Immunotherapy response and resistance: Dominant mechanisms in Merkel cell carcinoma

Thomas Pulliam

A dissertation submitted in the partial fulfillment of requirements for the degree of:

Doctor of Philosophy

University of Washington

2023

Reading Committee:

Paul Nghiem (Chair)
Aude Chapuis
David Koelle

Program authorized to offer degree:
Molecular and Cellular Biology

University of Washington

Abstract

Immunotherapy response and resistance:
Dominant mechanisms in Merkel cell carcinoma

Thomas Pulliam

Chair of the Supervisory Committee:
Professor Paul Nghiem
Molecular and Cellular Biology

Merkel cell carcinoma (MCC) is a rare, but deadly skin cancer that is rapidly increasing in incidence. Programed death-1 (PD-1) pathway blockade has been successful in treating MCC, but it is not effective for all patients. PD-1 therapy works by reinvigorating exhausted T cells, but major resistance mechanisms in MCC are currently unknown. Data from other cancers and murine models have described many mechanisms of immunotherapy resistance including terminal exhaustion in T cells, an immunosuppressive environment tumor microenvironment, T cell exclusion from the tumor, downregulation of antigen presentation and a lack of immunogenic antigens. To overcome PD-1 blockade resistance, several strategies are being pursued that target these different mechanisms. However, prioritization of clinical trials is challenging in rare cancers like MCC where only a few trials can be carried out simultaneously.

In **Chapter 1 and 2**, we describe the current state of immunotherapy for MCC and challenges in the treatment of this cancer.

In **Chapter 3**, we characterized cancer-specific T cells in 35 MCC patients and found that higher MCPyV-specific CD8 T-cell frequency in pre-treatment blood correlated with response to immunotherapy. Single cell RNA sequencing revealed that MCPyV-specific CD8 T cells in blood had increased stem/memory signatures and decreased exhaustion signatures compared to those in tumors. This suggests that the blood acts a reservoir of cancer-specific T cells at earlier stages of exhaustion. However, longitudinal samples showed emergence of immunotherapy resistance via downregulation of MHC-I despite abundant circulating cancer-specific CD8 T cells. This was studied in greater detail in **Chapter 4**. There we detail a second patient with secondary resistance to PD-1 pathway blockade despite the presence of cancer-specific CD8 T cells in the patient's tumor and blood. This patient's tumor lacked MHC-I expression, which was partially restored with an intralesional STING agonist. The patient experienced a durable partial response to treatment.

Chapters 5, 6 and 7 further describe antigen-specific T cells and the development of exhaustion in these cells. In **Chapter 5,** we detail neoantigen-specific T cells and show that these cells were predominantly CD4 restricted. These cells were prevalent in a patient with a profound response to anti-PD-L1 and exhibited a T_H1 phenotype that could support anti-tumor immunity. **Chapter 6** describes how the development of terminal exhaustion in T cells is potentiated by IL-2 signaling. **Chapter 7** describes the tumor microenvironment in human tumors using a novel bioinformatic method and spatially linked RNA sequencing.

The next three chapters describe new clinical trials based in part on the data presented in the previous chapters: Triple immune checkpoint blockade targeting PD-1, TIM3 and LAG3 (**Chapter 8**), therapeutic vaccination (**Chapter 9**) or inhibition of ATR (**Chapter 10**).

Finally, **Chapters 11 and 12** describe advancements in clinical management in MCC and how more personal minimal management can lead to improved patient care. We show that anti-PD-1 therapy dosing can be reduced in patients who respond to PD-1 blockade with compromising response (**Chapter 11**). We also investigate the importance of surgical margins and radiotherapy in MCC and demonstrate that tissue sparing surgery and adjuvant radiation can achieve protect against local recurrences when used in combination (**Chapter 12**).

We have used our extensive and unique repository of clinically annotated MCC blood and tumor tissues, along with clinical trial specimens, to characterize cancer-specific T cells and elucidate mechanisms of immunotherapy response and resistance in MCC, particularly an absence of circulating MCPyV-specific CD8 T cells. These studies have helped us define the mechanisms by which some patients mediate superior disease control and contributed to our goal of improving therapeutic options for patients with advanced MCC.

Dedication

To my family
To Mom. For your empathy as you pursue your PhD.
To Dad. For keeping me grounded.
To Anna and Alex. For your constant support and love.
And to Blair and Dell. For reminding me why we do this work.

Acknowledgements

First, I would like to thank Dr. Nghiem for his constant support, cheerleading and, of course, pastries. Being a good physician-scientist requires detailed knowledge of the field, but also the ability to connect with patients and communicate science effectively to diverse audiences. I joined this lab because of Dr. Nghiem's strengths in all of these areas and am so grateful for his mentorship.

I would also like to thank my committee for their guidance and support as I have pursued my PhD: Dr. Koelle for his guidance in studying antigen-specific T cells; Dr. Chapuis for sharing data reagents and whose lab trained me in single cell RNAseq; Dr. Campbell for her constant support and vast knowledge of the tumor micro-environment; Dr. Stetson for his pioneering knowledge of the STING pathway; and Dr. Overbaugh for her professional guidance.

I would also like to thank all my colleagues in the Nghiem lab, at the Fred Hutch Cancer Center, and at the University of Washington for their insightful discussions. In particular, I would like to thank Saumya Jani and Haroldo Rodriguez for always being willing to assist in experiments, share code, review manuscripts and their perspicacious scientific judgement.

I am grateful to all of our funding sources, particularly the National Institutes of Health for awarding me an individual MD/PhD fellowship (F30), and to our philanthropic donors for their support of our research.

And finally, I would like to thank all the patients who participated in clinical trials and who donated blood and tissue for research purposes, without which this work would not have been possible.

Table of Contents

*Equal contribution

Chapter 1. Introduction to Merkel cell carcinoma (MCC) and immunotherapy

Merkel cell carcinoma background and immunobiology

Merkel cell carcinoma (MCC) is a rare and deadly skin cancer[1-3] that is rapidly rising in incidence with ~3,000 new diagnoses in 2022, up from 1,200 in the year 2000.[4] In the US, 80% of MCC cases are caused by the Merkel cell polyomavirus (MCPyV), while the remaining 20% are caused by UV mutations.[5] Recent trials of programed death-1 (PD-1) pathway blockade have been highly successful with roughly half of patients achieving long term disease control, leading to the first two FDA approvals of any drug for MCC.[6,7] While these are beneficial therapies, they are not sufficient for roughly half of patients and it is imperative to understand the differences between patients who respond and do not respond so that we can design and move new therapies forward appropriately.

PD-1 pathway blockade is thought to work by reinvigorating T cell exhaustion, a dysfunctional state characterized by diminished function, reduced proliferative capacity, and increased inhibitory signals.[8-11] By blocking the interaction of PD-1 and its major ligand, PD-L1, these exhausted cells can regain function. However, the reason some patients do not respond to therapy is still unclear. Both tumor intrinsic and extrinsic PD-1 therapy resistance mechanisms have been described in other cancers. Specific tumor extrinsic mechanisms of PD-1 immune evasion include T cell exclusion from the tumor,[12] creation of an immunosuppressive environment inside the tumor,[13] and progression of exhaustion in CD8 T cells beyond the point of reversibility with PD-1 blockade.[14] Tumor intrinsic mechanisms of evasion include a lack of antigens for T cell recognition[15] and loss or downregulation of proteins required for antigen presentation to T cells.[16] Several strategies are being pursued in MCC and other cancers to overcome resistance to PD-1 blockade including therapeutic vaccination, transfer of transgenic T cells, and combination checkpoint blockade. Each of these therapies target different populations of T cells (i.e., naïve or insufficiently primed, clonally deleted, or terminally exhausted T cells), however which mechanisms underlie PD-1 blockade failure is unknown. This makes prioritization of clinical trials difficult, a particular problem in a rare cancer such as MCC where few trials can be carried out simultaneously.

MCC offers a unique ability to study immunotherapy response and resistance due to the viral nature of most MCC tumors. In non-virally driven tumors, the immune system recognizes mutations unique to cancer cells (neoantigens) or proteins that are upregulated in tumor cells but absent in most healthy tissue (tumor associated antigens; TAA). Neoantigens are particularly difficult to study since they vary between patients, so reagents need to be customized for each individual patient. This is a costly and difficult process. TAA are shared across patients, however because they are self-proteins, central and peripheral tolerance promote deletion and anergy in these cells. In contrast, tumor-viral antigens are truly non-self and shared across patients, allowing the study of antigen-specific immune responses across large cohorts of patients.

MCPyV-driven MCC is a particularly ideal tumor for studying these antigen-specific immune cells because: (1) MCPyV is a relatively small DNA virus and only two viral proteins are required for oncogenic transformation in humans; and (2) patients with virally-driven MCC have very new somatic mutations, which means that we can almost comprehensively study the anti-tumor immune response by focusing on MCPyV-specific responses. Oncogenesis by MCPyV requires two rare mutagenic events potentially promoted by UV exposure. The first is viral integration into the host genome, and the second is truncation of an MCPyV oncoprotein, the Large T antigen (LT). Truncation of LT renders MCPyV unable to replicate, while retaining the ability to drive cell cycle progression and to induce carcinogenesis.[17] MCPyV also expresses small T antigen (ST)

which also has oncogenic functions separate from LT.[17,18] Importantly, these viral oncoproteins are persistently expressed in MCC tumors and are absent in normal tissues, and are thereby ideal antigens for adaptive immune responses. We use these facts and a large panel of MHC-I multimers to characterize cancer-specific CD8 T cells in MCC patients over the course of immunotherapies.

Thematic nature of studies

This dissertation is a compilation of 10 publications and manuscripts that focus on current clinical care of Merkel cell carcinoma patients and use cellular and molecular tools to understand how current treatment could be improved. **Chapter 2** provides an overview of the care of Merkel cell carcinoma when I began my PhD. The subsequent chapters detail mechanisms of response or resistance to the therapies described in this chapter.

The major body of my work is detailed in **Chapter 3**. This study used samples from a trial of neoadjuvant PD-1 pathway blockade to determine why only a portion of patients respond to anti-PD-(L)1 therapies. We found that patients who did not have circulating cancer-specific CD8 T cells in their blood had poor responses to PD-1 blockade. We then describe the phenotype of these circulating cancer-specific CD8 T cells to show they are less exhausted than cancer-specific CD8 T cells in tumors. Because only the subset of less exhausted CD8 T cells expand following PD-1 pathway blockade[19-21], we believe the blood represents a reservoir of these less exhausted cells and that their frequency is correlated with response to initial anti-PD-(L)1 treatment. We note in **Chapters 3 and 4** however, that the frequency of circulating cancer-specific T cells is only predictive for initial PD-1 pathway blockade. We describe a patient who initially had these circulating cells prior to treatment, but the tumor cells downregulated MHC-I to evade detection by antigen-specific T cells.

In **Chapter 4,** we describe how STING agonism can yield durable clinical response in an MCC patient with secondary resistance to PD-1 pathway blockade. This study shows that cancer-specific T cells are present in a patient's tumor and blood at the time of recurrence, but MHC-I is absent on the tumor cells. Intralesional STING agonism increased MHC-I on the tumor cells and resulted in a durable partial response in this patient.

Chapters 5-7 further detail cancer-specific T cells and the development of exhaustion in these cells. **Chapter 5** continues the study of cancer-specific T cells in immunotherapy treated MCC patients. The differences in T cell responses to MCPyV oncoviral antigens and tumor neoantigens are not known. Whereas most prior studies of cancer-specific T cells in MCC have focused on MCPyV-specific T cells, we sought to characterize neoantigen-specific T cells in a patient with virus negative patient in this study. **Chapter 6** studies how IL-2 signaling in cancer-specific T cells leads to terminal exhaustion in these cells. **Chapter 7** describes a novel technique to study the tumor microenvironment at a near single cell level using spatial transcriptomics and single-cell RNA sequencing.

While **Chapters 3-6** detail immunotherapy response and resistance to current treatments, **Chapters 8-10** describe treatments that are in development and entering clinical trials. **Chapter 8** describes a clinical trial proposal to treat PD-(L)1-refractory MCC with a combination of anti-PD-1, anti-LAG3 and anti-TIM3 antibodies. This trial was in part based on data generated and shown in **Chapter 3** that shows that many patients who do not respond do PD-1 pathway blockade alone have cancer-specific CD8 T cells in their tumors, but these cells have upregulated several additional immune checkpoints and are thus too exhausted to respond to PD-(L)1 blockade alone. **Chapters 9 and 10** describe two approaches to increase the numbers

of cancer-specific CD8 T cells by either direct vaccination or *in situ* vaccination using ATR inhibition.

Chapters 11 and 12 demonstrate how advancements in clinical management of MCC can improve patient care through personalized minimal management. In **Chapter 11**, we show that patients who respond to PD-1 blockade can receive fewer doses of anti-PD-1 therapy while maintaining durable responses. Additionally, in **Chapter 12**, the significance of surgical margins and radiotherapy in MCC is explored. We demonstrate that a combination of tissue sparing surgery and adjuvant radiation can achieve high rates of recurrence free survival.

Together these studies characterize cancer-specific T cells and describe immunotherapy resistance mechanisms in MCC. Furthermore, they provide rationale for three upcoming therapeutic avenues for Merkel cell carcinoma: combination checkpoint blockade, therapeutic vaccination, and ATR inhibition.

Review

Clinical Cancer Research

Merkel Cell Carcinoma in the Age of Immunotherapy: Facts and Hopes

Aric Colunga[1], Thomas Pulliam[1], and Paul Nghiem[1,2,3]

Abstract

Merkel cell carcinoma (MCC) is a rare (~2,000 U.S. cases/year) but aggressive neuroendocrine tumor of the skin. For advanced MCC, cytotoxic chemotherapy only infrequently (<10% of cases) offers durable clinical responses (>1 year), suggesting a great need for improved therapeutic options. In 2008, the Merkel cell polyomavirus (MCPyV) was discovered and is clonally integrated in approximately 80% of MCC tumors. The remaining 20% of MCC tumors have large numbers of UV-associated mutations. Importantly, both the UV-induced neoantigens in virus-negative tumors and the MCPyV T antigen oncogenes that are required for virus-positive tumor growth are immunogenic. Indeed, antigen-specific T cells detected in patients are frequently dysfunctional/"exhausted," and the inhibitory ligand, PD-L1, is often present in MCC tumors. These findings led to recent clinical trials involving PD-1 pathway blockade in advanced MCC. The combined data from these trials involving three PD-1 pathway blocking agents—avelumab, pembrolizumab, and nivolumab—indicated a high frequency of durable responses in treated patients. Of note, prior treatment with chemotherapy was associated with decreased response rates to PD-1 checkpoint blockade. Over the past year, these striking data led to major changes in advanced MCC therapy, including the first-ever FDA drug approval for this disease. Despite these successes, approximately 50% of patients with MCC do not persistently benefit from PD-1 pathway blockade, underscoring the need for novel strategies to broaden antitumor immune responses in these patients. Here, we highlight recent progress in MCC including the underlying mechanisms of immune evasion and emerging approaches to augment the efficacy of PD-1 pathway blockade. *Clin Cancer Res; 24(9); 2035–43. ©2017 AACR.*

Introduction

Merkel cell carcinoma (MCC) is a rare (~2,000 U.S. cases/year) but aggressive skin cancer with a high risk of recurrence (27%–31%; refs. 1–3). Although MCC is rare, its incidence is rising steadily (4, 5). Risk factors include advanced age, sun/UV exposure, and chronic immunosuppression (~8% of patients with MCC have hematologic malignancy, solid organ transplant, or HIV/AIDS; ref. 6). Although 92% of patients with MCC are not immunosuppressed, individuals who have chronic T-cell dysfunction have an increased likelihood of developing MCC (10- to 30-fold; refs. 6–8). Only 4% of MCC cases occur in patients under 50 years of age, and MCC risk increases significantly with every additional decade of life (4, 9), likely due in part to increased immune senescence. The disease-associated mortality of MCC is 46% within 5 years (10), highlighting the need for improved therapeutic strategies.

Presentation/Diagnosis

The presentation of MCC can be challenging for physicians to recognize (Fig. 1), in part, due to its rarity. In two thirds of cases, physicians suspect a benign lesion based on clinical appearance (6). The following mnemonic summarizes features associated with MCC: Asymptomatic, Expanding rapidly, in an Immunesuppressed patient Older than 50 and on UV-exposed skin (AEIOU; ref. 6). As 89% of MCCs had three or more of these features (6), this mnemonic is sensitive; however, it is not specific for MCC, as such lesions may often represent another nonmelanoma skin cancer or a benign lesion such as an inflamed cyst. MCC diagnosis is confirmed through pathologic review of a biopsied lesion. Pathologic sections of MCC exhibit small cells with little cytoplasm (Fig. 1). The histologic recognition of MCC was greatly facilitated by the determination that perinuclear, coarsely granulated CK20 (KRT20) staining is present in 90% of MCC cases (11, 12).

Virus-induced MCC

Early studies indicated that MCC can be linked to decreased immune function. One key study found that patients with HIV have a 13-fold increased MCC risk compared with population controls (8). Also, case reports have described the uncommon, spontaneous regression of MCC tumors under a variety of scenarios, further indicating a link to the immune system (13–15). These data collectively suggested that MCC may be linked to a pathogen. In 2008, the Merkel cell polyomavirus (MCPyV) was discovered, and it is now clear that this virus plays a key role in the majority of MCC cases (16).

MCPyV is a member of the polyomavirus family comprised of nonenveloped, double-stranded DNA viruses and is the first virus from this family known to cause cancer in humans. MCPyV-specific antibodies have been detected in approximately 45% of children and in 80% of individuals 50 years or older, indicating that it is highly prevalent in the population (17).

[1]Division of Dermatology, Department of Medicine, University of Washington, Seattle, Washington. [2]Seattle Cancer Care Alliance, Seattle, Washington. [3]Clinical Research Division, Fred Hutchinson Cancer Research Center, Seattle, Washington.

Corresponding Author: Paul Nghiem, University of Washington, 850 Republican Street, Box 358050, Seattle, WA 98109. Phone: 206-221-4594; Fax: 206-221-4364; E-mail: pnghiem@uw.edu

doi: 10.1158/1078-0432.CCR-17-0439

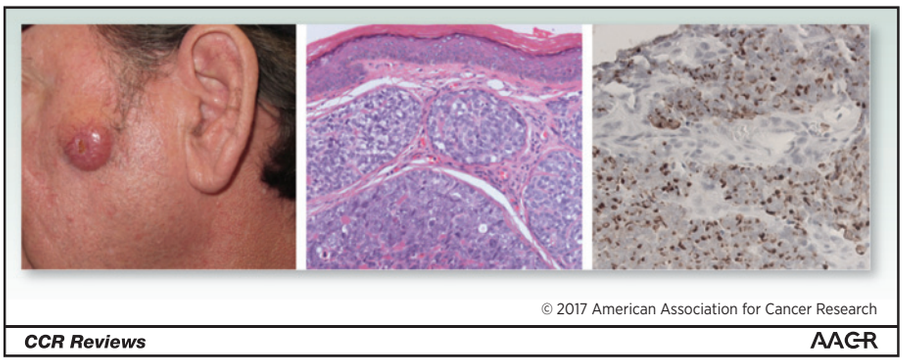

Figure 1.
Clinical and histologic appearance of MCC. Left, clinical appearance of an MCC arising on the left cheek of a 55-year-old man. The tumor was red, firm, nontender, and rapidly growing on sun-exposed skin. The differential diagnosis would include other types of nonmelanoma skin cancer. Center, intradermal tumor with pleiomorphic cells with large nuclei and scant cytoplasm. Right, cytokeratin 20 (CK20) IHC staining exhibits the characteristic perinuclear expression of CK20, a highly diagnostic finding for MCC.

Interestingly, despite this high prevalence, MCPyV has not been shown to cause any disease other than when it very rarely leads to MCC. We now understand key aspects of the mystery of how a virus with an extremely high incidence leads to a cancer that is very rare.

MCPyV-related oncogenesis requires two separate events likely accounting for its rarity: (i) The circular double-stranded genome must be linearized and integrated into the host genome, perhaps after a DNA-damaging event (MCPyV-positive tumors frequently occur on sun-exposed skin), and (ii) the virus must be mutated, with loss of expression of the C-terminus of the large T (LT) antigen that is required for viral DNA replication (Fig. 2). Virus-induced MCC is driven, in part, by expression of truncated large T antigen that binds to and inactivates the tumor suppressor Rb (RB1; Fig. 2; ref. 18), promoting cell-cycle progression and uncontrolled proliferation (19, 20). Small T (sT) inhibits the proteasomal degradation of large T (21) as well as the oncoprotein cMyc (MYC) and cyclin E (CCNE1; ref. 21). Both large T and small T have been demonstrated to drive transformation in mammalian cells *in vitro* (18, 20, 22); however, numerous attempts to generate mouse models of MCC at best only partially emulate the disease in adult animals (23–25). These data indicate that additional, as yet undetermined factors are required for induction of MCPyV-associated MCC. Although several groups have successfully generated xenografts using MCC cell lines and postoperative tumor tissue, engraftment can be done only in NOD SCID IL2Rgamma$^{-/-}$ (NSG) mice, which have a severely impaired immune system. These xenograft models mimic the gross pathologic features of the corresponding patient's tumor but fail to recapitulate the tumor–immune interactions that are now understood to greatly affect patient outcomes. *In vitro* experiments have demonstrated that ongoing expression of MCPyV oncoproteins is required for survival of virus-positive MCC cells (26–28). These persistently expressed non–self-antigens can potently elicit host immune recognition, and the limited size of MCPyV T antigens (<400 amino acids) has facilitated immune studies of MCPyV-specific T-cell responses (29–32).

Antibodies to MCPyV T Antigen Correlate with Tumor Burden

The robust response to MCPyV-positive tumors can include both T-cell and humoral components (33–35). At the time of diagnosis, approximately half of MCC patients make antibodies to MCPyV oncoproteins. Knowing a patient's serostatus (MCPyV positive or negative) can be helpful for his or her subsequent care. The prognosis of seronegative patients is less favorable (42% higher risk of recurrence than seropositive patients; refs. 35, 36), and thus, these patients need to be followed closely with scans (36). For seropositive patients, antibody titers correlate with tumor burden (33, 34), and a rising titer is an early indicator of disease recurrence (33). These findings have recently been validated in a large prospective cohort (36), and the test is now included in the 2018 National Comprehensive Cancer Network (NCCN) guidelines for MCC (37). Effective surveillance is relevant to patient care because if disease recurrence is discovered early (when tumor burden is lower), immunotherapy may be more effective (38).

UV-induced MCC

Some MCC tumors have no MCPyV detectable by either DNA-PCR or IHC, which raised the question of whether virus-negative MCC exists or whether viral detection techniques were insufficient (39). Recent studies have demonstrated that MCPyV-negative MCC tumors do indeed exist, with variable incidence around the world (~20% in United States/Europe vs. 76% in Australia; see Fig. 2; refs. 40–43). Strikingly, virus-negative MCC is among the most mutated of all solid tumors, including melanoma and non–small cell lung cancer (40–42). These mutations are mostly UV signature mutations (40–42). The high mutational burden (187–4,707 somatic single-nucleotide variants per exome) in MCC correlates to frequent amino acid changes and large numbers of UV-induced neoantigens (42). The most common mutations found in MCPyV-negative MCC are in *p53* (*TP53*; 75% of cases) and *Rb* (67% of cases), commonly resulting in loss of functional protein expression (42). However, activating mutations also comprise a large proportion of the *p53* mutations detected (45% of *p53* mutations in MCC; ref. 42).

Chemotherapy: The Previous Standard of Care

Definitive treatment of primary MCC includes surgery and/or radiation. This has been quite well established, and the consensus is summarized in the 2018 NCCN guidelines (37). Historically, chemotherapy was the preferred treatment option for advanced MCC despite a lack of data rigorously assessing its benefit in this setting. Recently, several careful retrospective studies have been carried out in the United States and Europe

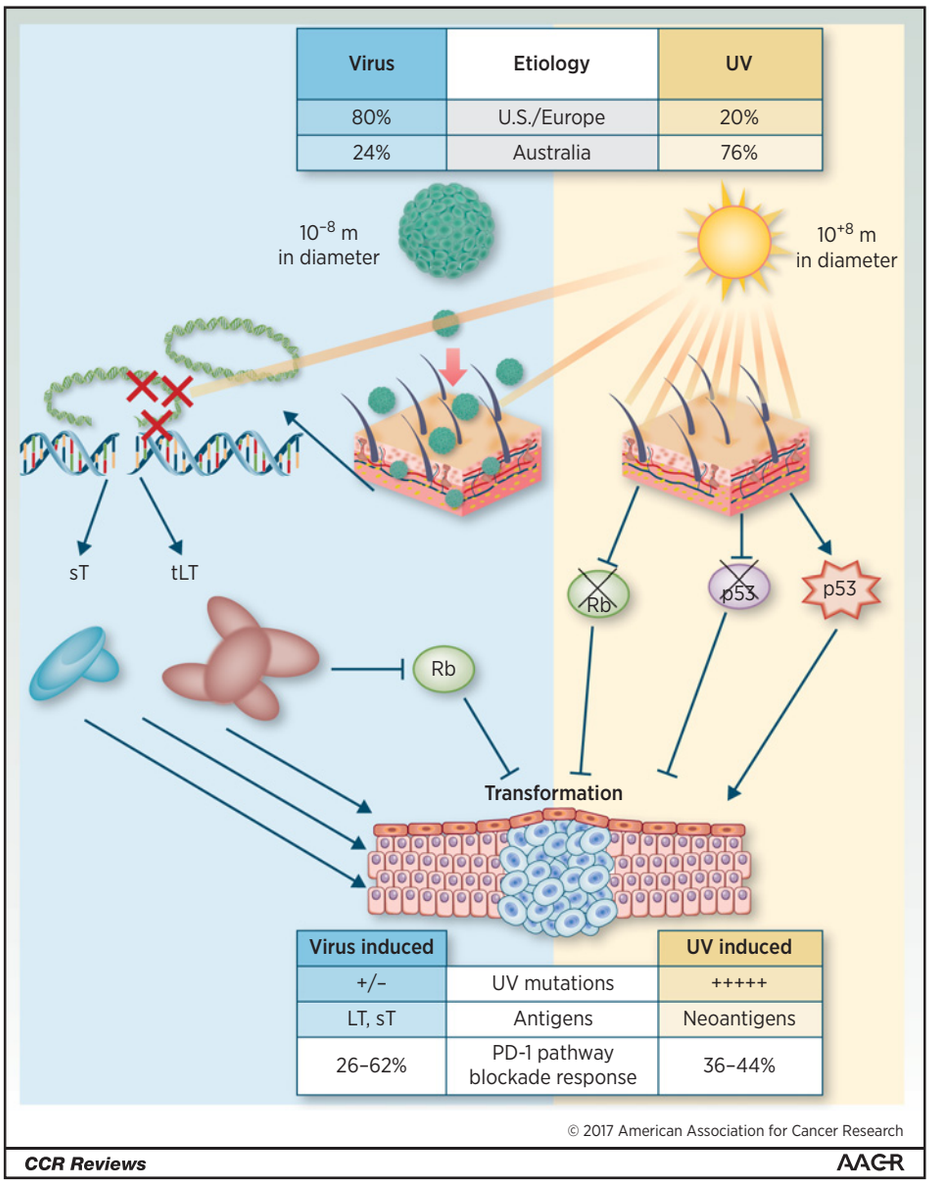

Figure 2.
Comparison of virus-positive and virus-negative MCC tumors. This schematic depicts the two major causes of MCC, their prevalence, differences in their potential immune targets, and frequencies of response to immune therapy. Top, differences in MCC prevalence—United States (U.S.)/Europe versus Australia. Left, virus-induced tumorigenesis—the highly prevalent MCPyV is often found on normal skin. Rarely, MCPyV will integrate into the host genome, and through a separate rare event, large T will become truncated (tLT; depicted by red Xs) prior its C-terminal. Expression of the sT and tLT viral oncogenes is tumorigenic through multiple pathways including inhibition of wild-type cellular Rb (see text). Right, UV-induced tumorigenesis—sun exposure results in the generation of many UV signature mutations (C→T mutations). The most common of which are in *Rb* and *p53*. Rb is frequently found to be inactivated in UV-induced MCC tumors (67%). Mutation of *p53* includes both activating and inactivating mutations (16, 18–21, 40–43, 71–75).

that document chemotherapy response rates and their durability (summarized in Table 1). A U.S. academic center–based study of 62 patients with distant metastatic MCC showed a first-line chemotherapy objective response rate (ORR) of 55%; however, the median progression-free survival (PFS) was only 94 days after chemotherapy initiation, and the median overall survival was 9.5 months (44). Second-line chemotherapy was even less favorable, with an ORR of 23% and a median PFS of

Table 1. Selected data for chemotherapy and anti-PD1/PD-L1 in MCC

	Chemotherapy		Nivolumab	Avelumab	Pembrolizumab
Line	1st line	2nd line	≥1st line	≥2nd line	1st line
Cohort size	62–67	20–30	22	88	25
Agent	Etoposide and platinum-based agent[b]	Topotecan[b]	Anti–PD-1	Anti–PD-L1	Anti–PD-1
ORR	31%–55%	9%–23%	68%	32%	56%
9-month PFS[a]	15%–26%	0%–3%	N/A[c]	33%	56%
Publications	Becker, 2017[d] (46); Cowey, 2017 (45); Iyer, 2016 (44)		Topalian, 2017 (52)	Kaufman, 2016 (54)	Nghiem, 2016 (50)

[a]Values estimated from charts.
[b]Most commonly used agents.
[c]9-Month PFS is not yet available; however, 3-month median PFS is 82%.
[d]Data for second-line chemotherapy only.

61 days (44). An independent study of 67 patients with metastatic MCC in the US Oncology Network also assessed responses to first- and second-line chemotherapy (45). This study found a first-line chemotherapy ORR of only 31%, with a median PFS of 4.6 months. Patients on their second or later line of chemotherapy had an ORR of 20% and a median PFS of 2.1 months (45). In a cohort of 34 patients from Europe whose disease had progressed following at least one line of chemotherapy, the patients' next line of chemotherapy had only a 9% ORR and a median duration of response of 1.9 months (46). These studies indicate that although MCC has a relatively high response rate to chemotherapy in the first line, responses are typically short-lived and resistance develops quickly. Multiple mechanisms are likely involved with the disappointing long-term benefit of chemotherapy in MCC. These may include its immunosuppressive effects in the setting of this immunogenic cancer as well as established mechanisms such as resistance to apoptosis (47).

Immunotherapy: A New Standard of Care

Over the last decade, several lines of evidence have suggested that immune status is linked to clinical outcomes in MCC, indicating that augmenting cell-mediated immunity could be beneficial. An early study focusing on tumor-infiltrating lymphocytes found that patients with robust $CD8^+$ lymphocyte infiltration into MCC tumors had 100% MCC-specific survival compared with 60% survival in those with little or no $CD8^+$ infiltration (48). These data indicated that infiltration by CD8 T cells had profound prognostic value and that augmenting immune function could benefit patients with MCPyV-driven MCC. The specificity of $CD8^+$ lymphocytes was then studied, and MCPyV oncoprotein–specific cells were found to be present in MCC patient blood and enriched in patients' tumors (29, 30). Importantly, signs of dysfunction were evident in MCPyV-specific $CD8^+$ T cells from patients, as they expressed both PD-1 (PDCD1) and Tim3 (HAVCR2), the combination of which suggests functional exhaustion (29). When the tumor microenvironment was investigated, 49% of 49 tumors contained PD-L1 (CD274, typically expressed on antigen-presenting cells) and expression tended to correlate with the presence of intratumoral lymphocytes (49). In aggregate, these findings made a compelling case for testing PD-1 pathway blockade in MCC.

To date, three antibodies targeting the PD-1 axis have been studied in MCC, with all three showing substantial response rates and impressive durability of responses (summarized in Table 1). Although the numbers of patients studied are small compared with other more prevalent cancer types, these early trials have demonstrated frequent therapeutic durability, whereas there was previously little hope for patients with advanced MCC. A National Cancer Institute–sponsored clinical trial studied pembrolizumab (anti–PD-1) in 25 patients with advanced MCC who had not received prior systemic therapy. The investigators found an ORR to pembrolizumab of 56% including a 16% complete response rate. Of the 14 responsive patients, the response duration ranged from at least 2.2 months to at least 9.7 months. Overall, the trial had an estimated PFS of 67% at 6 months. Pembrolizumab was effective in both virus-negative and virus-positive tumors (ORR of 62% and 44% respectively, not significantly different; ref. 50). The early results of this trial led to pembrolizumab being listed as a treatment option for advanced disease in the 2017 NCCN guidelines for MCC (51).

An international, single arm, open-label trial of nivolumab (anti–PD-1) included both patients who had and who had not received prior chemotherapy (36% and 64%, respectively). In this study, 15 of 22 patients (68%) had objective responses, and PFS at 3 months was 82% with the trial still ongoing (52).

A large international clinical trial studied avelumab (anti–PD-L1) in 88 patients with distant metastatic disease who had previously received at least one line of chemotherapy. This trial found an ORR of 33%, with a complete response rate of 11%. At 6 months, PFS was 40%, and the estimated PFS at 1 year was 30%. As with pembrolizumab, avelumab was found to be effective in both virus-positive and virus-negative tumors (ORR of 26% and 35%, respectively, not significantly different; refs. 53, 54). In March 2017, these remarkable data in chemotherapy-refractory MCC led to the first-ever FDA approval of a drug for this cancer. Avelumab was granted accelerated approval in advanced MCC in patients at least 12 years of age whether or not they have previously received chemotherapy (55).

Now that avelumab has been approved for treatment of advanced MCC, an important question remains: namely, whether treatment with PD-1 pathway blockade in the adjuvant setting is appropriate and/or beneficial for treatment of this aggressive disease. As with other cancer treatments in general, catching and treating the tumor early correlates with improved prognosis. This possibility, in the context of PD-1 pathway blockade in primary MCC, will be addressed by two (one of which is double blinded and randomized) clinical trials that are now recruiting (Table 2).

Anti–PD-1 checkpoint blockade therapies have proven to be well tolerated in a majority of patients. However, altering the balance of immune homeostasis can induce autoimmunity that results in grade 3 or grade 4 toxicity in 10% to 22% of cases (56, 57). As such, informed consent of patients is critical, particularly because immune-related adverse events (irAE) are typically idiosyncratic, making their early recognition and treatment challenging.

Importantly, the unique therapeutic benefits of these agents raise the question of whether they are indicated in patients who have a known autoimmune condition or previous irAE to ipilimumab. Indeed, patients with MCC exhibit higher numbers of autoimmune conditions than the population at large. Treatment of autoimmune disease is a major known iatrogenic cause of chronic, severe immune suppression that can increase the risk of multiple cancer types, including MCC (58). A recent retrospective analysis of 52 melanoma patients with prior autoimmune disease treated with PD-1 pathway blockade found comparable ORRs (33%) to those observed in clinical trials that have excluded patients with autoimmunity (59). Although 20 (38%) patients had a flare of autoimmune disease and another 15 (29%) developed other irAEs, only eight patients exhibited grade 3 toxicity of a preexisting autoimmune process or irAE, and just two patients permanently discontinued treatment. A separate study of 67 patients who had prior major ipilimumab toxicities exhibited a 40% ORR with PD-1 blockade (59). In this cohort, 25 (37%) patients experienced recurrence of ipilimumab-induced irAEs or developed new/different irAEs. Although 14 (21%) patients exhibited grade 3 to 4 irAEs, only eight (21%) patients discontinued therapy. In both of these cohorts, a majority of the immune toxicities could

Table 2. Selected immune therapy clinical trials for Merkel cell carcinoma

NCT identifier	Trial arms	Recruitment status	Phase	Targeted enrollment	Comments	Publications
Anti–PD-1/PD-L1 monotherapy						
NCT02155647	Avelumab as ≥2nd line	Active, not recruiting	II	88	28 of 88 chemotherapy-refractory patients achieved a response including eight complete responses (ORR = 32%)	Kaufman, 2016 (54)
NCT02155647	Avelumab as 1st line	Recruiting	II	112	Preliminary results show an objective response in 11 of 16 patients (ORR = 69%)	D'Angelo, 2017 (76)
NCT02267603	Pembrolizumab as 1st line	Active, not recruiting	II	50	Four of 25 patients evaluated had a complete response and 10/25 had a partial response (ORR = 56%)	Nghiem, 2016 (50)
NCT02488759	Nivolumab as 1st or ≥2nd line	Active, not recruiting	I/II	25	22 patients initially evaluated on nivolumab alone, 12 had a partial response, and three had a complete response (ORR = 68%)	Topalian, 2017 (52)
NCT02196961	Avelumab as adjuvant versus observation following resection	Recruiting	II	113	Only in Europe[a]	
NCT03271372	Avelumab as adjuvant 1st line	Recruiting	III	100	Stage III/IIIB nodal disease, randomized, double blinded	
Checkpoint blockade combination therapy						
NCT02488759	Nivolumab ± anti-LAG3 (BMS-9861016) ± ipilimumab (many arms)	Recruiting	I/II	500	Cohort of patients with virus-associated cancers	
NCT03071406	Ipilimumab + nivolumab versus ipilimumab + nivolumab + stereotactic body radiation therapy	Recruiting	II	50		
Innate immunity agents and cytokines						
NCT02035657	TLR-4 agonist, GLA-SE	Completed	I	10	Two of three patients with local nodal disease had a complete response, and two of seven patients with distant metastatic disease had stable disease	Bhatia, 2016 (60)
NCT01440816	IL12-EP	Completed	II	15	Four of 15 patients treated with IL12 had an objective response	Bhatia, 2015 (61)
Cell-based therapies						
NCT02584829	Autologous MCPyV-specific CD8 cells + avelumab + MHC upregulation versus avelumab + MHC upregulation	Recruiting	I/II	20	Four of four patients had responses with 3/4 complete responses	Paulson, 2017 (66)
NCT02465957	NK cells (activated NK-92) + ALT-803 (modified IL15)	Closed	II	24	Initial three patients showed no major toxicities, and at least one patient had a response	Bhatia, 2016 (64)
Oncolytic virus therapies						
NCT02819843	T-VEC versus T-VEC + hypofractionated radiotherapy	Recruiting	II	34	Cohort of melanoma and MCC	
NCT02978625	T-VEC + nivolumab	Not yet recruiting	II	68	Cohort of refractory lymphomas and refractory nonmelanoma skin cancers	
Biomarker-guided combination therapy						
NCT03167164	Avelumab, bevacizumab, capecitabine, cisplatin, cyclophosphamide, 5-fluorouracil, leucovorin, nab-paclitaxel, omega-3-acid ethyl esters, stereotactic body radiation therapy, ALT-803, NK-92 (many arms)	Not yet recruiting	I/II	67	Treatment customized on the basis of tumor-specific characteristics	

NOTE: Therapies in the order listed in table: avelumab = anti–PD-L1 (IgG1); pembrolizumab = anti–PD-1 (IgG4); nivolumab = anti–PD-1 (IgG4); ipilimumab = anti–CTLA-4; GLA-SE = glucopyranosyl lipid A in stable emulsion, a TLR-4 agonist; F16-IL = anti-tenascin C mAb–IL2 fusion protein; IL12-EP = IL12 plasmid administered with electroporation; MHC upregulation via radiation or intratumoral IFNβ administration; NK-92 = activated, irradiated, allogenic natural killer cells; ALT-803 = IL15 superagonist complex; bevacizumab = anti-VEGF; T-VEC = talimogene laherparepvec, an engineered herpes oncolytic virus.
[a]Unless otherwise noted, trials include sites within the United States.

be controlled by symptom management, oral steroids, and/or steroid sparing agents (>80% of all irAEs observed). Taken as a whole, this study indicates that, after appropriate informed consent discussions with the patient, PD-1 pathway blockade may be considered despite the presence of prior autoimmune disease or ipilimumab-induced irAEs (59).

New Immunotherapy Trials: A Diverse Pipeline

Despite the greatly improved durable responses observed through PD-1 checkpoint blockade therapy compared with chemotherapy, major challenges remain in systemic therapy for MCC in that nearly half of patients do not derive durable benefit from these drugs. To address this issue, numerous clinical trials are underway for MCC, at least nine of which involve immune therapy (Table 2). These trials involve four general strategies that will be summarized below: (i) "removing an additional brake" (i.e., CTLA-4) on the immune system, (ii) "stepping on the gas" by using innate or other immune agonists, (iii) "adding more troops" by infusing more of the relevant cells into the patient, and (iv) "weaponizing viruses" that can specifically target and kill cancer cells while preserving normal tissues.

Activated T cells express CTLA-4 (CTLA4) that suppresses their function after CTLA-4 binds its cognate receptor (CD80/CD86) on an antigen-presenting cell. In this way, CTLA-4 acts as a central type of immunologic "brake." Anti–CTLA-4 antibody (ipilimumab) blocks this binding and allows the T cell to remain in a more active state. Ipilimumab efficacy in MCC is now being determined in clinical trials (Table 2). One trial enrolling patients in Germany will assess the safety and efficacy of ipilimumab or avelumab in the adjuvant setting following surgical resection of local MCC in comparison with resection alone. The ipilimumab arm of this trial has recently closed, whereas the arm investigating avelumab in the adjuvant setting is currently enrolling. In patients where PD-1 pathway blockade is ineffective, one hypothesis is that further augmentation of the immune response is required, possibly via CTLA-4. In a U.S.-based trial, 50 patients with metastatic MCC are being enrolled to test the safety and efficacy of the combination of nivolumab (anti–PD-1) and ipilimumab with and without stereotactic body radiation that can debulk the tumor and may induce immunogenic cell death. The combination of ipilimumab with PD-1 pathway blockade is also being performed in melanoma, and safety data from these trials would be expected to be similar.

Intratumoral immune infiltration and immune recognition/activation is regulated by pro- and anti-inflammatory molecules within the tumor–immune microenvironment. To increase the activity of antitumoral immune responses, several strategies seek to "step on the gas" by adding immune agonists that can reinvigorate antitumor T-cell responses. In a proof-of-concept trial, a Toll-like receptor-4 (TLR4) agonist, glucopyranosyl lipid-A stable emulsion (GLA-SE), was intratumorally injected into superficial MCC tumors (Table 2; ref. 60). In this trial, two of three patients with stage IIIB MCC were recurrence-free at 23+ and 19+ months with one patient having a pathologic complete response after two injections of this TLR-4 agonist (60). In a second cohort, two of seven patients with stage IV MCC had partial responses and were progression free after 13 months at the time of publication. Encouragingly, responses correlated with increased T-cell infiltration and activation of proinflammatory genes (60), providing proof of concept of this therapeutic approach.

Another trial of patients with superficial/accessible MCC tumors explored the utility of intratumoral electroporation of DNA encoding the potent proinflammatory cytokine IL12 (IL12A; Table 2; ref. 61). In this study, three of three patients with local disease who received definitive surgery and/or radiotherapy at 4 weeks after one cycle of three IL12 treatments had recurrence-free survival of 2+, 9, and 32+ months, with one patient having a pathologic complete response (61). In a second arm of this trial involving 12 patients with metastatic disease, partial responses were seen in three patients and stable disease was seen in one patient (61). Treatment corresponded with induction of IL12 and TNFα (TNF) expression in the tumor microenvironment as well as enhanced T-cell infiltration over baseline. Encouragingly, 40% of the injected lesions exhibited regression (30% complete and 10% partial), and another 40% were stable (61). Regression of noninjected lesions was also observed, and no grade 3 or higher adverse events were reported. Although very preliminary, these results highlight the potential of local IL12 administration.

Cell-based therapy is an emerging immunotherapeutic approach, particularly in the setting of certain types of immune evasion. MCC evades immune detection through a variety of mechanisms, including downregulation of HLA class I molecules required for antigen presentation, which occurs in 74% to 84% of MCC tumors (62, 63). Natural killer (NK) cells typically target cells that downregulate HLA class I expression. An NK cell–based trial that accepts patients whose tumors were refractory to prior checkpoint therapy involves biweekly infusions of activated, irradiated, allogeneic NK-92 cells (Table 2). Thus far in this study, three patients treated with NK cells showed no major toxicities and although very preliminary, one patient, who had not responded to PD-1 pathway blockade, had a complete response (64).

MCPyV-positive MCC tumors require expression of viral T antigen oncoproteins (26–28). In patients with certain HLA types, MCPyV oncoprotein–specific T cells can be isolated and expanded *ex vivo* prior to therapeutic infusion. In one trial utilizing this strategy (Table 2), three of four patients given T cells plus HLA upregulation (tumor-targeted radiation or interferon) progressed, whereas one that had an initial complete response subsequently progressed after 14 months. It was found that the infused T cells frequently became dysfunctional/"exhausted" upon transfer (65, 66). As such, avelumab (anti–PD-L1) has been added in combination with these autologous virus-specific T cells. In this combined-therapy cohort, all four patients treated with a regimen including T cells, HLA upregulation, and avelumab experienced objective responses, with three complete responses at last follow-up (65, 66). These early results, in a limited set of patients, highlight the potential for the rational design and implementation of transgenic T-cell receptors against virus-positive MCC tumors.

A mechanistically relevant therapy, recently approved for melanoma, is the oncolytic virotherapeutic tamilogene laherparepvec (T-VEC; ref. 67). The viral genes have been mutated so that the construct is replication-defective in normal cells, but constitutively active proliferative pathways in tumor cells allow the virus to replicate and kill those cells. The T-VEC design also includes a granulocyte macrophage colony-stimulating factor (GM-CSF, CSF2) expression cassette to induce a proinflammatory immune response. T-VEC is currently being investigated in two trials that include MCC (Table 2). In the first trial, T-VEC is used alone or in combination with hypofractionated radiotherapy. Another trial combines T-VEC with nivolumab (anti–PD-1) to augment the immune response in conjunction with T-VEC–mediated killing.

On the Horizon

The diversity of drugs in development and currently being tested in clinical trials greatly outstrips our understanding of the cellular and molecular mechanisms at play (68). Indeed, nearly half of patients do not derive persistent benefit from PD-1 pathway blockade and neither tumor viral status nor biomarker studies accurately identify patients who will not respond (50, 66). In addition, mutation, adaptation, and selection for therapeutically resistant cells are remarkably powerful processes that continue to blunt therapeutic efficacy for all classes of drugs, including immunotherapy (68). To begin to address questions of response and nonresponse, a comprehensive, unbiased examination of host and tumor immune interactions in the tumor microenvironment is required.

MCC offers a particularly fertile hunting ground for studying the immune responses to cancers more broadly due to: (i) the unique relevance of MCC as a model for studying immunogenic cancers (e.g., viral oncoprotein vs. high UV-mutational load); (ii) the robust immune evasion, likely through multiple mechanisms, required for a tumor to persist despite such a heavy viral/neoantigen burden; (iii) the small size of the MCPyV T antigen oncogenes that greatly facilitates immunologic studies; and (iv) the generation of tumor-specific reagents that facilitate both studies of the antitumor immune response and improved therapy. As such, investigations of MCC are poised to contribute to the understanding of the biology of cancer immunogenicity.

Now more than ever, we are able to delve into the cellular and molecular complexities within any given tumor. The cost of next-generation sequencing technologies is rapidly decreasing. Single-cell sequencing is capable of analyzing hundreds to thousands of cells from small core biopsies making serial analysis of tumor tissues following therapy both more feasible and less invasive. Also, an ever-increasing number of targets can be stained using multiplexed IHC in combination with more sophisticated nucleic acid *in situ* hybridization techniques. In an attempt to combine this arsenal of molecular tools with clinical medicine, one trial will determine the genetic, transcriptomic, and proteomic details of a patient's tumor to customize therapy with immune and more traditional approaches (Table 2).

Detailed molecular analyses of the interactions within the tumor microenvironment in response to various immunotherapies will generate insights into therapeutically relevant targets (69, 70). Importantly, proper assessment of therapeutic efficacy or failure requires that serial tumor biopsies be obtained both before and after immune therapy despite their high costs and logistical challenges. With the recent striking progress in immune therapies for MCC, the diverse pipeline of agents, and forthcoming improvements in our ability to assess the tumor microenvironment, the future for MCC immunotherapy is very encouraging.

Disclosure of Potential Conflicts of Interest

P. Nghiem reports receiving commercial research grants from Bristol-Myers Squibb and is a consultant/advisory board member for EMD Serono and Merck. No potential conflicts of interest were disclosed by the other authors.

Acknowledgments

P. Nghiem and A. Colunga were supported by NIH K24-CA139052, NIHR01CA176841, Kelsey Dickson Fund of the Prostate Cancer Foundation, UW MCC Patient Gift Fund (to A. Colunga), and the Bloom endowment at University of Washington. T. Pulliam was supported by 5T32GM007266.

Received August 8, 2017; revised October 12, 2017; accepted December 1, 2017; published OnlineFirst December 7, 2017.

References

1. Mattavelli I, Patuzzo R, Torri V, Gallino G, Maurichi A, Lamera M, et al. Prognostic factors in Merkel cell carcinoma patients undergoing sentinel node biopsy. Eur J Surg Oncol 2017;43:1536–41.
2. Jouary T, Kubica E, Dalle S, Pages C, Duval-Modeste AB, Guillot B, et al. Sentinel node status and immunosuppression: recurrence factors in localized Merkel cell carcinoma. Acta Derm Venereol 2015;95:835–40.
3. Liang E, Brower JV, Rice SR, Buehler DG, Saha S, Kimple RJ. Merkel cell carcinoma analysis of outcomes: a 30-year experience. PLoS One 2015;10: e0129476.
4. Agelli M, Clegg LX. Epidemiology of primary Merkel cell carcinoma in the United States. J Am Acad Dermatol 2003;49:832–41.
5. Hodgson NC. Merkel cell carcinoma: changing incidence trends. J Surg Oncol 2005;89:1–4.
6. Heath M, Jaimes N, Lemos B, Mostaghimi A, Wang LC, Penas PF, et al. Clinical characteristics of Merkel cell carcinoma at diagnosis in 195 patients: the AEIOU features. J Am Acad Dermatol 2008;58:375–81.
7. Miller RW, Rabkin CS. Merkel cell carcinoma and melanoma: etiological similarities and differences. Cancer Epidemiol Biomarkers Prev 1999; 8:153–8.
8. Engels EA, Frisch M, Goedert JJ, Biggar RJ, Miller RW. Merkel cell carcinoma and HIV infection. Lancet 2002;359:497–8.
9. Albores-Saavedra J, Batich K, Chable-Montero F, Sagy N, Schwartz AM, Henson DE. Merkel cell carcinoma demographics, morphology, and survival based on 3870 cases: a population based study. J Cutan Pathol 2010;37:20–7.
10. Lemos B, Nghiem P. Merkel cell carcinoma: more deaths but still no pathway to blame. J Invest Dermatol 2007;127:2100–3.
11. Chan JK, Suster S, Wenig BM, Tsang WY, Chan JB, Lau AL. Cytokeratin 20 immunoreactivity distinguishes Merkel cell (primary cutaneous neuroendocrine) carcinomas and salivary gland small cell carcinomas from small cell carcinomas of various sites. Am J Surg Pathol 1997; 21:226–34.
12. Moll R, Lowe A, Laufer J, Franke WW. Cytokeratin 20 in human carcinomas. A new histodiagnostic marker detected by monoclonal antibodies. Am J Pathol 1992;140:427–47.
13. O'Rourke MG, Bell JR. Merkel cell tumor with spontaneous regression. J Dermatol Surg Oncol 1986;12:994–6.
14. Vandeven N, Nghiem P. Complete spontaneous regression of Merkel cell carcinoma metastatic to the liver: did lifestyle modifications and dietary supplements play a role? Glob Adv Health Med 2012;1:22–3.
15. Walsh NM. Complete spontaneous regression of Merkel cell carcinoma (1986–2016): a 30 year perspective. J Cutan Pathol 2016;43:1150–4.
16. Feng H, Shuda M, Chang Y, Moore PS. Clonal integration of a polyomavirus in human Merkel cell carcinoma. Science 2008;319:1096–100.
17. Tolstov YL, Pastrana DV, Feng H, Becker JC, Jenkins FJ, Moschos S, et al. Human Merkel cell polyomavirus infection II. MCV is a common human infection that can be detected by conformational capsid epitope immunoassays. Int J Cancer 2009;125:1250–6.
18. Borchert S, Czech-Sioli M, Neumann F, Schmidt C, Wimmer P, Dobner T, et al. High-affinity Rb binding, p53 inhibition, subcellular localization, and transformation by wild-type or tumor-derived shortened Merkel cell polyomavirus large T antigens. J Virol 2014;88:3144–60.
19. Richards KF, Guastafierro A, Shuda M, Toptan T, Moore PS, Chang Y. Merkel cell polyomavirus T antigens promote cell proliferation and inflammatory cytokine gene expression. J Gen Virol 2015;96:3532–44.
20. Cheng J, Rozenblatt-Rosen O, Paulson KG, Nghiem P, DeCaprio JA. Merkel cell polyomavirus large T antigen has growth-promoting and inhibitory activities. J Virol 2013;87:6118–26.

21. Kwun HJ, Shuda M, Feng H, Camacho CJ, Moore PS, Chang Y. Merkel cell polyomavirus small T antigen controls viral replication and oncoprotein expression by targeting the cellular ubiquitin ligase SCFFbw7. Cell Host Microbe 2013;14:125–35.
22. Shuda M, Kwun HJ, Feng H, Chang Y, Moore PS. Human Merkel cell polyomavirus small T antigen is an oncoprotein targeting the 4E-BP1 translation regulator. J Clin Invest 2011;121:3623–34.
23. Shuda M, Guastafierro A, Geng X, Shuda Y, Ostrowski SM, Lukianov S, et al. Merkel cell polyomavirus small T antigen induces cancer and embryonic Merkel cell proliferation in a transgenic mouse model. PLoS One 2015;10: e0142329.
24. Verhaegen ME, Mangelberger D, Harms PW, Vozheiko TD, Weick JW, Wilbert DM, et al. Merkel cell polyomavirus small T antigen is oncogenic in transgenic mice. J Invest Dermatol 2015;135:1415–24.
25. Verhaegen ME, Mangelberger D, Harms PW, Eberl M, Wilbert DM, Meireles J, et al. Merkel cell polyomavirus small T antigen initiates Merkel cell carcinoma-like tumor development in mice. Cancer Res 2017;77:3151–7.
26. Houben R, Shuda M, Weinkam R, Schrama D, Feng H, Chang Y, et al. Merkel cell polyomavirus-infected Merkel cell carcinoma cells require expression of viral T antigens. J Virol 2010;84:7064–72.
27. Schrama D, Hesbacher S, Angermeyer S, Schlosser A, Haferkamp S, Aue A, et al. Serine 220 phosphorylation of the Merkel cell polyomavirus large T antigen crucially supports growth of Merkel cell carcinoma cells. Int J Cancer 2016;138:1153–62.
28. Houben R, Adam C, Baeurle A, Hesbacher S, Grimm J, Angermeyer S, et al. An intact retinoblastoma protein-binding site in Merkel cell polyomavirus large T antigen is required for promoting growth of Merkel cell carcinoma cells. Int J Cancer 2012;130:847–56.
29. Afanasiev OK, Yelistratova L, Miller N, Nagase K, Paulson K, Iyer JG, et al. Merkel polyomavirus-specific T cells fluctuate with Merkel cell carcinoma burden and express therapeutically targetable PD-1 and Tim-3 exhaustion markers. Clin Cancer Res 2013;19:5351–60.
30. Iyer JG, Afanasiev OK, McClurkan C, Paulson K, Nagase K, Jing L, et al. Merkel cell polyomavirus-specific CD8(+) and CD4(+) T-cell responses identified in Merkel cell carcinomas and blood. Clin Cancer Res 2011;17:6671–80.
31. Lyngaa R, Pedersen NW, Schrama D, Thrue CA, Ibrani D, Met O, et al. T-cell responses to oncogenic Merkel cell polyomavirus proteins distinguish patients with Merkel cell carcinoma from healthy donors. Clin Cancer Res 2014;20:1768–78.
32. Miller NJ, Church CD, Dong L, Crispin D, Fitzgibbon MP, Lachance K, et al. Tumor-infiltrating Merkel cell polyomavirus-specific T cells are diverse and associated with improved patient survival. Cancer Immunol Res 2017;5:137–47.
33. Paulson KG, Carter JJ, Johnson LG, Cahill KW, Iyer JG, Schrama D, et al. Antibodies to Merkel cell polyomavirus T antigen oncoproteins reflect tumor burden in Merkel cell carcinoma patients. Cancer Res 2010;70: 8388–97.
34. Samimi M, Molet L, Fleury M, Laude H, Carlotti A, Gardair C, et al. Prognostic value of antibodies to Merkel cell polyomavirus T antigens and VP1 protein in patients with Merkel cell carcinoma. Br J Dermatol 2016;174:813–22.
35. Touze A, Le Bidre E, Laude H, Fleury MJ, Cazal R, Arnold F, et al. High levels of antibodies against Merkel cell polyomavirus identify a subset of patients with Merkel cell carcinoma with better clinical outcome. J Clin Oncol 2011;29:1612–9.
36. Paulson KG, Lewis CW, Redman MW, Simonson WT, Lisberg A, Ritter D, et al. Viral oncoprotein antibodies as a marker for recurrence of Merkel cell carcinoma: a prospective validation study. Cancer 2017; 123:1464–74.
37. National Comprehensive Cancer Network. Merkel cell carcinoma. In: NCCN Clinical Practice Guidelines in Oncology Version 1.2018 ed: Fort Washington, PA: National Comprehensive Cancer Network, Inc; 2017.
38. Nishino M, Giobbie-Hurder A, Ramaiya NH, Hodi FS. Response assessment in metastatic melanoma treated with ipilimumab and bevacizumab: CT tumor size and density as markers for response and outcome. J Immunother Cancer 2014;2:40.
39. Rodig SJ, Cheng J, Wardzala J, DoRosario A, Scanlon JJ, Laga AC, et al. Improved detection suggests all Merkel cell carcinomas harbor Merkel polyomavirus. J Clin Invest 2012;122:4645–53.
40. Wong SQ, Waldeck K, Vergara IA, Schroder J, Madore J, Wilmott JS, et al. UV-associated mutations underlie the etiology of MCV-negative Merkel cell carcinomas. Cancer Res 2015;75:5228–34.
41. Harms PW, Vats P, Verhaegen ME, Robinson DR, Wu YM, Dhanasekaran SM, et al. The distinctive mutational spectra of polyomavirus-negative Merkel cell carcinoma. Cancer Res 2015;75:3720–7.
42. Goh G, Walradt T, Markarov V, Blom A, Riaz N, Doumani R, et al. Mutational landscape of MCPyV-positive and MCPyV-negative Merkel cell carcinomas with implications for immunotherapy. Oncotarget 2016;7: 3403–15.
43. Garneski KM, Warcola AH, Feng Q, Kiviat NB, Leonard JH, Nghiem P. Merkel cell polyomavirus is more frequently present in North American than Australian Merkel cell carcinoma tumors. J Invest Dermatol 2009;129:246–8.
44. Iyer JG, Blom A, Doumani R, Lewis C, Tarabadkar ES, Anderson A, et al. Response rates and durability of chemotherapy among 62 patients with metastatic Merkel cell carcinoma. Cancer Med 2016;5:2294–301.
45. Cowey CL, Mahnke L, Espirito J, Helwig C, Oksen D, Bharmal M. Real-world treatment outcomes in patients with metastatic Merkel cell carcinoma treated with chemotherapy in the USA. Future Oncol 2017; 13:1699–710.
46. Becker JC, Lorenz E, Ugurel S, Eigentler TK, Kiecker F, Pfohler C, et al. Evaluation of real-world treatment outcomes in patients with distant metastatic Merkel cell carcinoma following second-line chemotherapy in Europe. Oncotarget 2017;8:79731–41.
47. Pommier Y, Sordet O, Antony S, Hayward RL, Kohn KW. Apoptosis defects and chemotherapy resistance: molecular interaction maps and networks. Oncogene 2004;23:2934–49.
48. Paulson KG, Iyer JG, Tegeder AR, Thibodeau R, Schelter J, Koba S, et al. Transcriptome-wide studies of Merkel cell carcinoma and validation of intratumoral CD8+ lymphocyte invasion as an independent predictor of survival. J Clin Oncol 2011;29:1539–46.
49. Lipson EJ, Vincent JG, Loyo M, Kagohara LT, Luber BS, Wang H, et al. PD-L1 expression in the Merkel cell carcinoma microenvironment: association with inflammation, Merkel cell polyomavirus and overall survival. Cancer Immunol Res 2013;1:54–63.
50. Nghiem PT, Bhatia S, Lipson EJ, Kudchadkar RR, Miller NJ, Annamalai L, et al. PD-1 blockade with pembrolizumab in advanced Merkel-cell carcinoma. N Engl J Med 2016;374:2542–52.
51. Merkel cell carcinoma. In: NCCN Clinical Practice Guidelines in Oncology. Version 1.2017 ed. Fort Washington (PA): National Comprehensive Cancer Network; 2016.
52. Topalian SL, Bhatia S, Hollebecque A, Awada A, De Boer JP, Kudchadkar RR, et al. Non-comparative, open-label, multiple cohort, phase 1/2 study to evaluate nivolumab (NIVO) in patients with virus-associated tumors (CheckMate 358): efficacy and safety in Merkel cell carcinoma (MCC) [abstract]. In: Proceedings of the American Association for Cancer Research Annual Meeting 2017; 2017 Apr 1–5; Washington, DC. Philadelphia (PA): AACR; 2017. Abstract nr CT074.
53. Kaufman HL, Russell JS, Hamid O, Bhatia S, Terheyden P, D'Angelo SP, et al. Durable responses to avelumab (anti-PD-L1) in patients with Merkel cell carcinoma progressed after chemotherapy: 1-year efficacy update [abstract]. In: Proceedings of the American Association for Cancer Research Annual Meeting 2017; 2017 Apr 1–5; Washington, DC. Philadelphia (PA): AACR; 2017. Abstract nr CT079.
54. Kaufman HL, Russell J, Hamid O, Bhatia S, Terheyden P, D'Angelo SP, et al. Avelumab in patients with chemotherapy-refractory metastatic Merkel cell carcinoma: a multicentre, single-group, open-label, phase 2 trial. Lancet Oncol 2016;17:1374–85.
55. U.S. Food and Drug Administration. FDA approves first treatment for rare form of skin cancer; 2017. Available from: https://www.fda.gov/newsevents/newsroom/pressannouncements/ucm548278.htm.
56. Robert C, Schachter J, Long GV, Arance A, Grob JJ, Mortier L, et al. Pembrolizumab versus ipilimumab in advanced melanoma. N Engl J Med 2015;372:2521–32.
57. El Osta B, Hu F, Sadek R, Chintalapally R, Tang SC. Not all immune-checkpoint inhibitors are created equal: meta-analysis and systematic review of immune-related adverse events in cancer trials. Crit Rev Oncol Hematol 2017;119:1–12.
58. DePry JL, Reed KB, Cook-Norris RH, Brewer JD. Iatrogenic immunosuppression and cutaneous malignancy. Clin Dermatol 2011;29:602–13.

59. Menzies AM, Johnson DB, Ramanujam S, Atkinson VG, Wong ANM, Park JJ, et al. Anti-PD-1 therapy in patients with advanced melanoma and preexisting autoimmune disorders or major toxicity with ipilimumab. Ann Oncol 2017;28:368–76.
60. Bhatia S, Ibrani D, Vandeven N, Miller N, Shinohara M, Byrd D, et al. Pilot study of intratumoral G100, toll-like receptor-4 (TLR4) agonist, therapy in patients with Merkel cell carcinoma (MCC). J Clin Oncol 34:15s, 2016 (suppl; abstr 3021).
61. Bhatia S, Iyer J, Ibrani D, Blom A, Byrd D, Parvathaneni U, et al. Intratumoral delivery of interleukin-12 DNA via in vivo electroporation leads to regression of injected and non-injected tumors in Merkel cell carcinoma: final results of a phase 2 study. Eur J Cancer 2015;51:S104.
62. Paulson KG, Tegeder A, Willmes C, Iyer JG, Afanasiev OK, Schrama D, et al. Downregulation of MHC-I expression is prevalent but reversible in Merkel cell carcinoma. Cancer Immunol Res 2014;2:1071–9.
63. Ritter C, Fan K, Paschen A, Reker Hardrup S, Ferrone S, Nghiem P, et al. Epigenetic priming restores the HLA class-I antigen processing machinery expression in Merkel cell carcinoma. Sci Rep 2017;7:2290.
64. Bhatia S, Burgess M, Zhang H, Lee T, Klingemann H, Soon-Shiong P, et al. Adoptive cellular therapy (ACT) with allogeneic activated natural killer (aNK) cells in patients with advanced Merkel cell carcinoma (MCC): preliminary results of a phase II trial. National Harbor (MD): NantKwest; 2016. Available from: https://nantkwest.com/sitc-2016-ank-mcc/.
65. Chapuis AG, Afanasiev OK, Iyer JG, Paulson KG, Parvathaneni U, Hwang JH, et al. Regression of metastatic Merkel cell carcinoma following transfer of polyomavirus-specific T cells and therapies capable of re-inducing HLA class-I. Cancer Immunol Res 2014;2:27–36.
66. Paulson KG, Perdicchio M, Kulikauskas R, Wagener F, Church CD, Bui K, et al. Augmentation of adoptive T-cell therapy for Merkel cell carcinoma with avelumab. J Clin Oncol 35:15s, 2017 (suppl; abstr 3044).
67. Andtbacka RH, Kaufman HL, Collichio F, Amatruda T, Senzer N, Chesney J, et al. Talimogene laherparepvec improves durable response rate in patients with advanced melanoma. J Clin Oncol 2015;33:2780–8.
68. Chen DS, Mellman I. Elements of cancer immunity and the cancer-immune set point. Nature 2017;541:321–30.
69. Taube JM, Klein A, Brahmer JR, Xu H, Pan X, Kim JH, et al. Association of PD-1, PD-1 ligands, and other features of the tumor immune microenvironment with response to anti-PD-1 therapy. Clin Cancer Res 2014; 20:5064–74.
70. Fusi A, Festino L, Botti G, Masucci G, Melero I, Lorigan P, et al. PD-L1 expression as a potential predictive biomarker. Lancet Oncol 2015;16: 1285–7.
71. Becker JC, Houben R, Ugurel S, Trefzer U, Pfohler C, Schrama D. MC polyomavirus is frequently present in Merkel cell carcinoma of European patients. J Invest Dermatol 2009;129:248–50.
72. Kassem A, Schopflin A, Diaz C, Weyers W, Stickeler E, Werner M, et al. Frequent detection of Merkel cell polyomavirus in human Merkel cell carcinomas and identification of a unique deletion in the VP1 gene. Cancer Res 2008;68:5009–13.
73. Mangana J, Dziunycz P, Kerl K, Dummer R, Cozzio A. Prevalence of Merkel cell polyomavirus among Swiss Merkel cell carcinoma patients. Dermatology 2010;221:184–8.
74. Schmitt M, Wieland U, Kreuter A, Pawlita M. C-terminal deletions of Merkel cell polyomavirus large T-antigen, a highly specific surrogate marker for virally induced malignancy. Int J Cancer 2012;131:2863–8.
75. Shuda M, Feng H, Kwun HJ, Rosen ST, Gjoerup O, Moore PS, et al. T antigen mutations are a human tumor-specific signature for Merkel cell polyomavirus. Proc Natl Acad Sci U S A 2008;105:16272–7.
76. D'Angelo SP, Russell J, Hassel JC, Lebbe C, Chmielowski B, Rabinowits G, et al. First-line (1L) avelumab treatment in patients (pts) with metastatic Merkel cell carcinoma (mMCC): preliminary data from an ongoing study. J Clin Oncol 35:15s, 2017 (suppl; abstr 9530).

Title

Cancer-specific CD8 T cell frequency at baseline in blood correlates with response to PD-1 blockade in Merkel cell carcinoma

Authors

Thomas Pulliam[1],
Saumya Jani[1],
Lichen Jing[2],
Ana Jojic[6],
Carolyn Shasha[6],
Heeju Ryu[6],
Jiajia Zhang[3],
Rima Kulikauskas[1],
Candice Church[1],
Charlie Garnett-Benson[4],
Ted Gooley[6],
Evan Newell[6],
Aude Chapuis[6],
Kelly Paulson[5],
Kellie Smith[3],
Drew Pardoll[3],
David M Koelle[2],
Suzanne Topalian[3],
Paul Nghiem[1]

1. Dermatology/Medicine, U. of WA, Seattle, WA
2. Dept. of Medicine, U. of WA, Seattle, WA
3. Bloomberg~Kimmel Institute for Cancer Immunotherapy, Johns Hopkins U., Baltimore, MD
4. Bristol Myers Squibb, Princeton, NJ
5. Swedish Cancer Institute, Seattle, WA
6. Fred Hutch Cancer Center,

Abstract (148/~150 words)

Understanding immunotherapy response and resistance is challenging due to difficulty identifying cancer-specific CD8 T cells. Merkel cell carcinoma (MCC) is typically driven by Merkel cell polyomavirus (MCPyV), facilitating identification of cancer-specific T cells across patients. We characterized cancer-specific T cells in 35 MCC patients, including from a neoadjuvant anti-PD-1 trial. Higher MCPyV-specific CD8 T-cell frequency in pre-treatment blood (but not tumors) correlated with response (p=0.0056). Single cell RNAseq revealed MCPyV-specific CD8 T cells in blood with increased stem/memory signatures and decreased exhaustion signatures relative to their intratumoral counterparts. Number of circulating cancer-specific T cells is likely most linked to primary response to immunotherapy as longitudinal samples documented emergence of additional resistance mechanisms, amidst abundant circulating cancer-specific CD8 T cells. These results suggest that blood acts as an important reservoir of cancer-specific CD8 T cells and suggests adoptive cell therapies may be particularly effective in patients without such cells.

Body (4087/4000 words)

Introduction

Immunotherapies that inhibit the PD-1 pathway have revolutionized oncological treatment, but PD-1 pathway blockade is not sufficient for most patients with metastatic disease[1,2]. Many immunotherapy resistance mechanisms have been identified targeting diverse pathways and cell types[3]. However, these mechanisms are thought to ultimately work by disrupting the interaction between functional cancer-specific T cells and cancer cells. Most prior studies of cancer-specific T cells in human cancers have focused on intratumoral CD8 T cells, but it is likely that CD8 T cells in lymph and blood may also play a key role in mediating immunotherapy responses systemically. Murine models have shown that cancer-specific CD8 T cells in lymph nodes are less exhausted than their intratumoral counterparts[4] and stopping the trafficking of these cells into tumors abrogates PD-1 blockade efficacy[5] In mouse models, these less exhausted T cell subsets undergo expansion during PD-1 pathway blockade and are responsible for tumor regression[6-8]. Other studies in humans have shown that there is substantial trafficking of CD8 T cell clones (some of which are likely cancer-specific) between blood and tumors during immunotherapy[9-11] suggesting that peripheral CD8 T cells may be playing a role in mediating clinical responses. Indeed, in a study of head and neck cancer, patients with higher levels of activated CD8 T cells (CD38+, HLA-DR+) in blood were more likely to respond to immunotherapy. A portion of the CD8 T cells in this study were reactive to the MAGEA1 cancer-testis antigen[12] and thus presumed to be cancer-specific.

The paucity of studies of cancer-specific CD8 T cells in humans is due in part to difficulties in identifying these cells and their cognate antigens. In most cancers, adaptive immune responses develop against unique mutations (neoantigens) or against self-proteins expressed within the tumor but not elsewhere (tumor associated antigens; TAA). Since neoantigens vary between patients, customized immune reagents must be developed for each patient. This makes it difficult to utilize a large cohort needed to identify associations between clinical outcomes and cancer-specific T cell frequency or phenotype. Studies that have identified and profiled cancer-specific CD8 T cells show they have increased inhibitory receptors and characteristics of exhaustion[13-15]. Meanwhile, studies of TAA-specific CD8 T cells have shown an inconsistent relationship between their frequency and clinical outcome[16-19]. Tumor associated antigens are often shared across patients, facilitating the study of T cells specific for these proteins. However, relative to neoantigens or oncoviral antigens, TAAs have disadvantages because they are self-proteins. This means both central and peripheral tolerance have resulted in deletion or anergy of many TAA-specific T cells[20,21]. A virally driven cancer can facilitate the study of cancer-specific immune responses since its oncoproteins are non-self, required for tumor growth, and are shared across multiple patients.

To study such cancer-specific CD8 T cells, we focused on Merkel cell carcinoma (MCC), a rare neuroendocrine skin cancer with a high response rate (>50%) to PD-1 pathway blockade[22]. These tumors are driven by the Merkel cell polyomavirus (MCPyV) in ~80% of cases[23]. Oncogenesis by MCPyV requires two rare mutagenic events potentially promoted by UV exposure: truncation of the large T antigen (LT) and integration of the MCPyV genome into a human chromosome[23]. Importantly, these viral oncoproteins are persistently expressed in MCC tumors and are absent in normal tissues, thereby providing ideal antigens for development of adaptive anti-cancer immune responses. MCPyV oncoproteins are also small (~400 amino acids), allowing a more comprehensive profiling of virus-specific T cells than is possible in large oncogenic viruses[22]. Of note, immune responses to MCPyV oncoproteins are absent in healthy persons and in patients with non-polyomavirus-driven MCC[24,25].

This suggests the immune responses against these MCPyV oncoproteins are cancer-specific and not a response to background levels of MCPyV which is frequently present on normal human skin. Furthermore, the low tumoral mutational burden in virally driven MCC (median 7 predicted neoantigens per exome compared to 173 in virus negative MCC) suggests that these oncoproteins are responsible for eliciting an anti-tumor immune response[26]. In the current study, we use MHC-I multimers containing an MCPyV peptide to study cancer-specific CD8 T cells in the tumor and blood of MCC patients who did or did not respond to anti-PD-(L)1 immunotherapy.

Results

Frequency of MCPyV-specific CD8 T cells in blood strongly correlates with anti-PD-1 therapy response

The MCPyV small and large T antigens are the major oncogenic drivers of MCC[27]. A panel of MHC-I multimers containing peptides from the MCPyV-oncoproteins was assembled to identify cancer-specific T cells from virus-positive MCC patients. To augment the panel of existing MCPyV-specific multimers, tumor infiltrating lymphocytes (TIL) from pre- and post-nivolumab treatment tumors were expanded and cocultured with artificial antigen presenting cells transfected with relevant MHC-I and MCPyV T antigen vectors (**Figure 1**; see methods). TIL that produced IFN-gamma in response to stimulation with T antigens presented by patient-matched HLAs, were then cultured with overlapping peptide pools to identify the minimal epitopes.

This approach led to the identification of 2 novel epitopes (one A*68:01 restricted, one B*57:01 restricted; **Supplementary Figure 1**) that were then combined with known MCPyV-epitopes[28] to create a panel of 16 MHC-I tetramers covering 15 unique HLA types (Supplementary **Table 1**). These tetramers were then used to stain peripheral blood mononuclear cells (PBMC) from pre- and on-treatment blood draws of patients who received neoadjuvant nivolumab (**Figure 2A, Supplementary Figure 2**). In this trial, patients with MCC tumors that were surgically resectable received two doses of nivolumab followed by complete surgical resection of clinically evident disease at 4 weeks following the first dose (see methods and reference[29] for details). Resected tumors were evaluated using recently described universal methods for evaluating residual tumor following immune therapy (see methods and references[37,38] for details). Patients whose tumor bed and associated lymph nodes no longer contained any viable tumor cells were designated to have had a pathological complete response (pCR). Tumors with any residual viable tumor cells were defined non-pathological complete responses (non-pCR).

The presence of circulating MCPyV-specific CD8 T cells was highly correlated with response. In patients with detectable MCPyV-specific CD8 T cells in blood and available pathological response data, 8 of 10 patients had pCR. In contrast 0 of 5 patients without detectable MCPyV-specific T cells had non-pCR ($p = 0.0019$, Fisher's exact test; **Figure 2B, Supplementary Table 2**). Quantity of these cells was also highly correlated with response. The mean number of MCPyV-specific CD8 T cells was 10-fold higher in the 8 patients with pCR (0.015% of peripheral CD8 T cells) as compared to the 7 patients with non-pCR (0.0015%; $p=0.0056$ Wilcoxon test; **Figure 2B**). Indeed, 4 of the 7 patients with non-pCR did not have any detectable MCPyV-specific CD8 T cell in their peripheral blood.

Presence of MCPyV-specific CD8 T cells in the blood also correlated with recurrence-free survival. Patients that had detectible MCPyV-specific CD8 T cells prior to treatment had 75% recurrence free survival (RFS) at two years compared to 0% RFS in patients without detectable MCPyV-specific T cells in their blood (**Figure 2C**, $p = 0.0018$ log rank test over entire treatment period). Given the importance of validating these findings, a second cohort (**Figure 1**) was

identified. This additional cohort also showed an association between the presence of circulating MCPyV-specific CD8 T cells and clinical response (p = 0.045 log rank test; **Supplementary Figure 3**), but had limited power because 92% of patients responded to PD-1 pathway blockade in that cohort. In the neoadjuvant-nivolumab study, the presence of MCPyV-specific CD8 T cells was predictive of pathological response with a sensitivity of 100% and a specificity of 75% (AUC = 0.98). Similarly, in the validation cohort, frequency of MCPyV-specific T cells in the blood was also predictive of response with an AUC of 0.95.

MCPyV-specific CD8 T cells in blood express markers of activation/exhaustion

Given the correlation between cancer-specific CD8 T cells frequency in blood samples and clinical response, it was important to assess the functional state of these cells. A highly multiplexed (29-parameter) flow cytometry panel was optimized to study CD8 T cell phenotype and exhaustion. MCPyV-specific CD8 T cells in blood expressed high levels of exhaustion-associated proteins TOX and PD-1, low levels of the stem-promoting transcription factor TCF1, and comparable levels of T-bet and EOMES compared to CD8 T cells that demonstrated canonical patterns of exhaustion (PD-1+, TIM3+/-, CXCR5+/-, **Figure 3A**, **Supplementary Figure 4A, B**, references[6-8]). While responding patients had larger numbers of MCPyV-specific CD8 T cells, unbiased analyses showed that these cancer-specific cells shared a highly similar phenotype across pre- and post-nivolumab timepoints and patients (both responders and non-responders; **Figure 3D**). These MCPyV-specific cells mapped to exhausted/activated clusters (**Figure 3C, Supplementary Figure 4D, E**) corresponding to areas of high PD-1, Ki67 and HLA-DR expression within UMAP plots (**Figure 4E, F**).

The expression pattern of exhaustion-associated markers in cancer-specific CD8 T cells was stable over the course of immunotherapy (**Figure 3D, Supplementary Figure B, D, E**). However, there was significant downregulation of PD-1 on MCPyV-specific CD8 T cells after anti-PD-1 therapy initiation (**Supplementary Figure 4B, C**). Of note, this was not due to competition between nivolumab and the fluorescently labeled anti-PD-1 antibody, as a clone known to bind an epitope distinct from that of nivolumab was used (clone MIH4[30])

An unbiased analysis of T cell and NK cells showed expansion of proliferating CD4 and CD8 T cells 2 weeks after the start of immunotherapy in patients with pCR (CD4 T: p = 0.0015; CD8 T p = 0.021 in pCR, CD4 T p = 0.47; CD8 T p = 0.13 in non-pCR; **Supplementary Figure 5**).

An interpretable machine learning algorithm optimized for flow cytometry data (FAUST[31]) was also used to find pre-treatment T cell phenotypes correlated with clinical response (**Supplementary Figure 6A**). This algorithm identified 1102 unique combinations of expression markers (clusters) among circulating CD8 T cells. Three of these clusters had an association with pathological response (FDR <0.05) and were also ~5 fold enriched for MCPyV-specific CD8 T cells (>0.5% of each cluster was MCPyV-specific; **Supplementary Figure 6A, B**). Backwards phenotype selection was then used to identify which markers in each cluster are most strongly correlated with clinical response. This analysis identified PD-1, Granzyme B and Eomes as the markers most associated with clinical response (**Supplementary Figure 5C**). These three markers were enriched in MCPyV-specific CD8 T cells (33% of MCPyV-specific cells compared to only 4% of CD8 T cells of unknown-specificity; **Supplementary Figure 5D**).

Concentrations of 20 serum proteins from neoadjuvant nivolumab treated patients were also measured but no association with response or time point was observed (**Supplementary Figure 7A**). Similarly, there was no correlation between clinical response and frequency of circulating myeloid derived suppressor cells (MDSC; CD14+, lineage- HLA-DR negative/low) in blood of neoadjuvant treated patients (**Supplementary Figure 7B**). MCC viral status or

proportion of MCPyV-specific CD8 T cells were also uncorrelated to MDSC frequency (**Supplementary Figure 7C, D**).

MCPyV CD8 T cells are present in tumors regardless of anti-PD-1 response

Given the correlation between response and the frequency of MCPyV-specific CD8 T cells in blood, we quantitated these cells in pre- and post-treatment tumor specimens. Given limited sample quantity, we used an alternative approach to quantify MCPyV-specific CD8 T cells in tumor specimens. MHC-I multimers to MCPyV and selected other viral antigens were used to determine CD8 T cell specificity linked with paired alpha-beta TCRseq (see **Supplementary Table 3** for a list of all epitopes used). These T cell specificities could then be connected for a given patient to TCR-beta sequencing of T cells within tumor specimens that were not amplified or manipulated (**Figure 4A**; see methods). This approach identified 152 unique TCRs of known specificity to a viral antigen (**Figure 4B**, **Supplementary Table 4**). Bulk beta TCRseq of 14 tumors revealed a total of 2,485,223 TCRs, with 353,098 being unique. To validate our approach, we compared the biochemical similarity of these TCRs of known specificity using TCRdist3 (**Supplementary Figure 8**; see methods). TCRs that bound the same MHC-I multimer (balls with same color) were more likely to share similar TCR sequences (connection via a black line). TCRs of known specificity were then matched to all TCR beta sequences from that patient's tumor specimens to determine the frequency of each MCPyV-specific T cell clonotype (**Figure 4C**). A MCPyV-specific CD8 T cell clonotype was the most frequent clonotype in 5 of the 8 patients who had an available pre-treatment tumor specimen. MCPyV-specific T cell clones were detected in 7 of these 8 patients (**Figure 4C**).

Unlike in peripheral blood, the frequency of MCPyV-specific CD8 T cells in tumor tissues did not correlate with pathologic response. As shown in **Figure 4F**, in patients with a pathological complete response, 0.86% of cells in pre-treatment and 0.45% of cells in post-treatment tumors were MCPyV-specific CD8 T cells. In contrast, for patients who did not achieve a pCR, 0.25% of pre-treatment and 1.56% of cells in post-treatment were MCPyV-specific CD8 T cells (**Figure 4F**). T cells with a TCR that was identical or highly similar (identified via TCRdist3) to a TCR of known MCPyV-specificity were categorized as meta-specific for MCPyV. Frequency of such MCPyV-meta-specific T cells also did not significantly correlate with response. Specifically, these cells represented 0.94% and 1.0% of cells in pre- and post-treatment specimen in pCR patients and 0.26% of cells in pre-treatment and 1.56% of cells in post-treatment tissues of patients with non-pCR (**Figure 4G**). In patients with pCR, mean intratumoral CD8 T cell frequency (of any specificity) increased from 9.6% of all cells prior to anti-PD-1 blockade to 41.9% of all cells following treatment ($p = 0.0078$; **Figure 4D**). In contrast, CD8 T cell frequency in patients with non-pCR underwent a more modest expansion from 5.4% to 18.5% ($p=0.15$; **Figure 4D**). A slight increase in Simpson productive clonality was noted in patients with non-pCR from 7.9 to 11.7 while a decrease was noted in patients with pCR from 11.2 to 5.85 though neither of these were significant (**Figure 4E**)

Of note, because T cell receptors described here could be further developed for therapeutic transgenic T cell therapies. TCRs described in **Supplementary Table 4** would cover 87% of MCC patients with virally driven tumors with at least one MHC matched TCR and 37% of patients with an two alleles to protect against allele specific MHC downregulation (**Supplementary Figure 9**).[32]

MCPyV-specific CD8 T cells in blood are less exhausted than intratumoral counterparts

Given that MCPyV-specific CD8 T cell frequency correlated with response in the blood but not the tumor, we next sought to investigate phenotypic differences between cancer-specific T cells in the different compartments. Because the neoadjuvant nivolumab trial did not collect tumor

digests from which MCPyV-specific T cells could be isolated (**Figure 5A**), we used matched tumor and blood samples from 8 patients with advanced resectable disease (cohort 3 in **Figure 1**). Cellular indexing of transcriptomes and epitopes by sequencing (CITEseq) was performed on these samples together with MHC-I multimers labeled with a unique DNA barcode and fluorophore for identification of antigen-specific CD8 T cells (**Figure 5A**, see methods). This led to identification of 51,555 unique single cells that passed quality control metrics (24,065 from tumors and 27,431 cells from blood; **Supplemental Figure 10A, B and C**). Clustering revealed major lineages of NK, CD4, CD8, B, myeloid, and tumor cells through expression of common genes and proteins (**Supplemental Figure 10A, D and F**). Blood specimens from two patients were not usable and a third patient only had a small number of tumor-resident cells that passed quality control filters due to high necrosis in the tumor (**Supplemental Figure 10E**).

Subclustering of CD8 T cells revealed 7 clusters consisting of naïve, memory, effector, senescent, gamma-delta T cells, progenitor exhausted and terminally exhausted CD8 T cells (**Figure 5B, Supplemental Figure 10G, H**). Progenitor and terminally exhausted clusters represented most of the tumor-resident CD8 T cells with the remaining cell populations being more dominant in blood (**Figure 5B, Supplemental Figure 10H, 10D, 10G**). Memory, exhaustion, and senescence signature scores showed predominance of an exhaustion phenotype in intratumoral CD8 T cells and while memory or senescent phenotypes were dominant among circulating cells (**Figure 5C; Supplementary Table 5**, see methods). MCPyV-specific CD8 T cells from tumors were most likely to be present in the progenitor exhausted or terminally exhausted clusters (90-100% of intratumoral MCPyV-specific CD8 T cells; **Figure 5E**). In contrast, MCPyV-specific CD8 T cells from the blood were more likely to fall into the effector cluster (33-100% of circulating MCPyV-specific CD8 T cells; **Figure 5E**) with fewer cells in exhausted clusters than MCPyV-specific CD8 T cells from tumors ($p = 0.0016$; **Figure 5F**).

This is further supported by pseudo time analyses which showed a “tumor path” and “blood path” following the tissue origin of these cells (**Supplementary Figure 11A, B**). The tumor path tracked along increases in CD39 and decreases in CD127 consistent with development of an exhausted phenotype. The blood path meanwhile correlated with increased CD57 expression and decreased CD28 expression, consistent with development of a senescent phenotype (**Supplementary Figure 11C, D**). This was supported by expression of exhaustion-associated genes on the tumor path and senescence genes in the blood path (**Supplementary Figure 11E**).

Direct comparison of antigen-specific CD8 T cells from blood or tumor tissues showed that MCPyV-specific CD8 T cells had higher levels of checkpoint molecules including PDCD1 (PD-1), HAVCR2 (TIM3), LAG3 and CTLA4 than their CMV-specific counterparts (**Figure 5D**). Furthermore, the MCPyV-specific CD8 T cells in tumor tissues had higher levels of these checkpoint molecules than their counterparts from blood (**Figure 5D**). In contrast, the stem/memory markers TCF7, SELL (CD62L), IL7R, and LEF1 are all more highly expressed in MCPyV-specific CD8 T cells in blood than MCPyV-specific T cells in tumors (**Figure 5D**). We also observed higher levels of AP-1 subunits (FOS and JUN) and lower levels of NFAT1 subunits (NFAT1C1 and NFATC2) in circulating MCPyV-specific CD8 T cells compared to intratumoral MCPyV-specific CD8 T cells, consistent with a more exhausted state in intratumoral cells[33] (**Figure 5D**). Difference in effector molecules were also seen between MCPyV-specific T cells in blood compared to in tumors with higher levels of Granzyme A and M in circulating CD8 T cells with tumors (**Figure 5D**). CXCL13 on the other hand was exclusively expressed by intratumoral MCPyV-specific CD8 T cells, consistent with this being a marker for cancer-specific T cells in tumors[34] (**Figure 5D**)

To compare MCPyV-specific CD8 T cells to antigen-specific T cells from other malignancies, we integrated these cells *in silico* into an existing dataset from Eberhardt et al of HPV-specific CD8 T cells from HPV-driven head and neck tumors[14]. Cells from both studies were clustered into stem, transitory and terminally differentiated populations as in the Eberhardt et al study (**Supplementary Figure 12 A, D**). MCPyV-specific CD8 T cells separated based on their tissue of origin (blood versus tumor). While ~75% of MCPyV-specific T cells fell into the terminally differentiated cluster regardless of tumor of origin, circulating MCPyV-specific cells made up 79% of the stem cluster while intratumoral cells made up 94% of the transitory population (**Supplementary Figure 12 B, C**).

Transcriptional regulatory network analysis via SCENIC[35] was performed on CD8 T cells and identified 535 regulatory networks (regulons) associated with transcription factors (**Supplemental Figure 13A, 13B, 13C**). Regulons associated with the AP-1 complex (FOS, JUN) were more highly expressed in naïve and memory CD8 T cells whereas regulons associated with effector function and terminal differentiation (EOMES, TBX21, IRF1, IRF8, STAT3, CREM) were more associated with terminally differentiated clusters of exhausted and senescent cells (**Supplemental Figure 13C, 13C**). MCPyV-specific CD8 T cells in tumors exhibited higher expression of exhaustion associated regulons IRF4, BATF and PRDM1 than CMV-specific CD8 T cells or MCPyV-specific T CD8 T cells in blood (**Supplemental Figure 13F, 13F**).

MHC-I downregulation during secondary resistance to PD-1 pathway blockade.

Given the association between frequency of MCPyV-specific CD8 T cells in blood and initial response to PD-1 pathway blockade, we next sought to assess the role of these cells in acquired (secondary) resistance. We identified a patient who was treated with anti-PD-L1 therapy with an initial partial response (RECIST1.1). This patient continued treatment for 1 year then electively stopped treatment.18 months after starting anti-PD-L1 therapy, the patient experienced a recurrence which was not responsive to restarting anti-PD-L1 therapy (**Figure 6A**). CITEseq was performed on the peripheral blood of this patient to identify MCPyV-specific CD8 T cells and identify TCR sequences of 49 unique clonotypes specific for a B*37:01 restricted epitope (**Figure 6B**). Bulk TCRseq of blood at 6 time points along this patient's treatment show that these cancer-specific CD8 T cells represent 0.04% of all T cells in blood before treatment, expand to 0.15% of T cells following treatment initiation and further expand to 0.53% of T cells at the time of recurrence following anti-PD-L1 reinitiation (**Figure 6C**). 21 novel clones expanded following initial treatment initiation (blue shades, **Figure 6C, 6D**) including the two most frequent cancer-specific TCRs at the time of recurrence. Immunohistochemistry of the tumor before treatment shows an immune excluded tumor with ample tumor oncoprotein and dispersed MHC-I expression on 46% of tumor cells (**Figure 6E, 6F**). In contrast, the tumor at the time of recurrence shows an "immune cold" tumor with little to no MHC-I expression on 4.6% of tumor cells (**Figure 6E, 6F**).

Discussion

Only a small subset of T cells recognize cancer antigens and the unique nature of tumor antigens in most patients' cancers make identification of such T cells difficult. However, cancer-specific T cells are likely critical in mediating immunotherapy responses. In this study, we leveraged the fact that tumor antigens are shared among patients with polyomavirus-driven Merkel cell carcinoma to study cancer-specific T cell responses in 35 patients. This allowed us to identify correlations between cancer-specific CD8 T cells and clinical responses in patients treated with PD-1 pathway blockade.

Through analyzing many parameters, we found that the major association with response to PD-1 pathway blockade was a higher frequency of MCPyV-specific CD8 T cells in blood. Patients with more circulating cancer-specific T cells were far more likely to have complete pathological responses and longer recurrence-free survival. These cells exhibited evidence of progression towards a dysfunctional phenotype, as demonstrated by low levels of TCF1 and high levels of PD-1 and TOX.

In contrast to the correlation between response and MCPyV-specific T cell frequency in blood, the frequency of these cells in tumors was not significantly correlated with response in this cohort. It is possible that in a larger cohort, intratumoral T cells would also correlate with response. Indeed, a sophisticated study of melanoma-associated antigens did see a correlation between expanded MART1-specific T cell frequency and immunotherapy response among 60 melanoma patients ($p = 0.041$). Regardless, the correlation of response we observed was much higher for MCPyV-specific CD8 T cell frequency in blood than their frequency in tumors. This suggested that these cells in blood may be playing a unique role in the immunotherapy response which we could explore using single cell RNAseq. We used barcoded MHC-I multimers on tumor and blood samples from MCC patients to identify these cells for further transcriptional analyses. MCPyV-specific T cells in tumors exhibited characteristics of terminal exhaustion including high levels of immune checkpoints, low NFAT expression despite high AP-1 subunit expression and high expression of PRDM1 and IRF4 regulatory networks[36-38]. In contrast to MCPyV-specific CD8 T cells within tumors, MCPyV-specific T cells in blood expressed fewer genes associated with exhaustion and more genes associated with a stem-like phenotype including expression of lymph homing receptors and TCF7 (encodes TCF1). In murine studies of dysfunctional CD8 T cells, TCF1-expressing cells undergo proliferation following PD-1 pathway blockade and maintain more effector capacity than TCF1-negative cells[6-8]. Furthermore, the presence of TCF1-expressing CD8 T cells in human tumors positively correlates with immunotherapy response[39].

These data support a model where the blood acts as a reservoir of cancer-specific CD8 T cells at an early stage of exhaustion that are capable of expansion and mediating clinical responses. However, these data were only studied in the setting of primary resistance. Analyses of a patient with secondary resistance to PD-1 pathway blockade showed a high frequency of peripheral cancer-specific CD8 T cells before initial treatment that remained high throughout response and increased at the time of recurrence. However, at the time of recurrence the tumor downregulated MHC-I suggesting this may also be a relevant immune evasion mechanism in the setting of secondary resistance.

Our findings that an absence of peripheral cancer-specific CD8 T cells is correlated with poor response to anti-PD-1 therapy indicates that a subset of patients could benefit from adoptive cellular therapies in the first line setting. It is also possible that combination therapy with other immune checkpoint inhibitors could benefit anti-PD-(L)1 therapy refractory patients by restoring function to intratumoral cancer-specific T cells, if they do not have a reservoir of circulating cancer-specific T cells. These data also suggest treatments ideal for primary immunotherapy resistance may differ from those ideal for secondary resistance and suggest that treatments reversing MHC-I downregulation could be beneficial in this setting[40]. Additionally, future developments and sequencing based techniques and TCR prediction tools could allow this to be developed as a biomarker for anti-PD-1 therapy response.

METHODS

Study design and participants

The samples in cohort 1 (**Figure 1**) were collected as part of a neoadjuvant nivolumab trial (NCT02488759; reference[29]). Briefly, patients who met the criteria were 18 years or older, had an Eastern Cooperative Oncology Group performance score of 0 or 1, and had their MCC confirmed through pathology. The patients had tumors that could be biopsied before treatment and were considered surgically resectable. This included stage IIA-IIIB disease with tumors measuring at least 2 cm, or smaller tumors with noticeable regional lymph node metastases or treatable in-transit metastases, stage IV diseases with only a few metastases, or local and regional recurrences with total tumor size of at least 1 cm. Patients were not eligible if they had brain metastases, another type of cancer within the past 3 years, a history of autoimmune issues, or required immunosuppressive medications, or if they had previously received treatment with drugs that modulate T-cells. After 2 doses of nivolumab (4 weeks after initial dose) surgery was carried out and the extent of pathological response was determined [29]. These criteria were described by Stein et al wherein a pathological complete response (pCR) was defined as “absence of residual viable invasive cancer on hematoxylin and eosin evaluation of completely resected tumor specimens including all sampled lymph nodes” [41,42]. Tumors with any viable tumor cells remaining were categorized as non-pathological complete response (non-pCR).

Samples in cohorts 2 and 3 (**Figure 1**) were collected with informed consent for research use and were approved by the Fred Hutch Cancer Center institutional review board, in accordance with the Declaration of Helsinki (2013) as part of observational registry studies focusing on Merkel cell carcinoma. Cohort 2 was designed by selecting all patients in our >1,500 patient database who were treated with immune checkpoint inhibitors (pembrolizumab, nivolumab, avelumab or ipilimumab with nivolumab) as first line systemic therapy. Patients were further selected if they had a PBMC collected within 45 days before the start of treatment. HLA typing and tumor viral status were determined as previously described [29]. This resulted in 26 patients included in this cohort for further analysis. Patient response data was assessed via patient chart review. Patient samples for cohort 3 were selected based on availability of frozen viable tumor tissues with frozen PBMC within 30 days of tumor collection. Patient samples were further selected to only include virus positive tumors and without immunosuppression.

Blood collection and processing

Heparinized whole blood from MCC patients was processed at the Specimen Processing Lab (Fred Hutchinson Cancer Center). Peripheral blood mononuclear cells (PBMC) were isolated by routine Ficoll density gradient centrifugation and cryopreserved in liquid nitrogen.

Tumor digestion processing

Fresh MCC tumor specimens from needle cores, punch biopsies, or surgical excisions were enzymatically digested as described[43]. All single-cell suspensions were cryopreserved in Freezing Medium [50% human serum (Valley Biomedical), 40% RPMI (Corning), and 10% DMSO (Sigma-Aldrich)] in liquid nitrogen.

To expand T cells from tumors, tumor tissue was chopped into small pieces and placed in a culture along with 10^6 allogenic irradiated peripheral blood mononuclear cells (PBMCs), Remel phytohemagglutinin-purified mitogen (1.6 µg/mL; ThermoFisher), human recombinant IL15 (10 ng/mL; R&D Systems), and human natural interleukin 2 (32 U/mL; Hemagen, Columbia, MD).

Epitope discovery and epitope mapping

We used previously described methods to discover novel MCPyV epitopes in expanded T cells[28,44,45]. In brief, HLA cDNA were either cloned from PBMC from HLA-typed persons or obtained ready-to-use from the International Histocompatibility Working Group gene bank housed at Fred Hutchinson Cancer Center (Seattle, WA[46]). The protocol for cloning of HLA cDNA from PBMC has been previously detailed and was performed exactly as described previously[45].

MCPyV LT AA 1-327 or full-length ST AA 1-186 with a carboxy-terminus six-histidine addition were cloned into the Nature Technology Corporation (NTC) 9385R vector[47] (PMID: 25142448; Nature Technology Company). These plasmids encode an identical 78 AA N-terminal CT domain. The NTC plasmids were based on Genbank HM011538.1. LT AA 1-259 from MCVw156 (Genbank HM355825.1) was separately cloned into pDEST103, a vector constructed in our laboratory[44].

To screen TIL for reactivity to MCPyV epitopes, first artificial antigen-presenting cells (aAPC) were created. Cos-7 cells (ATCC) were cotransfected for 24 hours with HLA plasmid, and MCPyV plasmid. After two days, 10^5 TIL were added and 24–48 hours later, supernatant IFNγ was measured by ELISA[48]. IFNγ results were reported as the mean and the SD of the mean (SD) in the figures. Positive candidate HLA was used for further fine epitopes mapping with 13 mer OLP.

Fine epitope mapping was performed using 95 overlapping T-Ag peptides (OLP; **Supplementary Table 6;**-Genscript) as previously described [49]. Peptides covering LT AA 1-281 and the unique region of ST were 13 AA long with 9 AA overlap and based on MCPyV 350 (Genbank FJ173805.1;[49]). Peptides were tested individually at 1 µg/mL final concentration by addition to Cos-7 cells 48 hours after HLA transfection. TILs (10^5) were added 1–2 hours later, and 24–48-hour supernatants were tested for IFNγ by ELISA as indicated above. Alternatively, OLP were matrix-pooled into rows and columns of 9–10 peptides/pool and tested at 1 µg/mL final concentration each. Peptides at positive (mean ELISA OD450 value > 0.2) pool intersection(s) were retested for confirmation. For some assays, aAPCs were peptide-pulsed at 10 µg/mL for 1 hour and PBS-washed before adding responder cells to reduce T-cell auto-presentation. The HLA-peptide binding prediction algorithm was performed using netMHCpan 4.0 [50].Positive pools were deconvoluted to individual peptides in follow-up assays.

Flow cytometry

PBMCs from the neoadjuvant-anti-PD-1 and definitive anti-PD-(L)1 cohorts (**Figure 1**) were analyzed by flow cytometry. Briefly, frozen tubes of PBMC were thawed at 37 C, followed by dropwise addition of complete media (RPMI, 10% Fetal bovine serum, 1x penicillin/streptomycin, 1x l-glutamine). DNAse I (10 units/ml) was added and cells were rested for 1 hour. Cells were counted using a hemacytometer and split into tubes of 1-3 million cells. Cells were washed twice with PBS followed by addition of dasatinib (100 nM) and live dead staining buffer (Live dead Blue; ThermoFisher) and incubated at 37C for 10 minutes. MHC-I

multimers were then added. If a sample had more potential MHC matches than tubes of 1-3 million cells, multiple MHC-I multimers for the same virus were added to a tube. Antibodies against chemokine or cytokine receptors were then added and samples were incubated for 30 minutes (See **Supplementary Table 7** for antibodies used). Antibodies against other cell surface receptors were then added and incubated at room temperature for 30 minutes. Cells were then washed twice with autoMACS running buffer (Miltenyi) and permeabilized using the Foxp3/Transcription factor staining buffer set (eBioscience) and washed twice with the kit permeabilization buffer. Intracellular antibodies were then added and incubated at room temperature for 1 hour. Cells were washed twice with permeabilization buffer and fixed in 1% paraformaldehyde. Antibody capture beads or amine reactive beads (ThermoFisher) were used to compensate each fluorophore in the experiment. Stained cells were analyzed by the Cytek Aurora spectral analyzer at the University of Washington, Department of Immunology's Cell Analysis Facility. Spectral unmixing was performed using SpectroFlo software. Visualization and Initial gating selecting for single cells, lymphocytes and live cells was performed in FlowJo v.10 (FlowJo LLC; **Supplementary Figure 14**). Subsequent analyses were performed in R (See below).

Single cell RNAseq sample preparation

Frozen tumor and PBMC single cell suspensions from cohort 3 (**Figure 1**) were analyzed by cellular indexing of transcripts and epitopes by sequencing (CITEseq). Frozen tubes were thawed at 37 C, followed by dropwise addition of 1 ml complete media (RPMI, 10% Fetal bovine serum, 1x penicillin/streptomycin, 1x l-glutamine). Equivolume of complete media was continuously added 4 additional times (dropwise with gentle mixing in between additions,total volume of 32 ml). Cells were then washed twice with 4 C PBS, counted using a hemacytometer and transferred to FACS tubes (Fisher Scientific). Live dead stain was then added (FVS780; BD Biosciences), followed by a blocking buffer to bring samples to 0.5% BSA, 5% TruStain FcX buffer (Biolegend), 100 nM dasatinib, and 50 µg salmon sperm. Samples were then incubated on ice for 10 minutes followed by the following reagents in order: DNA oligo labeled MHC-matched MHC-I multimers, hashtag antibodies to identify sample origin in subsequent pooling steps, fluorophore labeled antibodies, DNA oligo labeled antibodies. Cells were then incubated on ice for 30 minutes and washed three times. Cells were then sorted on an Aria II Cell sorter (BD Biosciences). Dead cells and debris were excluded, and samples were enriched for MHC multimer binding cells. Cells were sorted into cold complete media, pooled and immediately prepared for sequencing (see below).

scRNA-seq and scV(D)J-seq library preparation and sequencing

Single cell suspensions were collected from either tumor or blood samples and brought to a concentration of 700-1,200 viable cells per microliter using a hemacytometer. These single cell suspensions were then loaded into the appropriate microfluidic chip (chip G; 10x Genomics) and run through a Chromium controller to obtain Gel Beads-in-Emulsion (10x Genomics). Resulting cell suspensions then went through a library preparation process for single-cell RNA sequencing (scRNA-seq) along with paired scV(D)J-seq for T-cell receptor (TCR) and B-cell receptor (BCR) clonotypes using the 5′ transcriptome kit with feature barcoding (V1.1; 10x Genomics) following the manufacturer's guidelines. The complementary DNA libraries were then sequenced using a NovaSeq instrument (Illumina) with 2 × 92 base pair paired-end reads aiming for an average of 20,000 reads per cell per 10x Genomics guidelines.

Beta TCR receptor profiling

DNA was extracted from frozen peripheral blood mononuclear cells or formalin-fixed paraffin-embedded (FFPE) tumor biopsy material (20 μm thick molecular curls or material scraped from pre-cut slides) using QIAamp DNA Blood Mini Kit or QIAamp DNA FFPE tissue kit, respectively (Qiagen). Resulting samples were submitted to Adaptive Biotechnologies for TCRβ sequencing and normalization as previously described [51].

Immunohistochemistry

Standard immunohistochemistry was performed on formalin fixed paraffin embedded tissues with antibodies recognizing Merkel cell polyomavirus (CM2B4 clone at 1:50 dilution, Santa Cruz, CA, USA), class I MHC (EMR8-5 clone at 1:8000 dilution, MBL International, MA, USA), and cytokeratin 20 (Dako clone Ks20.8 at 1:200 dilution, Agilent, CA, USA). Multiplex immunohistochemistry was performed with a panel of antibodies including CD8 (clone 144B/Dako/fluor 520 opal/concentration 0.2 ug/mL), CD3 (Sp7/Thermo/fluor opal 650), HLA-DR (EP96/BSB/ 0.125 ug/mL/fluor opal 690), C56 (123.C3/BSB 1 ug/mL/fluor 540), and PD-L1 (E1L3N 0.5 ug/mL). We also attempted PD-1 staining with antibody clone D4W2J however non-specific staining was observed and PD-1 was thus excluded from analysis. Quantitative image analysis was performed with HALO software.

MHC multimer preparation

Allophycocyanin (APC)-labeled MHC-I tetramers were used for flow cytometry experiments and prepared by the Immune Monitoring Lab at Fred Hutch Cancer Center. Tetramers were titered using samples of known positivity. DNA oligo and fluorophore labeled MHC-I dextramers were prepared by Immudex. These multimers were used for staining expanded T cells as directed. MHC tetramers used for scRNAseq were created using MHC-I easYmers (Immunaware) and PE or APC and DNA oligo streptavidins (Biolegend). A full list of all epitopes used is provided in **Supplementary Tables 1 and 3**.

MHC multimer gating and analysis

For MHC-I multimer gating on flow cytometry analyses, samples were grouped by MHC-I multimer. Gates were manually drawn for each sample while blinded by tumor viral status, response, or patient identity. If a sample was stained with more than epitope, then the sample was included in all potential epitopes and then the gate was drawn at the maximum value of all potential epitopes. Median gate values were then calculated for each individual epitope and all gates were redrawn resulting in 144 FACS plots that were then reviewed by a second person with experience in tetramer staining (C.C.) who was also blinded to tumor viral status, response, or patient identity. Any variations in gating values were then discussed and, if appropriate, gates were edited. Once final gate values were established, frequency of MCPyV-specific CD8 T cells in the blood of patients with virally driven or non-virally driven cancer were calculated (**Supplementary Figure 2D**). These results supported accurate gating as no patients with non-MCPyV driven cancer had more than 1 in 10,000 CD8 T cells binding to MHC-I tetramers containing MCPyV oncoprotein peptides. This limit of detection is similar to prior study of MCPyV-specific CD8 T cells in healthy controls.[24] Phenotypic similarity was also used to confirm gate values. Given a priori knowledge of the phenotype of MCPyV-specific CD T cells (naïve, largely PD-1+, [24]), the cumulative portion of cells that were naïve or PD-1 positive were calculated as a function of decreased tetramer intensity (**Supplementary Figure 2B, C**). These results further validated the gating of MCPyV-specific T cells. Since the gate values drawn were concordant with this approach, no further adjustments were made using this approach.

For gating of antigen-specific CD8 T cells in single cell RNAseq data, the counts of MHC-I multimer unique molecular identifiers (UMIs) were used. A similar approach was used as above where gates were manually drawn for each sample while blinded by tumor viral status, response, or patient identity and then reviewed by a second person (S.J.) who was also blinded to these factors. TCR beta sequences of cells of known specificity were then compared to TCRs of known specificity in the VDJ database [52]. After comparison, 15/16 TCRbetas that were found in the database were accurately matched. The non-matched TCR was reviewed and MHC-I count values appeared in ranges of other matched cells suggesting this TCR could recognize different peptides in different HLA context with a different TCRalpha.

Flow cytometry data analysis

Live, CD19-, CD14- lymphocytes fcs files were loaded into a gating set object in R using flowWorkspace (v.4.6.0). Fluorescent data was transformed using the biexponential function. Fluorescent-minus-one samples were used to draw gates at the 99th percentile which were then used as the minimum gate for the markers CCR4, CCR6, CCR7, CD45RA, CD4, CD8, CXCR5 CD28, CD56, CD3, FOXP3, TCF1, and Ki67. Gates were adjusted upward as appropriate based on visual inspection. Markers of activated T cells including LAG3, TIM3, HLA-DR, TBET, EOMES, PD-1, Granzyme B, Granzyme K, and TOX were gated similarly with the 99th percentile of naïve cells acting as an additional minimum gate. UMAP dimensionality reduction was performed using uwot (v.0.1.14). clustering was performed using phenograph (v.0.99.1) and faust (v.0.5.5). Visualization was performed using ggplot2 (v.3.4.0) or FlowJo (v.10.8.1).

Single cell RNAseq data analysis

Raw sequencing reads were aligned to the hg38 genome using Cell Ranger v.3.1. Filtered counts matrices of transcripts and feature barcoding counts were loaded into a SingleCellExperiment object for further analyses in R (v.4.1.2). Sample hash deconvolution was performed using DropletUtils (v.1.14.2). Doublets detection and removal was performed using scds (v.1.10.0) in conjunction with doublets detected during hash deconvolution. Cells with less than 800 transcript reads, less than 250 genes detected or more than 10% of mitochondrial DNA were excluded as low quality. Comparisons of excluded and kept cells was performed to ensure no cell populations were disproportionally removed. This showed mitochondrial genes, MALAT1 (a transcript associated with dying cells), and hemoglobin genes were the only genes disproportionally represented in the removed cells. Cells were size-normalized and log transformed using scuttle (v.1.4.0).

Cells from different runs were then integrated using the mutual nearest neighbor method though the batchelor package (v1.10.0). UMAP dimensionality reduction was performed using the integrated values. Clustering was performed using the integrated transcript values and feature barcoding reads through the walktrap algorithm on a nearest neighbor graph (scran v.1.22.1). Numbers of clusters was varied by scaling the number of nearest neighbors (k) during graph construction followed by analysis via clustree (v.0.5.0). Clusters were then labeled as major cell lineages of CD4 T cells, CD8 T cells, B cells, myeloid cells, erythrocytes, NK cells and tumor cells through expression of key genes including MS4A1, CD19, CD4, CD8A, CD3E, CD3D, GZMB, NCAM1, HLA-DRA, PTPRC, NKG7 and the MCPyV oncoproteins. Cluster labels were then validated by investigating the portion of cluster with productive BCR or TCR rearrangements. Cell lineages were then isolated in silico and split into major lineages and dimensionality reduction and clustering was re-performed as above. Cells were scored for expression of memory and exhaustion gene sets (see below) using the UCell (v.1.99.1)

package. Pseudotime analyses was performed using slingshot (v.2.2.1) using the naïve CD8 T cell population as the starting population. Pseudotime heatmap was created by fitting a spline to each gene shown against pseudotime.

Single cell transcriptional regulatory networks in CD8 T cells were analyzed using SCENIC (v.1.2.4) as previously described [35]. Briefly, genes with more than 488 total counts across all CD8 T cells and cells with more than 163 genes were isolated for subsequent analysis. Correlations between transcription factors and genes were determined and GENIE3 was used to establish regulatory networks. SCENIC was then used to score the expression of these regulatory networks in each cell. UMAP dimensionality reduction was reperformed based on these regulons. MCPyV-specific CD8 T cells were isolated and integrated into a large single cell RNAseq dataset of HPV-specific CD8 T cells from HPV driven head and neck cancer [14]. Each dataset was rescaled using SCTransform (Seurat). Integration features (genes) were selected based on their variability across both datasets followed by removal of TCR and BCR V, D and J genes and mitochondrial genes. Seurat was then used to integrate the datasets using the HPV dataset as an anchor and a k.weight of 40.

Plots were made using scater (v.1.22.0), Seurat (v.4.3.0) or ggplot2 (3.4.0).

Gene set derivation from previous studies

Single cell RNAseq datasets from 4 studies containing diverse populations of CD8 T cells from human tumors[13,39,53,54] were used to create a compendium of labeled clusters along with genes positively or negatively associated with each cluster (**Supplementary Table 5**). Clusters with synonymous labels were renamed and grouped. Genes associated with clusters with p values of less than 0.05 and average log fold changes greater than 0.5 were selected for further inclusion. An “exhaustion” gene signature was developed for genes that were associated with exhausted clusters (labeled as exhausted, progenitor exhausted, terminally exhausted, exhausted cycling) in at least 3 of 4 datasets (74 total genes). Similarly, a “memory” gene signature was developed for genes that were associated with memory clusters (labeled as naïve, memory or central memory) in at least 2 of 3 datasets that had these populations (12 total genes). Immune checkpoints included in the exhaustion gene set were manually identified as PDCD1, LAG3, TIGIT, HAVCR2, CD276, ENTPD1, CD73, ADORA2A, and CTLA4.

Statistics

The statistical tests applied were two-sided unless specified otherwise. T tests were used to compare differences between two groups unless otherwise noted. When comparing more than two groups, the nonparametric Kruskal–Wallis test was used. Multiple hypothesis testing was done with the Benjamini–Hochberg method unless noted differently. Fisher's exact test was used to evaluate differences between two categorical variables. The ROC analysis was used to measure classification accuracy, which was expressed as the AUC. Pearson (r) or Spearman (ρ) correlation was used to determine linear concordance, and a two-sided t-test was used to see if the result was significantly different from zero. The significance levels and HRs for Kaplan–Meier analyses were calculated using a two-sided log-rank test. All statistical analysis was carried out using R v.4.1+.

Acknowledgements: Victoria L. Campbell deposited epitopes into IEDB.
Figures created with Biorender

Citations

1. Yarchoan, M., Hopkins, A. & Jaffee, E.M. Tumor Mutational Burden and Response Rate to PD-1 Inhibition. *N Engl J Med* **377**, 2500-2501 (2017).
2. Gandini, S., Massi, D. & Mandala, M. PD-L1 expression in cancer patients receiving anti PD-1/PD-L1 antibodies: A systematic review and meta-analysis. *Crit Rev Oncol Hematol* **100**, 88-98 (2016).
3. Vesely, M.D., Zhang, T. & Chen, L. Resistance Mechanisms to Anti-PD Cancer Immunotherapy. *Annu Rev Immunol* **40**, 45-74 (2022).
4. Huang, Q.*, et al.* The primordial differentiation of tumor-specific memory CD8(+) T cells as bona fide responders to PD-1/PD-L1 blockade in draining lymph nodes. *Cell* **185**, 4049-4066 e4025 (2022).
5. Fransen, M.F.*, et al.* Tumor-draining lymph nodes are pivotal in PD-1/PD-L1 checkpoint therapy. *JCI Insight* **3**(2018).
6. Utzschneider, D.T.*, et al.* T Cell Factor 1-Expressing Memory-like CD8(+) T Cells Sustain the Immune Response to Chronic Viral Infections. *Immunity* **45**, 415-427 (2016).
7. He, R.*, et al.* Follicular CXCR5- expressing CD8(+) T cells curtail chronic viral infection. *Nature* **537**, 412-428 (2016).
8. Im, S.J.*, et al.* Defining CD8+ T cells that provide the proliferative burst after PD-1 therapy. *Nature* **537**, 417-421 (2016).
9. Sidhom, J.W.*, et al.* Deep learning reveals predictive sequence concepts within immune repertoires to immunotherapy. *Sci Adv* **8**, eabq5089 (2022).
10. Wu, T.D.*, et al.* Peripheral T cell expansion predicts tumour infiltration and clinical response. *Nature* **579**, 274-278 (2020).
11. Yost, K.E.*, et al.* Clonal replacement of tumor-specific T cells following PD-1 blockade. *Nat Med* **25**, 1251-1259 (2019).
12. Luoma, A.M.*, et al.* Tissue-resident memory and circulating T cells are early responders to pre-surgical cancer immunotherapy. *Cell* **185**, 2918-2935 e2929 (2022).
13. Oliveira, G.*, et al.* Phenotype, specificity and avidity of antitumour CD8(+) T cells in melanoma. *Nature* **596**, 119-125 (2021).
14. Eberhardt, C.S.*, et al.* Functional HPV-specific PD-1(+) stem-like CD8 T cells in head and neck cancer. *Nature* **597**, 279-284 (2021).
15. Caushi, J.X.*, et al.* Transcriptional programs of neoantigen-specific TIL in anti-PD-1-treated lung cancers. *Nature* **596**, 126-132 (2021).
16. Li, P.*, et al.* Clinical Correlation of Function and TCR vbeta Diversity of MAGE-C2-Specific CD8(+) T Cell Response in Esophageal Cancer. *J Immunol* **209**, 1039-1047 (2022).
17. Tauber, C.*, et al.* Inefficient induction of circulating TAA-specific CD8+ T-cell responses in hepatocellular carcinoma. *Oncotarget* **10**, 5194-5206 (2019).
18. Tada, H.*, et al.* Dynamic alterations of circulating T lymphocytes and the clinical response in patients with head and neck squamous cell carcinoma treated with nivolumab. *Cancer Immunol Immunother* **71**, 851-863 (2022).
19. Palata, O.*, et al.* Detection of tumor antigens and tumor-antigen specific T cells in NSCLC patients: Correlation of the quality of T cell responses with NSCLC subtype. *Immunol Lett* **219**, 46-53 (2020).
20. Overwijk, W.W.*, et al.* gp100/pmel 17 is a murine tumor rejection antigen: induction of "self"-reactive, tumoricidal T cells using high-affinity, altered peptide ligand. *J Exp Med* **188**, 277-286 (1998).
21. Alves, P.M.*, et al.* Immunogenicity of the carcinoembryonic antigen derived peptide 694 in HLA-A2 healthy donors and colorectal carcinoma patients. *Cancer Immunol Immunother* **56**, 1795-1805 (2007).
22. Becker, J.C.*, et al.* Merkel cell carcinoma. *Nat Rev Dis Primers* **3**, 17077 (2017).

23. Feng, H., Shuda, M., Chang, Y. & Moore, P.S. Clonal integration of a polyomavirus in human Merkel cell carcinoma. *Science* **319**, 1096-1100 (2008).
24. Miller, N.J.*, et al.* Tumor-Infiltrating Merkel Cell Polyomavirus-Specific T Cells Are Diverse and Associated with Improved Patient Survival. *Cancer Immunol Res* **5**, 137-147 (2017).
25. Hansen, U.K.*, et al.* Extended T-Cell Epitope Landscape in Merkel Cell Polyomavirus Large T and Small T Oncoproteins Identified Uniquely in Patients with Cancer. *J Invest Dermatol* **142**, 239-243 e213 (2022).
26. Goh, G.*, et al.* Mutational landscape of MCPyV-positive and MCPyV-negative Merkel cell carcinomas with implications for immunotherapy. *Oncotarget* **7**, 3403-3415 (2016).
27. DeCaprio, J.A. Molecular Pathogenesis of Merkel Cell Carcinoma. *Annu Rev Pathol* **16**, 69-91 (2021).
28. Jing, L.*, et al.* Prevalent and Diverse Intratumoral Oncoprotein-Specific CD8(+) T Cells within Polyomavirus-Driven Merkel Cell Carcinomas. *Cancer Immunol Res* **8**, 648-659 (2020).
29. Topalian, S.L.*, et al.* Neoadjuvant Nivolumab for Patients With Resectable Merkel Cell Carcinoma in the CheckMate 358 Trial. *J Clin Oncol* **38**, 2476-2487 (2020).
30. Zappasodi, R.*, et al.* Non-conventional Inhibitory CD4(+)Foxp3(-)PD-1(hi) T Cells as a Biomarker of Immune Checkpoint Blockade Activity. *Cancer Cell* **33**, 1017-1032 e1017 (2018).
31. Greene, E.*, et al.* New interpretable machine-learning method for single-cell data reveals correlates of clinical response to cancer immunotherapy. *Patterns (N Y)* **2**, 100372 (2021).
32. Paulson, K.G.*, et al.* Acquired cancer resistance to combination immunotherapy from transcriptional loss of class I HLA. *Nat Commun* **9**, 3868 (2018).
33. Martinez, G.J.*, et al.* The transcription factor NFAT promotes exhaustion of activated CD8(+) T cells. *Immunity* **42**, 265-278 (2015).
34. Lowery, F.J.*, et al.* Molecular signatures of antitumor neoantigen-reactive T cells from metastatic human cancers. *Science* **375**, 877-884 (2022).
35. Van de Sande, B.*, et al.* A scalable SCENIC workflow for single-cell gene regulatory network analysis. *Nat Protoc* **15**, 2247-2276 (2020).
36. Jung, I.Y.*, et al.* BLIMP1 and NR4A3 transcription factors reciprocally regulate antitumor CAR T cell stemness and exhaustion. *Sci Transl Med* **14**, eabn7336 (2022).
37. Shin, H.*, et al.* A role for the transcriptional repressor Blimp-1 in CD8(+) T cell exhaustion during chronic viral infection. *Immunity* **31**, 309-320 (2009).
38. Man, K.*, et al.* Transcription Factor IRF4 Promotes CD8(+) T Cell Exhaustion and Limits the Development of Memory-like T Cells during Chronic Infection. *Immunity* **47**, 1129-1141 e1125 (2017).
39. Sade-Feldman, M.*, et al.* Defining T Cell States Associated with Response to Checkpoint Immunotherapy in Melanoma. *Cell* **175**, 998-1013 e1020 (2018).
40. Lee, P.C.*, et al.* Reversal of viral and epigenetic HLA class I repression in Merkel cell carcinoma. *J Clin Invest* **132**(2022).
41. Cottrell, T.R.*, et al.* Pathologic features of response to neoadjuvant anti-PD-1 in resected non-small-cell lung carcinoma: a proposal for quantitative immune-related pathologic response criteria (irPRC). *Ann Oncol* **29**, 1853-1860 (2018).
42. Stein, J.E.*, et al.* Pan-Tumor Pathologic Scoring of Response to PD-(L)1 Blockade. *Clin Cancer Res* **26**, 545-551 (2020).
43. Longino, N.V.*, et al.* Human CD4(+) T Cells Specific for Merkel Cell Polyomavirus Localize to Merkel Cell Carcinomas and Target a Required Oncogenic Domain. *Cancer Immunol Res* **7**, 1727-1739 (2019).

44. Jing, L.*, et al.* Cross-presentation and genome-wide screening reveal candidate T cells antigens for a herpes simplex virus type 1 vaccine. *J Clin Invest* **122**, 654-673 (2012).
45. Koelle, D.M. Expression cloning for the discovery of viral antigens and epitopes recognized by T cells. *Methods* **29**, 213-226 (2003).
46. Petersdorf, E.W.*, et al.* 16th IHIW: international histocompatibility working group in hematopoietic cell transplantation. *Int J Immunogenet* **40**, 2-10 (2013).
47. Williams, J.A. Improving DNA vaccine performance through vector design. *Curr Gene Ther* **14**, 170-189 (2014).
48. Koelle, D.M.*, et al.* CD8 CTL from genital herpes simplex lesions: recognition of viral tegument and immediate early proteins and lysis of infected cutaneous cells. *J Immunol* **166**, 4049-4058 (2001).
49. Iyer, J.G.*, et al.* Merkel cell polyomavirus-specific CD8(+) and CD4(+) T-cell responses identified in Merkel cell carcinomas and blood. *Clin Cancer Res* **17**, 6671-6680 (2011).
50. Jurtz, V.*, et al.* NetMHCpan-4.0: Improved Peptide-MHC Class I Interaction Predictions Integrating Eluted Ligand and Peptide Binding Affinity Data. *J Immunol* **199**, 3360-3368 (2017).
51. Robins, H.S.*, et al.* Comprehensive assessment of T-cell receptor beta-chain diversity in alphabeta T cells. *Blood* **114**, 4099-4107 (2009).
52. Goncharov, M.*, et al.* VDJdb in the pandemic era: a compendium of T cell receptors specific for SARS-CoV-2. *Nat Methods* **19**, 1017-1019 (2022).
53. Guo, X.*, et al.* Global characterization of T cells in non-small-cell lung cancer by single-cell sequencing. *Nat Med* **24**, 978-985 (2018).
54. Oh, D.Y.*, et al.* Intratumoral CD4(+) T Cells Mediate Anti-tumor Cytotoxicity in Human Bladder Cancer. *Cell* **181**, 1612-1625 e1613 (2020).

Supplementary Tables:

Supplementary Table 1: Summary of MHC-I tetramers used in FACS experiments on PBMC specimen (cohorts 1 & 2).

			Number of patients with allele	
Virus	HLA	Peptide	pCR	Non-pCR
MCPyV	A*02:01	KLLEIAPNC	4	2
MCPyV	A*03:01	AAFKRSCLK	1	0
MCPyV	A*03:01	RSGGFSFGK	1	0
MCPyV	A*11:01	RSGGFSFGK	0	1
MCPyV	A*24:02	EWWRSGGFSF	2	0
MCPyV	A*68:01	STPNGTSVPR	1	1
MCPyV	B*07:02	APNCYGNIPL	2	0
MCPyV	B*08:01	LNRKEREAL	0	1
MCPyV	B*15:01	FSFGKAYEY	1	1
MCPyV	B*35:01	FSFGKAYEY	2	0
MCPyV	B*35:02	FPWEEYGTL	0	0
MCPyV	B*35:02	HPDKGGNPVIM	0	0
MCPyV	B*37:01	KEWWRSGGF	0	0
MCPyV	B*44:02	KEWWRSGGF	1	1
MCPyV	B*57:01	GTTKFKEWW	1	0
MCPyV	B*57:01	FSFGKAYEY	1	0

Supplementary Table 2: MCPyV-specific CD8 T cells frequency in the peripheral blood broken down by patient and pathological response. **Bolded** HLA types indicate available MCPyV-tetramer. **Bolded and underlined** HLAs have 2 different epitopes (tetramers). **Bolded alone** have a single epitope (tetramer)

Publication ID	Viral Status	C1D1 Tetramer Frequency (% CD8)	C2D1 Tetramer Frequency (% CD8)	Prior to Resection Tetramer frequency (% CD8)	Response Site	Response Central	HLA	Total # of epitopes
1	Pos	0.015	NA	0	Non-pCR	Non-pCR/MPR	A0101 **A0301 B0801** B2707 C0701 C1502	3
2	Pos	0	0	0.00262	Non-pCR	Non-pCR/MPR	A0217 A2301 B1801 B4403 C0401 C1203	0
3	Pos	0	0.01155	0.00377	Non-pCR	Non-pCR/MPR	**A0201 A6801** B1801 **B4402** C0501 C0701	3
4	Pos	NA	NA	NA	pCR	pCR		
5	Pos	0.033	0.086	NA	pCR	pCR	**A0201 A0201 B1501** B4001 C0304 C0304	2
6	Pos	0.0752	NA	NA	pCR	pCR	**A0201 A2402 B0702 B4402** C0501 C0702	4
7	Pos	0.27	NA	0.108	pCR	pCR	**A0301 A2402 B3501** B5501 C0303 C0401	4
8	Pos	0.139	0.46	0.341	pCR	pCR	A0101 A2601 B4901 **B5701** C0602 C0701	2
9	Pos	0.00911	0.026734	0.05006	NE	NE	**A0201 A1101** B1501 B4001 C0304 C0401	2
10	Pos	0.014	0.012	0.013	pCR	NE	**A0201** A2501 **B0702** B3901 C0702 C1203	2
11	Pos	0.015	NA	0.00208	pCR	NT	**A0201** A2601 B3503 B3901 C0401 C1203	1
12	Pos	0.00884	NA	NA	NA	NA	**A0201 A6801** B1302 B5101 C0602 C1502	2
13	Pos	0	0.01364	NA	NA	NA	**A0201 A0201 B1501** B4001 C0303 C0304	2
14	Pos	0.04544	NA	NA	NA	NA	**A0201 A2402 B4402** B5601 C0102 C0501	3
15	Pos	0.072	0.12	0.018	pCR	NE	A0205 A2601 **B3501** B1801 C0401 C0701	1
16	Neg	0	0.00182	0.003983	Non-pCR	Non-pCR/MPR	**A0301** A2403 B1402 **B3501** C0401 C0802	3
17	Pos	0.074	0.31	0	pCR	pCR	A2601 **A6801** B5801 B5802 C0602 C0701	1
18	Neg	0	0.0079	0.00275	Non-pCR	Non-pCR/MPR	A0101 **A2402 B3501** **B3501** C0401 C0401	3
19	Pos	0	0	0	Non-pCR	MPR	A0101 A0101 **B0702** B1402 C0602 C0702	1
20	Neg	0.00282	NA	0.003137	Non-pCR	MPR	**A0301 A1101 B0702** **B0702** C0702 C1604	4

21	Neg	NA	0.00133	NA	pCR	pCR	**A0201 A2402 B1501** B1801 C0304 C0701	3
22	Neg	NA	0	0.00476	pCR	pCR	**A0201 A0201** B5001 B5101 C0602 C1402	1
23	Pos	0.03	NA	0.016	Non-pCR	MPR	**A0201** A3201 B1401 **B1501** C0304 C0802	2
24	Neg	0	0	0.00559	pCR	pCR	**A0201 A2402 B1501 B4402** C0303 C0501	4
25	Neg	0.00496	NA	0.00259	Non-pCR	Non-pCR/MPR	A0205 **A2402** B1402 B1501 C0303 C0802	2
26	Neg	0	NA	NA	pCR	pCR	**A0201 A0201 B0702 B4402** C0501 C0702	3
27	Neg	0.000642	0.00113	NA	Non-pCR	NT	**A2402** A3301 B1302 B1402 C0602 C0802	1
28	Pos	NA	0	NA	pCR	pCR	**A0301** A2601 **B0702** B3801 C0702 C1203	3
29	Neg	0	NA	0	Non-pCR	Non-pCR/MPR	A0101 **A0301 B0801 B3501** C0401 C0701	4
30	Pos	0.00483	0.00126	0	Non-pCR	NT	**A1101 A1101** B5001 B5601 C0102 C0602	1
31	Neg	0.00124	0.000646	0.000825	pCR	pCR	A0101 **A6801 B3701** B5101 C0602 C1502	2
32	Pos	0	NA	0	Non-pCR	NT	**A0201 A0201** B4403 **B5701** C0602 C1601	3
33	NE	0	0	NA	pCR	NE	A2402 A2501 B1801 B5109 C0102 C1203	0
34	Neg	0	0	0	pCR	NT	**A0201 A0301 B0702** B4901 C0701 C0702	4
35	NT	0.01877	NA	0.03493	NA	NA	A0101 **A0201 B0801 B4402** C0501 C0701	3
36	NT	0.014	0	NA	NA	NA	A0101 **A2402** B1517 B1801 C0701 C1203	1

Supplementary Table 3: MHC-I multimers used to identify MCPyV, Flu, CMV or EBV specific CD8 T cells identified from expanded T cells from neoadjuvant nivolumab trial (Cohort 1) or single cell RNAseq of direct ex vivo tumor and blood specimen (Cohort 3).

Virus	protein	sequence	HLA
CMV	pp50	VTEHDTLLY	A*01:01
Flu	NP	CTELKLSDY	A*01:01
Flu	M	GILGFVFTL	A*02:01
EBV	BMLF1	GLCTLVAML	A*02:01
CMV	pp65	NLVPMVATV	A*02:01
MCPyV	Common T	KLLEIAPNC	A*02:01
MCPyV	Common T	AAFKRSCLK	A*03:01
MCPyV	LT	RSGGFSFGK	A*03:01
CMV	IE-1	KLGGALQAK	A*03:01
Flu	NP	ILRGSVAHK	A*03:01
EBV	EBNA-3A	RLRAEAQVK	A*03:01
MCPyV	LT	RSGGFSFGK	A*11:01
MCPyV	ST	DYCLLHLHLF	A*24:02
MCPyV	LTA	EWWRSGGFSF	A*24:02
CMV	pp65	QYDPVAALF	A*24:02
Flu	PB1	SYINRTGTF	A*24:02
MCPyV	LT	STPNGTSVPR	A*68:01
MCPyV	LT	APIYGTTKF	B*07:02
MCPyV	Common T	HPDKGGNPV	B*07:02
MCPyV	Common T	APNCYGNIPL	B*07:02
CMV	pp65	RPHERNGFTVL	B*07:02
CMV	pp65	TPRVTGGGAM	B*07:02
EBV	EBNA-3A	RPPIFIRRL	B*07:02
MCPyV	Common T	LNRKEREAL	B*08:01
CMV	pp65	ELRRKMMYM	B*08:01
EBV	EBNA-3A	FLRGRAYGL	B*08:01
MCPyV	LT	FSFGKAYEY	B*15:01
MCPyV	LT	FSFGKAYEY	B*35:01
CMV	pp65	IPSINVHHY	B*35:01
EBV	EBNA-1	HPVGEADYFEY	B*35:01
MCPyV	ST	FPWEEYGTL	B*35:02
MCPyV	LT	KEWWRSGGF	B*37:01
MCPyV	LT	KEWWRSGGF	B*44:02
MCPyV	LT	GTTKFKEWW	B*57:01
MCPyV	LT	FSFGKAYEY	B*57:01
MCPyV	LT	DEVDEAPIY	B18:01

Supplementary Table 4: MCPyV, Flu, CMV or EBV specific CD8 T cells identified from expanded T cells from neoadjuvant nivolumab trial (Cohort 1) or single cell RNAseq of direct ex vivo tumor and blood specimen (Cohort 3).

Supplementary Table 5: List of gene sets used in this study. Signatures derived from references[13,39,53,54].

Supplementary Table 6: List of overlapping peptides and pools used in this study.

Supplementary Table 7: List of FACS and CITEseq antibodies used in this study.

T cell phenotyping panel					
Marker	**Fluorophore**	**Vendor**	**Clone**	**ul/test**	**Note**
CD3	AF532	Invitrogen	UCHT1	0.31	Intracellular
CD4	BUV805	BD	SK3	0.63	Surface
CD8	BV570	Biolegend	RPA-T8	0.63	Surface
MCC-Tetramer	APC		MCC specific		Pre-incubation
Live/Dead	Live dead Blue	ThermoFisher		0.5	Pre-incubation
CD14	BB700	BD	MφP9	0.625	Surface
CD19	BB700	BD	SJ25C1	0.15625	Surface
CCR7 (CD197)	BV605	Biolegend	GO43H7	5	Pre-incubation
CD45RA	BUV563	BD	HI100	0.16	Surface
CXCR3	Pacific blue	Biolegend	G025H7	1.25	Pre-incubation
CXCR5	BV480	BD	RF8B2	2.5	Pre-incubation
Tbet	BV785	Biolegend	4B10	0.63	Intracellular
PD1 (CD279)	AF488	Invitrogen	MIH4	5	Surface
Lag3	BV421	Biolegend	11C3C65	1.25	Intracellular
FoxP3	PE-Cy5	Invitrogen	PCH101	0.63	Intracellular
Tim3	BV650	BD	7D3	0.63	Surface
GZMK	PerCP-eF710	Invitrogen	G3H69	0.16	Intracellular
Tox	PE	Invitrogen	TXRX10	5	Intracellular
Eomes	PE-eF610	Invitrogen	WD1928	1.25	Intracellular
GZMB	APC-Fire750	Biolegend	QA16A092	0.31	Intracellular
CD28	BUV737	BD	CD28.2	2.5	Surface
CD56	BUV395	BD	NCAM16.2	5	Surface
CCR6	BUV496	BD	11A9	1.25	Pre-incubation
Ki67	AF700	Biolegend	B56	0.625	Intracellular
CCR4	BUV615	BD	1G1	5	Pre-incubation
TCF7	PE-Cy7	Cell Signaling Technology	C63D9	1.25	Intracellular
HLA-DR	BV711	Biolegend	L243	0.625	Surface
Control antibodies (for compensation)					
CD7	APC	BD	M-T701	1	Pre-incubation

scRNAseq FACS Sorting panel					
Marker	**Fluorophore**	**Vendor**	**Clone**	**ul/test**	**Note**
CD3	AF488	Biolegend	Sk7	2.5	Surface
CD4	AF700	Invitrogen	OKT4	2	Surface
CD8	BV570	Biolegend	SK1	0.63	Surface
CD19	BV421	BD	HIB19	0.31	Surface
CD56	PE-Cy7	BD	NCAM16.2	5	Surface

scRNAseq CITEseq antibodies				
Marker	**Barcode**	Clone	**ul/test**	**Vendor**
CD11b	GACAAGTGATCTGCA	ICRF44	0.0625	Biolegend
CD4	TGTTCCCGCTCAACT	RPA-T4	0.0625	Biolegend
CD39	TTACCTGGTATCCGT	A1	0.0625	Biolegend
CD3	CTCATTGTAACTCCT	UCHT1	0.0625	Biolegend
CD8a	GCTGCGCTTTCCATT	RPA-T8	0.0625	Biolegend
CD16	AAGTTCACTCTTTGC	3G8	0.0625	Biolegend
CD86	GTCTTTGTCAGTGCA	IT2.2	0.125	Biolegend
CD195	CCAAAGTAAGAGCCA	J418F1	0.125	Biolegend
CD27	GCACTCCTGCATGTA	O323	0.125	Biolegend
CD127	GTGTGTTGTCCTATG	A019D5	0.125	Biolegend
CD274	GTTGTCCGACAATAC	29E.2A3	0.125	Biolegend
CD28	TGAGAACGACCCTAA	CD28.2	0.125	Biolegend
CD107a	CAGCCCACTGCAATA	H4A3	0.125	Biolegend
CD62L	GTCCCTGCAACTTGA	DREG-56	0.125	Biolegend
CD45	TCCCTTGCGATTTAC	2D1	0.125	Biolegend
CD21	AACCTAGTAGTTCGG	Bu32	0.125	Biolegend
CD38	CCTATTCCGATTCCG	HB-7	0.125	Biolegend
CD14	TCTCAGACCTCCGTA	M5E2	0.25	Biolegend
CD15	TCACCAGTACCTAGT	W6D3	0.25	Biolegend

CD20	TTCTGGGTCCCTAGA	2H7	0.25	Biolegend
IgG1	GCCGGACGACATTAA	MOPC-21	0.25	Biolegend
IgG2a	CTCCTACCTAAACTG	MOPC-173	0.25	Biolegend
IgG2b	ATATGTATCACGCGA	MPC-11	0.25	Biolegend
CD137	CAGTAAGTTCGGGAC	4B4-1	0.25	Biolegend
CD56	TTCGCCGCATTGAGT	QA17A16	0.25	Biolegend
CD196	GATCCCTTTGTCACT	G034E3	0.25	Biolegend
CD183	GCGATGGTAGATTAT	G025H7	0.25	Biolegend
CD123	CTTCACTCTGTCAGG	6H6	0.25	Biolegend
CD1c	GAGCTACTTCACTCG	L161	0.25	Biolegend
CD57	AACTCCCTATGGAGG	QA17A04	0.25	Biolegend
CD272	GTTATTGGACTAAGG	MIH26	0.25	Biolegend
CD40	CTCAGATGGAGTATG	5C3	0.25	Biolegend
HLA-DR	AATAGCGAGCAAGTA	L243	0.25	Biolegend
CD278	CGCGCACCCATTAAA	C398.4A	0.25	Biolegend
CD69	GTCTCTTGGCTTAAA	FN50	0.25	Biolegend
CD194	AGCTTACCTGCACGA	L291H4	0.25	Biolegend
CD11c	TACGCCTATAACTTG	S-HCL-3	0.25	Biolegend
CD71	CCGTGTTCCTCATTA	CY1G4	0.25	Biolegend
CD19	CTGGGCAATTACTCG	HIB19	0.5	Biolegend
CD25	TTTGTCCTGTACGCC	BC96	0.5	Biolegend
CD45RO	CTCCGAATCATGTTG	UCHL1	0.5	Biolegend
CD279	ACAGCGCCGTATTTA	EH12.2H7	0.5	Biolegend
TIGIT	TTGCTTACCGCCAGA	A15153G	0.5	Biolegend
CD103	GACCTCATTGTGAAT	Ber-ACT8	0.5	Biolegend
CD185	AATTCAACCGTCGCC	J252D4	0.5	Biolegend
CD366	TGTCCTACCCAACTT	F38-2E2	0.5	Biolegend
CD141	GGATAACCGCGCTTT	M80	0.5	Biolegend
CD303	GAGATGTCCGAATTT	201A	0.5	Biolegend
CD152	ATGGTTCACGTAATC	BNI3	0.5	Biolegend
CXCR6	GACAGTCGATGCAAC	K041E5	0.5	Biolegend
Hashtag1	GTCAACTCTTTAGCG	LNH-94; 2M2	0.5	Biolegend
Hashtag2	TGATGGCCTATTGGG	LNH-94; 2M3	0.5	Biolegend
Hashtag3	TTCCGCCTCTCTTTG	LNH-94; 2M4	0.5	Biolegend
Hashtag4	AGTAAGTTCAGCGTA	LNH-94; 2M5	0.5	Biolegend
Hashtag5	AAGTATCGTTTCGCA	LNH-94; 2M6	0.5	Biolegend
Hashtag6	GGTTGCCAGATGTCA	LNH-94; 2M7	0.5	Biolegend
Hashtag7	TGTCTTTCCTGCCAG	LNH-94; 2M8	0.5	Biolegend
Hashtag8	CTCCTCTGCAATTAC	LNH-94; 2M9	0.5	Biolegend
Hashtag9	CAGTAGTCACGGTCA	LNH-94; 2M10	0.5	Biolegend
Hashtag10	ATTGACCCGCGTTAG	LNH-94; 2M11	0.5	Biolegend

Due to size of tables, Supplementary Tables 4, 5 and 6 are not included here. Please email thpullia@uw.edu, Pulliam.thomas@gmail.com or pnghiem@uw.edu for an electronic copy.

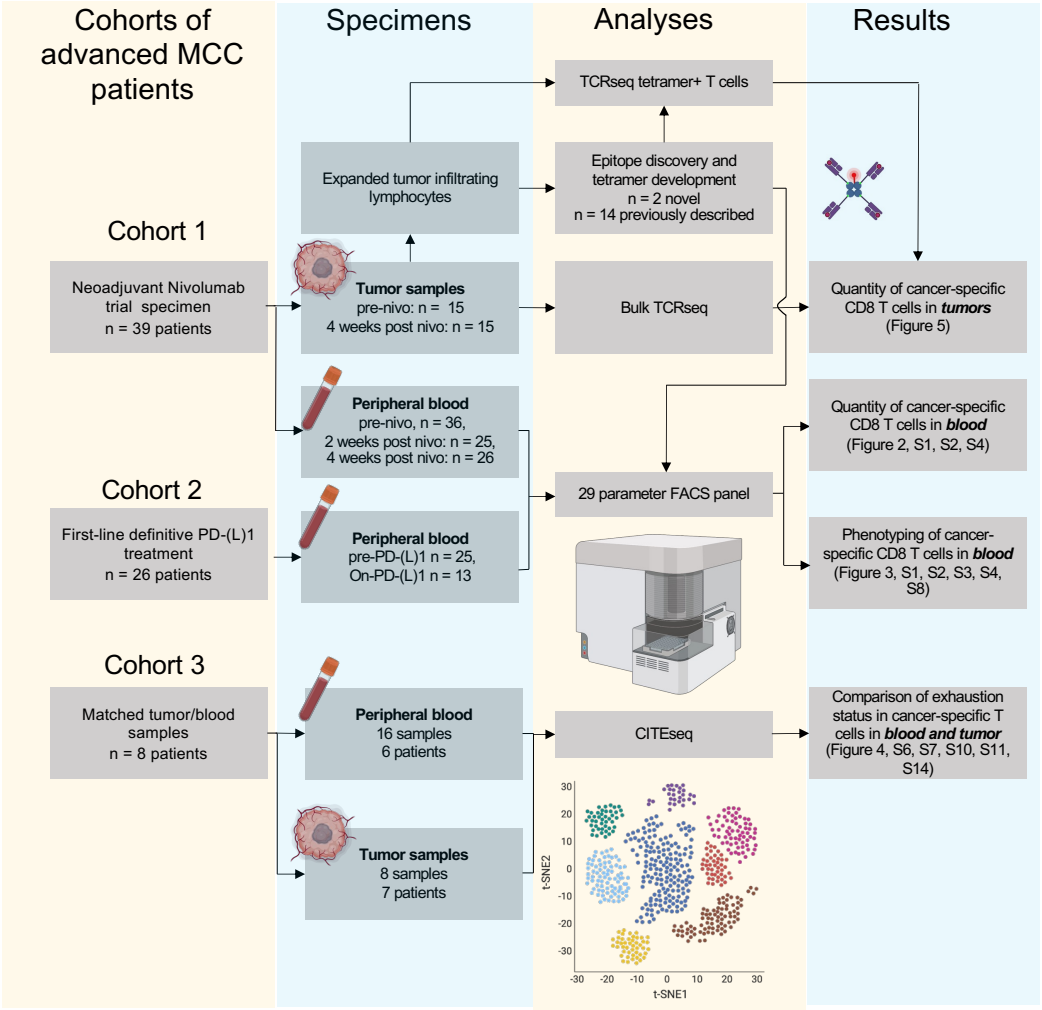

Figure 1. Overview of patient cohorts studied, analyses performed and result outputs (figures)

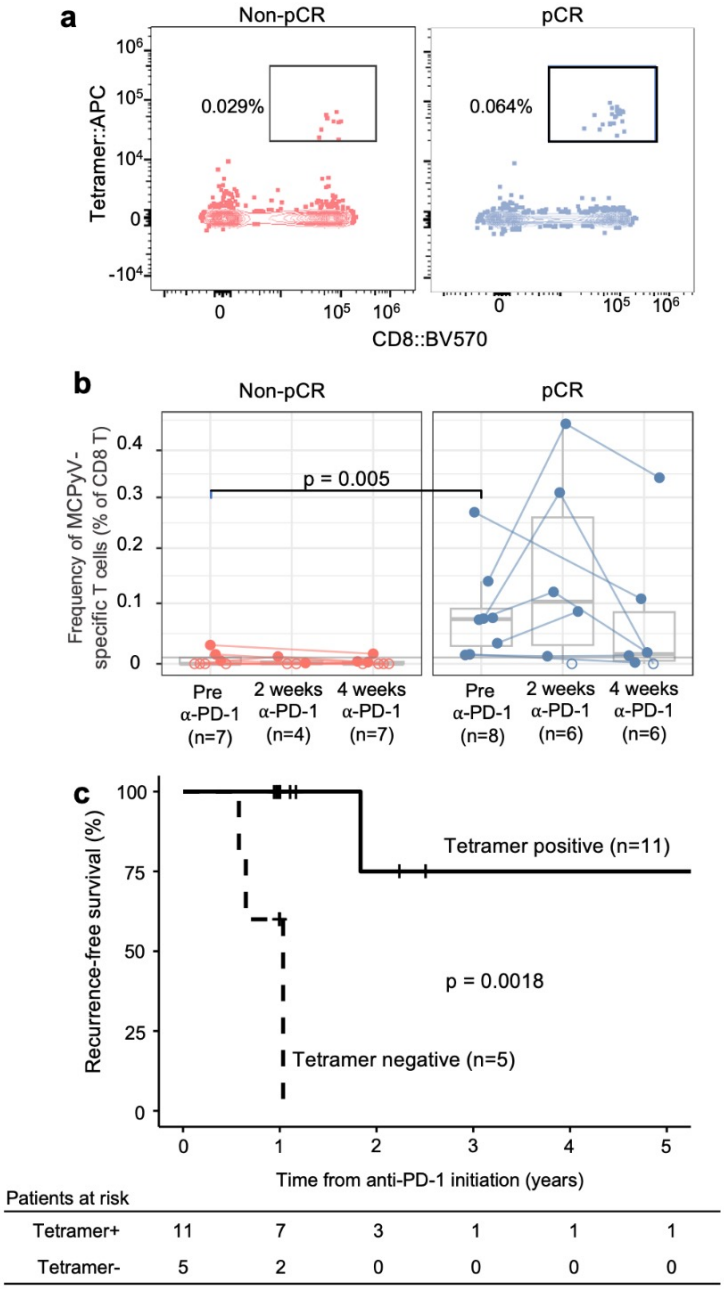

Figure 2. Associations between clinical outcomes and relative frequency of MCPyV-specific CD8 T cells in blood

A. Example of MHC-I tetramer staining for a B*18:01 allele containing an MCPyV peptide from a representative patient with a non-pathological complete response (left) and a patient with a pathological complete response (right). Frequencies shown represent the portion of tetramer binding T cells as a portion of CD8 T cells

B. Comparison of MCPyV-specific CD8 T cell frequencies in patients who did or did not have a pathological complete response. Hollow points represent no detectable MCPyV-specific CD8 T cells. Statistical differences in MCPyV-specific T cell frequency prior treatment measured using two sided Wilcoxon rank sum test.

C. Kaplan-Meier plot of recurrence-free survival in patients with detectable MCPyV-specific CD8 T cells (tetramer positive) or undetectable levels (tetramer negative). Limit of detection at 1 in 10,000 CD8 T cells (Supplemental figure 1). Recurrence events defined as tumor recurrence or death due to any cause as in original trial protocol. Statistical differences in recurrence free survival measured by log rank test.

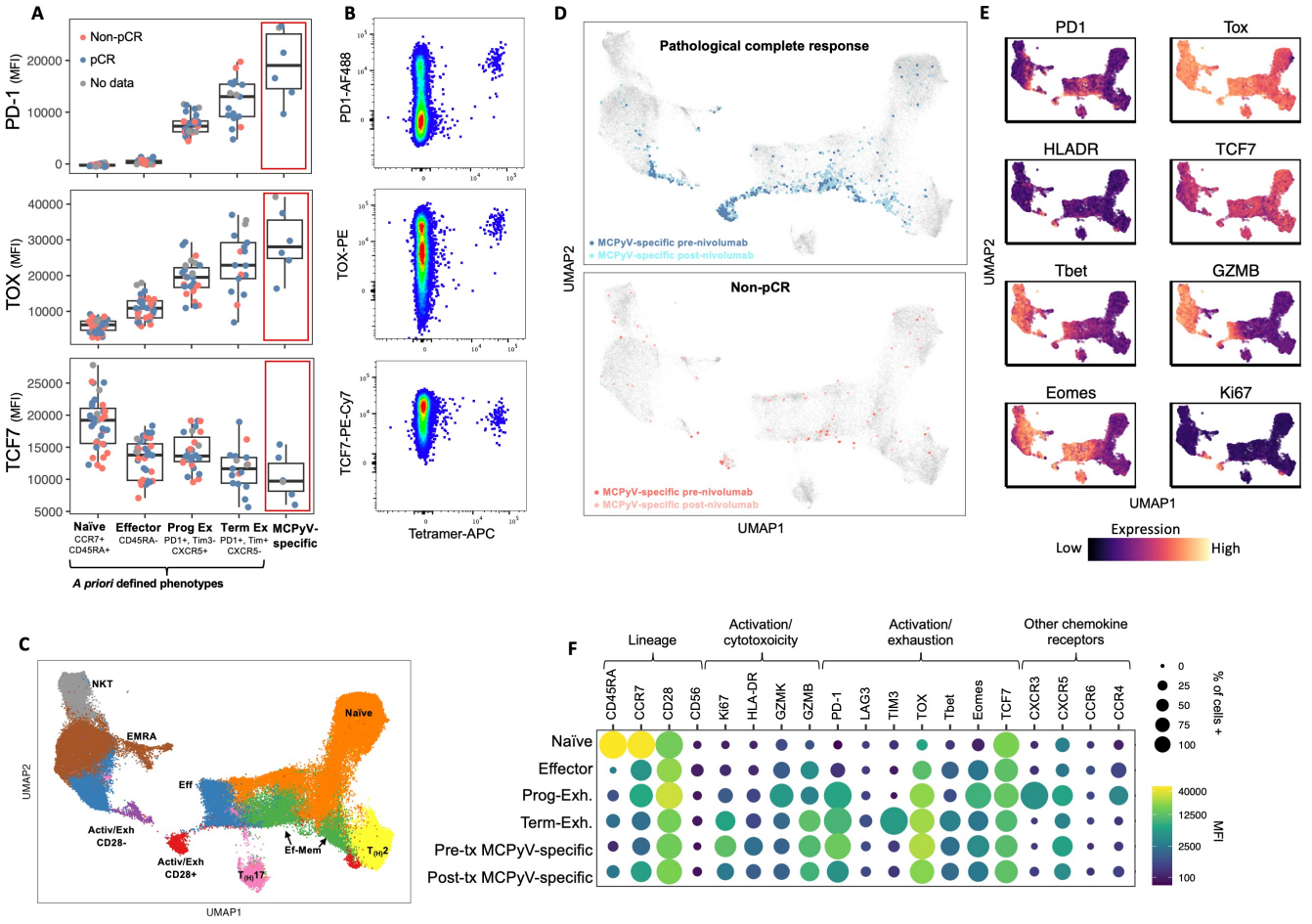

Figure 3: Circulating cancer-specific CD8 T cells exhibit characteristics of exhaustion and were detected in patients with pathological complete responses

A. Expression of key exhaustion markers in CD8 T cell populations or tetramer+ CD8 T Cells from pre-nivolumab samples. Populations with less than 10 cells were excluded

B. Representative FACS plot of CD8 T cells showing tetramer fluorescence versus the exhaustion markers used in panel A

C. UMAP plots of CD8 T cells from blood. Cells grouped, colored and labeled using phonograph clustering (PMID: 26095251)

D. UMAP plots of CD8 T cells as in panel C. MCPyV-specific T cells in patients with pCR (top) or non-pCR (bottom)

E. Expression of 8 differentiation-related proteins using same UMAP overlay as panels C and D

F. Relationship of protein expression in defined populations and MCPyV-specific CD8 T cells. As indicated in legends, size of each circle represents the portion of cells positive for that marker via canonical flow cytometry gating. color represents the median fluorescence intensity of each protein in each population

Abbreviations: MFI, median fluorescence intensity; AF488, Alexa Fluor 488; PE, phycoerythrin; APC allophycoerythrin, UMAP; uniform manifold approximation and projection; GZMB, Granzyme B; Proj Ex, progenitor exhausted; Term Ex, terminal exhausted; MCPyV, Merkel cell polyomavirus; EMRA, Effector-memory RA positive; Activ/exh, Activated/exhausted; tx, treatment

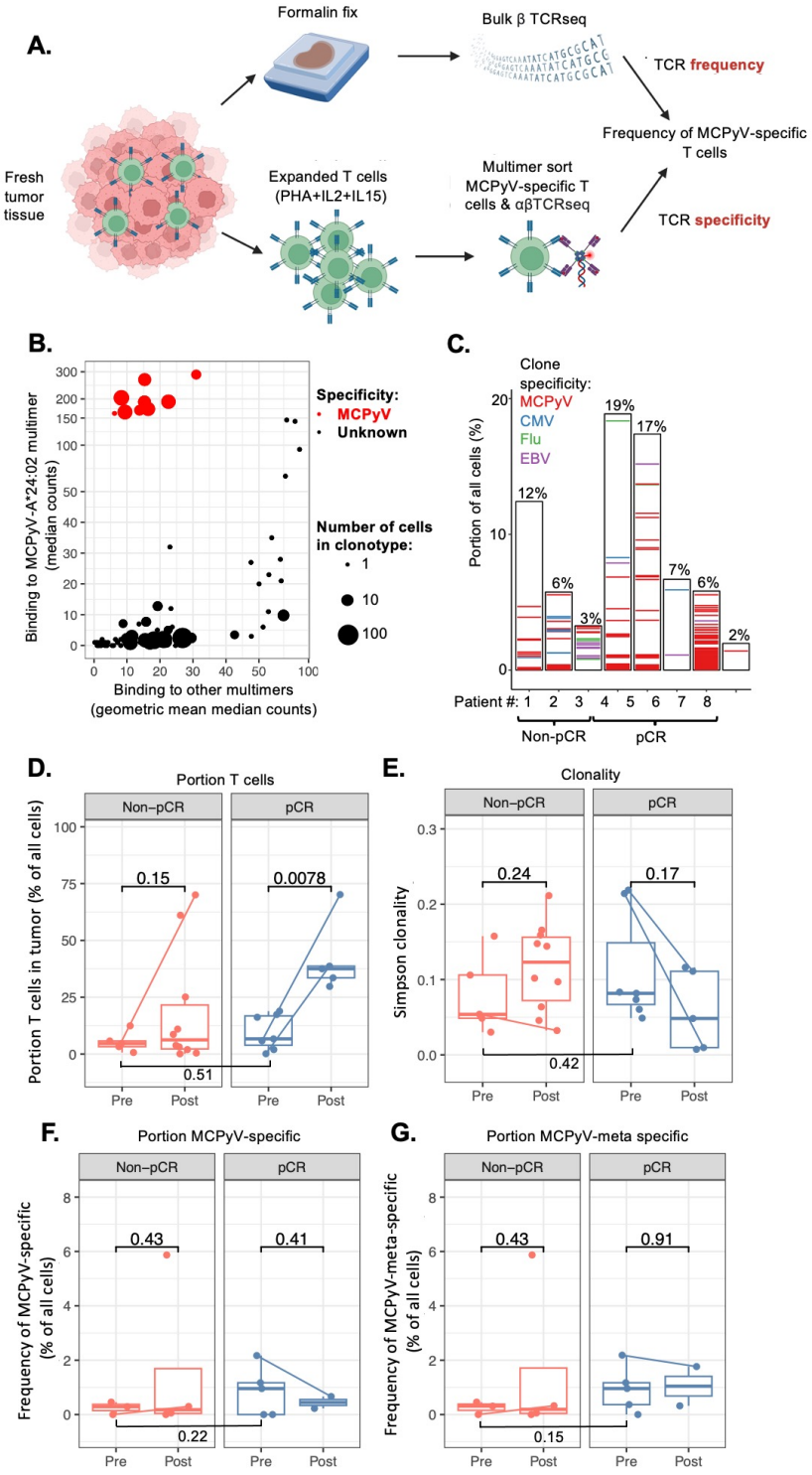

Figure 4. MCPyV-specific T cells are present in tumors regardless of anti-PD-1 therapy response

A. Graphical schematic describing experimental approach to identifying antigen-specific intratumoral CD8 T cells.

B. Representative plot of multimer binding to tumor infiltrating lymphocytes expanded from a from a single patient's tumor. Cells with identical alpha and beta TCR chains (clonotypic) were grouped with number of cells per clonotype as indicated. Median multimer counts were calculated for each multimer and clonotype. Biexponential axis transformation was used for visualization.

C. Extent of T cell infiltration and anti-viral specificity in pre-treatment tumors from 8 patients with pathologic complete response (pCR) or non-pCR as indicated. Bar height represents the proportion of all tumor cells that are T cells (indicated by % atop bar). Color of individual bars indicates viral specificity as per legend (MCPyV, EBV, CMV or Flu). Thickness of each colored bar is proportional to the number of T cells in a virus-specific clonotype. White portions of bar represent T cell clonotypes of unknown specificity.

D. Frequency of T cells with productive TCRs in tumor specimens before and after immunotherapy in patients who had a pCR (right) or did not (left). Patients with paired pre- and post-biopsy

E. Simpson clonality of productive TCRs in tumor specimens before and after immunotherapy in patients who had a pCR (right) or did not (left).

F. Frequency of MCPyV-specific T cells as a fraction of T cells in tumor specimens before and after immunotherapy in patients who had a pCR (right) or did not (left).

G. Frequency of CD8 T cells with an exact match to a MCPyV-specific TCR or a similar TCR (TCRdist radius <= 9) as a fraction of all cells in tumor specimens before and after immunotherapy in patients who had a pCR (right) or did not (left).

Abbreviations: Non-pCR, non-pathological complete response; pCR pathological complete response; TCR, T cell receptor

p values: ns >= 0.05; * <0.05; **<0.01, *** <0.001, ****<0.0001. All statistical tested using T tests

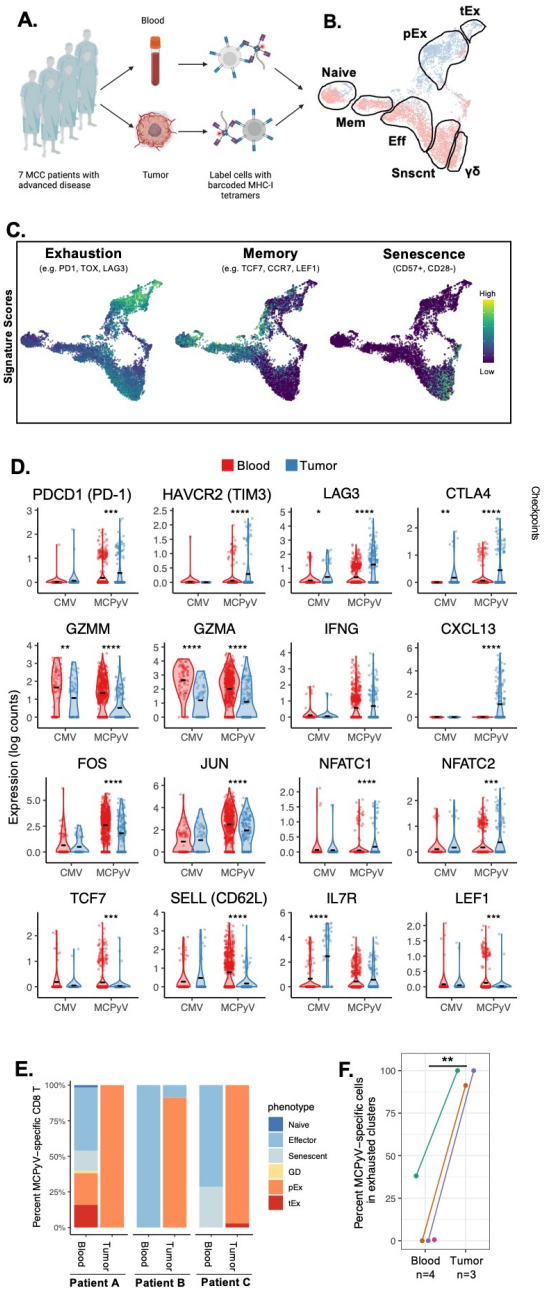

Figure 4 Transcriptomic & proteomic profiling of antigen-specific CD8 T cells in matched tumors and blood.

A. Schematic of experimental design. Matched tumor and blood specimens from 7 patients (cohort 3 in Figure 1) were labeled with barcoded MHC-I multimers and CITEseq was performed.

B. UMAP plot of CD8 T cells colored by origin from blood (pink) or tumor (blue). Clusters outlined in black.

C. UMAP plots (yellow equals high expression) of indicated gene signatures for different T cell programs of interest

D. Violin plots of exhaustion, memory, and checkpoint gene sets for MCPyV- and CMV-specific CD8 T cells from tumor or blood

E. Portions of MCPyV-specific T cells in each cluster as in B.

F. Comparison of frequency of MCPyV-specific CD8 T cells in each cluster as in E. p = 0.0016 using unpaired t.test

Abbreviations: Mem, memory; Eff, effector; Snscnt, Senescent; GD/**γδ** Gamma Delta T cells; pEx, progenitor exhausted, tEx; terminally exhausted.

p values: ns >= 0.05; * <0.05; **<0.01, *** <0.001, ****<0.0001

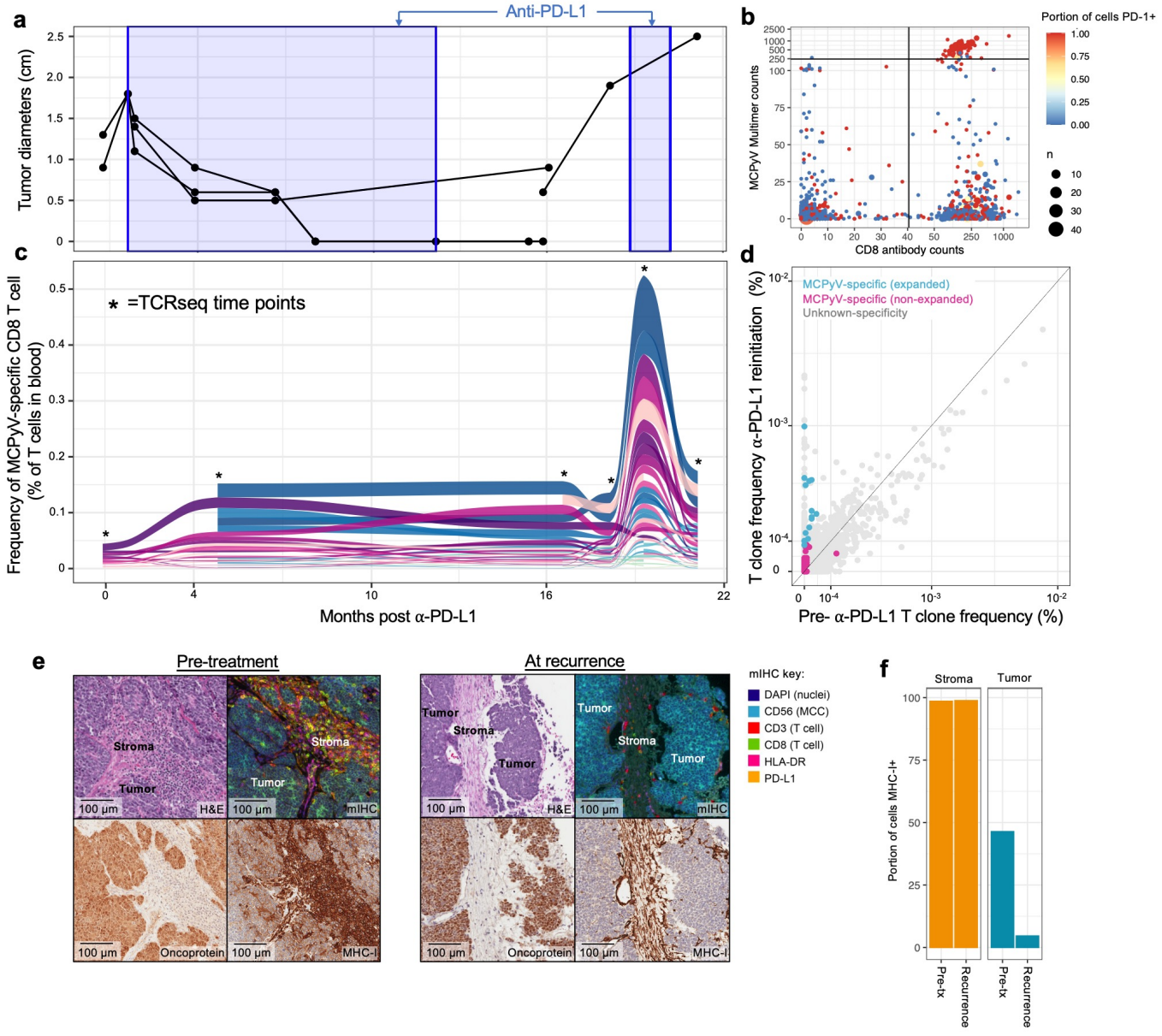

Figure 6. MHC-I downregulation during secondary resistance to PD-1 pathway blockade.

a. Clinical course of patient treatment. Patient had an initial partial response via RESIST criteria followed by recurrent disease. Each line represents an individual lesion. Periods of anti-PD-L1 treatment shaded in blue.

b. Frequency of T cell clones prior to immunotherapy compared to at the time of secondary resistance. Expanded clones determined via statistical difference between pre immunotherapy sample and immunotherapy reinitiation samples (beta binomial test; $p < 0.01$).

c. Alluvial plot of MCPyV-specific CD8 T cell clones as a portion of all T cells in blood. Cells present prior to anti-PD-L1 therapy colored in magenta shades. Cells appearing following anti-PD-L1 initiation shaded blue. Asterisks represent timepoints where TCRseq was performed.

d. Expression of pan-HLA-ABC on tumor cells at pre-treatment and secondary resistance time points.

e. Histology, MCPyV T antigen expression, and HLA-ABC expression on pre-treatment and secondary resistant tumors. Bottom left square is H&E and low magnification. Bottom right square is multiplexed IHC image with key to right of figure. Scale bars vary by sample and are indicated below images.

f. Quantification of MHC expression on stroma or tumor cells shown in panel e.

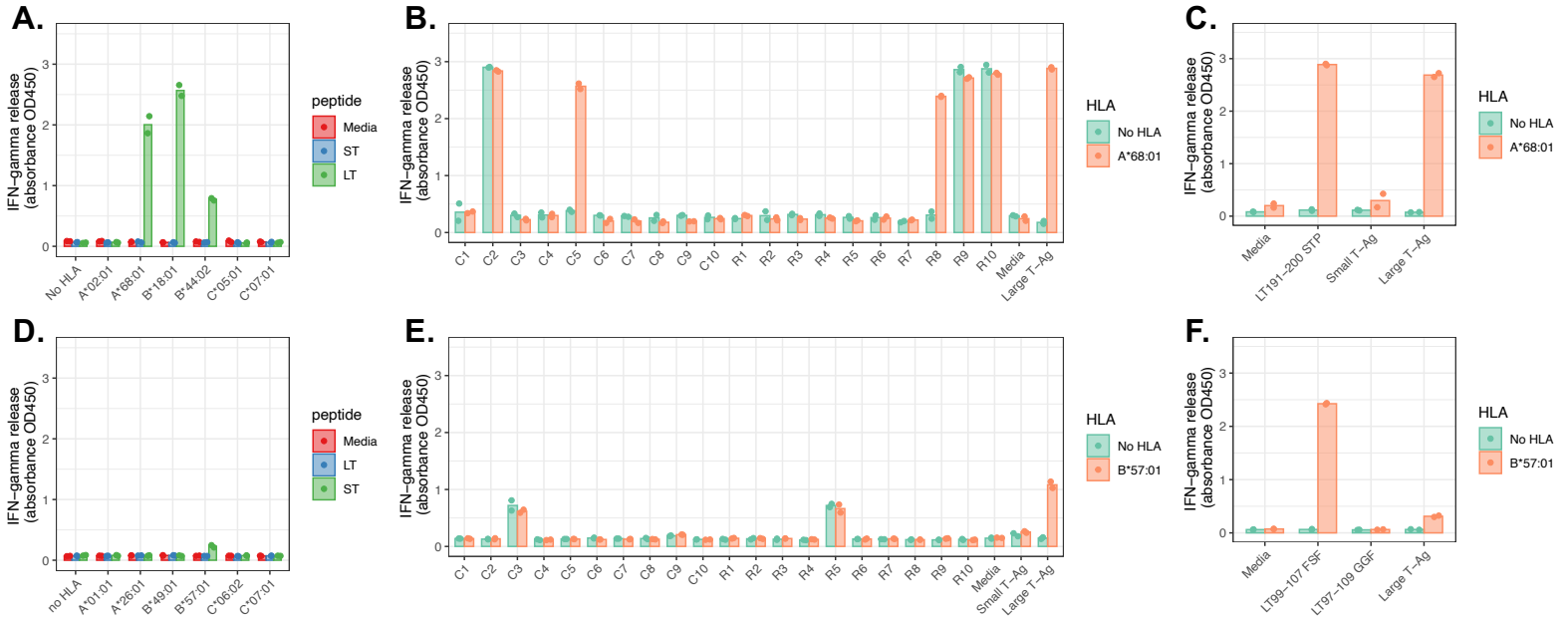

Supplemental Figure 1. Data illustrating MCPyV T-Ag CD8+ T-cell epitope discovery using artificial antigen presenting Cos7 cells (aAPC) for novel A*68:01(top) and B*57:01 (bottom) restricted MCPyV epitopes.

A. Subject 3's TILs were incubated with aAPCs after 48 hours co-transfected with HLA-A*02:01, A*68:01, B*18:01 or B*44:02 and MCPyV ST or LT

B. Subject 3′s TILs were incubated with A*68:01–transfected aAPCs and pulsed with matrix T-Ag peptides (no wash after peptides pulse). TILs were incubated with aAPCs either transfected with no HLA cDNA (left) A*68:01 (center). Details were described in PMID: 32179557.

C. A*68:01 transfected or HLA unstransfected COS-7 were pulsed with predicted peptide LT191-200 STP, or media or co-transfected with small T antigen or large T antigen expression plasmids. TIL from subject 3 were added after pulsed peptide washing

D. Subject 8 TILs were incubated with aAPCs after 48 hours co-transfected with HLA-A*01:01, A*26:01, B*49:01 or B*57:01 and with MCPyV ST or LT

E. Subject 8′s TILs were incubated with aAPCs either transfected with no HLA cDNA (left) or B*57:01 (right) aAPCs and pulsed with matrix T-Ag peptides (no wash after peptides pulse).

F. B*57:01 transfected COS-7 or HLA unstransfected COS-7 were pulsed with predicted peptide LT99-107 FSF (this one was found in the 2020 paper, but restricted by B*15:01 and B*35:02, but novel B*57:01 in this paper), peptide LT97-107 GGF (This one is found in the previous 2020 paper also), or media or transfected with large T antigen expression plasmid. Subject 8 TIL were added and Interferon gamma release was measured.

All assays performed in duplicate. Each plotted point represents one replicate.

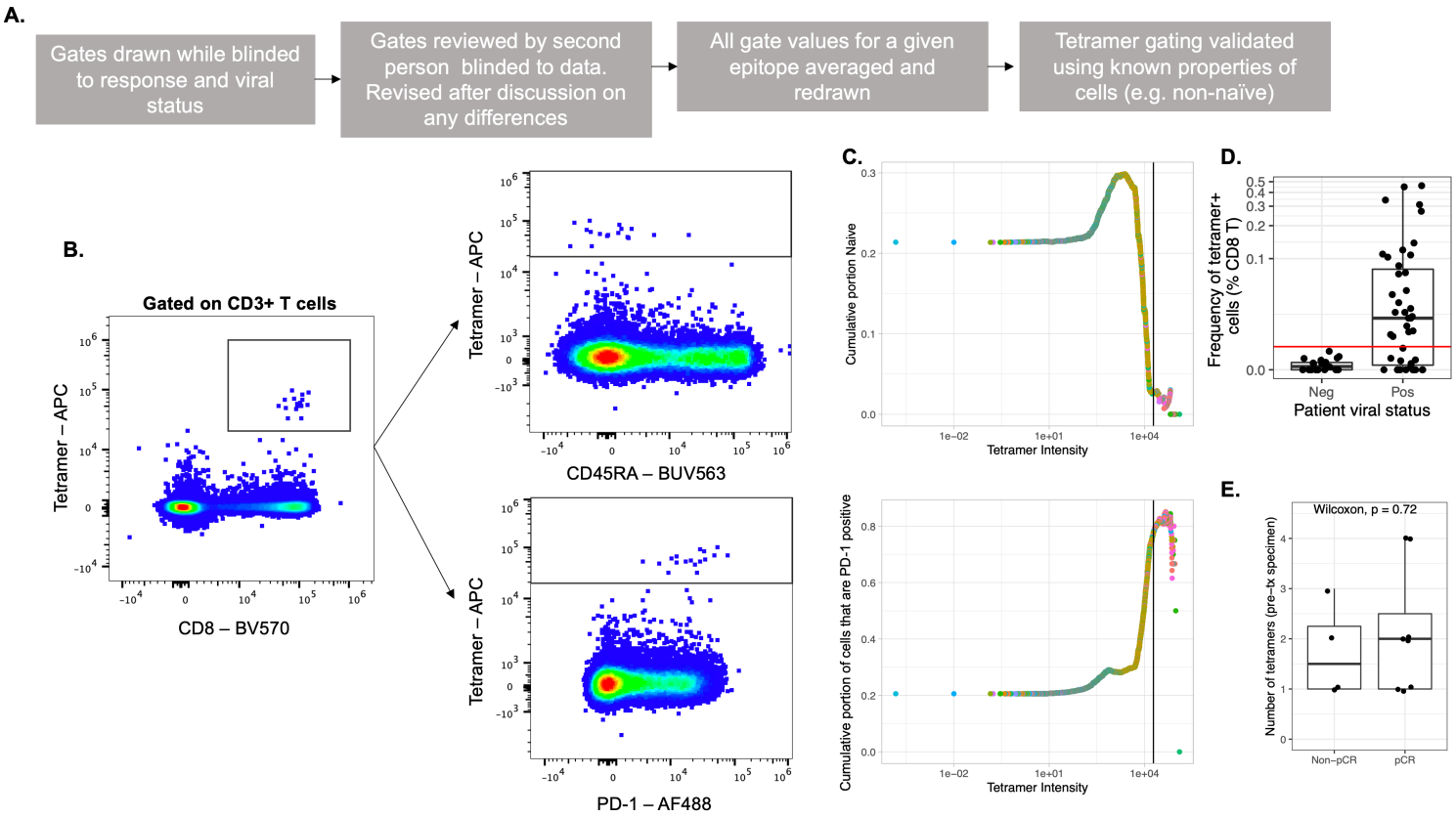

Supplemental figure 2. Tetramer gating strategy and validation approach

A. Flow chart of tetramer gating strategy

B. Example of PBMC stained with Tetramer FACS plots used to draw tetramer gate (left) and validation that gate follows known biology (right)

C. Cumulative density plot of portions of cells that are naïve (top) or PD-1+ (bottom) as a function of fluorescent intensity in the tetramer channel. Cumulative density is calculated from high tetramer intensity to low (ie right to left). Each individual point represents a CD8 T cell colored by the patient of origin.

D. frequency of tetramer positive cells in virus positive (Pos) or virus negative (Neg) patients. Each point represents a patients blood draw.

E. Comparison of the number of epitopes tested for patients that had complete pathological response or non-pathological complete responses

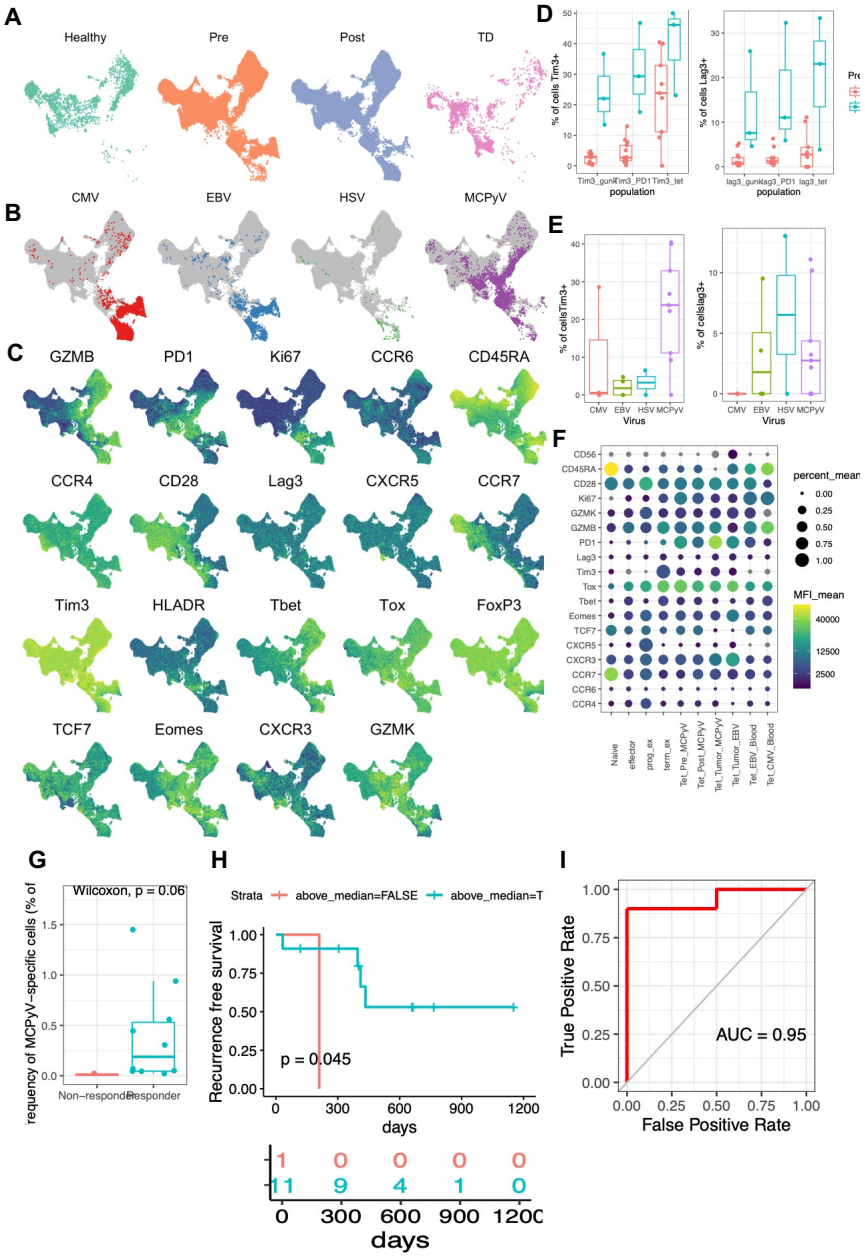

Supplemental figure 3. Validation cohort of flow cytometry on immunotherapy treated patients. All data gated on CD8 T cells.

A. UMAP plot of CD8 T cells from healthy control PBMC (far left) CD8 T cells from pre-treatment immunotherapy treated patients (center left) post-treatment immunotherapy treated patients (center right) or MCC tumor (far right). Each point represents a single cell. UMAP plot calculated using biexponetial transformed flow cytometry data. Same UMAP used in panels A, B and C.

B. UMAP plot colored by specificity of CD8 T cells

C. Expression of markers in UMAP space

D. Expression of TIM3 and LAG3 on MCC-specific T cells in blood or tumor tissues. Each point represents one patient

E. Expression of TIM3 and LAG3 on CD8T cells of various specificities. Each point represents one patient. All data from PBMC

F. Expression of FACS markers on various T cell populations and specificities. Data averaged across all patients. Size of points represents the portion of cells positive for each marker. Colors of points represents median fluorescent intensity

G. Frequency of MCPyV-specific CD8 T cells in patients who did or did not respond to anti-PD-(L)1 therapy.

H. Recurrence free survival of MCC patients following grouped by presence of MCPyV-specifc CD8 T cells above the threshold of detection (blue) or below threshold (red).

I. Receive operator characteristic curve showing predictive value of presence of MCPyV-specific CD8 T cells in blood for immunotherapy response.

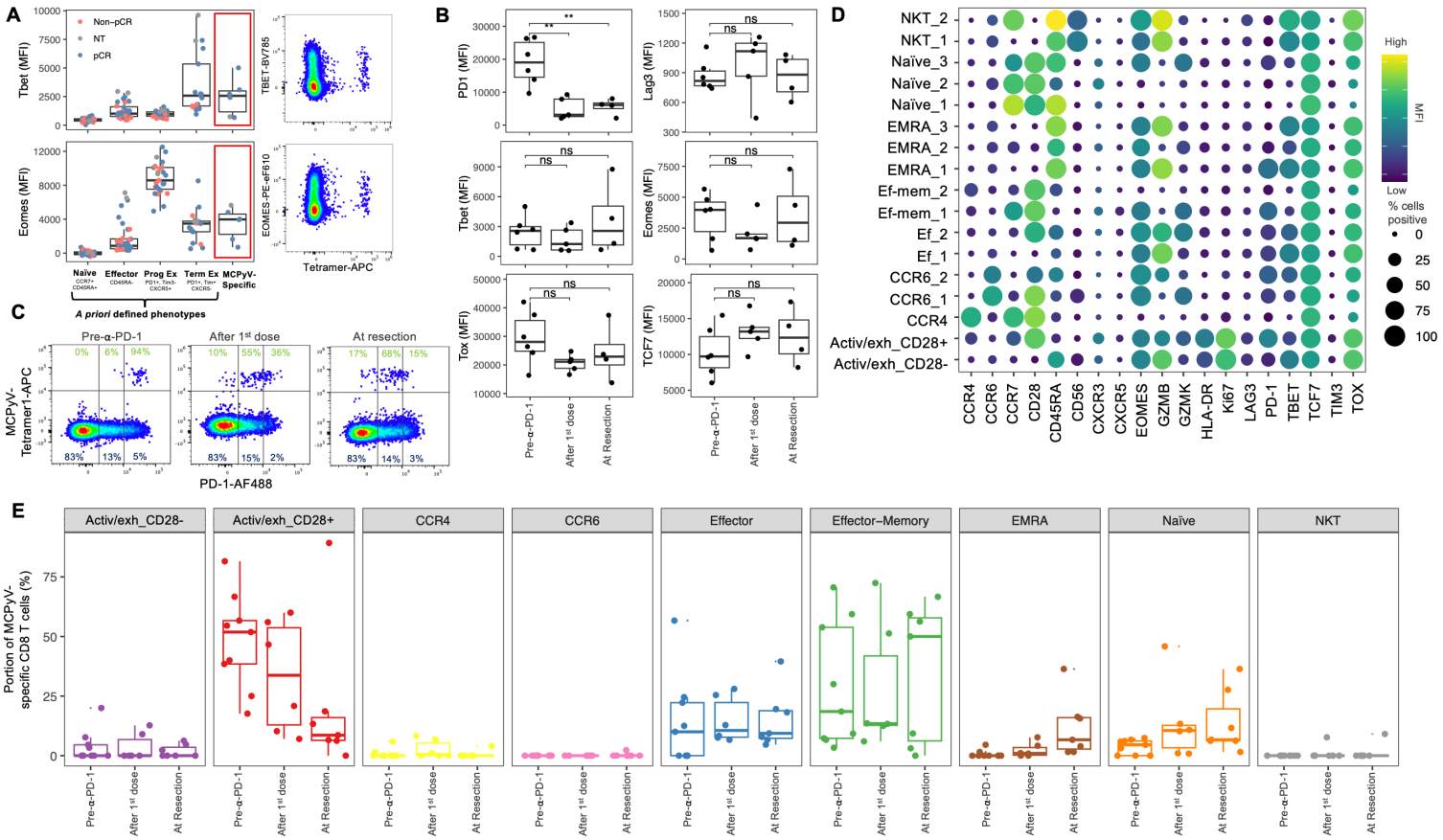

Supplemental figure 4. MCPyV-specific CD8 T cells downregulate PD-1 over the course of anti-PD-1 therapy.

A. Expression of T-bet and Eomes proteins in naïve, effector, progenitor exhausted, terminally exhausted and MCPyV-specific T cells via flow cytometry. Each point represents MCPyV-specific T cells from one patient at the pre-treatment time point. If a patient has less than 10 cells for a given population, that point was excluded.

B. Changes in expression of PD-1, LAG3, T-bet, Eomes, TOX and TCF7 protein expression in MCPyV-specific CD8 T cells over the course of anti-PD-1 therapy. Each point represents MCPyV-specific T cells from one patient at that time point. T tests were used for statistical significance. p values: ns = $p>0.05$; * = $p\leq0.05$; ** = $p\leq0.01$; *** = $p\leq0.001$; **** = $p\leq0.0001$

C. Representative Flow cytometry dot plots showing down regulation of PD-1 in MCPyV-specific CD8 T cells over the course of therapy. Gates drawn for PD-1 High, PD-1 middle and PD-1 negative cells. Percentages in top of plots (green) represent portion of tetramer+ (MCPyV-specific) cells. Percentages on bottom of plots (dark blue) represent portions of tetramer negative cells (unknown specificity).

D. Justification of phonograph clustering labels. CD8 T cells were clustered using flow cytometry data (panel E and Figure 2C) to assign phenotypic labels to each cluster, the MFI and portion of cells positive for each marker were tabulated for each cluster and plotted. Phenotypic labels y-axis labels) were then assigned based on the expression of these makers.

E. Phenotypes of MCPyV-specific CD8 T cells and changes over course of therapy. Each point represents MCPyV-specific T cells from one patient at the designated time point. If a patient has less than 10 cells for a given population, those point was excluded.

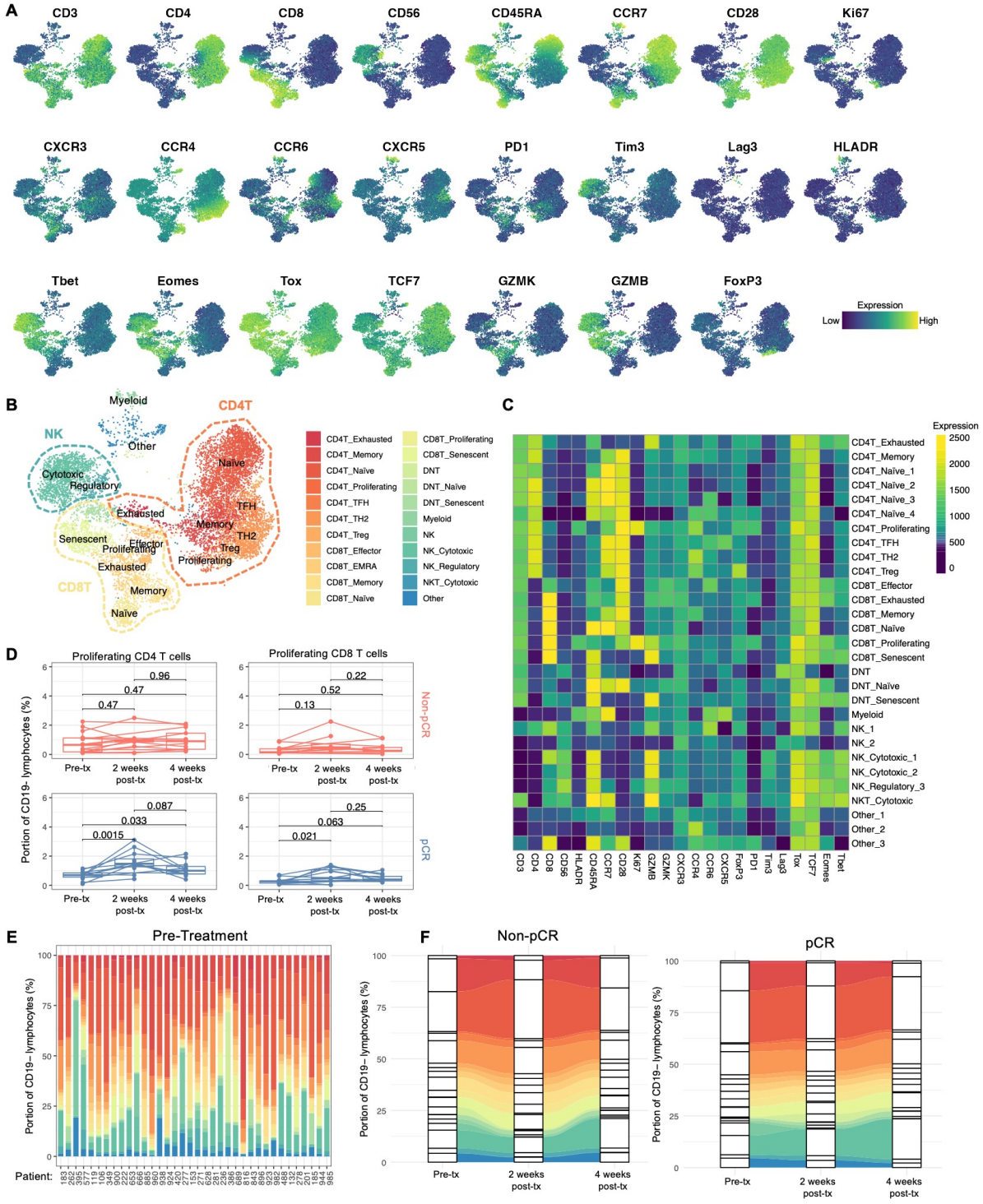

Supplemental figure 5. Analyses of bulk lymphocyte flow cytometry show association between pathological response and increases in proliferating CD4 and CD8 T cells in blood following anti-PD-1 blockade

A. UMAP plots of key markers of CD19- lymphocytes using 29 parameter flow cytometry data.

B. UMAP plot of same projection in A, pseudo colored by phonograph clustering.

C. Heatmap of each phonograph cluster (y axis) and the median expression of markers (x axis).

D. Frequency of proliferating CD4 (left) or CD8 (right) T cells over the course of neoadjuvant PD-1 blockage grouped by patients with non-pCRs (top) or pCRs (bottom). T tests were used to establish statistical significance.

E. Proportion of each phonograph cluster in each patient prior to treatment (Same color scale as panel B) .

F. Changes in proportions of phonograph clusters over the course of neoadjuvant PD-1 blockade. Proportions averaged across all patients with Non-pCRs (left) or pCRs (right).

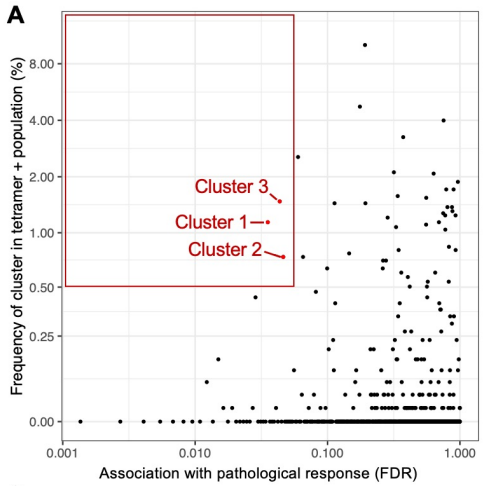

B

Marker	Cluster 1	2	3
CD28	+	+	-
GZMB	+	+	+
CCR7	+	+	-
Eomes	+	+	-
CCR4	-	-	-
GZMK	+	+	-
CD45RA	-	-	+
Tbet	-	-	-
CD56	-	-	-
PD1	+	+	-
CCR6	-	-	-
HLA-DR	+	-	-
TOX	+	+	+

C

		Ranking of most important markers in each cluster																
		1	2	3	4	5	6	7	8	9	10	11	12	13	14	15	16	17
Cluster 1a (Exhausted)	Markers	Eomes+	GZMB+	Ki67-	Tox+	CCR7+	CD28+	CD45RA-	CCR4-	Lag3-	CD56-	CCR6-	Tim3-	Tbet-	PD1+	CXCR5-	GZMK+	HLADR+
	p value	0.0208	0.0095	0.0069	0.0397	0.0391	0.027	0.0209	0.0184	0.0172	0.017	0.0171	0.0179	0.021	0.029	0.0373	0.0581	0.1676
Cluster 1b (Exhausted)	Markers	PD1+	GZMB+	CCR4-	CCR7+	HLADR+	Lag3-	Tbet-	Lag3-	CD28+	Tim3-	CD45RA-	CCR6-	CD56-	Eomes+	Ki67+	Tox+	CXCR5-
	p value	0.102	0.0008	0.0008	0.0765	0.0977	0.078	0.0595	0.0479	0.041	0.035	0.02889	0.0289	0.029	0.034	0.0445	0.0601	0.0836
Cluster 2 (Exhausted)	Markers	Eomes+	GZMB+	Ki67-	Tbet-	Tox+	CCR7+	HLADR-	GZMK+	CD45RA-	CCR4-	CCR6-	CD56-	CD28+	Lag3-	Tim3-	CXCR5-	PD1+
	p value	0.0208	0.0095	0.0069	0.0199	0.0302	0.03	0.0211	0.0172	0.0173	0.011	0.0107	0.0106	0.011	0.011	0.0115	0.0275	0.0497
Cluster 3 (Senescent)	Markers	Tbet-	Tox+	CD28-	CD45RA+	HLADR-	CD56-	Ki67-	Tim3-	CCR6-	CCR7-	GZMB+	CXCR5-	CCR4-	Lag3-	Eomes-	GZMK-	PD1-
	p value	0.416	0.486	0.0536	0.0367	0.0268	0.013	0.00984	0.0098	0.0992	0.011	0.011	0.0115	0.012	0.013	0.0404	0.0529	0.0747

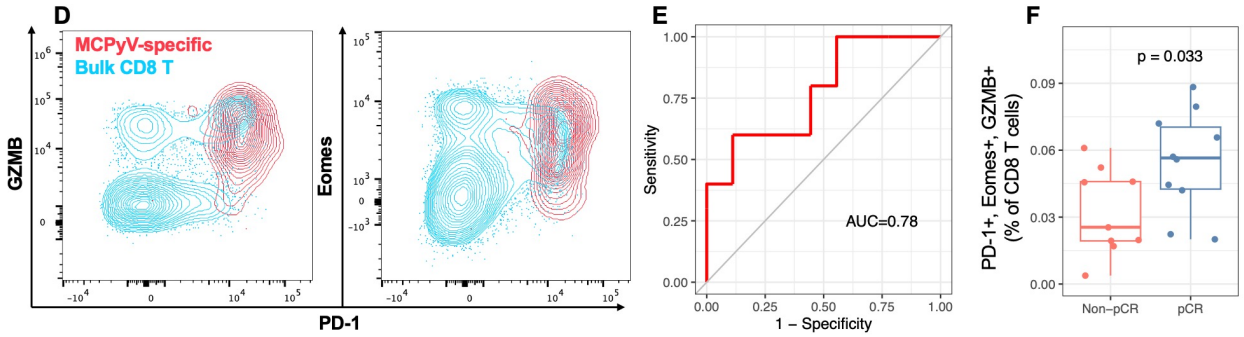

Supplemental figure 6. Machine learning algorithm identifies a PD-1+, Granzyme B+ and Eomes+ CD8 T cell population that is enriched for cancer-specific T cells and associates with response to PD-1 blockade. FAUST (PMID: 34950900) was used to iteratively gate CD8 T cells into unique clusters. Association of each cluster with pathological response (x axis) and enrichment in cancer-specific CD8 T cells (y axis). Each point represents one FAUST cluster averaged across all patients at the pre-treatment timepoint. Association with response calculated using T test of cluster frequency in patients with pCR versus non-pCR and adjusted for multiple comparisons using the Benjamini–Hochberg procedure. Clusters with a q value of less than 0.05 and more than 0.5% of MCPyV-specific T cells were selected for further analysis (red box)

A. Key identifying gating of clusters identified in panel A. Markers FAUST identified as most relevant to listed from top of table to bottom

B. Clusters identified in A were further analyzed using backwards phenotype selection to identify markers most important for differentiating pathological responses. Markers most important for identifying cells (left most markers) converged on PD-1, Granzyme B, and Eomes for cluster 1 and 2. Cluster 3 did not converge on a simple phenotype. Cluster 1 was further broken down into cluster 1a and cluster 1b after inclusion of all markers

C. Example FACS plot showing enrichment of PD-1, Eomes, and GZMB in MCPyV-specific T cells (red) compared to bulk CD8 T cells (blue)

D. Receive operator characteristic curve showing predictive capacity of portion PD-1+, Granzyme B+, Eomes+ CD8 T cells as a portion of all T cells in the peripheral blood before PD-1 blockade to predict pathological response

E. Boxplot of relative frequency of PD-1+, Granzyme B+, Eomes+ CD8 T cells in patients with non-pCR or pCR. P value calculated using T test

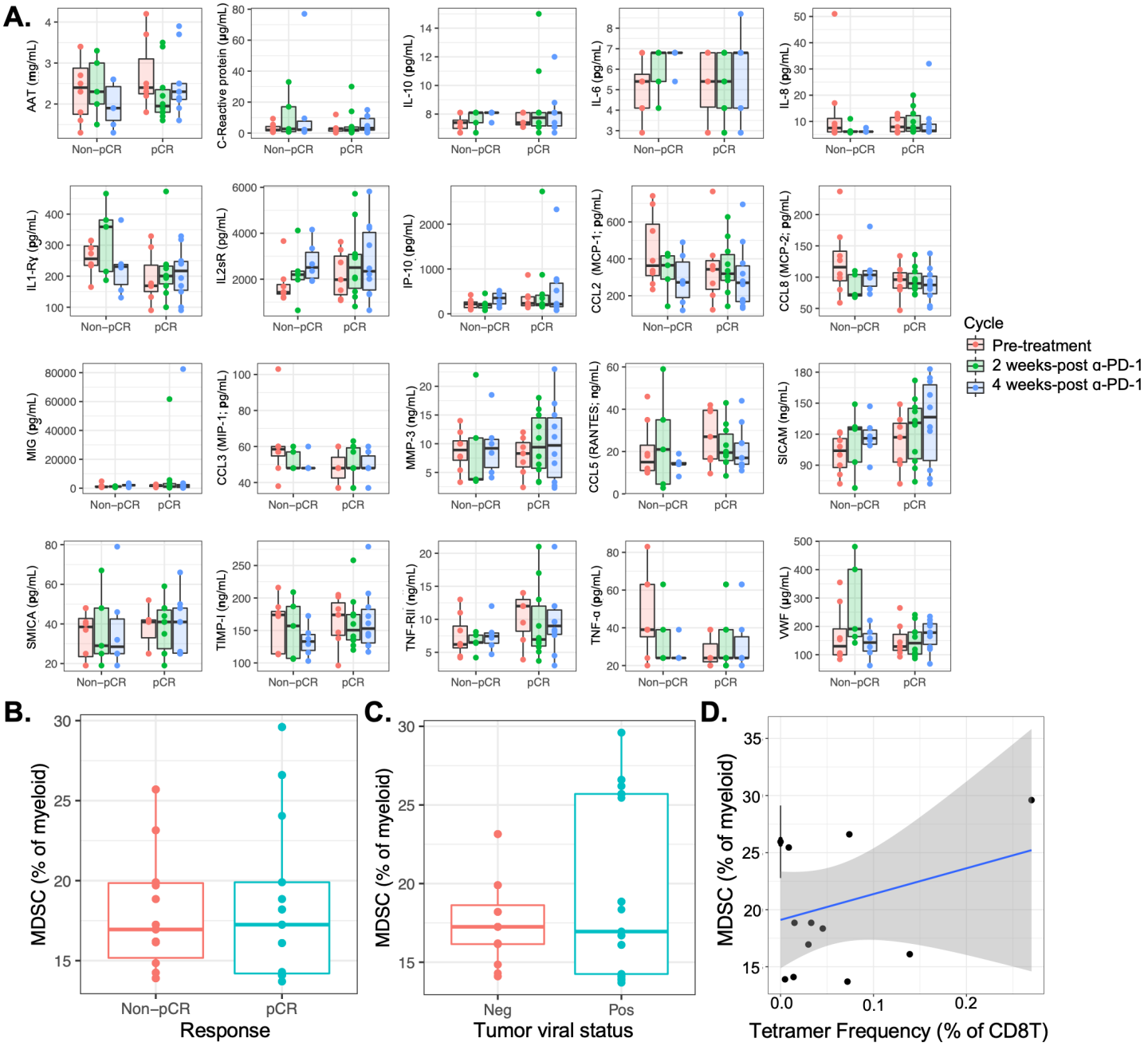

Supplemental figure 7. Association of pathological response and peripheral blood cytokines or myeloid derives suppressor cells (MDSC)

A. Concentrations of key cytokines in blood measured via Luminex assay in patients with pCRs (left) or non-pCRs (right) sub grouped by timepoint

B. Frequency of MDSCs as a portion of all myeloid cells in the peripheral blood at the pre-treatment timepoint grouped by pathological response at the pre-treatment timepoint

C. Frequency of MDSCs as a portion of all myeloid cells in the peripheral blood at the pre-treatment timepoint grouped by tumor viral status

D. Association of frequency of MDSCs and frequency of MCPyV-specific CD8 T cells in the peripheral blood at the pre-treatment timepoint

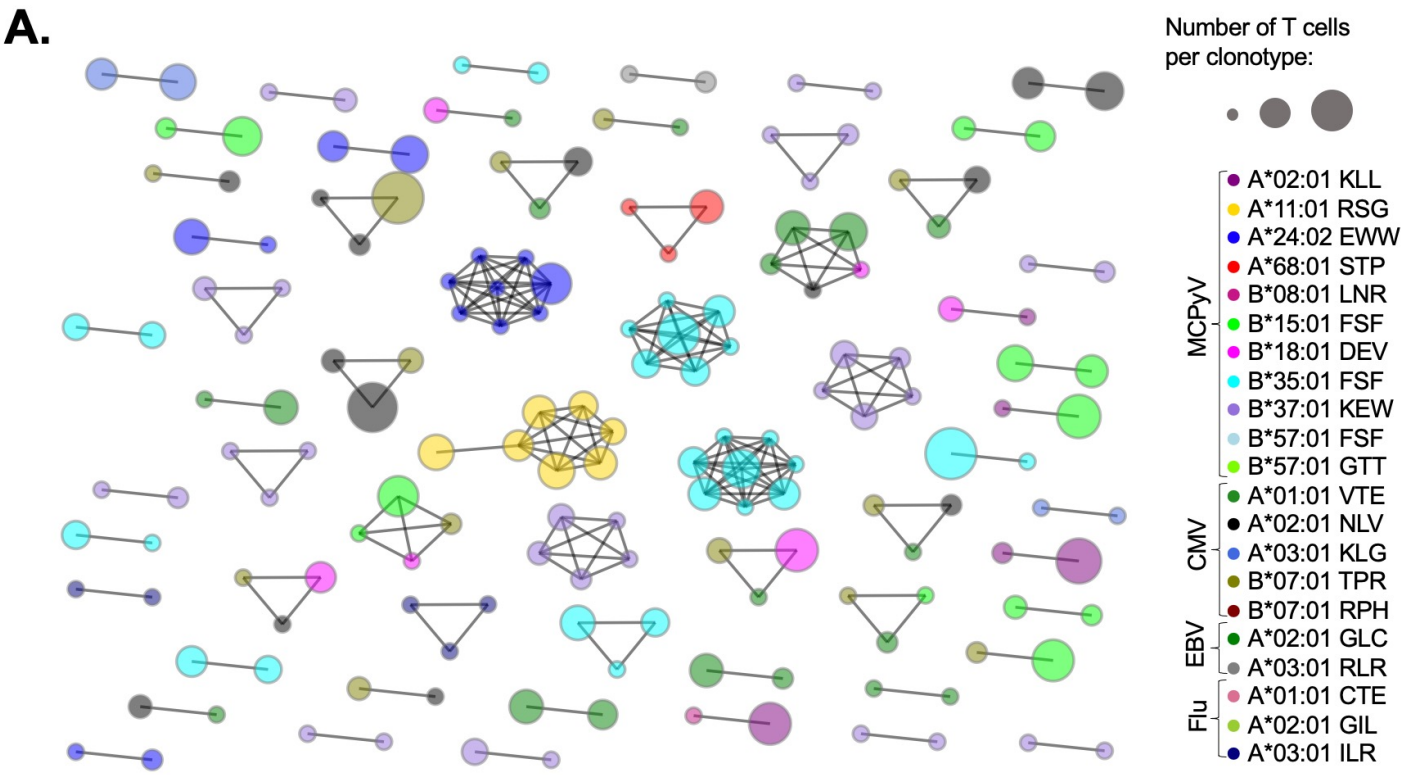

Supplemental figure 8. Network plot showing biochemical similar TCRs (nodes). Groupings of TCRs of same specificity (color) suggest these TCRs are biochemically similar. Each node is colored by its specificity and its size represents the number of clones detected. Biochemical similarity determined using TCRdist3 and a maximum radius of 15.

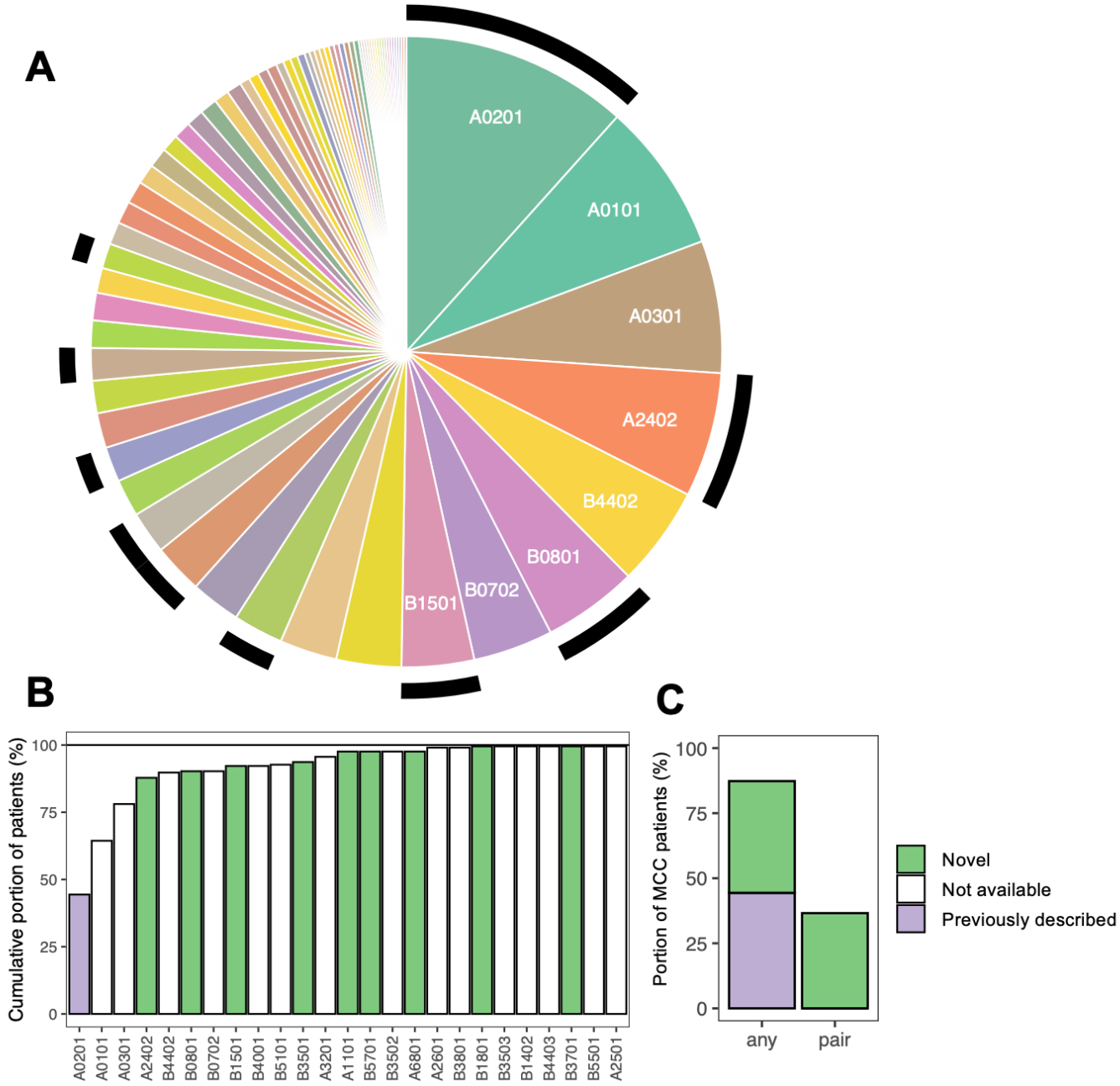

Supplemental figure 9. Novel TCR's described in this study could be used to treat a majority of virally driven MCC cases using transgenic T cells. High resolution HLA-typing was performed on 205 MCC patients in our Seattle based repository. Each individual TCR used in a transgenic T cell therapy could target a single HLA-type. Frequency of HLA types was determined in the relevant patient population to assess most common HLA types and prioritize TCR development

A. Most common TCRs and their relative frequency in the MCC patient population. Black bars highlight HLA-types with at least 1 cognate TCR described in this study which recognizes an MCPyV peptide in the HLA context. HLA types ordered from most common (top) to least common moving clockwise.
B. Cumulative coverage of HLA-types across the MCC patient population. Each bar represents the portion of MCC patients that have that HLA type or one of the prior HLA types moving from left to right. HLA types ordered from most to least common with 25 most common shown.
C. Portion of patients that could be treated with transgenic T cells expressing TCRs against one (left) or two alleles (right)

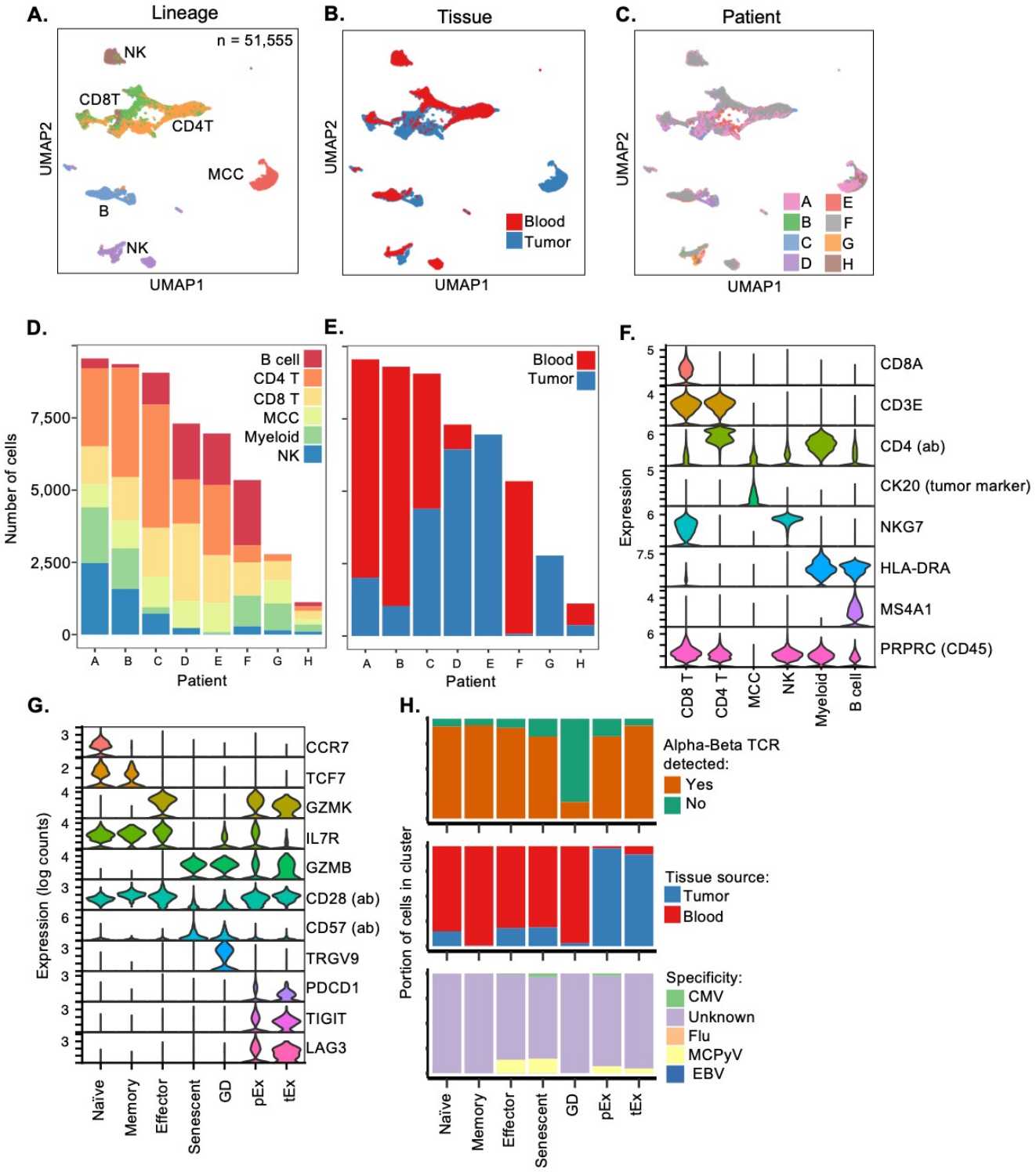

Supplemental figure 10. Justification of single cell RNAseq clustering of bulk cells and subclustering of CD8 T cells in Figure 4

A. UMAP plot of scRNAseq data from 51,555 cells isolated from tumor and blood samples from 8 patients. Cells were clustered and subsequently named according to the cell lineage (see panel F).

B. UMAP plot (as in panel A) colored by whether cells were isolated from tumor or blood specimens.

C. UMAP plot (as in panel A) colored by patient.

D. Bar plot of the number of cells contributed by each patient and colored by cell type

E. Bar plot of the number of cells contributed by each patient and colored by portions of cells from tumor or blood

F. Violin plots of phenotypic genes in CD8 T cells cell isolated *in silico* from bulk population shown in Panel A

G. Violin plots of cell lineage markers confirming cell types shown in panel A

H. Bar plots of the portions of cells in each phenotype in panel G by whether these cells had an alpha-beta TCR (top) originated from the tumor or blood (middle) or the specificity of each T cell (bottom)

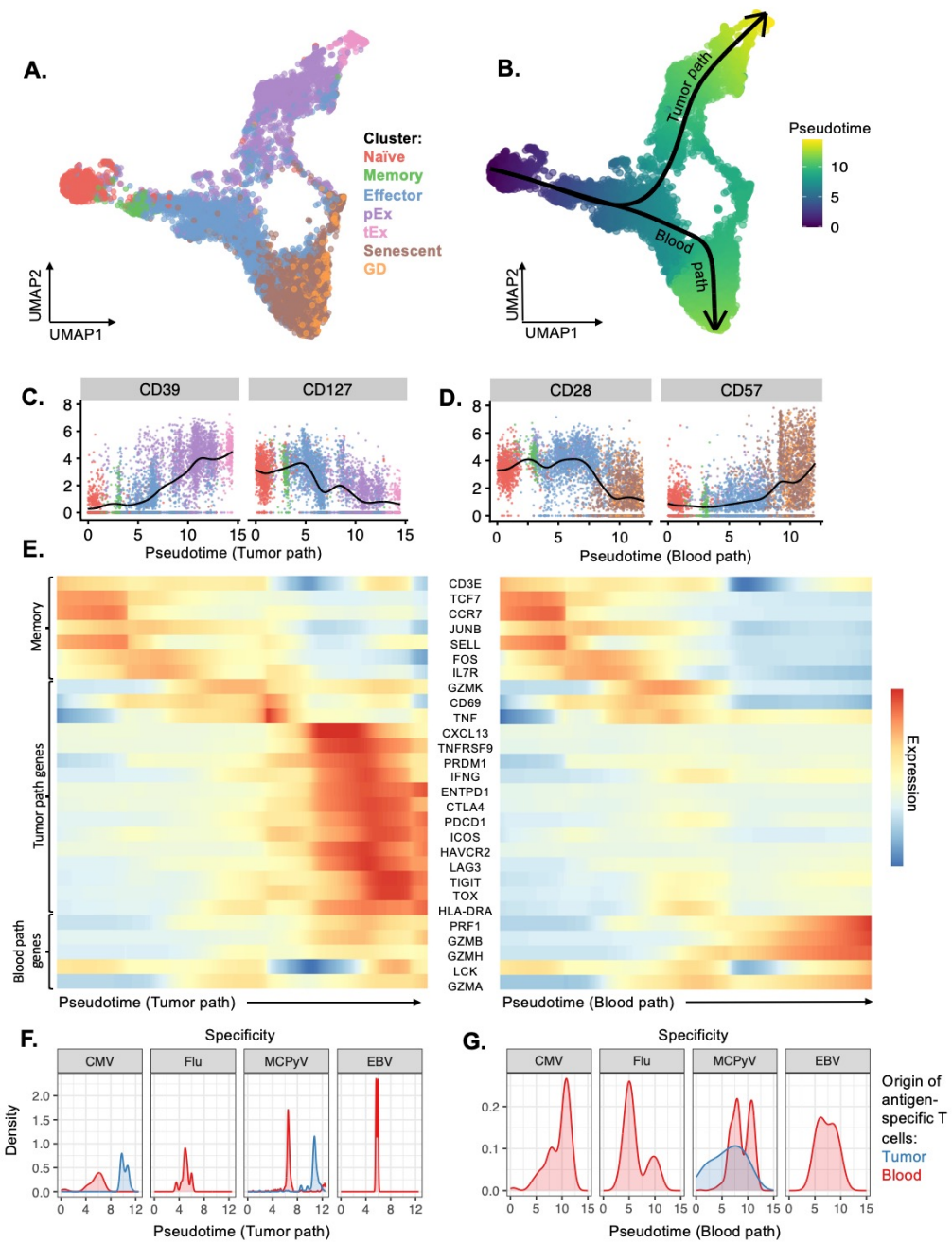

Supplemental Figure 11. Pseudotime analyses of CD8 T cells show a tumor trajectory and a blood trajectory. Data from single cell RNAseq of 8151 CD8 T cells

A. UMAP plot of CD8 T cells colored by the clustering and phenotypic identity

B. Trajectory analysis was performed on CD8 T cells shown in panel A which showed a bifurcated pathway with one pathway (tumor path) originated in in the naïve CD8 T cell cluster and terminating in the terminally exhausted T cell cluster while the other path (blood path) originated in the naïve CD8 T cell population and terminating in the gamma-delta and senescent clusters. Plot is colored by pseudotime along these paths.

C. Plot of CD39 and CD127 (IL7R) cell surface protein levels against pseudotime along the tumor path. Points colored according to their cluster identity as in A. Spline (black) tracks average of these markers over pseudotime.

D. Plot of CD28 and CD57 cell surface protein levels against pseudotime along the blood path. Points colored according to their cluster identity as in A. Spline (black) tracks average of these markers over pseudotime.

E. Heatmaps of memory, exhaustion and senescence genes along the tumor path pseudotime (left) or blood path pseudotime (right).

F. Histograms of CMV, Flu, MCPyV and EBV-specific CD8 T cells and their positions along the tumor path pseudotime

G. Histograms of CMV, Flu, MCPyV and EBV-specific CD8 T cells and their positions along the blood path pseudotime

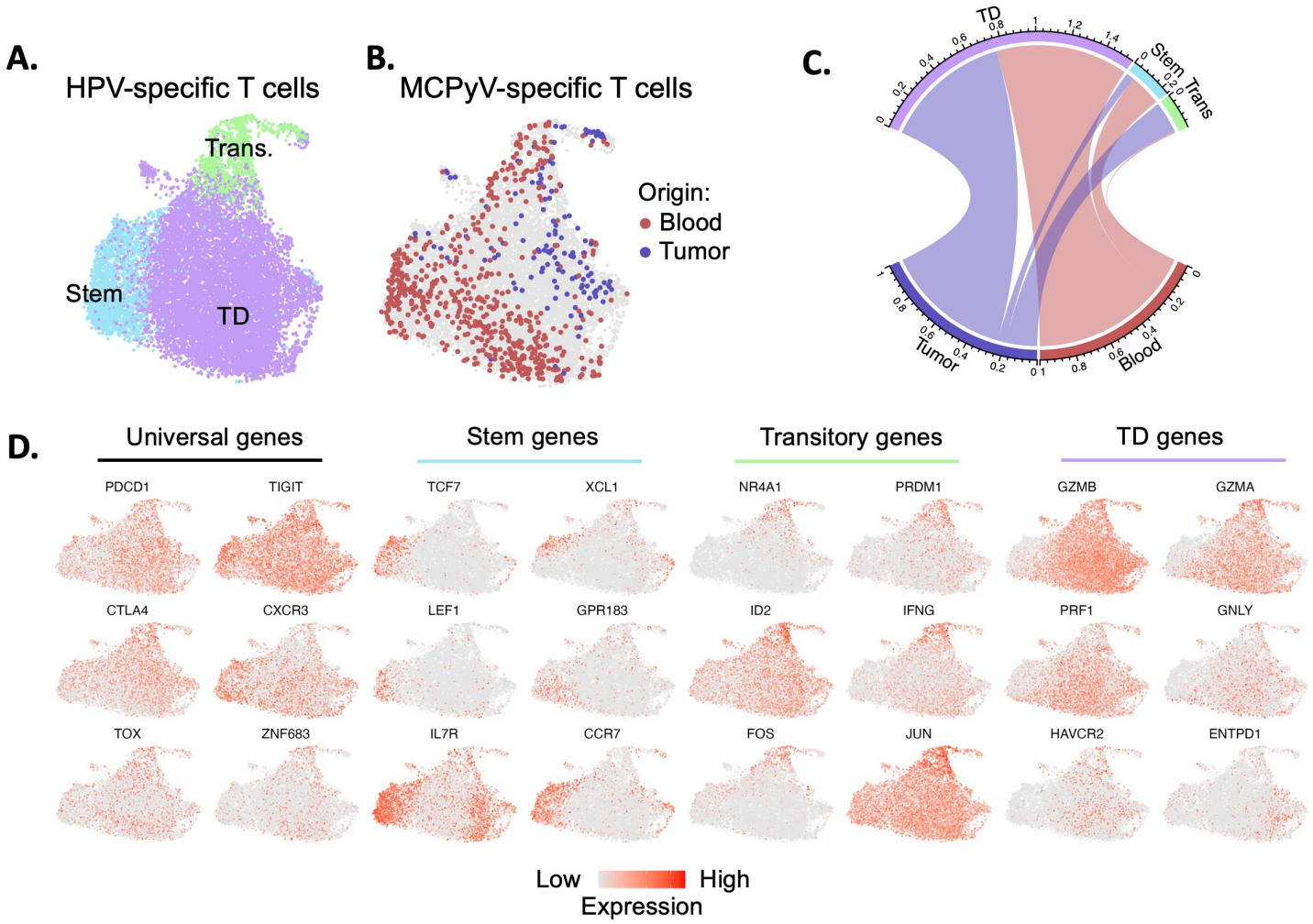

Supplemental figure 12. MCPyV-specific CD8 T cells from blood are phenotypically similar to stem-like HPV-specific CD8 T cells in virally driven head and neck cancer.
Single cell RNAseq MCPyV-specific CD8 T cells identified in Figure 3 and HPV-specific CD8 T cells from Eberhardt et al (PMID: **34471285**) were integrated *in silico*. Cells were clustered into Stem-like, transitory and terminally differentiated (TD) as in Eberhardt et al.
A. UMAP plot pseudo colored by cluster identity.
B. UMAP of MCPyV-specific CD8 T cells pseudocolored by anatomic origin on cells. HPV-specific cells in grey in background.
C. Chord diagram showing cluster identifies of MCPyV-specific CD8 T cells from tumor or blood (bottom) and their corresponding cluster identities
D. UMAP plots of expression of key exhaustion genes as in Eberhardt et al Figure 3 but including MCPyV-specific CD8 T cells.

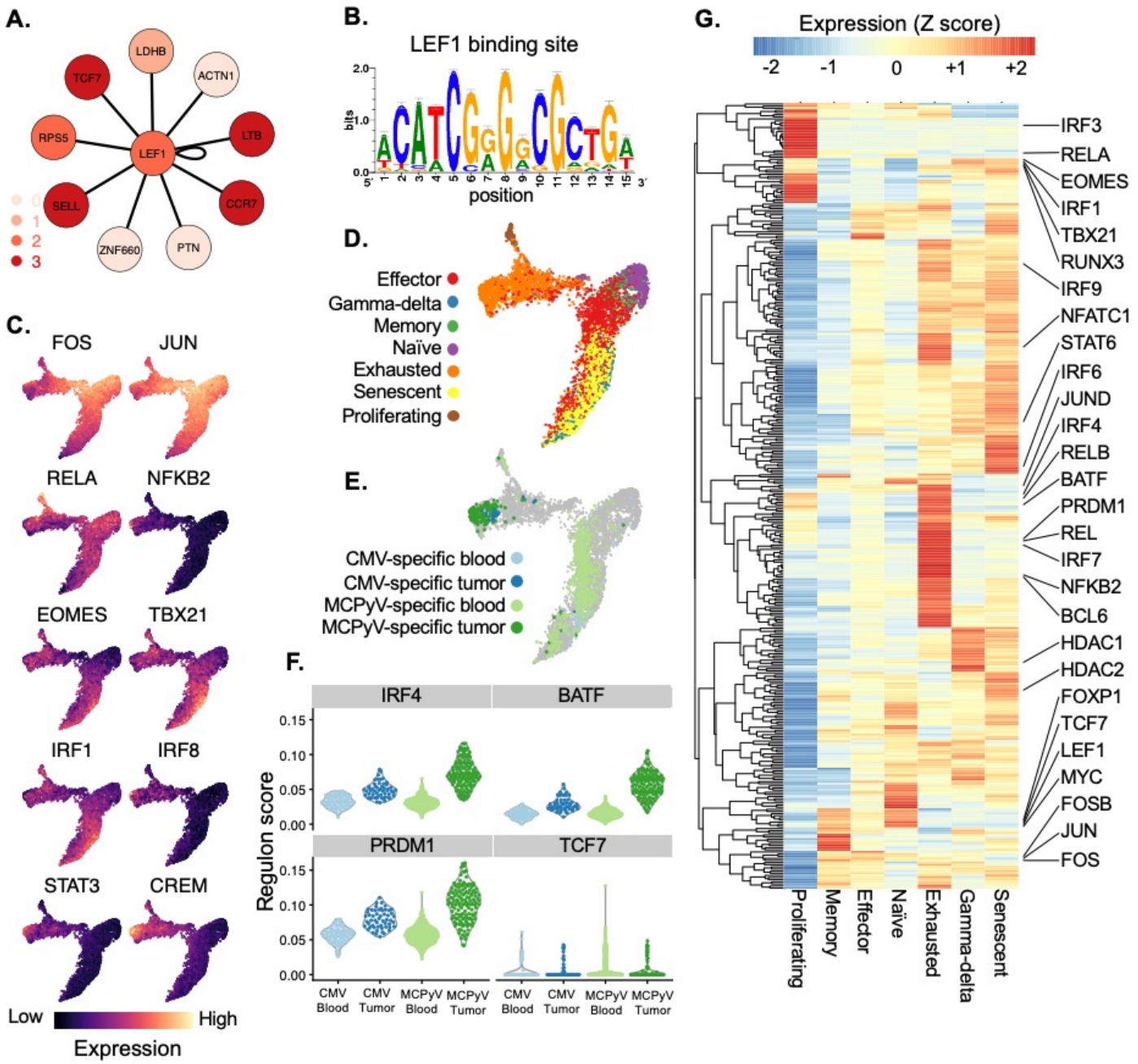

Supplemental figure 13. MCPyV-specific CD8 T cells in tumors exhibit activation of distinct regulatory networks associated with T cell exhaustion relative to MCPyV-specific CD8 T cells in blood.

A. Example of a regulatory network detected by SCENIC. The LEF1 transcription factor network regulates 10 genes shown in nodes. Each node is colored by its association with naïve or memory T cells in single cell RNAseq datasets from 3 prominent publications (see methods)

B. Pictogram of nucleotides associated with LEF1 binding as used in these analyses

C. UMAP plot calculated using regulon scores and showing expression of 10 key regulatory networks

D. UMAP as in panel C colored by CD8 T cell cluster identity.

E. UMAP as in panel C colored by CD8 T cell specificity and tissue of origin

F. Violin plots of expression of 4 regulatory networks important in CD8 T cell exhaustion in CMV- or MCPyV-specific cells from blood or tumor origin

G. Heatmap showing all regulatory networks and their expression in each of the CD8 T cell clusters shown in Panel D

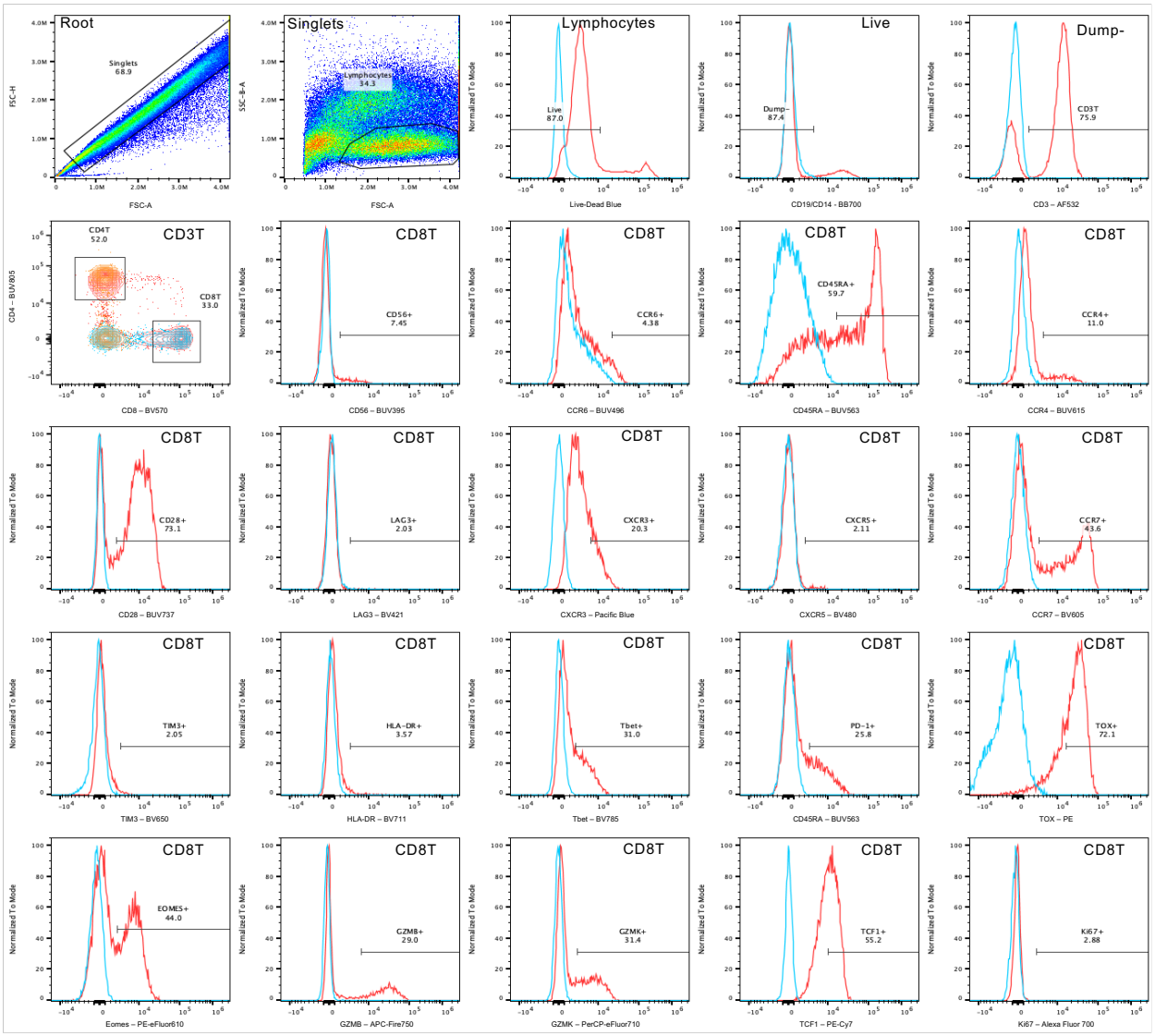

Sample
FMO
Second FMO (CD4/CD8 plot only)

Supplemental figure 14. Gating strategy of flow cytometry data from trial and validation cohorts Population in upper right corner represents parent population. Data from indicated FMO samples and a single representative patient.

Title

STING agonism leads to durable clinical response in a PD-L1 refractory patient: Tumor antigen-specific, single cell level biomarker analyses

Authors:
Thomas H. Pulliam[1],
Peter H. Goff[1,2,3],
Rashmi Bhakuni[1],
Saumya Jani[1],
Shira Tabachnick-Cherny[1],
Kimberly S. Smythe[2],
Brandon Seaton[2],
Lisa Tachiki[2, 4],
Rima Kulikauskas[1],
Paul Nghiem[1,2],
Shailender Bhatia[2,4]

1. Division of Dermatology, Department of Medicine University of Washington, Seattle, WA
2. Fred Hutchinson Cancer Center, Seattle WA
3. Department of Radiation Oncology, University of Washington, Seattle, WA
4. Division of Medical Oncology, Department of Medicine, University of Washington School of Medicine, Seattle, WA

Abstract

JITC abstract limit: 348/350 words

Background: PD-1 pathway blockade has revolutionized cancer care, but many patients do not durably benefit from these therapies. Novel treatments to engage anti-tumor immunity in this setting are needed. The stimulator of interferon genes (STING) protein, an innate sensor of cytoplasmic DNA, is a promising target with several agonists in development; however, recent clinical trials of these agents have not demonstrated efficacy for most patients. Here, we present detailed biomarker analyses of a patient with anti-PD-L1 refractory Merkel cell carcinoma that had a durable (~1 year), abscopal response to ADU-S100 (intralesional STING agonist) combined with anti-PD-1 blockade.

Methods: Tumor biopsies and peripheral blood acquired pre- and post-treatment were analyzed with single cell RNA sequencing, 27-color flow cytometry, T cell receptor sequencing and multiplexed immunohistochemistry (mIHC; post treatment tumor specimen only). Critically, cancer-specific CD8 T cells were identified using MHC-I tetramers containing peptides from the Merkel cell polyomavirus (MCPyV), the etiologic agent of this cancer. Cell lines and tumor specimens from 76 patients were used to evaluate STING expression and signaling in MCC.

Results:
High levels of cancer-specific T cells were observed in the tumor prior to ADU-S100 treatment (12% of T cells recognized an MCPyV epitope). These cancer-specific CD8 T cells exhibited characteristics of exhaustion including high TOX and low TCF1. Following STING agonist treatment, MCPyV-specific CD8 T cells expanded 3-fold with minimal phenotypic changes. An increase in antigen presentation on MCC tumor cells was also observed (1.8% of tumor cells were MHC-I positive before treatment compared to8.2% after treatment). This was not because ADU-S100 acts directly on tumor cells. mIHC analysis of 76 patients confirmed little or no STING expression in tumor cells, but high STING expression on infiltrating immune and stromal cells. Further *in vitro* studies showed MCPyV-positive MCC cell lines are STING deficient, and ADU-S100 did not induce interferon expression.

Conclusions: Our study suggests that STING agonists act on intratumoral immune cells to release interferons, which upregulate antigen presentation on tumor cells and allow tumor recognition by pre-existing cancer-specific T cells. Thus, patients with anti-PD-(L)1-refractory disease with reduced antigen-presentation may benefit from intralesional STING agonists.

Body
JITC limit: ~4600/5000 words

Introduction

Innate immune sensors of pathogen associated molecular patterns (PAMP) are important defenses against viral and bacterial pathogens. Due to their active immune-stimulating role, recent clinical trials have sought to use these agents to stimulate anti-tumor immunity[1]. Stimulator of interferon genes (STING) has been one promising PAMP sensor that has shown promise in pre-clinical mouse models[2-5]. The STING pathway senses cytoplasmic DNA through cyclic GMP-AMP synthase (cGAS), which then produces cyclic GMP-AMP as a second messenger. This, in turn, acts on STING to induce transcription of type I interferons and inflammatory cytokines via NF-kB and IRF3. The STING pathway is thought to have evolved to protect against DNA viruses that replicate in the cytoplasm of cells. However, it is often engaged by DNA damaging chemotherapies and radiation that can cause DNA release into the cytoplasm. Murine models have shown that these DNA damaging therapies lead to adaptive anti-tumor immune responses primarily through activation of STING in dendritic cells in the tumor microenvironment[6,7]. Given the role STING played in existing cancer therapies, novel agents designed to directly engage STING were developed. These STING agonists, when delivered intratumorally, increased intratumoral NK cells and activated CD8 T cells,[8,9] while also inducing both local and systemic anti-tumor immunity.

While intralesional therapies targeting the STING pathway have been successful in murine models, recent clinical trials have been disappointing with few durable responses. In one trial of an intralesional ADU-S100 in 47 patients with metastatic cancers, only one patient had a confirmed response via RECIST[10]. Of note, the responding patient had Merkel cell carcinoma. A separate trial of 106 patients, intralesional ADU-S100 in combination with anti-PD-1 (spartalizumab) yielded a 10% objective response rate with 10 patients achieving a partial response and 1 patient receiving a complete response[11]. One of the 11 patients with an objective response in this second trial also had Merkel cell carcinoma.

Merkel cell carcinoma (MCC) is a rare neuroendocrine cancer, that usually occurs in elderly and immunosuppressed patients[12]. As a highly immune responsive cancer, MCC tumors with CD8 T cell infiltration have a 100% MCC-specific survival compared to ~60% in non-infiltrated tumors[13]. Accordingly, MCC has a particularly high response rate to PD-1 pathway blockade, with more than half of patients experiencing a favorable response[14-17]. In the United States, 80% of MCC cases are driven by Merkel cell polyomavirus (MCPyV). These cases allow a unique opportunity to study cancer-specific immune responses by studying MCPyV-specific CD8 T cells. Of note, virus-driven MCC tumors typically have an extremely low tumor mutational burden and the small antigenic space of the oncoproteins has allowed for rigorous identification of HLA-restricted epitopes. Taken together, this means that we are able to identify cancer-specific T cell responses in a fairly comprehensive manner.

Herein, we describe a case study of a patient treated as part of an ADU-S100 and anti-PD-1 (spartalizumab) trial. This patient had an abscopal and durable partial response to ADU-S100 and anti-PD-1 treatment despite anti-PD-L1 refractory disease. We perform detailed immunophenotyping and single cell analyses of tumor cells and cancer-specific CD8 T cells to characterize this patient's response to STING agonism.

Results

Clinical MCC History and Response to ADU-S100 and anti-PD-1

A 63-year-old man presented with a 2 cm MCPyV-positive MCC tumor of the left knee which was initially treated with surgical resection (pathologic stage IIIB) and adjuvant radiotherapy (54 Gy to the primary and 50 Gy to inguinal nodes) as schematized in Figure 1A. Metastatic disease was subsequently confirmed at the left elbow prompting initiation of anti-PD-L1 therapy with avelumab. There was a complete response to immune checkpoint therapy, and it was electively discontinued after 1 year. Nine months later, a multifocal recurrence was diagnosed on the left lower extremity which proved refractory to rechallenge with avelumab.

The patient was subsequently enrolled on clinical trial (NCT03172936) and received 2 intratumoral injections of the STING agonist MIW815 (ADU-S100) and PD-1 inhibition with spartalizumab, both administered every 4 weeks. Two months after initiating trial therapy, no injectable lesions were clinically apparent. Both injected and non-injected lesions regressed, leading to a RECIST partial response (43% reduction in tumor burden in index lesions; Figure 1B). This response was durable for ~1 year after the two STING agonist injections withanti-PD-1 therapy given every 4 weeks until subsequent disease relapse in the left lower extremity. Representative PET/CT and CT images are shown for lesions with clinical response or stable disease and subsequent progression. Blood and tumor tissue were obtained pre- and post-STING agonist administration to analyze changes in the tumor microenvironment and peripheral blood.

Intralesional STING treatment increases intratumoral T cell infiltration

To investigate this patient's response to intralesional STING agonism, we first performed single cell RNAseq with feature barcoding (CITEseq) on pre- and post-treatment tumor and blood specimens to study cell populations and gene expression changes in an unbiased approach. DNA barcoded MHC-I tetramers containing MCPyV, CMV, or EBV peptides were used to identify antigen-specific T cells (Supplementary Figure 6). These data were then used to create a 27-color flow cytometry panel to study major cell populations observed in the scRNAseq data and rare cell populations that could have been missed due to the low-throughput nature of CITEseq (Figure 2a).

Unbiased clustering and dimensionality reduction primarily showed tumor and immune cells in the tumor microenvironment (70% and 28% of pre-treatment tumor, respectively) with remaining 2% of cells bearing markers of stromal/endothelial cells (CD34). Following intralesional STING agonist injection, tumor cells decreased to 49% of the TME which was matched with a 2-fold increase in T cells (Figure 2b, 2c). Further sub-clustering of tumor, T cell and myeloid populations (Supplemental figure 6) was then performed to determine if specific cell populations changed over the course of therapy. While both tumor cell populations (proliferating and non-proliferating) decreased over the course of immunotherapy, the most dramatic change was in the proliferating tumor cells which decreased from 17% of all cells in the TME before treatment to 5% following treatment (Figure 2d). Sub-clustering of T cells revealed that memory CD4 T cells, T_{REG} cells, CLA+ CD8 T cells, progenitor exhausted CD8 T cells, and terminally exhausted CD8 T cells each comprised more than 2% of the cells in the tumor microenvironment prior to STING treatment. All T cell populations appeared to increase proportionally following treatment (Figure 2e). No significant changes were observed in myeloid cells. However, a high portion of myeloid cells were plasmacytoid dendritic cells (2.7% of pre-treatment cells, marked by CD123 expression) which are specialized for sensing pathogen associated molecular patterns. An additional 2% of cells in the TME were classical dendritic cells (marked by high CD11c expression). Both dendritic cell populations expressed high levels of STING protein (supplemental figure 6).

Cancer-specific CD8 T cells expand in tumors following intralesional STING agonism
Given the increase in T cells observed following STING agonism, we sought to characterize the dynamics of antigen-specific T clones in the tumor and blood. To do this, a dual approach was used (Figure 3a). T cell specificity was identified using DNA barcoded MHC-I tetramers with paired CITEseq and V(D)J seq (Figure 3b). Gating of multimer positivity was confirmed by visualizing PD-1 positivity in these cells, which is known to be elevated in MCPyV-specific CD8 T cells[18]. This resulted in 12 TCR-sequences specific for an MCPyV epitope that can be presented in a B*37:01 allele. CD8 T cells specific for other MCPyV or other viral epitopes were detected at low levels and antigen-specific TCRs could not confidently be identified.

T cell frequency was quantified using bulk beta TCRseq and MCPyV-specific T cells were annotated using the specificity calls made above (Figure 3c). 0.03% of all cells in the blood were MCPyV-specific CD8 T cells prior to STING agonism. This was ~10 fold higher in the tumor (0.39% before STING agonism) After treatment, 0.04 % of cells in the blood and 0.93% of tumor cells were MCPyV-specific CD8 T cells. Expansion of T cells was largely proportionate with 8 of 5128 intratumoal clones significantly increasing in frequency following treatment and 20 of 5128 clones decreasing as a portion of all T cell ($p<0.01$; beta binomial test; supplementary figure 7). The results were similar for cancer-specific CD8 T cells where 1 of 12 MCPyV-specific clones expanded following STING treatment and 2 of 12 contracted as a portion of all T cells.

Cancer-specific CD8 T cells exhibit characteristics of exhaustion
We next sought to phenotype cancer-specific T cells in the tumor and blood. Unbiased clustering of scRNAseq of CD8 T cells yielded clusters of memory, naïve, progenitor exhausted, terminal exhausted effector, effector (intratumoral) and two gamma delta populations (Figure 4a, 4b). Expression of stem-like and memory genes was higher in CD8 T cells in blood while genes associated with exhaustion were higher in tumor tissues and highest in MCPyV-specific T cells (Figure 4c). MCPyV-specific CD8 T cells in tumors were largely confined to the terminally exhausted population defined by high expression of PDCD1 and CD39 (Figure 4b, 4d). The portion of MCPyV-specific CD8 T cells in the terminally exhausted population decreased slightly following STING agonism but low numbers of MCPyV-specific CD8 T cells in the pre-treatment timepoint limited analyses (Figure 4d). To circumvent the low capture efficiency of single cell RNAseq, flow cytometry was subsequently used as a higher throughput technique. These data show high expression of TOX, TCF7 and PD-1 proteins in MCPyV-specific CD8 T cells (99% PD-1+, 99% TOX+, 14% TCF1+, in pre-treatment samples, Figure 4e) from both blood and tumor tissue. This was unchanged following STING agonism, suggesting that treatment did not induce lasting phenotypic changes in cancer-specific CD8 T cells.

MCC tumor cells are STING deficient
To study the effect of STING agonism on either tumor, stroma or immune cells, we first confirmed STING expression in the TME by performing multiplexed immunohistochemistry on the studied patient's post-treatment tumor specimen. Previous studies of STING in MCC have suggested that this pathway is deficient in virus positive Merkel cell carcinomas[19]. We confirmed that the STING protein is absent in this patient's tumor cells via mIHC (Figure 5a). These data show absence of STING protein in tumor areas but prevalent STING expression in immune and stromal cells (Figure 5a). This was then confirmed broadly in further staining of 88 MCC tumors from 68 unique patients (Figure 5b). To confirm that MCC cells do not respond to ADU-S100 treatment, 4 MCC cell lines were treated with decreasing doses of ADU-S100. This did not result in any production of interferon beta (a downstream target of STING activation) in MCC cell lines, but did produce interferon beta in control monocytic THP-1 cells (Figure 5c).

Moreover, none of the virally-driven MCC cell lines tested produced detectable amounts of STING protein (Figure 5c).

Tumor cells upregulate MHC following STING agonism

To investigate if antigen presentation was increased following STING agonism, we investigated the expression of genes associated with antigen processing and presentation (Figure 6a). Tumor and non-tumor cells were isolated *in silico* (supplemental Figure 1) and a gene set of 18 genes associated with antigen presentation were used to measure this pathway in aggregate. Tumor cells upregulated expression of genes included in this gene set by 49% following STING agonism ($p<10^{-16}$). A more modest 4% increase was observed in non-tumor cells in the TME ($p=0.016$). Further analyses of these genes showed that most of this increase was largely driven by upregulation of beta 2 microglobin (Supplemental figure 2) in tumor cells following STING treatment ($p<10^{-16}$; Figure 6b). However, no change in beta 2 microglobulin expression was observed in other cells in the TME. This was validated at a protein level via FACS which showed 1.8% of tumor cells positive for MHC-I prior to STING treatment compared to 8.2% following STING treatment. Consistent with these findings, we observed increases in genes associated with interferon gamma or interferon alpha in most cell types in the TME following STING agonism (Supplemental figure 3a & 3b).

Discussion

STING agonists have shown great promise in pre-clinical models. However, clinical trials have shown limited responses with objective response rates between 2% and 10%[10,11]. To attempt to understand how STING agonism could yield anti-cancer immune response in humans, we studied a patient with virally-driven MCC who experienced a durable (1 year) response to combination intralesional STING agonism and anti-PD-1 therapy, despite a previous lack of response to anti-PD-L1 treatment. This patient had many (>10) tumors localized on the left leg. While only two of the lesions were injected, both injected and non-injected lesions responded to injections of the ADU-S100 STING agonist.

Our initial hypothesis was that ADU-S100 acted directly on STING in tumor cells. However, as we learned that MCC tumors are STING deficient[19], we set out to examine STING expression in the entire TME. Indeed, our results further supported the finding that the STING pathway is inactive in virally driven MCC. Given that the LxCxE motif that inactivates STING in adenovirus and human papillomavirus[20] is also present in the MCPyV large T antigen[21], it is plausible that MCPyV, the DNA virus that drives most MCC tumors, expresses viral proteins that inactivate STING to evade the immune system and support tumorigenesis.

Murine studies of STING's role in anti-cancer immunity have shown that STING activity is vital in dendritic cells, while being largely dispensable in tumor cells[6,7]. These dendritic cells release interferons following STING signaling, which in turn stimulates adaptive immunity and tumor regression. In the current study, we observed a high portion of dendritic cells in the treated patient's tumor (5% of all cells in the TME prior to treatment). We also observed an increase in interferon-beta and interferon-gamma induced genes following STING agonism. Interferons are known to regulate antigen presentation, and we saw an increase in MHC-I on MCC tumor cells following STING agonism (from 1.8% of cells expressing detectable MHC-I prior to treatment to 8.2% of cells after treatment). Since disruption of the antigen-presentation pathway is a well-known immune evasion mechanism in PD-1 pathway blockade, this may be particularly relevant.

The patient experienced regression of both injected and non-injected lesions (abscopal response). It is possible this was due to a systemic adaptive anti-cancer immune response. However, 93% of MCPyV-specific CD8 T cell clonotypes in the tumor following STING agonism had at least one clone present in the pre-treatment tumor suggesting novel CD8 T cell priming is not a driving factor in this patient's immune response. Furthermore, minimal changes were detected in MCPyV-specific phenotype or exhaustion status suggesting that a reversal of CD8 T cell exhaustion also does not explain the response seen in this patient. If this patient's immune response was not due to reversal of T cell dysfunction or priming of novel T cells, it is possible that this patient's abscopal response was due to spread of ADU-S100. Studies of mice have shown that ADU-S100 can spread to distal tumors[9] at high doses. The patient studied here received the highest dose of ADU-S100 tested in the trial (3200 mcg/injection) and all tumors were localized to the left leg. It is therefore possible that spread of ADU-S100 from the injected lesion could also explain this patient's abscopal response.

It is of note that 2 of the 4 MCC patients (50%) treated on two large trials of ADU-100 experienced objective responses compared to 10 of the 139 non-MCC patients (7%). This would be consistent with ADU-S100 upregulating antigen-presentation in tumor cells as this is a major immune evasion mechanism in MCC[22-25]. However, further study would be needed to validate this hypothesis.

Although initial trials of STING agonists have been disappointing, here we show that these agents can lead to durable immune responses in a PD-(L)1 refractory setting. Our results suggest that STING agonists may be particularly effective in tumors evading immune detection via MHC-I downregulation, and potentially less effective at priming novel anti-cancer CD8 T cell responses.

METHODS

Study design and participants

Samples were collected with informed consent for research use and were approved by the Fred Hutch Cancer Center institutional review board, in accordance with the Declaration of Helsinki (2013) as part of observational registry studies focusing on Merkel cell carcinoma (Fred Hutch Cancer Center IRB#6585). This patient presented to our institution as part of standard of care initially. Upon progression on anti-PD-L1, he was evaluated and enrolled in clinical trial with ADU-S100 and spartalizumab antibody (NCT03179236; PMID: 36282874). ADU-S100 was administered at 3200 mcg/injection every four weeks. One lesion was injected the first cycle and a separate lesions were injected the second week. Tumor biopsy was taken at 6 weeks after the first lesion injected. Blood was collected before and 1 year after treatment. Every four weeks, patient received spartalizumab administered at a dose of 400 mg until progression.

Blood collection and processing

Heparinized whole blood from MCC patients was processed at the Specimen Processing Lab (Fred Hutchinson Cancer Center). Peripheral blood mononuclear cells (PBMC) were isolated by routine Ficoll density gradient centrifugation and cryopreserved in liquid nitrogen.

Tumor digestion processing

Fresh MCC tumor specimens from needle cores, punch biopsies, or surgical excisions were enzymatically digested as described[26]. All single-cell suspensions were cryopreserved in Freezing Medium [50% human serum (Valley Biomedical), 40% RPMI (Corning), and 10% DMSO (Sigma-Aldrich)] in liquid nitrogen.

Flow cytometry

Frozen pre- and post-treatment PBMC and tumor digest samples were analyzed using flow cytometry. Tubes were thawed at 37°C and mixed with complete media (consisting of RPMI, 10% fetal bovine serum, 1x penicillin/streptomycin, and 1x l-glutamine). DNAse I was added at a concentration of 10 units/ml and the tubes were left to rest for an hour. The cells were counted using a hemacytometer and divided into tubes containing 1-3 million cells each. After two washes with PBS, dasatinib (100 nM) and live dead staining buffer (Live dead Blue; ThermoFisher) were added and the cells were incubated at 37°C for 10 minutes. The MHC-I multimers were then added, followed by the addition of antibodies against cell surface receptors (BV605 conjugated anti-E selectin (clone 68-5H11; BD), BUV395 conjugated anti-CD56 (clone NCAM16.2; BD), BUV615 conjugated anti-PD1 (clone EH12.1; BD), BV650 conjugated anti-PDL1 (clone 29E.2A3; Biolegend), PE-Cy7 conjugated anti-CLA (clone HECA-452; Biolegend), BV785 conjugated anti-CD163 (clone GHI/61; Biolegend), BUV805 conjugated anti-CD4 (clone SK3; BD), BV570 conjugated anti-CD8 (clone RPA-T8; Biolegend), BV711 conjugated anti-HLA-DR (clone L243; Biolegend), APC-Fire750 conjugated anti-CD123 (clone S18016F; Biolegend),

BUV563 conjugated anti-CD14 (clone MφP9; BD), BB700 conjugated anti-CD19 (clone SJ25C1; BD), BUV496 conjugated anti-HLA-ABC (clone W6/32; BD), V450 conjugated anti-CD66b (clone G10F5; BD), BUV737 conjugated anti-CD86 (clone 2331 (FUN-1); BD), BV510 conjugated anti-CD33 (clone WM53; Biolegend), BV480 conjugated anti-CD45 (clone HI30; BD), BV750 conjugated anti-CD34 (clone 563; BD), APC conjugated anti-CD11c (clone Bu15; Biolegend))were then added and incubated for 30 minutes at room temperature. The cells were washed twice with autoMACS running buffer (Miltenyi) and permeabilized using the Foxp3/Transcription factor staining buffer set (eBioscience), followed by two more washes with the permeabilization buffer. The intracellular antibodies (PE conjugated anti-TOX (clone Invitrogen; Invitrogen), AF488 conjugated anti-TCF7 (clone S33-966; BD), PE-CF594 conjugated anti-STING (clone T3-680; BD), AF532 conjugated anti-CD3 (clone UCHT1; Invitrogen), PE-Cy5 conjugated anti-FoxP3 (clone PCH101; Invitrogen), AF700 conjugated anti-Ki67 (clone Ki-67; Biolegend)) were then added and incubated for 1 hour at room temperature, followed by two washes with permeabilization buffer and fixation in 1% paraformaldehyde. Antibody capture beads or amine reactive beads (ThermoFisher) were used to balance each fluorophore in the experiment. The stained cells were then analyzed using the Cytek Aurora spectral analyzer at the University of Washington's Department of Immunology Cell Analysis Facility. Spectral unmixing was performed using SpectroFlo software and the initial gating, selecting for single cells, lymphocytes, and live cells, was performed in FlowJo v.10 (FlowJo LLC; supplementary figure 5). Further analysis was carried out in R.

Single cell RNAseq sample preparation

Frozen pre- and post-treatment PBMC and tumor digest samples were analyzed by cellular indexing of transcripts and epitopes by sequencing (CITEseq). Frozen tubes were thawed at 37 C, followed by dropwise addition of 1 ml complete media (RPMI, 10% Fetal bovine serum, 1x penicillin/streptomycin, 1x l-glutamine). Complete RPMI media was continuously added dropwise with gentle mixing in between up to a total volume of 32 ml. Cells were then washed twice with PBS, counted using a hemacytometer and transferred to FACS tubes (Fisher Scientific). Live dead stain was then added (FVS780; BD Biosciences), followed by a blocking buffer to bring samples to 0.5% BSA, 5% TruStain FcX buffer (Biolegend), 100 nM dasatinib, and 50 µg salmon sperm. Samples were then incubated on ice for 10 minutes. DNA oligo labeled MHC multimers were then added to patients with matched HLA types. Hashtag antibodies were added to identify sample origin in subsequent pooling steps. Fluorophore labeled antibodies were then added followed by DNA oligo labeled antibodies. Cells were then incubated on ice for 30 minutes and washed three times. Cells were sorted on an Aria II Cell sorter (BD Biosciences). Dead cells and debris were excluded and all live cell were sorted into cold complete media, pooled and immediately prepared for CITEseq (see below).

scRNA-seq and scV(D)J-seq library preparation and sequencing

Single cell suspensions were collected from either tumor or blood samples as above and counted using a hemacytometer. Single cell suspensions were then loaded into the appropriate microfluidic chip (chip G; 10x Genomics) in a chromium controller (10x Genomics). Resulting cell suspensions then went through a library preparation process for single-cell RNA sequencing (scRNA-seq) along with paired scV(D)J-seq for T-cell receptor (TCR) using the 5′ transcriptome kit with feature barcoding (V1.1; 10x Genomics) following the manufacturer's guidelines. The complementary DNA libraries were then sequenced using a NovaSeq instrument (Illumina) with 2 × 92 base pair paired-end reads aiming for an average of 20,000 reads per cell.

Beta TCR receptor profiling

Frozen peripheral blood mononuclear cells or formalin-fixed paraffin-embedded (FFPE) tumor biopsy material (20 µm thick molecular curls) were used for DNA extraction using QIAamp DNA Blood Mini Kit or QIAamp DNA FFPE tissue kit respectively (Qiagen). Resulting samples were submitted to Adaptive Biotechnologies for TCRβ sequencing and normalization as previously described (PMID: 19706884)

Immunohistochemistry

Formalin-fixed paraffin-embedded tissues were stained on a Leica BOND Rx autostainer using the Akoya Opal Multiplex IHC assay (Akoya Biosciences, Menlo Park, CA) with the following changes: Additional high stringency washes were performed after the secondary antibody and Opal fluor applications using high-salt TBST (0.05M Tris, 0.3M NaCl, and 0.1% Tween-20, pH 7.2-7.6). TCT was used as the blocking buffer (0.05M Tris, 0.15M NaCl, 0.25% Casein, 0.1% Tween 20, pH 7.6 +/- 0.1). All primary antibodies were incubated for 1 hour at room temperature. Antibodies against the following targets were used for staining: CD56 (clone cl123C3.D5; BioSB), CD8 (clone 144BI; DAKO) STING (clone SP338; Abcam) CD45 LCA clone 2B11+PD7/26; DAKO) FoxP3 (clone 236A/E7; eBioscience), CD163 (clone ERP324; BioSB) CD68 (clone PG-M1; DAKO).

Slides were mounted with ProLong Gold and cured for 24 hours at room temperature in the dark before image acquisition at 20x magnification on the Akoya PhenoImager HT Automated Imaging System. Images were spectrally unmixed using Akoya inForm software.

MHC multimer preparation

MHC tetramers used for scRNAseq were created using MHC-I easYmers (Immunaware. BV421-labeled streptavidin (Biolegend) was used to prepare tetramers for flow cytometry experiments. PE or APC and DNA oligo streptavidins (Biolegend) were used for scRNAseq experiments. Tetramers were titered using samples of known positivity. Tetramers for six epitopes were created matching this patients HLA typing: Influenza A (HLA A*02:01 containing GILGFVFTL peptide),Epstein-Barr virus (HLA A*02:01 containing GLCTLVAML peptide), cytomegalovirus (HLA A*02:01 containing NLVPMVATV peptide), and three MCPyV epitopes (HLA A*02:01 containing KLLEIANPC peptide; HLA A*11:01 containing RSGGFSFGK peptide and HLA A*37:01 containing KEWWRSGGF peptide).

Flow cytometry data analysis

Fcs files of live cells were loaded into a gating set object in R using flowWorkspace (v.4.6.0). Data from fluorescent markers was transform using the biexponential function. Fluorescent-minus-one (FMO) samples were used to draw minimum gates at the 99th percentile Gates were adjusted upward as appropriate based on visual inspection. UMAP dimensionality reduction was performed using uwot (v.0.1.14). clustering was performed using phenograph (v.0.99.1). Visualization was performed using ggplot2 (v.3.4.0) or FlowJo (v.10.8.1).

Single cell RNAseq data analysis

The raw sequencing reads were aligned to the hg38 genome using Cell Ranger v.3.1. The filtered count matrices of transcripts and feature barcoding counts were then loaded into an R

(v.4.1.2) SingleCellExperiment object for further analysis. The sample hash deconvolution was carried out using DropletUtils (v.1.14.2) and doublet detection and removal was done through scds (v.1.10.0) in conjunction with the doublets detected during hash deconvolution.

Low-quality cells with fewer than 800 transcript reads, fewer than 250 genes detected, or more than 10% of mitochondrial DNA were excluded from the analysis. A comparison of genes expressed in the removed low-quality cells and kept cells was done to ensure that no cell populations were removed disproportionately. The result showed that only mitochondrial genes, MALAT1 (a transcript associated with dying cells), and hemoglobin genes were disproportionately represented in the removed cells. The cells were size-normalized and log-transformed using scuttle (v.1.4.0).

The cells from different runs were then integrated using the mutual nearest neighbor method through the batchelor package (v1.10.0). UMAP dimensionality reduction was performed with the integrated values. Clustering was done using the integrated transcript values and feature barcoding reads through the walktrap algorithm on a nearest neighbor graph (scran v.1.22.1). The number of clusters was varied by adjusting the number of nearest neighbors (k) during graph construction, followed by analysis using clustree (v.0.5.0).

Clusters were then labeled as the major cell lineages of CD4 T cells, CD8 T cells, B cells, myeloid cells, erythrocytes, NK cells, and tumor cells through the expression of key genes, including MS4A1, CD19, CD4, CD8A, CD3E, CD3D, GZMB, NCAM1, HLA-DRA, PTPRC, NKG7, and the MCPyV oncoproteins. The cluster labels were validated by investigating the portion of the cluster with productive TCR rearrangements. The cell lineages were isolated in silico and split into major lineages, and dimensionality reduction and clustering were re-performed as described above.

The cells were scored for the expression of MHC and Interferon gene sets using the UCell (v.1.99.1) package. Plotting was performed using scater (v.1.22.0), Seurat (v.4.3.0), or ggplot2 (3.4.0).

Gene sets

Genes associated with antigen-presentation were taken from the antigen-presentation and processing dataset from Biocarta (PMID: 27374120). HLA genes B, C, E and F not originally included in the set were added for completeness. Genes associated with Interferon alpha or gamma signatures were taken from the respective hallmark gene sets (PMID: 26771021)

ADU-S100 stimulation

To assess MCC cell lines response to STING agonism, the virus positive cell lines WaGa, MKL1, MKL2, and MS-1 as well as monocytic cell line THP1 were treated with ADU-S100. 100,000 cells were plated in 0.25 ml of media. ADU-S100 (Medchemexpress) was added to bring final concentrations to 100, 20, 4, 0.8, 0.16, 0.032, 0.0064 or 0.00128 micromolar. Concentration of interferon beta was measured in media 48 hours later via ELISA (R&D Systems). All samples run in triplicate.

Western blot

WaGa, MKL1, MKL2, MS-1 and THP-1 cells were seeded in T75 flasks and maintained at 37oC in a humidified incubator supplied with 5% CO2. Cells were pelleted and lysed in ice-cold buffer containing 150 mM NaCl, 1.0% IGEPAL CA-630, 0.5% sodium deoxycholate, 0.1% SDS, 50 mM Tris (pH 8.0) and protease/phosphatase inhibitor cocktail (1:100; Cell Signaling Technology, USA). Soluble fractions from prepared cell lysates were collected after centrifugation at 13,000 rpm for 10 minutes at 4°C.

Next, normalized cell lysates (quantified using Bradford assay) were separated by 10% SDS-PAGE electrophoresis, transferred onto PVDF membranes, and immunoblotted with STING (1:1000; Cell Signaling Technology, USA) / β-actin (1:10,000; Sigma Aldrich, USA) primary antibody and anti-rabbit (1:2500; Cell Signaling Technology, USA) / anti-mouse (1:2500; Cell Signaling Technology, USA) horseradish peroxidase-conjugated secondary antibody respectively. Blotted proteins were visualized on X-ray films incubated with a high sensitivity ECL reagent (Sigma Aldrich, USA) inside a dark room.

Statistics

The statistical tests applied were two-sided unless specified otherwise. T tests were used to compare differences between two groups unless otherwise noted. When comparing more than two groups, the nonparametric Kruskal–Wallis test was used. Multiple hypothesis testing was done with the Bonferroni method unless noted differently. Fisher's exact test was used to evaluate differences between two categorical variables. All statistical analysis was carried out using R v.4.1+.

Acknowledgements:
Figure schematics created using biorender.com
“This research was supported by the Experimental Histopathology shared resource of the Fred Hutch/University of Washington Cancer Consortium (P30 CA015704)."

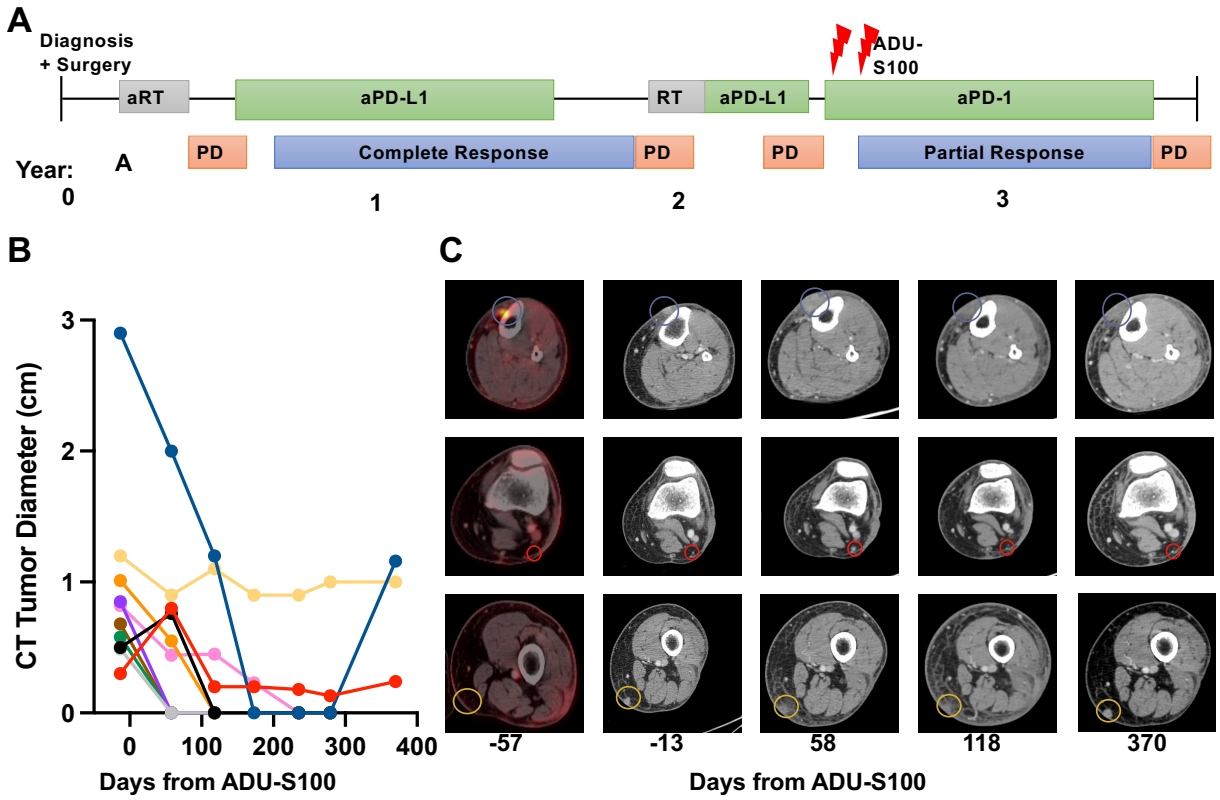

Figure 1. Clinical MCC course and characterization of partial response to injectable STING agonist + anti-PD-1 therapy.

A. Schematic of clinical history for a 63-year-old man diagnosed with stage IIIB MCC of the left lower extremity (LLE) and inguinal lymph nodes initially treated with wide local excision and lymph node dissection followed by adjuvant radiation (aRT). Metastatic progressive disease (PD) at the left elbow following primary treatment was treated with anti-PD-L1 (aPD-L1, avelumab) for 1 year and complete response was observed. Recurrent LLE disease was treated with RT and aPD-L1 therapy but progressed. He was enrolled on a trial clinical trial (NCT03172936) and received 2 intratumoral injections of the STING agonist MIW815 (ADU-S100) and PD-1 inhibition with spartalizumab, both administered every 4 weeks. No injectable lesions were clinically evident after 2 months of therapy, and partial response was maintained for 1 year with ongoing PD-1 therapy prior to PD in the LLE.

B. Size of RECIST index lesions throughout the time course depicts a partial response to therapy with a decrease in disease burden of 43%.

C. Representative CT and PET/CT images of LLE lesions are shown prior to, during, and at the time of disease progression.

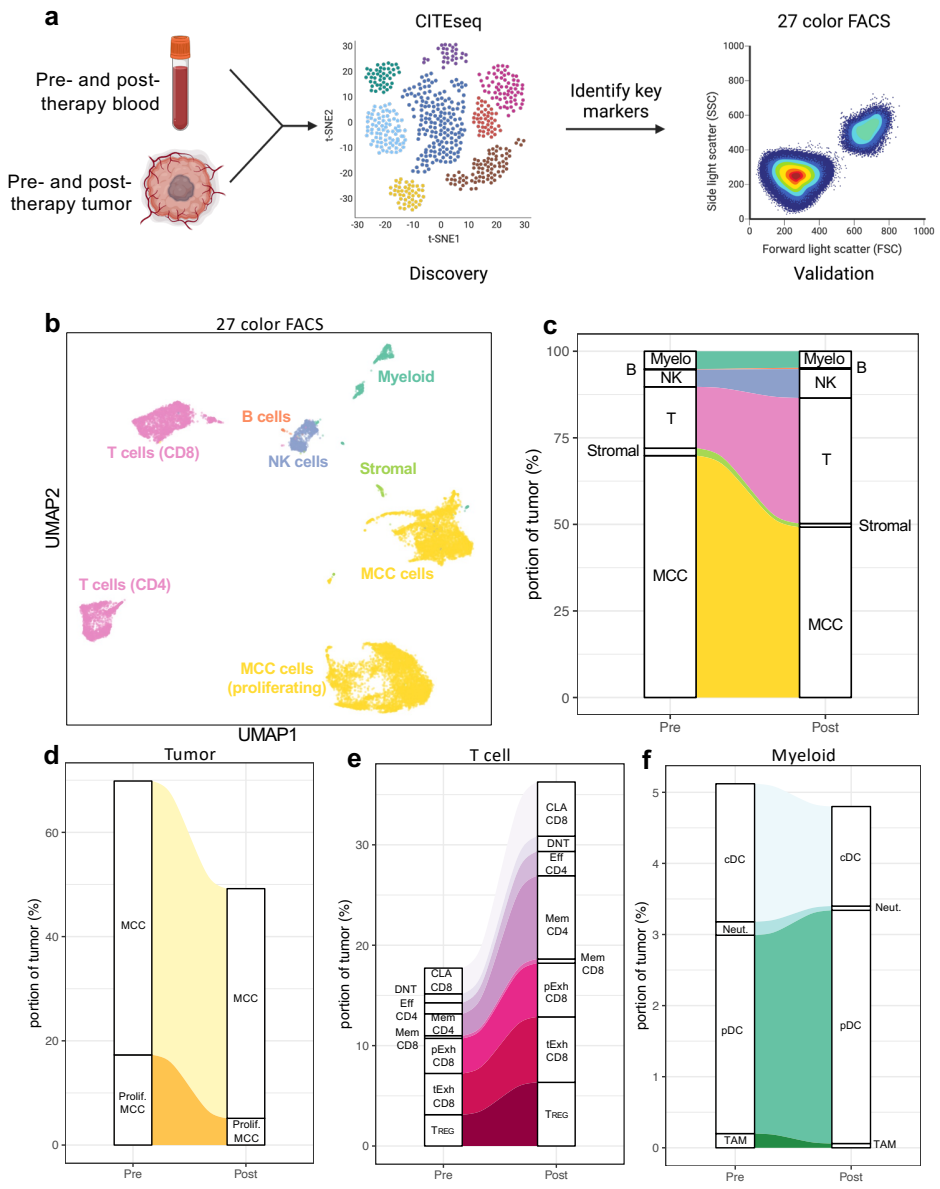

Figure 2. Intratumoral T cells increase following intralesional STING agonism

a. Experimental overview. CITEseq was performed on pre- and post-treatment tumor and blood specimens for unbiased analyses. Key markers and cell populations were identified and used to design a 27 color flow cytometry panel to validate samples in high throughput fashion to capture rare cell populations.

b. UMAP plot of 27 color flow cytometry data from pre- and post-STING agonist treatment. Each point represents one cell colored by cell lineage. Samples were subsetted to 10,000 cells per time point for visualization purposes

c. Alluvium plot of tumor composition before and after STING agonism showing expansion of T cells and contraction of tumor cells following treatment with STING agonist.

d. Alluvium plot of tumor of tumor cells sub clustered into proliferating MCC and non-proliferating cells showing contraction of both populations.

e. Alluvium plot of T cells showing an expansion of T cells following STING agonism. All T cells expanded similarly regardless of phenotype.

f. Alluvium plot of myeloid cells before and after STING agonist treatment. A predominance of plasmacytoid dendritic cells was noted but minimal changes occurred over the course of therapy.

g. Abbreviations: FACS: fluorescent activated cells sorting; UMAP: uniform manifold approximation projection; Myelo: Myeloid cells; NK: Natural killer cells; MCC: Merkel cell carcinoma; prolif: proliferating; CLA: cutaneous leukocyte antigen; DNT: double negative T cells; Mem: memory; pExh: progenitor exhausted; tExh: Terminally exhausted; cDC: classical dendritic cells; Neut: Neutrophil; pDC: plasmacytoid dendritic cells; TAM: tumor associated macrophage

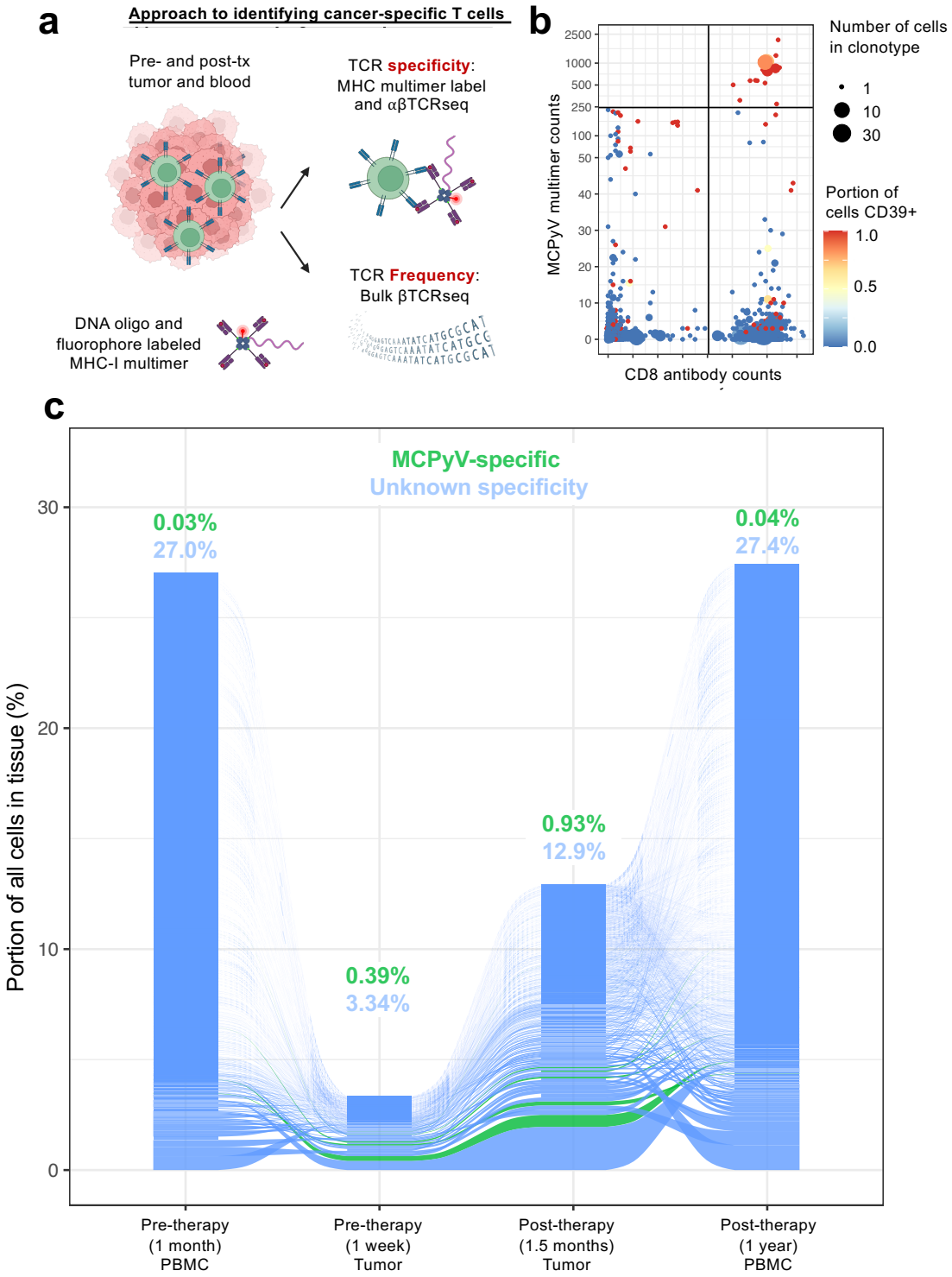

Figure 3. Intralesional STING treatment increases intratumoral T cell infiltration

a. Schematic of approach to quantifying frequency of MCPyV-specific CD8 T cells in tumor and blood specimens. Tumor or blood specimen were stained with DNA oligo and fluorophore labeled MHC tetramers and CITEseq with V(D)J seq was performed to identify specificity of TCRs. In parallel, beta-TCRseq was performed on tumor and blood specimen to quantify frequency of TCR clonotypes.

b. Gating of MCPyV-specific CD8 T cells via CITEseq. All cells with a single productive alpha and single productive beta TCR are shown. Cells with identical TCR sequences were grouped as clonotypes. X axis represents the median counts of CD8 antibody for each clonotype and y axis represents the median counts of an HLA-B*37:01 multimer containing a T antigen peptide.

c. Frequency of T cell clonotypes in tumor and blood before and after intralesional STING agonism. Alluvium plot where each alluvium represents and individual T cell clonotype. Clonotypes known to be MCPyV-specific are green. MCPyV-specific CD8 T cells were present in tumor and blood of patient

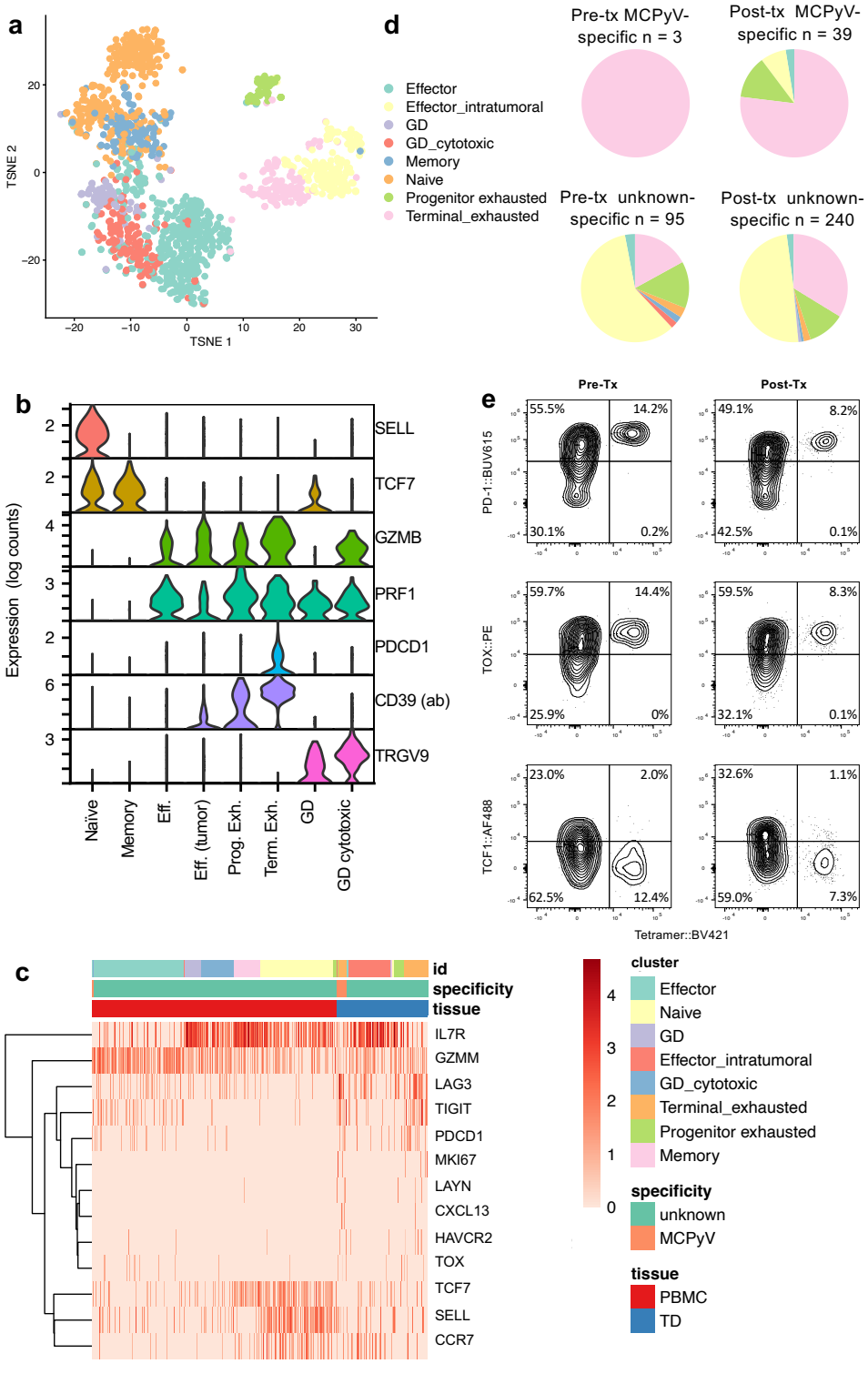

Figure 4. Cancer-specific CD8 T cells exhibit characteristics of exhaustion

a. TSNE plot of CD8 T cells isolated in silico from single cell RNAseq of patient tumor and blood specimen. Cells are colored by cluster.

b. Violin plots of expression of key genes in each cluster.

c. Heatmap of single cell RNAseq data of CD8 T cells from tumor or blood specimen.

d. Portion of MCPyV-specific CD8 T cells in tumors in each of 8 clusters. MCPyV-specific CD8 T cells in top pie charts and CD8 T cells of unknown specificity in bottom charts. Pre treatment specimen on left hand side and post-treatment on right.

e. FACS plots of CD8 T cells from tumors showing expression of proteins associated with exhaustion or stem like phenotypes in MCPyV-specific T cells

Abbreviations: GD: Gamma delta T cells, PBMC: peripheral blood mononuclear cells, TD: tumor digest, MCPyV: Merkel cell polyomavirus

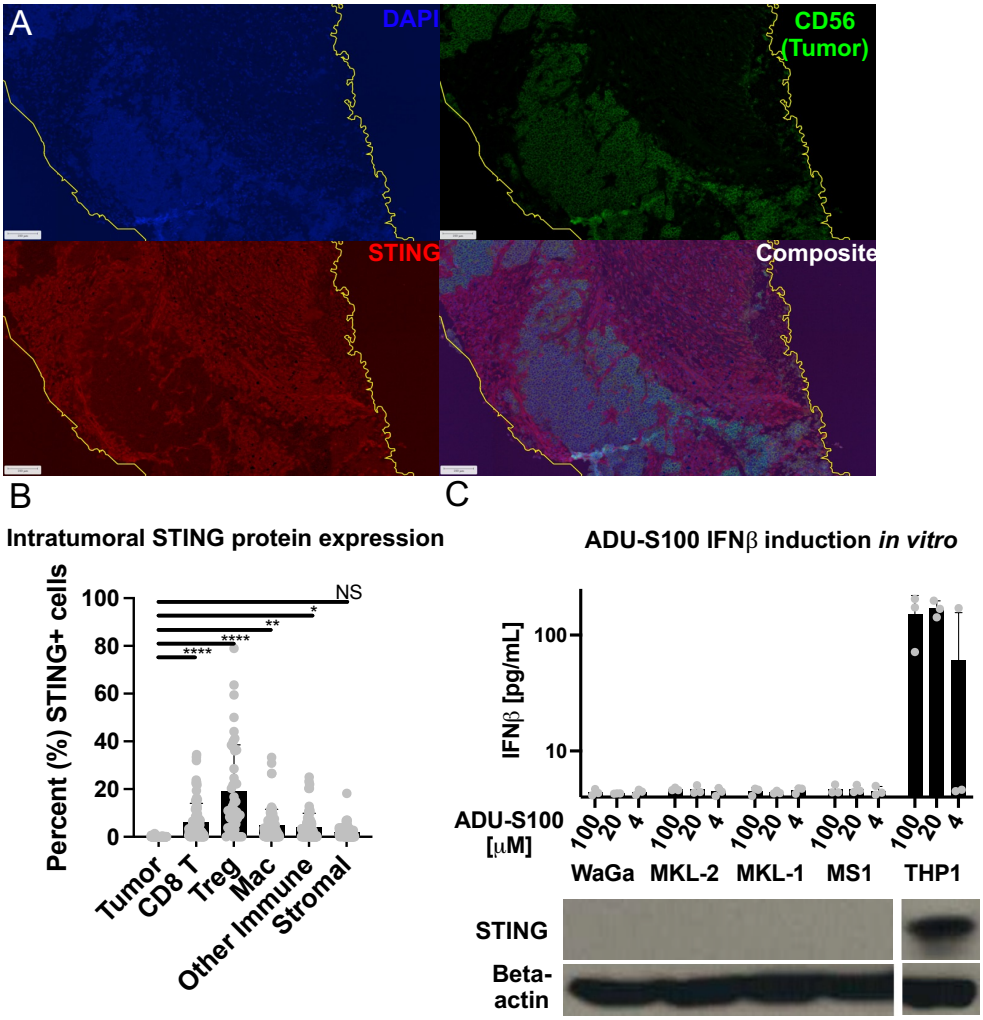

Figure 5. Merkel cell carcinoma are deficient in STING signaling

A. Multiplexed immunohistochemistry of post-ADU-S100 treated tumor. Areas of CD56 positivity (representing tumor) are non-overlapping with STING which is primarily expressed in stromal and immune tissues.

B. Quantification of STING expression. Each point represents 1 of 88 unique tumor specimens on a tissue microarray. STING is universially absent in MCC tumor cells. Tumor cells defined as CD56+, CD45-, CD8 T cells defined as CD8+, Treg cells defined as CD4+, FoxP3+, Macrophages defined as CD68+ or CD163+, Other immune cells defined as CD45+ cells which did not fall into prior categories, stromal cells defined as CD45-, CD56- cells.

C. MCC cell lines do not produce interferon-beta in response to ADU-S100 treatment. WaGa, MKL-2, MKL-1, MS1 MCC cells and THP1 cells (control monocytic cells) were all treated with decreasing doses of ADU-S100. None of the MCC cell lines produced detectable interferon-beta at any tested ADU-S100 concentration. These cells were all also deficient in STING protein (western blot, below).

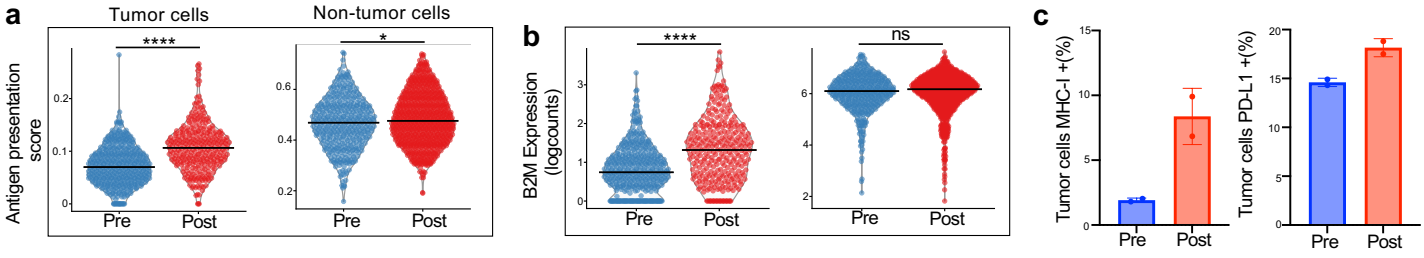

Figure 6. Tumor cells upregulate MHC following STING agonism.

A.scRNAseq data showing upregulation of antigen presentation genes following STING agonism on tumor cells. Tumor or non-tumor cells identified in silico. antigen presentation score calculated using 16 genes involved in the MHC-I antigen presentation pathway

B.B2M upregulation in tumor cells but not-non tumor cells following STING agonism.

C.Quantification of MHC-I and PD-L1 expression on tumor cells as shown in panel C. each data point represents 1 of 2 technical replicates.

T tests with bonferoni multiple comparison testing used for statistical significance. p value key: ns = p>0.05, * = p<0.05, ** = p<0.05, * = p<0.01, *** = p<0.001, **** = p<0.0001,

Abbreviations: MHC-I: major histocompatibility complex-I; FMO: Fluorescence minus one

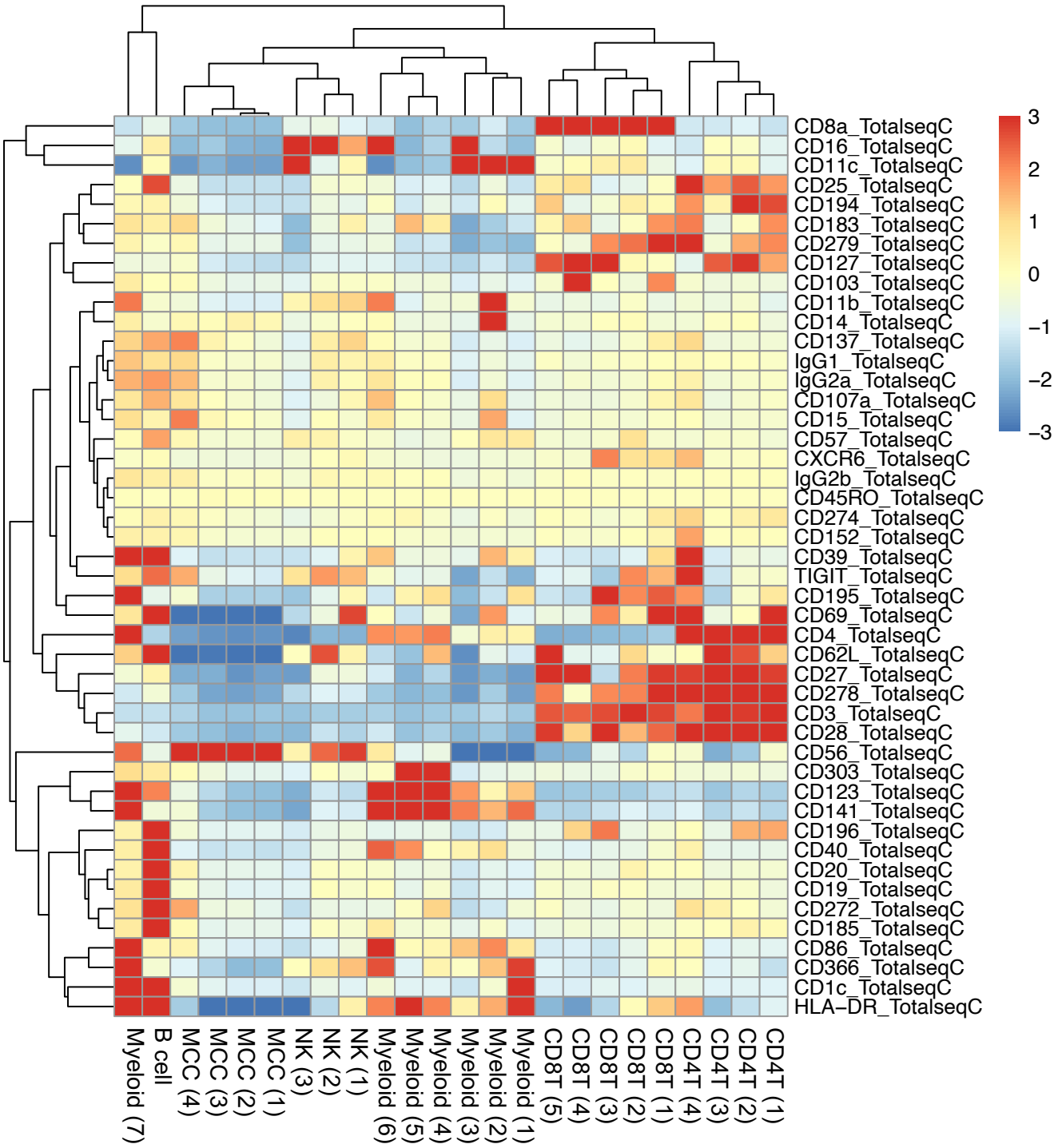

Figure 1. Clustering justification of single cell RNAseq. All clusters compared to all CITEseq antibodies to establish cell lineage identities.

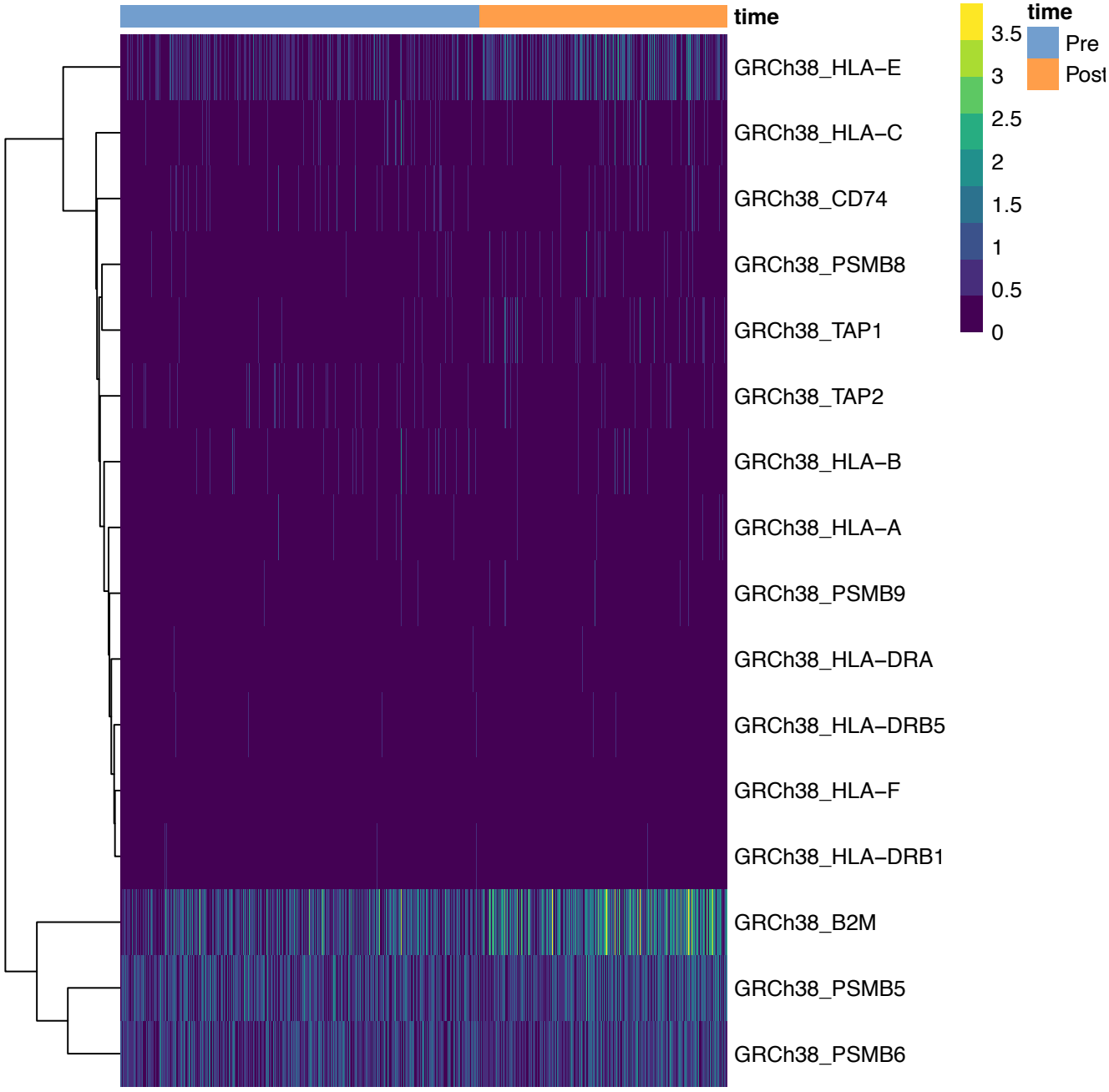

Supplemental Figure 2. Heatmap of genes associated with antigen presentation in MCC tumor cells before and after STING agonist treatment.

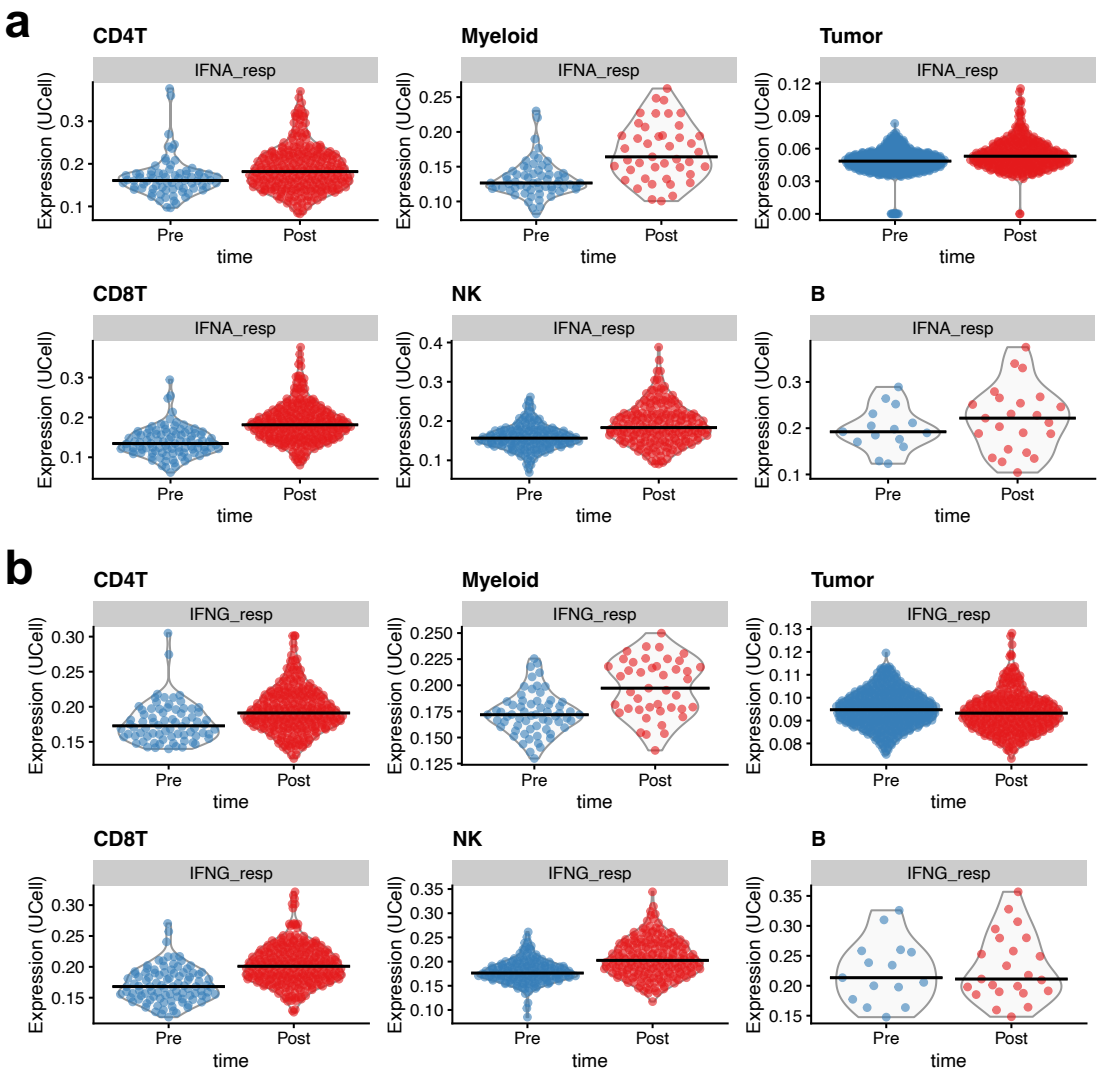

Figure 3. Interferon gene signatures are upregulated in cell in the tumor microenvironment following STING agonist treatment. Graphs broken down to show expression for individual cell lineages. Interferon alpha response signature shown in a (top), and interferon gamma signature shown in b (bottom)

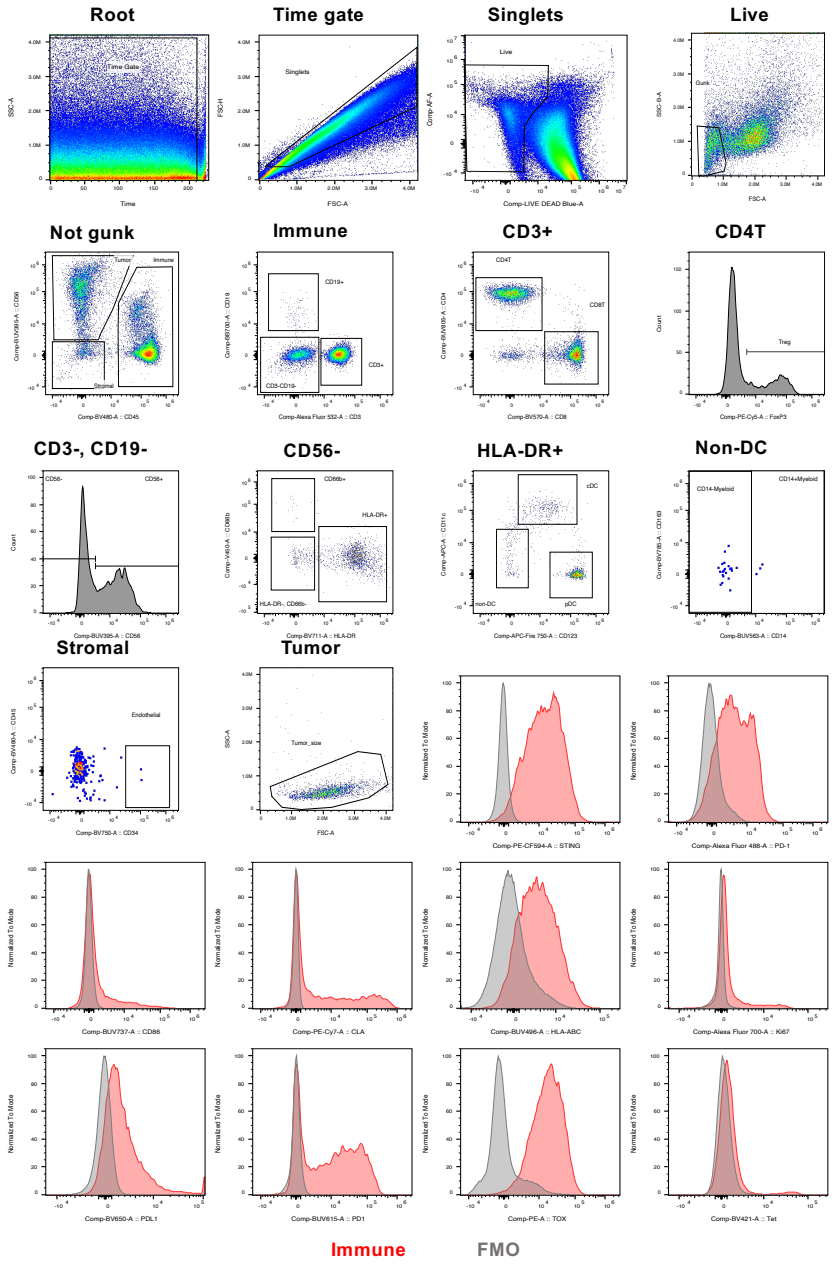

Supplemental figure 5. Flow cytometry gating strategy. Data shown for one tumor sample of patient treated with STING agonist.

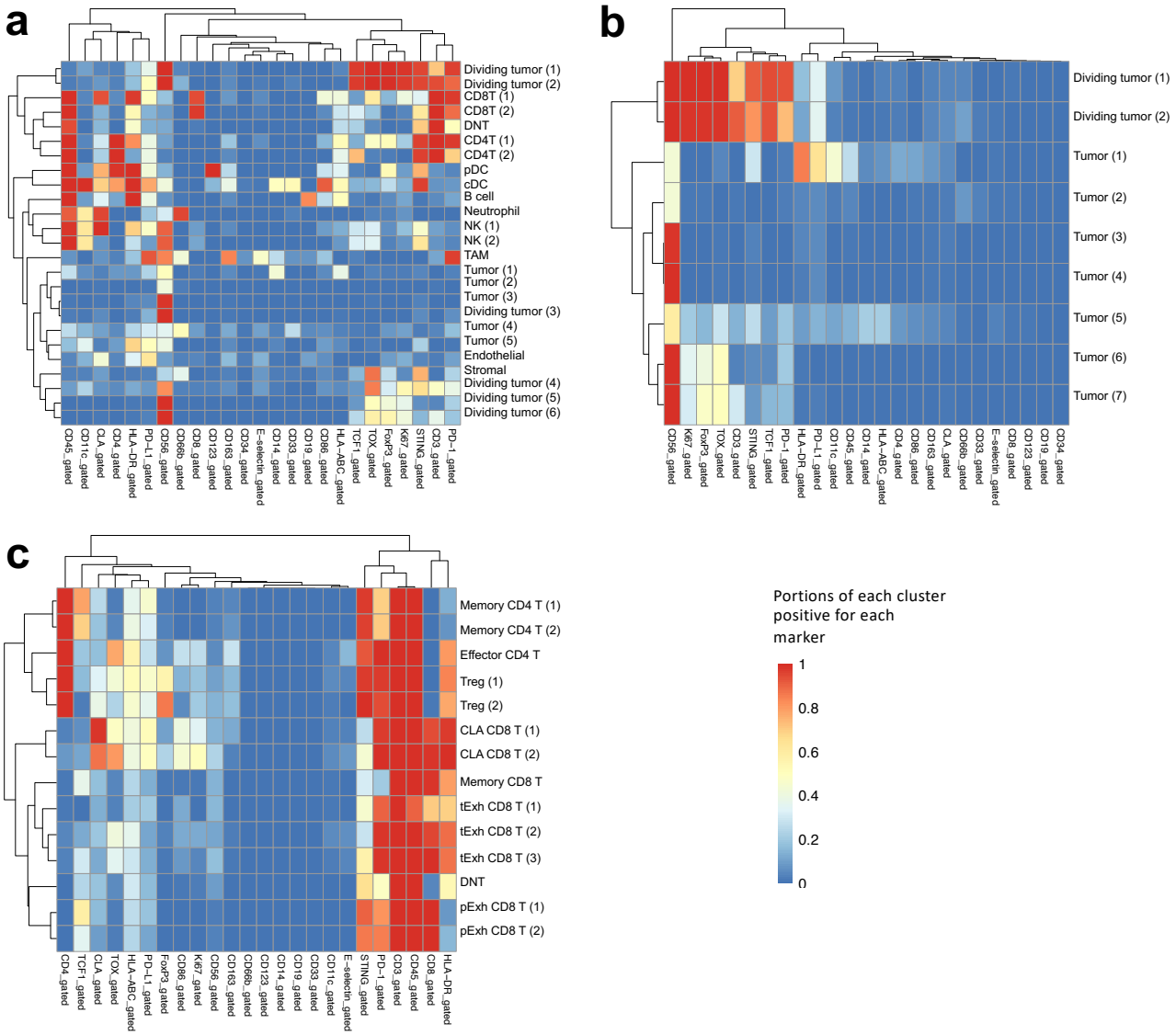

Supplemental Figure 6. Clustering and sub-clustering justification for FACS data. Heat map colored by portion of cells positive for each protein measured (x axis). Hierarchical clustering used to group cell populations (clusters) and markers.
A.All live cells clustered using phenograph.
B.Subclustering of Tumor cells
C.Subclustering of T cells

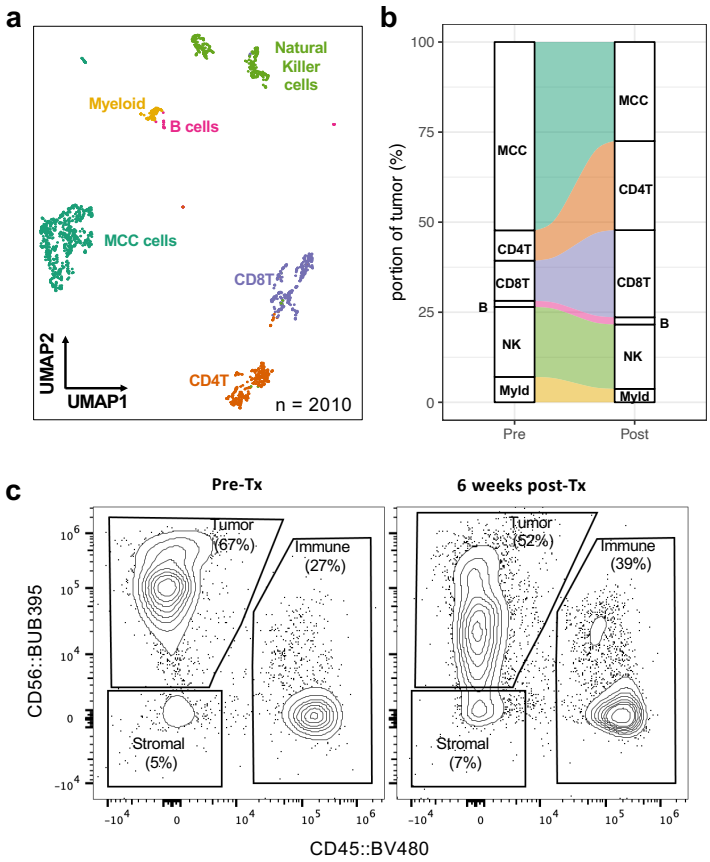

Supplemental figure 6. single cell RNAseq data and changes in tumor over course of therapy
a. UMAP plot of single cell RNAseq of pre and post-treatment tumor samples
b. Alluvium plot showing changes in cell populations after treatment
c. FACS plot confirming trends seen in panel b. Cells gated on live singlets.

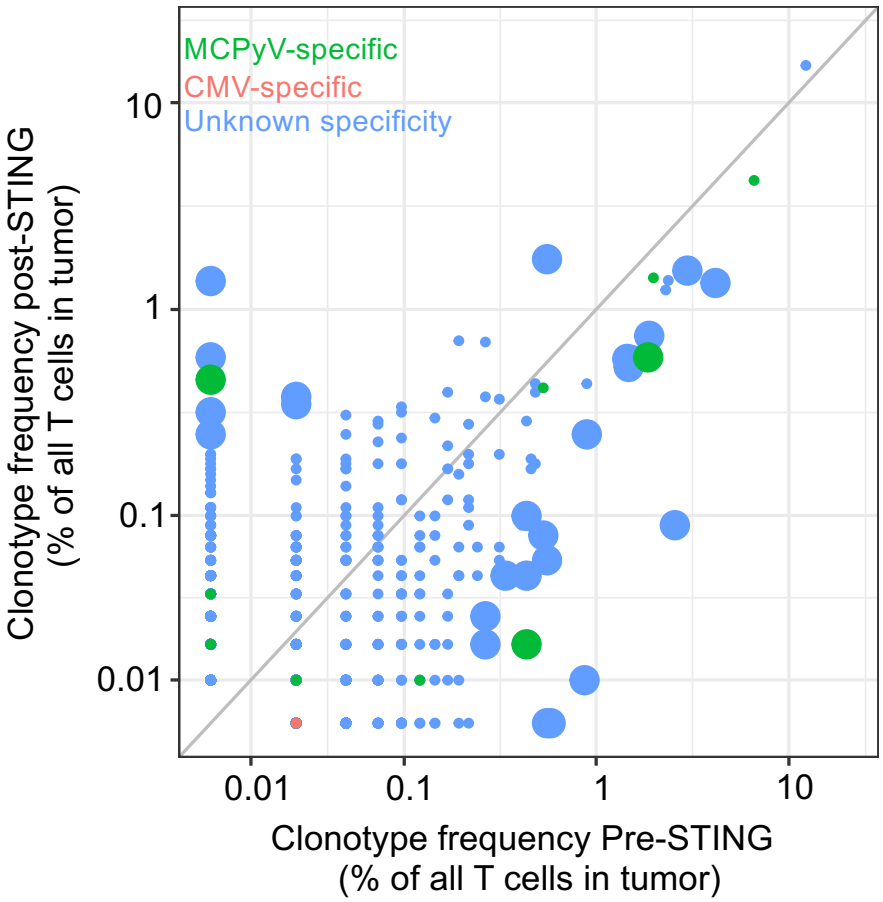

Supplemental figure 7. Differential abundance of T cell clonotypes in tumor before and after STING agonism. Each point represents an individual T cell clonotype. Clonotypes significantly expanded shown with large points. Clonotypes colored by specificity. Statistical significance assessed using betabinomial test and a p value of less than 0.01

Journal for ImmunoTherapy of Cancer

Transcriptional and functional analyses of neoantigen-specific CD4 T cells during a profound response to anti-PD-L1 in metastatic Merkel cell carcinoma

Candice Church ,[1] Thomas Pulliam ,[1] Natalie Longino,[1] Song Y Park ,[1] Kimberly S Smythe ,[2] Vladimir Makarov,[3,4] Nadeem Riaz ,[3] Lichen Jing ,[5] Robert Amezquita,[6] Jean S Campbell ,[2] Raphael Gottardo,[6,7,8] Robert H Pierce ,[2] Jaehyuk Choi ,[9] Timothy A Chan,[3,10] David M Koelle ,[5,11,12,13,14] Paul Nghiem [1,2]

To cite: Church C, Pulliam T, Longino N, *et al*. Transcriptional and functional analyses of neoantigen-specific CD4 T cells during a profound response to anti-PD-L1 in metastatic Merkel cell carcinoma. *Journal for ImmunoTherapy of Cancer* 2022;**10**:e005328. doi:10.1136/jitc-2022-005328

► Additional supplemental material is published online only. To view, please visit the journal online (http://dx.doi.org/10.1136/jitc-2022-005328).

CC and TP contributed equally.

Accepted 14 August 2022

For numbered affiliations see end of article.

Correspondence to
Dr Paul Nghiem;
pnghiem@uw.edu

ABSTRACT

Background Merkel cell carcinoma (MCC) often responds to PD-1 pathway blockade, regardless of tumor-viral status (~80% of cases driven by the Merkel cell polyomavirus (MCPyV)). Prior studies have characterized tumor-specific T cell responses to MCPyV, which have typically been CD8, but little is known about the T cell response to UV-induced neoantigens.

Methods A patient in her mid-50s with virus-negative (VN) MCC developed large liver metastases after a brief initial response to chemotherapy. She received anti-PD-L1 (avelumab) and had a partial response within 4 weeks. Whole exome sequencing (WES) was performed to determine potential neoantigen peptides. Characterization of peripheral blood neoantigen T cell responses was evaluated via interferon-gamma (IFNγ) ELISpot, flow cytometry and single-cell RNA sequencing. Tumor-resident T cells were characterized by multiplexed immunohistochemistry.

Results WES identified 1027 tumor-specific somatic mutations, similar to the published average of 1121 for VN-MCCs. Peptide prediction with a binding cut-off of ≤100 nM resulted in 77 peptides that were synthesized for T cell assays. Although peptides were predicted based on class I HLAs, we identified circulating CD4 T cells targeting 5 of 77 neoantigens. In contrast, no neoantigen-specific CD8 T cell responses were detected. Neoantigen-specific CD4 T cells were undetectable in blood before anti-PD-L1 therapy but became readily detectible shortly after starting therapy. T cells produced robust IFNγ when stimulated by neoantigen (mutant) peptides but not by the normal (wild-type) peptides. Single cell RNAseq showed neoantigen-reactive T cells expressed the Th1-associated transcription factor (T-bet) and associated cytokines. These CD4 T cells did not significantly exhibit cytotoxicity or non-Th1 markers. Within the pretreatment tumor, resident CD4 T cells were also Th1-skewed and expressed T-bet.

Conclusions We identified and characterized tumor-specific Th1-skewed CD4 T cells targeting multiple neoantigens in a patient who experienced a profound and durable partial response to anti-PD-L1 therapy. To our knowledge, this is the first report of neoantigen-specific T cell responses in MCC. Although CD4 and CD8 T cells recognizing viral tumor antigens are often detectible in virus-positive MCC, only CD4 T cells recognizing neoantigens were detected in this patient. These findings suggest that CD4 T cells can play an important role in the response to anti-PD-(L)1 therapy.

INTRODUCTION

Merkel cell carcinoma (MCC) is a rare and aggressive neuroendocrine skin cancer with an increasing incidence estimated to exceed 3200 cases per year in the USA by 2025.[1] Before the availability of immune checkpoint inhibitors, diagnosis with metastatic MCC had a grim outlook with a 20% relative survival rate at 3 years.[2] In contrast, the 3-year overall survival rate for first-line anti-PD-1 (pembrolizumab) in the Keynote-017 trial was 59%.[3] Accordingly, MCC tumors are thought to be immune sensitive as indicated by a >10 fold increase in incidence among immune suppressed patients[4 5] as well as a markedly lower risk of recurrence when tumors have brisk intratumoral CD8 infiltration.[6]

Roughly 80% of MCCs are driven by the Merkel cell polyomavirus (MCPyV), in which the viral DNA is clonally integrated into the host genome, and T-antigen oncoproteins are persistently expressed by tumor cells.[7] The remaining ~20% of cases are thought to be truly virus-negative MCC (VN-MCC) and are characterized by high UV-mutational burdens resulting in numerous potential neoantigens. Indeed, there are a median of 1121 protein-coding somatic single nucleotide variants

(SSNVs) per exome compared with a median of 13 SSNVs per exome in MCC tumors harboring MCPyV.[8–10] The MCPyV proteins that drive tumor cell growth have been shown to be immunogenic as evidenced by robust T and B cell responses specifically observed in MCC patients.[11 12] However, there is a paucity of data describing the immune response to individual tumor neoantigens in VN-MCCs. The different etiologies for virus-positive (VP) and VN-MCCs, as well as the immune sensitive nature of MCC, makes this an ideal cancer to study the important role of anti-tumor T cells, which can be applied to other solid tumors more broadly.

Programmed death-ligand 1 (PD-L1), a major ligand for programmed cell death-1 (PD-1), is frequently expressed in MCC patient tumor specimens on immune cells and in some cases on tumor cells.[13 14] MCC has a strikingly high response rate to agents targeting the PD-1 pathway (56–62%), making it one of the most PD-(L)1 responsive solid tumors studied to date.[3 15 16] The high response rate to PD-1 pathway blockade is consistent across multiple studies for both VP-MCC and VN-MCC. The immune response has been extensively studied for VP-MCC. It is clear that MCPyV oncoproteins are frequently recognized by CD8[12 17 18] and CD4 T cells,[17 19] the number and avidity of which correspond to clinical outcomes.[20] In contrast, little is known about the nature of the immune response in VN-MCC patients. Based on analogy to other cancers,[21–24] the abundant UV-induced neoantigens in VN-MCC are presumed to be relevant immune targets, but the contributions of CD8 vs CD4 T cells and nature of the response have not been characterized to the best of our knowledge.

Herein, we describe a patient with an impressive and rapid partial response (RECIST V.1.1)[25] to anti-PD-L1 (avelumab) that was deep and durable (87% reduction in tumor burden after the first 2 years of therapy and remained disease free 5 years after discontinuing treatment) despite a large burden of chemotherapy-refractory disease. Our results reveal robust CD4 T cell responses to patient-specific tumor neoantigens even though neoepitope peptides were selected using class I HLA binding prediction algorithms to identify CD8 T cell responses. Indeed, CD4 T cells were identified that selectively recognized five different neoantigens from this patient. These neoantigen-specific T cells actively secreted interferon gamma (IFNγ) and upregulated cellular activation markers when stimulated with neoantigens compared with wild-type normal self-antigens. Furthermore, detailed transcriptional analysis showed a T-helper (Th) 1 skewed T cell phenotype.

METHODS

Patient consent and specimens

Informed consent was received. HLA typing was performed via PCR at Bloodworks Northwest (Seattle, Washington, USA). Peripheral blood mononuclear cells were collected in heparinized tubes, ficolled and cryopreserved at the Fred Hutchinson Cancer Center (FHCC) Specimen Processing/Research Cell Bank (Seattle, Washington, USA). Formalin-fixed paraffin-embedded (FFPE) archival biopsy material was used for immunohistochemistry and DNA isolation. Tumor whole exome sequencing (WES) was performed on DNA from the tumor biopsy peripheral blood mononuclear cells (PBMCs), and somatic mutation and neoantigen calls were performed as previously described.[8] Neoantigen-specific peptides for immunoassays were selected based on HLA class I predicted binding affinity using NetMHCv3.4[26] (https://services.healthtech.dtu.dk/?NetMHC-3.4), with a cut-off of ≤100 nM (n=77 peptides). Neoepitopes were excluded from analysis if they were within genes that are not expressed in MCC.[6]

IFNγ enzyme-linked immunospot (ELISpot) assay

Cryopreserved PBMC were thawed and rested overnight in R10 (RPMI, 10% fetal bovine serum, 100 nmol/L L-glutamine, and 100 U/mL penicillin-streptomycin) at 37°C. Concurrently, 96-well MultiScreen-IP filter plates (Millipore) were coated with anti-IFNγ capture antibody (1-D1K, Mabtech) at a concentration of 10 µg/mL in and incubated overnight at 4°C. The next day, 1×10^5 PBMC/well were plated in R10 with either neoantigen peptide pools (containing 8–9 peptides each at 5 µg/mL), DMSO (negative control) or Staphylococcal enterotoxin B (SEB) as a positive control, in triplicate and incubated at 37°C overnight (online supplemental figure 1B). After 16 hours of culture, plates were developed.[27] Briefly, antibody coated 96-well plates were washed before incubation with detection antibody (7-B6-1; Mabtech), followed by Avidin-peroxidase (Vectastain ABC kit; Vector Labs), and AEC substrate (AEC kit; Vector Labs). Developed plates were scanned with a C.T.L. ELISpot reader and counted (ImmunoSpot 5.0 Software, C.T.L.). Wells with 2× above DMSO or with at least 10 spot forming units (SFU) were considered positive. Peptide pool hits were mapped to individual peptides in follow-up ELISpot assays. ELISpot experiments were performed as previously described with the addition of an anti-HLA class I antibody (clone W6/32, 10 µg/mL; Thermo Fisher) or anti-HLA-DR antibody (clone G46-6, 10 µg/mL; BD Biosciences) 30 min before peptides were added.

Generation and testing of T cell lines

On day 1, cryopreserved PBMC were thawed and allowed to rest overnight at 37°C in T cell media (TCM) (RPMI, 10% human serum, 10 mM HEPES, 50 µM β-mercaptoethanol, 100 nmol/L L-glutamine, 100 U/mL penicillin-streptomycin and 2 ng/mL IL-7). On day 2, the media was refreshed and volume adjusted so that PBMCs were at a concentration of 2×10^6 cells/mL. Each well of a 24-well plate had one neoantigen peptide or control peptide added at a concentration of 1 µg/mL. On day 3, 10 U/mL of recombinant human IL-2 was added. TCM and cytokines were refreshed every 2–3 days thereafter. On day 13, cells were washed and allowed to rest overnight without

cytokines. For functional readouts, 2.5×10^4 cultured cells were combined with 5×10^5 patient-derived LCLs (EBV-transformed lymphoblastoid cell line) in each well of a 96-well round bottomed plate. The antigen source was serial dilutions of the neoantigen peptide used to generate the cell lines or wild-type counterparts. Plates were incubated overnight at 37°C. Supernatants from cocultured cells were collected and assessed for IFNγ secretion via Ready-SET-Go human IFNγ ELISA per manufacturer's protocol (eBioscience).

Single cell sorting of antigen-specific T cells

Cryopreserved PBMC were thawed and cultured at 2×10^6 cells/mL in a 24-well plate with anti-CD40 at 500 ng/mL and each of the five neoantigen peptides as well as a control HIV NEF (RYPLTFGWCF) peptide at 1 µg/mL overnight at 37°C. After 16 hours, cells were stained for with LIVE/DEAD Fixable Violet Dead Cell Stain (Invitrogen), followed by lineage markers CD14 (clone M5E2, Biolegend), CD19 (clone HIB19, Biolegend), CD4 (clone SK3, eBioscience), CD8 (clone 3B5, Invitrogen) and activation-induced markers CD69 (clone L78, BD Biosciences), CD137 (clone 4-1BB, Biolegend) and CD154 (clone TRAP1, BD Bioscience). Single neoantigen-reactive CD4 cells were sorted into RNAlater (Thermo Fisher) based on coexpression of CD69, CD137 and CD154 on a BD FACSAria II (BD Biosciences).

Single-cell RNA sequencing and analysis

RNA from sorted cells was purified using RNA Solid Phase Reversible Immobilization beads (Beckman), and cDNAs were generated with Smart-Seq2 (Illumina). Purified DNA was quantified with a Qubit dsDNA High Sensitivity Assay Kit (Invitrogen) before library preparation (Nextera, Illumina). Paired-end, next-generation sequencing was performed. Kallisto (V.0.44.0) was used for pseudoalignment of sequencing reads to transcripts. All further single cell RNA sequencing (scRNAseq) analyses were performed in R (V.3.6.0) primarily using packages Seurat (V.3.2.1) and scater (V.1.22.0) for normalization and plotting. Cells with less than 2000 genes or more than 5% mitochondrial genes were removed as low quality. Gene counts were log-normalized and regressed using mitochondrial gene expression via the Seurat function SCTransform. Code is available on request.

Multiplex immunohistochemistry

FFPE tissues were stained on a Leica BOND Rx autostainer using the Akoya Opal Multiplex IHC assay (Akoya Biosciences, Menlo Park, California, USA) with the following changes: additional high stringency washes were performed after the secondary antibody and Opal fluor applications using high-salt Tris-buffered saline + 0.1% Tween-20 (0.05M Tris, 0.3M NaCl, and 0.1% Tween-20, pH 7.2–7.6). Tris-casein + 0.1% Tween was used as the blocking buffer (0.05M Tris, 0.15M NaCl, 0.25% Casein, 0.1% Tween 20, pH 7.6±0.1). All primary antibodies were incubated for 1 hour at room temperature. OPAL Polymer HRP Mouse plus Rabbit (Akoya Biosciences) was used for all secondary applications. Slides were mounted with ProLong Gold and cured for 24 hours at room temperature in the dark before image acquisition at 20× magnification on the Akoya Vectra 3.0 Automated Imaging System. Images were spectrally unmixed using Akoya Phenoptics inForm software and analyzed using HALO software (Indica Labs, Corrales, New Mexico, USA). Cell nuclei=DAPI, CTLA-4=clone BSB-88 OPAL 540, T-bet=-clone EP263 OPAL 570, CD4=clone EP204 OPAL 620, FoxP3=clone 236A OPAL 690, CD8=clone 144B OPAL 520, CD3=clone SP7 OPAL 690 and PD-L1=clone E1L3N OPAL 620.

RESULTS

Case presentation: clinical response to anti-PD-L1 therapy

A patient in her mid-50s with a previous history of breast cancer presented with a skin lesion on her chest, which was biopsied and diagnosed as VN-MCC based on positive staining for CK-20 and negative staining for MCPyV Large-T antigen (CM2B4 clone). Staging PET-CT scan revealed multiple metastatic tumors in the liver. Pathological evaluation a liver biopsy indicated metastatic MCC. The patient was treated with four cycles of cytotoxic chemotherapy (cisplatin and etoposide). After a brief partial response to chemotherapy that lasted less than 2 months, the patient progressed while still on treatment resulting in four liver masses, the largest two of which had diameters of 11 and 7.5 cm (figure 1A).

She received anti-PD-(L)1 (avelumab) as a second-line treatment and experienced a rapid decrease of tumor size within 4 weeks from treatment initiation (figure 1A). All four measurable lesions had significant shrinkage over the course of 29 months of anti-PD-L1 therapy. She did not experience any significant side effect other than grade 1 fatigue and remains in remission with a deep partial response (87% reduction in tumor burden) more than 7 years after beginning and 5 years after discontinuing anti-PD-L1 therapy. High-throughput T cell receptor sequencing (see online supplemental figure 3) of the tumor and on-treatment blood specimens showed an expansion of tumor-resident T cell clones in the blood suggesting an antitumor response that tracked with clinical response (figure 1A).

To understand this T cell response, we performed WES to identify tumor neoantigen mutations that could potentially be targeted by T cells. Neoantigen peptides were selected for synthesis based on prediction of their binding strength (see methods and figure 1B) to the following patient-specific HLA class I types: HLA-A*24:02, HLA-A*68:02, HLA-B*14:02, HLA-B*51:09, HLA-C*01:02 and HLA-C*08:02.

T cells recognize neoantigens and expand during profound clinical response

Following WES and mutant peptide identification, 77 potential neoantigen peptides were selected for synthesis

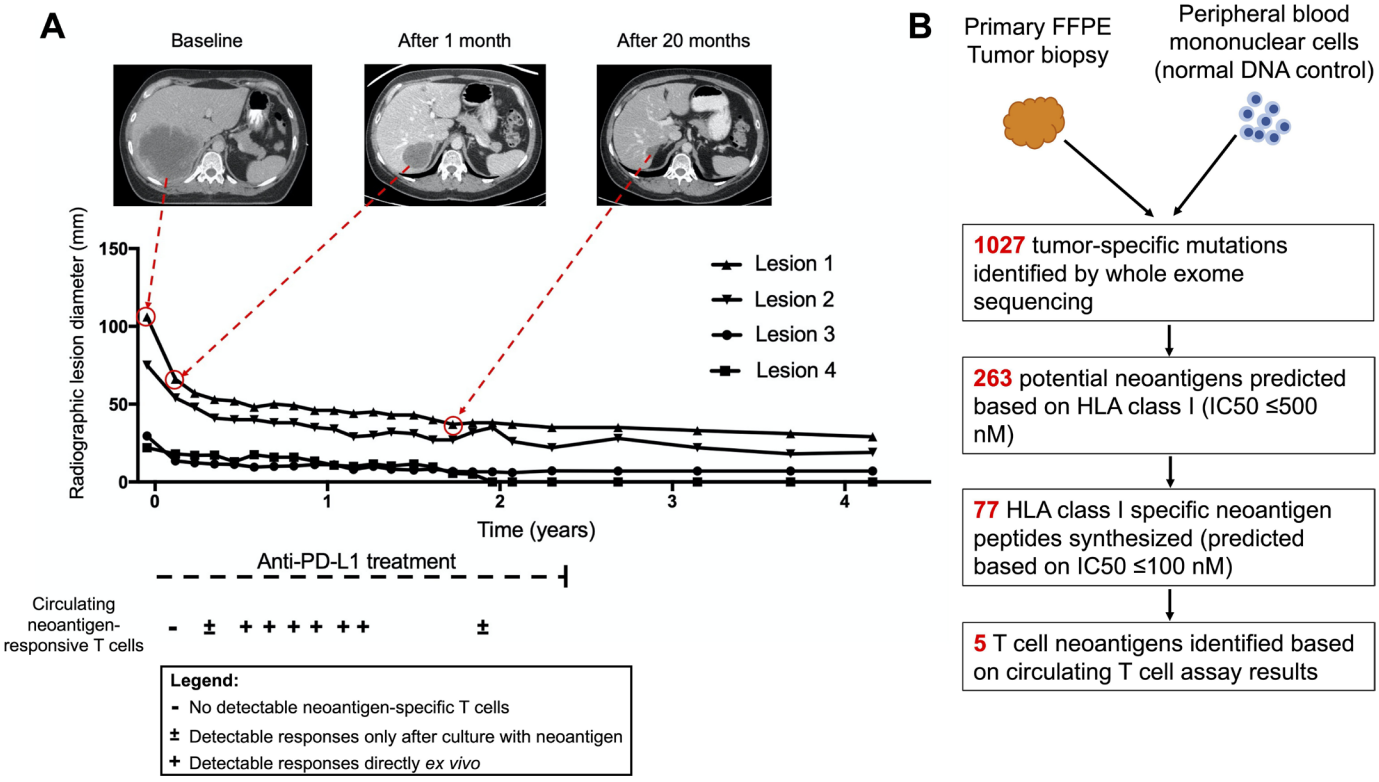

Figure 1 Clinical response to anti-PD-L1 therapy. (A) Timeline describing treatment, clinical response and T cell responses. Patient received four doses of cisplatin/etoposide and discontinued due to disease progression. Shortly thereafter, patient started anti-PD-L1 therapy (avelumab) and experienced a rapid partial response. Computed tomography (CT) scan of a tumor (lesion 1) in the liver before initiation of anti-PD-L1 therapy, after two doses of anti-PD-L and after 20 months of anti-PD-L1. Detection of neoantigen-specific T cells is denoted below the x axis: a '-' sign for no detectable neoantigen-specific T cells, a '±' sign for neoantigen-specific T cells detected after culture with target peptides, or a '+' for neoantigen-specific T cells detected directly ex vivo. (B) Tumor specific non-synonymous somatic mutations were identified via WES and compared against peripheral blood DNA for reference. WES, whole exome sequencing.

based on whether their predicted binding affinity for any cognate HLA class I allele was less than or equal to 100 nM (online supplemental figure 1A and table 1). Neoantigen peptides were pooled (online supplemental figure 1B), and patients PBMC from 6 months post-treatment initiation were assessed for response to peptides in an IFNγ ELISpot. Eleven neoantigen peptide pools elicited IFNγ secretion from T cells (online supplemental figure 1C), and then individual reactive peptides were then identified. Due to limited patient PBMC, only peptides from the strongest IFNγ pool hits were tested in follow-up IFNγ ELISpot assays.

Of the 18 individual peptides tested, five neoantigen peptides were considered positive based on responses above the baseline threshold (greater than 10 SFU/5×10^5 PBMC cells; online supplemental figure 1D). The following genes, and specific amino acid changes, elicited a positive IFNγ ELISpot result: *CASR* (P39S), *DMXL2* (P154S), *RNF38* (P287L), *TANGO6* (R172S), and *ZNF280C* (R301M). To the best of our knowledge, none of the mutations are considered driver mutations.

To determine if IFNγ secretion was specific for mutant neoantigen peptides and not a response against self-antigens, we performed an IFNγ ELISpot with side-by-side neoantigen and self (wild-type) peptides (figure 2A). Four of the five self-peptides tested did not elicit a T cell response; however, the self-peptide originating from the *RNF38* gene stimulated~45% of the IFNγ response that was induced by the mutant/neoantigen version of that peptide. To determine the sensitivity of neoantigen responses, we performed a dose–response curve in T cell lines specific for two of the mutant peptides, *TANGO6* and *ZNF280C*. Results of the dose–response experiments show specificity for the mutated form of the peptides as indicated by response to the neoantigen peptides versus wild type as low as 1 µg/mL (figure 2C,D).

After identifying neoantigen T cell epitopes, we used serially collected PBMC to determine kinetics. We were unable to detect T cell responses in the blood until ~4 months after anti-PD-L1 treatment initiation, consistent with either expansion or migration of epitope-specific T cells during immunotherapy. Furthermore, we were unable find epitope-specific T cell responses directly *ex vivo* after tumors markedly shrank (76% reduction at~22 months post treatment initiation).

Neoantigen-specific T cells are HLA class II restricted CD4+, CD8- T cells

To determine if IFNγ-positive T cells responding to neoantigen peptides were restricted by HLA class I or HLA class

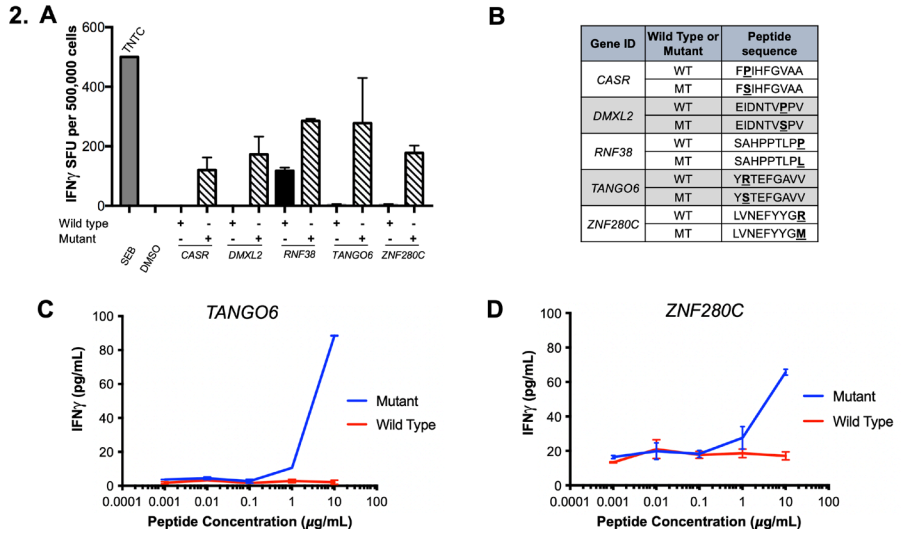

Figure 2 Circulating T cells recognize tumor-specific neoantigens. (A) Top: PBMC was tested for neoantigen T cell specificity by comparing IFNγ reactivity of mutant and wild-type peptides (5 µg/mL). Detection at twice the DMSO control level or >10 SFU per 5×10^5 PBMC were considered positive. Experiments were performed in triplicate. The mean is plotted, and SD is indicated by error bars. (B) Table of mutant peptides with reactivity in direct *ex vivo* IFNγ ELISpot and wild type peptide homologs. (C and D) T-cell line dose response curves for neoantigen peptides from the *TANGO6* (C) and *ZNF280C* (D) genes. Experiments performed in duplicate or triplicate. The mean is plotted and error bars represent SD from the mean. ELISpot, enzyme-linked immunospot; IFNγ, interferon gamma; SFU, spot forming units; TNTC, too numerous to count.

II, we performed an IFNγ ELISpot with the addition of blocking antibodies specific for either HLA class I A, B, and C, or the HLA class II loci. Addition of HLA class II specific antibodies to ELISpot wells blocked production of IFNγ spots (figure 3A) indicating that T cell responsiveness was HLA-DR restricted.

To confirm these findings, we measured the upregulation of three activation-induced T cell surface markers: CD69,[28] CD137,[29] and CD154[30] on CD4 T cells and two activation-induced cell markers, CD69 and CD137, on CD8 T cells after stimulation with neoantigen peptides. The specimen used was PBMC from ~7 months after

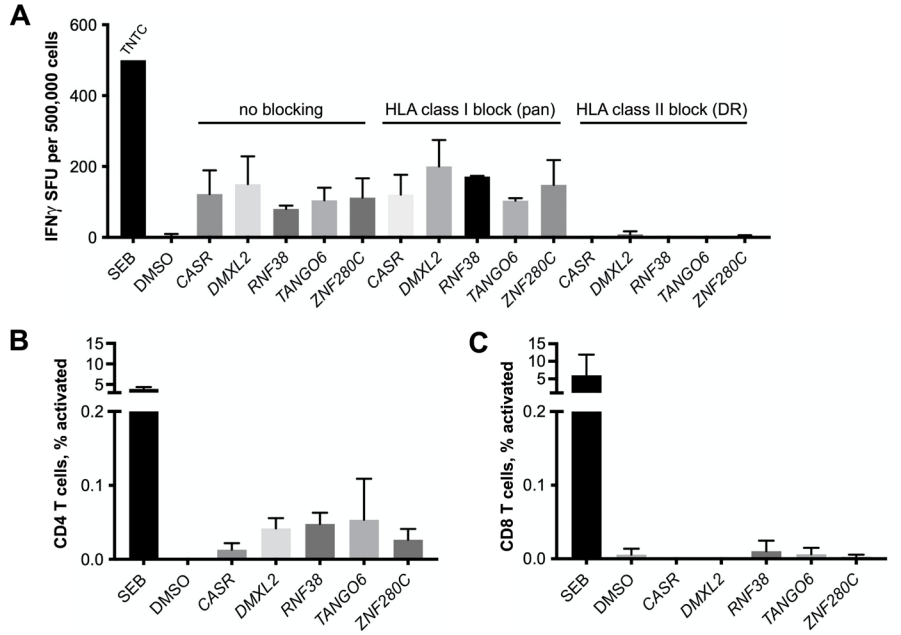

Figure 3 Neoantigen-specific T cells are HLA class II restricted and CD4 T cells upregulate activation markers on peptide stimulation. (A) IFNγ ELISpot incorporating anti-HLA class I antibody clone W6/32 or anti-HLA class II DR clone G46-6. Experiments were performed with two to six replicates. Positive responses were indicated by twice the DMSO control level or >10 SFU per 5×10^5 PBMC. (B and C) Per cent of CD4 T cells (B) that upregulate all three activation markers (CD69, CD137 and CD154) or CD8 T cells (C) that upregulate two activation markers (CD69 and CD137) after stimulation with each neoantigen peptide. Results are an average of two flow cytometry experiments; error bars indicate the SD. ELISpot, enzyme-linked immunospot.

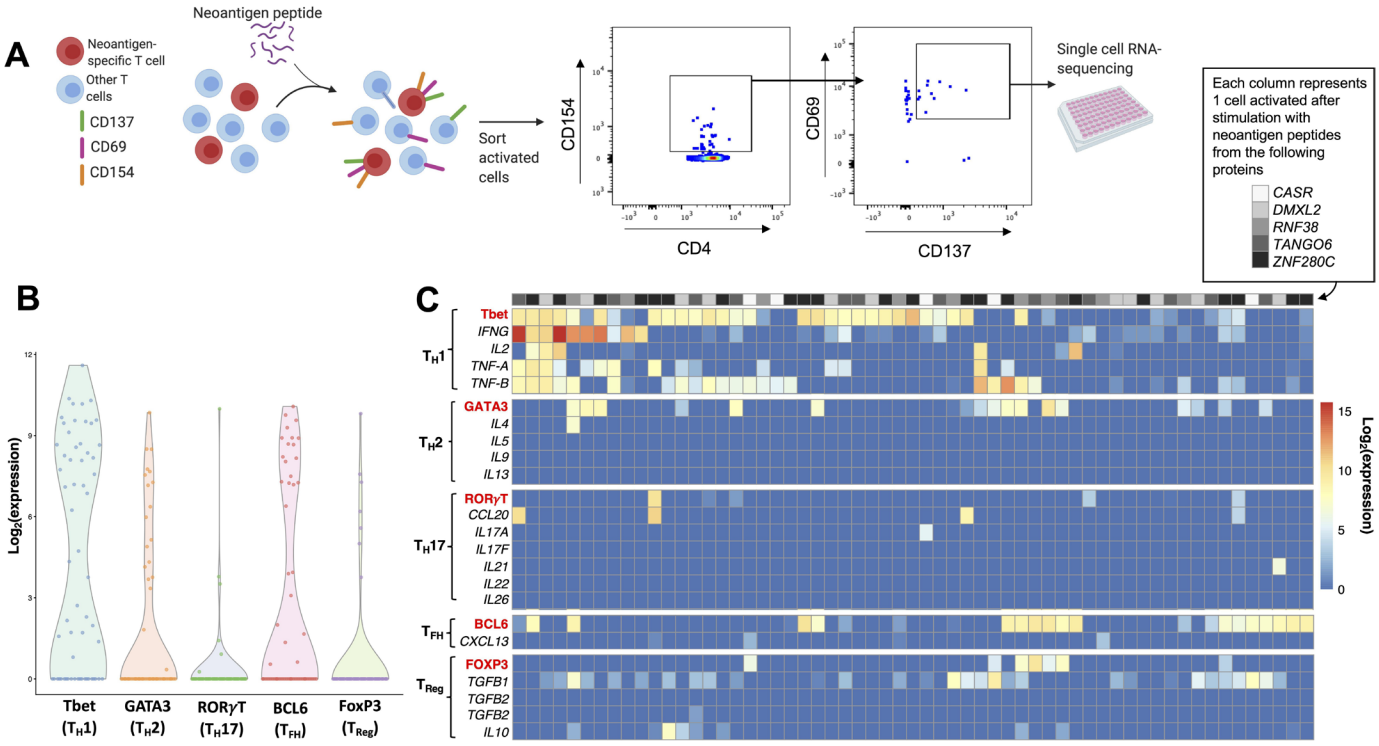

Figure 4 Neoantigen-specific CD4 T cells have a Th1-skewed transcriptional phenotype. (A) Overview of experimental method. Peripheral blood mononuclear cells were stimulated for 16 hours with neoantigen peptides and CD4 T cells were single-cell sorted into a 96 well plate based on upregulation of three activation markers (CD69, CD137 and CD154, representative dot plots shown). (B) Sorted CD4 T cell T-bet RNA levels were significantly elevated when compared with other CD4 T cell master regulator transcription factors (p values as compared with T-bet were: p<0.001 for GATA3, RORγT and FoxP3, and p<0.01 for BCL6). (C) RNA expression of effector cytokines indicates a Th1 skewed phenotype.

initiation of anti-PD-L1 therapy at a time the patient had experienced a partial response. Measurement by flow cytometry showed that all five of the neoantigens stimulated upregulation of the three activation markers on CD4+ but not CD8+ T cells (figure 3B,C).

IFNγ detection via flow cytometry can be difficult due to low secretion and infrequent numbers of T cells, as is common with antigen-specific CD4 T cells. To overcome this limitation, PBMCs were cultured with individual neoantigen peptides to first expand the T cell populations. Intracellular production of IFNγ was then assessed after restimulation with the corresponding neoantigen peptide for each culture condition. CD4 T cells, and not CD8 T cells, produced IFNγ in response to re-stimulation with neoantigen peptides, confirming our direct *ex vivo* findings (online supplemental figure 2A,B).

Single-cell transcriptional profiling of neoantigen-reactive CD4 T cells

To determine the transcriptional phenotype of neoantigen-specific T cells, we sorted CD4 T cells that upregulated activation markers CD69, CD137 and CD154 *ex vivo* in response to stimulation with neoantigen peptides (figure 4A). Single cell RNAseq was then used to characterize T cell phenotypes. Expression of CD4 T cell subset master transcription factor mRNAs showed a plurality of cells expressing the Th1-associated transcription factor (T-bet), suggesting that a Th1 phenotype is the most common phenotype that the neoantigen-specific CD4 T cells develop. This is further supported by the expression of cytokine mRNAs that showed a predominance of the Th1-weighted cytokines IFNγ, tumor necrosis factor alpha (TNFα) and IL-2 (figure 4B,C).

Tumor microenvironment exhibits a T cell excluded phenotype involving T-bet expressing CD4 T cells

To determine the T cell characteristics into and around the pre-therapy tumor, we used multiplex immunohistochemistry. While the tumor did not have appreciable infiltrating immune cells, the peritumoral and stromal areas had abundant CD3+, CD8+ and PD-L1+ cells indicating an 'excluded' T cell phenotype (figure 5A,B).

We also used a separate phenotyping panel to characterize CD4 T cells at the tumor edge. CD4+/T-bet+ cells were abundant while CD4+/FoxP3+ cells were not, indicating a predominantly inflammatory (Th1) response (figure 5A bottom and C).

DISCUSSION

The use of anti-PD-(L)1 agents in MCC has changed patient management and dramatically improved long-term outcomes for a substantial subset of patients with advanced disease. Indeed, the first-line response rate for MCC (~56–62%) is essentially the highest among solid tumors.[31–35] Across multiple trials, the response rate

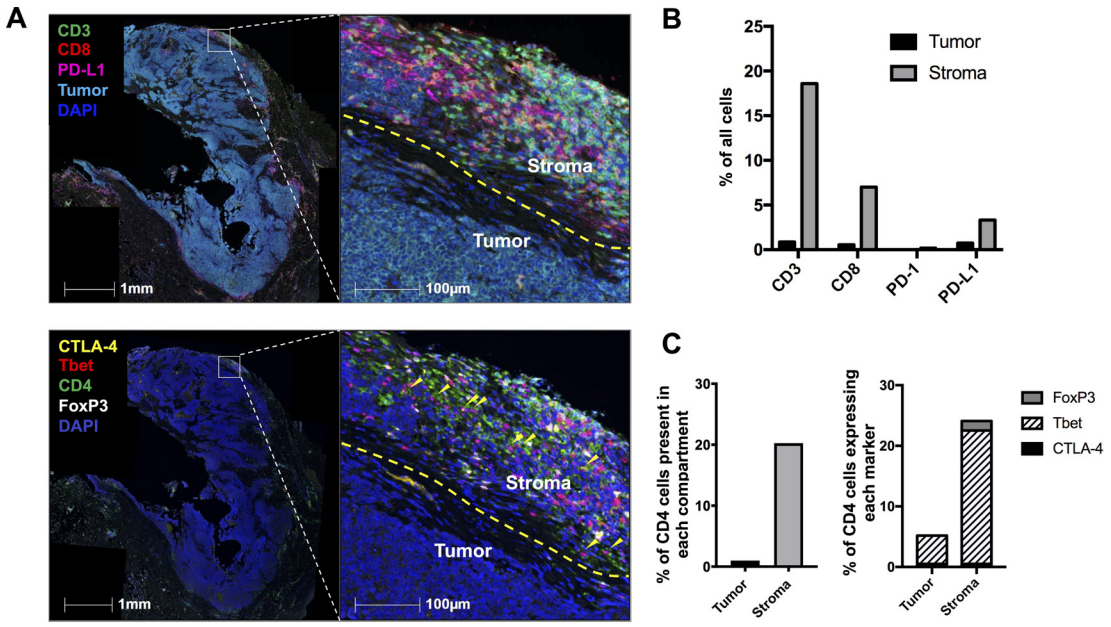

Figure 5 Primary tumor exhibits a T cell-excluded phenotype. (A) Top: representative image of multicolor staining for adaptive immune markers. Light blue=tumor (CD56), green=CD3, red=CD8, magenta=PD-L1, dark blue=cell nuclei. Bottom: representative image of multicolor staining for CD4 phenotyping in tumor. Dark blue=cell nuclei, green=CD4, yellow=CTLA-4, red=T bet, and white=FoxP3. Yellow arrowheads indicate examples of CD4+T-bet+ cells. (B) Staining was quantified with HALO software. Per cent of cells expressing CD3, CD8, PD-1, and PD-L1 within the tumor and on the peritumoral edge (stroma). (C) Left: per cent CD4 cells in the tumor or stroma; right: proportion of CD4 cells expressing each of the phenotypic markers listed.

has been similarly high for both VN-MCC and VP-MCC patients.[3 16 36]

VP-MCC has frequently been used to understand the immunological correlates of response and tumor antigen-specific T cells, due to the invariant MCPyV oncoprotein antigens expressed by these virally driven tumors. In contrast, relevant tumor-specific T cell responses have not been characterized in VN-MCCs to the best of our knowledge. Accordingly, we sought to determine whether neoantigen-specific T cells were associated with a deep and durable, partial response to anti-PD-L1 therapy in a patient with VN-MCC.

A screen of 77 putative neoantigen peptides lead to identification of five T cell responses that preferentially recognized the mutated version of a peptide (neoepitope) as compared with its wild type counterpart (figure 2A). Although the initial goal was to characterize CD8 T cell responses by selecting neoantigen peptides predicted to bind to class-I HLA, all neoantigen-reactive T cells identified were CD4+ and recognized neoepitopes in the context of class-II HLA (figure 2). Similar results have been reported for therapeutic vaccination wherein neoantigen peptides optimized for presentation on class-I HLA elicited in a surprisingly robust expansion of epitope-specific CD4 as well as CD8 T cells.[21 22 37] The fact that only CD4 T cells were identified using potential neoantigen peptides in the present study contrasts with prior findings in VP-MCC for which the majority of T cell responses identified have been CD8+.[17 19 20 38]

To understand the role these cancer-specific CD4 T cells were playing in this patient's clinical response to anti-PD-L1 therapy, we sought to quantify and phenotype these cells over the course of treatment. When studying their quantity, we observed that these CD4 T cells increased in the weeks following initiation of anti-PD-L1 (figure 1A). However, several months after the patient experienced a partial response, CD4 T cell responses became undetectable. This potentially could be due to the reduction in tumor neoantigens and subsequent contraction of the neoantigen-specific T cell population. This finding is consistent with previously published studies of MCPyV-specific T cell activity that reproducibly decreased in MCC patients shortly after surgical removal of their tumors.[38] We also sought to functionally characterize these neoantigen-specific T cells because CD4 T cells are known to have diverse potential roles within the tumor microenvironment. While one proposed mechanism for antitumor activity of CD8 T cells is direct killing of tumor cells, it is becoming more evident that cancer-specific CD4 T cells are a critical aspect of the antitumor response. Indeed, in experimental mouse models in which CD4 T cells were depleted, mice could no longer control tumors, suggesting that the CD4 T cell response is required for antitumor immunity.[39 40]

There are multiple potential 'helper' roles for antitumor CD4 T cells. In MCC, perhaps the most significant role may be secretion of IFNγ to upregulate HLA class I molecules, in turn making tumor cells visible to cytotoxic CD8 T cells.[41] This is particularly relevant in MCC because 85% of MCC tumors downregulate HLA class I molecules, and this downregulation is reversible with stimulation by interferons.[42 43] CD4 T cells can also have

direct cytotoxic effects on tumors through production of granzyme and perforin[44 45] or immunosuppressive function in the case of regulatory T cells.[46] Importantly, CD4 T cells are crucial for the formation of tertiary lymphoid structures in the tumor microenvironment.[47–49] These structures of coordinated B and CD4 T cells are associated with improved survival across several cancer types including MCC[50] and likely lead to improved antitumor immunity via increased support for cancer-specific CD8 T cells.[51]

To determine which of many roles neoantigen-specific CD4 T cells were playing in this patient's clinical response, we phenotyped these cells via scRNAseq (figures 3B and 4A). We observed a Th1 pattern (figure 4C), consistent with the observation in figure 2 that neoantigen-reactive T cells release IFNγ in response to their cognate neoantigen peptide. Furthermore, these cells express T-bet, the canonical transcription factor that enforces a Th1 phenotype and supports CD8 T cell function (figure 4B). To confirm that intratumoral CD4 T cells had a Th1 phenotype in the tumor microenvironment, multiplexed immunohistochemistry was performed. This showed an 'immune excluded' tumor with numerous T cells on the tumor periphery and very few within the tumor itself (figure 5A). The most frequently expressed master transcription factor in CD4+ cells in both tumor and stroma was T-bet, further suggesting these cells are Th1 skewed (figure 5C). These data show that neoantigen-specific CD4 T cells were present in this patient, increased over the course of anti-PD-L1 therapy and had a Th1 phenotype that could improve antitumor immunity via promotion of an inflamed tumor microenvironment.

It is noteworthy that neoantigen-specific CD8 T cells were not detected despite this patient's dramatic clinical response. There are several possibilities that could explain this perplexing finding. Even though data for *in silico* predictions of relevant peptides is robust, it is possible that not all immunogenic neoantigen peptides were appropriately identified. Additionally, high-avidity CD8 T cells could have been present but later deleted.[52] T cells with higher avidity TCRs for their cognate peptide-HLA molecules may be particularly prone to exhaustion and elimination, and higher peptide-HLA affinities are associated with higher TCR avidity.[52] Pertinent to this, only neoantigens with predicted peptide-HLA affinities of <100 nM were used in this study. Alternatively, it is possible that CD4 T cells were directly cytotoxic as appears to be the case in bladder cancer and melanoma, both of which are known to express HLA class II in some cases.[44 45] However, we do not believe this is the case for two main reasons: (1) HLA class II is typically not expressed on MCC tumor cells[43] and thus there would be no target ligand available for CD4 T cell recognition and possible cytotoxic activity (online supplemental figure 4) and (2) scRNAseq data revealed no significant expression of cytotoxic perforin or granzymes in the neoantigen-specific CD4 T cells (data not shown), further suggesting that it would be unlikely for these cells to be directly responsible for this patient's tumor regression.

Another potential explanation for why neoantigen-specific CD8 T cells were not detected is that the sensitive assays required to identify these rare cells depend on inducible cytokine secretion or activation marker expression. IFNγ inducibility is lost late in the process of CD8 T cell exhaustion, after suppression of other key cytokines such as IL-2 and TNFα. If neoantigen-specific CD8 T cells were too dysfunctional to release IFNγ or upregulate activation markers, then they would not be detectable via these functional assays. We have previously observed this contrast for MCPyV-specific CD8 T cells in blood, for which tetramer-positive populations are detectable in some patients who have absent IFNγ ELISpot responses *ex vivo*.[17] Additionally, the frequency of neoantigen-specific CD8 T cells in the blood may have been below the threshold of IFNγ ELISpot assays (less than 1 in 50,000). It is possible that neoantigen-specific CD4 T cells could also have greatly outnumbered their CD8 counterparts in the blood but could have been present in the tumor at sufficient frequency to mediate regression seen in this patient (figure 5). Regardless, this study suggests that future clinical trials of immunotherapies, including possible therapeutic vaccination for MCC,[53] should include both CD4 and CD8 T cell biomarker analyses to further elucidate the role of both T cell subsets.

While many studies have characterized cancer-specific CD8 T cells,[52 54 55] the focus has recently shifted to investigating the role of CD4 T cells in immunotherapy largely in part to emerging technologies. In this study, we report that neoantigens can elicit a CD4 T cell immune response in MCC and that tumor-specific T cells expand in the periphery following immunotherapy in a patient with a profound durable response. Future and ongoing clinical trials aiming to boost the CD4 immune response via adoptive T cell transfer (NCT03747484) or therapeutic vaccination[53 56] could further strengthen this response and improve antitumor immunity. Immunotherapy as well as personalized vaccination strategies, which often result in robust tumor-specific CD4 T cells, should be considered for MCC patients including those with chemotherapy-refractory disease. Reinvigorating and generating new CD4 and CD8 T cell responses are key to eliminating tumors and providing patients with long-term clinical benefit.

Author affiliations
[1]Division of Dermatology, Department of Medicine, University of Washington, Seattle, WA, USA
[2]Clinical Research Division, Fred Hutchinson Cancer Research Center, Seattle, Washington, USA
[3]Human Oncology and Pathogenesis Program, Memorial Sloan Kettering Cancer Center, New York, New York, USA
[4]Center for Immunotherapy and Precision Immuno-oncology, Lerner Research Institute, Cleveland Clinic, Cleveland, Ohio, USA
[5]Department of Medicine, University of Washington, Seattle, Washington, USA
[6]Biostatistics Bioinformatics and Epidemiology Division, Fred Hutchinson Cancer Center, Seattle, Washington, USA
[7]Lausanne University Hospital, Lausanne, Vaud, Switzerland

[8]Swiss Institute of Bioinformatics, Lausanne, Switzerland
[9]Department of Dermatology, Biochemistry & Molecular Genetics, Northwestern University Feinberg School of Medicine, Chicago, Illinois, USA
[10]Center for Immunotherapy and Precision Immuno-oncology, Cleveland Clinic, Cleveland, Ohio, USA
[11]Vaccine and Infectious Diseases Division, Fred Hutchinson Cancer Center, Seattle, Washington, USA
[12]Department of Global Health, University of Washington, Seattle, WA, USA
[13]Department of Laboratory Medicine and Pathology, University of Washington, Seattle, WA, USA
[14]Benaroya Research Institute, Seattle, WA, USA

Twitter Robert Amezquita @robamezquita, Raphael Gottardo @raphg, Jaehyuk Choi @jaehyukchoimd and Paul Nghiem @paulnghiem

Acknowledgements We would like to thank the patient and her family for their participation in this research. Ryan O'Malley, University of Washington, for radiographic assistance; William Kwok, Benaroya Institute, for guidance on CD4 T cell studies; Ti Cai, Zhen Su, and Kevin Chin, EMD Serono, for study support.

Contributors CC, TP, NL, JSC, JC, TC, DK and PN were involved in the conception, design, and planning of the study. CC, TP, NL, SP, KS, VM, NR, and LJ collected data. CC, TP, NL, SP, RA, RG, RHP, JC, TC, DK, and PN analyzed and interpreted data. CC, TP, and PN drafted, critically reviewed and revised the manuscript for important intellectual content. PN, CC and TP are responsible for overall content. All authors reviewed the manuscript and agree with its content and submission.

Funding Supported by the National Cancer Institute (NCI) Grants No. P01 CA225517 (PN) and F30 CA254168 (TP). This work was also supported by the National Institutes of Health/NCI Cancer Center Support Grant in Seattle Grant No. P30 CA015704. We would like to acknowledge support from the Merkel cell carcinoma (MCC) patient gift fund at the University of Washington, the Kelsey Dickson MCC Challenge Grant from the Prostate Cancer Foundation.

Competing interests PN reports personal fees from Pfizer, Inc, Bristol Myers Squibb, EMD Serono, Rain Therapeutics, Almirall, and Instill Bio. In addition, PN has pending patents for 'Merkel cell polyomavirus T antigen-specific TCRs and uses thereof' and 'Novel epitopes as T cell targets in Merkel Cell Carcinoma (MCC)'. CC has a pending patent 'Merkel cell polyomavirus T antigen-specific TCRs and uses thereof'. VM reports a patent (#EP3090066A2), Determinants of cancer response to immunotherapy. NR reports grants from REPARE Therapuetics, Repertoire Immune Medicines, and from Bristol Myers Squibb. RA is an employee of and reports stocks in Pfizer. JSC reports stock from Sensei Bio. RG reports personal fees from Takeda, Ozette Technologies, and Modulus Therapeutics. RHP is an employee of and reports stock in Sensei Bio. TC reports stock from Gritstone Bio, grants from Pfizer and InterVenn, personal fees from Illumina, and royalties from PGDx. Additionally, TC has a patent 'Use of TMB to identify immunotherapy responders licensed to PGDx'. DK reports grants from Sensei Bio and a pending patent related to 'high-affinity T-cell receptors that target the Merkel polyomavirus'.

Patient consent for publication Not applicable.

Ethics approval This study was conducted in accordance with the Declaration of Helsinki and the International Conference on Harmonisation Guidelines for Good Clinical Practice. This study was approved by the Fred Hutchinson Cancer Center (FHCC) Institutional Review Board (IRB Protocol #6585). Patient provided written informed consent and the protocol was approved by the Institutional Review Board at the Fred Hutchinson Cancer Center.

Provenance and peer review Not commissioned; externally peer reviewed.

Data availability statement Data are available on reasonable request.

ORCID iDs
Candice Church http://orcid.org/0000-0003-1582-8292
Thomas Pulliam http://orcid.org/0000-0003-3511-6348
Song Y Park http://orcid.org/0000-0003-4366-1821
Kimberly S Smythe http://orcid.org/0000-0002-2329-8298
Nadeem Riaz http://orcid.org/0000-0001-9873-5862
Lichen Jing http://orcid.org/0000-0002-5938-4171
Jean S Campbell http://orcid.org/0000-0002-9187-2204
Robert H Pierce http://orcid.org/0000-0002-2677-144X
Jaehyuk Choi http://orcid.org/0000-0003-2379-2226
David M Koelle http://orcid.org/0000-0003-1255-9023
Paul Nghiem http://orcid.org/0000-0003-2784-963X

REFERENCES

1 Paulson KG, Park SY, Vandeven NA, *et al*. Merkel cell carcinoma: current US incidence and projected increases based on changing demographics. *J Am Acad Dermatol* 2018;78:457–63.
2 Lemos BD, Storer BE, Iyer JG, *et al*. Pathologic nodal evaluation improves prognostic accuracy in Merkel cell carcinoma: analysis of 5823 cases as the basis of the first consensus staging system. *J Am Acad Dermatol* 2010;63:751–61.
3 Nghiem P, Bhatia S, Lipson EJ, *et al*. Three-year survival, correlates and salvage therapies in patients receiving first-line pembrolizumab for advanced Merkel cell carcinoma. *J Immunother Cancer* 2021;9:e002478.
4 Heath M, Jaimes N, Lemos B, *et al*. Clinical characteristics of Merkel cell carcinoma at diagnosis in 195 patients: the AEIOU features. *J Am Acad Dermatol* 2008;58:375–81.
5 Paulson KG, Iyer JG, Blom A, *et al*. Systemic immune suppression predicts diminished Merkel cell carcinoma-specific survival independent of stage. *J Invest Dermatol* 2013;133:642–6.
6 Paulson KG, Iyer JG, Tegeder AR, *et al*. Transcriptome-wide studies of Merkel cell carcinoma and validation of intratumoral CD8+ lymphocyte invasion as an independent predictor of survival. *J Clin Oncol* 2011;29:1539–46.
7 Feng H, Shuda M, Chang Y, *et al*. Clonal integration of a polyomavirus in human Merkel cell carcinoma. *Science* 2008;319:1096–100.
8 Goh G, Walradt T, Markarov V, *et al*. Mutational landscape of MCPyV-positive and MCPyV-negative Merkel cell carcinomas with implications for immunotherapy. *Oncotarget* 2016;7:3403–15.
9 Knepper TC, Montesion M, Russell JS, *et al*. The genomic landscape of Merkel cell carcinoma and Clinicogenomic biomarkers of response to immune checkpoint inhibitor therapy. *Clin Cancer Res* 2019;25:5961–71.
10 Wong SQ, Waldeck K, Vergara IA, *et al*. UV-associated mutations underlie the etiology of MCV-negative Merkel cell carcinomas. *Cancer Res* 2015;75:5228–34.
11 Carter JJ, Paulson KG, Wipf GC, *et al*. Association of Merkel cell polyomavirus-specific antibodies with Merkel cell carcinoma. *J Natl Cancer Inst* 2009;101:1510–22.
12 Jing L, Ott M, Church CD, *et al*. Prevalent and diverse intratumoral oncoprotein-specific CD8$^+$ T cells within polyomavirus-driven merkel cell carcinomas. *Cancer Immunol Res* 2020;8:648–59.
13 Lipson EJ, Vincent JG, Loyo M, *et al*. PD-L1 expression in the Merkel cell carcinoma microenvironment: association with inflammation, Merkel cell polyomavirus and overall survival. *Cancer Immunol Res* 2013;1:54–63.
14 Nghiem PT, Bhatia S, Lipson EJ, *et al*. PD-1 blockade with pembrolizumab in advanced Merkel-cell carcinoma. *N Engl J Med* 2016;374:2542–52.
15 D'Angelo SP, Russell J, Lebbé C, *et al*. Efficacy and safety of first-line Avelumab treatment in patients with stage IV metastatic Merkel cell carcinoma: a Preplanned interim analysis of a clinical trial. *JAMA Oncol* 2018;4:e180077.
16 Topalian SL, Bhatia S, Amin A, *et al*. Neoadjuvant nivolumab for patients with resectable Merkel cell carcinoma in the CheckMate 358 trial. *J Clin Oncol* 2020;38:2476–87.
17 Iyer JG, Afanasiev OK, McClurkan C, *et al*. Merkel cell polyomavirus-specific CD8$^+$ and CD4$^+$ T-cell responses identified in Merkel cell carcinomas and blood. *Clin Cancer Res* 2011;17:6671–80.
18 Samimi M, Benlalam H, Aumond P, *et al*. Viral and tumor antigen-specific CD8 T-cell responses in Merkel cell carcinoma. *Cell Immunol* 2019;344:103961.

19 Longino NV, Yang J, Iyer JG, *et al*. Human CD4+ T cells specific for merkel cell polyomavirus localize to merkel cell carcinomas and target a required oncogenic domain. *Cancer Immunol Res* 2019;7:1727–39.
20 Miller NJ, Church CD, Dong L, *et al*. Tumor-infiltrating merkel cell polyomavirus-specific T cells are diverse and associated with improved patient survival. *Cancer Immunol Res* 2017;5:137–47.
21 Ott PA, Hu Z, Keskin DB, *et al*. An immunogenic personal neoantigen vaccine for patients with melanoma. *Nature* 2017;547:217–21.
22 Kreiter S, Vormehr M, van de Roemer N, *et al*. Mutant MHC class II epitopes drive therapeutic immune responses to cancer. *Nature* 2015;520:692–6.
23 Rizvi NA, Hellmann MD, Snyder A, *et al*. Cancer immunology. Mutational landscape determines sensitivity to PD-1 blockade in non-small cell lung cancer. *Science* 2015;348:124–8.
24 Samstein RM, Lee C-H, Shoushtari AN, *et al*. Tumor mutational load predicts survival after immunotherapy across multiple cancer types. *Nat Genet* 2019;51:202–6.
25 Eisenhauer EA, Therasse P, Bogaerts J, *et al*. New response evaluation criteria in solid tumours: revised RECIST guideline (version 1.1). *Eur J Cancer* 2009;45:228–47.
26 Nielsen M, Lundegaard C, Worning P, *et al*. Reliable prediction of T-cell epitopes using neural networks with novel sequence representations. *Protein Sci* 2003;12:1007–17.
27 Hosken N, McGowan P, Meier A, *et al*. Diversity of the CD8+ T-cell response to herpes simplex virus type 2 proteins among persons with genital herpes. *J Virol* 2006;80:5509–15.
28 Ziegler SF, Ramsdell F, Alderson MR. The activation antigen CD69. *Stem Cells* 1994;12:456–65.
29 Wölfl M, Kuball J, Eyrich M, *et al*. Use of CD137 to study the full repertoire of CD8+ T cells without the need to know epitope specificities. *Cytometry A* 2008;73:1043–9.
30 Möller JF, Möller B, Wiedenmann B, *et al*. CD154, a marker of antigen-specific stimulation of CD4 T cells, is associated with response to treatment in patients with chronic HCV infection. *J Viral Hepat* 2011;18:e341–9.
31 Bhanegaonkar A, Liu FX, Boyd M, *et al*. Real-World clinical outcomes in patients with locally advanced or metastatic Merkel cell carcinoma treated in U.S. oncology clinical practices: results from SPEAR-Merkel. *Oncologist* 2021;26:e1633–43.
32 Yarchoan M, Albacker LA, Hopkins AC, *et al*. PD-L1 expression and tumor mutational burden are independent biomarkers in most cancers. *JCI Insight* 2019;4:126908. doi:10.1172/jci.insight.126908
33 Lahman MC, Paulson KG, Nghiem PT, *et al*. Quality is king: fundamental insights into tumor antigenicity from virus-associated Merkel cell carcinoma. *J Invest Dermatol* 2021;141:1897–905.
34 Hasmat S, Howle JR, Karikios DJ, *et al*. Immunotherapy in advanced Merkel cell carcinoma: Sydney West cancer network experience. *J Med Imaging Radiat Oncol* 2021;65:760–7.
35 Levy S, Aarts MJB, Eskens FALM, *et al*. Avelumab for advanced Merkel cell carcinoma in the Netherlands: a real-world cohort. *J Immunother Cancer* 2020;8:e001076.
36 D'Angelo SP, Lebbé C, Mortier L, *et al*. First-line avelumab in a cohort of 116 patients with metastatic Merkel cell carcinoma (JAVELIN Merkel 200): primary and biomarker analyses of a phase II study. *J Immunother Cancer* 2021;9:e002646.
37 Keskin DB, Anandappa AJ, Sun J, *et al*. Neoantigen vaccine generates intratumoral T cell responses in phase Ib glioblastoma trial. *Nature* 2019;565:234–9.
38 Afanasiev OK, Yelistratova L, Miller N, *et al*. Merkel polyomavirus-specific T cells fluctuate with Merkel cell carcinoma burden and express therapeutically targetable PD-1 and Tim-3 exhaustion markers. *Clin Cancer Res* 2013;19:5351–60.
39 Dranoff G, Jaffee E, Lazenby A, *et al*. Vaccination with irradiated tumor cells engineered to secrete murine granulocyte-macrophage colony-stimulating factor stimulates potent, specific, and long-lasting anti-tumor immunity. *Proc Natl Acad Sci U S A* 1993;90:3539–43.
40 Hung K, Hayashi R, Lafond-Walker A, *et al*. The central role of CD4(+) T cells in the antitumor immune response. *J Exp Med* 1998;188:2357–68.
41 Ben Khelil M, Godet Y, Abdeljaoued S, *et al*. Harnessing Antitumor CD4+ T Cells for Cancer Immunotherapy. *Cancers* 2022;14:14010260. doi:10.3390/cancers14010260
42 Paulson KG, Tegeder A, Willmes C, *et al*. Downregulation of MHC-I expression is prevalent but reversible in Merkel cell carcinoma. *Cancer Immunol Res* 2014;2:1071–9.
43 Lee PC, Klaeger S, Le PM, *et al*. Reversal of viral and epigenetic HLA class I repression in Merkel cell carcinoma. *J Clin Invest* 2022;132.
44 Oh DY, Kwek SS, Raju SS, *et al*. Intratumoral CD4+ T cells mediate anti-tumor cytotoxicity in human bladder cancer. *Cell* 2020;181:e13:1612–25.
45 Cachot A, Bilous M, Liu Y-C, *et al*. Tumor-specific cytolytic CD4 T cells mediate immunity against human cancer. *Sci Adv* 2021;7:3348. doi:10.1126/sciadv.abe3348
46 Ahmadzadeh M, Pasetto A, Jia L, *et al*. Tumor-infiltrating human CD4+ regulatory T cells display a distinct TCR repertoire and exhibit tumor and neoantigen reactivity. *Sci Immunol* 2019;4:4310. doi:10.1126/sciimmunol.aao4310
47 Petitprez F, de Reyniès A, Keung EZ, *et al*. B cells are associated with survival and immunotherapy response in sarcoma. *Nature* 2020;577:556–60.
48 Wieland A, Patel MR, Cardenas MA, *et al*. Defining HPV-specific B cell responses in patients with head and neck cancer. *Nature* 2021;597:274–8.
49 Cabrita R, Lauss M, Sanna A, *et al*. Tertiary lymphoid structures improve immunotherapy and survival in melanoma. *Nature* 2020;577:561–5.
50 Nakamura M, Magara T, Kano S, *et al*. Tertiary lymphoid structures and chemokine landscape in virus-positive and virus-negative Merkel cell carcinoma. *Front Oncol* 2022;12:811586.
51 Lowery FJ, Krishna S, Yossef R, *et al*. Molecular signatures of antitumor neoantigen-reactive T cells from metastatic human cancers. *Science* 2022;375:877–84.
52 Oliveira G, Stromhaug K, Klaeger S, *et al*. Phenotype, specificity and avidity of antitumour CD8+ T cells in melanoma. *Nature* 2021;596:119–25.
53 Tabachnick-Cherny S, Pulliam T, Church C, *et al*. Polyomavirus-driven Merkel cell carcinoma: prospects for therapeutic vaccine development. *Mol Carcinog* 2020;59:807–21.
54 Eberhardt CS, Kissick HT, Patel MR, *et al*. Functional HPV-specific PD-1+ stem-like CD8 T cells in head and neck cancer. *Nature* 2021;597:279–84.
55 Caushi JX, Zhang J, Ji Z, *et al*. Transcriptional programs of neoantigen-specific TIL in anti-PD-1-treated lung cancers. *Nature* 2021;596:126–32.
56 Blass E, Ott PA. Advances in the development of personalized neoantigen-based therapeutic cancer vaccines. *Nat Rev Clin Oncol* 2021;18:215–29.

SUPPLEMENTAL MATERIAL

Transcriptional and functional analyses of neoantigen-specific CD4 T cells during a profound response to anti-PD-L1 in metastatic Merkel cell carcinoma

TABLE OF CONTENTS

Figure S1: Selection and design of peptide pools and T cell responses

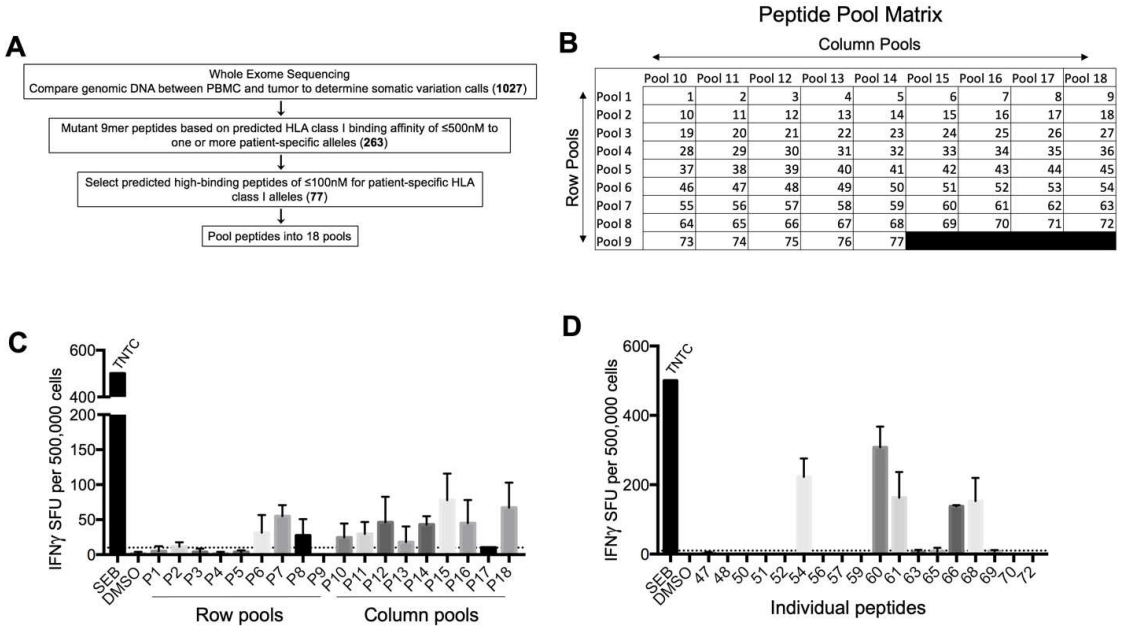

A) Overview of pipeline to identify tumor specific mutations, HLA class I restricted neoantigens and **B)** peptide pool design. **C)** IFNγ secretion in response to neoantigens. Pools of neoantigen peptides were used to probe PBMC directly ex vivo in an IFNγ ELISpot assay. 2x spot forming units (SFU) above DMSO control or >10 SFU and above were considered positive. n=4 technical replicates, the mean is graphed and error bars indicate standard deviation . **D)** Positive peptide pools were broken down to individual neoantigen peptides. n=2 technical replicates, the mean is graphed and error bars indicate standard deviation.

Figure S2: Flow cytometry assessment of IFNγ shows CD4 T cell reactivity to neoantigens

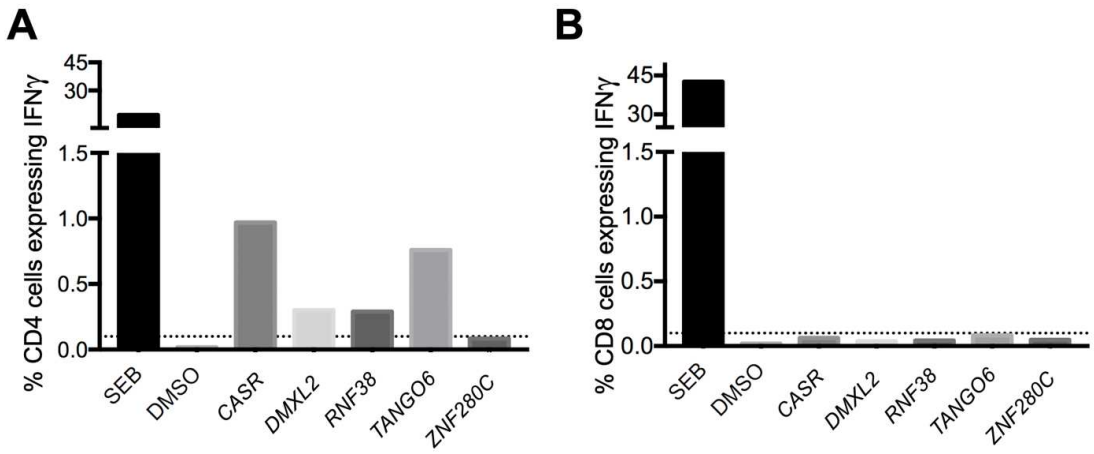

PBMC were cultured with each neoantigen peptide and supporting cytokines. After 14 days, T cell cultures were re-challenged with appropriate peptides. IFNγ expression by CD4 **(A)** and CD8 **(B)** T cells were assessed by flow cytometry. Cutoff for positivity set at 0.1% (dotted line). n=1 flow cytometry experiment.

Figure S3: Characterization of tumor-associated T cell receptor clones

A

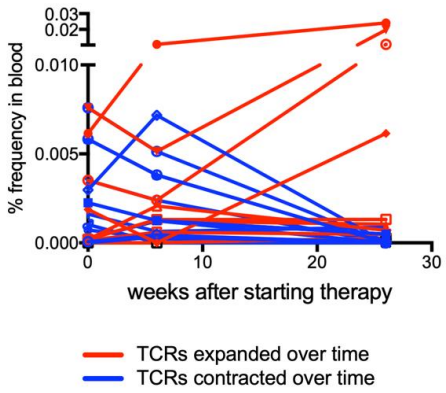

B TCR beta chain sequences of neoantigen-specific T cells sorted following activation induced markers from blood

Neoantigen	TCRB CDR3 amino acid	V beta family	% in tumor
CASR	CAISEADGGYTF	TRBV10-3*00	0
	CASSIQGYGASGANVLTF	TRBV19*00	0
DMXL2	CASSPDPDWGGNEQFF	TRBV28*00	0
	CSGVSSSYEQYF	TRBV20-1*00	0
	CASSEARAQHNEQFF	TRBV2*00	0
	CASSLAEGAYEQYF	TRBV7-2*00	0
	CASSLGRGDTEAFF	TRBV11-3*00	0
RNF38	CASSIRGLNEKLFF	TRBV12-4*00,TRBV12-3*00	0
	CASTGLPGNEKLFF	TRBV2*00	0
	CASSLGQGANTGELFF	TRBV7-6*00,TRBV7-7*00	0
	CATSRTRDRGTEAFF	TRBV15*00	0
TANGO6	CASSIGTSGLEQFF	TRBV6-5*00,TRBV06-08*01	0.21%
	CSARGQREAFF	TRBV20-1*00	0
	CASSQGITYEQYF	TRBV3-1*00	0
	CATSDTRGTGGEKLFF	TRBV24-1*00	0
	CAWRGASVSYEQYF	TRBV30*00	0
ZNF280C	CSVPDSIEQFF	TRBV29-1*00	0
	CASTSDRGRVQPQHF	TRBV12-4*00,TRBV12-3*00	0
	CSASRTSGRGGYF	TRBV20-1*00	0
	RASSLEREGPHEQFF	TRBV7-3*00	0

A) Tumor specific clonotypes were identified (TCR beta CDR3) in biopsy material and were then used as "barcodes" to track circulating T cell clones in the peripheral blood over time. Differentially expressed clonotypes (as determined by Fisher's exact test) are shown in red for upregulated and blue for downregulated TCRs. **B**) TCR beta amino acid sequences of neoantigen-specific CD4 T cells sorted from peripheral blood based on upregulation of CD154, CD137 and CD69 after stimulation with indicated neoantigens. One CD4 T cell clone isolated based on activation markers from PBMC was also found in the tumor biopsy.

Figure S4: Merkel cell carcinomas do not express HLA-DR

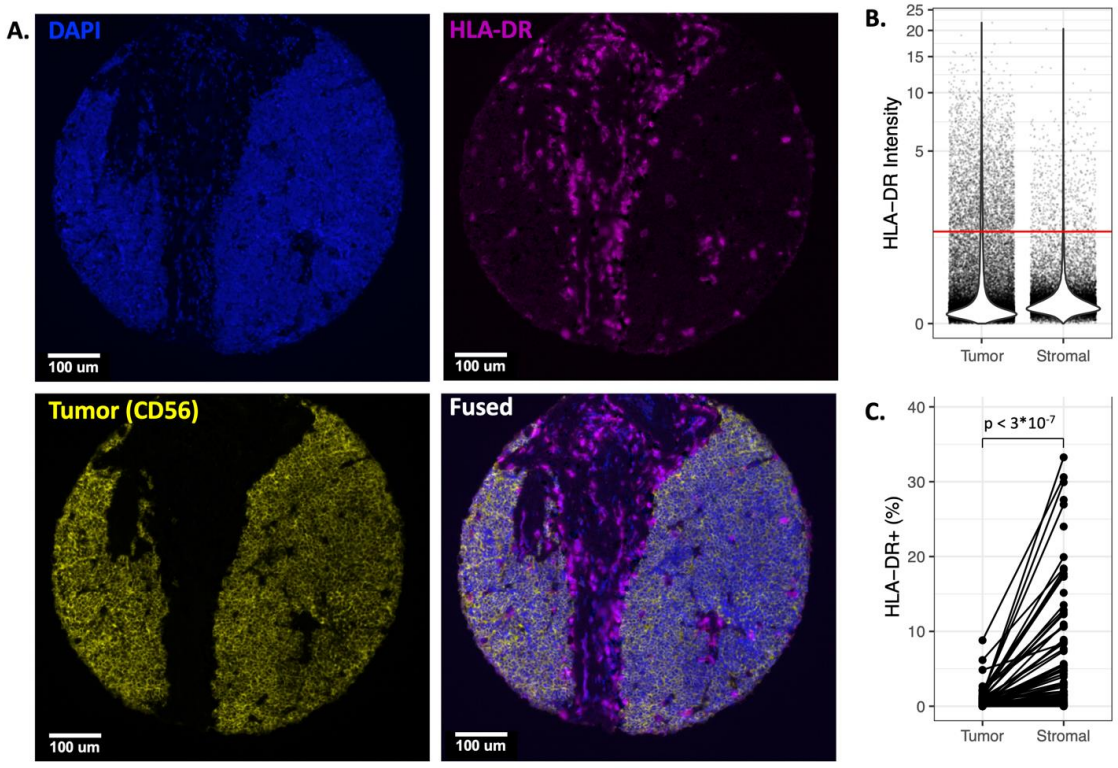

A) HLA-DR expression within the tumor and stroma revealed by mIHC staining of a representative tumor within an MCC tissue microarray (TMA). **B)** Intensity of HLA-DR expression among ~500,000 cells within the tumor or stroma across 76 unique MCC patient tumors. **C)** Paired frequency within each TMA core of HLA-DR+ tumor or stromal cells.

Table S1: List of 77 neoantigen-specific peptides used in immunoassays

Neoantigen peptides were selected based upon HLA class I predicted binding affinity using NetMHCv3.4 (https://services.healthtech.dtu.dk/?NetMHC-3.4), with a cut-off of ≤100nM (n=77 peptides). HLA class I and binding affinities (IC50 in nM) are shown.

Gene Name	Wild type sequence	Mutant sequence	Amino acid change	HLA allele prediction	IC50 (nM) of wild sequence	IC50 (nM) of mutant (neoantigen) sequence
XKR3	msftisfIi	msftisfNi	I74N	A6802	6	3
NAIF1	sAtaaaatv	sTtaaaatv	A159T	A6802	61	11
USP22	ittyvsfPl	ittyvsfSl	P429S	A6802	6	17
FANCD2	qmllcpfPf	qmllcpfLf	P1468L	A2402	75	26
ABHD8	mltgvTdgi	mltgvldgi	T6I	A6802	25	38
UBAP2	stavnscsP	stavnscsL	P82L	A6802	13273	53
VPS13B	dafPwtisl	dafSwtisl	P1153S	A6802	37	64
TSHZ1	Slakaaspi	Flakaaspi	S620F	C0802	2953	77
DRD3	fviySsvvs	fviyFsvvs	S192F	A6802	213	94
MAD2L1BP	etsStqepl	etsFtqepl	S38F	A6802	6	4
GCFC2	dtsiSfppv	dtsiLfppv	S93L	A6802	18	11
WWP1	ltVvldglv	ltAvldglv	V137A	A6802	76	18
OXR1	Dtehstnev	Ntehstnev	D390N	A6802	54	28
CD53	evlGmsfal	evlRmsfal	G199R	A6802	17	40
CNBD1	fisqsfhsF	fisqsfhsI	F235I	A6802	5138	54
CLN6	vfplewfPl	vfplewfSl	P75S	A2402	81	66
VPS8	qvfEflirl	qvfKflirl	E757K	A6802	25	77
NLRP7	yPdcklqtl	yLdcklqtl	P873L	C0802	262	97
NIPSNAP3A	Gvfhteyga	Evfhteyga	G182E	A6802	1801	7
CHD5	eaidrfnaP	eaidrfnaL	P1089L	A6802	7457	12
GPR52	mvlfriTsv	mvlfriIsv	T271I	A6802	19	18
KCNJ11	tlasarGpl	tlasarEpl	G366E	A6802	64	29
MAGEA1	vsarvRfff	vsarvCfff	R291C	A2402	160	41
NLRP5	lwmrDktli	lwmrNktli	D762N	A2402	124	54

VIT	sysngvqSl	sysngvqLl	S123L	A2402	285	68
TANGO6	yRtefgavv	yStefgavv	R172S	C0802	762	80
FBXO33	tavelErfv	tavelKrfv	E303K	A6802	237	99
EPB41	etepTvhhl	etepIvhhl	T618I	A6802	38	7
SIDT1	Gnmvashpi	Enmvashpi	G351E	A6802	3747	13
SLC38A10	ttfyvmvGf	ttfyvmvEf	G245E	A6802	19	20
USP44	Gntcymnsv	Entcymnsv	G279E	A6802	7309	30
ZFAND5	stSeksrnv	stFeksrnv	S84F	A6802	214	45
CACNA1F	dtfpqalIT	dtfpqalII	T692I	A6802	1939	55
NAPA	esvkeydSi	esvkeydFi	S268F	A6802	194	68
OPLAH	iciSvgaev	iciFvgaev	S720F	A6802	247	81
SEMA4A	tengfSypv	tengfLypv	S500L	A6802	60	99
MYO18B	Ssppplfsv	Fsppplfsv	S24F	A6802	15	7
CACNA1G	fGnyvlfnl	fSnyvlfnl	G951S	A6802	173	13
ORC1	itaiknsSv	itaiknsFv	S771F	A6802	56	22
IMMT	taaipPesl	taaipLesl	P617L	A6802	48	31
PTPRJ	Smasfdcev	Fmasfdcev	S721F	A6802	128	45
DSEL	fvsfksGkl	fvsfksEkl	G448E	A6802	138	55
KIAA1033	fvPdlediv	fvSdlediv	P946S	A6802	91	68
ZNF280C	fyygRhegv	fyygMhegv	R301M	A6802	5983	84
DUOX2	eisvvkaEl	eisvvkaKl	E1278K	A6802	32	100
ZSCAN9	etpgpReal	etpgpKeal	R67K	A6802	6	9
COPB1	maanviPvl	maanviSvl	P403S	A6802	79	13
PROM1	niiPvldei	niiSvldei	P242S	A6802	14	24
CPXM1	qDadpwfqv	qNadpwfqv	D169N	A6802	125	33
MAGI3	maytdtGmi	maytdtEmi	G307E	A6802	119	45
C1orf228	evggVltll	evggFltll	V105F	A6802	34	57
RNF38	sahpptlpP	sahpptlpL	P287L	A6802	12773	69
IPO11	liptLiesv	liptFiesv	L172F	A6802	146	85
ASTN1	tvmEdavev	tvmKdavev	E573K	A6802	5	9

DSCAM	esisiswSt	esisiswFt	S1110F	A6802	30	15
NOS3	Glgplhygv	Elgplhygv	G967E	A6802	6089	25
CPT1B	kylGvsspf	kylEvsspf	G634E	A2402	22	33
OSGIN2	tyitSvsrl	tyitFvsrl	S244F	A2402	72	49
ASCC3	nHhvaslsf	nYhvaslsf	H2139Y	A2402	3333	58
CASR	fPihfgvaa	fSihfgvaa	P39S	A6802	2430	73
IPO7	eaiihsPel	eaiihsSel	P103S	A6802	778	89
COL12A1	dtlySvnlv	dtlyFvnlv	S837F	A6802	18	10
AMBN	msfavpffP	msfavpffS	P31S	A6802	620	16
CDC45	atmslmesP	atmslmesL	P341L	A6802	12614	26
HSPA12B	lrffrEhal	lrffrKhal	E182K	B1402	37	34
PARP15	gvagvtSra	gvagvtFra	S31F	A6802	225	50
UBE3C	Sfarhyyfl	Ffarhyyfl	S813F	A2402	32	58
IPO5	liPyldnlv	liSyldnlv	P498S	A6802	94	73
MARCH7	nvpsasevP	nvpsasevL	P281L	A6802	16953	93
CCDC67	stmpplppS	stmpplppL	S526L	A6802	223	11
TNPO2	evRqssfal	evWqssfal	R681W	A6802	305	16
C12orf29	mPcvfvtev	mScvfvtev	P12S	A6802	703	26
PIGB	cqlcSwftw	cqlcFwftw	S181F	A2402	78	36
PDZRN3	tPyglyyps	tSyglyyps	P661S	A6802	1713	51
DMXL2	eidntvPpv	eidntvSpv	P154S	A6802	537	62
MAP3K1	svssSthft	svssFthft	S846F	A6802	237	74
COL15A1	frdfaisvV	frdfaisvM	V96M	C0802	45	93
HIV nef	rypltfgwcf	n/a	n/a	A2402	8	n/a

TABLE S2: Patient-specific neoantigen peptides and predicted HLA class II binding

Wild type and mutant 17mer peptides are listed. *Predicted CD8 epitopes used in immunoassays are bolded, mutant residues are underlined. Class II core peptide predictions are shown and binding affinities (via Net MHCv3.4) are listed.

HLA Restriction	Gene	Wild type 17mer	Mutant 17mer*	Class II core peptide	IC50 (nM) Wild Type	IC50 (nM) Mutant
DRB1*04:01	*CASR*	DIILGGLFPIHFGVAAK	DIILGGL**F<u>S</u>IHFGVAA**K	LGGLFSIHF	1055	294
DRB1*04:01	*DMXL2*	EEEIDNTVPPVLNDWKC	EE**EIDNTV<u>S</u>PV**LNDWKC	IDNTVSPVL	4764	1367
DRB1*04:01	*RNF38*	SAHPPTLPPSAPLQFLT	**SAHPPTLPL<u></u>**SAPLQFLT	TLPLSAPLQ	4175	1852
DRB1*04:01	*TANGO6*	GVGVPLRYRTEFGAVVQ	GVGVPLR**Y<u>S</u>TEFGAVV**Q	LRYSTEFGA	281	208
DRB1*04:01	*ZNF280C*	LVNEFYYGRHEGVTEKE	**LVNEFYYG<u>M</u>**HEGVTEKE	FYYGMHEGV	1219	492
DRB1*11:01	*CASR*	DIILGGLFPIHFGVAAK	DIILGGL**F<u>S</u>IHFGVAA**K	LGGLFSIHF	1892	1047
DRB1*11:01	*DMXL2*	EEEIDNTVPPVLNDWKC	EE**EIDNTV<u>S</u>PV**LNDWKC	IDNTVSPVL	8915	10377
DRB1*11:01	*RNF38*	SAHPPTLPPSAPLQFLT	**SAHPPTLPL<u></u>**SAPLQFLT	TLPLSAPLQ	14494	867
DRB1*11:01	*TANGO6*	GVGVPLRYRTEFGAVVQ	GVGVPLR**Y<u>S</u>TEFGAVV**Q	LRYSTEFGA	287	529
DRB1*11:01	*ZNF280C*	LVNEFYYGRHEGVTEKE	**LVNEFYYG<u>M</u>**HEGVTEKE	FYYGMHEGV	90	44

Materials and Methods

IFNγ detection via flow cytometry

T cell lines were co-cultured with Carboxyfluorescein succinimidyl ester (CFSE, Invitrogen) labeled, peptide loaded (5µg/ml), patient derived LCLs in the presence of anti-CD28 and anti-CD49d mAbs (BD Biosciences), and brefeldin A for 12–16 hours[1 2]. Overnight cultured cells were stained with anti-CD3, -CD4, -CD8, -CD14 and -CD19. After a cytofix/cytoperm step (BD Biosciences), cells were intracellularly stained with anti-IFNγ (BD Biosciences), washed and data collected on a FACSCanto II (BD Biosciences).

T cell receptor sequencing

Neoantigen-reactive CD4 T cells were sorted and cDNAs generated from single cells (as described above). cDNAs were used for paired TCR alpha and beta sequencing of the complementarity determining region 3 (CDR3) for each gene as previously described.[3] TCR alpha and beta CDR3 sequences were analyzed with the MiXCR program with the IMGT databased used as a reference.[4 5] TCR Immunoseq™: A DNeasy Kit (Qiagen) was used to isolate DNA from formalin fixed paraffin-embedded (FFPE) tissue and from peripheral blood and were submitted to Adaptive Biotechnology (Seattle, WA) for *TCB* CDR3 sequencing and data processing.

References

1. Posavad CM, Wald A, Hosken N, et al. T cell immunity to herpes simplex viruses in seronegative subjects: silent infection or acquired immunity? *J Immunol* 2003;170(8):4380-8. doi: 10.4049/jimmunol.170.8.4380 [published Online First: 2003/04/12]
2. Jing L, Chong TM, McClurkan CL, et al. Diversity in the acute CD8 T cell response to vaccinia virus in humans. *J Immunol* 2005;175(11):7550-9. doi: 10.4049/jimmunol.175.11.7550 [published Online First: 2005/11/23]
3. Jing L, Ott M, Church CD, et al. Prevalent and Diverse Intratumoral Oncoprotein-Specific CD8(+) T Cells within Polyomavirus-Driven Merkel Cell Carcinomas. *Cancer Immunol Res* 2020;8(5):648-59. doi: 10.1158/2326-6066.CIR-19-0647 [published Online First: 2020/03/18]
4. Ilca FT, Neerincx A, Wills MR, et al. Utilizing TAPBPR to promote exogenous peptide loading onto cell surface MHC I molecules. *Proc Natl Acad Sci U S A* 2018;115(40):E9353-E61. doi: 10.1073/pnas.1809465115 [published Online First: 2018/09/15]
5. Lefranc MP, Giudicelli V, Duroux P, et al. IMGT(R), the international ImMunoGeneTics information system(R) 25 years on. *Nucleic Acids Res* 2015;43(Database issue):D413-22. doi: 10.1093/nar/gku1056 [published Online First: 2014/11/08]

Programming of stem-like and terminally exhausted T cell fate by divergent IL-2 signals during priming

AUTHORS: Ryma Toumi[1,#], Hanxi Xiao[1,#], Thomas Pulliam[2], Rucha Deo[1], Jim Reed[1], Paul Nghiem[2,3], Surojit Sarkar[1,4,5,★] and Vandana Kalia[1,5,★]

AFFILIATIONS:

[1]Ben Towne Center for Childhood Cancer Research, Seattle Children's Research Institute, Seattle WA 98101

[2] Department of Medicine, Dermatology Division, University of Washington School of Medicine, Seattle, WA 98195

[3] Vaccine and Infectious Disease Division, Fred Hutchinson Cancer Research Center, Seattle WA 98109

[4] Department of Pathology, University of Washington School of Medicine, Seattle, WA 98195

[5] Department of Pediatrics, University of Washington School of Medicine, Seattle, WA 98195

[#]Equal contributors

[★]Corresponding authors sarkarkalia@gmail.com

ONE SENTENCE SUMMARY: Programming CD8 T cell exhaustion outcomes by IL-2

ABSTRACT

The stem-like self-renewing subset of antigen-specific CD8 T cells is critical for maintaining long-term resistance during chronic infections and cancer, and is an important checkpoint blockade immunotherapy target for functional reinvigoration and disease control[1-7]. Hence, there is vigorous interest in understanding the ontogenesis of stem-like CD8 T cells, and in defining the signals that promote their development. Here, we show a crucial fate-deterministic role of IL-2 in programming the development of stem-like exhausted CD8 T cells. *In vivo* fate-tracking experiments reveal that strong IL-2 signals drive terminal differentiation, whereas tempered IL-2 signals program the development of TCF-1^{Hi} stem-like CD8 T cells, capable of long-term persistence and potent responsiveness to anti-PD-1 therapy in later stages of chronic viral infection. In the context of tumors as well, single cell RNA-seq analyses of total or antigen-specific (tetramer+ or neoantigen-specific) tumor infiltrating lymphocytes from melanoma, human papillomavirus+ head and neck cancer, and lung cancer patients show an inverse relationship of IL-2 signaling signature with T cell stemness and checkpoint blockade therapy outcomes. Our studies further show that the rheostatic control of exhausted T cell fates by differential IL-2 signals is physiologically mediated through differential cell surface expression of IL-2Rα during early stages of T cell activation, which in turn is pioneered during priming by distinct dendritic cell subsets. Notably, moderation of *in vivo* IL-2 signals during priming promotes the development of stem-like TCF-1^{Hi} lineage, thus supporting a unique mechanism of improving clinical immunotherapy outcomes by enhancing the development of long-lived, therapy-responsive stem-like cells with vigorous effector expansion capabilities.

MAIN

Exhausted virus-specific CD8 T cells critically restrain pathogen outgrowth despite functional impairment[8]. This property is ascribed to a small subset of stem-like CD8 T cells, which have been recently identified within the exhausted CD8 T cell pool of chronic viral infections as well as cancer[1-7,9-12]. Distinguishable from terminally exhausted CD8 T cells by higher expression of T cell factor-1 (TCF-1) and lower expression of inhibitory receptors, the stem-like exhausted CD8 T cells are capable of self-renewal, and have been shown to continually seed the transient pool of functional effector cells for mediating host-virus stand-off[5,7,13,14]. Importantly, TCF-1^{Hi} stem-like exhausted CD8 T cells undergo vigorous expansion and functional reinvigoration in response to PD-1 checkpoint blockade immunotherapy (CBI), and are crucial for reducing viral loads and tumor burdens post-therapy[2-4,6,10,15]. TCF-1^{Hi} stem-like CD8 T cells have also been delineated in a multitude of human cancers such as head and neck cancer[16], melanoma[10,17], lung cancers[18-21] and hepatocellular carcinoma (HCC)[22]. Hence, inducing stem-like T cells is a highly desirable goal in chronic infections and cancers for mediating long-term disease control, and for the therapeutic success of anti-PD-1 therapy as well as adoptive T cell transfer (ACT) therapeutic interventions. However, while our understanding of the transcriptional regulation of T cell exhaustion is quite extensive with several known factors such as TOX, Blimp-1, E2A, T-bet, Eomes, BACH-2, BATF, IRF-4 and Myb[3,5,14,23-34], we know very little about the ontogenesis of TCF-1^{Hi} stem-like CD8 T cells, and the signals that drive their initial generation and subsequent development in the context of chronic antigenic settings.

Association of TCF-1^{Hi} stem-like CD8 T cells with lower IL-2Rα expression during early stages of chronic viral infection.

Key features of T cell exhaustion are distinguishable early during CD8 T cell responses to chronic LCMV infection[5,11-13,35-37], and are proposed to be programmed during initial priming and expansion. Towards gaining insight into the exhausted CD8 T cell fate programming events, we evaluated the expression of TCF-1 in virus-specific CD8 T cells during early stages of murine infection with $LCMV_{Cl-13}$. Consistent with the notion of early programming of the stem-like CD8 T cell lineage, putative TCF-1^{Hi} GzmB^{Lo} stem-like cells, were distinguishable from TCF-1^{Lo} GzmB^{Hi} effector-like subsets (Fig 1a). As in the case of stem-like exhausted CD8 T cells isolated from late stages of chronic infection, the TCF-1^{Hi} GzmB^{Lo} stem-like cells isolated during early stages of infection showed preferential enrichment in secondary lymphoid organs (spleen and lymph nodes) compared to peripheral lung and liver sites (Fig 1a, Extended Data Fig 1a). Intriguingly, we noted reduced expression of IL-2Rα (CD25) – the IL-2R component which renders high affinity IL-2 binding – in TCF-1^{Hi} cells compared to TCF-1^{Lo} cells (Fig 1a, Extended Data Fig 1a). Reduced expression of IL-2Rα in TCF-1^{Hi} GzmB^{Lo} cells was associated with lower expression of the common IL-2Rβ-chain (CD122) and largely similar expression of the common IL-2Rγ-chain (CD132) (Fig 1a). At the mRNA level as well, T-distributed stochastic neighbor embedding (t-SNE) analysis of scRNA-seq data[35] confirmed inverse expression pattern of TCF-1 with CD25 in chronic infection model (Fig 1b). As shown previously[5,35], TCF-1 expression correlated directly with Slamf6, Bcl-2 and CD62L, and inversely with proliferation marker Ki-67, inhibitory receptor Tim3 and effector molecule GzmB (Fig 1b, Extended Data Fig 1b). The TCF-1^{Hi} CD25^{Lo} and TCF-1^{Lo} CD25^{Hi} antigen-specific cells distinguishable during the activation and early expansion phase, were not

functionally exhausted, as evidenced by vigorous production of IFN-γ and TNF-α effector cytokine upon restimulation with cognate antigen, albeit the TCF1^{Hi} cells exhibited a modest trend towards decreased IFN-γ expression (Extended Data Fig 2). Importantly, inverse association between the expression of CD25 and TCF-1 occurred similarly in TCR-transgenic as well as endogenous antigen-specific CD8 T cells of distinct specificities (D^{b}Gp33- and D^{b}GP276-specific tetramer+ endogenous CD8 T cells; data shown in Extended Fig 3a, 3b). Likewise, the precursor frequency of antigen-specific CD8 T cells also did not have a bearing on the generation of CD25^{Lo} TCF-1^{Hi} GzmB^{Lo} stem-like cells during chronic LCMV infection (Extended Data Fig 3c). While the kinetics of appearance of CD25^{Lo} TCF-1^{Hi} GzmB^{Lo} stem-like cells was slightly faster at higher precursor frequencies (Extended Data Fig 3c), the final CD8 T cell outcome during later stages of exhaustion was independent of their initial precursor frequencies (Extended Data Fig 4a-c). Collectively, these data demonstrate heterogeneity in early priming events during chronic viral infection, and establish an inverse association of IL-2Rα expression with TCF-1^{Hi} stem-like subset.

We next sought to determine whether TCF-1^{Hi} CD25^{Lo} CD8 T cells identifiable during early stages of priming and expansion give rise to stem-like progenitor exhausted CD8 T cells during later stages of viral chronicity. We FACS-purified CD25^{Lo} and CD25^{Hi} D^{b}GP33-specific CD8 T cells from day 4.5 LCMV$_{Cl\text{-}13}$ infection, and tracked their long-term fate following adoptive transfer into infection-matched recipients (Fig 1c). Equal numbers of purified CD25^{Lo} donors (enriched for TCF-1^{Hi} Tim-3^{Lo} cells) and CD25^{Hi} donors (enriched for TCF-1^{Lo} Tim-3^{Hi} cells) (Extended Data Fig 5a) were transferred into congenically distinct infection-matched recipient mice. Prior to adoptive transfer, CD25^{Hi} cells expressed higher levels of most inhibitory receptors analyzed (PD-1, Tim-3, Lag-3) (Extended Data Fig 5b), and key transcription factors implicated in regulating effector and

terminally exhausted CD8 T cell differentiation (Blimp-1, T-bet, Eomesodermin and Tox) (Extended Data Fig 5c). $CD25^{Hi}$ cells also showed higher expression of cell proliferation markers (BrdU, Ki-67 and cMyc) (Extended Data Fig 5d), and were larger in size (Extended Data Fig 5e). These differences between $CD25^{Hi}$ and $CD25^{Lo}$ subsets were largely independent of their activation status, as both subsets showed potent upregulation of activation markers CD44 and CD69, and downregulation of CD127 and CD62L relative to naïve cells (Extended Data Fig 5e).

Notwithstanding these initial differences, consistent with similar expression levels of pro-survival molecule Bcl-2 (Extended Data Fig 5d), the $CD25^{Hi}$ and $CD25^{Lo}$ donors engrafted similarly. Both donors also expanded to largely similar levels at the peak of CD8 T cell expansion (day 8 post-infection with $LCMV_{Cl\text{-}13}$) (Extended Data Fig 6a). The $CD25^{Lo}$ donors (enriched in TCF-1^{Hi} Tim-3^{Lo} cells at the time of purification) maintained higher proportions of TCF-1^{Hi} Tim-3^{Lo} $GzmB^{Lo}$ stem-like cells compared to $CD25^{Hi}$ donors (Fig 1d), and preferentially localized to secondary lymphoid organs (spleen and lymph nodes) compared to peripheral lung and liver sites (Extended Data Fig 6b). However, with progression of infection, there was a striking decline in the numbers of $CD25^{Hi}$ donors, which largely disappeared, and were 10-20-fold lower in numbers than their $CD25^{Lo}$ counterparts at day 24 post-infection in all tissues analyzed (Fig 1e). Greater recovery of $CD25^{Lo}$ donors was associated with higher proportions of TCF-1^{Hi} $GzmB^{Lo}$ (Extended Data Fig 6c) $CD62L^{Hi}$ $Slamf6^{Hi}$ (Extended Data Fig 6d) stem-like cells, and lesser degree of exhaustion as evidenced by fewer donors co-expressing three or more inhibitory receptors (PD-1, Tim-3, Lag-3, 2B4) compared to the small surviving population of $CD25^{Hi}$ donors (Fig 1f). In contrast, consistent with a more terminally exhausted phenotype, $CD25^{Hi}$ donors also expressed higher levels of Tbet/Eomes ratio (Fig 1g, Extended Data Fig 6e). Notably, the $CD25^{Lo}$ and $CD25^{Hi}$ donor cells,

minimally impacted the infectious milieu as demonstrated by largely similar endogenous D^bGP33-specific CD8 T cell responses over time (Extended Data Fig 7a), and similar proportions of stem-like cells (Extended Data Fig 7b) and PD-1 expression (Extended Data Fig 7c) in endogenous virus-specific CD8 T cells from the recipients. Collectively, these data demonstrate that $CD25^{Lo}$ TCF-1^{Hi} cells distinguishable during early stages of priming and expansion preferentially differentiate into stem-like progenitor exhausted CD8 T cells during later stages of viral chronicity.

Stem-like TCF-1^{Hi} progenitor CD8 T cells arising from IL-2Rα^{Lo} precursors exhibit augmented responsiveness to PD-1 checkpoint blockade immunotherapy during exhaustion.

Compared to TCF-1^{Lo} terminally exhausted CD8 T cells, TCF-1^{Hi} progenitor exhausted CD8 T cells mount superior expansion in response to PD-1 CBI in both chronic infection and tumor model studies[2-4,6,10,15]. Hence, we next assessed this key functional property of stem-like TCF-1^{Hi} progenitor cells arising from $CD25^{Lo}$ precursors programmed during early stages of priming and expansion. As in Fig 1, $CD25^{Lo}$ and $CD25^{Hi}$ D^bGP33-specific CD8 T cells were FACS-purified from day 4.5 $LCMV_{Cl\text{-}13}$ infection, adoptively transferred in equal numbers into infection-matched recipient mice, and allowed to differentiate under conditions of viral chronicity. The recipient mice were then subjected to PD-1 checkpoint blockade immunotherapy, and donor cell expansion, phenotype and function was assessed (Fig 2a). Consistent with their stem-like less exhausted TCF-1^{Hi} Tim-3^{Lo} $GzmB^{Lo}$ $Slamf6^{Hi}$ $CD62L^{Hi}$ phenotype (Fig 1f-g, Extended Data Fig 6c-e), the $CD25^{Lo}$ donors mounted significantly greater expansion in response to PD-1 CBI compared to $CD25^{Hi}$ donors in all tissues analyzed (PBMC, spleen, lymph node, lung and liver) (Fig 2b, 2c).

However, minimal differences were observed in effector differentiation between $CD25^{Lo}$ and $CD25^{Hi}$ donors, as evidenced by largely similar levels of expression of GzmB, PD-1 and TNF-α following PD-1 CBI (Fig 2d, 2e). Notably, the responsiveness (expansion and effector differentiation) of endogenous D^bGP33-specific CD8 T cells of recipient mice remained unaltered to anti-PD-1 therapy, regardless of $CD25^{Lo}$ or $CD25^{Hi}$ donors being adoptively transferred into them (Extended Data Fig 8), thus lending further support to the data in Extended Data Fig 7 showing that the adoptively transferred donor cells do not perturb the infectious milieu of recipient mice with respect to viral loads, immune factors, etc. Together, these data establish that functionally potent TCF-1^{Hi} stem-like progenitor cells – capable of vigorous expansion in response to anti-PD-1 therapy – develop from $CD25^{Lo}$ precursors programmed during early stages of chronic viral infection. These observations prompted us to hypothesize that tempered IL-2 signals during T cell priming serve to program the long-lived self-renewing subset of stem-like exhausted CD8 T cells capable of robust responses to anti-PD-1 therapy.

Functional role of T cell-specific IL-2 signals in programming TCF-1^{Hi} stem-like precursors during chronic LCMV infection.

Higher expression of IL-2Rα was associated with increased STAT-5 phosphorylation (Extended Data Fig 9a), increased expression of downstream metabolic regulator cMyc (Extended Data Fig 5d), and higher levels of glycolysis and respiration (as indicated by increased extracellular acidification rate and oxygen consumption rate in a Seahorse biochemical analysis; Extended Data Fig 9b-d). Hence, we next sought to directly query the implied role of differential IL-2 signals in programming the development of TCF-1^{Hi} and TCF-1^{Lo} CD8 T cells in chronic LCMV infection.

Towards this goal, we either increased IL-2 signals through exogenous administration of IL-2, or tempered IL-2 signals through *in vivo* antibody blockade during early stages of chronic LCMV infection (days 0-3.5), and assessed the development of TCF-1^{Hi} GzmB^{Lo} stem-like CD8 T cells (Fig 3a). Appropriate IL-2 signal modulation was confirmed by assessing the levels of key IL-2 signaling-dependent proteins, CD25 and GzmB (Fig 3b). At these early stages of TCR-driven proliferation, all three groups – untreated, IL-2 supplemented and IL-2 blocked – exhibited similar levels of activation, as assessed by significant upregulation of CD44 compared to naïve cells (Extended Data Fig 10a); underwent significant proliferation compared to naïve cells as assessed by largely similar BrdU incorporation, and expanded to largely similar levels (Extended Data Fig 10b). Additionally, in the short programming window of 3-5 days, we did not observe any significant alterations in Treg cells due to IL-2 manipulation (Extended Data Fig 10c).

As shown in Fig 3c, evident differences in the development of TCF-1^{Hi} antigen-specific CD8 T cells were noted with manipulation of IL-2 signals: whereas exogenous IL-2 administration from days 0-3.5 after LCMV$_{Cl-13}$ infection led to reduced TCF-1^{Hi} GzmB^{Lo} cells, IL-2 blockade led to augmentation of TCF-1^{Hi} GzmB^{Lo} cells compared to untreated cells, in most secondary lymphoid and nonlymphoid tissues analyzed (spleen, lymph node, lung, liver) (Fig 3c, Extended Data Fig 10d). The donor cells primed in polarized high or low IL-2 conditions maintained their initial program, such that donors receiving increased IL-2 signals from days 0-3.5 remained lower for TCF-1^{Hi} GzmB^{Lo} cells even a week after adoptive transfer into infection-matched recipients with physiologic levels of IL-2 (Fig 3d). In contrast, day 3.5 donors programmed with tempered IL-2 signals remained higher for TCF-1^{Hi} GzmB^{Lo} cells following transfer into infection-matched recipients (Fig 3d). Increased IL-2 signaling specifically impaired the development of the TCF-1^{Hi}

Tim-3^{Lo} stem-like subset, while mediating modest decrease in the intermediate TCF-1^{Lo} Tim-3^{Lo} subset, and a modest increase in the TCF-1^{Lo} Tim-3^{Hi} subset (Extended Data Fig 10e). Reduced IL-2 signaling showed the inverse outcome. Notably, adoptive transfer of day 3.5 donors into day 3.5-infection matched recipients was conducted at low precursor frequencies, and did not alter the differentiation program of endogenous D^{b}GP33-specific CD8 T cells, as indicated by similar numbers of endogenous D^{b}GP33-specific CD8 T cells, which also contained largely similar levels of TCF-1^{Hi} GzmB^{Lo} cells regardless of receiving untreated, IL-2 treated or IL-2 blocked donors (Extended Data Fig 11). These data establish a key functional role of tempered IL-2 signals in programming the development of TCF-1^{Hi} lineage in chronic viral infection.

Enrichment of TCF-1^{Hi} cells in the CD25^{Lo} subset of virus-specific CD8 T cells (Fig 1), and the subsequent emergence of PD-1 checkpoint blockade immunotherapy responsive TCF-1^{Hi} stem-like progenitor cells from CD25^{Lo} precursors (Fig 2) further support the notion that IL-2 signal regulation might be acting at a T cell-specific level to program the generation of stem-like lineage, likely through physiologic modulation of CD25 expression. However, it is also plausible that IL-2 might drive the divergence of TCF-1^{Hi} and TCF-1^{Lo} CD8 T cell lineages through indirect effects on other immune cells such as effector CD4 T cells, Treg cells or APCs. Hence, we next engaged RNP-based Crispr/Cas9 methodology to specifically ablate CD25 expression in D^{b}GP33-specific CD8 T cells from day 0 (Fig 3e, Extended Data Fig 12) or day 2 (Extended Data Fig 13a) after priming and activation. We also used siRNA technology to transiently decrease CD25 expression between days 2-4 of priming and activation to query the timing of action of IL-2 signals in regulating the fate of TCF-1^{Hi} stem-like precursors (Extended Data Fig 14a). The development of TCF-1^{Hi} and TCF-1^{Lo} cells from wild-type (WT) and CD25 knockdown (KD) CD8 T cells was then

assessed at day 8 after $LCMV_{Cl-13}$ infection following transfer into naïve (in case of day 0 or siRNA-based transient knockdown) or day 2 infection-matched C57Bl/6 recipients (in case of day 2 knockdown) (Fig 3e, Extended Data Fig 12, 13, 14). WT D^bGP33-specific CD8 T cells were co-transferred with CD25 KD cells into the same recipient mice to ensure differentiation of both subsets in the same infectious milieu. The WT and KD donors were distinguishable from each other and from endogenous D^bGP33-specific CD8 T cells using congenic Ly/Thy markers. The efficiency of transfection (Extended Data Fig 12a) and CD25 knockdown was confirmed by flow cytometry at days 2 (Fig 3f), 5 and 8 (Extended Data Fig 12b) after electroporation of guide RNAs. In the case of day 2 CD25 knockdown, CD25 expression levels were confirmed to be reduced at day 4 after activation as well as day 8 after infection(Extended Data Fig 13b). In contrast to Crispr/Cas9-mediated deletion of *il2ra,* transient loss of CD25 was noted at day 2 after transfection in the case of siRNA-mediated knockdown, which was restored to WT levels at days 4 after knockdown and day 8 after infection (Extended Data Fig 14b).

In all three experimental conditions, we observed enhanced development of TCF-1^{Hi} $GzmB^{Lo}$, Tim-3^{Lo} stem-like CD8 T cells upon CD25 knockdown, compared to wild-type CD8 T cells in spleen (Fig 3e, Extended Data Fig 13c, 14c). Even in the nonlymphoid liver site, where TCF-1^{Hi} cells are typically found at lower levels compared to lymphoid organs, we saw modest increase in TCF-1^{Hi} cells upon CD25 knockdown from day 0 (Extended Data Fig 12c) or transiently from days 0-4 after stimulation (Extended Data Fig 14c). As is typical for exhausted cells[23-26], Tox was expressed at higher levels than naïve cells, albeit CD25 ablation was associated with modest increase in Tox expression (Extended Data Fig 14d). Ablation of CD25 from day 0 led to a greater enhancement of TCF-1^{Hi} $GzmB^{Lo}$, Tim-3^{Lo} stem-like progenitor exhausted CD8 T cells, compared

to ablation of CD25 from day 2 or between days 0-4, thus suggesting that CD25 continues to exert an impact on the development of TCF-1^{Hi} cells at least up to 4 days after infection. These data establish that CD25 serves as a T cell-specific physiologic regulator of TCF-1^{Hi} stem-like cell development during early stages of chronic viral infection by modulating IL-2 signals.

Late priming of CD8 T cells gives rise to IL-2Rα^{Lo} stem-like precursor CD8 T cells. In viral infections, IL-2 levels in the spleen typically peak around day 2 after infection and progressively decrease to baseline levels by day 6[38,39]. Hence, we hypothesized that T cell priming during later stages of expansion, when IL-2 levels are declining following chronic LCMV infection, may promote the development of TCF-1^{Hi} stem-like CD8 T cells. To test this, we adoptively transferred naïve D^{b}GP33-specific CD8 T cells at day 0, 1, 2 or 3 after infection, and analyzed the level of TCF-1^{Hi} GzmB^{Lo} Slamf6^{Hi} stem-like CD8 T cells in the secondary lymphoid (spleen and lymph node) and nonlymphoid tissues (liver and lung) at day 8.5 LCMV$_{Cl\text{-}13}$ after infection (Extended Data Fig 15). We noted that conditions of late priming and curtailed duration of stimulation (days 3-8.5) were more conducive to the development of stem-like CD8 T cells in all tissues analyzed, compared to prolonged stimulation from days 0-8.5 after infection (Extended Data Fig 15a-c). Curtailed stimulation during later stages from days 3-8.5 was also associated with lesser proliferation (as indicated by Ki-67 staining), lower level of Tim-3 expression and largely similar levels of PD-1 expression (Extended Data Fig 15d). Likewise, curtailing the duration of stimulation to early stages of infection (days 0-3.5 and days 0-5.5) induced higher levels of TCF-1^{Hi} GzmB^{Lo} stem-like virus-specific CD8 T cells, compared to longer durations of stimulation from days 0-6 or days 0-8 (Extended Data Fig 16a, 16b). However, the proportions of stem-like CD8 T cells were lower when

cells were stimulated during early stages of infection (when IL-2 levels are higher), than during later stages of priming when IL-2 levels decline (Extended Data Figure 15b, 16b). Early stimulation from days 0-5.5 induced about 10-15% TCF-1^{Hi} cells, compared to stimulation during later stages of expansion from days 3-8.5 stimulation, which induced about 40% TCF-1^{Hi} cells despite identical duration of stimulation (Extended Data Fig 15, 16). These data indicated that shorter duration of stimulation and later priming are more conducive for the development of TCF-1^{Hi} stem-like CD8 T cells.

To directly investigate whether priming during later stages of chronic LCMV infection better supports the development of TCF-1^{Hi} stem-like CD8 T cells compared to earlier stages, we next scanned how a 5.5 day window of stimulation from days 0-5.5, 1-6.5, 2-7.5 or 3-8.5 impacted the development of stem-like CD8 T cells (Fig 4a). Thus, maintaining the duration of stimulation the same (5.5 days), we controlled the timing of stimulation by adoptively transferring naïve D^{b}GP33-specific CD8 T cells at day 0, 1, 2 or 3 after infection, and analyzed the level of TCF-1^{Hi} GzmB^{Lo} Slamf6^{Hi} stem-like CD8 T cells. Stem-like CD8 T cells were maximally induced in the days 3-8.5 stimulation window in all secondary lymphoid (spleen and lymph node) and nonlymphoid tissues (liver and lung) analyzed (Fig 4b, Extended Data Fig 17a). We noted a progressive increase in TCF-1^{Hi} GzmB^{Lo} Slamf6^{Hi} stem-like CD8 T cells with later priming, such that donor cells transferred at day 3 after infection exhibited the highest proportions of stem-like antigen-specific CD8 T cells, whereas cells primed during early stages of infection (days 0-5.5) exhibited the least amounts (Fig 4b). No significant differences in proliferation, or expression of canonical inhibitory receptors Tim-3 and PD-1 was noted between groups, consistent with largely similar duration of antigenic stimulation (Extended Data Fig 17b). These findings implicate differential priming of

antigen-specific CD8 T cells during early versus late stages of expansion in chronic LCMV infection, and further demonstrate that longer duration of stimulation and stimulation during early stages of infection in higher IL-2 conditions are detrimental to the development of TCF-1^{Hi} stem-like CD8 T cells. In contrast, shorter duration of stimulation, during later stages of infection with lower IL-2 levels, are conducive for the development of stem-like $TCF1^{Hi}$ CD8 T cells during exhaustion.

To dissect differences in priming events during early versus late stages of chronic viral infection, we next characterized the dendritic cells (DC) subsets during distinct stages of chronic LCMV infection (days 0, 3.5, 5.5 and 8) using the subset distinguishing markers MHC-II, CD11c, CD11b, Ly6C, CCR2, CX3CR1 (Extended Data Fig 18a, 18b). We noted an evident decline in conventional DCs (cDC), and a concomitant increase in monocyte-derived DCs (moDC) with progression of infection (Fig 4c). We further compared the *in vivo* IL-2-production capabilities of cDC and moDC subsets during chronic LCMV infection. For this, we engaged the TdTomato IL-2 reporter mice[40]. As with $LCMV_{Cl\text{-}13}$-infected C57Bl/6 mice, we noted a skewing of DCs towards the moDC lineage at day 4 after $LCMV_{Cl\text{-}13}$ infection of TdTomato IL-2 reporter mice (Extended Data Fig 18c). With respect to IL-2 production, cDCs were preferentially enriched in the TdTomato+ population compared to moDCs, thus confirming that cDCs produced higher levels of IL-2 than moDCs *in vivo* during $LCMV_{Cl\text{-}13}$ infection (Fig 4d). To determine whether cDC and moDC subsets, expressing differential levels of IL-2, primed CD8 T cells differentially, we purified cDC and moDC subsets from day 3.5 after $LCMV_{Cl\text{-}13}$ infection, based on the expression of MHC-II, CD11b and CD11c gating scheme (Fig 4e, Extended Data Fig 18b). The subsets were further validated using distinguishing CCR2, Ly6C and Cx3CR1 markers (Extended Data Fig S18b), and purified DC subsets loaded with GP33 peptide antigen were used for stimulating naïve D^bGp33-specific CD8 T cells

(Fig 4e). Both DC subsets stimulated largely similar proliferative responses in D^bGP33-specific CD8 T cells (Fig 4f). However, activation of CD8 T cells was much stronger with cDC priming compared to moDC priming, as indicated by greater induction of CD44, CD25, CD69, PD-1 and downregulation of CD62L (Extended Data Fig 19). Consistent with less potent induction of CD25 in moDC-primed CD8 T cells, we observed significantly higher induction of $Slamf6^{Hi}$ $GzmB^{Lo}$ stem-like CD8 T cells following stimulation with moDCs, compared to cDCs (Fig 4g). In summary, these data demonstrate a preferential enrichment of moDCs with progression of chronic LCMV infection, which produce minimal amounts of IL-2 and prime preferential development of $Slamf6^{Hi}$ stem-like CD8 T cells compared to cDCs. These findings are consistent with preferential development of TCF-1^{Hi} stem-like CD8 T cells during later stages of chronic LCMV infection (Fig 4a, 4b), when moDCs predominate. Collectively, these data support the model that differential priming of antigen-specific CD8 T cells by cDCs and moDCs institute distinct programs of T cell differentiation during chronic LCMV infection through differential induction of CD25 expression and downstream IL-2 signaling.

Correlations of IL-2 signaling signature with stem-like lineage and checkpoint blockade immunotherapy responses in melanoma, head and neck cancer and lung cancer patients.

Analogous to chronic viral infections, functional exhaustion of tumor-reactive CD8 T cells is well established in solid tumors[8]. Importantly, recent studies have identified a wide spectrum of heterogeneity in exhausted CD8 T cell pool, ranging from stem-like to terminally exhausted tumor-reactive CD8 T cells in a variety of patient tumor samples including melanoma, lung carcinoma and head and neck cancer[10,16-21]. In order to explore a potential relationship between

IL-2 signaling and T cell exhaustion in patient solid tumor samples, we analyzed scRNA-seq data from melanoma, HPV+ head and neck cancer and lung carcinoma samples[10,16,21]. As in the case of LCMV-specific CD8 T cells, tumor infiltrating lymphocytes (TIL) from patient melanoma samples showed an inverse association between TCF-1 and IL-2 signaling signature genes in uniform manifold approximation and projection (UMAP) analyses of scRNA-seq data (Fig 5a). TILs expressing lower levels of gene encoding TCF-1 exhibited higher expression of Granzyme B, Tim-3 and PD-1 encoding genes, alongside increased IL-2 signaling signature genes such as STAT5 targets and Blimp-1 (encoded by *prdm1*) downstream of IL-2 (Fig 5a). In contrast, higher TCF-1 gene expression was directly related to higher CD62L and reduced IL-2 signaling signature genes (Fig 5a) as seen in LCMV-specific CD8 T cells (Fig 1b). Unsupervised clustering of CD8 T cells into stem-like, transitory effector-like and terminally exhausted subsets based on gene expression profiles (Extended Data Fig 20a, 20b) (as validated by relative enrichment of memory or exhaustion signatures; Fig 5b, Extended Data Fig 20c) further confirmed a preferential enrichment of IL-2 signaling signature in the more differentiated transitory effector and terminally exhausted subsets compared to the less-differentiated stem-like cells (Fig 5b). Importantly, IL-2 signaling signature was also found to be enriched in TILs of melanoma patients who did not benefit from checkpoint blockade (non-responders), whereas patients with robust responses to therapy (responders) showed significantly lower IL-2 signaling signature enrichment scores (Fig 5c, Extended Data Fig 20d). Thus, these data link IL-2 signaling with increased TIL exhaustion and poor responsiveness to PD-1 CBI in melanoma patients.

In virally-induced human papillomavirus (HPV)+ head and neck cancers as well, UMAP analysis of scRNA-seq data from HPV tetramer+ TILs showed inverse expression patterns of TCF-

1 with GzmB, Tim-3, PD-1 and IL-2 signaling, whereas higher TCF-1 expression correlated with higher CD62L expression, as in case of melanoma (Extended data Fig 21a). Importantly, we noted an evident enrichment of IL-2 signaling signature in terminally differentiated antigen-specific TIL subsets compared to the stem-like cells defined by unsupervised cluster analysis (Fig 5d,e; Extended Data Fig 21b, 21c). Consistent with higher IL-2 signaling in more differentiated HPV+ TILs, we noted increased expression of STAT5 targets downstream of IL-2 and Blimp-1 (Extended Data Fig 21d). Likewise, scRNA-seq data analysis of neoantigen-specific and influenza A virus-specific TILs from lung cancer patients (Extended Data Fig 22a, 22b) also showed preferential enrichment of exhaustion and IL-2 signaling signatures (Fig 5f) (including STAT5 and Blimp-1, Extended Data Fig 22c) compared to influenza A virus-specific T cells from the same environment, which were more memory-like (Fig 5f). Collectively, our studies show a direct regulatory effect of IL-2 signaling in the development of stem-like and terminally exhausted CD8 T cell lineages and checkpoint blockade immunotherapy responses during chronic viral infection and solid tumors.

IMPLICATIONS

IL-2 – an enigmatic cytokine, capable of effecting both immunostimulatory and immunosuppressive physiologic outcomes[39] – is shown here to act in a rheostatic manner to program the development of stem-like TCF-1^{Hi} exhausted CD8 T cell precursors at low signaling intensity, but drive terminal exhaustion under strong/prolonged signaling conditions. Our findings of *in vivo* fate programming of stem-like exhausted CD8 T cells by attenuated IL-2 signals in chronic viral infection, and direct association of increased IL-2 signaling with more terminal differentiation in intra-tumoral tumor-reactive T cells from patients with a variety of solid tumors such as melanoma, lung cancer and virally-induced head and neck cancer have implications in two main areas: first, for PD-1-based therapy of patients with chronic viral infections and solid tumors; and second for adoptive T cell therapeutic strategies for chronic viral infections and cancers.

The efficacy of PD-1 based therapies is critically dependent on the presence of TCF-1^{Hi} stem-like exhausted CD8 T cells, capable of vigorous expansion and differentiation into effector CTLs for expeditious and efficacious control of virus or tumors[2-4,6,10,15]. Given that new thymic emigrants continue to be recruited into the virus- or cancer-specific immune response even in established disease[3,41], our studies present regulated IL-2 signaling as a promising new preconditioning strategy that may be leveraged to improve clinical outcomes of PD-1-based therapies by shifting the balance in favor of stem-like exhausted CD8 T cell differentiation in ongoing cancers and chronic infections. This strategy to precondition an augmented response to PD-1-based therapies by IL-2 signal attenuation and augmentation of stem-like T cell subset prior to initiation of PD-1 checkpoint blockade is distinct from combination treatment with IL-2 and

PD-1 checkpoint blockade, which is designed to boost effector responses following release of PD-1 brakes[42]. Additionally, mechanisms that skew the balance of dendritic cells in favor of IL-2 non-producing subsets in the tumor microenvironment or during chronic infections may also be beneficial for augmenting T cell stemness and responsiveness to checkpoint blockade immunotherapy.

In the context of ACT, IL-2 has been classically used for expansion of therapeutic lymphocytes *in vitro* and for boosting their effector functions in patients following adoptive transfer[43]. *In vivo* IL-2 administration offers beneficial effects by boosting effector responses, and several IL-2 biologics with targeted effects on anti-tumor T cells (and not Treg cells) are being evaluated[43-45]. Our studies show that strong/prolonged IL-2 signaling eventually drives terminal exhaustion, whereas tempered IL-2 signals promote the generation of long-lived, multipotent stem-like antigen-specific T cells. These findings support the notion that tempering IL-2 signals during therapeutic T cell product generation will be beneficial for mediating long-term tumor control and immunosurveillance post-ACT by enhancing stem-like cells in the therapeutic product even in the controlled *in vitro* setting of T cell stimulation[46]. Moreover, our studies present IL-2Rα and other components of the IL-2 signaling axis such as IL-2Rβ[47], Blimp-1[48] and T cell-derived IL-2[49,50] as putative genetic engineering targets for enhancing the stemness and long-term therapeutic efficacy of TCR- or CAR-modified T cell monotherapy. This strategy is also expected to promote responsiveness of therapeutic product to subsequent PD-1 checkpoint blockade. Thus, our studies have broad implications in improving clinical outcomes of anti-PD-1 and ACT therapies for chronic infections and cancers by providing a unique preconditioning strategy of boosting long-lived, therapy-responsive stem-like CD8 T cells through IL-2 signal attenuation.

METHODS

Mice and infection

Four week old C57BL/6 mice were purchased from the Jackson Laboratory (Bar Harbor, ME, USA). Thy1.1+ and Ly5.1+ H-2D^{b}GP33-specific TCR-transgenic P14 mice, fully backcrossed onto the C57BL/6 background, were maintained in our colony. IL-2-Cre$^+$ mice were crossed with Rosa26 TdTomato reporter mice and bred in house. In all experiments, sex- and age-matched mice were used. All animals were used in accordance with SCRI Institutional Animal Care and Use Committee guidelines. LCMV Clone 13 strain (LCMV$_{Cl\text{-}13}$) was propagated, titered, and used for infections as previously[51]. Mice were injected intravenously (i.v.) with LCMV$_{Cl13}$ (2×10^6 PFU) 12-16 hrs following adoptive transfer of P14 cells.

Adoptive T cell transfer

To generate P14 chimeric mice, naïve C57Bl/6 mice were adoptively transferred with 2.5 x10^3 (Low dose) or 1x10^6 (High dose) WT D^{b}GP33-specific P14 CD8 T cells 12-16 hrs prior to infection with LCMV$_{Cl13}$. Early T cell priming and expansion were analyzed at Day 3.5 in case of high dose P14 chimeras, and at day 5.5 for low dose P14 chimeric mice. FACS-purified CD25^{Hi} or CD25^{Lo} CD8 T cells isolated at day 3.5 after infection were adoptively transferred into infection-matched recipients, at similar numbers (1x10^5-5x10^5). In the CD25 ablation experiments, naïve P14 cells that were permanently knocked down for CD25 expression (D0 CD25 KD) using Crispr/Cas9 or transiently ablated for CD25 expression using siRNA (Transient 25 KD) were co-transferred along with their respective WT P14 controls (~2x10^3) at 1:1 ratio into naïve recipient mice one day prior to LCMV$_{Cl\text{-}13}$ infection. Day 2 activated P14 CD8 T cells ablated for CD25 expression (D2 CD25 KD)

and WT P14 T cells were similarly co-transferred into infection matched recipient mice at 1:1 ratio of 200x10^3 cells of each type.

Flow cytometry and cell sorting

All antibodies were purchased from Biolegend (San Diego, CA, USA) except for TCF-1 (Cell signaling) and Slamf6 (BD Biosciences). MHC class I tetramers were made as described on the NIH tetramer core facility protocol and used as previously[52]. Single-cell suspensions from spleens, inguinal lymph nodes, lungs, livers or PBMCs from mice were prepared as previously[52-55]. All samples were resuspended in FACs buffer (1xPBS containing 1% FBS and 0.05% sodium azide) and stained with a fixable dead cell dye (LIVE/ DEAD zombie) along with extracellular fluorophore-conjugated antibodies to detect cell surface markers. For analysis of intracellular cytokines, splenocytes (2x10^6) were stimulated *in vitro* with 0.2µg/mL GP33-41 peptide in the presence of Brefeldin A for 5h, followed by surface staining for CD8, Ly5.1, Thy1.1, and Thy1.2. Cells were then washed and stained for IFN-γ, TNF-α and IL-2 using the BD Fixation/permeabilization kit (BD Bioscience). Staining of intranuclear transcription factors was performed using eBiosciences Foxp3/Transcription Factor Staining protocol. Phosphostaining was performed on splenocytes direct *ex vivo* or following *in vitro* stimulation with IL-2 in complete RPMI 1640 containing 10% FBS and β-mercaptoethanol (cRPMI) at 37˚C in 5% CO2. Cells were immediately fixed with 1.6% formaldehyde for 10 min followed by permeabilization in 80% ice-cold methanol for 30 min at 4ºC. After rehydration in FACs buffer cells were stained with anti-pSTAT5 on ice for 45 min as we have done previously[52]. For *in vivo* BrdU incorporation assay, mice were injected with 500µL BrdU (2mg/ml) intraperitoneally 12h prior to analysis using a BrdU

flow kit (BD Biosciences) as previously[53,54]. Sample acquisition was performed on LSRII Fortessa (BD Biosciences, San Jose, CA). Data analysis was performed with FlowJo v. 9.9 software.

For cell sorting of CD8 T cells or DC subsets, cells were enriched from total splenocytes using the EasySep Mouse CD8+ T cell Isolation Kit or the MojoSort Mouse Pan Dendritic Cell Isolation Kit (Biolegend), respectively at day 3.5 post infection. The enriched CD8 T cells were then FACS-sorted into $CD25^{Hi}$ and $CD25^{Lo}$ cells, following gating of Thy1.2- CD44+ P14 population. Isolated DCs were sorted into cDCs and moDCs based on CD11c, CD11b, Ly6c and CCR2 expression. Cells were sorted on JAZZ cell sorter (BD Bioscience) using a 70-micron nozzle.

In vivo treatment

For PD-1 checkpoint blockade immunotherapy studies, $CD25^{Hi}$ and $CD25^{Lo}$ recipient mice were treated intraperitoneally (I.P.) with PBS containing anti-PD-L1 monoclonal antibody (200μg/mouse, clone 10F.9G2, BioXcell) as previously[52]. PDL-1 blockade was performed every three days starting from day 16 to day 25 post infection for a total of three injections. To regulate IL-2 signals during priming (Day 0 to Day 3.5 post infection), mice were treated with high dose hIL-2 (15,000 IU, administered twice-daily through intraperitoneal route). IL-2 signaling blockade was performed using a combination of JES61A12 and S4B6 anti-IL-2 antibodies at 200μg/ml (BioXCell) injected once daily through intraperitoneal route. Control mice received sterile 1X PBS.

T cell activation and electroporation

CD8+ T cells were enriched from total splenocytes using the EasySep Mouse CD8+ T cell Isolation kit (Stem Cell). For permanent or transient CD25 ablation experiments at day 0, 4-6 x 10^6 P14 CD8 T cells were plated in 6 well plates and pre-cultured in IL-7 (10ng/ml, PeproTech) at 37°C, 5% CO2 for 24 hrs prior to electroporation. For ablation of CD25 at day 2 post-activation, purified naïve P14 CD8 T cells were plated at 3x10^6 cells/well in αCD3/αCD28 coated 6 well plates. Cells were pre-activated for 48h at 37°C, 5% CO2 prior to electroporation. Note that the preparation of CRISPR/Cas9 reagents was conducted based on guidance provided by IDT Alt-R CRISPR-Cas9 system. Naïve cells were resuspended in T buffer (Invitrogen MPK1096) and electroporated using 2200V, 10ms, 3 pulses, while activated CD8 T cells were resuspended in R buffer (Invitrogen MPK1096) and electroporated using 1600V, 10ms, 3 pulses. Following Neon transfection P14 CD8 T cells were transferred into warm cRPMI. Cells were rested at 37°C, 5% CO2 for 20-30min. The electroporation efficiency was evaluated for ATTO uptake by flow cytometry. Naïve and effector CD8 T cells were then plated on αCD3/αCD28 coated plates for activation and stained for CD25 expression 48h and 96h post electroporation.

DCs and P14 CD8 T cell co-culture

cDCs and moDCs subsets were harvested and sorted from spleens of infected mice at day 3.5-4.0 after infection with $LCMV_{Cl\text{-}13}$. For *in vitro* analysis of cell proliferation, 5x 10^4 of purified naïve P14 CD8 T cells were labeled with 5,6-carboxyfluorescein diacetate succinimidyl ester (CFSE) (Invitrogen, Carlsbad, CA) and co-cultured with GP33-loaded moDC or cDC (1 x 10^4 APCs) at a 5:1 ratio for 72h at 37°C as previously described (*Shin et al., 2019*).

Seahorse Assay

Oxygen consumption (OCR) and extracellular acidification rates (ECAR) were measured using the XFe96 well Seahorse Analyzer (Agilent). Day 3.5 Sorted $CD25^{Hi}$ and $CD25^{Lo}$ were adhered onto Seahorse cell culture plates using poly-L-lysine (Sigma) at $1.5x10^5$ cells per well. Agilent Seahorse XF Cell Mito Stress Test Kit was used to perform Mitostress test in the presence of 10mM glucose (Agilent) with addition of Oligomycin, FCCP, Rotenone/Antimycin A and finally 2-Deoxyglucose (20mM) to obtain the zero-point value of extracellular acidification.

RNA-seq Data analyses

Mouse samples: scRNA-seq (10x Genomics) data (GSE119943) from splenocytes isolated from P14 chimeric mice (adoptively transferred with 5000 D^bGP33-specific P14 CD8 T cells) at day 4.5 after infection with $LCMV_{Cl\text{-}13}$[35] were analyzed using Seurat (Version 2). Briefly, cells with percentage of mitochondrial genes below 0.05% were included. Cells with highest numbers of detected genes (top 0.2%) or lowest numbers of detected genes (bottom 0.2%) were considered as outliers and excluded from downstream analyses. Raw UMI counts were normalized to UMI count per million total counts and log-transformed. Variable genes were selected based on average expression and dispersion. Principal component analysis (PCA) analysis was performed using variable genes. T-distributed stochastic neighbor embedding (t-SNE) plots were generated based on selected PCA dimensions and unsupervised graph-based clustering was used to partition cells into clusters based on their transcriptomes. Each dot corresponds to one individual cell. Marker genes were identified by Seurat function FindAllMarkers.

Melanoma datasets: A single cell RNA-seq dataset of CD45+ cells from melanoma tumors was downloaded from gene expression omnibus (GEO; GSE120575)[10]. Data were loaded into a Seurat object and clustered using the associated Seurat packages. Cells in T cell clusters with >1 CD8A transcript, >1 CD3E transcript and <2 CD4 transcripts were isolated in silico for further analysis. These cells were again clustered, and dimensionality reduction was performed using the Seurat packages. Frequency of CD8 T cells in the two clusters with the highest IL2 signaling scores (see below) were compared in patients who responded or did not respond to therapy. T tests were used to assign statistical significance between response groups.

HPV-associated cancer datasets: Single cell RNA-seq dataset of HPV-tetramer sorted CD8 T cells from HPV associated malignancies was downloaded from GEO (GSE180268)[16]. Doublets were removed using the scds package. Low quality cells that contained >7% mitochondrial genes, <700 detected genes or <2,500 unique molecular identifiers were removed. Data from different patients were integrated using the linear regression and the batchelor package. Further clustering and dimensionality reduction was performed using the Seurat package.

Lung cancer patient samples: Gene expression matrices and TCR VDJ sequences from T cells isolated from non-small cell lung cancer tumors were downloaded from GEO (GSE176021)[21]. Gene expression data for each patient were loaded into Seurat objects (version 4.1) and integrated using IntegrateData and associated functions in Seurat. Antigen specificity was assigned by mapping VDJ sequences of known neoantigen or viral specificity to gene expression data with matching cell barcodes for each patient. Low quality cells (>7% mitochondrial genes

or <700 features) were removed. CD4, CD8A and CD8B gene expression was imputed using the SAVER package (version 1.1) and used to select for CD8 T cells. Subsequent clustering and dimensionality reduction were performed using the Seurat package.

Gene set scoring: Gene set signatures were scored using the UCell package (version 1.99). The IL2 signature gene set (FUNG_IL2_SIGNALING_1) and STAT5 targets downstream of IL-2 gene set (FUNG_IL2_TARGETS_WITH_STAT5_BINDING_SITES_T1) were downloaded from the molecular signatures database. The exhaustion and memory scores were compiled from overlapping genes in previously published datasets. Wilcoxon signed-rank tests were used to assign statistical significance.

Code availability: Code used to analyze human single cell RNA-seq data included R version 4.1.2 and the following publicly available packages: AUCell version 1.16 for ranking gene expression, SAVER version 1.1 for CD4, CD8A and CD8B gene imputation, scds version 1.10 for doublet detection, Seurat version 4.1, scater version 1.22 and scran version 1.22 for data manipulation and plotting, Monocle version 2.22 for pseudotime analyses and UCell version 1.99 for gene set scoring. Full code used to analyze human scRNA-seq datasets is available at https://github.com/thpulliam/IL2-exhaustion

Statistics

Paired or unpaired Student's t-test was used as indicated to evaluate differences between sample means. Paired analysis was conducted in experimental settings where WT and CD25KD CD8 T

cells were cotransferred into the same host. Unpaired t-test was used to compare sample means when WT and KD or $CD25^{Hi}$ and $CD25^{Lo}$ cells were transferred into separate hosts, or to compare sample means of treated and untreated groups from *in vitro* or *in vivo* studies. A one-way analysis of variance (ANOVA) with Tukey's post-hoc test was used for experiments with 3 or more groups to compare means across distinct groups. All statistical analysis was conducted using GraphPad Prism 5 Software (GraphPad Software, Inc.). P values of statistical significance are depicted by asterisk per the Michelin guide scale: * ($P \leq 0.05$), ** ($P \leq 0.01$), and *** ($P \leq 0.001$) in the figures. In cases where statistically significant differences were not observed, no asterisk marks are included.

ACKNOWLEDGMENTS

The authors would like to thank Shruti Bhise, Heather Maylor-Hagen and Yevgeniy Yuzefpolskiy for technical assistance. **Funding:** This work was supported by research funding from the Pediatric Cancer Research Foundation to SS, the Rachel Lynn Henley Foundation to VK, the Hopes and Smiles For Children Foundation to VK, In Concert for Cancer Foundation to VK and the National of Health (AI132819, AI103748 and to SS; 5P30CA015704 and AI154363 to VK; CA225517 to PN). **Author contributions:** RT, HX, RD and JR carried out experiments, analyzed data and prepared figures. TP analyzed data, prepared figures and wrote the results and methods section pertaining to human scRNA-seq data. RT wrote the methods section and figure legends for the mouse studies. PN provided critical input on the key aspects of scRNA-seq data analysis in human samples. VK and SS conceptualized the project, designed the experiments, analyzed data, interpreted the results, prepared figures, and wrote the manuscript. All authors assisted with figure or manuscript editing. **Competing Interests:** None**. Data Availability:** All data associated with this study are in the paper or supplementary materials. Microarray datasets are publicly available from previous studies at the National Center for Biotechnology Information GEO database under accession numbers GSE119943, GSE176021, GSE180268 and GSE120575.

REFERENCES

1 Utzschneider, D. T. *et al.* T Cell Factor 1-Expressing Memory-like CD8(+) T Cells Sustain the Immune Response to Chronic Viral Infections. *Immunity* **45**, 415-427, doi:10.1016/j.immuni.2016.07.021 (2016).

2 Im, S. J. *et al.* Defining CD8+ T cells that provide the proliferative burst after PD-1 therapy. *Nature* **537**, 417-421, doi:10.1038/nature19330 (2016).

3 He, R. *et al.* Follicular CXCR5- expressing CD8(+) T cells curtail chronic viral infection. *Nature* **537**, 412-428, doi:10.1038/nature19317 (2016).

4 Wu, T. *et al.* The TCF1-Bcl6 axis counteracts type I interferon to repress exhaustion and maintain T cell stemness. *Sci Immunol* **1**, doi:10.1126/sciimmunol.aai8593 (2016).

5 Chen, Z. *et al.* TCF-1-Centered Transcriptional Network Drives an Effector versus Exhausted CD8 T Cell-Fate Decision. *Immunity* **51**, 840-855 e845, doi:10.1016/j.immuni.2019.09.013 (2019).

6 Siddiqui, I. *et al.* Intratumoral Tcf1(+)PD-1(+)CD8(+) T Cells with Stem-like Properties Promote Tumor Control in Response to Vaccination and Checkpoint Blockade Immunotherapy. *Immunity* **50**, 195-211 e110, doi:10.1016/j.immuni.2018.12.021 (2019).

7 Hudson, W. H. *et al.* Proliferating Transitory T Cells with an Effector-like Transcriptional Signature Emerge from PD-1(+) Stem-like CD8(+) T Cells during Chronic Infection. *Immunity* **51**, 1043-1058 e1044, doi:10.1016/j.immuni.2019.11.002 (2019).

8 McLane, L. M., Abdel-Hakeem, M. S. & Wherry, E. J. CD8 T Cell Exhaustion During Chronic Viral Infection and Cancer. *Annu Rev Immunol* **37**, 457-495, doi:10.1146/annurev-immunol-041015-055318 (2019).

9 Brummelman, J. *et al.* High-dimensional single cell analysis identifies stem-like cytotoxic CD8(+) T cells infiltrating human tumors. *J Exp Med* **215**, 2520-2535, doi:10.1084/jem.20180684 (2018).

10 Sade-Feldman, M. *et al.* Defining T Cell States Associated with Response to Checkpoint Immunotherapy in Melanoma. *Cell* **175**, 998-1013 e1020, doi:10.1016/j.cell.2018.10.038 (2018).

11 Kallies, A., Zehn, D. & Utzschneider, D. T. Precursor exhausted T cells: key to successful immunotherapy? *Nat Rev Immunol* **20**, 128-136, doi:10.1038/s41577-019-0223-7 (2020).

12 Utzschneider, D. T. *et al.* Early precursor T cells establish and propagate T cell exhaustion in chronic infection. *Nat Immunol* **21**, 1256-1266, doi:10.1038/s41590-020-0760-z (2020).

13 Zander, R. *et al.* CD4(+) T Cell Help Is Required for the Formation of a Cytolytic CD8(+) T Cell Subset that Protects against Chronic Infection and Cancer. *Immunity* **51**, 1028-1042 e1024, doi:10.1016/j.immuni.2019.10.009 (2019).

14 Beltra, J. C. *et al.* Developmental Relationships of Four Exhausted CD8(+) T Cell Subsets Reveals Underlying Transcriptional and Epigenetic Landscape Control Mechanisms. *Immunity* **52**, 825-841 e828, doi:10.1016/j.immuni.2020.04.014 (2020).

15 Miller, B. C. *et al.* Subsets of exhausted CD8(+) T cells differentially mediate tumor control and respond to checkpoint blockade. *Nat Immunol* **20**, 326-336, doi:10.1038/s41590-019-0312-6 (2019).

16 Eberhardt, C. S. *et al.* Functional HPV-specific PD-1(+) stem-like CD8 T cells in head and neck cancer. *Nature* **597**, 279-284, doi:10.1038/s41586-021-03862-z (2021).

17 Li, H. *et al.* Dysfunctional CD8 T Cells Form a Proliferative, Dynamically Regulated Compartment within Human Melanoma. *Cell* **176**, 775-789 e718, doi:10.1016/j.cell.2018.11.043 (2019).
18 Guo, X. *et al.* Global characterization of T cells in non-small-cell lung cancer by single-cell sequencing. *Nat Med* **24**, 978-985, doi:10.1038/s41591-018-0045-3 (2018).
19 Clarke, J. *et al.* Single-cell transcriptomic analysis of tissue-resident memory T cells in human lung cancer. *J Exp Med* **216**, 2128-2149, doi:10.1084/jem.20190249 (2019).
20 Thommen, D. S. *et al.* A transcriptionally and functionally distinct PD-1(+) CD8(+) T cell pool with predictive potential in non-small-cell lung cancer treated with PD-1 blockade. *Nat Med* **24**, 994-1004, doi:10.1038/s41591-018-0057-z (2018).
21 Caushi, J. X. *et al.* Transcriptional programs of neoantigen-specific TIL in anti-PD-1-treated lung cancers. *Nature* **596**, 126-132, doi:10.1038/s41586-021-03752-4 (2021).
22 Zheng, C. *et al.* Landscape of Infiltrating T Cells in Liver Cancer Revealed by Single-Cell Sequencing. *Cell* **169**, 1342-1356 e1316, doi:10.1016/j.cell.2017.05.035 (2017).
23 Alfei, F. *et al.* TOX reinforces the phenotype and longevity of exhausted T cells in chronic viral infection. *Nature* **571**, 265-269, doi:10.1038/s41586-019-1326-9 (2019).
24 Khan, O. *et al.* TOX transcriptionally and epigenetically programs CD8(+) T cell exhaustion. *Nature* **571**, 211-218, doi:10.1038/s41586-019-1325-x (2019).
25 Scott, A. C. *et al.* TOX is a critical regulator of tumour-specific T cell differentiation. *Nature* **571**, 270-274, doi:10.1038/s41586-019-1324-y (2019).
26 Seo, H. *et al.* TOX and TOX2 transcription factors cooperate with NR4A transcription factors to impose CD8(+) T cell exhaustion. *Proc Natl Acad Sci U S A* **116**, 12410-12415, doi:10.1073/pnas.1905675116 (2019).
27 Shin, H. *et al.* A role for the transcriptional repressor Blimp-1 in CD8(+) T cell exhaustion during chronic viral infection. *Immunity* **31**, 309-320, doi:10.1016/j.immuni.2009.06.019 (2009).
28 Scott-Browne, J. P. *et al.* Dynamic Changes in Chromatin Accessibility Occur in CD8(+) T Cells Responding to Viral Infection. *Immunity* **45**, 1327-1340, doi:10.1016/j.immuni.2016.10.028 (2016).
29 Sen, D. R. *et al.* The epigenetic landscape of T cell exhaustion. *Science* **354**, 1165-1169, doi:10.1126/science.aae0491 (2016).
30 Kao, C. *et al.* Transcription factor T-bet represses expression of the inhibitory receptor PD-1 and sustains virus-specific CD8+ T cell responses during chronic infection. *Nat Immunol* **12**, 663-671, doi:10.1038/ni.2046 (2011).
31 Doering, T. A. *et al.* Network analysis reveals centrally connected genes and pathways involved in CD8+ T cell exhaustion versus memory. *Immunity* **37**, 1130-1144, doi:10.1016/j.immuni.2012.08.021 (2012).
32 Yao, C. *et al.* BACH2 enforces the transcriptional and epigenetic programs of stem-like CD8(+) T cells. *Nat Immunol* **22**, 370-380, doi:10.1038/s41590-021-00868-7 (2021).
33 Seo, H. *et al.* BATF and IRF4 cooperate to counter exhaustion in tumor-infiltrating CAR T cells. *Nat Immunol* **22**, 983-995, doi:10.1038/s41590-021-00964-8 (2021).
34 Man, K. *et al.* Transcription Factor IRF4 Promotes CD8(+) T Cell Exhaustion and Limits the Development of Memory-like T Cells during Chronic Infection. *Immunity* **47**, 1129-1141 e1125, doi:10.1016/j.immuni.2017.11.021 (2017).

35 Yao, C. *et al.* Single-cell RNA-seq reveals TOX as a key regulator of CD8(+) T cell persistence in chronic infection. *Nat Immunol* **20**, 890-901, doi:10.1038/s41590-019-0403-4 (2019).
36 Barber, D. L. *et al.* Tuberculosis following PD-1 blockade for cancer immunotherapy. *Sci Transl Med* **11**, doi:10.1126/scitranslmed.aat2702 (2019).
37 Abdel-Hakeem, M. S. *et al.* Epigenetic scarring of exhausted T cells hinders memory differentiation upon eliminating chronic antigenic stimulation. *Nat Immunol* **22**, 1008-1019, doi:10.1038/s41590-021-00975-5 (2021).
38 Kalia, V. *et al.* Prolonged interleukin-2Ralpha expression on virus-specific CD8+ T cells favors terminal-effector differentiation in vivo. *Immunity* **32**, 91-103, doi:S1074-7613(10)00008-7 [pii] 10.1016/j.immuni.2009.11.010 (2010).
39 Kalia, V. & Sarkar, S. Regulation of Effector and Memory CD8 T Cell Differentiation by IL-2-A Balancing Act. *Front Immunol* **9**, 2987, doi:10.3389/fimmu.2018.02987 (2018).
40 Yamamoto, M. *et al.* Ontogeny and localization of the cells produce IL-2 in healthy animals. *Cytokine* **61**, 831-841, doi:10.1016/j.cyto.2012.11.026 (2013).
41 Vezys, V. *et al.* Continuous recruitment of naive T cells contributes to heterogeneity of antiviral CD8 T cells during persistent infection. *J Exp Med* **203**, 2263-2269, doi:10.1084/jem.20060995 (2006).
42 West, E. E. *et al.* PD-L1 blockade synergizes with IL-2 therapy in reinvigorating exhausted T cells. *J Clin Invest* **123**, 2604-2615, doi:10.1172/JCI67008 (2013).
43 Hernandez, R., Poder, J., LaPorte, K. M. & Malek, T. R. Engineering IL-2 for immunotherapy of autoimmunity and cancer. *Nat Rev Immunol*, doi:10.1038/s41577-022-00680-w (2022).
44 Levin, A. M. *et al.* Exploiting a natural conformational switch to engineer an interleukin-2 'superkine'. *Nature* **484**, 529-533, doi:10.1038/nature10975 (2012).
45 Mitra, S. *et al.* Interleukin-2 activity can be fine tuned with engineered receptor signaling clamps. *Immunity* **42**, 826-838, doi:10.1016/j.immuni.2015.04.018 (2015).
46 Mo, F. *et al.* An engineered IL-2 partial agonist promotes CD8(+) T cell stemness. *Nature* **597**, 544-548, doi:10.1038/s41586-021-03861-0 (2021).
47 Beltra, J. C. *et al.* IL2Rbeta-dependent signals drive terminal exhaustion and suppress memory development during chronic viral infection. *Proc Natl Acad Sci U S A* **113**, E5444-5453, doi:10.1073/pnas.1604256113 (2016).
48 Rutishauser, R. L. *et al.* Transcriptional repressor Blimp-1 promotes CD8(+) T cell terminal differentiation and represses the acquisition of central memory T cell properties. *Immunity* **31**, 296-308, doi:S1074-7613(09)00323-9 [pii] 10.1016/j.immuni.2009.05.014 (2009).
49 Kahan, S. M. *et al.* Intrinsic IL-2 production by effector CD8 T cells affects IL-2 signaling and promotes fate decisions, stemness, and protection. *Sci Immunol* **7**, eabl6322, doi:10.1126/sciimmunol.abl6322 (2022).
50 Toumi, R. *et al.* Autocrine and paracrine IL-2 signals collaborate to regulate distinct phases of CD8 T cell memory. *Cell Rep* **39**, 110632, doi:10.1016/j.celrep.2022.110632 (2022).
51 Wherry, E. J. *et al.* Molecular signature of CD8+ T cell exhaustion during chronic viral infection. *Immunity* **27**, 670-684, doi:S1074-7613(07)00454-2 [pii] 10.1016/j.immuni.2007.09.006 (2007).

52 Kalia, V. *et al.* Metabolic regulation by PD-1 signaling promotes long-lived quiescent CD8 T cell memory in mice. *Sci Transl Med* **13**, eaba6006, doi:10.1126/scitranslmed.aba6006 (2021).
53 Kalia, V., Penny, L. A., Yuzefpolskiy, Y., Baumann, F. M. & Sarkar, S. Quiescence of Memory CD8(+) T Cells Is Mediated by Regulatory T Cells through Inhibitory Receptor CTLA-4. *Immunity* **42**, 1116-1129, doi:10.1016/j.immuni.2015.05.023 (2015).
54 Khan, A. A., Penny, L. A., Yuzefpolskiy, Y., Sarkar, S. & Kalia, V. MicroRNA-17~92 regulates effector and memory CD8 T-cell fates by modulating proliferation in response to infections. *Blood* **121**, 4473-4483, doi:10.1182/blood-2012-06-435412 (2013).
55 Sarkar, S. *et al.* Functional and genomic profiling of effector CD8 T cell subsets with distinct memory fates. *J Exp Med* **205**, 625-640, doi:jem.20071641 [pii] 10.1084/jem.20071641 (2008).
56 Lowery, F. J. *et al.* Molecular signatures of antitumor neoantigen-reactive T cells from metastatic human cancers. *Science* **375**, 877-884, doi:10.1126/science.abl5447 (2022).

FIGURE LEGENDS

FIGURE 1. TCF-1^{Hi} stem-like CD8 T cell lineage is preferentially associated with reduced IL-2R expression during T cell priming in chronic viral infection.

(a) Inverse expression patterns of TCF-1 and IL-2R in LCMV-specific CD8 T cells during early stages of T cell activation and expansion in response to chronic LCMV infection. WT D^{b}GP33-specific P14 cells (2.5x10^{3}, low dose, endogenous precursor frequencies) were adoptively transferred into naïve B6 mice, which were subsequently infected with LCMV$_{Cl13}$. Flow-cytometry plot of TCF-1 and GzmB co-expression in splenic P14 CD8 T cells are shown at day 5.5 post-infection. Histograms and bar graphs depict levels of CD25 expression on TCF-1^{Hi} (Light blue) or TCF-1^{Lo} (Gold) gated P14 T cells.

(b) scRNA-seq data support lower expression of IL-2Rα in cells expressing higher levels of markers associated with stem-like CD8 T cells in chronic LCMV infection. Single-cell transcript levels of *tcf7*, *gzmb*, *il2ra*, *slamf6*, *pdcd1*, *havcr2*, *sell*, *bcl2* and *mki67* are illustrated in t-SNE plots from LCMV-specific CD8 T cells 4.5 days after LCMV$_{Cl-13}$ infection (Transcript levels are color-coded: grey, not expressed; purple, expressed).

(c) Experimental set-up to investigate the long-term exhausted CD8 T cell fate outcomes of CD25^{Hi} and CD25^{Lo} LCMV-specific CD8 T cells isolated during priming. WT P14 cells (1x10^{6}) were adoptively transferred into naïve B6 recipient mice and then infected with LCMV$_{Cl13}$ 1 day later. CD25^{Lo} and CD25^{Hi} cells were FACS purified 3.5 days after LCMV$_{Cl13}$ infection. Congenically mismatched CD25^{Hi} or CD25^{Lo} donor cells (~1x10^{5}) were transferred into infection-matched C57Bl/6 mice.

(d) TCF1^{Hi} GzmB^{Lo} cells preferentially arise from CD25^{Lo} donors. Flow-cytometry plots of TCF-1 and GzmB co-expression in transferred CD25^{Hi} or CD25^{Lo} donor cells are presented from the indicated tissues, 8 days after infection. Representative flow data are shown along with a bar graph of % stem-like TCF-1^{Hi} GzmB^{Lo} CD8 T cells.

(e) Preferential survival of CD25^{Lo} donors enriched in TCF1^{Hi} stem-like CD8 T cells during late stages of chronic LCMV infection. Bar graphs show numbers of CD25^{Hi} and CD25^{Lo} donor CD8 T cells in indicated tissues at day 24 after LCMV$_{Cl13}$ infection.

(f) Increased expression of multiple inhibitory receptors on terminally exhausted CD8 T cells arising from CD25^{Hi} precursors. SPICE (simplified presentation of incredibly complex evaluations) plots illustrating co-expression of the inhibitory receptors (IR) PD-1, Tim-3, LAG3, 2B4 on transferred CD25^{Hi} or CD25 ^{Lo} P14 CD8 T cells are presented.

(g) Relative expression of T-bet and eomesodermin transcription factors in CD25^{Lo} and CD25^{Hi} donors. Bar graphs depict the expression of T-bet and Eomes on FACS sorted and transferred CD25^{Hi} (Red) or CD25^{Lo} (Blue) P14 CD8 T cells at day 8 post-infection; grey histograms show endogenous CD44^{lo} naïve CD8 T cells. Number represents MFI of respective marker. Bar graphs display mean and SEM. Data are representative of at least two independent experiments with n=5-10 mice per group. Unpaired Student t-test was used with statistical significance in difference of means represented as * ($P \leq 0.05$), ** ($P \leq 0.01$), *** ($P \leq 0.001$).

FIGURE 2. Stem-like TCF-1^{Hi} progenitor CD8 T cells arising from IL-2Rα precursors exhibit augmented responsiveness to PD-1 checkpoint blockade immunotherapy during exhaustion.

(a) Experimental set-up. $CD25^{Lo}$ and $CD25^{Hi}$ cells were FACS purified at day 3.5 after infection, and adoptively transferred into infection-matched congenically distinct recipient mice (as in Fig 1). Mice were subsequently treated with anti-PD-L1 antibody (200 μg) every 3 days from day 15 to 24, and donor cells were assessed for expansion and effector function.

(b) Longitudinal analysis of $CD25^{Lo}$ and $CD25^{Hi}$ donors in blood of chronically infected mice. Numbers of $CD8^{+}$ $Ly5.1^{+}$ donor cells per $10x10^{6}$ PBMC are depicted at indicated time points after infection. Bar graphs show fold expansion of donor cells at day 22 in blood after infection in treated and untreated groups receiving $CD25^{Lo}$ or $CD25^{Hi}$ donor cells. Data are representative of 2 independent experiments with n=4-6 mice per group.

(c) Absolute numbers of donor cells in the presence or absence of anti-PD-L1 blockade therapy. Bar graphs show absolute numbers of donor cells in indicated tissues. Numbers above bars depict fold-change in numbers of donor cells after treatment with aPD-L1.

(d) Expression of effector molecule granzyme B and inhibitory receptor PD-1 in $CD25^{Lo}$ and $CD25^{Hi}$ donors in response to anti-PD-L1 blockade therapy. Representative histograms and composite bar graphs show GzmB and PD-1 expression in donor CD8 T cells in the spleen at day 24 after infection. Numbers depict mean fluorescence intensity (MFI) of expression of respective markers.

(e) Expression of effector cytokines by $CD25^{Lo}$ and $CD25^{Hi}$ donors in response to anti-PD-L1 blockade therapy. Bar graphs show % IFN-γ and TNF-α double positive donor cells, and MFI of TNF-α expression in $CD25^{Hi}$ and $CD25^{Lo}$ donor CD8 T cells from spleens following *in vitro* stimulation of splenocytes with GP33 peptide for 5 hrs.

Bar graphs display mean, and SEM. Data are representative of at least 2 independent experiments with n=4-6 mice per group. One-way ANOVA with Tukey post-test was used to

compare differences between groups. Statistical significance in difference of means is represented as * ($P \leq 0.05$), ** ($P \leq 0.01$), *** ($P \leq 0.001$).

FIGURE 3. Attenuation of IL-2 signals in virus-specific CD8 T cells promotes the generation of TCF-1^{Hi} stem-like precursors during exhaustion.

(a) Experimental setup for IL-2 enhancement or attenuation during T cell priming of chronic LCMV infection. Naïve C57Bl/6 mice adoptively transferred with $1x10^6$ P14 CD8 T cells were infected with $LCMV_{Cl13}$, and were treated intraperitoneally with PBS, high dose IL-2 (1.5×10^4 IU) or anti-IL-2 complex from days 0-3.5 after infection. LCMV-specific CD8 T ($4x10^5$) cells were isolated from splenocytes at day 3.5 post-infection, characterized, and transferred into infection-matched recipients. Donor cells were analyzed 6 days following transfer (Day 9 post- infection).

(b) Activation and effector molecule expression under distinct IL-2 stimulatory conditions. Bar graphs show the MFI of expression of CD25 and GzmB on donor cells in the untreated (UnTx) (Black), IL-2-treated (Red) and αIL-2 treated groups (Blue) at day 3.5 post-infection.

(c) Assessment of stem-like precursors with IL-2 supplementation or blockade during T cell priming. Representative flow-cytometry plots of TCF-1 and GzmB co-expression on donor CD8 T cells, and composite bar graphs showing % TCF1^{Hi} GzmB^{Lo} stem-like precursors in the SPL at day 3.5 post-infection. Data are representative of 3-4 independent experiments with n=4-6 mice per group.

(d) Persistence of stem-like CD8 T cell precursors primed under conditions of IL-2 attenuation. Representative flow-cytometry plots of TCF-1 and GzmB co-expression on donor CD8 T cells, and composite bar graphs showing % TCF1^{Hi} GzmB^{Lo} stem-like precursors in the SPL 6 days after

adoptive transfer (~9 days after $LCMV^{Cl-13}$ infection) of donor cells primed under IL-2 supplementation or blockade conditions for 3.5 days.

(e) Experimental setup to query the CD8 T cell-intrinsic role of CD25 in programming TCF-1^{Hi} stem-like lineage through IL-2 signal modulation. The gene encoding IL-2Rα was knocked out using RNP-based CRISPR-Cas9 technology. Naïve P14 CD8 T cells were electroporated with guide RNA targeting *il2ra* gene. Equal numbers of WT CD8 T cells or CD25 knockdown (KD) cells were adoptively co-transferred into naïve mice, which were then infected with $LCMV_{Cl-13}$. Donor LCMV-specific CD8 T cells were analyzed after 8 days of infection.

(f) The efficiency of CRISPR-Cas9-mediated deletion of *il2ra.* Representative histogram plots show the expression of CD25 in WT (Red), CD25 ^{KD} (Blue) and naïve cells (Gray) P14 CD8 T cells after 48hr of *in vitro* stimulation by plate bound anti-CD3 and anti-CD28.

(g) Assessment of $TCF1^{Hi}$ stem-like precursors in CD25 ablated CD8 T cells. Representative flow-cytometry plots of TCF-1 and GzmB or TCF-1 and Tim-3 co-expression on D0 ablated CD25 donor CD8 T cells in the spleen, along with composite bar graphs of % stem-like TCF-1^{Hi} $GzmB^{Lo}$ CD8 T cells are presented.

Data are representative of at least 2 independent repeats with n=3 mice per group (mean ± SEM). Paired Student t-test was used with statistical significance in difference of means represented as * ($P \leq 0.05$), ** ($P \leq 0.01$), *** ($P \leq 0.001$). To compare differences between groups one-way ANOVA with Tukey post-test was used. Statistical significance in difference of means is represented as * ($P \leq 0.05$), ** ($P \leq 0.01$), *** ($P \leq 0.001$).

FIGURE 4. Late priming of CD8 T cells gives rise to IL-2Ra^{Lo} stem-like precursor CD8 T cells.

(a) Experimental setup. LCMV $_{Cl13}$ infected C57Bl/6 mice were adoptively transferred with $2.5x10^3$ of WT P14 at day 0, 1, 2 and 3 after infection. Donor CD8 T cells were analyzed 5.5 days after P14 transfer.

(b) Characterization of stem-like CD8 T cell fates upon early versus late priming in $LCMV_{Cl-13}$ infection. Representative flow cytometry plots of TCF-1 and GzmB or TCF-1 and Slamf6 co-expression on donor CD8 T at indicated time-points (days 5.5, 6.5, 7.5 or 8.5) after infection are presented. Bar graphs depict % stem-like TCF-1^{Hi} $GzmB^{Lo}$ CD8 T cells in the SPL (top), or iLN, LVR and LNG (Bottom) at 5.5 days after P14 transfer.

(c) Characterization of conventional (cDC) and monocyte-derived (moDC) DCs during early stages of $LCMV_{Cl-13}$ infection. Bar graphs show mean and SEM of frequencies and absolute numbers of $MHCII^+$ $Ly6G^-$ cDC ($CD11c^+$) (orange) and moDCs ($CD11b^+$) (brown) in spleens on days 3.5, 5.5 and day 8 after $LCMV_{Cl-13}$ infection. The subsets were further confirmed using Ly6C, CCR2 and CX3CR1 markers.

(d) Relative *in vivo* IL-2 production capability of cDC and moDC subsets during $LCMV_{Cl-13}$ infection. IL-2-Cre ROSA/tdTomato IL-2 reporter mice were infected with $LCMV_{Cl13}$, and moDC and cDC were isolated from spleen 4 days after infection. Bar graphs depict % cDC (Orange) or moDC (Brown) gated subsets that are TdT+. Cells were gated and analyzed on $MHCII^+$ $Ly6G^-$ population.

(e) Experimental setup to query distinctive T cell priming by cDC and moDC subsets. B6 mice were infected with $LCMV_{Cl13}$. Conventional and monocyte-derived DC subsets were purified and sorted by flow cytometry at day 3.5 after infection, and co-cultured ($1x10^4$ cells) with CFSE labeled GP33-specific P14 CD8 T cells ($5x10^5$) for 3 days in the presence of GP_{33-41} peptide.

(f) T cell proliferation upon stimulation with cDC or moDC subsets. Representative histograms gated on donor P14 cells depict CFSE dilution 3 days post co-culture with cDC and moDC. Bar graphs show frequency of donor P14 T cells in each cell division.

(g) Phenotypic characterization of T cells primed by cDC or moDC subsets. Representative flow-cytometry plots show Slamf6 and GzmB or CD25 expression on GP33-specific CD8 T cells 3 days after activation. Bar graph depict % Slamf6^{Hi} GzmB^{Lo} and Slamf6^{Hi} CD25^{Lo} GP33- specific CD8 T cells.

Data are representative of 2 independent experiments with n=3-5 mice per group. To compare differences between groups one-way ANOVA with Tukey post-test was used. Statistical significance in difference of means is represented as * ($P \leq 0.05$), ** ($P \leq 0.01$), *** ($P \leq 0.001$).

FIGURE 5. IL-2 signaling signatures are inversely associated with TCF-1^{Hi} lineage and anti-PD-1 responses in melanoma, HPV+ head and neck cancer and lung cancer patients.

(a) Expression of key exhaustion and memory genes and IL2 signaling score in CD8 T cells in melanoma tumors from checkpoint blockade immunotherapy treated patient dataset originally published in Sade-Feldman et al., 2018[10]. UMAP plots of scRNA-seq of CD8 T cells from 48 melanoma tumors for activation/exhaustion associated genes (*pdcd1, havcr2, gzmb*), stem cell associated genes (*tcf7, sell*) or a composite IL2 signature (FUNG_IL2_SIGNALING_1). Genes containing STAT5 binding sites and Blimp-1 (encoded by *prdm1*) downstream targets of IL-2 are also presented as UMAP plots. Genes downstream of IL2 signaling that also contain STAT5 binding sites (FUNG_IL2_TARGETS_WITH_STAT5_BINDING_SITES_T1) were used to calculate the STAT5 Target Binding score.

(b) Exhaustion signature scores are shown for indicated CD8 T cell clusters from melanoma tumors and across pseudotime. Signature of genes from the FUNG_IL2_SIGNALING_1 dataset was created and scored across the Naïve (N), Effector (E), Stem-like (T_{St}) exhausted, Trasitory-exhausted (T_{Tr}), and Terminally differentiated exhausted (T_{TD}) clusters.

(c) Association between immunotherapy response and IL2 signature scores in CD8 T cells. The frequency of CD8 T cells from either of the clusters with high IL2-signatures (T_{Tr} and T_{TD}) as a portion of all CD8 T cells were compared between patients who responded or did not respond to checkpoint blockade. Wilcoxon ranked-sum test used to establish statistical significance.

(d) Phenotypes of HPV-specific CD8 T cells in HPV driven tumors. CD8 T cells binding to MHC-I tetramers containing HPV peptides were sorted using flow cytometry and scRNA-seq was performed on the sorted cells from 12 patients. Unbiased clustering and UMAP plots were generated as described in the original publication[16]. Unbiased clusters were labeled as stem-like (T_{St}), transitory (T_{Tr}) or terminally differentiated (T_{TD}) based on their expression of memory and exhaustion genes and concordance with the original publication.

(e) IL2 signature score in exhausted CD8 T cell clusters identified in panel d from HPV+ head and neck tumors. A signature score of genes from the FUNG_IL2_SIGNALING_1 dataset was created and scored across the clusters. Statistical significance was assigned using Wilcoxon signed-rank tests.

(f) Violin plots of exhaustion, memory and IL2 signaling related gene signatures in neoantigen and influenza-specific CD8 T cells from NSCLC samples. CD3 T cells from 15 non-small cell lung cancer (NSCLC)-tumors were isolated and single cell RNA-seq was performed on these cells. In parallel the MANAFEST and viraFEST assays were performed to identify mutation associated

neoantigens (MANA) or influenza specific T cell receptors. Cancer-specific signature MANA score was derived from Lowery et al., 2022[56]. CD8 T cells with either MANA or influenza-specific T cells were isolated *in silico* and UMAP plots of these cells were performed on dataset originally published in Caushi et al., 2021[21]. Signature scores were calculated using expression of exhaustion- or memory -associated genes and genes downstream of IL2 signaling (FUNG_IL2_SIGNALING_1). Wilcoxon ranked-sum tests were used to assign statistical significance. Statistical significance represented as * ($P \leq 0.05$), ** ($P \leq 0.01$), *** ($P \leq 0.001$).

EXTENDED DATA FIGURES AND TABLES

Extended Data Fig 1. Markers of stem-like CD8 T cell lineage are inversely related to IL-2Ra expression during early stages of chronic viral infection.

(a) WT P14 cells ($2.5x10^3$) were adoptively transferred into naïve B6 mice, which were subsequently infected with $LCMV_{Cl13}$. Representative flow-cytometry plots of CD25 and TCF-1 or GzmB co-expression in P14 CD8 T cells isolated from iLN, LVR and LNG at day 5.5 post-infection are shown.

(b) Flow-cytometry plots show CD25 and TCF-1, Slamf6, GzmB or Tim-3 co-expression in splenic P14 CD8 T cells at day 5.5 post-infection. Bar graphs depict the frequency of TCF-1^{Hi}, Slamf6^{Hi}, GzmB ^{Lo} and Tim-3 ^{Lo} P14 T cells on gated $CD25^{Lo}$ (Blue) or $CD25^{Hi}$ (Red) P14 T cells 5.5 days after infection. Data presented are representative of 2 independent experiments with at least 3 mice per group.

Extended Data Fig 2. Functional competence of $TCF1^{Hi}$ and TCF-1^{Lo} antigen-specific CD8 T cells during early stages of chronic LCMV infection.

WT P14 cells ($1x10^6$) were adoptively transferred into naïve B6 recipient mice and then infected with $LCMV_{Cl13}$ 1 day later. Representative flow cytometry plots of TNF-α+ and IFN-γ+ co-expression on gated TCF-1^{Hi} $GzmB^{Lo}$ or TCF-1^{Lo} $GzmB^{Hi}$ donor CD8 T cells at day3.5 post-infection are presented. Bar graphs depict MFI of IFN-γ and %TNF-α+ of IFN-γ+ in TCF-1^{Hi} (Light blue) or TCF-1^{Lo} (Gold) P14 T cells.

Extended Data Fig 3. Inverse association of TCF-1 and CD25 expression is evident in endogenous virus-specific CD8 T cells, and in TCR-transgenic CD8 T cells at low or high precursor frequencies.

(a) Representative flow cytometry plots show TCF-1 and CD25 expression on endogenous Gp33- and Gp276-specific CD8 T cells in the SPL, iLN, LVR and LNG at day 5.5 after infection.

(b) Bar graphs depict relative proportions of stem-like TCF-1^{Hi} CD8 T cells (Light blue) or terminally differentiated TCF-1^{Lo} CD8 T cells (Gold) in endogenous LCMV D^bGP33-, and D^bGP276-specific CD8 T cells in spleen at day 5.5 after infection.

(c) WT D^bGP33-specific P14 CD8 T Cells were adoptively transferred at high dose ($1x10^6$) or low dose ($2.5 x10^3$) into naïve B6 mice, which were subsequently infected with $LCMV_{Cl13}$ for 3.5 or 5.5 days respectively. Representative flow cytometry plots of TCF-1 and CD25 or TCF-1 and GzmB expression in P14 CD8 T cells on the indicated days post $LCMV_{Cl13}$ infection are presented. Bar graphs display mean and SEM. Paired and unpaired student t-test was used with statistical significance in difference of means represented as ** ($P \leq 0.01$), *** ($P \leq 0.001$).

Extended Data Fig 4. Similar developmental profiles of adoptively transferred virus-specific CD8 T cells purified from low or high precursor frequencies.

(a) Experimental setup. Chimeric C57Bl/6 mice were adoptively transferred with high dose ($1x10^6$) or low dose ($2.5 x10^3$) WT P14 CD8 T cells, and infected with $LCMV_{Cl13}$ for 3.5 or 5.5 days respectively. On the indicated days, donor cells were purified, and equal numbers of antigen specific CD8 T cells ($4x10^5$) were adoptively transferred into infection-matched recipients.

(b) Representative flow cytometry plots of TCF-1 with CD25 or Tim-3 in the SPL or TCF-1 and Tim-3 expression in donor CD8 T cells at day 26 post $LCMV_{Cl13}$ infection in the indicated tissues are

presented. Bar graphs show the % of TCF-1^{Hi} Tim-3^{Lo} CD8 T cells in the indicated tissues at day 26 post-infection).

(c) Quantification of MFI of PD-1 and Tim-3 expression on donor CD8 T cells in the indicated tissues at day 26 post-infection, purified and transferred at day 3.5 (Green) or day 5.5 (Purple) from high dose or low dose P14 chimeric mice, respectively, are presented as bar graphs. Paired and unpaired student t-test was used to compare statistical significance in difference of means.

Extended Data Fig 5. Markers of stem-like CD8 T cell lineage are inversely related to IL-2Rα expression during early stages of chronic viral infection.

(a) Characterization of FACS sorted CD25^{Hi} and CD25^{Lo} at day 3.5 post infection. Flow cytometry plot show TCF-1 and Tim-3 or TCF-1 and Slamf6 co-expression in splenic P14 CD8 T cells at day 3.5 post-infection before and after FACS sort.

(b-e) WT P14 cells (1x10^6) were adoptively transferred into naïve B6 recipient mice and then infected with LCMV$_{Cl13}$ 1 day later. Paired histograms and bar graphs show expression of the indicated markers on gated CD25^{Lo} (Blue) or CD25^{Hi} (Red) antigen specific CD8 T cells in spleen at day 3.5 post-infection; grey histograms show marker expression on endogenous CD44^{Lo} naïve CD8 T cells. Numbers represent MFI of expression of respective markers. Data are representative of 4 independent experiments (mean ± SEM) with at least 3 mice per group.

Extended Data Fig 6. Markers of stem-like CD8 T cell lineage are inversely related to IL-2Rα expression during early stages of chronic viral infection.

(a-b) Bar graphs show absolute numbers **(a)** and % localization **(b)** of donor cells in spleen (SPL), inguinal lymph nodes (iLN), liver (LVR) and lung (LNG) at day 8 after infection (~4.5 days after FACS purification and adoptive transfer into infection-matched recipients). % localization of donor cells in a given tissue was calculated as the number of donor cells in a given tissue/total number of donor cells in all tissues analyzed x 100.

(c) Representative flow cytometry plots of TCF-1 and GzmB expression in transferred $CD25^{Hi}$ or $CD25^{Lo}$ donor cells in the indicated tissues at 24 days after infection are shown. Bar graphs depict % stem-like TCF-1^{Hi} $GzmB^{Lo}$ donor CD8 T cells in indicated tissues at day 24 after infection.

(d) Representative flow cytometry plots of Slamf6 and CD62L expression on $CD25^{Hi}$ and $CD25^{Lo}$ CD8 T cells in the spleen at day 24 post infection are presented. Bar graphs depict % $Slamf6^{+}$ $CD62L^{+}$ CD8 T cells from all mice.

(e) Bar graphs depict the expression of T-bet and Eomes on FACS-purified and transferred $CD25^{Hi}$ (Red) or $CD25^{Lo}$ (Blue) P14 CD8 T cells at day 8 post-infection. Bar graphs display mean and SEM. Paired and unpaired student t-test was used with statistical significance in difference of means represented as* ($P \leq 0.05$), ** ($P \leq 0.01$), *** ($P \leq 0.001$).

Extended Data Fig 7: The adoptively transferred $CD25^{Lo}$ and $CD25^{Hi}$ donors minimally impact the endogenous virus-specific CD8 T cell responses.

(a) Longitudinal analysis of endogenous D^{b}GP33-CD8T cell expansion and contraction in blood at indicated times after infection.

(b) Representative flow cytometry plots of TCF-1 and GzmB expression in endogenous D^{b}GP33-CD8T cell-specific cells in the indicated tissues 24 days after infection. Bar graphs depict %

endogenous stem-like TCF-1^{Hi} GzmB^{Lo} cells in D^{b}GP33-specific CD8 T cells.

(c) Quantification of PD-1 expression on endogenous D^{b}GP33-CD8T cells in the indicated tissues at day 24 post-infection is summarized as bar graphs. Data representative of at least 4 mice per group (mean ± SEM). Paired and unpaired student t-test was used to compare statistical significance of difference in means as appropriate.

Extended Data Fig 8: Endogenous virus-specific CD8 T cell responses to PD-1 checkpoint blockade immunotherapy remain unaltered in chronically infected recipients of CD25^{Lo} and CD25^{Hi} donor cells.

(a) CD25^{Lo} and CD25^{Hi} cells were FACS purified at day 3.5 after infection, and adoptively transferred into infection-matched congenically distinct recipient mice (as in Fig 1). Mice were subsequently treated with anti-PD-L1 antibody (200 µg) every 3 days from day 15 to 24, and endogenous virus-specific CD8 T cells were assessed. Longitudinal analysis of endogenous D^{b}GP33-CD8T cell expansion and contraction in blood at indicated times after infection are presented. Bar graph depicts endogenous D^{b}GP33-specific CD8 T cell frequencies at day 22 post-infection.

(b) Histograms and bar graphs show GzmB, PD-1 and Tim-3 expression in endogenous D^{b}GP33-specific CD8 T cells in the spleen at day 24 post infection. Number represents MFI of respective marker. Bar graphs display mean and SEM. Paired and unpaired student t-test was used to compare difference of means between two groups. To compare differences between multiple groups one-way ANOVA with Tukey post-test was used with statistical significance in difference of means represented as * ($P \leq 0.05$), ** ($P \leq 0.01$), *** ($P \leq 0.001$).

Extended Data Fig 9. Differential IL-2 signals in CD25^{Lo} and CD25^{Hi} virus-specific CD8 T cells at priming.

(a) WT P14 cells ($2.5x10^3$) were adoptively transferred into naïve B6 mice, which were subsequently infected with $LCMV_{Cl13}$. Splenocytes were isolated from P14 chimeric mice at day 5.5 after $LCMV_{Cl13}$ infection. Cells were stimulated with 10nM IL-2 and intracellular p-STAT5 was assessed by flow cytometry. Histograms are gated on CD25^{Hi} (red) or CD25^{Lo} (Blue) CD8 T cells.

(b) Metabolic analysis was performed using CD25^{Hi} and CD25^{Lo} FACS-purified P14 CD8 T cells at day 3.5 post-infection in the presence of 10 mM glucose with indicated additions of oligomycin (oligo), trifluoromethoxy carbonylcyanide phenylhydrazone (FCCP), rotenone and antimycin A (Rot/AntiA), and 2-deoxyglucose (2DG). Line graphs show extracellular acidification (ECAR) and oxygen consumption (OCR) rates over time. Dashed vertical lines indicate pharmacologic interventions with Oligomycin, FCCP, Rotenone/AntimycinA and 2-deoxyglucose.

(c) Bar graphs show maximum ECAR and basal OCR on FACS sorted CD25^{Hi} or CD25^{Lo} at day 3.5 post-infection.

(d) Energy map for purified CD25^{Lo} (Blue) or CD25^{Hi} (Red) D^{b}GP33-specific CD8 T cells (n=8 for each mean depicted).

To compare differences between groups unpaired student t-test was used. Statistical significance in difference of means is represented as * ($P \leq 0.05$), ** ($P \leq 0.01$), *** ($P \leq 0.001$).

Extended Data Fig 10. Tempered IL-2 signals at priming lead to enhanced development of TCF1^{Hi} CD8 T cells.

(a) Representative histograms show CD44 expression on antigen-specific CD8 T cells (Black) on day 3.5 post-infection. Grey histograms depict endogenous $CD44^{Lo}$ naïve CD8 T cells. Numbers within histograms depict MFI of marker expression. Bar graphs depict the expression of CD44 in the untreated (UnTx) group (Black), IL-2-treated (Red) and αIL-2 treated (Blue) groups at day 3.5 post-infection.

(b) Representative histograms showing BrdU incorporation by the donor cells are presented. Numbers inside histograms depict MFI of BrdU. Numbers in histograms show MFI of BrdU staining for corresponding donor plots. Bar graphs depict the MFI and absolute numbers of the donor cells at day 3.5 post-infection for indicated groups of untreated, IL-2 treated or IL-2 blocked groups.

(c) Representative flow-cytometry plots show the frequency of $FoxP3^{+}CD4$ T regulatory cells (Treg) in the spleens of untreated or treated groups of mice at day 3.5 post-infection as indicated. Bar graph shows absolute numbers of Tregs in each group.

(d) Representative flow cytometry plots of TCF-1 and GzmB expression in gated $D^{b}GP33$-specific P14 CD8 T cells isolated from iLN and LNG at day 3.5 post-infection are presented. Bar graphs show % stem-like TCF-1^{Hi} $GzmB^{Lo}$ P14 CD8 T cells. Data are representative of 3 independent experiments with n=3 mice per group.

(e) Representative flow cytometry plots show TCF-1 and Tim-3 expression in donor cells isolated at day 9 after $LCMV_{Cl\text{-}13}$ infection, from recipient mice adoptively transferred with day 3.5 donor cells isolated from P14 chimeric mice that were untreated (Black), or treated with IL-2 (Red) or IL-2 blocking antibody (Blue) from days 0-3.5 post-infection. Bar graphs show the frequency of TCF-1^{Hi} Tim-3^{Lo}, TCF-1^{Lo} Tim-3^{Lo}, Tim-3^{Hi} TCF-1^{Lo} on donor CD8 T at day 9 post-infection.

To compare differences between groups one-way ANOVA with Tukey post-test was used. Statistical significance in difference of means is represented as * (P ≤ 0.05), ** (P ≤ 0.01), *** (P ≤ 0.001).

Extended Data Fig 11. Adoptive transfer of donor cells primed in distinct IL-2 signaling conditions does not alter the differentiation program of endogenous CD8 T cells to chronic LCMV infection.

(a) Bar graphs show numbers of D^bGP33-specific P14 donors and endogenous CD8 T cells in spleen at day 9 after infection in recipient mice adoptively transferred with day 3.5 donor cells isolated from P14 chimeric mice that were untreated (Black), or treated with IL-2 (Red) or IL-2 blocking antibody (Blue) from days 0-3.5 post-infection.

(b) Representative flow cytometry plots of TCF-1 and GzmB co-expression in endogenous LCMV D^bGP33 -specific CD8 T cells in spleen at day 9 post-infection are presented. Bar graphs depict % stem-like TCF-1^{Hi} $GzmB^{Lo}$ CD8 T cells. Data are representative of at least 3 mice per group (mean ± SEM). To compare differences between groups one-way ANOVA with Tukey post-test was used. Statistical significance in difference of means is represented as * (P ≤ 0.05), ** (P ≤ 0.01), *** (P ≤ 0.001).

Extended Data Fig 12. Knockdown of CD25 expression on antigen-specific CD8 T cells at day 0, before infection with $LCMV_{Cl\text{-}13}$ promotes the development of TCF-1^{Hi} stem-like CD8 T cells.

(a) Electroporation efficiency using the Neon Transfection System. Histogram plots show percent positive cells for ATTO™ 55O (Black) post electroporation of D2 activated CD8 T cells.

(b) Paired histograms and bar graphs show the expression of CD25 on WT P14 CD8 T cells transfected with scrambled (WT) or *il2ra* guide RNAs (CD25 knockdown, CD25 KD) prior to adoptive transfer into naive mice, which were infected $LCMV_{Cl\text{-}13}$. Data are presented for WT and CD25 KD gated donor cells from spleens at day 5 and day 8 post-infection. Numbers within histograms represent MFI.

(c) Representative flow cytometry plots of TCF-1 and GzmB expression in WT and CD25 KD donor CD8 T cells isolated from the LVR at day 8 post-infection. Bar graphs depict composite data for % stem-like TCF-1^{Hi} $GzmB^{Lo}$ CD8 T cells in gated donor populations from n=3-5 mice per group.

Extended Data Fig 13. Knockdown of CD25 expression on antigen-specific CD8 T cells at day 2 after infection with $LCMV_{Cl\text{-}13}$ promotes the development of TCF-1^{Hi} stem-like CD8 T cells.

(a) Experimental setup. Activated P14 CD8 T cells were electroporated with guide RNA targeting *il2ra* gene. Equal numbers of WT CD8 T cells or CD25 KD cells were adoptively co-transferred into Day 2 chronically infected mice. Donor antigen specific $CD8^+$ T cells were analyzed after 8 days of infection.

(b) The efficiency of CRISPR-Cas9-mediated deletion of *il2ra* on D2 activated P14 CD8 T cells was confirmed by flow cytometry after 48hr of *in vitro* stimulation by plate bound anti-CD3 and anti-CD28. Histograms show the expression of CD25 in WT (Red), CD25 KD (Blue) and naïve cells (Gray).

(c) Representative flow cytometry plots of TCF-1 and GzmB or TCF-1 and Tim-3 expression in D2 CD25-ablated donor CD8 T cells in spleens from day 8 $LCMV_{Cl\text{-}13}$-infected mice are shown. Bar graph depicts % stem-like TCF-1^{Hi} $GzmB^{Lo}$ CD8 T cells in gated WT and CD25 KD donor populations.

Extended Data Fig 14. Knockdown of CD25 expression on antigen-specific CD8 T cells at day 2 after infection with $LCMV_{Cl\text{-}13}$ promotes the development of TCF-1^{Hi} stem-like CD8 T cells.

(a) Experimental setup. Naïve P14 CD8 T cells were electroporated with short interfering RNA (siRNA) targeting CD25 mRNA (CD25 KD) or with controls (WT). Equal numbers of WT or CD25 KD donor P14 CD8 T cells were adoptively co-transferred into naïve mice, which were subsequently infected with $LCMV_{Cl\text{-}13}$. Donor antigen specific $CD8^+$ T were analyzed at day 8 post-infection.

(b) The efficiency of siRNA-mediated transient silencing of CD25 was confirmed by flow cytometry after 48hr of *in vitro* stimulation by plate bound anti-CD3 and anti-CD28. Cells were kept in culture for two more days to confirm the re-expression of CD25 on CD25 KD cells. CD25 expression levels were also assessed in WT and CD25 KD cells adoptively transferred into C57Bl/6 mice 8 days following infection with $LCMV_{Cl\text{-}13}$. Histograms show the expression of CD25 in WT (Red), CD25 KD (Blue) and naïve CD8 T cells (Gray). Corresponding bar graphs depict MFI of CD25 expression from n=3 mice.

(c) Representative flow cytometry plots of TCF-1 and GzmB or TCF-1 and Tim-3 co-expression on donor CD8 T cells isolated from spleens at day 8 after infection are presented. Bar graph depict % stem-like TCF-1^{Hi} $GzmB^{Lo}$ donor CD8 T cells in spleen and liver.

(d) Paired histogram and bar graphs show the expression levels of TOX on WT CD8 T cells and CD25 KD donor CD8 T cells isolated from spleens at day 8 post-infection. Data are representative of at least 2 independent repeats with n=3 mice per group (mean ± SEM). Paired Student t-test was used with statistical significance in difference of means represented as * ($P \leq 0.05$), ** ($P \leq 0.01$), *** ($P \leq 0.001$).

Extended Data Fig 15. Delayed priming and curtailed duration of stimulation of virus-specific CD8 T cells promotes the development of TCF-1^{Hi} stem-like CD8 T cells.

(a) Experimental setup. LCMV$_{Cl13}$-infected C57Bl/6 mice were adoptively transferred with 2.5x10^3 of WT P14 CD8 T cells at day 0, 1, 2 or 3 after infection. Donor CD8 T cells were analyzed 8.5 days after infection.

(b) Representative flow cytometry plots of TCF-1 and GzmB or TCF-1 and Slamf6 expression in donor CD8 T cells at day 8.5 post-infection are presented from spleen. Bar graphs depict % TCF-1^{Hi} GzmB^{Lo} CD8 T cells in the SPL (top) and iLN, LVR and LNG (Bottom) at 8.5 days after infection.

(c) Representative flow cytometry data for TCF-1 and GzmB expression on adoptively transferred donor CD8 T cells in iLN, LVR and LNG are presented. Virus-specific donor CD8 T cells were analyzed at day 8.5 post-infection.

(d) Representative histogram plots and corresponding bar charts show expression of the indicated markers on adoptively transferred D^{b}GP33-specific donor CD8 T cells in spleens at 8.5 days after stimulation; grey histograms show marker expression in endogenous CD44^{Lo} naïve CD8 T cells. Numbers within histograms represent MFI of expression of respective markers. Data are representative of 2 independent experiments with n=3 mice per group. To compare differences between groups one-way ANOVA with Tukey post-test was used. Statistical significance in difference of means is represented as * ($P \leq 0.05$), ** ($P \leq 0.01$), *** ($P \leq 0.001$).

Extended Data Fig 16. Shorter duration of stimulation promotes the development of TCF-1^{Hi} stem-like CD8 T cells.

(a) Experimental setup. $LCMV_{Cl13}$ infected B6 mice were adoptively transferred with $2.5x10^3$ of WT D^bGP33-specific P14 CD8 T cells at day 0 after infection. Donor CD8 T cells were analyzed at the indicated days post-infection in the spleens of infected mice.

(b) Representative flow cytometry plots of TCF-1 and GzmB expression on donor CD8 T cells in the SPL at the indicated days post-infection are presented. Bar graphs depict % $TCF\text{-}1^{Hi}$ $GzmB^{Lo}$ donor CD8 T cells in the spleen at indicated days post-infection. To compare differences between groups one-way ANOVA with Tukey post-test was used. Data are representative of 2 independent experiments with n=3 mice per group. Statistical significance in difference of means is represented as * ($P \leq 0.05$), ** ($P \leq 0.01$), *** ($P \leq 0.001$).

Extended Data Fig 17. Late priming of virus-specific CD8 T cells promotes the development of $TCF\text{-}1^{Hi}$ stem-like CD8 T cells.

(a) $LCMV_{Cl13}$ infected B6 mice were adoptively transferred with $2.5x10^3$ of WT P14 at days 0, 1, 2 or 3 after infection. Donor CD8 T cells were analyzed 5.5 days after P14 transfer. Representative flow cytometry plots show TCF-1 and GzmB expression on donor CD8 T cells isolated from spleens at day 5.5 post P14 adoptive transfer in the indicated tissues.

(b) Representative histogram plots and bar charts show levels of expression of the indicated markers on D^bGP33-specific CD8 T cells in spleens 5.5 days after adoptive transfer; grey histograms show marker expression in endogenous $CD44^{Lo}$ naïve CD8 T cells. Numbers within histograms represent MFI of expression of respective markers. Data are representative of 2 independent experiments with n=3 mice per group. To compare differences between groups

one-way ANOVA with Tukey post-test was used. Statistical significance in difference of means is represented as * ($P \leq 0.05$), ** ($P \leq 0.01$), *** ($P \leq 0.001$).

Extended Data Fig 18. Characterization of DC subsets during early versus late stages of CD8 T cell expansion in chronic LCMV infection.

(a,b) Representative flow cytometry plots show the gating strategy used to sort cDCs (CD11c+) and moDCs (CD11b+) from spleen samples of naïve **(a)** and day 3.5 $LCMV_{Cl\text{-}13}$-infected **(b)** C57Bl/6 mice. Histogram plots and bar charts show expression of the indicated markers on cDC (Orange) and moDC (Brown) populations. Numbers within histogram plots represent MFI of expression of respective markers.

(c) IL-2-Cre ROSA/tdTomato reporter mice were infected with $LCMV_{Cl13}$, and moDC and cDC were isolated from spleen 4 days after infection. Cells were gated and analyzed on $MHCII^{+}$ $Ly6G^{-}$ population. % cDC and moDC subsets are also presented as bar graphs.

(d) Representative histogram plots and corresponding bar graphs show phenotypic validation of the gated cDC and moDC subsets with respect to indicated markers. Data are representative of 2 independent experiments (mean ± SEM) with at least 3 mice per group. Paired Student t-test was used with statistical significance in difference of means represented as * ($P \leq 0.05$), ** ($P \leq 0.01$), *** ($P \leq 0.001$).

Extended Data Fig 19: T cell activation by distinct DC subsets.

B6 mice were infected with $LCMV_{Cl13}$, moDC and cDC were purified and sorted by flow cytometry at day 3.5 after-post infection. DC subsets were co-cultured ($1x10^4$ cells) with CFSE labeled P14

($5x10^5$) for 3 days in the presence of GP_{33-41} peptide. Representative histograms and corresponding bar graphs depict expression of the indicated markers of T cell activation on donor P14 CD8 T cells 3 days after co-culture with cDC or moDC subsets.

Extended Data Fig 20: scRNA-seq analysis of TILs from melanoma patients

(a) Heatmap of differentially expressed genes in 5 clusters from CD8 T cells in melanoma tumors from checkpoint blockade immunotherapy treated patients. Top differentially expressed genes in each of the 5 clusters are shown on each row. Columns represent individual cells grouped by the clusters they are classified into. Dataset originally published in Sade-Feldman et al., 2018[10].
(b) UMAP plot colored by clusters. Clustering shown in panel a was used to color cells in the same UMAP as in Figure 5a.
(c) Expression of memory signature in clusters and across pseudotime.
(d) Association between immunotherapy response and IL2 signature scores in CD8 T cells. The frequency of CD8 T cells from either of the clusters with high IL2-signatures (T_{Tr} and T_{TD}) as a portion of all CD45+ cells were compared between patients who responded or did not respond to checkpoint blockade. Wilcoxon ranked-sum test used to establish statistical significance.

Extended Data Fig 21: scRNA-seq analysis of TILs from head and neck cancer patients

(a) Expression of key exhaustion and memory genes and IL2 signaling score in HPV-specific CD8 T cells in HPV associated tumors from 15 patients. UMAP plots of scRNA-seq from CD8 T cells that bound HPV-MHC tetramers CD8 T illustrating activation/exhaustion associated genes

(*pdcd1*, *havcr2*, and *gzmb*), memory associated genes (*tcf7, sell*) or a composite IL2 signature (FUNG_IL2_SIGNALING_1). Dataset originally published in Eberhardt et al., 2021[16]

(b) Memory and exhaustion signature score in 3 clusters of HPV-specific cells from tumors. Signature scores of exhaustion and memory genes scored across Stem-like (T_{St}), Transitory (T_{TR}), and Terminally differentiated (T_{TD}) clusters.

(c) Heatmap of differentially expressed genes in 3 clusters from HPV-specific CD8 T cells. Top differentially expressed genes in each of the 2 clusters are shown in each row. Columns represent individual cells grouped by the clusters they are classified into.

(d) Expression of IL2 signature genes and gene encoding Blimp-1 (*prdm1*) in HPV-specific CD8 T cells. Genes downstream of IL2 signaling that also contain STAT5 binding sites (FUNG_IL2_TARGETS_WITH_STAT5_BINDING_SITES_T1) were used to calculate the STAT5 Target Binding score.

Extended Data Fig 22: scRNA-seq analysis of TILs from lung cancer patient tumor samples

(a) Heatmap of differentially expressed genes in T cells of various specificities in NSCLC. CD3 T cells from 15 non-small cell lung cancer (NSCLC)-tumors were isolated and single cell RNA-seq was performed on these cells. In parallel the MANAFEST and viraFEST assays were performed to identify mutation associated neoantigens (MANA) or influenza specific T cell receptors. CD8 T cells with either MANA or influenza-specific T cells were isolated in silico. Top differentially expressed genes for each specificity are shown in each row. Columns represent individual cells grouped by the T cell specificity based on their individual TCR sequences. Dataset was originally published in Caushi et al., 2021[21].

(b) UMAP plot of all CD8 T cells of known specificity in NSCLC. UMAP dimensionality reduction was performed on CD8 T cells of known specificity isolated in silico. Lower panel colored by exhaustion signature score.

(c) Violin plots of cancer-specific neoantigen STAT5 target and Blimp-1 (encoded by *prdm1*) scores in CD8 T cells of known specificity in NSCLC. Cancer-specific neoantigen score was derived from Lowery et al., 2022[56]. MANA and Influenza specific CD8 T cells were isolated *in silico* as in panel a. Wilcoxon ranked-sum tests were used to assign statistical significance. Statistical significance represented as * ($P \leq 0.05$), ** ($P \leq 0.01$), *** ($P \leq 0.001$).

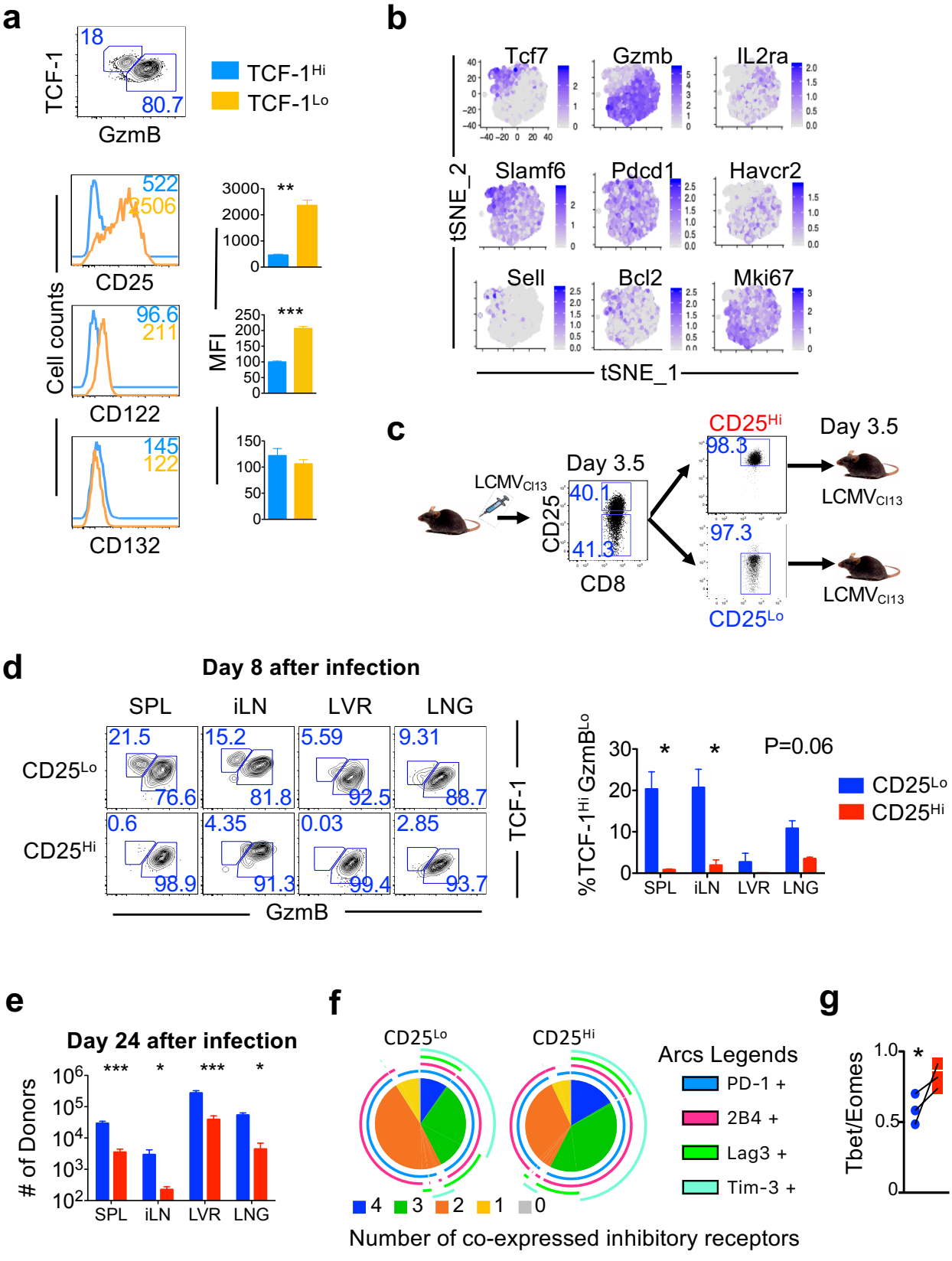
a
TCF-1
GzmB
18
80.7
TCF-1Hi
TCF-1Lo
CD25
522
2506
Cell counts
MFI
**
CD122
96.6
211
***
CD132
145
122
b
Tcf7
Gzmb
IL2ra
Slamf6
Pdcd1
Havcr2
Sell
Bcl2
Mki67
tSNE_2
tSNE_1
c
LCMVCl13
Day 3.5
CD25
CD8
40.1
41.3
CD25Hi
98.3
97.3
CD25Lo
Day 3.5
LCMVCl13
LCMVCl13
d
Day 8 after infection
SPL
iLN
LVR
LNG
CD25Lo
CD25Hi
21.5
76.6
15.2
81.8
5.59
92.5
9.31
88.7
0.6
98.9
4.35
91.3
0.03
99.4
2.85
93.7
TCF-1
GzmB
%TCF-1Hi GzmBLo
P=0.06
CD25Lo
CD25Hi
e
Day 24 after infection
# of Donors
f
CD25Lo
CD25Hi
Arcs Legends
PD-1 +
2B4 +
Lag3 +
Tim-3 +
4 3 2 1 0
Number of co-expressed inhibitory receptors
g
Tbet/Eomes

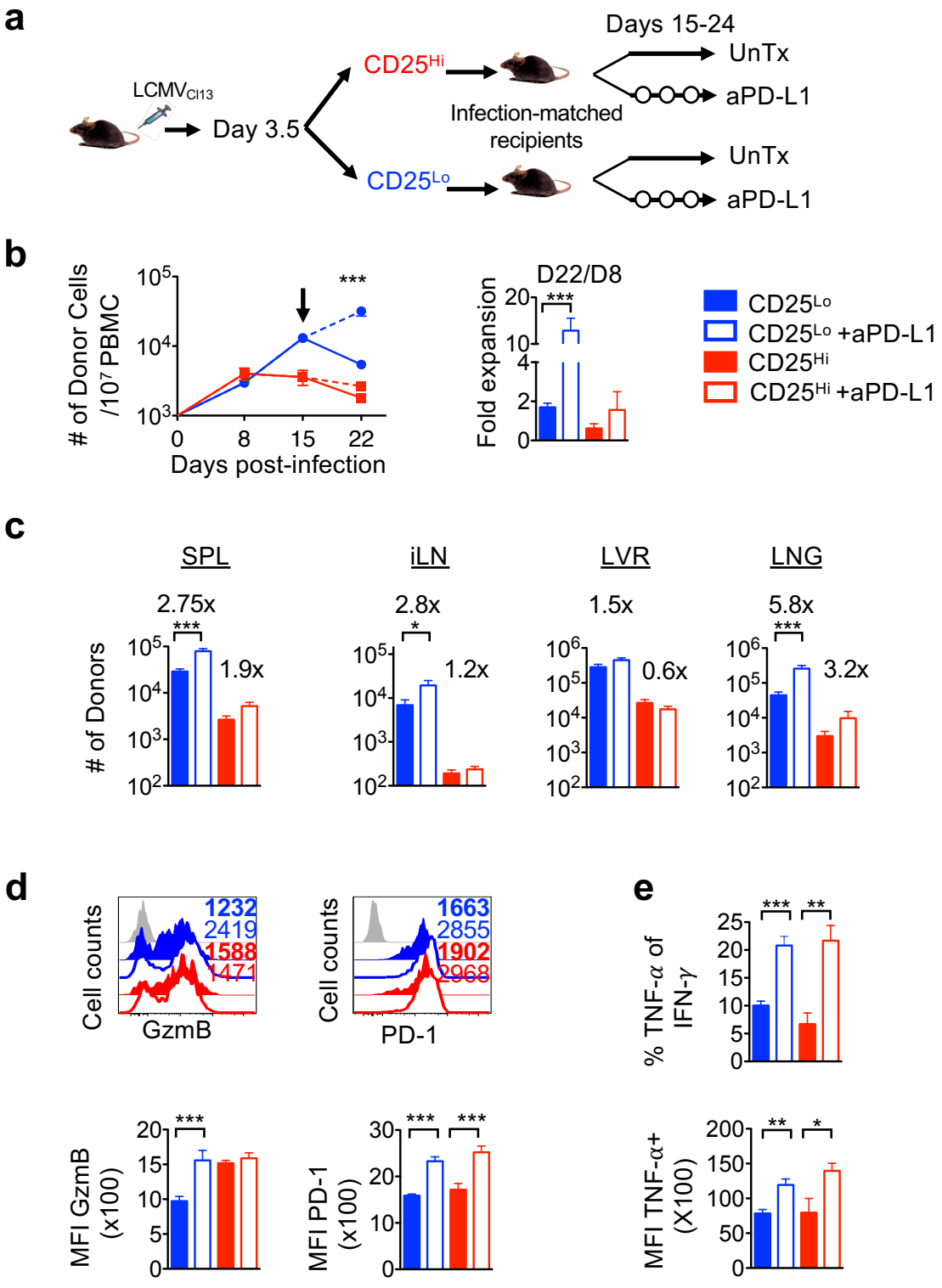
a
LCMV Cl13
Day 3.5
CD25Hi
CD25Lo
Infection-matched recipients
Days 15-24
UnTx
aPD-L1
UnTx
aPD-L1
b
# of Donor Cells /10^7 PBMC
Days post-infection
***
D22/D8
Fold expansion
***
CD25Lo
CD25Lo +aPD-L1
CD25Hi
CD25Hi +aPD-L1
c
SPL
iLN
LVR
LNG
# of Donors
2.75x
1.9x
2.8x
1.2x
1.5x
0.6x
5.8x
3.2x
d
Cell counts
1232
2419
1588
1471
GzmB
Cell counts
1663
2855
1902
2968
PD-1
MFI GzmB (x100)
MFI PD-1 (x100)
e
% TNF-α of IFN-γ
MFI TNF-α+ (X100)

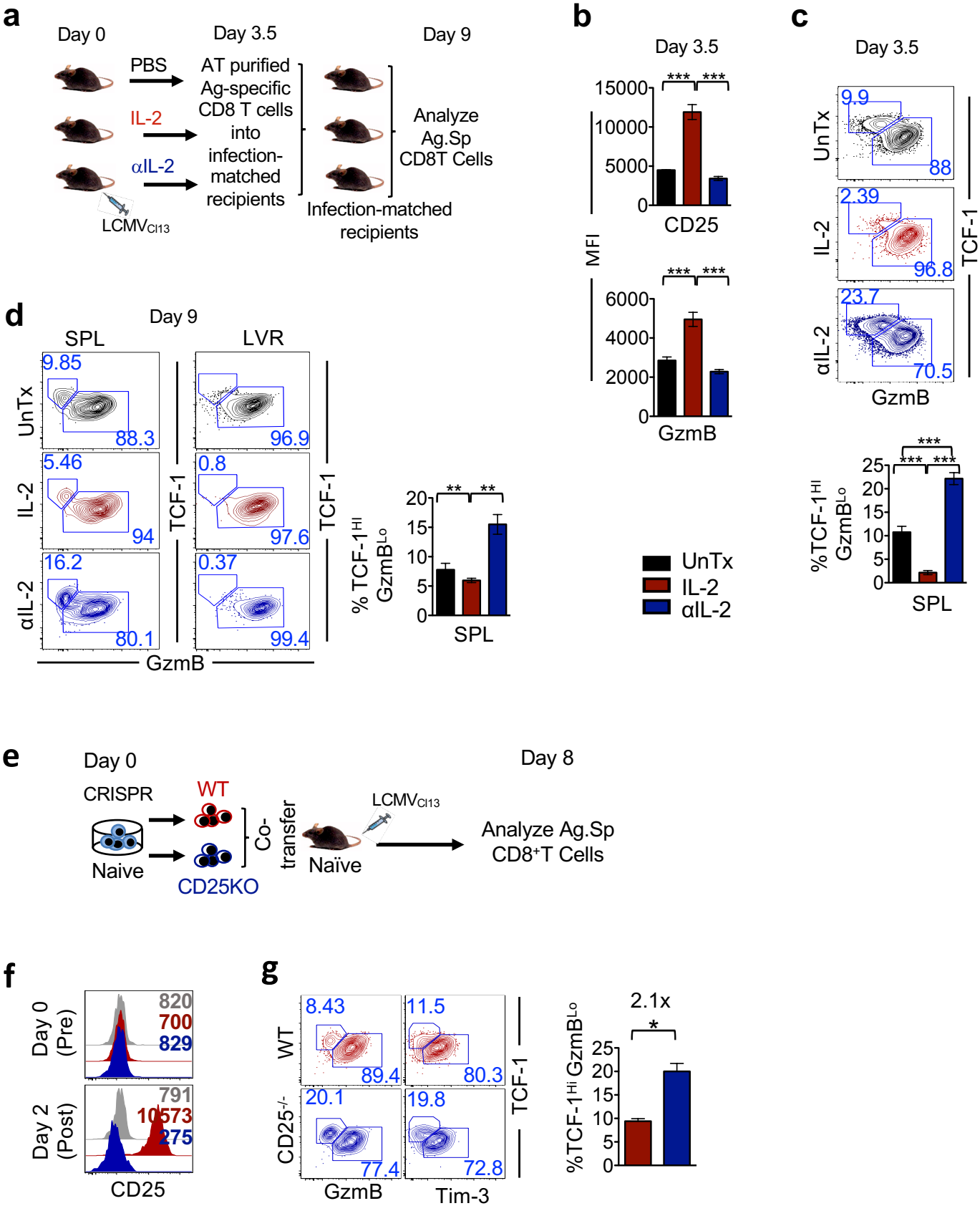
a
Day 0
Day 3.5
Day 9
PBS
IL-2
αIL-2
LCMVCl13
AT purified Ag-specific CD8 T cells into infection-matched recipients
Infection-matched recipients
Analyze Ag.Sp CD8T Cells
b
Day 3.5
MFI
CD25
GzmB
UnTx
IL-2
αIL-2
c
Day 3.5
UnTx
IL-2
αIL-2
TCF-1
GzmB
%TCF-1HI GzmBLo
SPL
d
Day 9
SPL
LVR
UnTx
IL-2
αIL-2
TCF-1
GzmB
%TCF-1HI GzmBLo
SPL
e
Day 0
CRISPR
WT
CD25KO
Naive
Co-transfer
LCMVCl13
Naïve
Day 8
Analyze Ag.Sp CD8+T Cells
f
Day 0 (Pre)
Day 2 (Post)
820
700
829
791
10573
275
CD25
g
WT
CD25-/-
8.43
89.4
11.5
80.3
20.1
77.4
19.8
72.8
TCF-1
GzmB
Tim-3
2.1x
%TCF-1HI GzmBLo

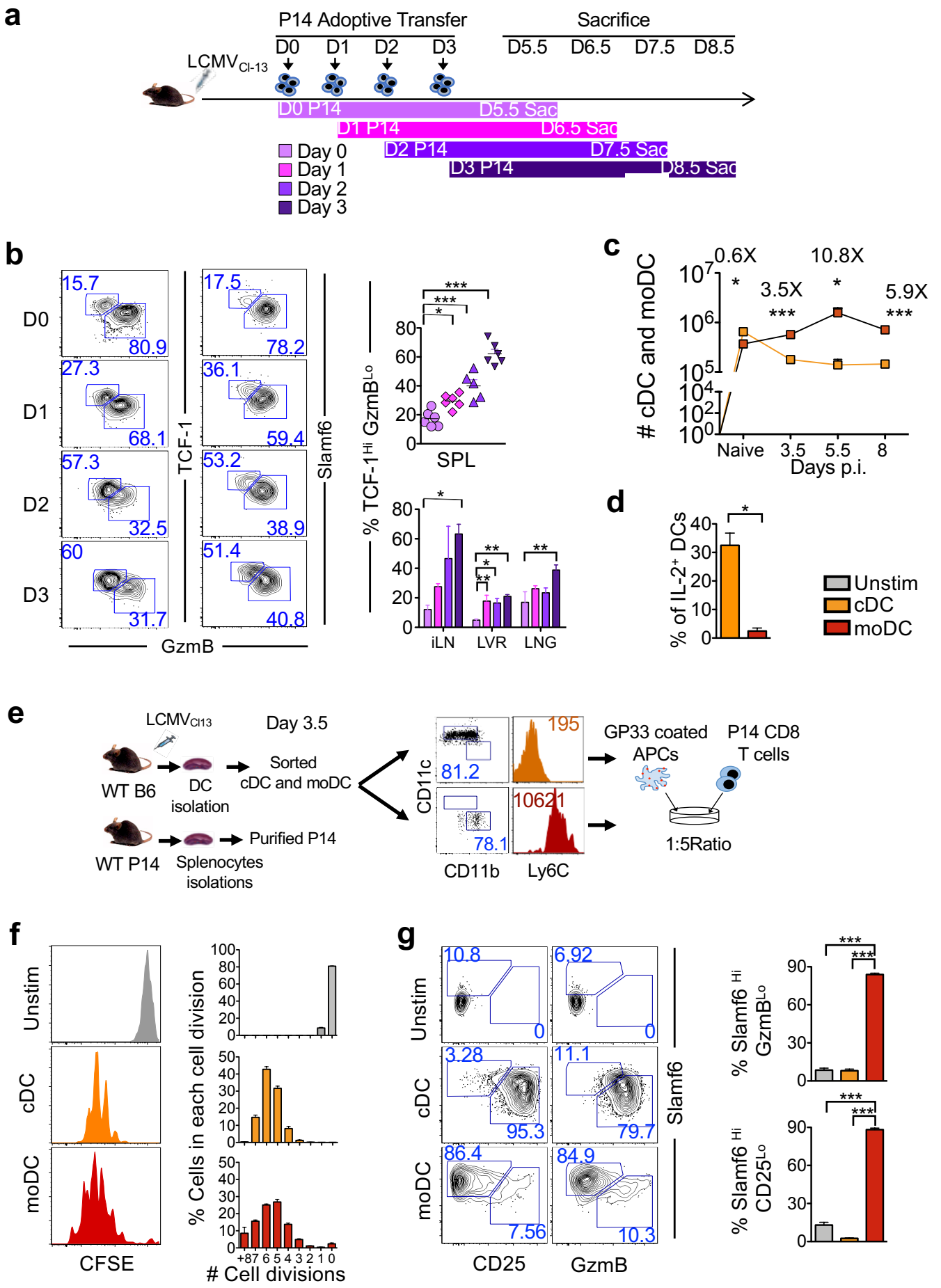
a
P14 Adoptive Transfer
Sacrifice
D0 D1 D2 D3
D5.5 D6.5 D7.5 D8.5
LCMV Cl-13
D0 P14
D5.5 Sac
D1 P14
D6.5 Sac
D2 P14
D7.5 Sac
D3 P14
D8.5 Sac
Day 0
Day 1
Day 2
Day 3
b
D0
D1
D2
D3
15.7
80.9
17.5
78.2
27.3
68.1
36.1
59.4
57.3
32.5
53.2
38.9
60
31.7
51.4
40.8
TCF-1
Slamf6
GzmB
% TCF-1Hi GzmBLo
SPL
iLN
LVR
LNG
c
cDC and moDC
0.6X
3.5X
10.8X
5.9X
Naive
3.5
5.5
8
Days p.i.
d
% of IL-2+ DCs
Unstim
cDC
moDC
e
LCMVCl13
Day 3.5
WT B6
DC isolation
Sorted cDC and moDC
WT P14
Splenocytes isolations
Purified P14
CD11c
81.2
195
78.1
10621
CD11b
Ly6C
GP33 coated APCs
P14 CD8 T cells
1:5Ratio
f
Unstim
cDC
moDC
CFSE
% Cells in each cell division
# Cell divisions
g
10.8
6.92
3.28
11.1
95.3
79.7
86.4
84.9
7.56
10.3
CD25
GzmB
Slamf6
% Slamf6 Hi GzmBLo
% Slamf6 Hi CD25Lo

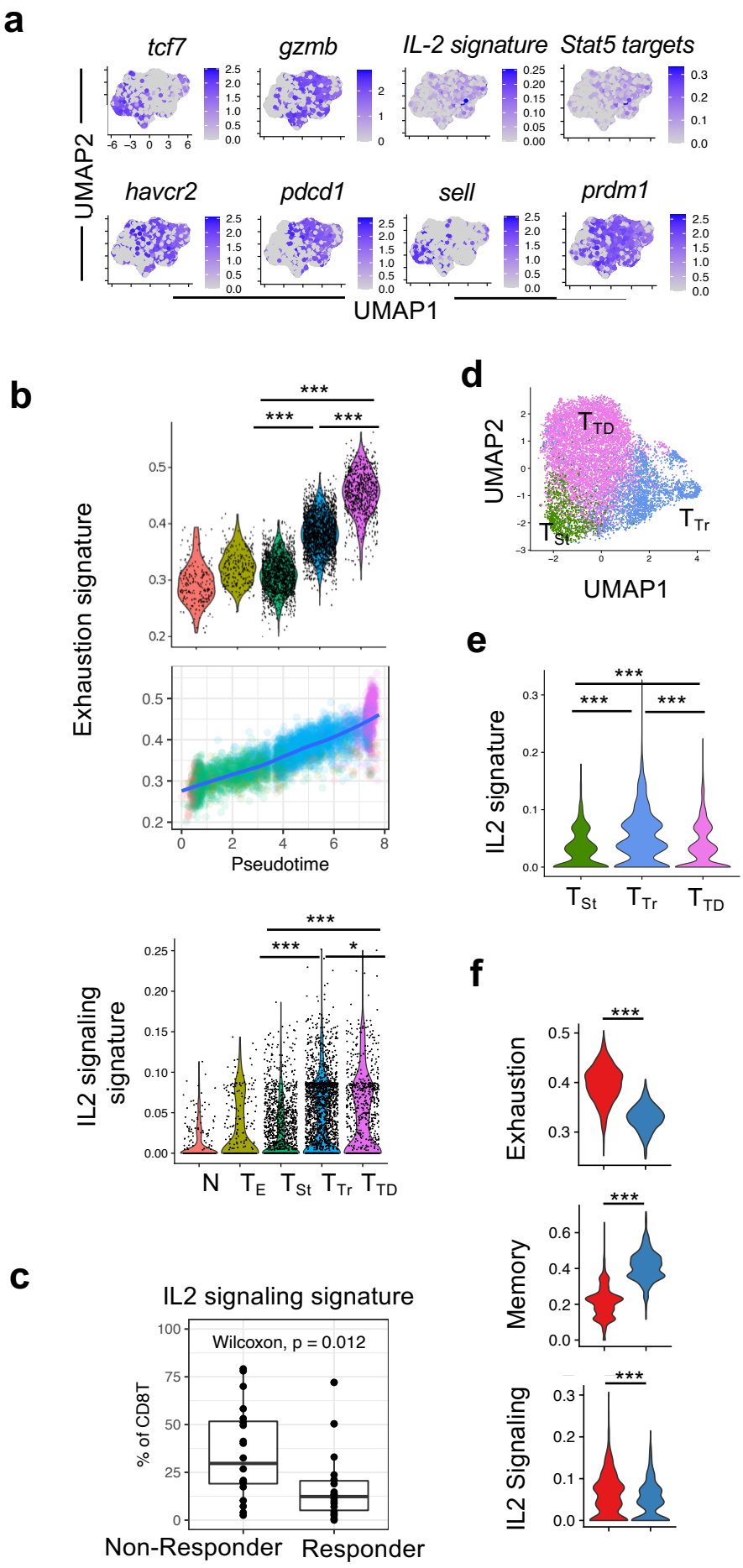
a
tcf7
gzmb
IL-2 signature
Stat5 targets
havcr2
pdcd1
sell
prdm1
UMAP2
UMAP1
b
Exhaustion signature
Pseudotime
IL2 signaling signature
N
TE
TSt
TTr
TTD
c
IL2 signaling signature
Wilcoxon, p = 0.012
% of CD8T
Non-Responder
Responder
d
UMAP2
UMAP1
TTD
TTr
TSt
e
IL2 signature
TSt
TTr
TTD
f
Exhaustion
Memory
IL2 Signaling

Extended Data Figures 1-22

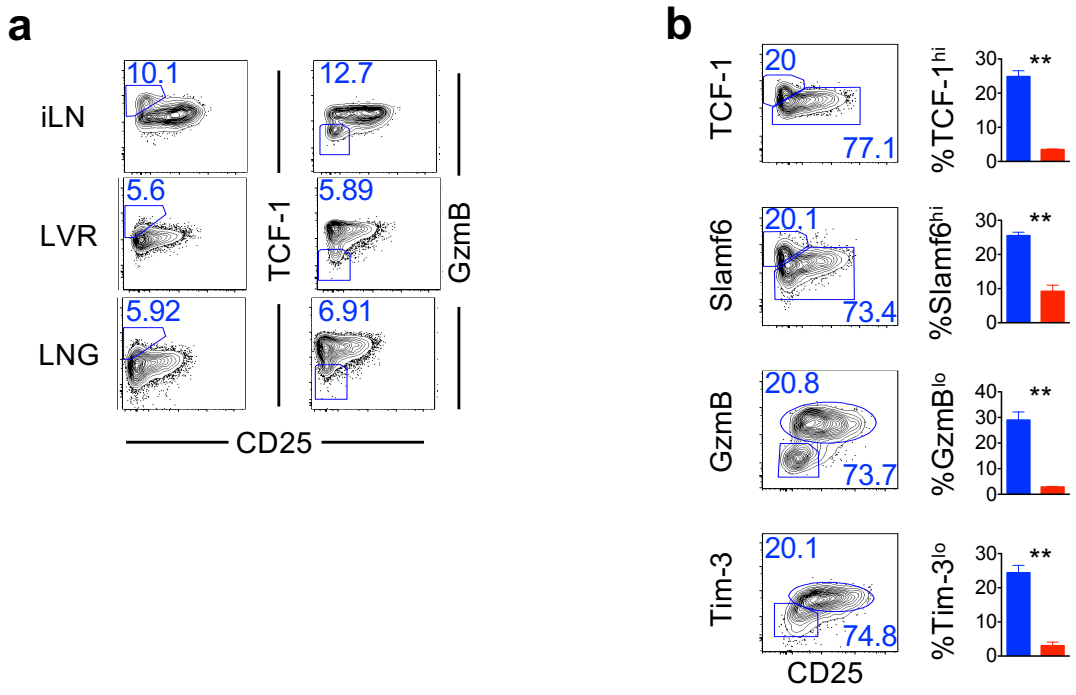

Extended Data Fig 1. Markers of stem-like CD8 T cell lineage are inversely related to IL-2Rα expression during early stages of chronic viral infection.
a) WT P14 cells ($2.5x10^3$) were adoptively transferred into naïve B6 mice, which were subsequently infected with $LCMV_{Cl13}$. Representative flow-cytometry plots of CD25 and TCF-1 or GzmB co-expression in P14 CD8 T cells isolated from iLN, LVR and LNG at day 5.5 post-infection are shown. **b)** Flow-cytometry plots show CD25 and TCF-1, Slamf6, GzmB or Tim-3 co-expression in splenic P14 CD8 T cells at day 5.5 post-infection. Bar graphs depict the frequency of TCF-1^{Hi}, Slamf6^{Hi}, GzmB ^{Lo} and Tim-3^{Lo} P14 T cells on gated $CD25^{Lo}$ (Blue) or $CD25^{Hi}$ (Red) P14 T cells 5.5 days after infection. Data presented are representative of 2 independent experiments with at least 3 mice per group.

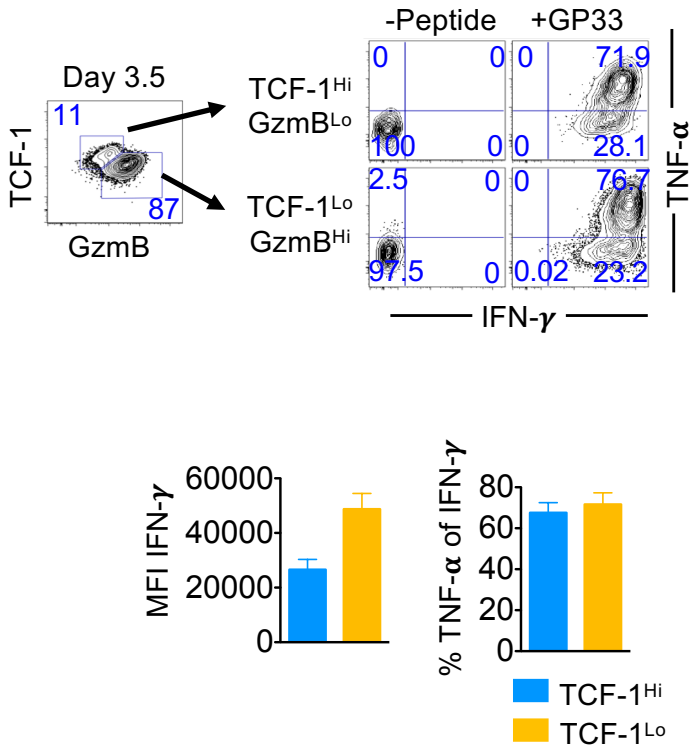

Extended Data Fig 2. Functional competence of TCF1^{Hi} and TCF-1^{Lo} antigen-specific CD8 T cells during early stages of chronic LCMV infection.
WT P14 cells (1x10^6) were adoptively transferred into naïve B6 recipient mice and then infected with LCMVCl13 1 day later. Representative flow cytometry plots of TNF-α+ and IFN-γ+ co-expression on gated TCF-1^{Hi} GzmB^{Lo} or TCF-1^{Lo} GzmB^{Hi} donor CD8 T cells at day3.5 post-infection are presented. Bar graphs depict MFI of IFN-γ and %TNF-α+ of IFN-γ+ in TCF-1^{Hi} (Light blue) or TCF-1^{Lo} (Gold) P14 T cells.

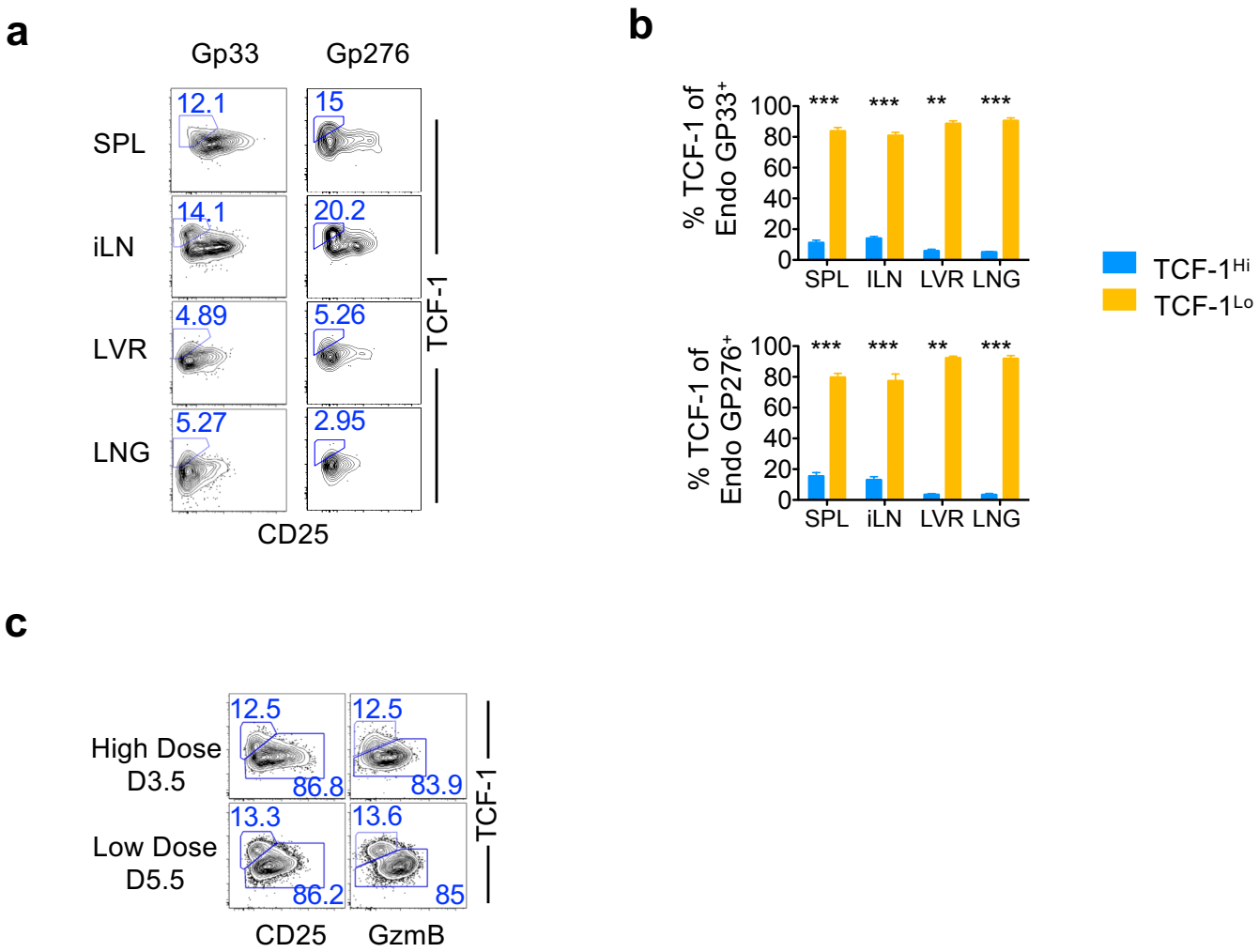

Extended Data Fig 3. Inverse association of TCF-1 and CD25 expression is evident in endogenous virus-specific CD8 T cells, and in TCR-transgenic CD8 T cells at low or high precursor frequencies.

(a) Representative flow cytometry plots show TCF-1 and CD25 expression on endogenous Gp33- and Gp276-specific CD8 T cells in the SPL, iLN, LVR and LNG at day 5.5 after infection.

(b) Bar graphs depict relative proportions of stem-like TCF-1^{Hi} CD8 T cells (Light blue) or terminally differentiated TCF-1^{Lo} CD8 T cells (Gold) in endogenous LCMV D^{b}GP33-, and D^{b}GP276-specific CD8 T cells in spleen at day 5.5 after infection.

(c) WT D^{b}GP33-specific P14 CD8 T Cells were adoptively transferred at high dose (1x10^{6}) or low dose (2.5 x10^{3}) into naïve B6 mice, which were subsequently infected with LCMV$_{Cl13}$ for 3.5 or 5.5 days respectively. Representative flow cytometry plots of TCF-1 and CD25 or TCF-1 and GzmB expression in P14 CD8 T cells on the indicated days post LCMV$_{Cl13}$ infection are presented. Bar graphs display mean and SEM. Paired and unpaired student t-test was used with statistical significance in difference of means represented as ** ($P \leq 0.01$), *** ($P \leq 0.001$).

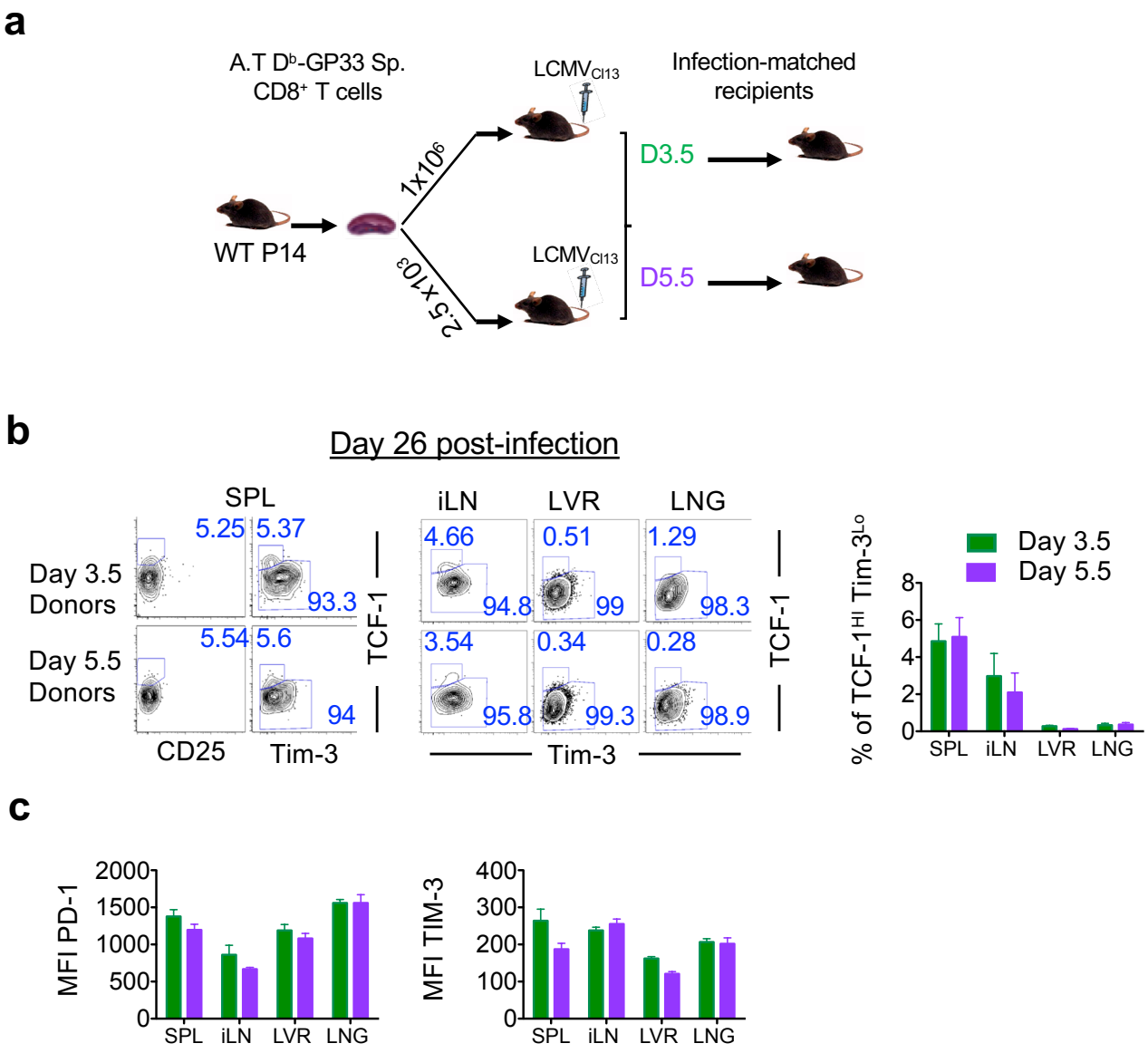

Extended Data Fig 4. Similar developmental profiles of adoptively transferred virus-specific CD8 T cells purified from low or high precursor frequencies.

(a) Experimental setup. Chimeric C57Bl/6 mice were adoptively transferred with high dose ($1x10^6$) or low dose ($2.5 x10^3$) WT P14 CD8 T cells, and infected with $LCMV_{Cl13}$ for 3.5 or 5.5 days respectively. On the indicated days, donor cells were purified, and equal numbers of antigen specific CD8 T cells ($4x10^5$) were adoptively transferred into infection-matched recipients.

(b) Representative flow cytometry plots of TCF-1 with CD25 or Tim-3 in the SPL or TCF-1 and Tim-3 expression in donor CD8 T cells at day 26 post $LCMV_{Cl13}$ infection in the indicated tissues are presented. Bar graphs show the % of TCF-1^{Hi} Tim-3^{Lo} CD8 T cells in the indicated tissues at day 26 post-infection).

(c) Quantification of MFI of PD-1 and Tim-3 expression on donor CD8 T cells in the indicated tissues at day 26 post-infection, purified and transferred at day 3.5 (Green) or day 5.5 (Purple) from high dose or low dose P14 chimeric mice, respectively, are presented as bar graphs. Paired and unpaired student t-test was used to compare statistical significance in difference of means.

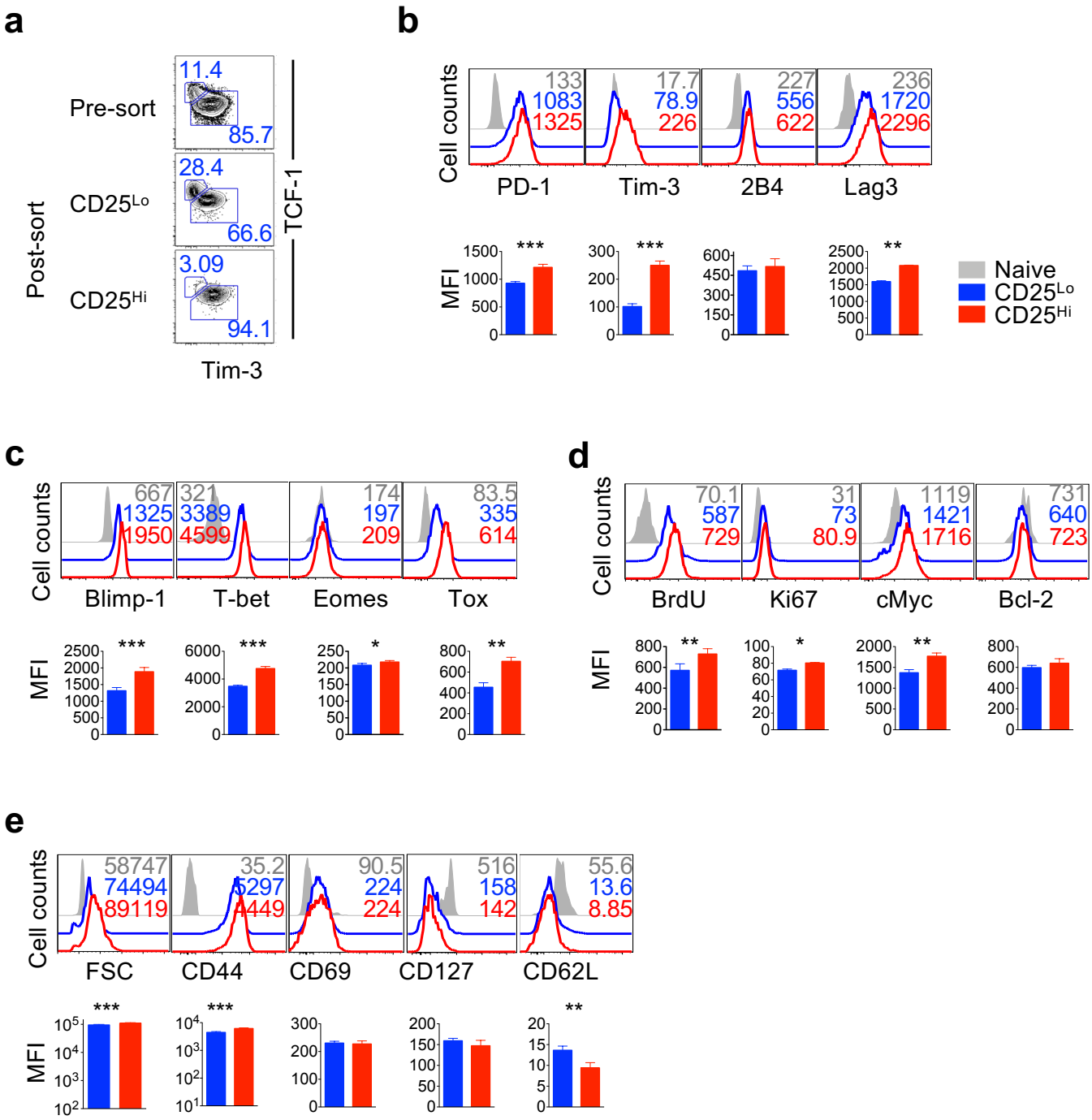

Extended Data Fig 5. Markers of stem-like CD8 T cell lineage are inversely related to IL-2Rα expression during early stages of chronic viral infection.

(a) Characterization of FACS sorted CD25^{Hi} and CD25^{Lo} at day 3.5 post infection. Flow cytometry plot show TCF-1 and Tim-3 or TCF-1 and Slamf6 co-expression in splenic P14 CD8 T cells at day 3.5 post-infection before and after FACS sort.

(b-e) WT P14 cells (1x10^6) were adoptively transferred into naïve B6 recipient mice and then infected with LCMV$_{Cl13}$ 1 day later. Paired histograms and bar graphs show expression of the indicated markers on gated CD25^{Lo} (Blue) or CD25^{Hi} (Red) antigen specific CD8 T cells in spleen at day 3.5 post-infection; grey histograms show marker expression on endogenous CD44^{Lo} naïve CD8 T cells. Numbers represent MFI of expression of respective markers. Data are representative of 4 independent experiments (mean ± SEM) with at least 3 mice per group.

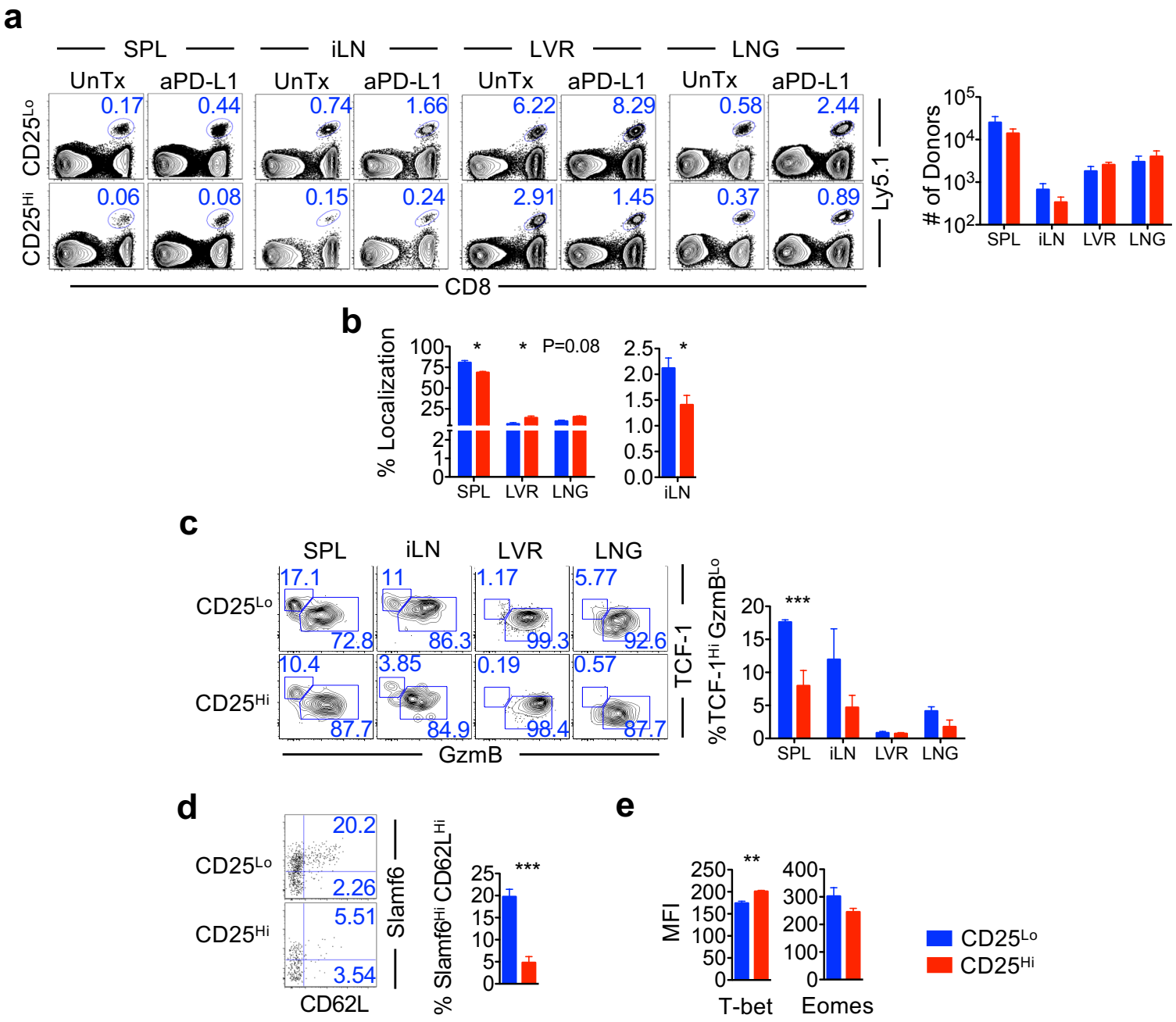

Extended Data Fig 6. CD25^{Lo} donors are enriched for long-lived stem-like exhausted CD8 T cells.

(a) Representative flow-cytometry plots and quantification (bar graphs) of donor cells at day 24 after infection in the indicated tissues. Bar graphs show absolute numbers **(a)** and % localization **(b)** of donor cells in spleen (SPL), inguinal lymph nodes (iLN), liver (LVR) and lung (LNG) at day 8 after infection (~4.5 days after FACS purification and adoptive transfer into infection-matched recipients). % localization of donor cells in a given tissue was calculated as the number of donor cells in a given tissue/total number of donor cells in all tissues analyzed x 100. **(c)** Representative flow cytometry plots of TCF-1 and GzmB expression in transferred CD25^{Hi} or CD25^{Lo} donor cells in the indicated tissues at 24 days after infection are shown. Bar graphs depict % stem-like TCF-1^{Hi} GzmB^{Lo} donor CD8 T cells in indicated tissues at day 24 after infection.

(d) Representative flow cytometry plots of Slamf6 and CD62L expression on CD25^{Hi} and CD25^{Lo} CD8 T cells in the spleen at day 24 post infection are presented. Bar graphs depict % Slamf6^{+} CD62L^{+} CD8 T cells from all mice.

(e) Bar graphs depict the expression of T-bet and Eomes on FACS-purified and transferred CD25^{Hi} (Red) or CD25^{Lo} (Blue) P14 CD8 T cells at day 8 post-infection. Bar graphs display mean and SEM. Paired and unpaired student t-test was used with statistical significance in difference of means represented as* (P ≤ 0.05), ** (P ≤ 0.01), *** (P ≤ 0.001).

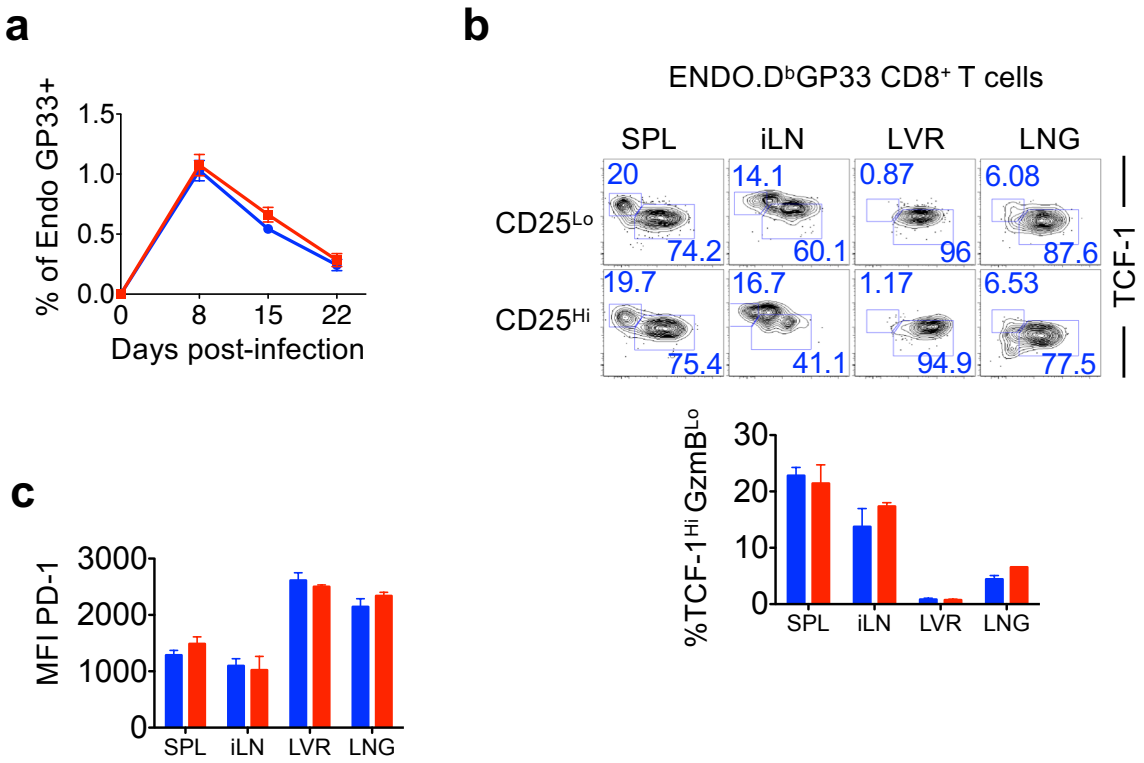

Extended Data Fig 7. The adoptively transferred CD25^{Lo} and CD25^{Hi} donors minimally impact the endogenous virus-specific CD8 T cell responses.

(a) Longitudinal analysis of endogenous D^{b}GP33-CD8T cell expansion and contraction in blood at indicated times after infection.

(b) Representative flow cytometry plots of TCF-1 and GzmB expression in endogenous D^{b}GP33-CD8T cell-specific cells in the indicated tissues 24 days after infection. Bar graphs depict % endogenous stem-like TCF-1^{Hi} GzmB^{Lo} cells in D^{b}GP33-specific CD8 T cells.

(c) Quantification of PD-1 expression on endogenous D^{b}GP33-CD8T cells in the indicated tissues at day 24 post-infection is summarized as bar graphs. Data representative of at least 4 mice per group (mean ± SEM). Paired and unpaired student t-test was used to compare statistical significance of difference in means as appropriate.

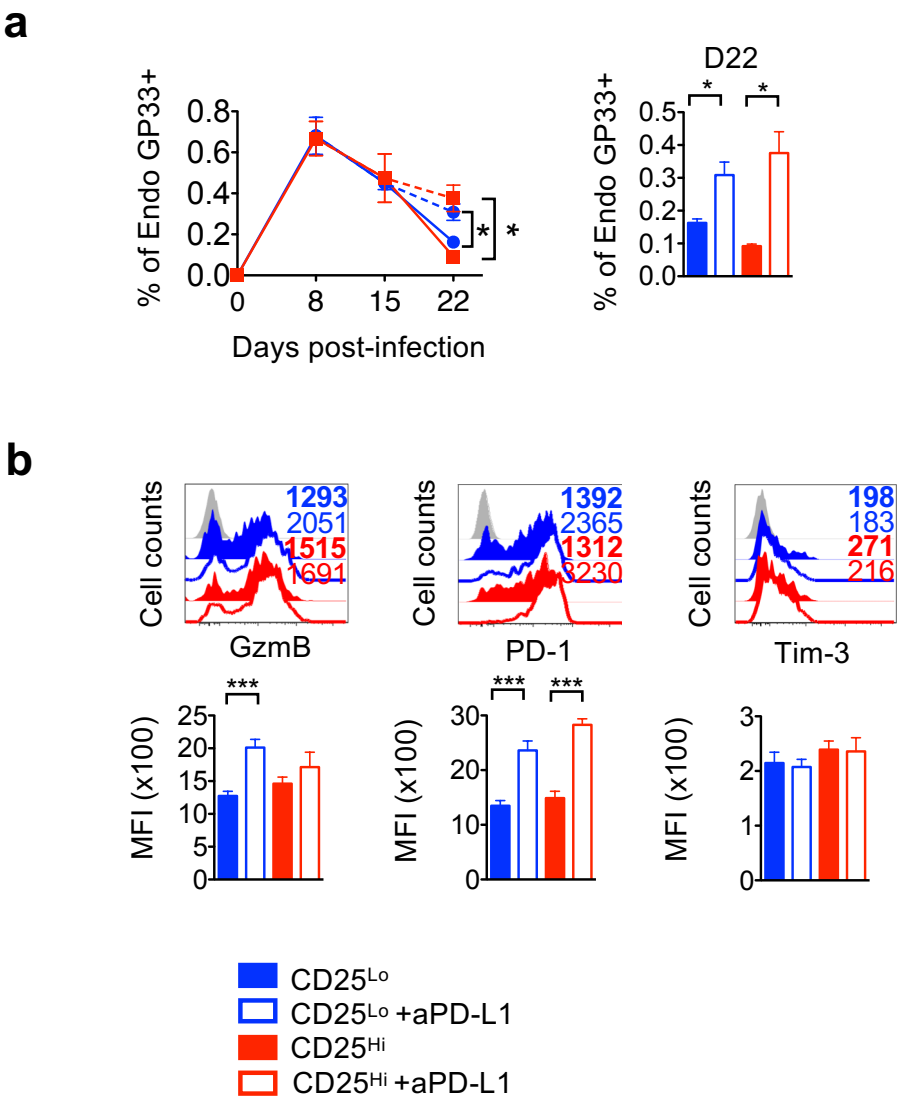

Extended Data Fig 8. Endogenous virus-specific CD8 T cell responses to PD-1 checkpoint blockade immunotherapy remain unaltered in chronically infected recipients of CD25^{Lo} and CD25^{Hi} donor cells.

(a) CD25^{Lo} and CD25^{Hi} cells were FACS purified at day 3.5 after infection, and adoptively transferred into infection-matched congenically distinct recipient mice (as in Fig 1). Mice were subsequently treated with anti-PD-L1 antibody (200 µg) every 3 days from day 15 to 24, and endogenous virus-specific CD8 T cells were assessed. Longitudinal analysis of endogenous D^{b}GP33-CD8T cell expansion and contraction in blood at indicated times after infection are presented. Bar graph depicts endogenous D^{b}GP33-specific CD8 T cell frequencies at day 22 post-infection.

(b) Histograms and bar graphs show GzmB, PD-1 and Tim-3 expression in endogenous D^{b}GP33-specific CD8 T cells in the spleen at day 24 post infection. Number represents MFI of respective marker. Bar graphs display mean and SEM. Paired and unpaired student t-test was used to compare difference of means between two groups. To compare differences between multiple groups one-way ANOVA with Tukey post-test was used with statistical significance in difference of means represented as * ($P \leq 0.05$), ** ($P \leq 0.01$), *** ($P \leq 0.001$).

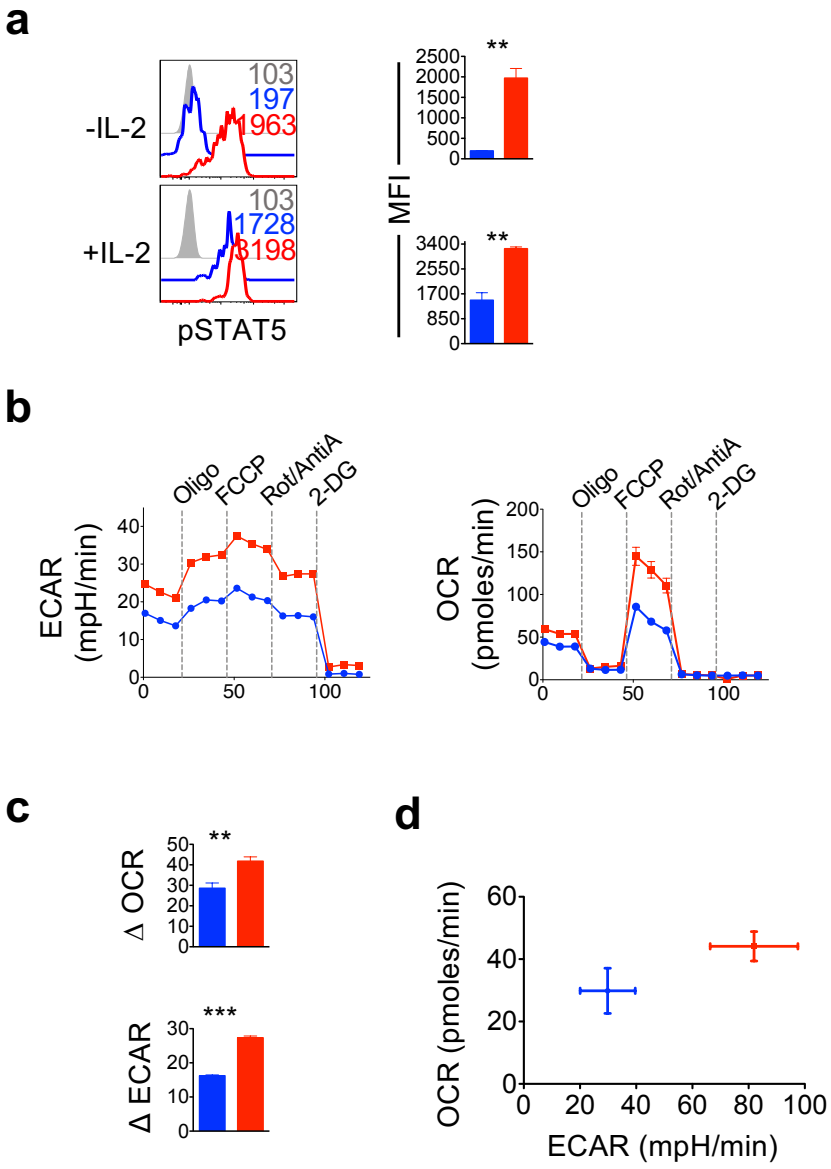

Extended Data Fig 9. Differential IL-2 signals in CD25^{Lo} and CD25^{Hi} virus-specific CD8 T cells at priming.

(a) WT P14 cells (2.5x10^3) were adoptively transferred into naïve B6 mice, which were subsequently infected with LCMV$_{Cl13}$. Splenocytes were isolated from P14 chimeric mice at day 5.5 after LCMV$_{Cl13}$ infection. Cells were stimulated with 10nM IL-2 and intracellular p-STAT5 was assessed by flow cytometry. Histograms are gated on CD25^{Hi} (red) or CD25^{Lo} (Blue) CD8 T cells.

(b) Metabolic analysis was performed using CD25^{Hi} and CD25^{Lo} FACS-purified P14 CD8 T cells at day 3.5 post-infection in the presence of 10 mM glucose with indicated additions of oliomycin (oligo), trifluoromethoxy carbonylcyanide phenylhydrazone (FCCP), rotenone and antimycin A (Rot/AntiA), and 2-deoxyglucose (2DG). Line graphs show extracellular acidification (ECAR) and oxygen consumption (OCR) rates over time. Dashed vertical lines indicate pharmacologic interventions with Oligomycin, FCCP, Rotenone/AntimycinA and 2-deoxyglucose.

(c) Bar graphs show maximum ECAR and basal OCR on FACS sorted CD25^{Hi} or CD25^{Lo} at day 3.5 post-infection.

(d) Energy map for purified CD25^{Lo} (Blue) or CD25^{Hi} (Red) D^{b}GP33-specific CD8 T cells (n=8 for each mean depicted).

To compare differences between groups unpaired student t-test was used. Statistical significance in difference of means is represented as * (P ≤ 0.05), ** (P ≤ 0.01), *** (P ≤ 0.001).

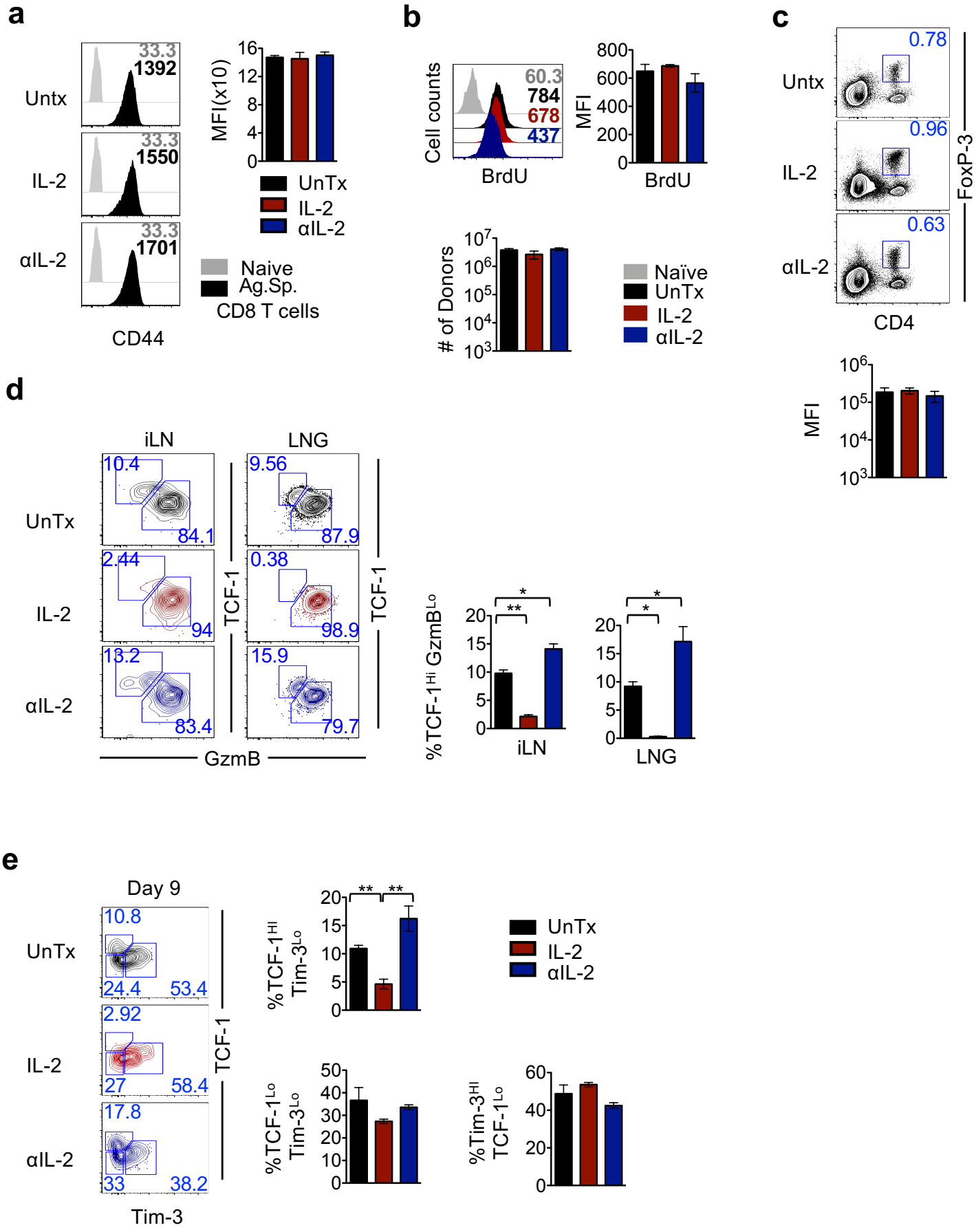

Extended Data Fig 10. Tempered IL-2 signals at priming lead to enhanced development of TCF1^{Hi} CD8 T cells. *(continued on next page)*

Extended Data Fig 10. Tempered IL-2 signals at priming lead to enhanced development of TCF1^{Hi} CD8 T cells.

(a) Representative histograms show CD44 expression on antigen-specific CD8 T cells (Black) on day 3.5 post-infection. Grey histograms depict endogenous CD44^{Lo} naïve CD8 T cells. Numbers within histograms depict MFI of marker expression. Bar graphs depict the expression of CD44 in the untreated (UnTx) group (Black), IL-2-treated (Red) and αIL-2 treated (Blue) groups at day 3.5 post-infection.

(b) Representative histograms showing BrdU incorporation by the donor cells are presented. Numbers inside histograms depict MFI of BrdU. Numbers in histograms show MFI of BrdU staining for corresponding donor plots. Bar graphs depict the MFI and absolute numbers of the donor cells at day 3.5 post-infection for indicated groups of untreated, IL-2 treated or IL-2 blocked groups.

(c) Representative flow-cytometry plots show the frequency of FoxP3^{+}CD4 T regulatory cells (Treg) in the spleens of untreated or treated groups of mice at day 3.5 post-infection as indicated. Bar graph shows absolute numbers of Tregs in each group.

(d) Representative flow cytometry plots of TCF-1 and GzmB expression in gated D^{b}GP33-specific P14 CD8 T cells isolated from iLN and LNG at day 3.5 post-infection are presented. Bar graphs show % stem-like TCF-1^{Hi} GzmB^{Lo} P14 CD8 T cells. Data are representative of 3 independent experiments with n=3 mice per group.

(e) Representative flow cytometry plots show TCF-1 and Tim-3 expression in donor cells isolated at day 9 after LCMV$_{Cl\text{-}13}$ infection, from recipient mice adoptively transferred with day 3.5 donor cells isolated from P14 chimeric mice that were untreated (Black), or treated with IL-2 (Red) or IL-2 blocking antibody (Blue) from days 0-3.5 post-infection. Bar graphs show the frequency of TCF-1^{Hi} Tim-3^{Lo}, TCF-1 ^{Lo} Tim-3^{Lo} , Tim-3^{Hi} TCF-1 ^{Lo} on donor CD8 T at day 9 post-infection.

To compare differences between groups one-way ANOVA with Tukey post-test was used. Statistical significance in difference of means is represented as * ($P \leq 0.05$), ** ($P \leq 0.01$), *** ($P \leq 0.001$).

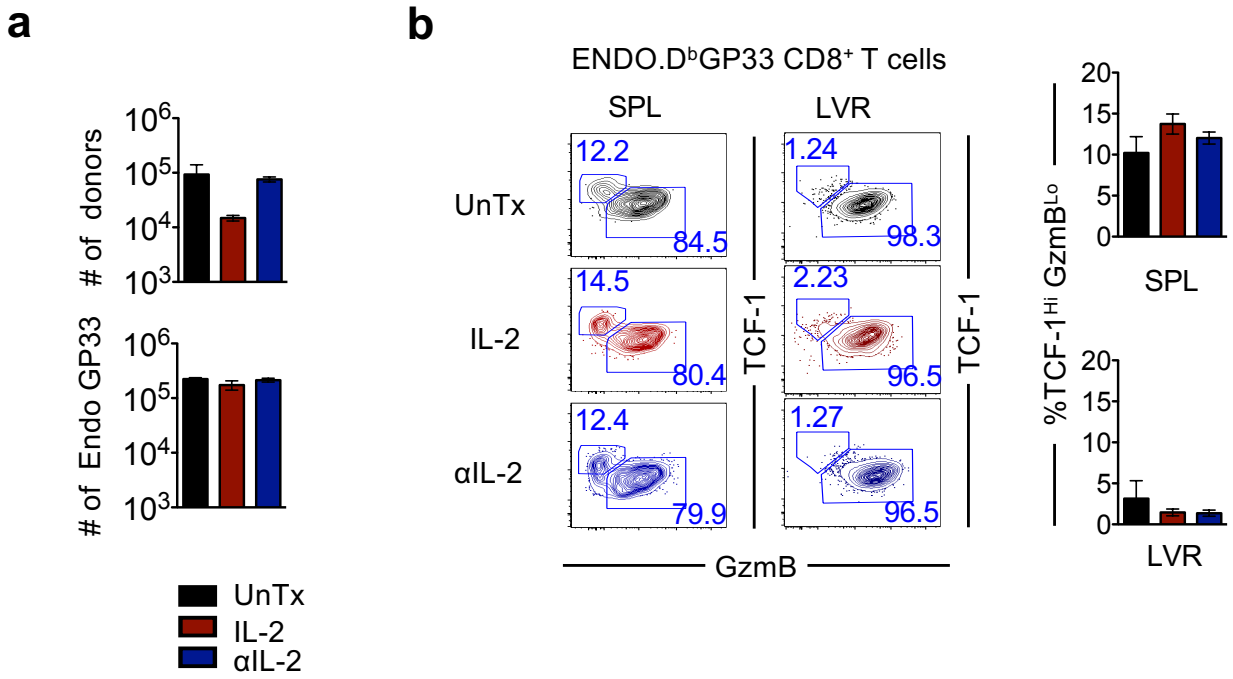

Extended Data Fig 11. Adoptive transfer of donor cells primed in distinct IL-2 signaling conditions does not alter the differentiation program of endogenous CD8 T cells to chronic LCMV infection.

(a) Bar graphs show numbers of D^bGP33-specific P14 donors and endogenous CD8 T cells in spleen at day 9 after infection in recipient mice adoptively transferred with day 3.5 donor cells isolated from P14 chimeric mice that were untreated (Black), or treated with IL-2 (Red) or IL-2 blocking antibody (Blue) from days 0-3.5 post-infection.

(b) Representative flow cytometry plots of TCF-1 and GzmB co-expression in endogenous LCMV D^bGP33 -specific CD8 T cells in spleen at day 9 post-infection are presented. Bar graphs depict % stem-like TCF-1^{Hi} $GzmB^{Lo}$ CD8 T cells. Data are representative of at least 3 mice per group (mean ± SEM). To compare differences between groups one-way ANOVA with Tukey post-test was used. Statistical significance in difference of means is represented as * ($P \leq 0.05$), ** ($P \leq 0.01$), *** ($P \leq 0.001$).

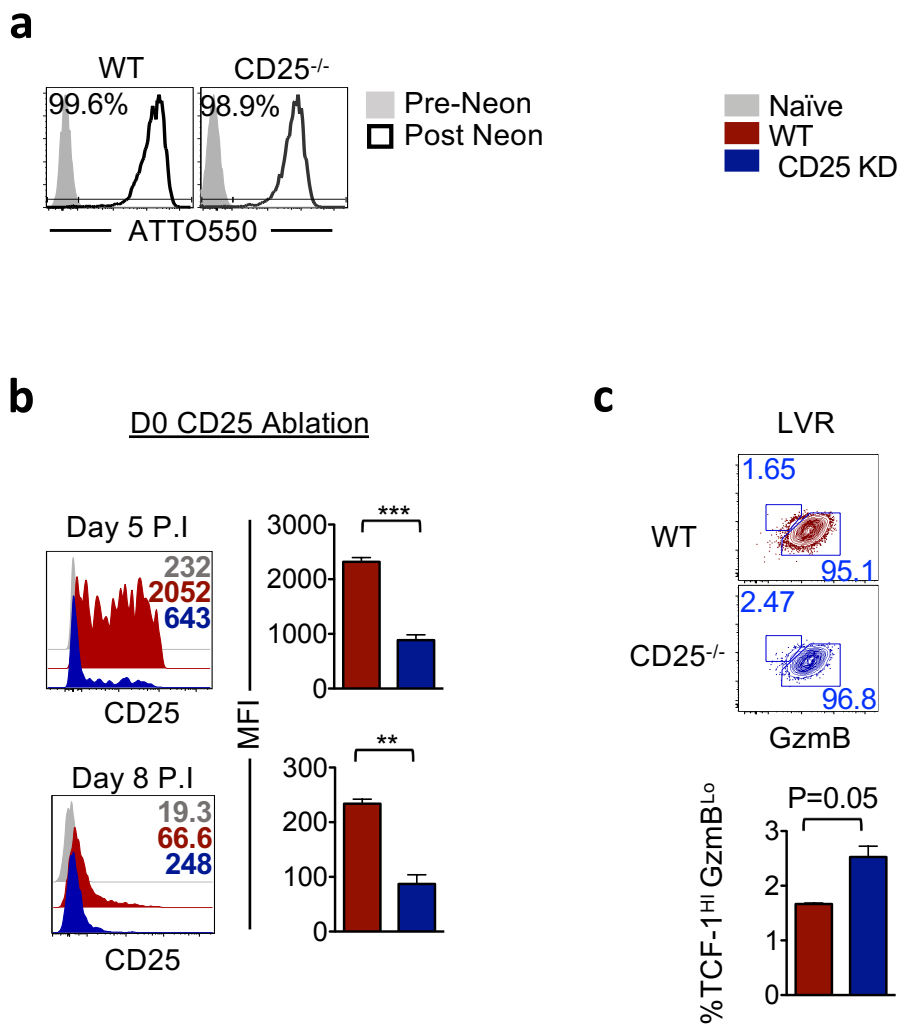

Extended Data Fig 12. Knockdown of CD25 expression on antigen-specific CD8 T cells at day 0, before infection with $LCMV_{Cl\text{-}13}$ promotes the development of TCF-1^{Hi} stem-like CD8 T cells.
(a) Electroporation efficiency using the Neon Transfection System. Histogram plots show percent positive cells for ATTO™ 55O (Black) post electroporation of D2 activated CD8 T cells.
(b) Paired histograms and bar graphs show the expression of CD25 on WT P14 CD8 T cells transfected with scrambled (WT) or *il2ra* guide RNAs (CD25 knockdown, CD25 KD) prior to adoptive transfer into naive mice, which were infected $LCMV_{Cl\text{-}13}$. Data are presented for WT and CD25 KD gated donor cells from spleens at day 5 and day 8 post-infection. Numbers within histograms represent MFI.
(c) Representative flow cytometry plots of TCF-1 and GzmB expression in WT and CD25 KD donor CD8 T cells isolated from the LVR at day 8 post-infection. Bar graphs depict composite data for % stem-like TCF-1^{Hi} $GzmB^{Lo}$ CD8 T cells in gated donor populations from n=3-5 mice per group.

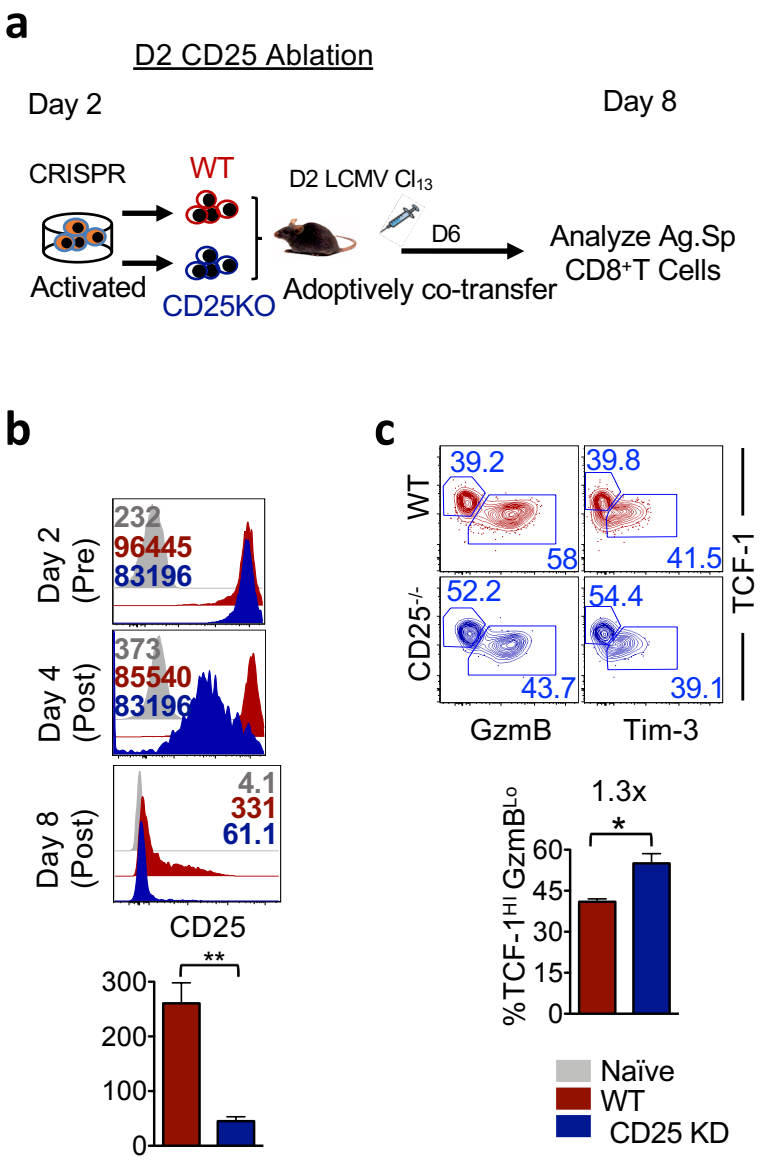

Extended Data Fig 13. Knockdown of CD25 expression on antigen-specific CD8 T cells at day 2 after infection with LCMV$_{Cl-13}$ promotes the development of TCF-1^{Hi} stem-like CD8 T cells.
(a) Experimental setup. Activated P14 CD8 T cells were electroporated with guide RNA targeting *il2ra* gene. Equal numbers of WT CD8 T cells or CD25 KD cells were adoptively co-transferred into Day 2 chronically infected mice. Donor antigen specific CD8$^+$ T cells were analyzed after 8 days of infection.
(b) The efficiency of CRISPR-Cas9-mediated deletion of *il2ra* on D2 activated P14 CD8 T cells was confirmed by flow cytometry after 48hr of *in vitro* stimulation by plate bound anti-CD3 and anti-CD28. Histograms show the expression of CD25 in WT (Red), CD25 KD (Blue) and naïve cells (Gray).
(c) Representative flow cytometry plots of TCF-1 and GzmB or TCF-1 and Tim-3 expression in D2 CD25-ablated donor CD8 T cells in spleens from day 8 LCMV$_{Cl-13}$-infected mice are shown. Bar graph depicts % stem-like TCF-1^{Hi} GzmB^{Lo} CD8 T cells in gated WT and CD25 KD donor populations.

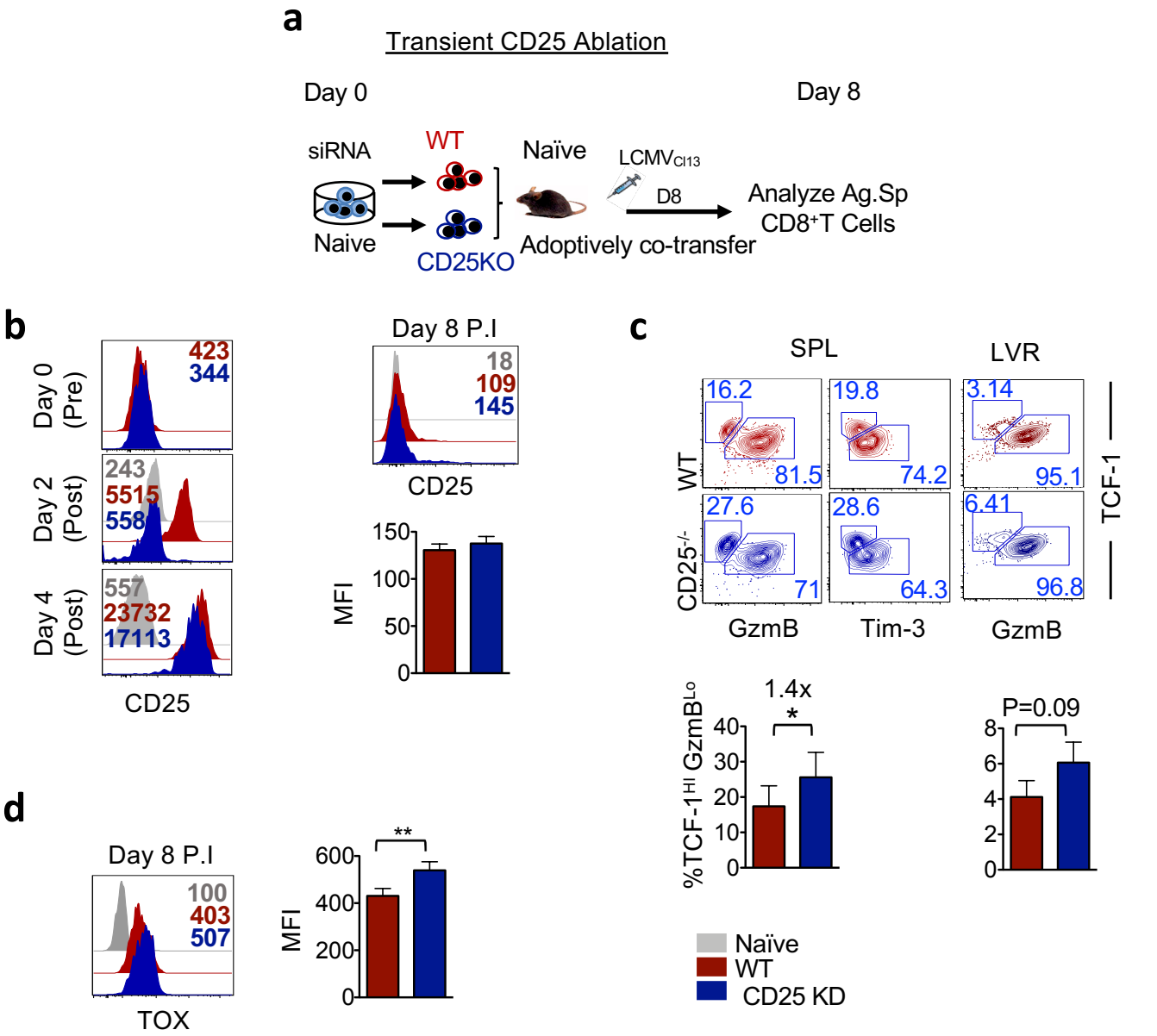

Extended Data Fig 14. Knockdown of CD25 expression on antigen-specific CD8 T cells at day 2 after infection with $LCMV_{Cl-13}$ promotes the development of TCF-1^{Hi} stem-like CD8 T cells.
(a) Experimental setup. Naïve P14 CD8 T cells were electroporated with short interfering RNA (siRNA) targeting CD25 mRNA (CD25 KD) or with controls (WT). Equal numbers of WT or CD25 KD donor P14 CD8 T cells were adoptively co-transferred into naïve mice, which were subsequently infected with $LCMV_{Cl-13}$. Donor antigen specific $CD8^+$ T were analyzed at day 8 post-infection.
(b) The efficiency of siRNA-mediated transient silencing of CD25 was confirmed by flow cytometry after 48hr of *in vitro* stimulation by plate bound anti-CD3 and anti-CD28. Cells were kept in culture for two more days to confirm the re-expression of CD25 on CD25 KD cells. CD25 expression levels were also assessed in WT and CD25 KD cells adoptively transferred into C57Bl/6 mice 8 days following infection with $LCMV_{Cl-13}$. Histograms show the expression of CD25 in WT (Red), CD25 KD (Blue) and naïve CD8 T cells (Gray). Corresponding bar graphs depict MFI of CD25 expression from n=3 mice.
(c) Representative flow cytometry plots of TCF-1 and GzmB or TCF-1 and Tim-3 co-expression on donor CD8 T cells isolated from spleens at day 8 after infection are presented. Bar graph depict % stem-like TCF-1^{Hi} $GzmB^{Lo}$ donor CD8 T cells in spleen and liver.
(d) Paired histogram and bar graphs show the expression levels of TOX on WT CD8 T cells and CD25 KD donor CD8 T cells isolated from spleens at day 8 post-infection. Data are representative of at least 2 independent repeats with n=3 mice per group (mean ± SEM). Paired Student t-test was used with statistical significance in difference of means represented as * ($P \leq 0.05$), ** ($P \leq 0.01$), *** ($P \leq 0.001$).

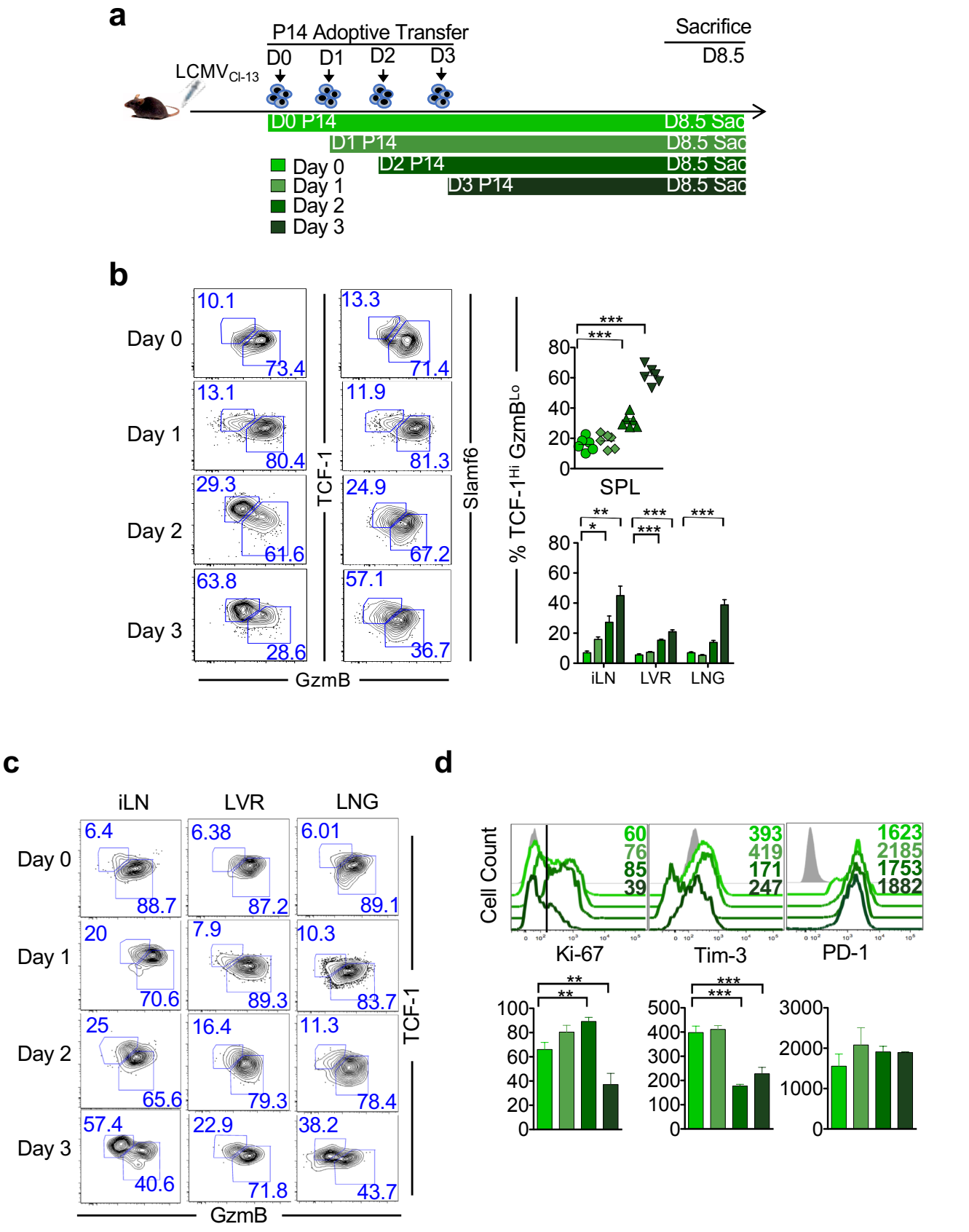

Extended Data Fig 15. Delayed priming and curtailed duration of stimulation of virus-specific CD8 T cells promotes the development of TCF-1^{Hi} stem-like CD8 T cells. *(continued on next page)*

Extended Data Fig 15. Delayed priming and curtailed duration of stimulation of virus-specific CD8 T cells promotes the development of TCF-1^{Hi} stem-like CD8 T cells.
(a) Experimental setup. $LCMV_{Cl13}$-infected C57Bl/6 mice were adoptively transferred with $2.5x10^3$ of WT P14 CD8 T cells at day 0, 1, 2 or 3 after infection. Donor CD8 T cells were analyzed 8.5 days after infection.
(b) Representative flow cytometry plots of TCF-1 and GzmB or TCF-1 and Slamf6 expression in donor CD8 T cells at day 8.5 post-infection are presented from spleen. Bar graphs depict % TCF-1^{Hi} GzmB^{Lo} CD8 T cells in the SPL (top) and iLN, LVR and LNG (Bottom) at 8.5 days after infection. **(c)** Representative flow cytometry data for TCF-1 and GzmB expression on adoptively transferred donor CD8 T cells in iLN, LVR and LNG are presented. Virus-specific donor CD8 T cells were analyzed at day 8.5 post-infection.
(d) Representative histogram plots and corresponding bar charts show expression of the indicated markers on adoptively transferred D^{b}GP33-specific donor CD8 T cells in spleens at 8.5 days after stimulation; grey histograms show marker expression in endogenous CD44^{Lo} naïve CD8 T cells. Numbers within histograms represent MFI of expression of respective markers. Data are representative of 2 independent experiments with n=3 mice per group. To compare differences between groups one-way ANOVA with Tukey post-test was used. Statistical significance in difference of means is represented as * ($P \leq 0.05$), ** ($P \leq 0.01$), *** ($P \leq 0.001$).

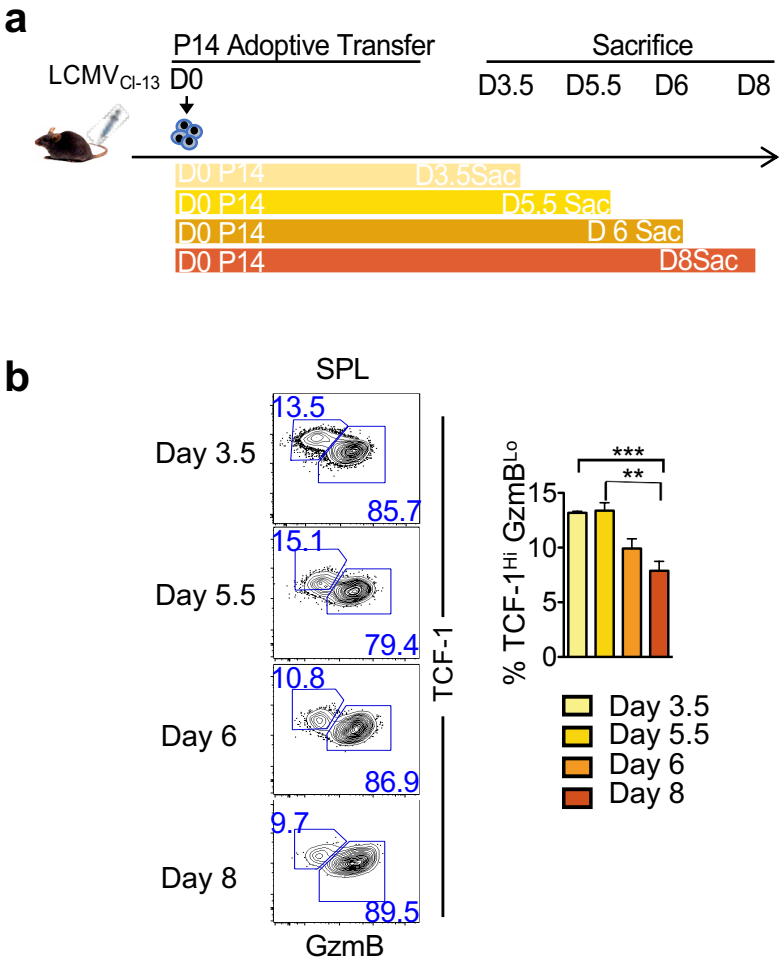

Extended Data Fig 16. Shorter duration of stimulation promotes the development of TCF-1^{Hi} stem-like CD8 T cells.
(a) Experimental setup. LCMV$_{Cl13}$ infected B6 mice were adoptively transferred with 2.5x10^3 of WT D^{b}GP33-specific P14 CD8 T cells at day 0 after infection. Donor CD8 T cells were analyzed at the indicated days post-infection in the spleens of infected mice.
(b) Representative flow cytometry plots of TCF-1 and GzmB expression on donor CD8 T cells in the SPL at the indicated days post-infection are presented. Bar graphs depict % TCF-1^{Hi} GzmB^{Lo} donor CD8 T cells in the spleen at indicated days post-infection. To compare differences between groups one-way ANOVA with Tukey post-test was used. Data are representative of 2 independent experiments with n=3 mice per group. Statistical significance in difference of means is represented as * ($P \leq 0.05$), ** ($P \leq 0.01$), *** ($P \leq 0.001$).

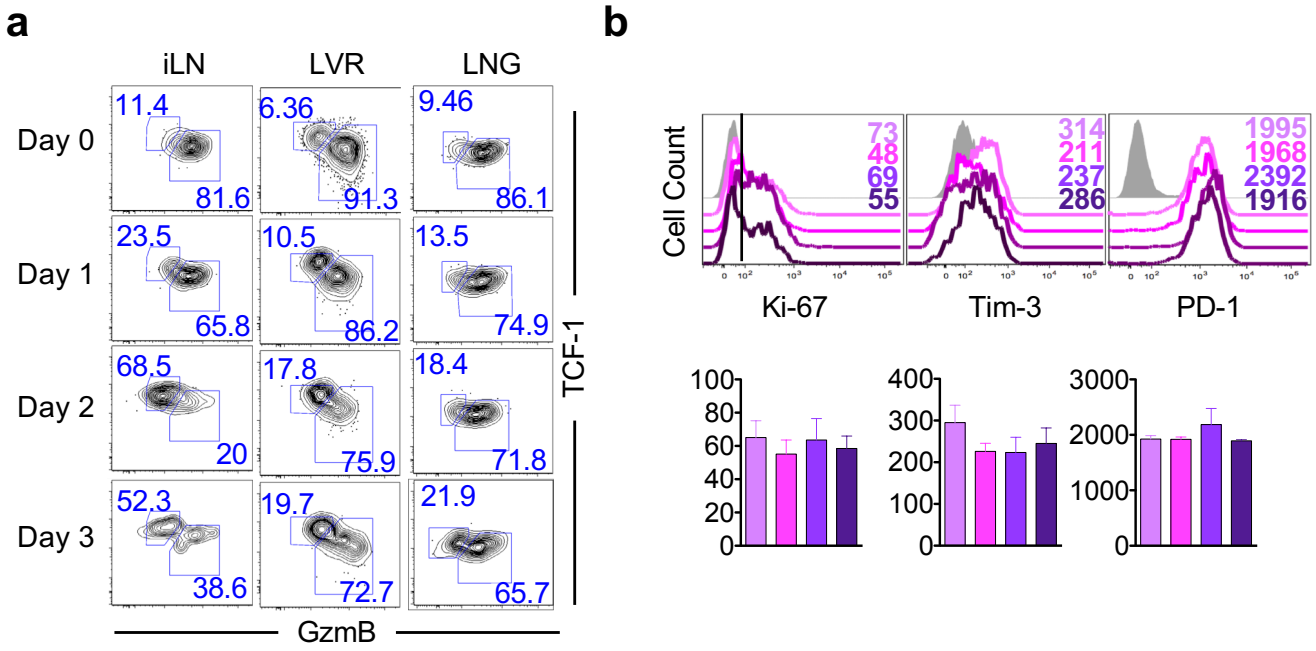

Extended Data Fig 17. Late priming of virus-specific CD8 T cells promotes the development of TCF-1^{Hi} stem-like CD8 T cells.

(a) LCMV $_{Cl13}$ infected B6 mice were adoptively transferred with 2.5x10^3 of WT P14 at days 0, 1, 2 or 3 after infection. Donor CD8 T cells were analyzed 5.5 days after P14 transfer. Representative flow cytometry plots show TCF-1 and GzmB expression on donor CD8 T cells isolated from spleens at day 5.5 post P14 adoptive transfer in the indicated tissues.

(b) Representative histogram plots and bar charts show levels of expression of the indicated markers on D^{b}GP33-specific CD8 T cells in spleens 5.5 days after adoptive transfer; grey histograms show marker expression in endogenous CD44^{Lo} naïve CD8 T cells. Numbers within histograms represent MFI of expression of respective markers. Data are representative of 2 independent experiments with n=3 mice per group. To compare differences between groups one-way ANOVA with Tukey post-test was used. Statistical significance in difference of means is represented as * ($P \leq 0.05$), ** ($P \leq 0.01$), *** ($P \leq 0.001$).

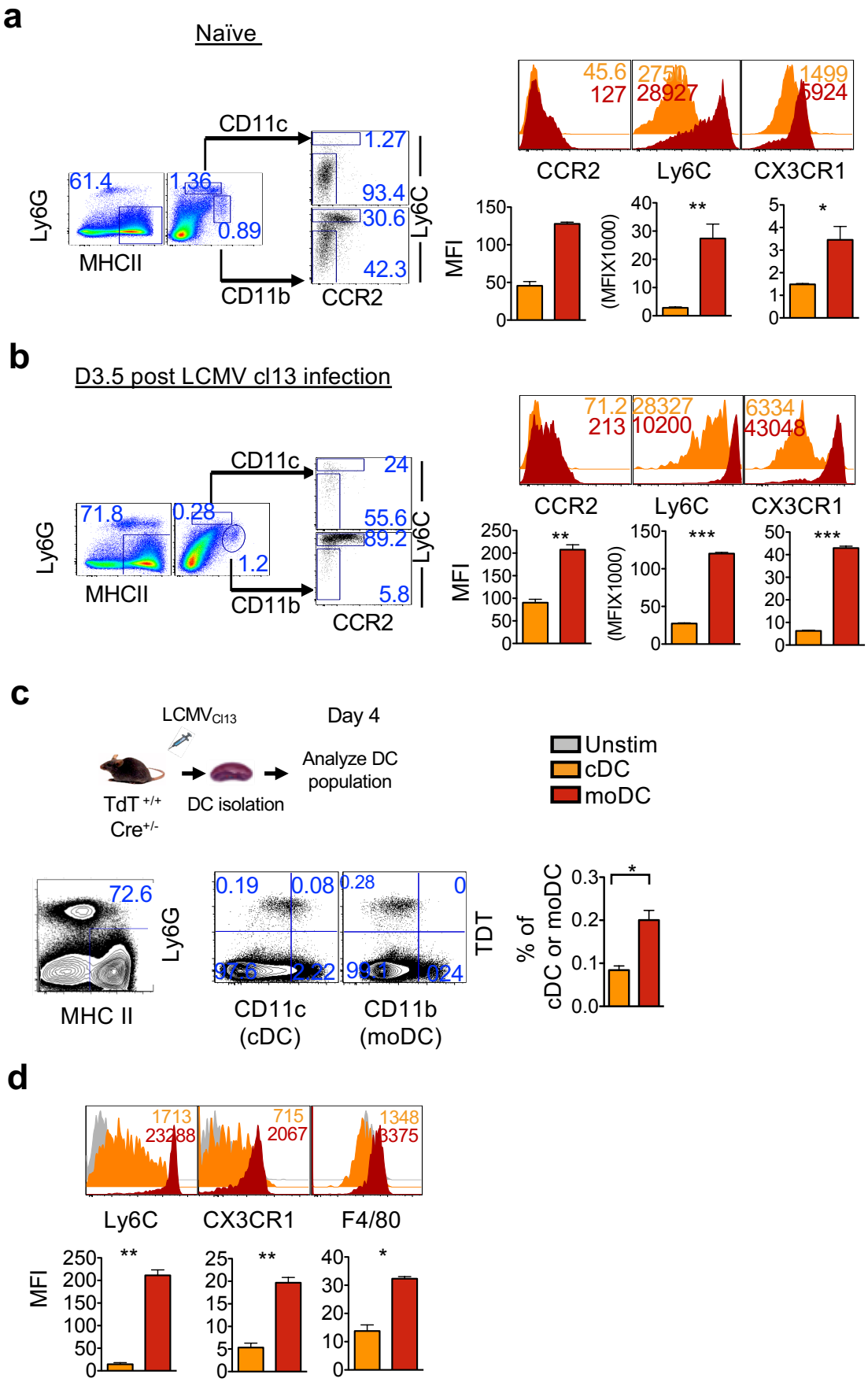

Extended Data Fig 18. Characterization of DC subsets during early versus late stages of CD8 T cell expansion in chronic LCMV infection. *(continued on next page)*

Extended Data Fig 18. Characterization of DC subsets during early versus late stages of CD8 T cell expansion in chronic LCMV infection.

(a,b) Representative flow cytometry plots show the gating strategy used to sort cDCs (CD11c+) and moDCs (CD11b+) from spleen samples of naïve **(a)** and day 3.5 $LCMV_{Cl\text{-}13}$-infected **(b)** C57Bl/6 mice. Histogram plots and bar charts show expression of the indicated markers on cDC (Orange) and moDC (Brown) populations. Numbers within histogram plots represent MFI of expression of respective markers.

(c) lL-2-Cre ROSA/tdTomato reporter mice were infected with $LCMV_{Cl13}$, and moDC and cDC were isolated from spleen 4 days after infection. Cells were gated and analyzed on $MHCII^{+}$ $Ly6G^{-}$ population. % cDC and moDC subsets are also presented as bar graphs.

(d) Representative histogram plots and corresponding bar graphs show phenotypic validation of the gated cDC and moDC subsets with respect to indicated markers. Data are representative of 2 independent experiments (mean ± SEM) with at least 3 mice per group. Paired Student t-test was used with statistical significance in difference of means represented as * ($P \leq 0.05$), ** ($P \leq 0.01$), *** ($P \leq 0.001$).

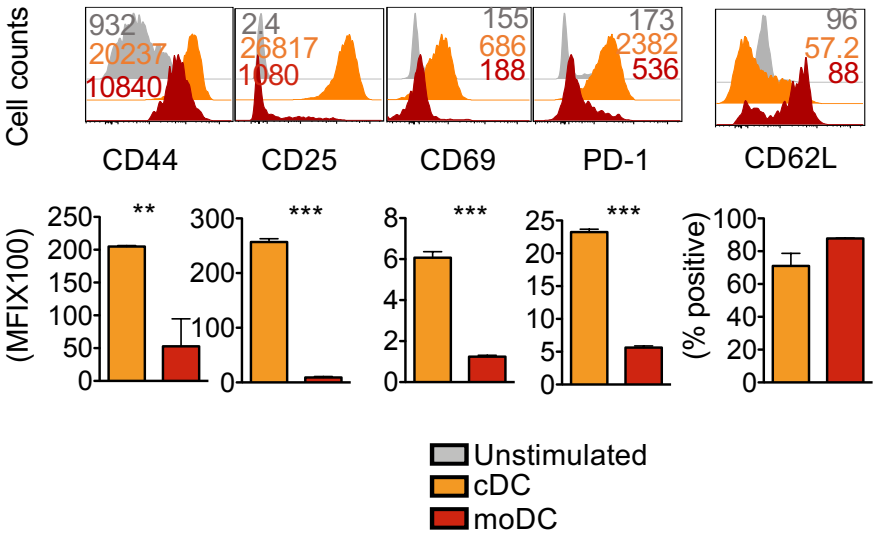

Extended Data Fig 19. T cell activation by distinct DC subsets.
B6 mice were infected with $LCMV_{Cl13}$, moDC and cDC were purified and sorted by flow cytometry at day 3.5 after-post infection. DC subsets were co-cultured ($1x10^4$ cells) with CFSE labeled P14 ($5x10^5$) for 3 days in the presence of GP_{33-41} peptide. Representative histograms and corresponding bar graphs depict expression of the indicated markers of T cell activation on donor P14 CD8 T cells 3 days after co-culture with cDC or moDC subsets.

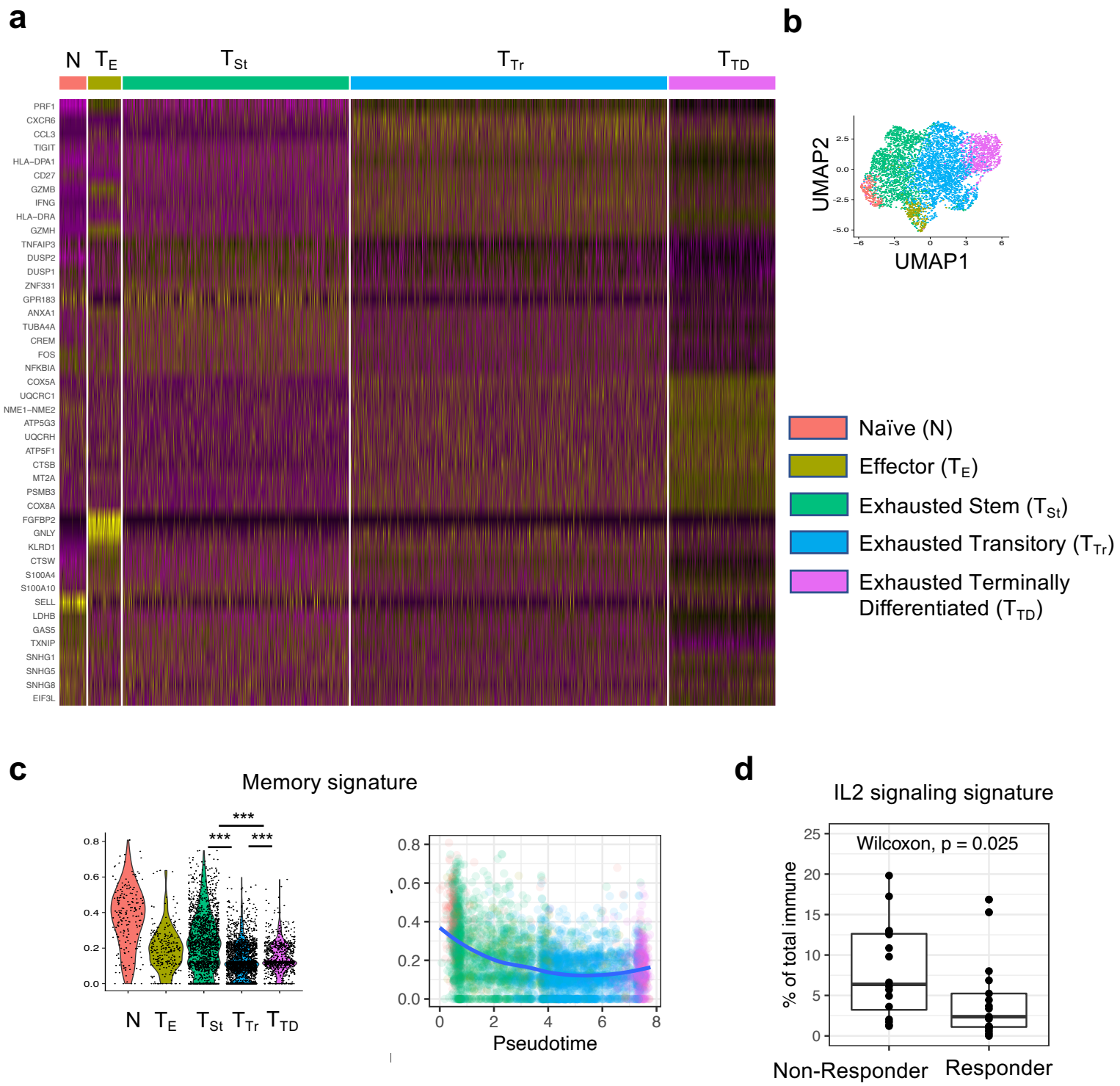

Extended Data Fig 20. scRNA-seq analysis of TILs from melanoma patients.

(a) Heatmap of differentially expressed genes in 5 clusters from CD8 T cells in melanoma tumors from checkpoint blockade immunotherapy treated patient dataset originally published in Sade-Feldman et al., 2018[10]. Top differentially expressed genes in each of the 5 clusters are shown on each row. Columns represent individual cells grouped by the clusters they are classified into. **(b)** UMAP plot colored by clusters. Clustering shown in panel a was used to color cells in the same UMAP as in Figure 5a.

(c) Expression of memory signature in clusters and across pseudotime.

(d) Association between immunotherapy response and IL2 signature scores in CD8 T cells. The frequency of CD8 T cells from either of the clusters with high IL2-signatures (transitory T_{Tr} and terminally differentiated T_{TD}) as a portion of all CD45+ cells were compared between patients who responded or did not respond to checkpoint blockade. Wilcoxon ranked-sum test used to establish statistical significance.

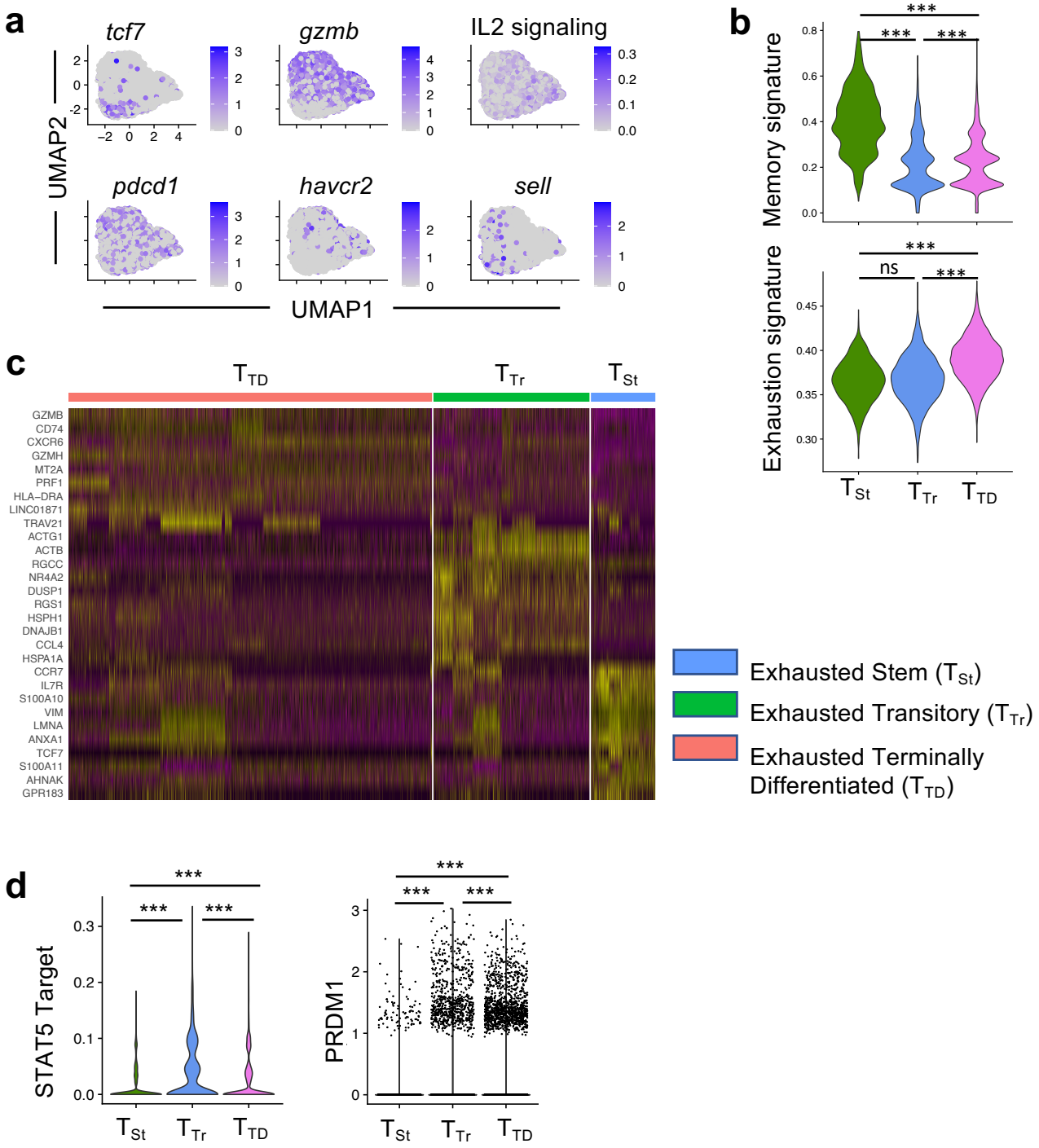

Extended Data Fig 21. scRNA-seq analysis of TILs from head and neck cancer patients.

(a) Expression of key exhaustion and memory genes and IL2 signaling score in HPV-specific CD8 T cells in HPV associated tumors from 15 patient dataset originally published in Eberhardt et al., 2021[16]. UMAP plots of scRNAseq from CD8 T cells that bound HPV-MHC tetramers CD8 T illustrating activation/exhaustion associated genes (*pdcd1, havcr2, gzmb*), memory associated genes (*tcf7, sell*) or a composite IL2 signature (FUNG_IL2_SIGNALING_1).

(b) Memory and exhaustion signature score in 3 clusters of HPV-specific cells from tumors. Signature scores of exhaustion and memory genes scored across Stem-like (T_{St}), Transitory (T_{TR}), and Terminally differentiated (T_{TD}) clusters.

(c) Heatmap of differentially expressed genes in 3 clusters from HPV-specific CD8 T cells. Top differentially expressed genes in each of the 2 clusters are shown in each row. Columns represent individual cells grouped by the clusters they are classified into.

Expression of IL2 signature genes and gene encoding Blimp-1 (*prdm1*) in HPV-specific CD8 T cells.

(d) Genes downstream of IL2 signaling that also contain STAT5 binding sites (FUNG_IL2_TARGETS_WITH_STAT5_BINDING_SITES_T1) were used to calculate the STAT5 Target Binding score.

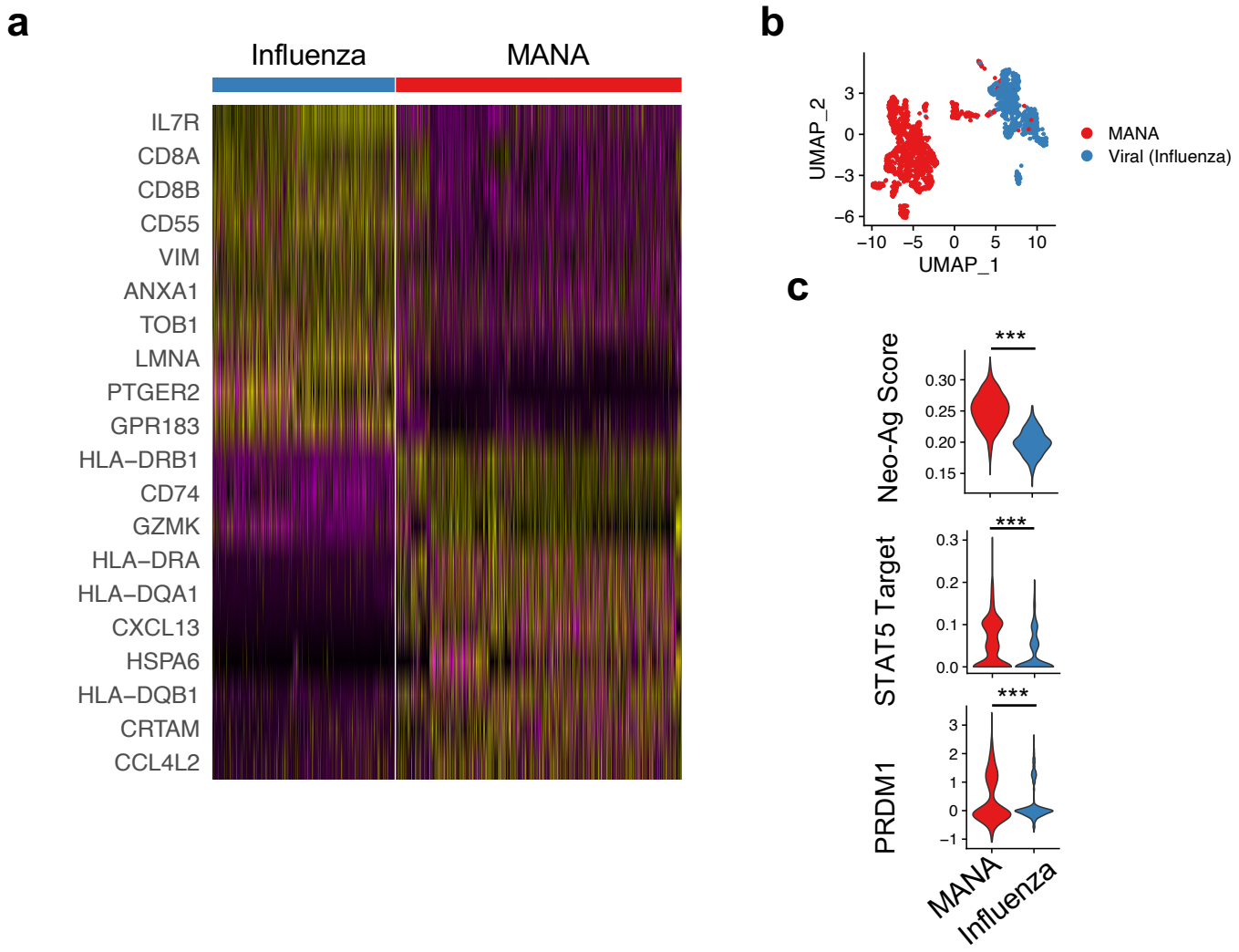

Extended Data Fig 22. scRNA-seq analysis of TILs from lung cancer patient tumor samples.
(a) Heatmap of differentially expressed genes in T cells of various specificities in NSCLC. CD3 T cells from 15 non-small cell lung cancer (NSCLC)-tumors were isolated and single cell RNAseq was performed on these cells as originally published in Caushi et al., 2021[21]. In parallel the MANAFEST and viraFEST assays were performed to identify mutation associated neoantigens (MANA) or influenza specific T cell receptors. CD8 T cells with either MANA or influenza-specific T cells were isolated in silico. Top differentially expressed genes for each specificity are shown in each row. Columns represent individual cells grouped by the T cell specificity based on their individual TCR sequences.
(b) UMAP plot of all CD8 T cells of known specificity in NSCLC. UMAP dimensionality reduction was performed on CD8 T cells of known specificity isolated in silico. Lower panel colored by exhaustion signature score.
(c) Violin plots of cancer-specific neoantigen STAT5 target and Blimp-1 (encoded by prdm1) scores in CD8 T cells of known specificity in NSCLC. Cancer-specific neoantigen score was derived from Lowery et al., 2022[56]. MANA and Influenza specific CD8 T cells were isolated in silico as in panel a. Wilcoxon ranked-sum tests were used to assign statistical significance. Statistical significance represented as * ($P \leq 0.05$), ** ($P \leq 0.01$), *** ($P \leq 0.001$).

nature biotechnology

ARTICLES

https://doi.org/10.1038/s41587-021-00935-2

Spatial transcriptomics at subspot resolution with BayesSpace

Edward Zhao[1,2], Matthew R. Stone[3], Xing Ren[1], Jamie Guenthoer[4], Kimberly S. Smythe[5], Thomas Pulliam[6], Stephen R. Williams[7], Cedric R. Uytingco[7], Sarah E. B. Taylor[7], Paul Nghiem[5,6,8], Jason H. Bielas[3,9,10] and Raphael Gottardo[1,2] ✉

Recent spatial gene expression technologies enable comprehensive measurement of transcriptomic profiles while retaining spatial context. However, existing analysis methods do not address the limited resolution of the technology or use the spatial information efficiently. Here, we introduce BayesSpace, a fully Bayesian statistical method that uses the information from spatial neighborhoods for resolution enhancement of spatial transcriptomic data and for clustering analysis. We benchmark BayesSpace against current methods for spatial and non-spatial clustering and show that it improves identification of distinct intra-tissue transcriptional profiles from samples of the brain, melanoma, invasive ductal carcinoma and ovarian adenocarcinoma. Using immunohistochemistry and an in silico dataset constructed from scRNA-seq data, we show that BayesSpace resolves tissue structure that is not detectable at the original resolution and identifies transcriptional heterogeneity inaccessible to histological analysis. Our results illustrate BayesSpace's utility in facilitating the discovery of biological insights from spatial transcriptomic datasets.

Knowledge of the spatial location of transcript expression can provide vital insights into biological function and pathology. Single-cell RNA sequencing (scRNA-seq) achieves high-throughput and high-resolution profiling of gene expression, but because tissue is dissociated for sample preparation, spatial information is not retained. Recent methods for high-throughput profiling of gene expression while retaining spatial information allow analyses to be made within the context of the biological tissue[1]. Studies performed with the Spatial Transcriptomics (ST) platform and the improved Visium platform have already generated insights into diverse areas such as tumor heterogeneity[2,3], brain function[4] and the pathophysiology of sepsis[5]. The primary technological limitation of these spatial gene expression platforms is resolution, with the unit of observation being spots that are 100 µm in diameter on the ST platform and 55 µm in diameter on the Visium platform. As such, the number of cells within a spot may range from one to 30 on the Visium platform and up to 200 on the older ST platform, depending on the biological tissue[6]. Alternative approaches include fluorescence in situ hybridization (FISH) technologies, such as seqFISH and multiplexed error-robust FISH, and other recently developed spatial sequencing methods, such as Slide-seq and ZipSeq[7–10]. While these methods provide increased resolution, most are lower throughput, less sensitive, rely on custom protocols or are not widely available.

Here, we propose BayesSpace, a computational method that uses the neighborhood structure in spatial transcriptomic data to increase the resolution to the subspot level (Fig. 1a). Our method draws from the existing literature for use of Bayesian statistics to achieve super-resolution images[11–13]. In contrast to existing deconvolution methods using scRNA-seq data[14–16], the enhanced-resolution modeling of BayesSpace, which approaches single-cell resolution with the Visium platform, does not require independent single-cell data and allows us to infer the spatial arrangement of subspots. While integration with scRNA-seq is appealing, it may be costly if matched samples are used or introduce bias if publicly available references are used. Furthermore, deconvolved mixtures are still only spatially resolved at the original scale of the ST or Visium technology, and the neighborhood structure of cell types cannot be recovered.

In addition, there is a need for new statistical methods for the analysis of spatial gene expression data that efficiently use the available spatial information. Clustering is an important step in the analysis of such data that allows downstream analyses, such as cell type or tissue annotation and differential expression, to provide unbiased biological insights. Existing analyses of spatial gene expression data often rely on clustering methods for non-spatial scRNA-seq data[2,4]. The additional spatial information available from ST and Visium can help address the analytical challenges of sparsity and noise by smoothing over adjacent spots, which are more likely to have similar transcriptomic profiles. Zhu et al.[17] proposed a hidden Markov random field model (HMRF) for clustering of low-resolution in situ hybridization data into distinct spatial domains by jointly modeling gene expression and spatial neighborhood structure[17]. This approach was later adapted for use with high-throughput spatial transcriptomic data through selection of spatially differentially expressed genes before clustering[18]. Another recently developed spatial clustering algorithm is stLearn, which uses deep learning

[1]Vaccine and Infectious Disease Division, Fred Hutchinson Cancer Research Center, Seattle, WA, USA. [2]Department of Biostatistics, University of Washington, Seattle, WA, USA. [3]Fred Hutch Innovation Laboratory, Immunotherapy Integrated Research Center, Fred Hutchinson Cancer Research Center, Seattle, WA, USA. [4]Human Biology Division, Fred Hutchinson Cancer Research Center, Seattle, WA, USA. [5]Clinical Research Division, Fred Hutchinson Cancer Research Center, Seattle, WA, USA. [6]Department of Medicine, Division of Dermatology, University of Washington, Seattle, WA, USA. [7]10x Genomics, Pleasanton, CA, USA. [8]Seattle Cancer Care Alliance, Seattle, WA, USA. [9]Translational Research Program, Public Health Sciences Division, Fred Hutchinson Cancer Research Center, Seattle, WA, USA. [10]Department of Pathology, University of Washington, Seattle, WA, USA. ✉e-mail: rgottard@fredhutch.org

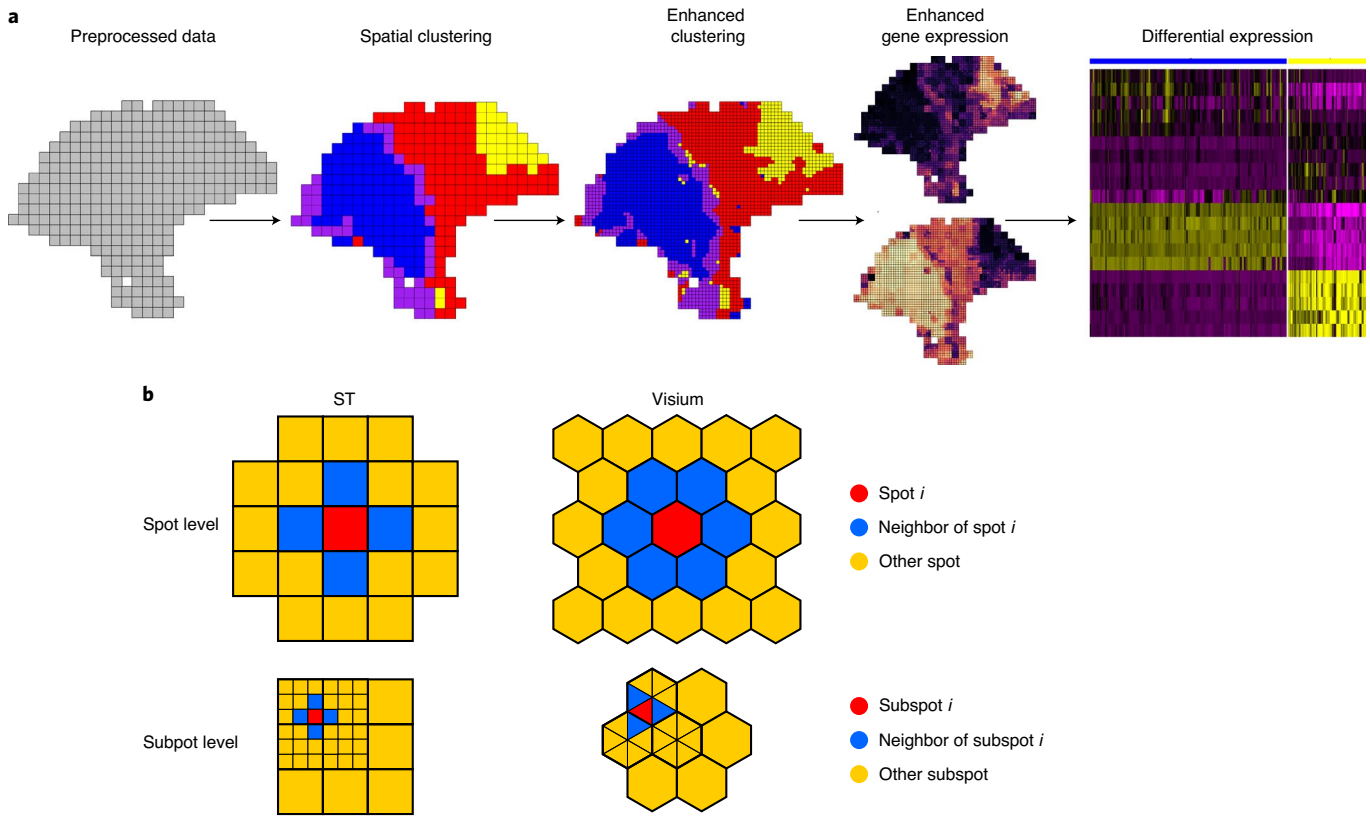

Fig. 1 | The BayesSpace workflow. a, The BayesSpace workflow begins with preprocessed ST or Visium data. Data are spatially clustered to infer regions with similar expression profiles. These clusters can be refined via enhanced clustering to provide a higher-resolution spatial map. Enhanced clustering also provides the basis for predicting gene expression at the higher resolution, which can be used in further differential expression analyses. **b**, From geometric representations of spatial distribution of spots in the ST and Visium technologies, neighbors can be identified for each spot based on shared edges (top). Each spot can be subdivided into subspots, which again have natural edge-based neighbors (bottom).

features extracted from histopathological images as well as expression of neighboring spots to spatially smooth data[19].

BayesSpace enables spatial clustering by modeling a low-dimensional representation of the gene expression matrix and encouraging neighboring spots to belong to the same cluster via a spatial prior (Fig. 1b). Our method draws from previously developed spatial statistics methods for image analysis and microarray data[20,21]. Compared with previous approaches, BayesSpace allows for a more flexible specification of the clustering structure and error term than alternative approaches. From a user perspective, BayesSpace is accessible in that it takes the widely used Bioconductor SingleCellExperiment object as input[22], does not require the additional task of marker gene preselection and involves minimal parameter tuning.

Using several datasets, we show that BayesSpace improves the identification of spatially distributed tissue domains through spatial clustering and enhances the resolution of gene expression maps. We use immunohistochemistry as a ground truth in two cancer samples to validate that our enhanced-resolution clustering identifies a tissue structure consistent with cell surface markers, and we report examples of transcriptional heterogeneity in the tumor microenvironment not achievable by immunohistochemical analyses alone. Furthermore, using in silico spatial transcriptomic datasets generated from aggregating scRNA-seq data, we show that BayesSpace can recover the true spatial structure at near single-cell resolution.

Results

Spatial clustering improves identification of known layers in brain tissues. Recently, Maynard et al.[4] presented Visium spatial expression profiles of 12 dorsolateral prefrontal cortex (DLPFC) samples, as well as manual annotations of the six cortical layers and white matter for each sample as part of the spatialLIBD package[4] (Fig. 2a). Maynard et al.[4] annotated DLPFC layers by considering cytoarchitecture and selected gene markers. Here, we evaluate BayesSpace's ability to identify distinct layer-specific expression profiles and compare its performance to other spatial and non-spatial clustering methods. Specifically, we compare the performance of four non-spatial algorithms commonly applied to scRNA-seq data, *k*-means, mclust[23], Louvain[24] and SC3 (ref. [25]); two recently published spatial clustering algorithms, HMRF (as implemented in the Giotto package)[18] and stLearn[19]; and the clustering partitions originally reported by Maynard et al.[4] in the spatialLIBD package, which involve Walktrap clustering of spatial coordinates and principal components (PCs) calculated from highly variable genes (HVGs) or known layer-specific marker genes. Following the methodology of Maynard et al.[4], we use the adjusted Rand index (ARI) to quantify similarity between cluster labels and manual annotations, which are considered the ground truth.

BayesSpace substantially outperforms the original spatialLIBD clustering partitions, as well as all non-spatial clustering algorithms and spatial clustering methods developed for spatial transcriptomic data (Fig. 2b). BayesSpace and the non-spatial methods were applied on 15 PCs calculated from the top 2,000 HVGs. Spatial clustering methods Giotto and stLearn were implemented based on the original authors' recommended parameters (Supplementary Note). We also show Giotto and stLearn results using precomputed PCs from BayesSpace to provide a more controlled comparison, although we found that this did not improve either method's

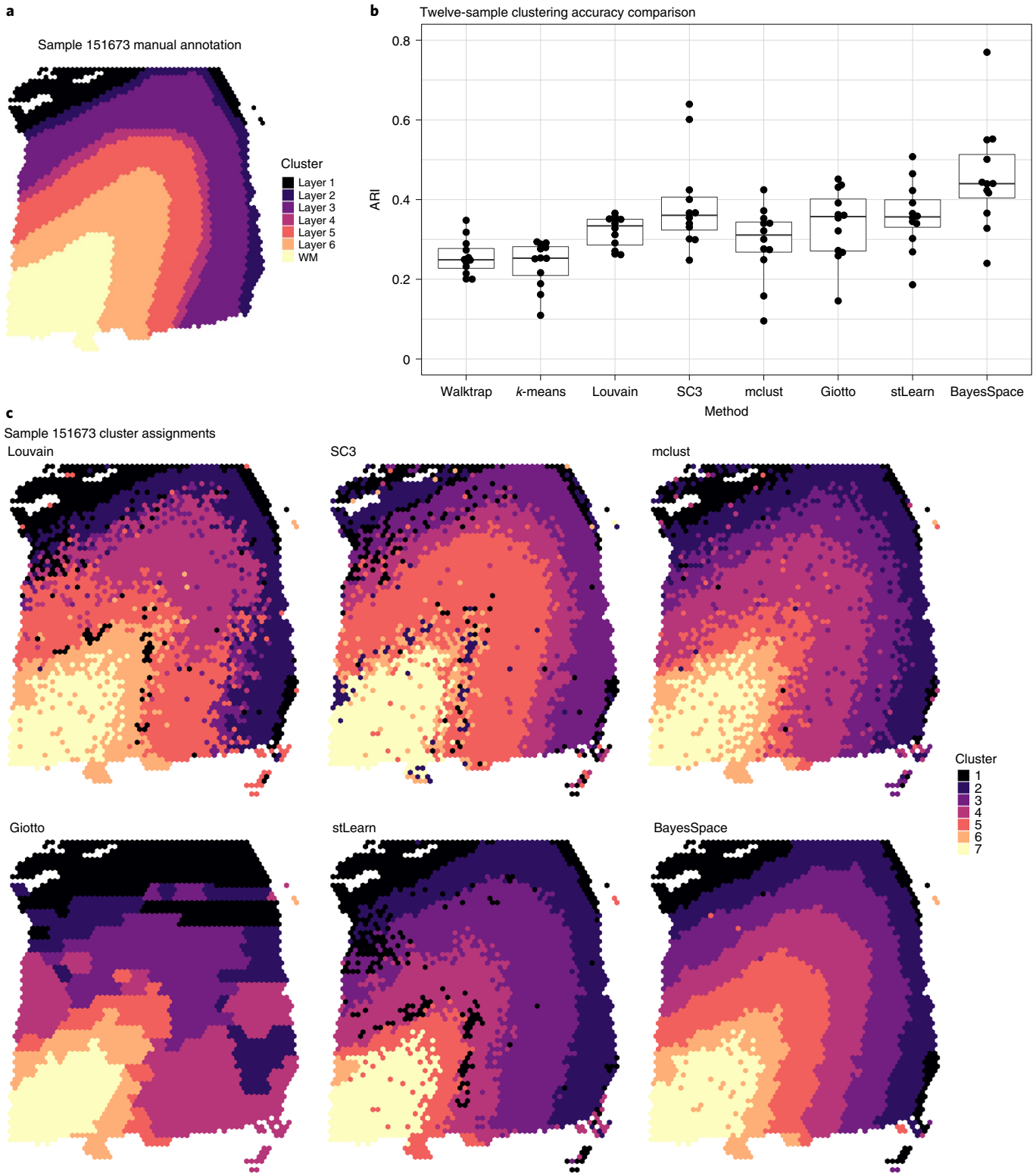

Fig. 2 | BayesSpace improves computational resolution of layers in the DLPFC. a, Ground truth. We highlight the manually annotated six DLPFC layers and white matter (WM) in sample 151673 from the spatialLIBD dataset. Annotated layers for the remaining samples can be found in the original publication[4]. **b**, Summary of clustering accuracy in all twelve samples. The ARI is used to compare similarity between cluster labels from each method against the manually annotated layers for all twelve samples. In the boxplot, the center line, box limits and whiskers denote the median, upper and lower quartiles and 1.5× interquartile range, respectively. **c**, Cluster assignments generated by non-spatial (top) and spatial (bottom) methods for sample 151673.

performance (Supplementary Fig. 1). As an example, in sample 151673, we found that only SC3 (ARI = 0.42), mclust (ARI = 0.42), stLearn (ARI = 0.37) and BayesSpace (ARI = 0.55) generated clusters that qualitatively followed the expected layer pattern (Fig. 2c). Most clustering partitions aside from BayesSpace exhibited substantial noise and lack of clear spatial separation between clusters.

By contrast, BayesSpace leveraged spatial information to smooth the data and provided distinct layers of clusters. The *t*-distributed error model that BayesSpace uses is particularly robust against outliers in clusters, which may be driven by technical artifacts generated during sample preparation or downstream analyses (Supplementary Fig. 2). Additionally, BayesSpace's runtime and memory footprints are comparable to those of other spatial clustering methods, requiring 27 min of wall time and 9.6 GB of memory in this sample (Supplementary Fig. 3).

Increased resolution clustering leads to identification of known tissue structures missed by other methods. We used BayesSpace to analyze a melanoma ST sample first annotated and described by Thrane et al.[2]. As the manual annotation identified regions of melanoma, stroma and lymphoid tissue and left an additional area unannotated (Fig. 3a), we ran spatial clustering with $k=4$ clusters (Fig. 3b). The resulting clusters corresponded well with the manually annotated tissue types. Furthermore, the melanoma tissue was split into the central region of the tumor and an outer ring of mixed tumor and lymphoid tissue. BayesSpace enhanced spatial clustering provided a higher-resolution map of the tissue types (Fig. 3c). Notably, the enhancement identified lymphoid regions along the tumor border and possible immune infiltration into the tumor that could not be discerned at the original resolution. These regions were also largely not identified by other clustering methods (Supplementary Fig. 4). While most clustering methods identified heterogeneity between the periphery and the center of the tumor, only SC3, Giotto and subspot-level BayesSpace identified lymphoid regions proximal to the tumor, with BayesSpace providing higher resolution and more robust signal (Supplementary Fig. 4). Finally, we also ran BayesSpace at the spot level using five and six clusters, identifying potential heterogeneity within the stroma region (Supplementary Fig. 4).

Using the enhanced PCs, we can generate high-resolution maps of individual genes or expression profiles for major cell types as described in the Methods. Differential expression analysis performed on enhanced-resolution gene expression indicated that the lymphoid regions had a distinct expression profile. We observed elevated expression of lymphocyte markers such as *CD52* and *MS4A1* and lower expression of melanoma markers such as *MCAM* and *SPP1* relative to that of the surrounding tumor border (Supplementary Fig. 4). Enhanced-resolution differential expression analysis between the four clusters highlighted additional spatial variation in gene expression (Fig. 3d). In the stroma (cluster 2), expression levels were higher for extracellular matrix proteins such as those encoded by *DCN* and *COL3A1*. Furthermore, we revealed intratumor heterogeneity between the border and center of the tumor (clusters 1 and 3, respectively), with higher chemokine (*CXCL9*, *CXCL10*) activity at the border and elevated expression of genes related to cell proliferation (*HSPB1*) and metastasis (*ATP1A1*) at the center[26,27].

We defined tumor cell (*PMEL*), fibroblast (*COL1A1*), B cell (*CD19*, *MS4A1*), T cell (*CD2*, *CD3D*, *CD3E*, *CD3G*, *CD7*) and macrophage (*CD14*, *FCGR1A*, *FCGR1B*) expression profiles based on one or more marker genes from existing literature[28]. The enhanced expression profiles provided noticeably higher spatial resolution (Fig. 3e). In particular, we could more clearly observe immune expression on the periphery of the tumor. The contrast between *PMEL* expression in the tumor, stroma and lymphoid tissue was also more apparent with enhanced resolution.

Immunohistochemistry validates enhanced-resolution clusters. To validate our enhanced-resolution clustering and gene expression, we analyzed an unreported breast cancer sample: an estrogen receptor-positive (ER^+), progesterone receptor-negative (PR^-), human epidermal growth factor receptor (HER)2-amplified (HER^+) invasive ductal carcinoma (IDC) prepared on the Visium platform with immunofluorescence staining for 4,6-diamidino-2-phenylindole (DAPI) (staining nuclei) and CD3 (staining T cells) (Supplementary Note and Supplementary Fig. 5). We additionally analyzed a dataset published by 10x Genomics: an endometrial adenocarcinoma of the ovary (ovarian cancer; OC) sequenced on the Visium platform and stained with immunofluorescence for DAPI, pan-cytokeratin (staining epithelial tissue) and CD45 (staining leukocytes) (Supplementary Fig. 6). After examination by a pathologist, out-of-focus and overexposed regions were excluded from the analysis (Methods and Supplementary Figs. 7 and 8). Cell segmentation of in-focus areas (IDC, $n=2{,}929$ of 4,727 spots; OC, $n=2{,}041$ of 3,493 spots) identified a median of 21 cells per spot in the IDC tissue and 19 cells per spot in the OC tissue, along with a median of three cells per subspot in both tissues (Supplementary Figs. 7 and 8).

We applied BayesSpace to cluster the IDC sample into ten clusters and the OC sample into eight clusters at spot and subspot resolution, selecting the number of clusters based on the negative log-likelihood curve (Supplementary Figs. 9 and 10). We analyzed anti-CD3 and anti-CD45 intensity in the in-focus area of each tissue section (Fig. 4a,f, respectively), finding that the immunofluorescence signal correlated well with the corresponding enhanced gene expression (Pearson's $r=0.53$ in the IDC; Fig. 4b,g). In both samples, we identified clusters enriched for the respective immune immunofluorescence signal and dichotomized the clusters into CD3- or CD45-rich and CD3- or CD45-poor areas (Fig. 4c,h and Supplementary Figs. 9 and 10). From this, we identified regions of interest (ROI) between the spot-level and enhanced clustering: areas where the enhancement increased the observed heterogeneity and many subspots flipped from immune rich to immune poor or vice versa. We highlight six of these ROI in Fig. 4d,i to demonstrate that enhanced clustering qualitatively improves concordance of clustering with the underlying immunohistochemical stain. Specifically, we present regions where, compared to the coarser spot-level clustering, the enhanced-resolution clustering detects subspots with high underlying immunofluorescence stain intensity and refines the boundary between immune-rich and immune-poor areas.

To quantify the improvement at enhanced resolution, we compared the distribution of immunofluorescence intensity between subspots that changed classification after enhancement (for

Fig. 3 | Enhanced-resolution clustering identifies tumor-proximal lymphoid tissue in a melanoma sample. a, The original histopathological annotations of H&E-stained tissue ($N=1$ tissue section, $n=293$ spots) revealed a section of melanoma (black) adjacent to tumor-proximal lymphoid tissue (yellow) and a region of stroma (red), separating these from a larger section of tumor-distal lymphoid tissue (yellow)[2]. Adapted from ref. [2] with permission from the American Association for Cancer Research. Spatial clustering (**b**) and enhancement (**c**) generate biologically meaningful spatial domains corresponding to the original annotations. Enhanced-resolution clustering identified tumor-proximal lymphoid tissue (cluster 4, yellow), which was not resolved at spot-level clustering. **d**, Differential expression analysis between the four clusters highlighted spatial differences in the expression of immune genes, cancer markers and genes encoding extracellular matrix proteins. **e**, For each of the five major cell types, the observed total spot-level expression (as measured by the summed log-normalized counts) of the defined marker genes (left) is shown alongside the corresponding enhanced-resolution expression (right). We show spatial expression plots for tumor cells (*PMEL*), fibroblasts (*COL1A1*), macrophages (*CD14*, *FCGR1A*, *FCGR1B*), B cells (*CD19*, *MS4A1*) and T cells (*CD2*, *CD3D*, *CD3E*, *CD3G*, *CD7*).

example, immune rich at the spot level and immune poor after enhancement) and subspots that maintained their classification (for example, immune rich at both the spot and subspot level). We found a significant difference in the intensity of subspots that changed classification compared to those that maintained their spot-level status (Fig. 4e,j), indicating that BayesSpace's resolution enhancement

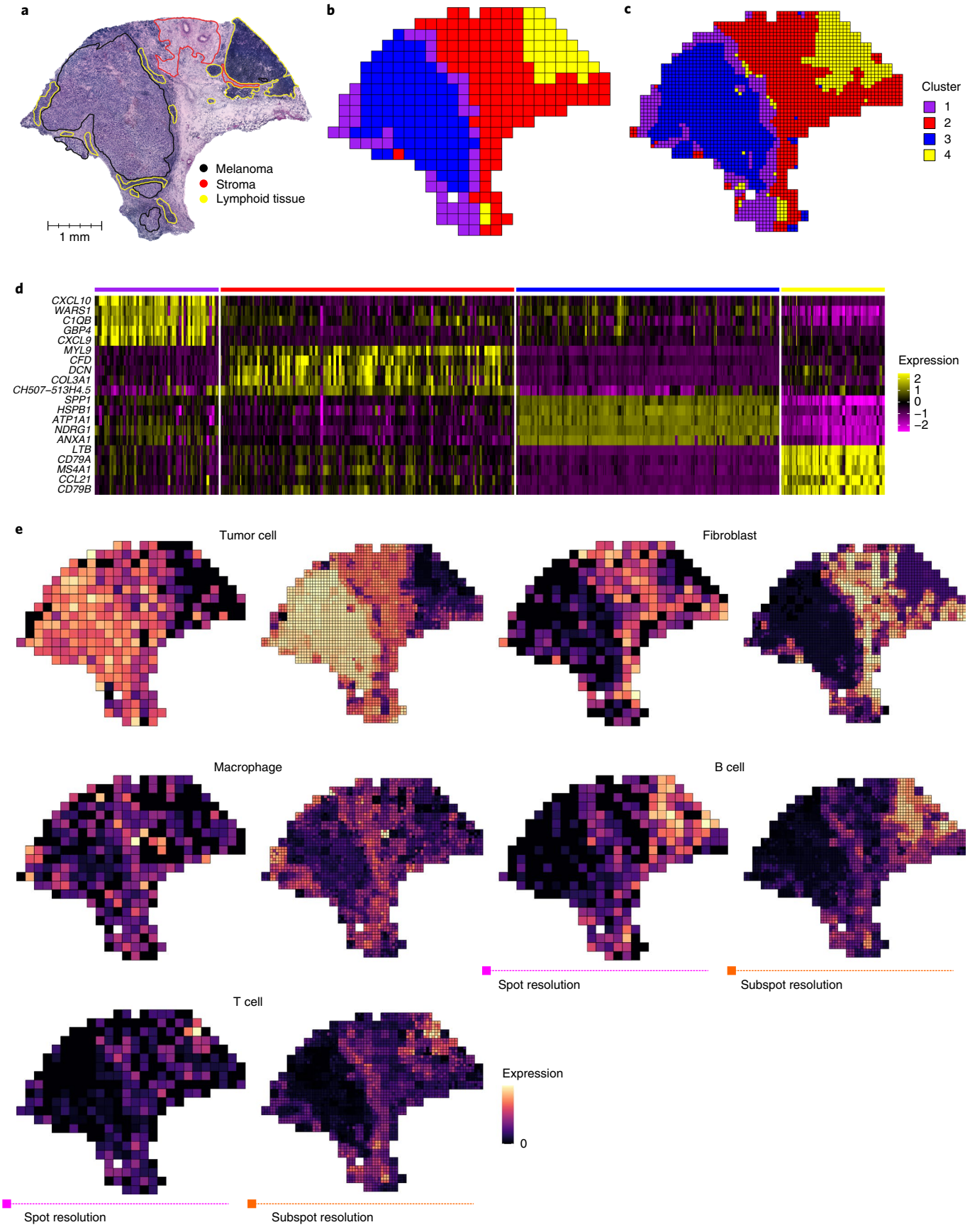

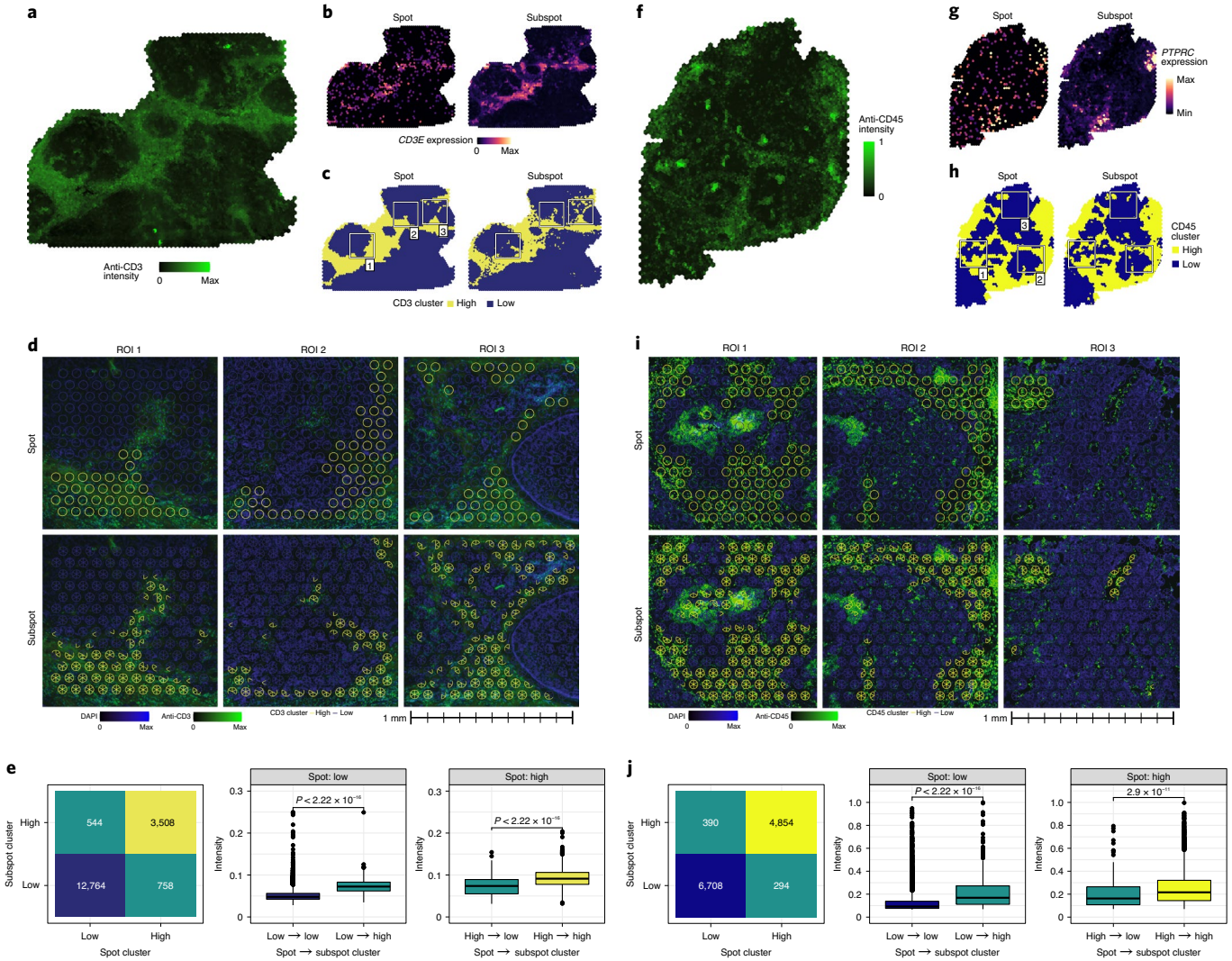

Fig. 4 | Immunohistochemistry validates BayesSpace enhancement in an IDC sample and an OC sample. a, Average intensity of the anti-CD3 immunofluorescent stain in the IDC. Intensity was scaled to the range (0,1) for visualization. **b**, Log-normalized gene expression of *CD3E* measured on the Visium platform (left, 'spot') and enhanced with BayesSpace (right, 'subspot'). **c**, Dichotomized clustering of Visium gene expression values. After clustering the tissue section into ten clusters, the clusters were binned by their median anti-CD3 stain intensity into CD3 'high' and CD3 'low' clusters, shown here. White squares outline three ROI where the enhanced clustering revealed areas of increased heterogeneity. **d**, Zoomed-in views of the $n=3$ ROI. Each panel shows a 1-mm^2 area of the immunofluorescence image. DAPI intensity is shown in blue, and anti-CD3 intensity is shown in green. Overlaid on each panel in the top row is the spot-level clustering. Each circle corresponds to the position and size (55-μm diameter) of a spot on the Visium array and is colored based on whether it belongs to a CD3 'high' (yellow) or CD3 'low' (blue) cluster. The bottom row contains a similar overlay of the enhanced-resolution subspot clustering, where the circles are now subdivided into six wedges corresponding to the positions of subspots in the BayesSpace model. As in the spot overlay, the subspots are colored based on their cluster membership. **e**, Summary of subspot reassignment after enhancement. On the left, we show a contingency table describing the number of subspots ($n=17{,}574$) that belong to a CD3 'high' or 'low' cluster at the spot level and at the subspot level. Using two-sided Wilcoxon rank-sum tests, we also show that anti-CD3 intensity in subspots that are reassigned to a 'high' cluster is significantly higher ($P<2.22\times10^{-16}$) than that in those that remain in a 'low' cluster (center) and that subspots that are reassigned to a 'low' cluster have a significantly lower ($P<2.22\times10^{-16}$) anti-CD3 intensity than that in those that remain in a 'high' cluster (right). **f**–**j**, Panels for the OC mirror those for the IDC, with anti-CD45 intensity replacing anti-CD3 intensity and *PTPRC* (CD45) gene expression replacing that of *CD3E*. In **e**, we show $n=12{,}246$ subspots. In **i**, we show $n=3$ ROI. In **j**, using two-sided Wilcoxon rank-sum tests, we show that anti-CD45 intensity in subspots that are reassigned to a 'high' cluster is significantly higher ($P<2.22\times10^{-16}$) than that in those that remain in a 'low' cluster (center) and that subspots that are reassigned to a 'low' cluster' have a significantly lower ($P=2.9\times10^{-11}$) anti-CD45 intensity than that in those that remain in a 'high' cluster (right). All reported *P* values are unadjusted values.

improves the accuracy of expression-based clustering with respect to an orthogonal immunohistochemistry signal.

BayesSpace distinguishes intratumoral heterogeneity in IDC. We further analyzed the IDC tissue section to identify clusters of biological relevance. Pathologist annotation identified regions of predominantly invasive carcinoma (IC), carcinoma in situ and benign hyperplasia, from which we derived ground-truth labels for each spot (Fig. 5a and Supplementary Fig. 11). The clusters were largely consistent with histopathological annotations (cluster purity = 0.839; Fig. 5b and Supplementary Figs. 9 and 11), and we identified five clusters that corresponded to annotated regions of

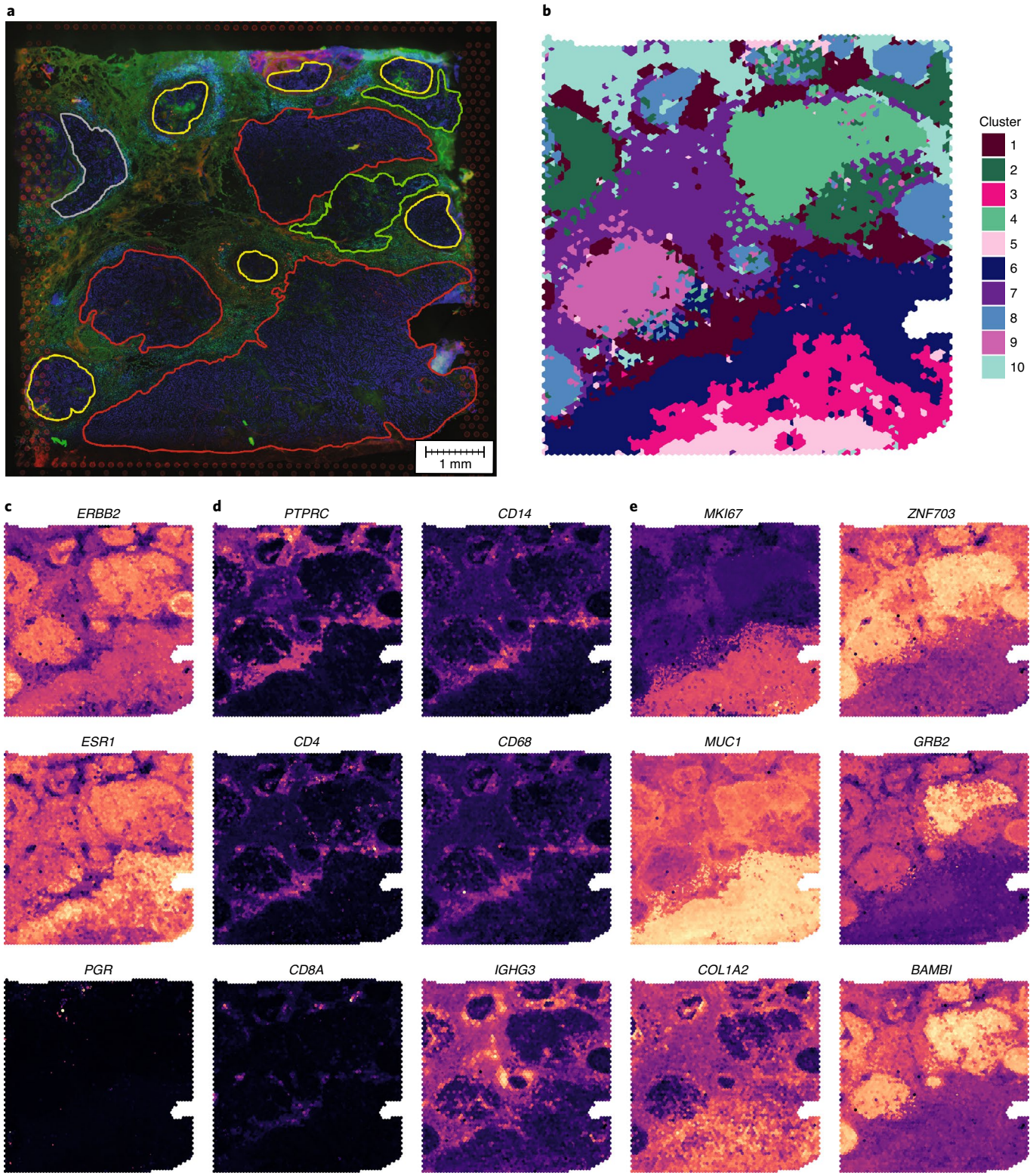

Fig. 5 | BayesSpace identifies transcriptional heterogeneity within an IDC. a, Immunofluorescent imaging of the tissue section ($N=1$ tissue section, $n=4{,}727$ spots) and histopathological annotations. DAPI intensity is shown in blue, anti-CD3 intensity is shown in green, and the Visium fiducial frame is shown in red. Annotated regions of IC are outlined in red, those of carcinoma in situ are outlined in yellow, those of benign hyperplasia are outlined in green, and those of unclassified tumor are outlined in gray. **b**, Enhanced BayesSpace clustering. **c**, Spatial expression of genes coding for HER2 (*ERBB2*) and ER (*ESR1*) and PR (*PGR*). **d**, Spatial expression of immune genes *PTPRC* (CD45), *CD4*, *CD8A*, *CD14*, *CD68* and *IGHG3*. **e**, Spatial expression of proliferation marker *MKI67* (Ki-67), markers of tumor progression *MUC1* and *COL1A2*, the oncogene *ZNF703*, *GRB2* (coding for the growth factor receptor protein) and *BAMBI* (coding for transforming growth factor (TGF)-β pseudoreceptor).

predominantly IC (3–6 and 9), one cluster that encompassed all annotated regions of carcinoma in situ (8), one cluster that coincided with the annotated benign hyperplasia and an invasive-appearing area (2) and three clusters corresponding to predominantly non-tumor areas (1, 7 and 10; Supplementary Fig. 11). We note that, without hematoxylin and eosin (H&E) stains or an immunofluorescent stain for a tumor marker, the tumor–stroma interface could not be fully delineated histologically and BayesSpace's enhanced clustering identified heterogeneity within the tissue that was not reflected in the annotated boundaries but was clearly supported by key tumor marker genes (Fig. 5c–e). This further supports our previous validation with immunofluorescence (Fig. 4).

Spatial expression patterns of known marker genes and differential expression analysis between these clusters were largely in accord with clinical and histopathological annotations. Consistent with the clinical report of $ER^+PR^-HER2^+$ IDC, we observed high expression levels of genes coding for HER2 (*ERBB2*) and ER (*ESR1*) throughout the tumor clusters and minimal expression of the gene coding for PR (*PGR*) in the sample (Fig. 5c and Supplementary Fig. 12). The non-tumor clusters 1, 7 and 10 were characterized by the expression of immune genes, with *PTPRC* (leukocyte-common antigen CD45) highly expressed in these clusters. We found that these clusters corresponded to distinct spatial transcriptional patterns. Cluster 1 was enriched for signatures of cell-mediated immunity, including marker genes expressed by T cells (*CD4*, *CD8A*, *CD8B*) and macrophages (*CD14*, *CD68*), while clusters 7 and 10 were enriched for genes involved in humoral immunity, particularly those encoding immunoglobulin chains (for example, *IGHG3*; Fig. 5d and Supplementary Figs. 12–15). Compared to other non-tumor clusters, cluster 7 was also enriched for expression of *ERBB2* and tumor-associated genes, such as *ZNF703*, suggesting that this cluster represents a mixture of tumor and immune cells. Analysis of non-tumor subspots (clusters 1, 7 and 10) with CIBERSORT was consistent with differential expression results, predicting subspots in cluster 1 to have a greater abundance of T cells, while clusters 7 and 10 had higher proportions of B and plasma cells (Supplementary Fig. 16).

We found similar heterogeneity within the invasive tumor clusters. Clusters 3, 5 and 6 displayed elevated expression of known markers of cell proliferation, including genes encoding Ki-67 (*MKI67*) and cyclins, as well as genes associated with tumor progression, invasion and proliferation, including *COL1A2* (refs. [29–31]), *MUC1* (refs. [32–35]) and *MMP11* (refs. [30,31,36]) (Fig. 5e and Supplementary Figs. 13, 15 and 17). Clusters 4 and 9 showed increased expression of *ZNF703*, an oncogene in the more aggressive, ER^+ luminal B breast cancer subtype[37,38] as well as that of *GRB2*, a gene implicated in breast cancer tumorigenesis[39,40] and *BAMBI*, encoding a pseudoreceptor for TGF-β[41], the signaling pathway of which is implicated in progression to invasion[32] (Fig. 5e). These spatial expression patterns suggest a transcriptional heterogeneity among compartments of invasive tumor inaccessible to histopathological analysis, demonstrating the superiority of spatial transcriptomic data over immunofluorescence alone.

BayesSpace enhances gene expression patterns to near single-cell resolution on in silico spatial data. We conducted several simulations to demonstrate that BayesSpace clustering and resolution enhancement outperform existing methods. In the first simulation, for which we simulated data modeled on two of our experimental datasets (see Methods for details), results showed that BayesSpace spot-level clustering consistently outperformed all other methods in both the simulated melanoma and ovarian datasets (Fig. 6a). Giotto, another spatial clustering method, also outperformed all non-spatial methods but provided slightly worse performance than BayesSpace. Among the non-spatial methods, mclust and Louvain clustering performed decently.

In the second simulation, we showed that BayesSpace enhanced-resolution clustering outperformed the optimal clustering that can be achieved at the spot level in melanoma and ovarian samples that were simulated at the subspot level (Fig. 6b). In each dataset, the enhanced clustering ARI exceeded the optimal spot-level clustering in all 20 simulated replicates. This indicates that BayesSpace is able to increase the resolution of data to better recapture finer details of the ground truth.

In the third simulation, we demonstrated that BayesSpace enhanced-resolution clustering can increase the resolution of data that were simulated from real, aggregated single cells (see Methods for details). BayesSpace captures the spatial distribution of clusters better than optimal spot-level clustering, as illustrated in the spatial representation of enhanced clustering results from one replicate (Fig. 6c). In regions with high mixing of cell types, there is little to no information available to resolve cluster labels at the subspot level, but BayesSpace is still able to closely approximate the overall tissue structure at the spot level. In these cases, although it is easy to miss isolated cells due to the signal being diluted out from the aggregation of multiple cells at the spot level, we found that BayesSpace was still able to recover some of these populations. The simulation results further supported our melanoma analyses in which our enhanced analysis recovered lymphoid structure near the tumor that was not apparent at the spot level. In all, BayesSpace enhanced clusters recapture the ground truth better than all other methods, again highlighting the superior performance of our method (Fig. 6d) and showing that BayesSpace is able to successfully enhance the resolution of spot-level data.

Enhanced-resolution clustering resolves keratinocyte structure in squamous cell carcinoma. Finally, we also used BayesSpace to analyze a squamous cell carcinoma Visium sample first described by Ji et al.[42]. H&E-stained tissue annotated by a pathologist revealed tumor borders and other major tissue structures (Supplementary Fig. 18). We defined expression profiles for the major cell types present in the sample based on known marker genes from the literature: keratinocytes (*KRT1*, *KRT5*, *KRT10*, *KRT14*), melanocytes (*MLANA*, *DCT*, *PMEL*), myeloid cells (*LYZ*) and T cells (*CD2*, *CD3D*, *CD3E*, *CD3G*, *CD7*)[28,42]. Keratinocytes were further separated into basal keratinocytes (*KRT5*, *KRT14*) and suprabasal keratinocytes (*KRT1*, *KRT10*), as products of *KRT5* and *KRT14* form heterodimers that localize to the basal layer of the epidermis, while products of *KRT1* and *KRT10* form heterodimers that localize to the suprabasal layer[43]. We show that our enhanced spatial gene expression plots delineate the border between the basal and suprabasal layers more precisely than spot-level plots (Supplementary Figs. 18 and 19) and similarly find that the enhanced expression of marker genes for melanocytes, myeloid cells and T cells better match the expected patterns based on annotated tissue structures (Supplementary Fig. 18).

Discussion

BayesSpace seamlessly integrates into the spatial transcriptomic analysis workflow by taking as input preprocessed data via the widely used Bioconductor SingleCellExperiment data structure. The output is likewise stored in a SingleCellExperiment object that can be used for downstream analyses. The methods are all implemented as an R package that is openly accessible on Bioconductor.

We have demonstrated the utility of BayesSpace in identifying spatial clusters with similar expression profiles and enhancing the resolution of spatial transcriptomics. BayesSpace overcomes both the challenge in efficiently using spatial information to inform the clustering of expression data and the limited resolution of current spatial transcriptomic technology. While there are similarities in the spatial prior specification between BayesSpace and Giotto (HMRF), we highlight several differences between the methods. BayesSpace is a spatial transcriptomic model-based clustering method that uses a t-distributed error model to identify spatial clusters that are more robust to the presence of outliers caused by

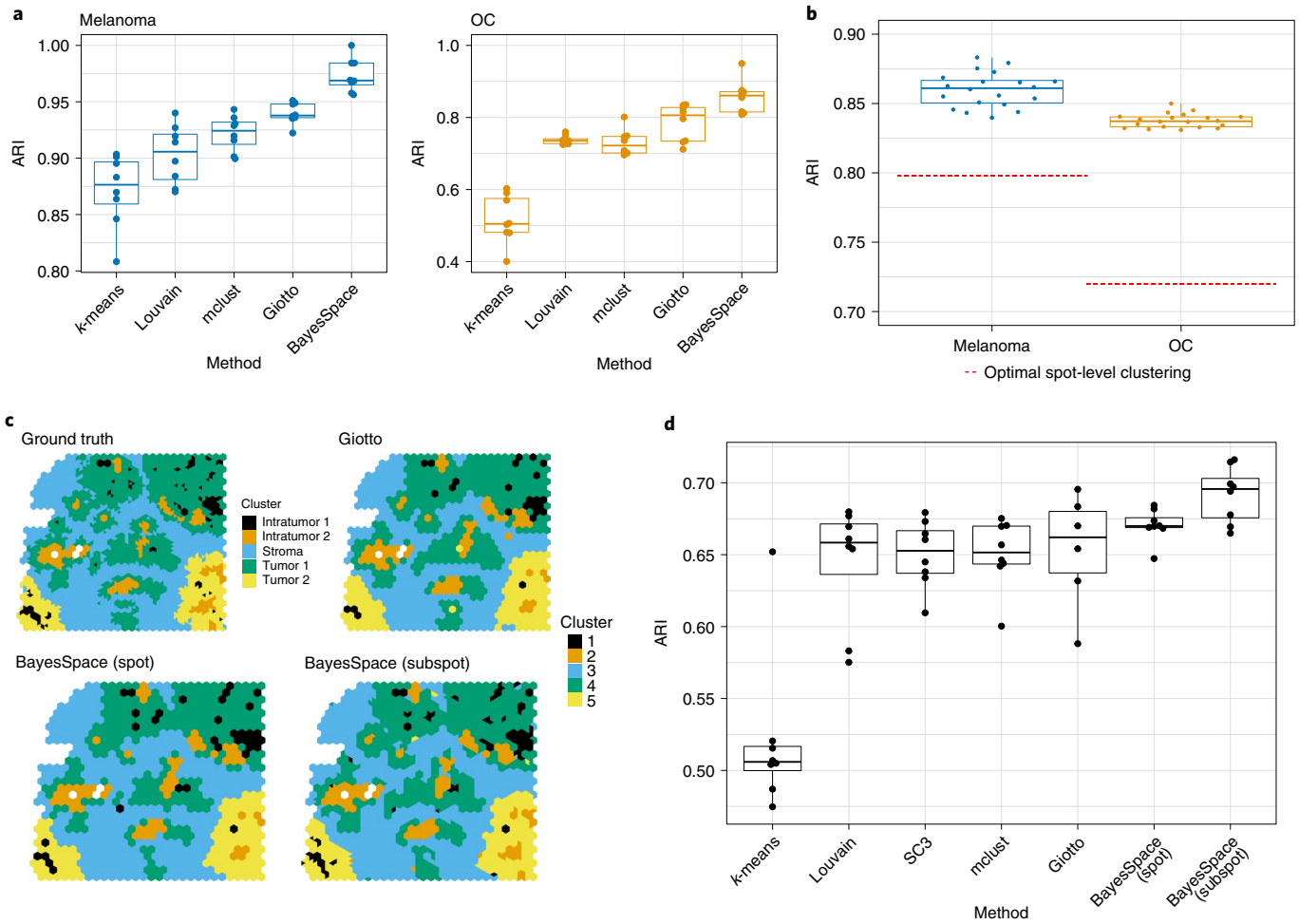

Fig. 6 | BayesSpace outperforms spatial and non-spatial clustering methods with simulated data. a, In $N=8$ replicates simulated from the melanoma sample and $N=8$ replicates simulated from the OC sample, BayesSpace spot-level clustering outperforms other clustering methods. **b**, In $N=20$ replicates for the simulation performed at the subspot level, BayesSpace enhanced clustering outperforms the optimal spot-level clustering (red dotted line). **c**, In the third simulation using single-cell data, the ground truth is derived from expert annotation of an immunofluorescence staining image corresponding to the OC sample (top left). Examples of clustering partitions generated by BayesSpace at the spot and subspot levels as well as by the next best method (Giotto) are also shown. **d**, BayesSpace clustering at the spot level slightly outperforms competing methods, while BayesSpace enhancement to the subspot level generally provides substantially higher performance than that of other methods in recapturing ground-truth clusters among the $N=8$ simulation replicates. In all boxplots, the center line, box limits and whiskers denote the median, upper and lower quartiles and 1.5× interquartile range, respectively.

technical noise. BayesSpace also uses Markov chain Monte Carlo (MCMC) to estimate model parameters, while HMRF uses expectation–maximization, which might not explore the space as efficiently[44]. BayesSpace also differs from Giotto (HMRF) in that it uses a fixed precision matrix rather than a variable precision matrix across clusters, which we found to improve the stability of estimates without compromising clustering performance (Supplementary Fig. 20) and in that it uses a more reliable method for detecting the spatial neighborhood network.

Studies have not achieved subspot resolution of spatial transcriptomic data without requiring the use of additional information aside from spatial coordinates. Immunohistochemical analyses in the IDC and OC tissue sections provide validation that our subspot model accurately refines and reflects the spatial structure of the underlying tissue. Enhancement of gene expression analysis at subspot resolution allows downstream differential expression analyses to compare finer and more biologically meaningful clusters. Our analyses of differential expression in the IDC tissue section identify transcriptional heterogeneity within regions of invasive tumor that appear histologically indistinct. While histological analysis of this tissue was limited by available immunofluorescent stains, notably lacking a tumor marker or H&E stains, our results suggest the potential for spatial transcriptomics and BayesSpace to capture previously uncharacterized spatial patterns of gene expression.

The resolution enhancement approaches single-cell resolution, with approximately three cells per subspot for data acquired with the Visium platform, without the need for external single-cell data. However, there is potential for the enhanced data to be integrated with external single-cell data through deconvolution or label-transfer methods. For example, it may be possible to enhance the resolution of spot-level cell-type proportion estimates by using a Dirichlet regression model with enhanced PCs as predictors. Integration with single-cell data has the potential to improve our ability to resolve cell types in dense and complex tissues, and it is a future direction of our research.

While our work focused on the ST and Visium platforms from 10x Genomics, BayesSpace should be applicable to other platforms in which spots are arranged on a lattice. Slight modifications may be needed so that our spatial model can be used with a different neighborhood structure. Because BayesSpace models a lower-dimensional

representation of data (that is, principal component analysis (PCA)), it should also be applicable to other dimensional-reduction techniques such as uniform manifold approximation and projection and possibly be applied to other data types such as protein markers and multiomics. Finally, it may also be possible to extend BayesSpace to jointly cluster spots from multiple samples given appropriate data normalizations.

Online content

Any methods, additional references, Nature Research reporting summaries, source data, extended data, supplementary information, acknowledgements, peer review information; details of author contributions and competing interests; and statements of data and code availability are available at https://doi.org/10.1038/s41587-021-00935-2.

Received: 10 September 2020; Accepted: 26 April 2021;
Published online: 3 June 2021

References

1. Ståhl, P. L. et al. Visualization and analysis of gene expression in tissue sections by spatial transcriptomics. *Science* **353**, 78–82 (2016).
2. Thrane, K., Eriksson, H., Maaskola, J., Hansson, J. & Lundeberg, J. Spatially resolved transcriptomics enables dissection of genetic heterogeneity in stage III cutaneous malignant melanoma. *Cancer Res.* **78**, 5970–5979 (2018).
3. Berglund, E. et al. Spatial maps of prostate cancer transcriptomes reveal an unexplored landscape of heterogeneity. *Nat. Commun.* **9**, 2419 (2018).
4. Maynard, K. R. et al. Transcriptome-scale spatial gene expression in the human dorsolateral prefrontal cortex. *Nat. Neurosci.* **24**, 425–436 (2021).
5. Janosevic, D. et al. The orchestrated cellular and molecular responses of the kidney to endotoxin define a precise sepsis timeline. *eLife* **10**, e62270 (2021).
6. Saiselet, M. et al. Transcriptional output, cell types densities and normalization in spatial transcriptomics. *J. Mol. Cell Biol.* **12**, 906–908 (2020).
7. Lubeck, E., Coskun, A. F., Zhiyentayev, T., Ahmad, M. & Cai, L. Single-cell in situ RNA profiling by sequential hybridization. *Nat. Methods* **11**, 360–361 (2014).
8. Chen, K. H., Boettiger, A. N., Moffitt, J. R., Wang, S. & Zhuang, X. Spatially resolved, highly multiplexed RNA profiling in single cells. *Science* **348**, aaa6090 (2015).
9. Rodriques, S. G. et al. Slide-seq: a scalable technology for measuring genome-wide expression at high spatial resolution. *Science* **363**, 1463–1467 (2019).
10. Hu, K. H. et al. ZipSeq: barcoding for real-time mapping of single cell transcriptomes. *Nat. Methods* **17**, 833–843 (2020).
11. Gavin, J. & Jennison, C. A subpixel image restoration algorithm. *J. Comput. Graph. Stat.* **6**, 182–201 (1997).
12. Ripley, B. D. The use of spatial models as image priors. In *Spatial Statistics and Imaging: Papers from the Research Conference on Image Analysis and Spatial Statistics held at Bowdoin College, Brunswick, Maine, Summer 1988* **20**, 309–340 (Institute of Mathematical Statistics, 1991).
13. Tipping, M. E. & Bishop, C. M. Bayesian image super-resolution. In *Proc. 15th Int. Conf. Neural Information Processing Systems* (eds. Becker, S., Thrun, S. & Obermayer, K.) 1303–1310 (2002).
14. Andersson, A. et al. Single-cell and spatial transcriptomics enables probabilistic inference of cell type topography. *Commun. Biol.* **3**, 565 (2020).
15. Cable, D. M. et al. Robust decomposition of cell type mixtures in spatial transcriptomics. *Nat. Biotechnol.* https://doi.org/10.1038/s41587-021-00830-w (2021).
16. Elosua-Bayes, M., Nieto, P., Mereu, E., Gut, I. & Heyn, H. SPOTlight: seeded NMF regression to deconvolute spatial transcriptomics spots with single-cell transcriptomes. *Nucleic Acids Res.* https://doi.org/10.1093/nar/gkab043 (2021).
17. Zhu, Q., Shah, S., Dries, R., Cai, L. & Yuan, G. C. Identification of spatially associated subpopulations by combining scRNAseq and sequential fluorescence in situ hybridization data. *Nat. Biotechnol.* **36**, 1183–1190 (2018).
18. Dries, R. et al. Giotto: a toolbox for integrative analysis and visualization of spatial expression data. *Genome Biol.* **22**, 78 (2021).
19. Pham, D. T. et al. stLearn: integrating spatial location, tissue morphology and gene expression to find cell types, cell–cell interactions and spatial trajectories within undissociated tissues. Preprint at *bioRxiv* https://doi.org/10.1101/2020.05.31.125658 (2020).
20. Besag, J. *On the statistical analysis of dirty pictures. J. R. Stat. Soc. Ser. B* **48**, 259–279 (1986).
21. Gottardo, R., Besag, J., Stephens, M. & Murua, A. Probabilistic segmentation and intensity estimation for microarray images. *Biostatistics* **7**, 85–99 (2006).
22. Amezquita, R. A. et al. Orchestrating single-cell analysis with Bioconductor. *Nat. Methods* **17**, 137–145 (2020).
23. Fraley, C., Raftery, A. E. & Murphy, T. B. mclust version 4 for R: normal mixture modeling for model-based clustering, classification, and density estimation. *R. J.* **8**, 289–317 (2012).
24. Blondel, V. D., Guillaume, J. L., Lambiotte, R. & Lefebvre, E. Fast unfolding of communities in large networks. *J. Stat. Mech. Theory Exp.* **2008**, P10008 (2008).
25. Kiselev, V. Y. et al. SC3: consensus clustering of single-cell RNA-seq data. *Nat. Methods* **14**, 483–486 (2017).
26. Wang, H. X. et al. HSPB1 deficiency sensitizes melanoma cells to hyperthermia induced cell death. *Oncotarget* **7**, 67449–67462 (2016).
27. Mathieu, V. et al. The sodium pump α1 sub-unit: a disease progression-related target for metastatic melanoma treatment. *J. Cell. Mol. Med.* **13**, 3960–3972 (2009).
28. Tirosh, I. et al. Dissecting the multicellular ecosystem of metastatic melanoma by single-cell RNA-seq. *Science* **352**, 189–196 (2016).
29. Mori, K. et al. CpG hypermethylation of collagen type I α 2 contributes to proliferation and migration activity of human bladder cancer. *Int. J. Oncol.* **34**, 1593–1602 (2009).
30. Knudsen, E. S. et al. Progression of ductal carcinoma in situ to invasive breast cancer is associated with gene expression programs of EMT and myoepithelia. *Breast Cancer Res. Treat.* **133**, 1009–1024 (2012).
31. Lee, S. et al. Differentially expressed genes regulating the progression of ductal carcinoma in situ to invasive breast cancer. *Cancer Res.* **72**, 4574–4586 (2012).
32. Hu, M. et al. Regulation of in situ to invasive breast carcinoma transition. *Cancer Cell* **13**, 394–406 (2008).
33. Hattrup, C. L. & Gendler, S. J. MUC1 alters oncogenic events and transcription in human breast cancer cells. *Breast Cancer Res.* **8**, R37 (2006).
34. Besmer, D. M. et al. Pancreatic ductal adenocarcinoma mice lacking mucin 1 have a profound defect in tumor growth and metastasis. *Cancer Res.* **71**, 4432–4442 (2011).
35. Behrens, M. E. et al. The reactive tumor microenvironment: MUC1 signaling directly reprograms transcription of *CTGF*. *Oncogene* **29**, 5667–5677 (2010).
36. Zhang, X. et al. Insights into the distinct roles of MMP-11 in tumor biology and future therapeutics (Review). *Int. J. Oncol.* **48**, 1783–1793 (2016).
37. Holland, D. G. et al. *ZNF703* is a common luminal B breast cancer oncogene that differentially regulates luminal and basal progenitors in human mammary epithelium. *EMBO Mol. Med.* **3**, 167–180 (2011).
38. Sircoulomb, F. et al. *ZNF703* gene amplification at 8p12 specifies luminal B breast cancer. *EMBO Mol. Med.* **3**, 153–166 (2011).
39. Daly, R., Binder, M. & Sutherland, R. Overexpression of the *Grb2* gene in human breast cancer cell lines. *Oncogene* **9**, 2723–2727 (1994).
40. Tari, A. M., Hung, M. C., Li, K. & Lopez-Berestein, G. Growth inhibition of breast cancer cells by Grb2 downregulation is correlated with inactivation of mitogen-activated protein kinase in EGFR, but not in ErbB2, cells. *Oncogene* **18**, 1325–1332 (1999).
41. Onichtchouk, D. et al. Silencing of TGF-signalling by the pseudoreceptor BAMBI. *Nature* **401**, 480–485 (1999).
42. Ji, A. L. et al. Multimodal analysis of composition and spatial architecture in human squamous cell carcinoma. *Cell* **182**, 497–514 (2020).
43. Sümer, C., Boz Er, A. B. & Dinçer, T. Keratin 14 is a novel interaction partner of keratinocyte differentiation regulator: receptor-interacting protein kinase 4. *Turk. J. Biol.* **43**, 225–234 (2019).
44. Liu, W. Unsupervised learning approaches for the finite mixture models: EM versus MCMC. In *2010 International Conference on Cyber-Enabled Distributed Computing and Knowledge Discovery* **2010**, 498–501 (IEEE, 2010).

Methods

Data description. We applied BayesSpace to samples from five spatial gene expression datasets, of which four were generated on the newer Visium platform. All Visium samples that were obtained directly from 10x Genomics were procured from BioIVT:ASTERAND. Details on dataset processing and availability are provided in the Supplementary Information. The first dataset included twelve human DLPFC samples from three individuals run on the Visium platform[4]. Briefly, each sample contained approximately 4,000 spots that were manually annotated to belong to one of six DLPFC layers or white matter. The second dataset involved melanoma samples run on the ST platform[2]. From this dataset, we analyzed the second replicate from biopsy 1 because it contained regions annotated as lymphoid tissue and was also described extensively in the original paper. Biopsy 1 contains 293 spots covered by tissue. The third dataset is publicly available from the 10x Genomics website and includes matching Visium spatial gene expression (3,493 spots) and immunofluorescence staining of an endometrial adenocarcinoma of the ovary. The sample was stained with an anti-cytokeratin antibody, an anti-human CD45 antibody and DAPI. The fourth dataset is from an IDC sample prepared on the Visium platform (4,727 spots) and stained with an anti-human CD3 antibody and DAPI. The final dataset included data from ten human skin squamous cell carcinomas profiled on either the ST or the Visium platform[42]. Among the two samples run on the Visium platform, we chose to analyze that from patient 4 (P4) as the data quality was higher as shown in the original paper. Sample P4 contains 722 spots covered by tissue.

Preprocessing and dimension reduction. In all datasets, raw gene expression counts were log transformed and normalized using library size[45,46]. PCA was then performed on the top 2,000 most HVGs. Two thousand HVGs provided the best clustering performance in our benchmarks (Supplementary Fig. 21). In downstream analyses, we modeled the top 15 PCs from the Visium libraries, and we modeled the top seven PCs from the sample prepared on the ST platform (melanoma). The choice to model PCs rather than the full gene expression profile allows for a more tractable probabilistic model, avoiding the need for cumbersome multivariate discrete distributions. PCs are commonly used in clustering analysis of gene expression data. Here, we recommend modeling the top 15 PCs to capture as much of the variability in the data as possible while limiting the rapid increase in space that occurs with higher dimensions, although users may choose to model a different number of PCs or HVGs using the BayesSpace R package. Modeling more than 15 PCs did not provide substantial improvements in clustering performance but increased runtime and memory usage in our benchmarks (Supplementary Fig. 21). In the melanoma sample, many of the higher PCs exhibited higher numbers of extreme outliers (Supplementary Fig. 22) and significantly less variance, suggesting that they most likely represent technical variability. Because the older ST technology has lower coverage, sequencing depth and throughput, fewer PCs are necessary for modeling.

Spatial clustering model. BayesSpace implements a fully Bayesian model with a Markov random field before encouraging spots of the same cluster to be close to one another. Such models have been widely used in image analysis, including analyses of microarray images[20,21]. ST and Visium spots are arranged on square and hexagonal lattices, which provide a natural way to define a neighborhood structure (Fig. 1b). For each spot i, a low d-dimensional representation y_i (for example, PCs) of the gene expression vector can be obtained. We model the data as follows:

$$(y_i|z_i = k, w_i) \sim N\left(y_i;\mu_k, w_i^{-1}\Lambda^{-1}\right)$$

$z_i \in \{1, \ldots, q\}$ denotes the latent cluster that i belongs to, μ_k denotes the mean vector for cluster k, Λ denotes the precision matrix, and w_i denotes an unknown (observation-specific) scaling factor. We assume a common (fixed) precision matrix across clusters because the number of unknown parameters in the precision matrix quickly rises with higher numbers of clusters and numbers of PCs modeled. In practice, we found that the variable precision model often required strong priors for parameter estimation. We also assume that the common precision matrix is unconstrained as there is correlation between PCs after conditioning on cluster, even though PCs are marginally uncorrelated (Supplementary Fig. 20). On real data, variable and independent precision models both performed poorly relative to the unconstrained, fixed precision model.

The number of clusters q is determined by prior biological knowledge when available or otherwise by the elbow of the pseudo-log-likelihood plot (Supplementary Figs. 9 and 10). We place the following priors on μ_k, Λ and w_i:

$$\mu_k \overset{\text{i.i.d.}}{\sim} N\left(\mu_0, \Lambda_0^{-1}\right),$$

$$\Lambda \overset{\text{i.i.d.}}{\sim} \text{Wishart}_d\left(\alpha, \text{diag}\left(\beta\right)_d^{-1}\right),$$

$$w_i \overset{\text{i.i.d.}}{\sim} \Gamma\left(\tfrac{\nu}{2}, \tfrac{\nu}{2}\right),$$

where μ_0, Λ_0, α and β are fixed hyperparameters. By default, we set μ_0 to be the empirical mean vector of the data, which is generally the zero vector for PCA input. Λ_0 is set to 0.01 times the identity matrix to provide a weak prior that will be dominated by the data when there are spots assigned to the cluster. Similarly, we set $\alpha = 1$ and $\beta = 0.01$ to provide a weak prior for the precision matrix. ν denotes a fixed degrees-of-freedom parameter to control the heaviness of tails and was set to $\nu = 4$, which was previously shown to overcome the influence of outlier spots during clustering[21]. We also assume that y_i and w_i are independent. As such, when marginalizing over w_i, our normal likelihood becomes a multivariable t distribution with a mean of 0 and covariance matrix $\frac{\nu}{\nu-2}\Lambda^{-1}$. This formulation allows us to use a simple Gibbs sampling for updating most of the parameters because the observations are normally distributed when conditioning on w_i. w_i values can also be interpreted as weights; the model will simply estimate a small weight value for any potential outlying data value. This provides robustness against outliers that can be commonly encountered in these types of data (Supplementary Fig. 2). Estimation of parameters is carried out using an MCMC method. We initialize $\boldsymbol{z}$ using a non-spatial clustering method such as mclust by default[23]. Alternative initializations can also be supplied as a label vector. Next, iteratively and sequentially, each μ_k, Λ and w_i is updated via Gibbs sampling, and each z_i is updated via the Metropolis–Hastings algorithm. Specifically, each z_i is updated by taking into account both the likelihood and spatial prior information. The Markov random field prior is given by the Potts model:

$$\pi\left(z_i\right) = \exp\left(\frac{\gamma}{\left|\langle ij\rangle\right|} \times 2\sum_{\langle ij\rangle} I\left(z_i = z_j\right)\right),$$

where $\langle i\, j\rangle$ denotes all spots j that are neighbors of i, I represents the indicator function, and γ is a fixed parameter controlling the strength of the smoothing. In this way, neighboring spots are encouraged to belong to the same cluster. Further details on the MCMC algorithm are provided in the Supplementary Information. Model fitting diagnostics are provided in Supplementary Figs. 2 and 20.

Spatial clustering model at enhanced resolution. To enhance the resolution of the clustering map, we segmented each spot into subspots and again leveraged spatial information using the Potts model spatial prior. Specifically, we segmented each ST spot into nine subspots and each Visium spot into six subspots (Fig. 1b). For ST, we used nine subspots to help increase the resolution of data from lower-resolution technology, because ST spots are 100 µm in diameter, while Visium spots are 55 µm in diameter. This translates into more than a threefold difference in area. In the IDC and OC samples, Visium spots are estimated to contain a median of around 20 cells; therefore, subspots will generally represent the expression of a few cells, rather than that of potentially dozens of cells at the spot level (Supplementary Figs. 7 and 8).

Relative to the spot-level clustering method, model specification and parameter estimation is largely similar for enhanced-resolution clustering, although the unit of analysis is now the subspot rather than the spot. As gene expression is not observed at the subspot level, it is modeled as another latent variable that is also estimated through MCMC. The latent expression of each subspot j that is part of spot i is denoted as y_{ij}^*, initialized to be y_i and then updated via the Metropolis–Hastings algorithm. In each iteration and for each spot, the new proposal is given by $y_{ij}^{*\prime} = y_{ij}^* + \varepsilon_{ij}$ for each subspot, such that the error $\varepsilon_{ij} \sim N(0, \sigma^2 I_d)$, where σ^2 is a small fixed parameter and $\sum_j \varepsilon_{ij} = 0$. In effect, this jitters the latent expression value of each subspot within a spot while keeping the total expression of the spot fixed. The proposal is accepted or rejected based on the conditional likelihood of the proposal given the other parameters. We set σ^2 such that the acceptance rate ranges from 25% to 40% of iterations on average to maximize the efficiency of the Metropolis–Hastings algorithm[47]. A weak Gaussian prior is placed on the latent expression to ensure that the jittered values do not drift too far away from y_i. Aside from replacing y_i with y_{ij}^*, all other steps of the MCMC algorithm remain the same as in the spot-level clustering method. Model fitting diagnostics are provided in Supplementary Fig. 20. Intuitively, the enhancement procedure reassigns the total expression within a spot to its constituent subspots by leveraging spatial information, ultimately generating a higher-resolution spatial clustering map.

Mapping high-resolution PCs to high-resolution gene expression space. While BayesSpace can provide higher-resolution maps of spatial transcriptomic patterns, the modeling is carried out on the PC space, and an additional step is necessary to map the PC values back to the original log-normalized gene expression space. BayesSpace implements two options for predicting high-resolution gene expression: linear regression and nonlinear regression using XGBoost (default)[48]. In either case, a model is trained for each gene for which the outcome is the measured gene expression at the spot level and the predictors are the PCs generated from the original data. The fitted model can then be used to predict gene expression from the high-resolution PCs estimated using enhanced-resolution clustering. The enhanced gene expression values can be visualized spatially and analyzed via differential expression methods (Fig. 1a). In our analyses, we used the two-sided Wilcoxon rank-sum test as implemented in Seurat to identify the top differentially expressed genes, and also we used Seurat for heatmap visualization of the centered and scaled gene expression values[49].

Simulations. Using several simulations, we evaluated the performance of BayesSpace. The first simulation compared BayesSpace spot-level clustering to other non-spatial and spatial clustering methods: *k*-means, Louvain, mclust, SC3 and Giotto. We could not evaluate stLearn in simulation due to the need for an image as input. The simulated data were based on the melanoma and OC samples introduced in the earlier results. Eight replicates of simulated melanoma and OC PCs were generated from *t*-distributions with means, precision and spot labels determined by spot-level clustering results of the real melanoma and OC samples, respectively (Fig. 3b and Supplementary Fig. 23). Other clustering methods were implemented as described in the Supplementary Information with the true cluster number provided as input. BayesSpace was also implemented with the true cluster number provided as input. Performance was assessed using the ARI between ground-truth spot labels and clustering results.

In the second simulation, we evaluated the performance of BayesSpace subspot-level enhanced clustering. We simulated 20 replicates from *t*-distributions with means, precision and labels based on real melanoma and OC samples, but, unlike for the previous simulation, we generated subspots using the enhanced clustering results as the ground truth (Figs. 3c and 4d). The simulated subspot-level PCs were averaged to provide spot-level PCs that were given as input to BayesSpace. We can use the modal ground-truth label of the subspots within each spot to generate an optimal spot-level clustering for each dataset (Supplementary Fig. 23). The ARI between this optimal spot-level clustering and the subspot-level ground truth represents the highest ARI that can be achieved when all subspots within a spot must belong to the same cluster, as is the case with spot-level clustering.

In the third simulation, we sampled data from real single cells rather than simulating PCs. Here, we sampled single cells from scRNA-seq profiling of patients with high-grade serous OC (HGSOC)[50]. The single cells can be sampled into subspots on the OC Visium sample, providing another way to evaluate the performance of BayesSpace clustering and enhancement relative to other methods without relying on model-based data generation. Given the limited number of single cells, we used only the positions from a portion of the OC Visium sample. Ground-truth cluster labels were derived from expert single-cell level annotation of tumor and stroma compartments within the immunofluorescence stain image associated with the OC sample. In each subspot, the ground truth was assigned using the modal annotation of the single cells located within the subspot. Consequently, the ground-truth assignment takes into account gaps between spots in spatial transcriptomic technologies, and the clusters represent realistic biological spatial domains.

To add complexity to the simulation, we separated the tumor compartment into two ground-truth clusters and introduced two additional intratumoral clusters that represent heterogeneity within tumors. Thus, the simulation included a total of five spatial ground-truth clusters, including the stroma compartment cluster. The single-cell sampling strategy is shown in Supplementary Table 1, with single cells randomly drawn from single-cell clusters into corresponding spatial clusters in each of the eight simulation replicates. As raw counts were not available in the HGSOC dataset, pseudocounts were obtained by back transforming log-normalized counts, and simulated data were generated by aggregating across all subspots within a spot. The data were then processed to generate PCs as described for real data in the Methods. Because HGSOC single-cell clusters are very well separated, we also added random noise to each simulated PC equal to 25% of its variance, thus adding additional complexity to our simulation. This process also made our simulation more realistic when comparing the generated PCs to PCs derived from experimental data (Supplementary Fig. 22).

Reporting Summary. Further information on research design is available in the Nature Research Reporting Summary linked to this article

Data availability

Datasets analyzed in this paper are available in raw form from their original authors (see details in the Supplementary Note), and the SingleCellExperiment objects that we prepared for analysis with BayesSpace are available through the BayesSpace package. Raw count matrices, images and spatial data from the IDC sample are accessible on the 10x Genomics website at https://support.10xgenomics.com/spatial-gene-expression/datasets.

Code availability

BayesSpace is available as a Bioconductor package at http://www.bioconductor.org/packages/release/bioc/html/BayesSpace.html, and the source code is publicly available at https://github.com/edward130603/BayesSpace.

References

45. Lun, A. T. L., Bach, K. & Marioni, J. C. Pooling across cells to normalize single-cell RNA sequencing data with many zero counts. *Genome Biol.* **17**, 75 (2016).
46. McCarthy, D. J., Campbell, K. R., Lun, A. T. L. & Wills, Q. F. Scater: pre-processing, quality control, normalization and visualization of single-cell RNA-seq data in R. *Bioinformatics* **33**, 1179–1186 (2017).
47. Gelman, A., Roberts, G. O. & Gilks, W. R. Efficient Metropolis jumping rules. *Bayesian Stat.* **5**, 599–607 (1996).
48. Chen, T. & Guestrin, C. XGBoost: a scalable tree boosting system. In *Proceedings of the ACM SIGKDD International Conference on Knowledge Discovery and Data Mining* 785–794 (Association for Computing Machinery, 2016).
49. Stuart, T. et al. Comprehensive integration of single-cell data. *Cell* **177**, 1888–1902 (2019).
50. Izar, B. et al. A single-cell landscape of high-grade serous ovarian cancer. *Nat. Med.* **26**, 1271–1279 (2020).

Acknowledgements

This research was supported by funding from the National Institutes of Health (P01-CA225517, P30-CA015704 to R.G. and P.N.; T32-CA080416, F30-CA254168 to T.P.), the Immunotherapy and Data Science Integrated Research Centers at Fred Hutchinson to E.Z., M.R.S., X.R. and J.H.B. and the Scientific Computing Infrastructure at Fred Hutchinson funded by ORIP grant S10OD028685. We thank M. Lin and P.L. Porter for their pathological review of J.G.'s histological annotations, K.J. Cheung from the Fred Hutchinson Public Health Sciences and Human Biology Divisions for his suggestions in our analysis of the IDC sample, A. Moshiri from the UW Division of Dermatology for his review of T.P.'s histopathological annotations and Q. Nguyen and X. Tan at the University of Queensland for their assistance in applying stLearn.

Author contributions

E.Z. and R.G. formulated the method and wrote the paper. M.R.S. and E.Z. developed software. E.Z., M.R.S. and X.R. analyzed data. J.G., K.S.S. and T.P. contributed to annotation and interpretation of cancer samples. C.R.U., S.R.W. and S.E.B.T. prepared and contributed to analysis of the IDC sample. P.N., J.H.B. and R.G. supervised the project.

Competing interests

R.G. has received consulting income from Juno Therapeutics, Takeda, Infotech Soft, Celgene and Merck, has received research support from Janssen Pharmaceuticals and Juno Therapeutics and declares ownership in Ozette Technologies and stock ownership in 10x Genomics. S.R.W., C.R.U. and S.E.B.T. are employees of and hold shares in 10x Genomics. All other authors declare no conflicts of interest.

Additional information

Supplementary information The online version contains supplementary material available at https://doi.org/10.1038/s41587-021-00935-2.

Correspondence and requests for materials should be addressed to R.G.

Peer review information *Nature Biotechnology* thanks the anonymous reviewers for their contribution to the peer review of this work.

Reprints and permissions information is available at www.nature.com/reprints.

nature research

Corresponding author(s): Raphael Gottardo

Last updated by author(s): Apr 1, 2021

Reporting Summary

Nature Research wishes to improve the reproducibility of the work that we publish. This form provides structure for consistency and transparency in reporting. For further information on Nature Research policies, see our Editorial Policies and the Editorial Policy Checklist.

Statistics

For all statistical analyses, confirm that the following items are present in the figure legend, table legend, main text, or Methods section.

n/a	Confirmed	
☐	☒	The exact sample size (*n*) for each experimental group/condition, given as a discrete number and unit of measurement
☐	☒	A statement on whether measurements were taken from distinct samples or whether the same sample was measured repeatedly
☐	☒	The statistical test(s) used AND whether they are one- or two-sided *Only common tests should be described solely by name; describe more complex techniques in the Methods section.*
☒	☐	A description of all covariates tested
☐	☒	A description of any assumptions or corrections, such as tests of normality and adjustment for multiple comparisons
☐	☒	A full description of the statistical parameters including central tendency (e.g. means) or other basic estimates (e.g. regression coefficient) AND variation (e.g. standard deviation) or associated estimates of uncertainty (e.g. confidence intervals)
☐	☒	For null hypothesis testing, the test statistic (e.g. *F*, *t*, *r*) with confidence intervals, effect sizes, degrees of freedom and *P* value noted *Give P values as exact values whenever suitable.*
☐	☒	For Bayesian analysis, information on the choice of priors and Markov chain Monte Carlo settings
☒	☐	For hierarchical and complex designs, identification of the appropriate level for tests and full reporting of outcomes
☐	☒	Estimates of effect sizes (e.g. Cohen's *d*, Pearson's *r*), indicating how they were calculated

Our web collection on statistics for biologists contains articles on many of the points above.

Software and code

Policy information about availability of computer code

Data collection	No software was used.
Data analysis	Snakefiles and scripts used to process each dataset are available at https://github.com/msto/spatial-datasets, and processed datasets are accessible via the BayesSpace::getRDS() method. The BayesSpace software package was used to analyze the data. The BayesSpace software package has been submitted to Bioconductor, and the source code is publicly available at https://github.com/edward130603/BayesSpace. Immunofluorescence images were processed using Indica Labs HALO (High-plex FL module v3.2.1).

For manuscripts utilizing custom algorithms or software that are central to the research but not yet described in published literature, software must be made available to editors and reviewers. We strongly encourage code deposition in a community repository (e.g. GitHub). See the Nature Research guidelines for submitting code & software for further information.

Data

Policy information about availability of data

All manuscripts must include a data availability statement. This statement should provide the following information, where applicable:

- Accession codes, unique identifiers, or web links for publicly available datasets
- A list of figures that have associated raw data
- A description of any restrictions on data availability

The published datasets analyzed in this paper are available in raw form through their original authors (see details in Supplementary Information). The SingleCellExperiment objects we prepared for analysis with BayesSpace are available through the BayesSpace package.
• Dorsolateral prefrontal cortex
- Spatial data (Maynard et al. 2021). Figure 2. A SingleCellExperiment object containing the counts and spatial coordinates for all samples was downloaded using the spatialLIBD::fetch_data() method and then subset by sample.

• Melanoma
- Spatial data (Thrane et al. 2018). Figure 3. Counts matrices were downloaded from the Spatial Research website (https://www.spatialresearch.org/wp-content/uploads/2019/03/ST-Melanoma-Datasets_1.zip). Array row/column coordinates were obtained from the column labels of these matrices. An aligned image and pixel coordinates were not available for this sample.

• Invasive ductal carcinoma
- Spatial data (10x Genomics). Figures 4, 5. The counts matrix and spatial data generated by the SpaceRanger pipeline, along with the immunofluorescence stain image, were acquired from 10x Genomics. Raw counts matrices, images, and spatial data will be made accessible on GEO upon the publication of this manuscript.

• Ovarian cancer
- Spatial data (10x Genomics). Figure 4. The counts matrix and spatial data generated by the SpaceRanger pipeline, along with the immunofluorescence stain image, were downloaded from 10x Genomics' website. Data and details of the sample preparation and staining are available at https://support.10xgenomics.com/spatial-gene-expression/datasets/1.2.0/Parent_Visium_Human_OvarianCancer

• Squamous cell carcinoma
- Spatial data (Ji, Rubin, et al. 2020). Supplementary Figure 18. A counts matrix containing expression profiles from all samples and tissue positions were downloaded from GEO (accession GSE144239).

Field-specific reporting

Please select the one below that is the best fit for your research. If you are not sure, read the appropriate sections before making your selection.

☒ Life sciences ☐ Behavioural & social sciences ☐ Ecological, evolutionary & environmental sciences

For a reference copy of the document with all sections, see nature.com/documents/nr-reporting-summary-flat.pdf

Life sciences study design

All studies must disclose on these points even when the disclosure is negative.

Sample size	For the brain data, all twelve published samples were included in our analyses. For the melanoma data, we analyzed the ST sample that was analyzed the most in the original paper (Thrane et al., 2018). For OC, we analyzed the only whole-transcriptome sample available on the 10x Genomics website. For IDC, we had access to two replicates but chose to analyze the sample that had better imaging quality. For the SCC data, we analyzed the Visium sample that was of higher sequencing quality and was analyzed the most in the original paper (Ji et al., 2020). For all datasets, we used all spots that were detected to have expression as determined by the original publication.
Data exclusions	For each biopsy/slide, we used all spots that were detected to have expression as determined by the original publication. No data were excluded.
Replication	For the brain results, findings are replicated in 12 samples. For the cancer results, analyses were performed on four samples from different platforms and further supported by a number of simulation results based on the cancer data, each of which involves 8-20 replicates.
Randomization	Not relevant to the study since each biopsy/slide is analyzed separately. Any between-sample differences are not relevant since comparisons only involve groups of ST or Visium spots from a single biopsy/slide.
Blinding	J.G., K.S., and T.P., who annotated the histology and immunofluorescence features of the tumor samples, were blinded to the corresponding spatial transcriptomics data until they finished annotations.

Reporting for specific materials, systems and methods

We require information from authors about some types of materials, experimental systems and methods used in many studies. Here, indicate whether each material, system or method listed is relevant to your study. If you are not sure if a list item applies to your research, read the appropriate section before selecting a response.

Materials & experimental systems

n/a	Involved in the study
☒	☐ Antibodies
☒	☐ Eukaryotic cell lines
☒	☐ Palaeontology and archaeology
☒	☐ Animals and other organisms
☒	☐ Human research participants
☒	☐ Clinical data
☒	☐ Dual use research of concern

Methods

n/a	Involved in the study
☒	☐ ChIP-seq
☒	☐ Flow cytometry
☒	☐ MRI-based neuroimaging

A Proof-of-Concept Study of Combination Therapy with INCMGA00012 (Anti–PD-1), INCAGN02385 (Anti–LAG-3), and INCAGN02390 (Anti–TIM-3) in Participants with Advanced or Metastatic PD(L)-1 refractory Merkel Cell Carcinoma

University of Washington, Seattle WA
Shailender Bhatia, MD (Principal Investigator)
Natalie Miller, MD, PhD (Co-Investigator)

Incyte Biosciences International

Title:
A Proof-of-Concept Study of Combination Therapy with INCMGA00012 (Anti–PD-1), INCAGN02385 (Anti–LAG-3), and INCAGN02390 (Anti–TIM-3) in Participants with Advanced or Metastatic PD(L)-1 refractory Merkel Cell Carcinoma

Investigators:
Primary investigators: Natalie Miller, MD PhD (Senior oncology fellow) and Shailender Bhatia, MD (Professor, Medical oncology)
Co-Investigators: Ted Gooley, PhD (Professor, Biostatistics); Thomas Pulliam (MD-PhD student); Paul Nghiem, MD PhD (Professor, Dermatology); Incyte scientific team

Institutions:
University of Washington and Fred Hutchinson Cancer Center, Seattle, WA (USA)

Background and Rationale:
Merkel cell carcinoma (MCC) is an aggressive neuroendocrine skin cancer often caused by the Merkel cell polyomavirus (MCPyV). Tumors with both virus-positive and virus-negative MCC are often highly immunogenic and respond well to immune checkpoint inhibitor therapy, with an overall response rate (ORR) to first line systemic treatment with PD(L)-1 blockade of 40-56% (DiAngelo S, *JITC* 2021; Nghiem P, *NEJM* 2016). Approximately 3 in 4 responding patients will have durable responses > 6 months. However, there is a large unmet need for treatments for the >50% of MCC patients who experience disease progression despite PD(L)-1 blockade. Ipilimumab alone or in combination with PD-1 blockade has been investigated in PD-1 refractory MCC, but efficacy appears to be limited with ORR reported to be from 0% to 31% in relatively small number of patients (LoPiccolo J, *JITC* 2019; Shalout S, *JImmunot* 2022; Kim S, *Lancet* 2022).

Novel checkpoint inhibition via blockade of Lymphocyte Activation Gene-3 (LAG-3) and T-cell immunoglobulin mucin-3 (TIM-3) pathways holds significant promise. In a Phase III study with metastatic melanoma patients, combination of LAG-3 and PD-1 inhibition was associated with improved progression-free survival (PFS) from 4.6 to 10.1 months compared to PD-1 blockade alone in the first line setting (Tawbi H, *NEJM* 2022). The combination was also associated with activity in PD-1 treated melanoma patients with an ORR of 11.5% (N=61); LAG-3 expression >1% appeared to enrich for responses with an ORR of 18% (N=33)(Ascierto P, *ESMO* 2017). Our laboratory data suggests that both LAG-3 and TIM-3 inhibitory pathways are active and likely relevant in MCC. Co-expression of TIM-3 and PD-1 is significantly higher by flow cytometry on both MCPyV-specific T cells from PBMC as well as tumor infiltrating lymphocytes, compared to CMV- or EBV-specific T cells from the same patients (Afanasiev O, *CCR* 2013). More recent analysis of PBMC (n = 9) and tumor (n = 3) from PD(L)-1 naïve patients using a highly multiplexed flow cytometry panel revealed a higher expression of TIM-3 on MCPyV-specific T cells versus all CD8 T cells (23% vs 2.2% in PBMC, p = 0.001; 40 vs 24% from TIL, p = 0.069). Similarly, LAG-3 is more frequently expressed on MCPyV-specific T cells compared to all CD8 T cells in these patient samples (3.8% vs 1.5% from PBMC, p= 0.051, and 20% vs 13% from TIL, p= 0.26) (Pulliam T, *unpublished)*. Lastly, surface expression of both LAG-3 and TIM-3 increased over time on MCPyV-specific T cells from a patient who progressed on PDL-1 blockade (quantify, Pulliam T, unpublished). These preliminary data support the hypothesis that blockade of LAG-3 and TIM-3 could enhance the MCC-specific cytotoxic T cell response, synergizing with PD(L)-1 blockade, to lead to clinical benefit in MCC patients.

Study Hypothesis:

Combination therapy with triple checkpoint inhibitor blockade including anti-PD-1 (INCMGA00012), anti-LAG-3 (INCAGN02385), and anti-TIM-3 (INCAGN02390) will lead to clinical benefit in patients with advanced or metastatic Merkel Cell Carcinoma who are refractory to PD(L)-1 monotherapy.

Study Population:

1. Patients must have a biopsy-proven Merkel cell carcinoma (MCC). Patients with either MCPyV-positive or negative tumors are eligible.
2. Age 18 or older
3. Performance status by Eastern Cooperative Oncology Group (ECOG) of 0-2
4. Patients must meet a definition of primary or secondary anti-PD(L)-1 refractory as follows (Kluger H, *JITC*):
    a. Primary refractory: best response of progressive disease (PD) or stable disease (SD) < 6 mo, after at least 6 weeks of therapy
    b. Secondary refractory: PD after best response of complete response (CR), partial response (PR), or SD for >6 months, after at least 6 months of therapy
5. Patients must not have a history of serious immune-related adverse events from prior immunotherapy that could jeopardize patient safety with triple combination.
6. Patients who have previously been treated with prior systemic chemotherapy and/or prior immunotherapy combinations (i.e. ipilimumab plus nivolumab) are eligible.

Study Design:

1. This is a single institution, open label, non-randomized proof-of-concept study.
2. We plan to enroll **20 patients** with PD(L)-1 refractory MCC to receive treatment with INCAGN02385 (350 mg) + INCAGN02390 (400mg) every two weeks, along with INCMGA00012 (500mg) given every 4 weeks (NOTE: final dose and schedule will be determined with Incyte team based on the available clinical data from the ongoing Phase I/2 trial INCAGN 2385-201).
3. Imaging will be performed every 8 weeks (± 2 weeks) for the first 12 months, then every 12 weeks (± 4 weeks) thereafter.
4. We will obtain serial peripheral blood mononuclear cells (PBMC) at baseline and at selected time-points post-treatment for correlative studies as below.
5. Serial tumor biopsies will be obtained, when feasible, at baseline, at 4 weeks post-treatment, and at progression for correlative studies as below.

Endpoints:

Primary endpoint:

- Overall response rate (ORR), defined as the percentage of participants having a CR or PR, will be determined by investigator assessment of radiographic disease assessments per RECIST v1.1.

Secondary endpoints:

- Duration of response (DOR), defined as the time from earliest date of disease response (CR or PR) until earliest date of disease progression, will be determined by investigator assessment of radiographic disease per RECIST v1.1, or death from any cause, if occurring sooner than progression
- Disease control rate (DCR), defined as percentage of participants having CR, PR, or SD as best on-study response.

- Progression free survival (PFS), defined as the time from date of first dose of study treatment until the earliest date of disease progression, as determined by investigator assessment of objective radiographic disease per RECIST v1.1
- Overall survival
- Incidence and severity of adverse events, including irAEs and surgical complications.

Correlative analyses

Correlative studies to better understand mechanisms of response and resistance to checkpoint blockade is a major focus of our MCC program and we plan to perform rigorous biomarker studies on precious samples from this proposed trial. Our laboratory has considerable expertise in isolating MCPyV-specific T cells from the vast majority (~95%) of patients' blood and tumor samples. This would allow us to quantify and phenotype antigen-specific CD8+ T cells and their clonal dynamics over the course of trial, using existing TCRseq (Adaptive Biosciences), 26-color multiplexed flow cytometry, and/or CyTOF panels on samples from PBMC and/or tumor. In addition, we propose to assess T cell function via ELISPOT and/or intracellular cytokine staining via flow cytometry. Tumor microenvironment studies could be done utilizing spatial transcriptomics (RNAseq) via a platform from 10X genomics, to assess the baseline and post-treatment inflammation in responding and non-responding patients. To this end, we will obtain serial peripheral blood samples and tumor biopsies, when clinically feasible, at baseline and post-treatment.

Statistical plans

The primary objective of this single-arm proof-of-concept clinical trial is to assess whether there is a signal associated with the proposed treatment such that a larger definitive trial might be warranted in the targeted patient population. The primary endpoint for these purposes will be the objective response rate (ORR). The study will not be powered in the traditional sense, as in the PD-1 refractory MCC setting there is wide range of response rates with various therapies, making it difficult to assign a particular benchmark on which to improve. Rather we propose to enroll 20 patients or enroll for 2 years, whichever comes first. We will target an observed ORR of 25% as an outcome considered to be sufficiently strong to warrant further study, as long as other metrics such as durability of response appear to be favorable. If the true ORR is 30% or 35%, the probability of observing an ORR of 25% or more (5 or more responses among 20 patients) is 0.76 and 0.88, respectively. If the true ORR is 15%, the probability of observing an ORR of 25% or more is 0.17. And with 20 patients, a two-sided 80% confidence interval for the estimated ORR will extend from 0.126 to 0.374 when the true ORR is 25%, so that with 20 patients the estimated ORR will be reasonably precise. If there is a sufficiently strong signal observed in this trial, the data will be used to inform the design of future definitive trial.

After 10 patients have been enrolled and followed sufficiently long to assess ORR, if there are no responses, consideration will be given to terminating the trial due to lack of efficacy. The probability of such an occurrence is 0.056 if the true ORR is 25%. The decision to terminate will consider the totality of the data, including durability of response.

Anticipated outcomes and future directions

To the best of our knowledge, this study will be the first-ever investigation of LAG-3 or TIM-3 blockade in MCC patients, and therefore, also the first investigation of triple checkpoint blockade against LAG-3, TIM-3 and PD-1. Observation of clinically meaningful anti-tumor activity in this proof-of-concept study could provide strong preliminary data for a multi-center, registrational trial in the ~50% of patients with advanced MCC who progress despite PD(L)-1 monotherapy. In addition, it may support a subsequent front-line investigation of triple

checkpoint blockade, compared to PD(L)-1 monotherapy, in patients with newly diagnosed advanced or metastatic MCC. Last but not the least, the correlative studies from this proposal, especially the phenotypic and functional studies of cancer-specific T cells in peripheral blood and in tumor microenvironment, should shed light on the relevance of TIM-3 and LAG-3 in cancer immunotherapy, with implications not just for MCC, but other cancers as well.

Study budget:

References:

1. D'Angelo SP, Lebbé C, Mortier L, et al. First-line avelumab in a cohort of 116 patients with metastatic Merkel cell carcinoma (JAVELIN Merkel 200): primary and biomarker analyses of a phase II study. Journal for ImmunoTherapy of Cancer 2021;9:e002646. doi:10.1136/jitc-2021-002646
2. Nghiem PT, Bhatia S, Lipson EJ, et al. PD-1 Blockade with Pembrolizumab in Advanced Merkel-Cell Carcinoma. N Engl JMed. 2016;374:2542–2552.
3. Pires da Silva I, Ahmed T, Reijers ILM, et al. Ipilimumab alone or ipilimumab plus anti-PD-1 therapy in patients with metastatic melanoma resistant to anti-PD-(L)1 monotherapy: a multicentre, retrospective, cohort study. Lancet Oncol. 2021; 22:836–847.
4. LoPiccolo J, Schollenberger MD, Dakhil S, et al. Rescue therapy for patients with anti-PD-1-refractory Merkel cell carcinoma: a multicenter, retrospective case series. J Immunother Cancer. 2019 Jul 8;7(1):170. doi: 10.1186/s40425-019-0661-6.
5. Shalhout SZ, Emerick KS, Kaufman HL, et al. A Retrospective Study of Ipilimumab Plus Nivolumab in Anti-PD-L1/PD-1 Refractory Merkel Cell Carcinoma J Immunother. 2022; 45:299-302.
6. Kim S, Wuthrick E, Blakaj D, et al. Combined nivolumab and ipilimumab with or without stereotactic body radiation therapy for advanced Merkel cell carcinoma: a randomised, open label, phase 2 trial. Lancet. 2022; https://doi.org/10.1016/S0140-6736(22)01659-2
7. Tawbi HA, Schadendorf D, Lipson EJ, et al. Relatlimab and Nivolumab versus Nivolumab in Untreated Advanced Melanoma. N Engl JMed. 2022; 386:24-34.
8. Ascierto PA, Bono P, Bhatia S, et al. Abstract 4998 - Efficacy of BMS-986016, a Monoclonal Antibody That Targets Lymphocyte Activation Gene-3 (LAG-3), in Combination With Nivolumab in Pts With Melanoma Who Progressed During Prior Anti–PD-1/PD-L1 Therapy (mel prior IO) in All-Comer and Biomarker-Enriched Populations. Annals of Oncology, 2017; 28 (suppl_5): v605-v649. 10.1093/annonc/mdx440
9. Afanasiev OK, Yelistratova L, Miller N, et al. Merkel polyomavirus-specific T cells fluctuate with merkel cell carcinoma burden and express therapeutically targetable PD-1 and Tim-3 exhaustion markers. Clin Cancer Res. 2013 Oct 1;19(19):5351-60.
10. Kluger HM, Tawbi HA, Ascierto ML, et al. Defining tumor resistance to PD-1 pathway blockade: recommendations from the first meeting of the SITC Immunotherapy Resistance Taskforce. Journal for ImmunoTherapy of Cancer 2020;8:e000398. doi:10.1136/ jitc-2019-000398

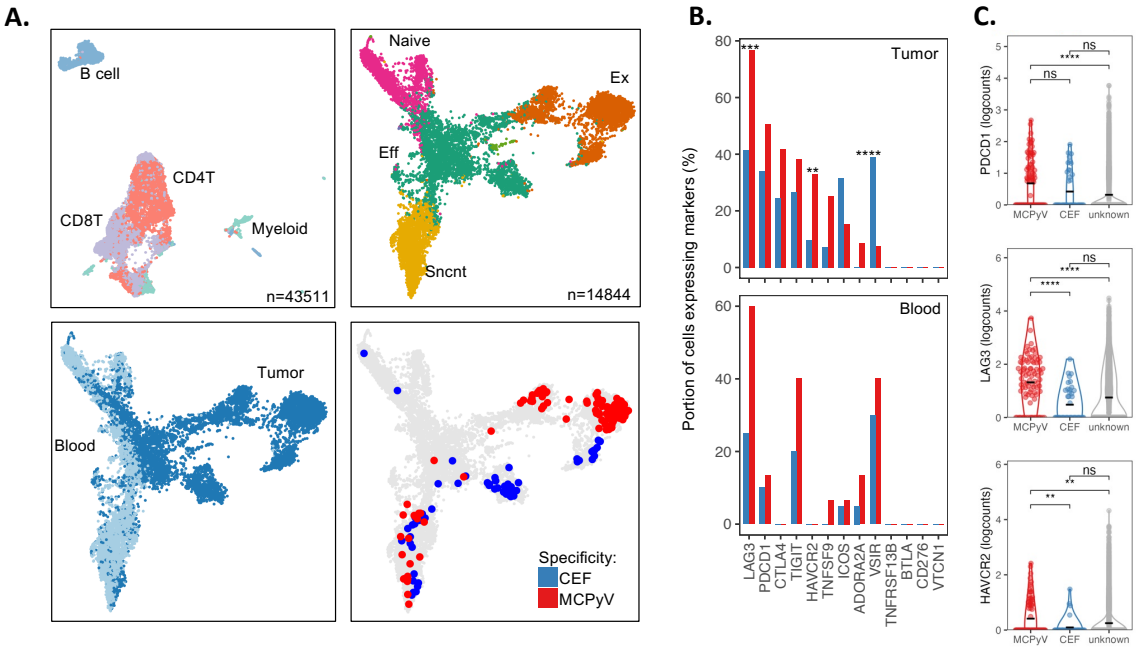

Figure 1. Single cell RNAseq of antigen-specific CD8 T cells and unbiased analyses of immune checkpoints on cancer-specific CD8 T cells. Tumor and blood specimens from 4 different patients were A. (top left) UMAP plot of all immune cells collected colored by major cell lineages. (top right) UMAP plot redrawn for CD8 T cells and clustered into major phenotypes. (bottom left) UMAP plot colored by anatomic origin of CD8 T cells. (bottom right) UMAP plot colored by known specificity of CD8 T cells mapped using CDR3s of known specificity.
B. Portions of MCPyV- or CEF-specific CD8 T cells that express each checkpoint molecule. Broken down by cells originating from tumor tissue (top) or blood (bottom)
C. Violin plot of experession of genes encoding PD-1, LAG3 and TIM3 in MCPyV-, or CEF-specific CD8 t cells or CD8 T cells of u,known specificity
Abbreviations: UMAP: uniform manifold approximation projection, MCPyV: Merkel cell polyomavirus, CEF: Cytomegalovirus, Epstein-Barr virus, or Influenza A, Eff: effector, Ex: Exhausted, Sncnt: senescent, CDR3: complementary determining region 3
Significance: P<0.0001: ****, p<0.001:***, p<0.01:**, p<0.05:*, p≥0.05: ns

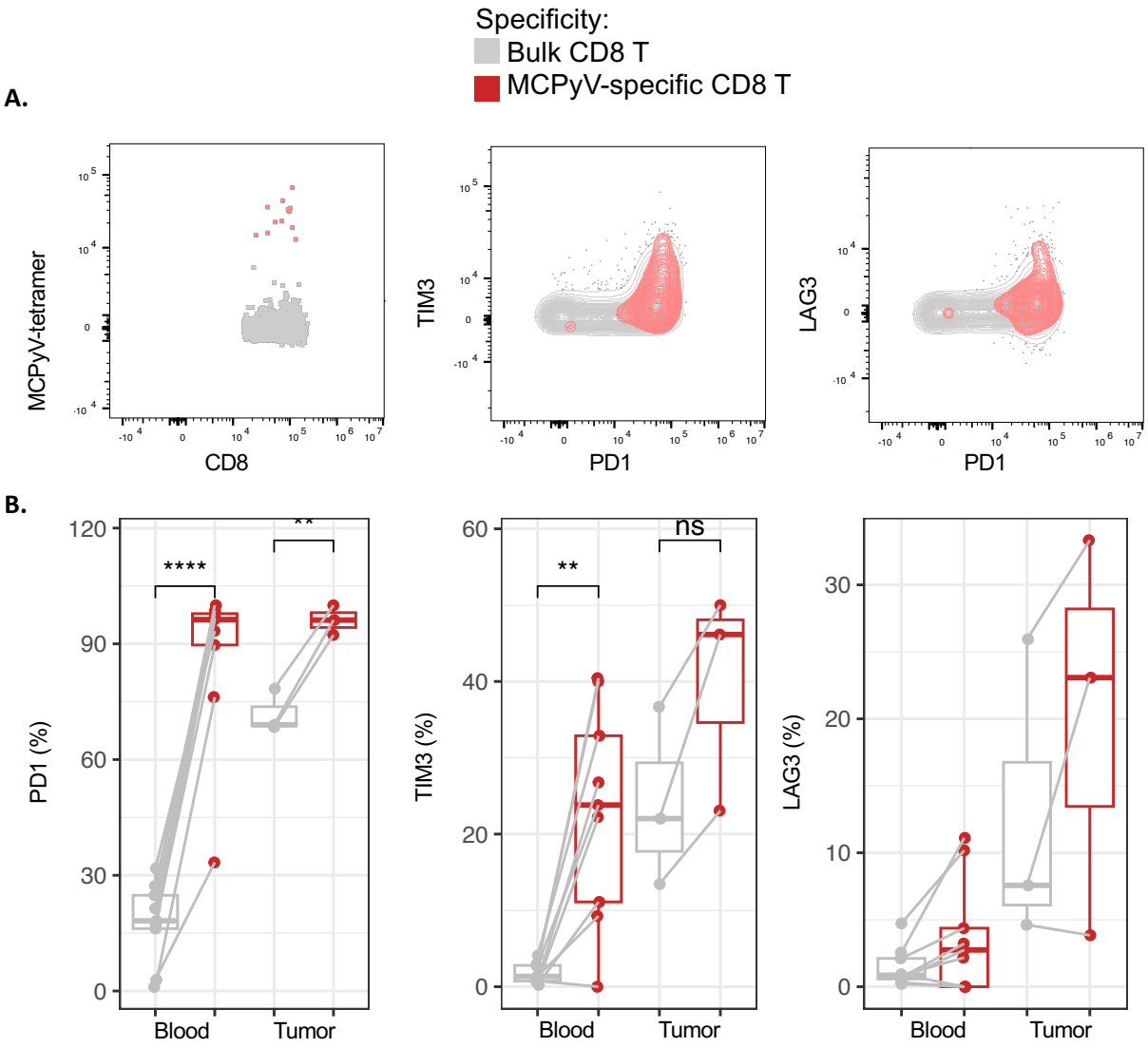

Figure 2. Cancer-specific CD8 T cells in tumors and blood express TIM3 and LAG3 proteins. Blood from 9 MCC patients immediately prior to receiving PD-1 pathway blockade and tumor samples from 3 immunotherapy naïve patients were stained using MHC tetramers and a highly multiplexed flow cytometry panel. Example FACS plots of Portions of different CD8 T cell populations positive for TIM3 (A) or LAG3 (B) are shown shown grouped by tissue source.

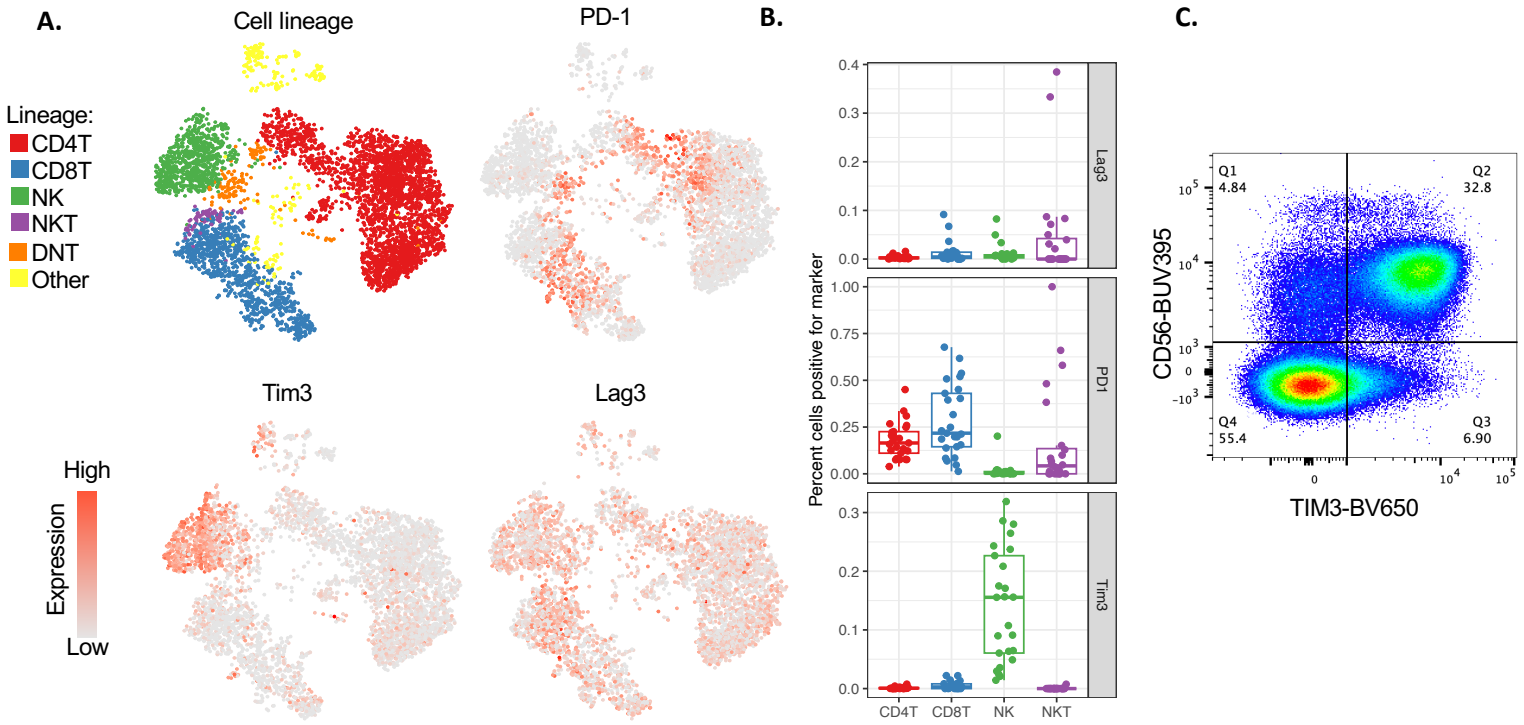

Figure 3. Expression of TIM3, LAG3 and PD-1 on Immune cell subsets.

A. A highly multiplexed flow cytometry panel was used to analyze blood specimens from 24 patients. Data was visualized on UMAP plots and cells were clustered into major cell lineages using phonograph clustering (top left). Protein expression of PD-1 TIM3, and LAG3 were visualized on the same projections.

B. Expression of LAG3, PD-1 and TIM3 in the major cell lineages visualized using box plots

C. FACS plot showing example staining of TIM3 on NK cell subset

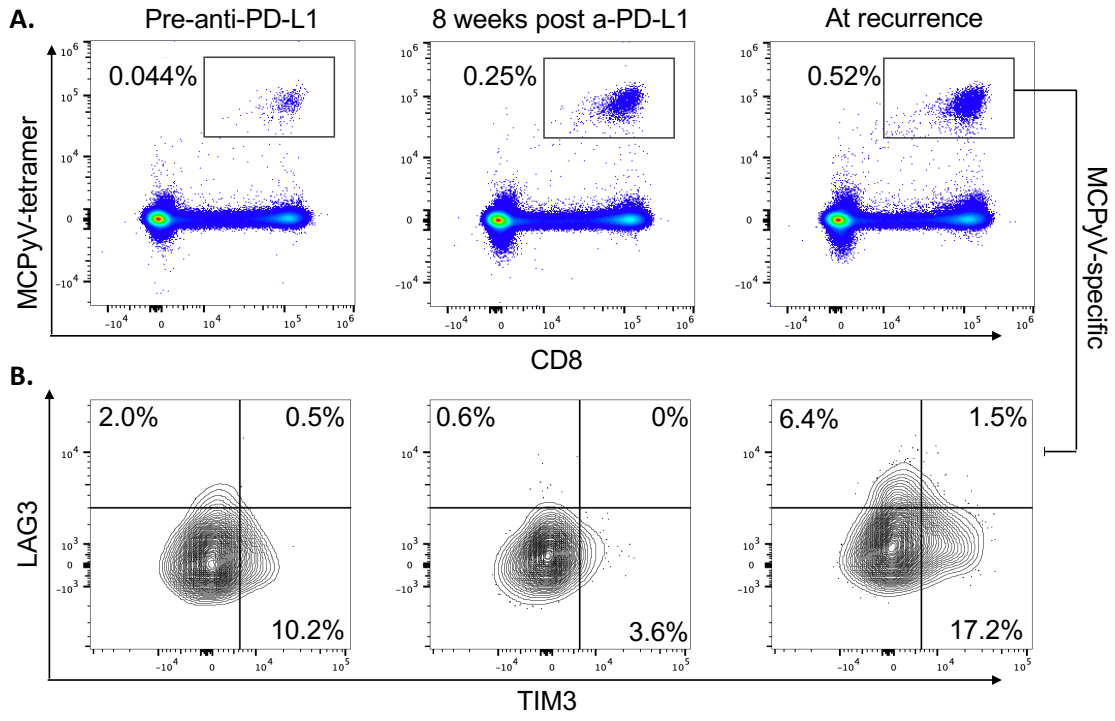

Figure 4. Cancer-specific CD8 T cells express TIM3 and LAG3 and these markers are increased following PD-1 pathway blockade failure. Serial blood draws were taken from a patient treated with avelumab (anti-PD-L1) who initially had a partial response to therapy but had a disease recurrence 16 months after starting therapy. These blood draws were stained using a highly multiplexed flow cytometry panel that included tetramers MHC containing peptides from the MCPyV tumor antigens.

A. MHC tetramer gating on CD3 T cells using an MHC B*37:01 restricted tetramer.

B. LAG3 and TIM3 expression on the tetramer positive cells in panel A.

Received: 4 February 2020 | Revised: 6 March 2020 | Accepted: 7 March 2020

DOI: 10.1002/mc.23190

IN PERSPECTIVE

Molecular Carcinogenesis WILEY

Polyomavirus-driven Merkel cell carcinoma: Prospects for therapeutic vaccine development

Shira Tabachnick-Cherny[1] | Thomas Pulliam[1] | Candice Church[1] | David M. Koelle[2,3,4,5,6] | Paul Nghiem[1,7,8]

[1]Department of Medicine, Division of Dermatology, University of Washington, Seattle, Washington

[2]Department of Medicine, Division of Allergy and Infectious Diseases, University of Washington, Seattle, Washington

[3]Translational Research Program, Benaroya Research Institute at Virginia Mason, Seattle, Washington

[4]Department of Laboratory Medicine, University of Washington, Seattle, Washington

[5]Department of Global Health, University of Washington, Seattle, Washington

[6]Vaccine and Infectious Diseases Division, Fred Hutchinson Cancer Research Center, Seattle, Washington

[7]Seattle Cancer Care Alliance, Seattle, Washington

[8]Clinical Research Division, Fred Hutchinson Cancer Research Center, Seattle, Washington

Correspondence
Paul Nghiem, MD, PhD, UW Medical Center at Lake Union, 850 Republican St, Seattle, WA 98109.
Email: pnghiem@uw.edu

Funding information
NIH, Grant/Award Numbers: NIH-P01-CA225517, NIH-T32-CA080416; Prostate Cancer Foundation Kelsey Dickson Team, Grant/Award Number: Science Courage Research Team Award; UW MCC Patient Gift Fund

Abstract

Great strides have been made in cancer immunotherapy including the breakthrough successes of anti-PD-(L)1 checkpoint inhibitors. In Merkel cell carcinoma (MCC), a rare and aggressive skin cancer, PD-(L)1 blockade is highly effective. Yet, ~50% of patients either do not respond to therapy or develop PD-(L)1 refractory disease and, thus, do not experience long-term benefit. For these patients, additional or combination therapies are needed to augment immune responses that target and eliminate cancer cells. Therapeutic vaccines targeting tumor-associated antigens, mutated self-antigens, or immunogenic viral oncoproteins are currently being developed to augment T-cell responses. Approximately 80% of MCC cases in the United States are driven by the ongoing expression of viral T-antigen (T-Ag) oncoproteins from genomically integrated Merkel cell polyomavirus (MCPyV). Since T-Ag elicits specific B- and T-cell immune responses in most persons with virus-positive MCC (VP-MCC), and ongoing T-Ag expression is required to drive VP-MCC cell proliferation, therapeutic vaccination with T-Ag is a rational potential component of immunotherapy. Failure of the endogenous T-cell response to clear VP-MCC (allowing clinically evident tumors to arise) implies that therapeutic vaccination will need to be potent anśd synergize with other mechanisms to enhance T-cell activity against tumor cells. Here, we review the relevant underlying biology of VP-MCC, potentially applicable therapeutic vaccine platforms, and antigen delivery formats. We also describe early successes in the field of therapeutic cancer vaccines and address several clinical scenarios in which VP-MCC patients could potentially benefit from a therapeutic vaccine.

KEYWORDS

cancer therapeutic vaccine, immunotherapy, MCPyV, Merkel cell carcinoma

1 | INTRODUCTION

Merkel cell carcinoma (MCC) is a rare neuroendocrine malignancy that typically occurs in the skin (recently reviewed by Harms et al[1]). The MCC recurrence rate ranges from 25% to 75% depending on the stage,[2] leading to a 33% to 46% disease-specific mortality.[3,4] The current incidence of MCC in the United States is ~2500 cases per year. However, a recent report documented a 95% increase in MCC incidence between the years 2000 and 2013, with ~3200 cases per year expected by 2025.[5] MCC has higher incidence rates among immunosuppressed populations and older persons with particularly elevated risk among Caucasian men.[1] The majority of MCC cases

[The corresponding author address is changed on April 02, 2020 after initial publication online]

(~80%) are associated with clonal integration of the Merkel cell polyomavirus (MCPyV) into the host genome.[6] The remaining ~20% of cases are caused by UV mutations alone and are associated with prolonged UV exposure.[1,7,8]

Primary MCPyV infection occurs during childhood. Infection is thought to be chronic, with viral DNA detected on the skin in more than 50% of healthy individuals.[9-12] The cell types infected[13] and possible health effects of commensal MCPyV infection require further study.

The most successful cancer vaccines to date are preventive vaccines for human papillomaviruses (HPV) and HBV. Because such a small minority of MCPyV-infected persons develop VP-MCC, a preventive vaccine for MCPyV is likely not cost-effective. In contrast, a therapeutic vaccine targeting the relevant MCPyV proteins may prevent disease recurrence and be helpful in specific populations with both limited and relapsed VP-MCC as detailed below.

2 | THE BIOLOGY OF POLYOMAVIRUS-DRIVEN MERKEL CELL CARCINOMA

Seroprevalence and viral detection studies indicate that MCPyV is widespread in healthy individuals (Figure 1). At baseline, healthy people have antibodies to certain MCPyV proteins, as indicated by the high prevalence of antibodies to viral capsid proteins.[15,16] In contrast, healthy individuals rarely have detectable antibody responses to MCPyV T-Ag (~1% of the population have borderline positive titers). This low immunogenicity of T-Ag may, in part, be due to limited expression of the T-Ag in the course of routine infection, and also the nuclear localization signal (NLS) within the C-terminal domain of the large T-Ag (LT) oncoprotein.[17] Nuclear targeting reduces antigen processing and presentation by HLA-class I, potentially accounting for low CD8 T-cell responses to T-Ag in healthy persons. In contrast to healthy individuals, patients with VP-MCC tumors often have T cells specific for MCPyV oncoproteins.[18] and also robust anti-T-Ag humoral immune responses.[16,19] Importantly, the magnitude of antibodies to MCPyV T-antigen oncoproteins (but not capsid proteins) correlates directly with tumor burden.[19] This association is the basis for a clinical test for tumor recurrence.[16,19] Such antibody responses suggest T-Ag oncoproteins are likely to be coordinated between helper CD4+ T cells and B cells, either in draining lymph nodes or potentially in organized lymphoid structures within or near tumors.[20-22]

Some studies demonstrate the presence of B cells in MCC tumors[23,24] and tertiary lymphoid structures (TLS), typically enriched with B cells, were identified in the periphery of MCC tumors.[24,25] The TLS in these MCC tumors contained CD4-, CD8-, and CD20-expressing cells (T and B cells), and correlated with recurrence-free survival.[24] The presence of TLS in VP-MCC may underlie the observed direct correlation of T-Ag antibodies with tumor burden if in fact T-Ag-specific B cells are activated within or reside in or near tumors. However, the roles of B cells and TLS remain understudied and further investigation is required to understand their function in MCC.

In order for MCPyV to cause VP-MCC, two rare events are required: (a) truncation of the large T (LT) antigen proximal to the C-terminal domains involved in viral DNA replication and (b) linearization and clonal integration of MCPyV into the host genome. After genome integration, VP-MCC tumors express a truncated form of LT protein, as well as full-length small T (ST) protein. Both T-Ag isoforms are involved in MCC tumor persistence and proliferation,[26,27] and drive tumorigenicity by distinct mechanisms. Truncation of the LT antigen deletes the helicase domain required for viral replication, preventing destruction of infected host cells through inappropriate DNA replication initiated within the viral sequence itself. Additionally, loss of NLS[28] results in redistribution of LT to the cytoplasm,[29] where it is accessible to the antigen processing machinery. Although MCPyV LT truncation mutations vary from patient to patient, the highly conserved N-terminal LXCXE motif that binds and inhibits the retinoblastoma tumor suppressor is invariably preserved.[30,31] Of interest, this motif may also bind the Stimulator of Interferon genes (STING) protein, and is preserved in other pathogenic viruses such as cancer-related human papillomavirus strains.[32] The ST antigen promotes cell survival and proliferation by multiple incompletely understood mechanisms. For example, the LT-stabilization domain (LSD) contributes by stabilization of truncated LT and induction of oncoproteins such as c-Myc and cyclin E.[33] A different mechanism of action to stabilization of the truncated LT by ST antigen was demonstrated in a recent study.[34] Additionally, ST can inhibit p53 activity in MCC cells via the canonical regulator of p53, MDM4.[35]

It is clear that VP-MCC survival is dependent on the continued expression of MCPyV T antigens. Indeed, many MCC patients have T-cell responses against ST and LT,[36-38] but tumors also downregulate class-I HLA,[39] suggesting not only dependence on oncoprotein T antigens for ongoing replication and survival but also active escape from immune pressure. This reliance on T-Ag expression and the presence of compensatory mechanisms suggests that MCPyV T-Ags provide an ideal target for a therapeutic vaccine if tumor immune evasion mechanisms can be overcome.

3 | MCPYV ONCOPROTEINS AS PROMISING TARGETS FOR IMMUNOTHERAPY

One of the major limitations in tumor immunology is the identification of appropriate tumor-specific immunological targets. Tumor neoepitopes are typically discovered through whole-exome sequencing, messenger RNA quantitation, and in silico prediction using patient HLA types. This complex, customized, and the expensive process has a challenging candidate-to-hit ratio.

Virus-induced cancers express "nonself" viral antigens that are foreign to the host, potentially increasing their inherent immunogenicity compared to overexpressed, nonmutated, tumor-associated antigens, such as NYESO-1. With a combined T-Ag oncoprotein size of approximately 400 amino acids and very little variation between MCPyV strains, several groups have used standard immunologic approaches to detect T-cell responses to MCPyV T-Ag.[36-38,40] Indeed, CD8 T cells appear to play a significant role in controlling MCC as patients who have brisk tumoral CD8 T-cell

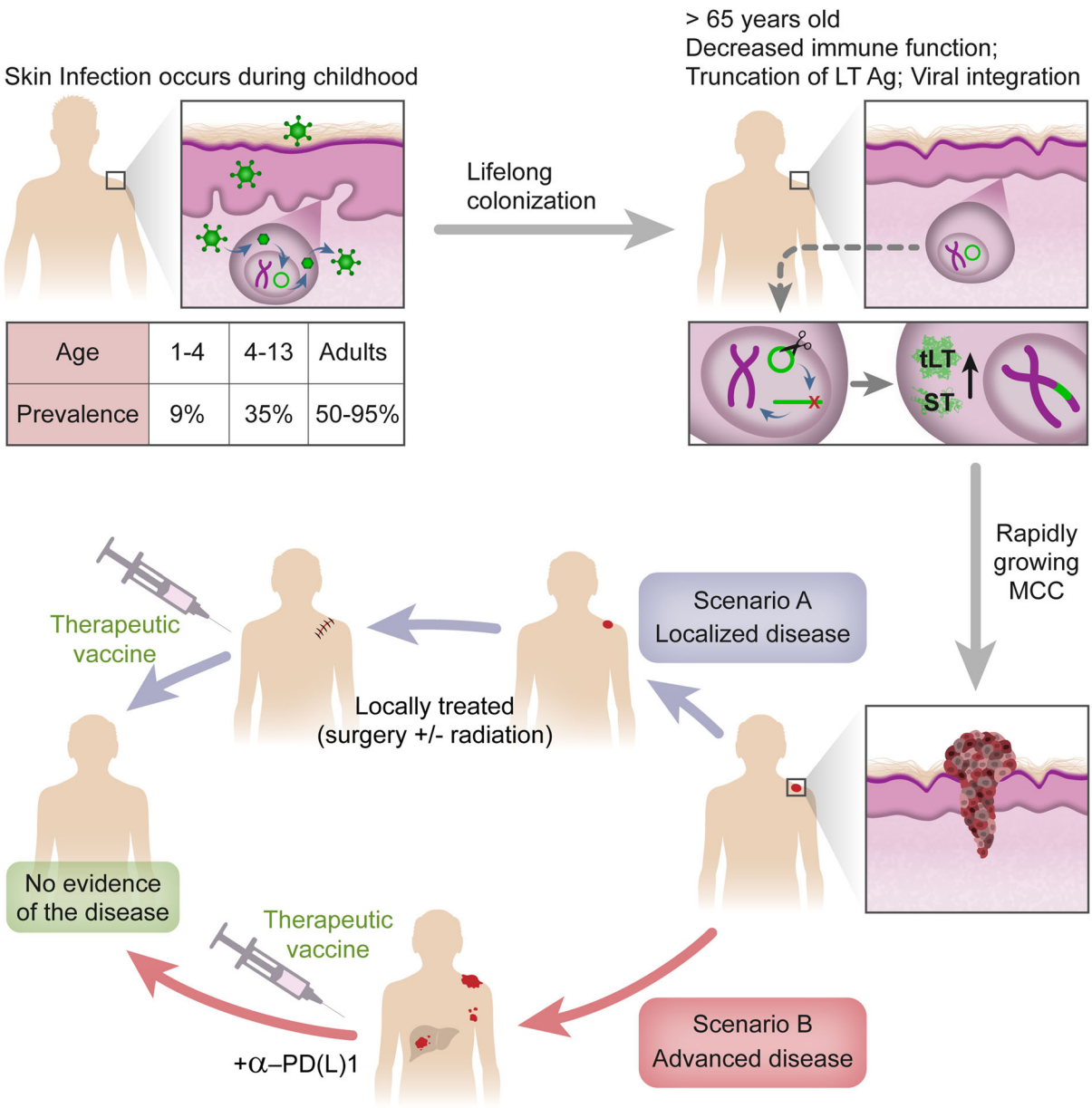

FIGURE 1 Etiology of virus-positive MCC and potential clinical scenarios for a therapeutic vaccine. Seroprevalence of polyomavirus-specific capsid antibodies indicates that MCPyV is common in the general population starting in childhood.[9,14] MCPyV then colonizes skin throughout life without causing known disease, except in rare cases when it integrates into the human genome and leads to MCC. This occurs mainly in persons aged over 65 and is likely to be driven by immune senescence and rare mutational events. Following viral integration, two oncoproteins, truncated Large T (tLT) and Small T (ST) antigens, are expressed and promote carcinogenesis. A therapeutic vaccine could potentially be tested in localized or advanced disease. MCC, Merkel cell carcinoma; MCPyV, Merkel cell polyomavirus

infiltration and a cytotoxic T-cell profile experience markedly improved outcomes.[41,42] Moreover, patients with greater intratumoral T-cell receptor diversity among their MCPyV-specific T cells also have significantly improved MCC-specific survival.[38]

The abundance of circulating MCPyV-specific T cells as measured by peptide-HLA tetramers generally tracks with tumor burden, often being elevated at diagnosis when a larger tumor burden is present and decreasing following successful reduction of the tumor by surgery or other modalities.[37] This fluctuation of MCPyV-specific T cells may very well be a reflection of the amount of tumor-viral antigen available and is consistent with the poor transition to long-lived memory cells. As noted above, the expansion of anti-MCPyV T-cell responses in MCC patients is supported by the detection of MCPyV-specific CD8 T cells in patients but not in healthy individuals.[18,37]

As observed in many cancers and infections, MCPyV-specific T cells are generally enriched at the site of disease, albeit blood is readily obtainable and thus the focus of many studies. Using an HLA-A*24:02-restricted epitope (LT92-101) a tetramer was developed which enabled recognition of MCPyV-specific T cells in the PBMC of 7 of 11 (64%) HLA-A*24:02-positive patients.[36,37] Another study of

27 individuals used a tetramer-enrichment strategy and identified nine potential T-Ag T-cell epitopes restricted by several population-prevalent HLA alleles (HLA-A*01, HLA-A*02, HLA-A*03, HLA-A*11, or HLA-B*07), exclusively in the PBMC of MCC patients and not in healthy individuals.[18]

While studying circulating T cells is important for understanding the immunogenicity and T-cell specificity, blood-based lymphocytes do not provide an accurate picture of their roles within the "battlefield" of the tumor microenvironment. Accordingly, studies have focused on detecting specific tumor-infiltrating lymphocyte (TIL) responses by both measuring cytokine production from CD8 T cells upon recognition of tumor-associated antigens and via HLA-peptide tetramers. The apparent proportion of VP-MCC TIL that include T-Ag-specific CD8 T-cell responses appears to vary with the technology used for detection (Figure 2). When a single HLA-appropriate tetramer was used in one report, 5 of 24 patients' TIL had detectable antigen-specific responses.[38] In another study, 6 of 21 TIL from VP-MCC subjects were positive when assayed with a limited panel of patient-matching artificial antigen-presenting cells (aAPC).[40] Recently, we used the aAPC approach to probe patients' TIL for multiple relevant HLA-A and B allelic variants.[43] This study detected T-Ag-specific CD8 TIL in the majority of biopsies (9 of 12) from persons with VP-MCC. While the true proportion of tumors infiltrated with T-Ag-specific CD8 T cells may vary between populations and assay methods, the failure of these cells to clear tumors by definition indicates that further augmentation of the endogenous response may be required.

CD4 T-cell responses, which are both essential for mediating humoral responses and for dendritic cell "licensing" (promoting the capacity of dendritic cells to stimulate cytotoxic T cells) and subsequent CD8 T-cell activation, have also been identified within TIL from VP-MCC. Indeed, a total of 6 distinct CD4 T-cell epitopes were detected within a limited region of LT. One epitope (LT209-228) was highly prevalent among MCC patients, as tetramer-positive cells were detected in 14 of 18 patients[44] (Figure 2).

These studies demonstrate that TIL from MCC tumors are often specific for MCPyV oncoproteins and that MCPyV-specific T-cells can also circulate. However, patient T-cell responses against epitope-HLA combinations predicted to be immunogenic are often not detectable. While knowledge of and assays for HLA-appropriate T-cell responses are rapidly advancing, it is likely that in some patients, certain HLA-peptide T-cell responses are not only below current detection thresholds but are actually absent. Indeed, the presence of clinically evident tumors implies that T-cell responses are frequently ineffective. A therapeutic vaccine could provide support to these cancer-specific T cells and promote antitumor immunity. Unlike preventive vaccines, a therapeutic vaccine is thought to improve immunity by supporting insufficiently primed T cells in addition to possibly stimulating naïve CD8 T cells. Supporting ineffectively primed T cells is particularly important since naïve T cells are produced in low numbers in older patients[45] and existing CD8 T cells have likely encountered cognate tumor antigen due to the large antigen burden of cancer. Improperly primed CD8 T cells have not seen their cognate antigen on dendritic cells with costimulatory signals. They exhibit decreased effector function and a state similar to exhaustion.[46,47] This is supported by recent studies showing therapeutic vaccination before immunotherapy preserves T-cell function and mediates tumor regression via induction of early exhausted (stem-like) CD8 T cells that respond to immune therapy.[48] Each of these concepts provides support for the development of a therapeutic vaccine that may enable tumor-specific T-cell responses to reach a functionally effective threshold, especially if combined with measures to enhance trafficking to tumors, overcome tumor endogenous immune escape factors and promote persistence of T cells.

4 | VACCINE DESIGN

4.1 | Target antigens

One of the first tasks when designing a therapeutic cancer vaccine is identifying an optimal antigen. In general, tumor antigens can be divided into cancer-associated antigens and cancer-specific antigens.[49] Cancer-associated antigens such as cancer-testis

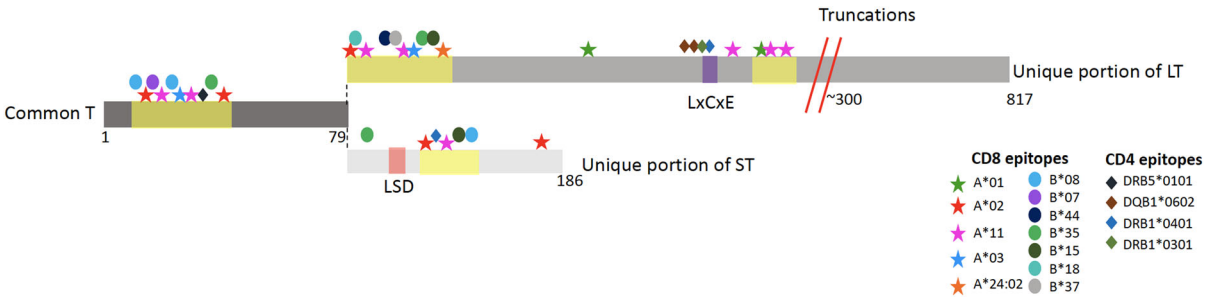

FIGURE 2 MCPyV (Merkel cell polyomavirus) large and small T oncoproteins and immune "hot zones." The common T sequence (middle-left) is shared between large T and small T. Top: unique portion of large T (LT). Bottom: unique portion of small T (ST). Common T encodes the region recognized by human antibodies to T-Ag. Yellow-highlighted areas indicate hot zones of enriched T-cell specific epitopes as detailed in the text. Documented HLA-restricting alleles are marked with either asterisk (HLA-A), ovals (HLA-B), or diamonds (HLA-DR/DQ). Large T truncations (red diagonal lines) occur approximately at amino acid 300; the exact location varies from patient to patient. The LXCXE motif (purple) is the retinoblastoma tumor suppressor-binding domain. The small T LSD domain (orange) is an LT-stabilization domain that also mediates other oncoprotein functions

antigens (ie, MAGE-A3) and overexpressed proteins (ie, HER-2/neu) are germline-coded antigens that may be expressed at low levels in healthy tissues or in gonadal tissues. Although these antigens are attractive vaccine targets because they are shared across many patients and cancers, they have numerous drawbacks including their dispensable nature to most cancers and frequent toxicity of immune responses to healthy tissues.[50,51] In contrast, tumor-specific antigens such as oncoviral and neoantigens are attractive since they are exclusively expressed in tumor tissue. Some oncoviral antigens, in particular, are ideal vaccine targets since they drive carcinogenesis and thus cannot be downregulated to avoid immune destruction. Oncoviral-antigens are also shared between patients so a vaccine would not need to be personalized for each patient. VP-MCC has two such oncoviral antigens, the MCPyV small and large T antigens (ST and LT). As noted above, there are well-documented T-cell responses to these antigens and autologous T-cell therapies targeting these antigens have induced clinical responses.[39,52] However, the endogenous T-cell response is often suboptimal with many patients having undetectable T-cell responses against known ST or LT antigens (see Section 3). When present, the T-cell responses exhibit characteristics of dysfunction.[37] These observations suggest that MCPyV ST and LT antigens are appealing candidates for a therapeutic MCC vaccine.

4.2 | Methods of antigen delivery: Protein and peptides

One of the simplest ways to deliver tumor antigens is polypeptides or whole protein. This approach is used for some preventive and therapeutic vaccines for infectious disease[53] and cancer.[54,55] A key benefit of the simple approach is that patients would not develop immunity against other vaccine components such as vector proteins. This allows multiple rounds of vaccination without limiting boosts due to the development of antivector adaptive immune responses. This is in contrast to viral-vectored vaccines where pre-existing immunity to viral-vector is associated with a weaker immune response, relating to adaptive immunity preventing or limiting vector infection and transduction.[56,57] However, since peptides alone are prone to induce tolerance, a danger signal must also be administered, typically an adjuvant compound (discussed below). Overall, the simplicity and safety of this approach make it an appealing option for a therapeutic vaccine (Table 1).

Whole proteins or protein antigens conjugated to immune-enhancing molecules, are preferred to peptides as they contain all potential epitopes within individual patients and the HLA-diverse population. Whole proteins also require endogenous antigen processing which promotes the presentation of biologically relevant cleavage peptides in the proper HLA context. However, in the specific case of MCPyV T-Ag, there is a possible risk of promoting oncogenesis by delivering unmodified oncoproteins, a concern shared by some other vaccine platforms (discussed below). To avoid this, multiple synthetic long peptides (SLP) covering the oncoprotein sequence can be used. This avoids the risk of carcinogenesis, has been shown to induce both CD4 and CD8 T-cell responses and to have antitumor activity for HPV,[78,79] and remains an attractive strategy for VP-MCPyV. To date, SLP-based vaccines appear to be most effective in early-stage cancers or carcinoma in situ.[78,79] An additional concern is the processing and presentation of HLA-binding minimal epitopes from SLP could differ from those derived from the whole protein.[80]

Peptide or protein antigens can also be modified to increase immunogenicity or selectively promote processing and presentation to T cells. One such approach is to covalently link the antigen of interest to an adjuvant. This ensures that the same APC that take up antigen receive additional danger signals and thus are competent to provide costimulatory signals to T cells. This approach has been successful in animal models that conjugate long peptides to a TLR agonists.[81-83] Peptides can also be expressed as fusions with proteins that direct them towards antigen processing machinery and HLA presentation.[84] Overall, polypeptides of various lengths are attractive for their general lack of toxicity, clinical experience, and ease of manufacturing. Several studies[54,55] have shown their ability to stimulate T-cell responses against tumor antigens.

4.3 | Methods of antigen delivery: Nucleic acids

Tumor antigens can also be encoded in nucleic acid products to express tumor antigens in vivo. This approach shares some of the design constraints and attractive options of subunit protein vaccines, with additional challenges and potential. For example, antigens, adjuvants, and targeting moieties can be included in a single construct. Nucleic acids also have auto-adjuvant activity, which can be further enhanced by the insertion of specific, stimulatory sequences. Cytoplasmic dsDNA stimulates immune responses via the cGAMP/STING pathway, and TLR9, while exogenous RNAs can signal through the RIG-I pathway and TLRs 3, 7, and 8.[85] These and other nucleic acid sensor pathways can promote robust immune responses against target antigens. A dose-sparing effect can be obtained using self-amplifying RNA molecules such as alphavirus replications, which encode an RNA-dependent RNA polymerase to increase the copy number of immune-stimulatory and antigen-encoding RNA in transduced cells.[63,64]

A DNA vaccine has been tested in an animal model of MCC. In these studies from Hung Lab, murine melanoma cells were engineered to express MCPyV tumor antigens.[86-88] Mice were then treated with a DNA vaccine expressing the ST or LT antigens, inducing tumor regression. Interestingly, initial studies using vaccination of LT antigen alone stimulated a strong CD4 response.[88] However, a follow-up study in which the LT antigen was conjugated to calreticulin a much more robust CD8 T-cell response was induced, possibly due to increased antigen uptake by cross-presenting dendritic cells.[87] These findings further support conjugating tumor antigens to other proteins that can modulate T-cell responses and may be particularly relevant for MCC.

TABLE 1 Comparison of antigen delivery platforms

Modality	Type	Rationale	Benefits	Drawbacks	Relevant citations or trials
Peptide	Neoantigen	Cancers often have mutations in proteins that can be recognized as nonself by T cells	Can target proteins necessary for cancer survival	Patient-specific, difficult to identify neoantigens that would drive strong immune responses	54,58
	Viral tumor antigen	Viral proteins are highly immunogenic, sometimes required for tumor growth	Shared across patients, truly foreign, highly immunogenic, often required for carcinogenesis	Not applicable for most cancers	59
	Tumor-associated antigen	Many cancers express antigens which would only otherwise be expressed in embryonic or gonadal tissues or lowly expressed in healthy tissues	Shared across patients	Since these are often not required for cancer survival, tumors can downregulate these proteins to evade an immune response	60
Nucleic Acid	DNA	Putative tumor antigens are encoded into DNA constructs which can then be delivered to patients where the antigens are transcribed and translated	Stable and inexpensive mechanism of antigen delivery, intrinsic adjuvanticity as can encode protein adjuvants	Difficulties in transfection, degradation by DNases	61
	Messenger RNA (mRNA)	Putative tumor antigens are encoded into mRNA constructs which can then be delivered to patients where the antigens are directly translated	RNA is highly immunogenic, can encode protein adjuvants	Also, difficulties in transfection, degradation by RNases	62
	Self-amplifying RNA	Viral RNA encodes an RNA polymerase in addition to tumor antigen(s), increasing both transcription and adjuvanticity	Higher levels of transcription and immunogenicity	Less tested	63,64
Cellular	Tumor cell	Tumor cells are expanded ex vivo and killed cells are injected with adjuvants. This does not require identifying individual neoantigens	Does not require identification of tumor antigens, tumor cells can be engineered to express adjuvants or even costimulatory signals	Potential autoimmune side effects, low proportion of neoantigens	65-67
	Dendritic cell	Dendritic cells are professional antigen-presenting cells primarily responsible for strong T-cell responses; can be expanded and treated with tumor antigens and infused into patients.	Allows direct presentation to T cells with costimulatory signals.	Difficult and expensive manufacturing. HLA diversity precludes an “off-the-shelf” product	68
Pathogen	Viral	Viral antigens can be encoded into viral vectors allowing efficient delivery to patients	More efficient delivery than nucleic acids	Immunity to vector complicates repeat vaccination	69
	Bacteria phages	Phages are well known to display antigens on their capsids which could be sources of antigen in a vaccine	Simple manufacturing (bacterial culture) contain some PAMPS (pathogen-associated molecular patterns)	No replication in eukaryotic cells	NCT04034225
	Bacterial	Bacteria expressing tumor antigens can be killed and used as a vaccine	Bacteria encode numerous immune agonists, relatively simple manufacturing	Difficulty in precise control over antigen and adjuvant levels	70-72

TABLE 1 (Continued)

Modality	Type	Rationale	Benefits	Drawbacks	Relevant citations or trials
In situ	Adjuvant-only vaccine	Intratumoral injection of adjuvant stimulates intratumoral dendritic cells and T cells	Does not require identification of tumor antigens, tumor cells can be engineered to express adjuvants or even costimulatory signals	Less likely to develop adaptive immune responses, Intratumoral environment is suboptimal site to stimulate T-cell responses due to suppressive characteristics	73,74
	Oncolytic viruses	Viruses attenuated to replicate in cancer cells but not healthy cells could drive a systemic adaptive immune response against tumor antigens in addition to local immune effects	Agnostic to tumor type, augments both innate and adaptive immune responses, replicative capacity of virus increases immunogenicity	Typically requires intralesional delivery which is not possible in some cases	75
	Radiation	In rare circumstances, radiation can induce systemic responses through an abscopal effect	Radiation has well-documented in-field tumoricidal effects independent of immunogenicity	Abscopal effect is rare and poorly understood	76,77

It is worth noting that nucleic acid-based vaccines can also incorporate features of peptide vaccines such as fusion to proteins that influence antigen trafficking, processing, and presentation or co-expression with a protein adjuvant. One example of how this could be pursued in MCC is a DNA vaccine that conjugates MCPyV ST or LT to lysosome-associated membrane glycoprotein (LAMP). This directs these antigens towards the lysosome and HLA-II presentation, to promote a CD4 response. This approach has been shown to be safe in phase I trials to induce allergen tolerance.[89] The use of LAMP to elicit functional antitumor responses to MCC is under active investigation in animal models.[84]

Despite their advantages, nucleic acid-based vaccines have not been reliably effective in humans. Several vaccines have had disappointing clinical trials with only a small fraction of patients developing T-cell responses against target antigens.[62,90,91] These trials tested numerous tumor-associated antigens in several cancer types including renal cell carcinoma, non–small-cell lung cancer, and melanoma. However, the vaccines induced weaker responses in humans than in animal models, possibly due to low antigen expression or differences in immune nucleic acid sensing pathways. As a result, no nucleic acid-based vaccine is currently licensed in humans. Promising adjuncts such as lipid nanoparticle or electroporation-based delivery systems and dose escalation can increase immunogenicity.[92] There is still substantial interest in nucleic acid-based vaccines[93] and these platforms will likely continue to improve.

4.4 | Methods of antigen delivery: Microbe-vectored vaccines

Microbes can also be used to deliver tumor antigens and stimulate adaptive immune responses. This approach is attractive since microbes can naturally stimulate a strong immune response. In general, there is a correlation between the replication competence of the vector and the strength of the immune response to the tumor antigens, as vector amplification increases the stimulation of pathogen-associated molecular patterns and antigen dose. The tradeoff, however, is that replication competence may bring with it virulence, especially in immune-compromised cancer patients, such that vector attenuation and safety need to be extremely carefully addressed in animal models and early-stage clinical trials. In addition, many pathogens have evolved immune evasion mechanisms, which need to be understood and engineered out of vaccine vectors to improve responses.[32,94,95] This issue, combined with microbe genome stability during manufacturing and the complexity of manufacturing add considerable time and expense to microbe-vectored vaccine workflows.

Several therapeutic cancer vaccine trials using pox or adenoviral vectors have been conducted in humans with mixed results. A trial using vaccinia and fowlpox vectors to express the NYESO-1 tumor-antigen in melanoma patients induced CD8 T-cell responses in a majority of patients (88%) by the conclusion of the trial. However, only 14% of patients had a clinical response to vaccination.[69]

Therapeutic vaccination vectors other than human viruses are also beginning to move into trials. The most common of these are *Listeria monocytogenes* engineered to express tumor antigens. An initial trial had sepsis-related adverse events but did induce T-cell responses to the vaccine target antigens.[96] Subsequent trials with additional vector attenuation have proven safer[70] and to improve survival in patients with refractory pancreatic cancer.[71] Another such approach uses bacteriophages to deliver cancer antigens of interest.[97,98] Phages have been known to be capable of promoting immunity in vivo since 1985.[99] An advantage of this approach is the ease and low cost of phage manufacture in bacterial culture. While at least one phage vaccine has reached the clinical stage for cancer (NCT03120832), overall this platform remains unproven and requires more immunogenicity and safety work. If multiple doses are used, the development of binding antibodies, known to occur after administration of some phages[100] could divert antigen either away or potentially even towards the antigen processing pathways required for T-cell responses, adding further complexity. In summary, microbe-based vaccines have several advantages including self-adjuvanticity and the potential for intracellular delivery of antigens. Although less developed than other vaccine formats, these platforms are likely to be of further interest in the near future (Table 1).

4.5 | Methods of antigen delivery: Cell-based vaccination

While the adoptive cell transfer has recently been clinically approved for the delivery of redirected T cells, cellular-based vaccine therapies can alternatively be used to stimulate endogenous T-cell responses. Tumor cells expanded and inactivated ex vivo can be reinfused back into patients where they can act as a source of antigen or even antigen-presenting cells.[101] Alternatively, autologous dendritic cells loaded with tumor antigens have the potential to present tumor peptides in the correct HLA context, together with costimulatory signals.

For inactivated tumor cells vaccines, a tumor biopsy is obtained and tumor cells are then expanded ex vivo.[102,103] The tumor cells can be modified to express adjuvants or costimulatory signals and then, they are killed or inactivated before administration back into patients. Large trials using this approach have shown modest efficacy in early-stage cancers in the early 2000s, however, the substantial cost in lower-risk cancers has hindered further development.[102,103]

Vaccination with dendritic cells (DC) includes loading antigen into DC ex vivo, which provides control over DC phenotype and maturation. Most such vaccines that now reach the clinical stage use cross-presenting DCs, with the potential to stimulate CD8 T cells in vivo upon readministration to the patient. A noteworthy example of DC vaccination is Sipuleucel-T, a Food and Drug Administration-approved vaccine for the treatment of castration-resistant metastatic prostate cancer. Although the clinical benefit of Sipuleucel-T is relatively modest (4-mo improved survival[104]), these trials provide a strong rationale for future trials of dendritic cell vaccines. These agents are limited by costly, complex, and time-consuming manufacturing and individualized nature and are thus most relevant for patients with particularly high-risk disease (Table 1).

4.6 | Adjuvants and in situ vaccination

Adjuvant selection is thought to be as important as choosing an antigen delivery system. Adjuvants can be broken down into two major categories: Innate immune agonists that largely target innate immune cells and cytokines that typically support T cells or APC. Innate immune adjuvants are usually small molecules that mimic molecular patterns found in bacteria or viruses such as nucleic acids or TLR agonists which are thought to act by activating relevant antigen-presenting cells.[85] Adaptive immune adjuvants are usually proteins which would normally be expressed by immune cells to support APC or T-cell growth or differentiation.[105]

The importance of adjuvants can be illustrated by "adjuvant-only" or in situ vaccines. In contrast to the above vaccination approaches which rely on delivering tumor antigens as part of a vaccine, in situ vaccines rely on endogenous antigens in the tumor and aim to improve responses to these antigens. Indeed, it is now recognized that some irradiation and cytotoxic chemotherapy regimens may work at least in part by promoting immunogenic cell death.[106,107] These "adjuvant-only" concepts have had moderate success in small MCC trials. GLA-100 is a stable emulsion of a synthetic TLR4 agonist and was tested in seven patients with metastatic MCC. This compound is thought to modulate innate immune cells such as macrophages in the tumor microenvironment so that they shift from a suppressive and towards an inflammatory phenotype. In this small trial, two patients had sustained partial responses in the target lesion.[73] A separate trial tested an IL-12-expressing plasmid in MCC using DNA electroporation directly into tumors. IL-12 supports T-cell differentiation and polarizes CD4 T cells towards a Th1 phenotype. In this trial, 3 of 10 patients with multiple metastatic lesions had partial responses, including in nontarget tumors.[74]

Encouraged by these results, two newer trials delivering immune agonists into tumors are ongoing. One approach targets the STING (NCT03172936). The STING pathway senses intracellular DNA and activates interferon signaling, known to be critical for immune responses following radiation.[108,109] STING agonists have been shown to reverse anti-PD-1 therapy resistance in animal models.[110] A separate trial investigating AST-008, a nanoparticle TLR9 agonist, is being studied for PD-(L)1 refractory MCC (NCT03684785). The nanoparticle formulation is designed to increase phagocytic APC uptake and delivery to endosomal TLR9.

In situ vaccine trials in MCC support the notion that adjuvants on their own can stimulate innate and adaptive immune cells. Combining these therapies with optimally delivered tumor antigen will likely further strengthen immune responses in MCC.

5 | EARLY SUCCESSES OF THERAPEUTIC VACCINES

5.1 | Personalized neoantigens vaccines

As mentioned above, tumor-associated antigens are often divided into two groups: (a) nonmutated self-antigens that may be tissue-specific and overexpressed in various cancers and (b) neoantigenic peptides derived from somatic mutations in cancer cell genomes.[111] Therapeutic cancer vaccines that target tumor-associated self-antigens often have low clinical efficacy and generate poor T-cell responses. Presumably, because it correlates with low-avidity T cells, as high avidity T cells targeting self-antigens are eliminated during thymic selection.[111,112] In contrast, neoantigens are ideal targets for therapeutic vaccines as the T-cell repertoire, including avidity, is not reduced by thymic selection.[113]

Because most cancer mutations are patient-specific, personalized approaches are appropriate for high tumor mutational burden (TMB) malignancies. Indeed, recent developments of in silico prediction approaches enable characterization and selection of neoantigens for personalized therapeutic vaccines.[54,55,114] Two groups provided clinical data demonstrating the promise of personalized neoantigen vaccines. Sahin et al[114] identified tumor-associated mutations in 13 patients with advanced melanoma. Using HLA data and epitope prediction tools, 10 peptides were selected per patient and administered as RNA vaccines. Eight patients (61%) who started the treatment without any detectable radiological lesions had a robust immune response and remained recurrence-free up to 23 months. The other patients relapsed after the initiation of the vaccine. Among these, one had a complete response after completion of the vaccine series and the second after receiving subsequent anti-PD-1 treatment.

Analyses of PBMC suggested that the majority of T-cell responses to these vaccines were de novo rather than boosts of pre-existing responses. CD4 T-cell responses dominated over CD8 recognition of vaccine epitopes, despite vaccine design targeting CD8 T cells as discussed above. In the second study, Ott et al[54] tested a peptide-based vaccine in six patients with previously untreated advanced melanoma. Patient-specific somatic mutations were identified, and twenty neoantigens were selected with HLA prediction tools. Thirty-amino acid-long peptides were injected with poly IC:LC adjuvant. Four patients (66%) who entered after surgical resection remained free from disease recurrence for 25 months. The other two patients who entered the study with lung metastases had complete responses after subsequent anti-PD-1 treatment. The vaccine stimulated both CD8 and CD4 PBMC interferon (IFN)-γ responses, with a preponderance of CD4 responses. T-cell receptor (TCR) analyses suggested that vaccine-elicited cells included de novo T-cell clonotypes.

Another vaccine (based on 20 personalized long peptides per patient) was recently tested in glioblastoma.[55] Glioblastoma is an immunologically "cold" tumor with a relatively low mutational burden.[115] While this trial did not result in clinical benefit, a significant benchmark was achieved by the demonstration of specific T-cell responses to a classically nonimmunogenic tumor. In addition to generating CD4 T-cell responses, patients had an increase in tumor-infiltrating T cells.

5.2 | HPV therapeutic vaccines

HPVs are circular DNA viruses. Some genotypes are associated with cervical, anal, vulval, and oropharyngeal cancers.[116] Similar to VP-MCC, a limited number of viral oncoproteins are persistently expressed in HPV-associated cancers and mechanistically drive cell proliferation. Prophylactic vaccination prevents HPV-associated neoplastic diseases when used before primary infection.[117] This great success has led to an interest in therapeutic vaccination that is administered after disease presentation.

HPV16 and HPV18-driven malignant transformation are strongly dependent on the E6 and E7 oncoproteins.[118,119] Many prototypes of therapeutic vaccines that induce T-cell responses to E6 and E7 have been developed.[59,61,120] Vaccination with mixed SLP (ISA101 vaccine) from HPV E6 and E7 oncoproteins with adjuvant in women with HPV16-positive vulvar intraepithelial neoplasia resulted in regression in 94% of patients, of whom 47% experienced a complete response.[59] This was associated with both CD8 and CD4 T-cell responses. An E6 and E7 DNA vaccine (VGX-3100) was tested in phase 2, double-blind trial in women with HPV16/18 positive precancerous conditions. Histopathological regression was observed in 49% of treated patients compared to 36% in the placebo group.[61] CD8 T-cell and antibody responses correlated with the histopathological regression. The vaccine is currently in phase III trials (NCT03185013 and NCT03721978).

In contrast to clinical responses in precancerous conditions,[59,61] E6 and E7 therapeutic cancer vaccines have yielded clinically disappointing results in patients with advanced or recurrent HPV16-related cancers,[121,122] despite the enhancement of blood T-cell responses. This suggests that vaccine-activated T cells are being inhibited by immunosuppression.[79] Therefore, synergism with approaches to overcome local and systemic immune suppression are rational to enhance the clinical activity of cancer vaccines in persons with established tumors. A phase-2 clinical trial that combined ISA101and PD-1 blockade, in patients with recurrent and invasive HPV16-associated malignancies, resulted in a 33% overall response rate (ORR) (8/24 subjects), higher than the 16% to 22% ORR with PD-1 blockade alone.[79] Similar trials are underway (NCT03260023).

HPV murine models support such combination therapy. A therapeutic vaccine combined with anti-PD-1 resulted in a better tumor regression when compared to anti-PD-1 treatment alone.[123-125] Moreover, it was shown that vaccines alone increased tumor-infiltrating CD8 T cells but also raised PD-1 expression levels. Combination of the vaccine with anti-PD-1 preserved tumor-infiltrating CD8 cells and reduced the numbers of T cells expressing PD-1,[123,125] and demonstrated synergistic antitumoral responses.

6 | BIOLOGICAL CONSIDERATIONS BEFORE CLINICAL IMPLEMENTATION

Selection of the appropriate treatment for MCC depends on many factors. Practice guidelines emphasize disease stage,[126] with the early disease typically being managed with surgery and radiation while more advanced disease is managed with systemic immunotherapies such as anti-PD-(L)1 blockade. We envision possible roles for therapeutic vaccination at both ends of the VP-MCC clinical spectrum.

6.1 | Adjuvant therapy for early MCC

Patients diagnosed with local MCC will often undergo surgical excision. Radiation of the excised area and the adjacent lymph nodes is also often included.[127] This combination is extremely effective in rendering patients free of detectable disease, but recurrences frequently arise near the primary tumor site, in the nodal region, and/or distantly.[1,127] Vaccination after local treatment could generate or enhance a systemic immune response that recognizes early emerging microscopic tumors and eliminates them by efficient effector responses. Therefore, a safe therapeutic vaccine to augment MCPyV immunity would be useful to help prevent MCC recurrence. With regard to clinical trials, an appealing alternative to adjuvant studies is the neoadjuvant setting, in which vaccine is initiated in the short window between diagnostic biopsy and excision. This provides an opportunity for histopathologic study of the removed tumor after potential immune-boosting. The conserved nature of MCPyV T-Ag allows consideration of a neoantigen trial as the vaccine candidate product would be off-the-shelf and ready to administer.

6.2 | Systemic/advanced disease

Patients with advanced disease currently receive PD-(L)1 blockade as the preferred first-line therapy. The response rates, 50% to 65%,[25,128] are higher than those for most other cancers. Unfortunately, approximately half of all treated patients do not experience prolonged benefit.[1,129] The fact that some MCC patients have modest or nondetectable T-cell immune responses to MCPyV antigens[37,38] suggests that a paucity of antigen-specific T cells capable of being functionally augmented by anti-PD-(L)1 may contribute to suboptimal clinical responses. Therefore, a combination of a therapeutic vaccine and PD-(L)1 inhibitor could potentially be beneficial for VP-MCC patients. Indeed, several studies in mice and humans suggest it is possible to both stimulate the T-cell function and prevent the induction of T-cell exhaustion. Such studies have demonstrated that vaccination increases the number of T cells infiltrating tumors.[55,114,123,124] The increase in T-cell number occurs by generating either de novo T-cell responses or by augmenting existing T-cell responses. However, in advanced disease, an increase of T-cell numbers by a therapeutic vaccine is usually not sufficient to clear tumors completely. Furthermore, alongside the increase in T-cell responses and infiltration into tumors, an increase in exhaustion markers, such as PD-1 on TIL and PD-L1 on tumor cells, is also often observed.[123,124] Importantly, mice treated simultaneously with a therapeutic vaccine and either anti-PD-1,[123] or anti-PD-L1[124] demonstrated prolonged T-cell stimulation and stronger suppression of tumor growth. Additionally, a clinical trial in men and women with recurrent HPV has tested anti-PD-1 treatment combined with a synthetic long peptide vaccine, leading to promising antitumor responses compared to PD-1 blockade alone.[79] These studies suggest that combining a cancer vaccine with PD-(L)1 blockade has significant clinical potential for VP-MCC.

The sequencing of vaccination and PD-(L)1 therapy was explored in a recent mouse study that showed how different treatment protocols result in distinct responses. Verma et al[48] showed that simultaneous PD-1 inhibitor and vaccination was beneficial, but pretreatment with PD-1 blockade before combination therapy abrogated responses. The inhibitory effect of pretreatment with anti-PD-1 was mediated by PD-1^{+}CD38^{hi} CD8 T cells, the depletion of which resulted in a more robust antitumor response and improved mice survival.

In the difficult setting of patients whose tumors are already refractory to anti-PD-(L)1, it may be beneficial to add additional therapy, such as a T-cell modulatory cytokine. A rational candidate is the immunomodulator, interleukin-12 (IL-12). IL-12 has been shown to be a potent producer of antitumor immunity,[130] which stimulates different effector cells (NK and T cells).[131] IL-12 has been broadly tested in the clinic; several studies have demonstrated that IL-12 treatment increases tumor-infiltrating lymphocytes and the circulating T-cell response in refractory settings.[132,133] Potentially, such a cytokine could restore some of the immune functions and support further benefit from a combined therapeutic vaccine with PD-(L)1 blockade.

7 | POTENTIAL CLINICAL TRIAL DESIGNS

It is mechanistically attractive to consider an up-front combination of therapeutic vaccination with anti-PD-(L)1 therapy, but it is probably not feasible to carry out such a trial in a rare disease with a relatively high response rate to anti-PD-(L)1 monotherapy. The establishment of incremental benefit for a therapeutic vaccine would require a large and expensive trial. For example, to detect an increase in response rate from 60% to 80%, ~162 patients would be required for a randomized trial, with 80% power to detect a difference of that magnitude.[134] A 20-percentage point improvement in the response rate is a very optimistic estimate, representing a 50% decrease in the number of nonresponders. The number of patients required for a trial is very sensitive to the assumed effect size. If the effect size is cut to 10% (60% response rate increases to 70% with vaccine) ~712 patients would be required for the trial.[134] Since the largest trial to date in advanced MCC (88 patients) required more than a dozen international sites,[135] it is likely impractical to explore the first-line combination of a therapeutic vaccine with PD-(L)1 blockade. The

greatest unmet need in MCC is to develop an effective therapy for patients with PD-(L)1 refractory VP-MCC. Because anti-PD-(L)1 refractory metastatic MCC has no proven effective therapy, even occasional responses in this setting could be clinically meaningful and indicative of the benefit of vaccine therapy.

For the adjuvant setting, clinical trial design is again challenging based on a relatively large number of patients required to determine efficacy. Statistically, adequate sample size depends on the number of anticipated events (recurrences) which varies significantly based on the stage at presentation. Higher-risk groups (eg, stage IIIB disease) would require fewer patients to meet statistical significance because ~70% of these patients are expected to recur after initial treatment. In this scenario, only 62 patients would need to be randomized to vaccine versus placebo to assess clinical benefit, assuming the vaccine reduced the recurrence rate by one half.[134] In contrast, for stage I (~20% risk of recurrence), a clinical trial would require nearly 400 patients, assuming the vaccine also reduced the recurrence rate by one half (to 10%) in this setting.[134] Since there are several other adjuvant trials being conducted (NCT03712605 and NCT03271372), and they focus on higher-risk patients, an adjuvant vaccine trial would likely need to preferentially enroll lower-risk patients, meaning target trial size may need to be ~200, based on appropriate risk stratification for the stage. Before embarking on a significant trial to assess efficacy in the adjuvant setting, a smaller feasibility and immunogenicity clinical trial would likely make sense after a candidate vaccine has been evaluated in a preclinical model. In this initial human study, the extent and persistence of anti-MCPyV immune responses to a vaccine could be assessed as outlined in the MCPyV oncoproteins section above. This analysis will be facilitated by the fact that after tumor removal, these immune responses typically fall very rapidly.

8 | CONCLUSIONS

The clinical efficacy of cancer vaccines has remained modest despite decades of effort. Different cancers pose distinct challenges that must be addressed in a customized manner. VP-MCC is an appealing candidate for a therapeutic vaccine because (a) MCC is an inherently immune-sensitive cancer, strongly associated with baseline immune status, and generally responsive to immunotherapies, (b) The small and conserved antigenic space of the relevant MCPyV-encoded oncoproteins are amenable to vaccine construction and well-defined immune monitoring tools such as tetramers and TCR sequencing,[37,38] (c) MCPyV viral antigens are inherently immunogenic, leading to robust B- and T-lymphocyte responses that can be readily detected throughout the clinical course.

Several studies that have characterized MCPyV-specific T cells in MCC tumors clearly demonstrate that T-cell infiltration, TCR diversity, and T-cell frequency are associated with better patient outcomes.[37,38,41] However, in most cases, these responses are not sufficient and T cells fail to clear tumors, indicating that augmentation of the endogenous response may be needed. Treatment with a therapeutic vaccine could potentially both enhance existing immune responses and induce de novo T-cell responses. Depending on the clinical scenario evaluated, as discussed above, vaccination could prevent late recurrences by eliminating micrometastases or could rescue patients with advanced disease who do not have initial or sustained responses to checkpoint inhibition.

Several factors suggest that VP-MCC is an interesting model of therapeutic vaccination. The viral oncoprotein is T-cell immunogenic providing a trackable biomarker to measure responses. Since both T- and B-cell responses drop after tumor removal,[19,37] persistent responses from the vaccine would contrast with naturally occurring transitory responses and help to differentiate the two. The clonotypic complexity of T-cell responses to LT can readily be followed in blood, tumor biopsies, and TIL[38,43] providing another biomarker for vaccine responses.

Because of the unique advantages of this disease, it should be a high priority for the field to explore therapeutic vaccination in this setting. It is likely that clinical trials of a therapeutic vaccine for VP-MCC will yield valuable insights relevant to other immunogenic cancers that may be more common.

ACKNOWLEDGMENTS

NIH-P01-CA225517, NIH-T32-CA080416, Prostate Cancer Foundation Kelsey Dickson Team Science Courage Research Team Award, and UW MCC Patient Gift Fund.

CONFLICT OF INTERESTS

DMK and PN are coinventors on institutionally owned US patent applications relevant to this article. DMK has received funding from Immunomics Therapeutics Incorporated relevant to this article. PN has received grant support from EMD-Serono and Bristol Myers Squibb as well as honoraria from Merck and EMD-Serono. Remaining authors declare that there are no conflict of interests.

ORCID

Shira Tabachnick-Cherny http://orcid.org/0000-0003-1595-4619
Thomas Pulliam http://orcid.org/0000-0003-3511-6348
Candice Church http://orcid.org/0000-0003-1582-8292
David M. Koelle http://orcid.org/0000-0003-1255-9023
Paul Nghiem http://orcid.org/0000-0003-2784-963X

REFERENCES

1. Harms PW, Harms KL, Moore PS, et al. The biology and treatment of Merkel cell carcinoma: current understanding and research priorities. *Nat Rev Clin Oncol*. 2018;15(12):763-776.
2. Harms KL, Healy MA, Nghiem P, et al. Analysis of prognostic factors from 9387 Merkel cell carcinoma cases forms the basis for the new 8th Edition AJCC Staging System. *Ann Surg Oncol*. 2016;23(11):3564-3571.
3. Agelli M, Clegg LX, Becker JC, Rollison DE. The etiology and epidemiology of Merkel cell carcinoma. *Curr Probl Cancer*. 2010;34(1):14-37.
4. Harms PW. Update on Merkel cell carcinoma. *Clin Lab Med*. 2017;37(3):485-501.
5. Paulson KG, Park SY, Vandeven NA, et al. Merkel cell carcinoma: Current US incidence and projected increases based on changing demographics. *J Am Acad Dermatol*. 2018;78(3):457-463 e452.

6. Feng H, Shuda M, Chang Y, Moore PS. Clonal integration of a polyomavirus in human Merkel cell carcinoma. *Science*. 2008; 319(5866):1096-1100.
7. Goh G, Walradt T, Markarov V, et al. Mutational landscape of MCPyV-positive and MCPyV-negative Merkel cell carcinomas with implications for immunotherapy. *Oncotarget*. 2016;7(3):3403-3415.
8. Wong SQ, Waldeck K, Vergara IA, et al. UV-associated mutations underlie the etiology of MCV-negative Merkel cell carcinomas. *Cancer Res*. 2015;75(24):5228-5234.
9. Chen T, Hedman L, Mattila PS, et al. Serological evidence of Merkel cell polyomavirus primary infections in childhood. *J Clin Virol*. 2011; 50(2):125-129.
10. Sourvinos G, Mammas IN, Spandidos DA. Merkel cell polyomavirus infection in childhood: current advances and perspectives. *Arch Virol*. 2015;160(4):887-892.
11. Coursaget P, Samimi M, Nicol JTJ, Gardair C, Touzé A. Human Merkel cell polyomavirus: virological background and clinical implications. *APMIS*. 2013;121(8):755-769.
12. Schowalter RM, Pastrana DV, Pumphrey KA, Moyer AL, Buck CB. Merkel cell polyomavirus and two previously unknown polyomaviruses are chronically shed from human skin. *Cell Host Microbe*. 2010;7(6):509-515.
13. Liu W, Yang R, Payne AS, et al. Identifying the target cells and mechanisms of Merkel cell polyomavirus infection. *Cell Host Microbe*. 2016;19(6):775-787.
14. Pastrana DV, Tolstov YL, Becker JC, Moore PS, Chang Y, Buck CB. Quantitation of human seroresponsiveness to Merkel cell polyomavirus. *PLOS Pathog*. 2009;5(9):e1000578.
15. Carter JJ, Paulson KG, Wipf GC, et al. Association of Merkel cell polyomavirus-specific antibodies with Merkel cell carcinoma. *J Natl Cancer Inst*. 2009;101(21):1510-1522.
16. Paulson KG, Lewis CW, Redman MW, et al. Viral oncoprotein antibodies as a marker for recurrence of Merkel cell carcinoma: a prospective validation study. *Cancer*. 2017;123(8):1464-1474.
17. Liu X, Hein J, Richardson SCW, et al. Merkel cell polyomavirus large T antigen disrupts lysosome clustering by translocating human Vam6p from the cytoplasm to the nucleus. *J Biol Chem*. 2011; 286(19):17079-17090.
18. Lyngaa R, Pedersen NW, Schrama D, et al. T-cell responses to oncogenic Merkel cell polyomavirus proteins distinguish patients with Merkel cell carcinoma from healthy donors. *Clin Cancer Res*. 2014;20(7):1768-1778.
19. Paulson KG, Carter JJ, Johnson LG, et al. Antibodies to Merkel cell polyomavirus T antigen oncoproteins reflect tumor burden in Merkel cell carcinoma patients. *Cancer Res*. 2010;70(21):8388-8397.
20. Helmink BA, Reddy SM, Gao J, et al. B cells and tertiary lymphoid structures promote immunotherapy response. *Nature*. 2020;577 (7791):549-555.
21. Petitprez F, de Reyniès A, Keung EZ, et al. B cells are associated with survival and immunotherapy response in sarcoma. *Nature*. 2020; 577(7791):556-560.
22. Seow DYB, Yeong JPS, Lim JX, et al. Tertiary lymphoid structures and associated plasma cells play an important role in the biology of triple-negative breast cancers. *Breast Cancer Res Treat*. 2020;180: 369-377.
23. Giraldo NA, Nguyen P, Engle EL, et al. Multidimensional, quantitative assessment of PD-1/PD-L1 expression in patients with Merkel cell carcinoma and association with response to pembrolizumab. *J Immunother Cancer*. 2018;6(1):99.
24. Behr DS, Peitsch WK, Hametner C, et al. Prognostic value of immune cell infiltration, tertiary lymphoid structures and PD-L1 expression in Merkel cell carcinomas. *Int J Clin Exp Pathol*. 2014;7(11): 7610-7621.
25. Nghiem PT, Bhatia S, Lipson EJ, et al. PD-1 blockade with pembrolizumab in advanced Merkel-cell carcinoma. *N Engl J Med*. 2016; 374(26):2542-2552.
26. Shuda M, Kwun HJ, Feng H, Chang Y, Moore PS. Human Merkel cell polyomavirus small T antigen is an oncoprotein targeting the 4E-BP1 translation regulator. *J Clin Invest*. 2011; 121(9):3623-3634.
27. Houben R, Shuda M, Weinkam R, et al. Merkel cell polyomavirus-infected Merkel cell carcinoma cells require expression of viral T antigens. *J Virol*. 2010;84(14):7064-7072.
28. Houben R, Angermeyer S, Haferkamp S, et al. Characterization of functional domains in the Merkel cell polyomavirus Large T antigen. *Int J Cancer*. 2015;136(5):E290-E300.
29. Borchert S, Czech-Sioli M, Neumann F, et al. High-affinity Rb binding, p53 inhibition, subcellular localization, and transformation by wild-type or tumor-derived shortened Merkel cell polyomavirus large T antigens. *J Virol*. 2014;88(6):3144-3160.
30. Arora R, Chang Y, Moore PS. MCV and Merkel cell carcinoma: a molecular success story. *Curr Opin Virol*. 2012;2(4):489-498.
31. Shuda M, Feng H, Kwun HJ, et al. T antigen mutations are a human tumor-specific signature for Merkel cell polyomavirus. *Proc Natl Acad Sci USA*. 2008;105(42):16272-16277.
32. Lau L, Gray EE, Brunette RL, Stetson DB. DNA tumor virus oncogenes antagonize the cGAS-STING DNA-sensing pathway. *Science*. 2015;350(6260):568-571.
33. Kwun HJ, Shuda M, Feng H, Camacho CJ, Moore PS, Chang Y. Merkel cell polyomavirus small T antigen controls viral replication and oncoprotein expression by targeting the cellular ubiquitin ligase SCFFbw7. *Cell Host Microbe*. 2013;14(2):125-135.
34. Dye KN, Welcker M, Clurman BE, Roman A, Galloway DA. Merkel cell polyomavirus tumor antigens expressed in Merkel cell carcinoma function independently of the ubiquitin ligases Fbw7 and beta-TrCP. *PLOS Pathog*. 2019;15(1):e1007543.
35. Park DE, Cheng J, Berrios C, et al. Dual inhibition of MDM2 and MDM4 in virus-positive Merkel cell carcinoma enhances the p53 response. *Proc Natl Acad Sci USA*. 2019;116(3):1027-1032.
36. Iyer JG, Afanasiev OK, McClurkan C, et al. Merkel cell polyomavirus-specific CD8(+) and CD4(+) T-cell responses identified in Merkel cell carcinomas and blood. *Clin Cancer Res*. 2011;17(21):6671-6680.
37. Afanasiev OK, Yelistratova L, Miller N, et al. Merkel polyomavirus-specific T cells fluctuate with Merkel cell carcinoma burden and express therapeutically targetable PD-1 and Tim-3 exhaustion markers. *Clin Cancer Res*. 2013;19(19):5351-5360.
38. Miller NJ, Church CD, Dong L, et al. Tumor-infiltrating Merkel cell polyomavirus-specific T cells are diverse and associated with improved patient survival. *Cancer Immunol Res*. 2017;5(2):137-147.
39. Paulson KG, Voillet V, McAfee MS, et al. Acquired cancer resistance to combination immunotherapy from transcriptional loss of class I HLA. *Nat Commun*. 2018;9(1):3868.
40. Samimi M, Benlalam H, Aumond P, et al. Viral and tumor antigen-specific CD8 T-cell responses in Merkel cell carcinoma. *Cell Immunol*. 2019;344:103961.
41. Paulson KG, Iyer JG, Tegeder AR, et al. Transcriptome-wide studies of Merkel cell carcinoma and validation of intratumoral CD8+ lymphocyte invasion as an independent predictor of survival. *J Clin Oncol*. 2011;29(12):1539-1546.
42. Paulson KG, Iyer JG, Simonson WT, et al. CD8+ lymphocyte intratumoral infiltration as a stage-independent predictor of Merkel cell carcinoma survival: a population-based study. *Am J Clin Path*. 2014;142(4):452-458.
43. Jing L, Ott M, Church CD, et al. High prevalence and diverse HLA restriction of intratumoral oncoprotein-specific CD8 T cells in polyoma virus-driven Merkel cell carcinoma. *Cancer Immunology Research*. 2020:canimm.0647.2019.
44. Longino NV, Yang J, Iyer JG, et al. Human CD4(+) T cells specific for Merkel cell polyomavirus localize to Merkel cell carcinomas and target a required oncogenic domain. *Cancer Immunol Res*. 2019;7(10): 1727-1739.

45. den Braber I, Mugwagwa T, Vrisekoop N, et al. Maintenance of peripheral naive T cells is sustained by thymus output in mice but not humans. *Immunity*. 2012;36(2):288-297.
46. Ahrends T, Spanjaard A, Pilzecker B, et al. CD4(+) T cell help confers a cytotoxic T cell effector program including coinhibitory receptor downregulation and increased tissue invasiveness. *Immunity*. 2017; 47(5):848-861.e845.
47. Smith CM, Wilson NS, Waithman J, et al. Cognate CD4(+) T cell licensing of dendritic cells in CD8(+) T cell immunity. *Nat Immunol*. 2004;5(11):1143-1148.
48. Verma V, Shrimali RK, Ahmad S, et al. PD-1 blockade in subprimed CD8 cells induces dysfunctional PD-1(+)CD38(hi) cells and anti-PD-1 resistance. *Nat Immunol*. 2019;20(9):1231-1243.
49. Hollingsworth RE, Jansen K. Turning the corner on therapeutic cancer vaccines. *NPJ Vaccines*. 2019;4:7.
50. Morgan RA, Chinnasamy N, Abate-Daga D, et al. Cancer regression and neurological toxicity following anti-MAGE-A3 TCR gene therapy. *J Immunother*. 2013;36(2):133-151.
51. Cameron BJ, Gerry AB, Dukes J, et al. Identification of a Titin-derived HLA-A1-presented peptide as a cross-reactive target for engineered MAGE A3-directed T cells. *Sci Transl Med*. 2013;5(197): 197ra103.
52. Chapuis AG, Afanasiev OK, Iyer JG, et al. Regression of metastatic Merkel cell carcinoma following transfer of polyomavirus-specific T cells and therapies capable of re-inducing HLA class-I. *Cancer Immunol Res*. 2014;2(1):27-36.
53. Cunningham AL, Lal H, Kovac M, et al. Efficacy of the herpes zoster subunit vaccine in adults 70 years of age or older. *N Engl J Med*. 2016;375(11):1019-1032.
54. Ott PA, Hu Z, Keskin DB, et al. An immunogenic personal neoantigen vaccine for patients with melanoma. *Nature*. 2017;547(7662):217-221.
55. Keskin DB, Anandappa AJ, Sun J, et al. Neoantigen vaccine generates intratumoral T cell responses in phase Ib glioblastoma trial. *Nature*. 2019;565(7738):234-239.
56. Nayak S, Herzog RW. Progress and prospects: immune responses to viral vectors. *Gene Ther*. 2010;17(3):295-304.
57. Buchbinder SP, Mehrotra DV, Duerr A, et al. Efficacy assessment of a cell-mediated immunity HIV-1 vaccine (the Step Study): a double-blind, randomised, placebo-controlled, test-of-concept trial. *Lancet*. 2008;372(9653):1881-1893.
58. Asa SL, Dardick I, Peter van Nostrand AW, Bailey DJ, Gullane PJ. Primary thyroid thymoma: a distinct clinicopathologic entity. *Hum Pathol*. 1988;19(12):1463-1467.
59. Kenter GG, Welters MJP, Valentijn ARPM, et al. Vaccination against HPV-16 oncoproteins for vulvar intraepithelial neoplasia. *N Engl J Med*. 2009;361(19):1838-1847.
60. Vantomme V, Dantinne C, Amrani N, et al. Immunologic analysis of a phase I/II study of vaccination with MAGE-3 protein combined with the AS02B adjuvant in patients with MAGE-3-positive tumors. *J Immunother*. 2004;27(2):124-135.
61. Trimble CL, Morrow MP, Kraynyak KA, et al. Safety, efficacy, and immunogenicity of VGX-3100, a therapeutic synthetic DNA vaccine targeting human papillomavirus 16 and 18 E6 and E7 proteins for cervical intraepithelial neoplasia 2/3: a randomised, double-blind, placebo-controlled phase 2b trial. *Lancet*. 2015;386(10008): 2078-2088.
62. Sebastian M, Schröder A, Scheel B, et al. A phase I/IIa study of the mRNA-based cancer immunotherapy CV9201 in patients with stage IIIB/IV non-small cell lung cancer. *Cancer Immunol Immunother*. 2019; 68(5):799-812.
63. Vogel AB, Lambert L, Kinnear E, et al. Self-amplifying RNA vaccines give equivalent protection against influenza to mRNA vaccines but at much lower doses. *Mol Ther*. 2018;26(2):446-455.
64. Brito LA, Kommareddy S, Maione D, et al. Self-amplifying mRNA vaccines. *Adv Genet*. 2015;89:179-233.
65. Harris JE, Ryan L, Hoover HC, et al. Adjuvant active specific immunotherapy for stage II and III colon cancer with an autologous tumor cell vaccine: Eastern Cooperative Oncology Group Study E5283. *J Clin Oncol*. 2000;18(1):148-157.
66. Berger M, Kreutz FT, Horst JL, Baldi AC, Koff WJ. Phase I study with an autologous tumor cell vaccine for locally advanced or metastatic prostate cancer. *J Pharm Pharm Sci*. 2007;10(2):144-152.
67. Fishman M, Hunter TB, Soliman H, et al. Phase II trial of B7-1 (CD-86) transduced, cultured autologous tumor cell vaccine plus subcutaneous interleukin-2 for treatment of stage IV renal cell carcinoma. *J Immunother*. 2008;31(1):72-80.
68. Small EJ, Schellhammer PF, Higano CS, et al. Placebo-controlled phase III trial of immunologic therapy with sipuleucel-T (APC8015) in patients with metastatic, asymptomatic hormone refractory prostate cancer. *J Clin Oncol*. 2006;24(19):3089-3094.
69. Odunsi K, Matsuzaki J, Karbach J, et al. Efficacy of vaccination with recombinant vaccinia and fowlpox vectors expressing NY-ESO-1 antigen in ovarian cancer and melanoma patients. *Proc Natl Acad Sci USA*. 2012;109(15):5797-5802.
70. Le DT, Brockstedt DG, Nir-Paz R, et al. A live-attenuated Listeria vaccine (ANZ-100) and a live-attenuated Listeria vaccine expressing mesothelin (CRS-207) for advanced cancers: phase I studies of safety and immune induction. *Clin Cancer Res*. 2012; 18(3):858-868.
71. Le DT, Wang-Gillam A, Picozzi V, et al. Safety and survival with GVAX pancreas prime and Listeria Monocytogenes-expressing mesothelin (CRS-207) boost vaccines for metastatic pancreatic cancer. *J Clin Oncol*. 2015;33(12):1325-1333.
72. Maciag PC, Radulovic S, Rothman J. The first clinical use of a live-attenuated Listeria monocytogenes vaccine: a phase I safety study of Lm-LLO-E7 in patients with advanced carcinoma of the cervix. *Vaccine*. 2009;27(30):3975-3983.
73. Bhatia S, Miller NJ, Lu H, et al. Intratumoral G100, a TLR4 agonist, induces antitumor immune responses and tumor regression in patients with Merkel cell carcinoma. *Clin Cancer Res*. 2019;25(4): 1185-1195.
74. Bhatia S, Longino NV, Miller NJ, et al. Intratumoral delivery of plasmid IL12 via electroporation leads to regression of injected and noninjected tumors in Merkel cell carcinoma. *Clin Cancer Res*. 2019; 26:598-607.
75. Andtbacka RHI, Kaufman HL, Collichio F, et al. Talimogene laherparepvec improves durable response rate in patients with advanced melanoma. *J Clin Oncol*. 2015;33(25):2780-2788.
76. Schaub SK, Stewart RD, Sandison GA, et al. Does neutron radiation therapy potentiate an immune response to Merkel cell carcinoma? *Int J Particle Ther*. 2018;5(1):183-195.
77. Cotter SE. Abscopal effect in a patient with metastatic Merkel cell carcinoma following radiation therapy: potential role of induced antitumor immunity. *Arch Dermatol*. 2011;147(7):870-872.
78. de Vos van Steenwijk PJ, Ramwadhdoebe TH, Löwik MJG, et al. A placebo-controlled randomized HPV16 synthetic long-peptide vaccination study in women with high-grade cervical squamous intraepithelial lesions. *Cancer Immunol Immunother*. 2012;61(9):1485-1492.
79. Massarelli E, William W, Johnson F, et al. Combining immune checkpoint blockade and tumor-specific vaccine for patients with incurable human papillomavirus 16-related cancer: a phase 2 clinical trial. *JAMA Oncol*. 2019;5(1):67-73.
80. Vyas JM, van der Veen AG, Ploegh HL. The known unknowns of antigen processing and presentation. *Nat Rev Immunol*. 2008;8(8): 607-618.
81. Zom GG, Khan S, Britten CM, et al. Efficient induction of antitumor immunity by synthetic toll-like receptor ligand-peptide conjugates. *Cancer Immunol Res*. 2014;2(8):756-764.
82. Kastenmüller K, Wille-Reece U, Lindsay RWB, et al. Protective T cell immunity in mice following protein-TLR7/8 agonist-conjugate

immunization requires aggregation, type I IFN, and multiple DC subsets. *J Clin Invest*. 2011;121(5):1782-1796.
83. Lynn GM, Sedlik C, Baharom F, et al. Peptide-TLR-7/8a conjugate vaccines chemically programmed for nanoparticle self-assembly enhance CD8 T-cell immunity to tumor antigens. *Nat Biotechnol*. 2020;38:320-332.
84. Heiland T, Rosean CB, Sinha P, et al. Abstract: Lysosomal-associated membrane protein-1-targeting of the large T antigen of Merkel cell polomavirus elicits potent CD4 + T cell responses. *First International Symposium on Merkel Cell Carcinoma*. 2019.
85. O'Neill LA, Golenbock D, Bowie AG. The history of toll-like receptors—redefining innate immunity. *Nat Rev Immunol*. 2013;13(6):453-460.
86. Gomez B, He L, Tsai Y, Wu TC, Viscidi RP, Hung CF. Creation of a Merkel cell polyomavirus small T antigen-expressing murine tumor model and a DNA vaccine targeting small T antigen. *Cell Biosci*. 2013;3(1):29.
87. Gomez BP, Wang C, Viscidi RP, et al. Strategy for eliciting antigen-specific CD8+ T cell-mediated immune response against a cryptic CTL epitope of Merkel cell polyomavirus large T antigen. *Cell & BioScience*. 2012;2(1):36.
88. Zeng Q, Gomez BP, Viscidi RP, et al. Development of a DNA vaccine targeting Merkel cell polyomavirus. *Vaccine*. 2012;30(7):1322-1329.
89. Su Y, Romeu-Bonilla E, Anagnostou A, Fitz-Patrick D, Hearl W, Heiland T. Safety and long-term immunological effects of CryJ2-LAMP plasmid vaccine in Japanese red cedar atopic subjects: a phase I study. *Human Vaccine Immunother*. 2017;13(12):2804-2813.
90. Rittig SM, Haentschel M, Weimer KJ, et al. Intradermal vaccinations with RNA coding for TAA generate CD8+ and CD4+ immune responses and induce clinical benefit in vaccinated patients. *Mol Ther*. 2011;19(5):990-999.
91. Weide B, Carralot JP, Reese A, et al. Results of the first phase I/II clinical vaccination trial with direct injection of mRNA. *J Immunother*. 2008;31(2):180-188.
92. Meyer M, Huang E, Yuzhakov O, Ramanathan P, Ciaramella G, Bukreyev A. Modified mRNA-based vaccines elicit robust immune responses and protect guinea pigs from ebola virus disease. *J Infect Dis*. 2018;217(3):451-455.
93. Servick K. This mysterious $2 billion biotech is revealing the secrets behind its new drugs and vaccines. Science: AAAS. Feb 1, 2017. http://doi.org/10.1126/science.aal0686
94. Quakkelaar ED, Redeker A, Haddad EK, et al. Improved innate and adaptive immunostimulation by genetically modified HIV-1 protein expressing NYVAC vectors. *PLOS One*. 2011;6(2):e16819.
95. Liu BL, Robinson M, Han ZQ, et al. ICP34.5 deleted herpes simplex virus with enhanced oncolytic, immune stimulating, and anti-tumour properties. *Gene Therapy*. 2003;10(4):292-303.
96. Dattananda CS, Rajkumari K, Gowrishankar J. Multiple mechanisms contribute to osmotic inducibility of proU operon expression in *Escherichia coli*: demonstration of two osmoresponsive promoters and of a negative regulatory element within the first structural gene. *J Bacteriol*. 1991;173(23):7481-7490.
97. Bao Q, Li X, Han G, Zhu Y, Mao C, Yang M. Phage-based vaccines. *Adv Drug Delivery Rev*. 2019;145:40-56.
98. Karbach J, Neumann A, Brand K, et al. Phase I clinical trial of mixed bacterial vaccine (Coley's toxins) in patients with NY-ESO-1 expressing cancers: immunological effects and clinical activity. *Clin Cancer Res*. 2012;18(19):5449-5459.
99. Smith GP. Filamentous fusion phage: novel expression vectors that display cloned antigens on the virion surface. *Science*. 1985;228(4705):1315-1317.
100. Smith LL, Buckley R, Lugar P. Diagnostic immunization with bacteriophage PhiX 174 in patients with common variable immunodeficiency/hypogammaglobulinemia. *Front Immunol*. 2014;5:410.
101. Enomoto Y, Bharti A, Khaleque AA, et al. Enhanced immunogenicity of heat shock protein 70 peptide complexes from dendritic cell-tumor fusion cells. *J Immunol*. 2006;177(9):5946-5955.
102. Vermorken JB, Claessen AM, van Tinteren H, et al. Active specific immunotherapy for stage II and stage III human colon cancer: a randomised trial. *Lancet*. 1999;353(9150):345-350.
103. Jocham D, Richter A, Hoffmann L, et al. Adjuvant autologous renal tumour cell vaccine and risk of tumour progression in patients with renal-cell carcinoma after radical nephrectomy: phase III, randomised controlled trial. *Lancet*. 2004;363(9409):594-599.
104. Cheever MA, Higano CS. PROVENGE (Sipuleucel-T) in prostate cancer: the first FDA-approved therapeutic cancer vaccine. *Clin Cancer Res*. 2011;17(11):3520-3526.
105. Zuniga-Pflucker JC. T-cell development made simple. *Nat Rev Immunol*. 2004;4(1):67-72.
106. Zhou J, Wang G, Chen Y, Wang H, Hua Y, Cai Z. Immunogenic cell death in cancer therapy: present and emerging inducers. *J Cell Mol Med*. 2019;23(8):4854-4865.
107. Galluzzi L, Buqué A, Kepp O, Zitvogel L, Kroemer G. Immunogenic cell death in cancer and infectious disease. *Nat Rev Immunol*. 2017;17(2):97-111.
108. Deng L, Liang H, Xu M, et al. STING-dependent cytosolic DNA sensing promotes radiation-induced type I interferon-dependent antitumor immunity in immunogenic tumors. *Immunity*. 2014;41(5):843-852.
109. Woo SR, Fuertes MB, Corrales L, et al. STING-dependent cytosolic DNA sensing mediates innate immune recognition of immunogenic tumors. *Immunity*. 2014;41(5):830-842.
110. Fu J, Kanne DB, Leong M, et al. STING agonist formulated cancer vaccines can cure established tumors resistant to PD-1 blockade. *Sci Transl Med*. 2015;7(283):283ra52.
111. Lee CH, Yelensky R, Jooss K, Chan TA. Update on tumor neoantigens and their utility: Why it is good to be different. *Trends Immunol*. 2018;39(7):536-548.
112. Pedersen SR, Sørensen MR, Buus S, Christensen JP, Thomsen AR. Comparison of vaccine-induced effector CD8 T cell responses directed against self- and non-self-tumor antigens: implications for cancer immunotherapy. *J Immunol*. 2013;191(7):3955-3967.
113. Snyder A, Makarov V, Merghoub T, et al. Genetic basis for clinical response to CTLA-4 blockade in melanoma. *N Engl J Med*. 2014;371(23):2189-2199.
114. Sahin U, Derhovanessian E, Miller M, et al. Personalized RNA mutanome vaccines mobilize poly-specific therapeutic immunity against cancer. *Nature*. 2017;547(7662):222-226.
115. Hodges TR, Ott M, Xiu J, et al. Mutational burden, immune checkpoint expression, and mismatch repair in glioma: implications for immune checkpoint immunotherapy. *Neuro Oncol*. 2017;19(8):1047-1057.
116. Otter S, Whitaker S, Chatterjee J, Stewart A. The human papillomavirus as a common pathogen in oropharyngeal, anal and cervical cancers. *Clin Oncol (R Coll Radiol)*. 2019;31(2):81-90.
117. Arbyn M, Xu L, Simoens C, Martin-Hirsch PP. Prophylactic vaccination against human papillomaviruses to prevent cervical cancer and its precursors. *Cochrane Database Syst Rev*. 2018;5:Cd009069.
118. Wise-Draper TM, Wells SI. Papillomavirus E6 and E7 proteins and their cellular targets. *Front Biosci*. 2008;13:1003-1017.
119. Vande Pol SB, Klingelhutz AJ. Papillomavirus E6 oncoproteins. *Virology*. 2013;445(1-2):115-137.
120. Grunwitz C, Salomon N, Vascotto F, et al. HPV16 RNA-LPX vaccine mediates complete regression of aggressively growing HPV-positive mouse tumors and establishes protective T cell memory. *Oncoimmunology*. 2019;8(9):e1629259.
121. van Driel WJ, Ressing ME, Kenter GG, et al. Vaccination with HPV16 peptides of patients with advanced cervical carcinoma: clinical evaluation of a phase I-II trial. *Eur J Cancer*. 1999;35(6):946-952.
122. van Poelgeest MIE, Welters MJP, van Esch EMG, et al. HPV16 synthetic long peptide (HPV16-SLP) vaccination therapy of patients

with advanced or recurrent HPV16-induced gynecological carcinoma, a phase II trial. *J Transl Med*. 2013;11:88.
123. Rice AE, Latchman YE, Balint JP, Lee JH, Gabitzsch ES, Jones FR. An HPV-E6/E7 immunotherapy plus PD-1 checkpoint inhibition results in tumor regression and reduction in PD-L1 expression. *Cancer Gene Ther*. 2015;22(9):454-462.
124. Lin PL, Cheng YM, Wu DW, et al. A combination of anti-PD-L1 mAb plus Lm-LLO-E6 vaccine efficiently suppresses tumor growth and metastasis in HPV-infected cancers. *Cancer Med*. 2017;6(9):2052-2062.
125. Liu Z, Zhou H, Wang W, Fu YX, Zhu M. A novel dendritic cell targeting HPV16 E7 synthetic vaccine in combination with PD-L1 blockade elicits therapeutic antitumor immunity in mice. *Oncoimmunology*. 2016;5(6):e1147641.
126. NCCN. Merkel cell carcinoma (Version 2.2019). https://merkelcell.org/wp-content/uploads/2017/10/MCC_v.2.2019-2.pdf. Accessed 31 January 2020.
127. Becker JC, Stang A, DeCaprio JA, et al. Merkel cell carcinoma. *Nat Rev Dis Primers*. 2017;3:17077.
128. Topalian SL, Bhatia S, Hollebecque A, et al. Abstract CT074: non-comparative, open-label, multiple cohort, phase 1/2 study to evaluate nivolumab (NIVO) in patients with virus-associated tumors (CheckMate 358): efficacy and safety in Merkel cell carcinoma (MCC). *Cancer Res*. 2017;77(13 suppl):CT074.
129. Nghiem P, Bhatia S, Lipson EJ, et al. Durable tumor regression and overall survival in patients with advanced Merkel cell carcinoma receiving pembrolizumab as first-line therapy. *J Clin Oncol*. 2019;37(9):693-702.
130. Colombo MP, Trinchieri G. Interleukin-12 in anti-tumor immunity and immunotherapy. *Cytokine Growth Factor Rev*. 2002;13(2):155-168.
131. Zundler S, Neurath MF. Interleukin-12: functional activities and implications for disease. *Cytokine Growth Factor Rev*. 2015;26(5):559-568.
132. Chiocca EA, Yu JS, Lukas RV, et al. Regulatable interleukin-12 gene therapy in patients with recurrent high-grade glioma: results of a phase 1 trial. *Sci Transl Med*. 2019;11(505):eaaw5680.
133. Bekaii-Saab TS, Roda JM, Guenterberg KD, et al. A phase I trial of paclitaxel and trastuzumab in combination with interleukin-12 in patients with HER2/neu-expressing malignancies. *Mol Cancer Ther*. 2009;8(11):2983-2991.
134. Sp. K Sample size calculator. https://clincalc.com/stats/samplesize.aspx. Accessed February 6, 2020.
135. Kaufman HL, Russell J, Hamid O, et al. Avelumab in patients with chemotherapy-refractory metastatic Merkel cell carcinoma: a multicentre, single-group, open-label, phase 2 trial. *Lancet Oncol*. 2016;17(10):1374-1385.

How to cite this article: Tabachnick-Cherny S, Pulliam T, Church C, Koelle DM, Nghiem P. Polyomavirus-driven Merkel cell carcinoma: Prospects for therapeutic vaccine development. *Molecular Carcinogenesis*. 2020;59:807–821. https://doi.org/10.1002/mc.23190

cancers

MDPI

Review

Intersection of Two Checkpoints: Could Inhibiting the DNA Damage Response Checkpoint Rescue Immune Checkpoint-Refractory Cancer?

Peter H. Goff [1,†], Rashmi Bhakuni [2,†], Thomas Pulliam [2], Jung Hyun Lee [2,3], Evan T. Hall [4,5] and Paul Nghiem [2,5,*]

1 Department of Radiation Oncology, University of Washington, Seattle, WA 98195, USA; goffp01@uw.edu
2 Division of Dermatology, Department of Medicine, University of Washington, Seattle, WA 98109, USA; rbhakuni@uw.edu (R.B.); thpullia@uw.edu (T.P.); jlee24@uw.edu (J.H.L.)
3 Institute for Stem Cell and Regenerative Medicine, Department of Bioengineering, University of Washington, Seattle, WA 98109, USA
4 Division of Medical Oncology, Department of Medicine, University of Washington, Seattle, WA 98109, USA; evanh@uw.edu
5 Clinical Research Division, Fred Hutchinson Cancer Research Center, Seattle, WA 98109, USA
* Correspondence: pnghiem@uw.edu
† These authors contributed equally to the work.

Simple Summary: Immunotherapies have revolutionized the management of advanced stage cancer; however, not all patients benefit given many cancers are resistant to immune checkpoint inhibitors. To support rapid growth, malignant cells frequently bypass the cell cycle checkpoints that normally ensure high-fidelity DNA replication prior to cell division. Therefore, cancer cells (lacking early cell cycle checkpoints) are under high replication stress and rely more heavily on the DNA damage response (DDR) for survival and growth. DDR pathways are long-recognized anti-neoplastic targets. Recently, preclinical studies have demonstrated unexpected crosstalk between these pathways and the immune system. Here, we discuss emerging evidence linking cell cycle biology and the DDR to innate and adaptive immunity. We present a rationale for why Merkel cell carcinoma could serve as a paradigm for studying DDR inhibitors as novel agents to overcome resistance to programmed cell death-1 (PD-1) pathway blockade.

Abstract: Metastatic cancers resistant to immunotherapy require novel management strategies. DNA damage response (DDR) proteins, including ATR (ataxia telangiectasia and Rad3-related), ATM (ataxia telangiectasia mutated) and DNA-PK (DNA-dependent protein kinase), have been promising therapeutic targets for decades. Specific, potent DDR inhibitors (DDRi) recently entered clinical trials. Surprisingly, preclinical studies have now indicated that DDRi may stimulate anti-tumor immunity to augment immunotherapy. The mechanisms governing how DDRi could promote anti-tumor immunity are not well understood; however, early evidence suggests that they can potentiate immunogenic cell death to recruit and activate antigen-presenting cells to prime an adaptive immune response. Merkel cell carcinoma (MCC) is well suited to test these concepts. It is inherently immunogenic as ~50% of patients with advanced MCC persistently benefit from immunotherapy, making MCC one of the most responsive solid tumors. As is typical of neuroendocrine cancers, dysfunction of p53 and Rb with upregulation of Myc leads to the very rapid growth of MCC. This suggests high replication stress and susceptibility to DDRi and DNA-damaging agents. Indeed, MCC tumors are particularly radiosensitive. Given its inherent immunogenicity, cell cycle checkpoint deficiencies and sensitivity to DNA damage, MCC may be ideal for testing whether targeting the intersection of the DDR checkpoint and the immune checkpoint could help patients with immunotherapy-refractory cancers.

Keywords: immune checkpoint inhibitors; ATR; ATM; DNA-PK; DNA damage response inhibitors; Merkel cell carcinoma; PD-1 pathway; cell cycle checkpoint; immunogenic cell death

Citation: Goff, P.H.; Bhakuni, R.; Pulliam, T.; Lee, J.H.; Hall, E.T.; Nghiem, P. Intersection of Two Checkpoints: Could Inhibiting the DNA Damage Response Checkpoint Rescue Immune Checkpoint-Refractory Cancer? *Cancers* **2021**, *13*, 3415. https://doi.org/10.3390/cancers13143415

Academic Editor: Kavita Y. Sarin

Received: 9 June 2021
Accepted: 5 July 2021
Published: 8 July 2021

1. Immunotherapy: Progress and Problems

Over the past decade, immune checkpoint inhibitors (ICIs) have progressed from early clinical trials to established pillars of treatment for many advanced solid malignancies [1]. There are now eight ICIs approved for a variety of indications which target programmed cell death-1 (PD-1) or its ligand, PD-L1, or cytotoxic T-lymphocyte-associated protein 4 (CTLA-4) [2–4]. Agents targeting PD-1 or PD-L1 (collectively "anti-PD-(L)1" therapies) have become dominant (seven of the eight approvals) in most settings given their higher efficacy and reduced toxicity relative to anti-CTLA-4 therapy [5–7]. Broadly speaking, these immune checkpoint pathways serve as negative regulators of T cell immunity. Their specific functions and patterns of cellular expression have been reviewed in detail [8,9]. The proportion of patients with advanced cancer who are eligible for ICI therapy increased from an estimated 1.5% in 2011 to 44% in 2018 [10], and increasing ICI utilization is associated with survival gains for patients with several advanced malignancies [11–14]. Despite the remarkable expansion in the number of agents and indications for ICIs in cancer therapy, response rates are affected by many factors and vary widely, as discussed below.

1.1. Clinical Efficacy of Immune Checkpoint Inhibitors

Response rates to ICIs vary widely by histology from essentially no benefit to greater than 50% in the most sensitive cancers [1]. Notably, many skin cancers are associated with a high tumor mutational burden (TMB) resulting from ultraviolet radiation (UV)-induced DNA damage [15,16]. Tumor neoantigens derived from DNA damage render them visible to anti-tumor T cells, and thus skin cancers are particularly sensitive to ICIs. The first FDA (United States Food and Drug Administration) approval granted for any ICI was for an anti-CTLA-4-targeting monoclonal antibody, ipilimumab, for melanoma in 2011 after showing a survival benefit in patients with pre-treated metastatic disease [17]. There have been many subsequent approvals for ICIs to treat skin cancers, and response rates for each of the following indications were in the impressive 30–60% range [18]. The majority of responses to ICIs are more durable than those achieved with chemotherapy or targeted therapies. Nivolumab (anti-PD-1) and pembrolizumab (anti-PD-1) were approved for melanoma in 2014 and 2015, respectively [19,20]. The combination of anti-PD-1 and anti-CTLA-4 agents was approved in 2015 for melanoma; overall survival at 5 years was 52% for ipilimumab/nivolumab vs. 44% for nivolumab alone [21]. Combining CTLA-4 and PD-1 inhibitors increases immune-related toxicities, although efforts are underway to optimize dosing to improve the tolerability of combined therapy [22]. Avelumab (anti-PD-L1) [23,24] and pembrolizumab [25,26] were approved for Merkel cell carcinoma (MCC) in 2017 and 2018, respectively. Cemiplimab (anti-PD-1) was approved for squamous cell carcinoma in 2018 [27] and for basal cell carcinoma [28] in 2021.

To increase response rates to ICIs across diverse cancer types, significant efforts have been made to identify biomarkers to inform patient selection. An increase in ICI responsiveness has been linked to a litany of factors that include tumor-intrinsic (e.g., high TMB [16] or PD-L1 expression [29]) and tumor-extrinsic factors (e.g., low neutrophil to lymphocyte ratio [30] and obesity [31,32]). Yet, no single factor or well-defined combination of factors has yielded a clinically reliable predictor of response to immunotherapy. Absent predictive markers, the typical approach is to empirically administer therapy to all eligible patients. As the average cancer patient treated with an ICI is not likely to have a meaningful response (although many histologies are highly responsive as above), some patients will experience significant toxicity without benefit. TMB can be readily determined and is one of the most clinically used, if imperfect, predictors of response to ICI [33]. Indeed, pembrolizumab was approved for treatment of all advanced solid tumors with a high TMB ($\geq$10 mutations/megabase) on the basis of an overall response rate of 29% [34].

1.2. Limitations of Current Immune Checkpoint Inhibitors

With the urgent need to increase response rates to ICIs, tremendous efforts have been made and are ongoing to optimally combine them with existing or novel therapies. Some

notable gains have been made in combining ICI with cytotoxic chemotherapy in lung [35] and esophageal cancers [36], for example. However, while chemotherapy reduces the systemic tumor burden, it also weakens the anti-tumor immune response (as lymphocytes are sensitive to cytotoxic agents), making this an approach that may not be suitable for all tumor types [37,38]. Combining radiation with ICI has been widely tested with some notable areas of success [39–43], although it may be immunosuppressive in some settings. Adding radiotherapy to immune therapy in ICI-resistant patients has generally not yielded a synergistic clinical benefit for unirradiated tumors despite very promising data in animal models and some early, promising clinical studies [39,44–46].

With new efforts to combine immune therapies to augment efficacy, immune related adverse events (irAEs) also become more prevalent. irAEs are immune responses induced by the relevant therapy against healthy tissues. The combination of immunotherapies has yielded some successes. Combining ipilimumab with anti-PD-1 agents in melanoma [21] or hepatocellular carcinoma (HCC) [47,48] may increase response rates modestly for resistant cancers but at the cost of a significant increase in the likelihood and severity of irAEs. Even for single-agent immunotherapy, irAEs are sometimes severe, may be irreversible and often lead to discontinuation of immunotherapy [49,50]. Despite the appeal of combing multiple immunotherapies to augment response rates, this approach will typically lead to greater irAE toxicities. One successful strategy to avoid augmented irAEs has been the use of intralesional immune-stimulating agents which typically do not increase systemic immune toxicity. Talimogene laherparepvec (T-VEC) is an oncolytic herpesvirus approved for intralesional melanoma injection [51]. T-VEC is well tolerated in combination with ICI and is being explored in immunotherapy-resistant disease [52,53].

1.3. New Approaches to Improve the Efficacy of ICI and Enhance Anti-Tumor Immunity

To expand the pool of patients benefitting from immunotherapy, efforts are underway to identify predictive biomarkers for ICI response in order to better select patients and inform future clinical trial design [54,55]. Novel therapies and combinations of existing treatments are also in development to aid patients with ICI-refractory disease. For example, the combination of ICI with molecularly targeted agents, such as the vascular endothelial growth factor receptor (VEGFR) inhibitor bevacizumab or multi-tyrosine kinase inhibitors (e.g., axitinib or cabozantinib), has shown promising efficacy in recent trials [56,57]. The development of agents targeting novel immune checkpoint proteins (e.g., lymphocyte activating 3 (Lag3), T cell immunoglobulin and mucin domain-containing protein 3 (Tim3)) is also well underway and could be combined with existing ICIs [58–60].

Identifying non-immune targets for anti-neoplastic drugs that may stimulate anti-tumor immunity, especially in the setting of ICI-refractory cancers, is particularly appealing because they are less likely to augment irAEs. Targets including cell cycle regulators (e.g., cyclin-dependent kinases or CDKs) and DNA damage response (DDR) proteins have long been of interest in cancer research. Clinically, the most advanced DNA damage repair-targeting agents are inhibitors of poly (ADP-ribose) polymerase (PARPi), which are actively being explored in combination with ICI [61–63]. PARPi have efficacy in BRCA-mutant (BRCA1/2 mutations) cancers deficient in homologous recombination (via "synthetic lethality") but are currently of limited utility outside of this setting [64]. The status of PARPi has been extensively summarized and is not the focus of this review [65]. Instead, several new drug candidates targeting central regulators of the DDR are of emerging significance. These include ATR (ataxia telangiectasia and Rad3-related), ATM (ataxia telangiectasia mutated) and DNA-PK (DNA-dependent protein kinase) for which several inhibitors have entered clinical trials in the past several years [66,67]. Exciting preclinical data suggest these new agents have the potential to synergize with ICIs, potentially without increasing immune-related toxicity.

2. Crosstalk between the DNA Damage Response and Innate and Adaptive Immunity

Surgery, radiation and chemotherapy are the traditional three pillars of cancer therapy. The latter two selectively induce DNA damage in rapidly dividing tumor cells in contrast to healthy, normal tissues which divide less frequently. Accordingly, DDR pathways and cell cycle checkpoint biology have been intensely studied for decades with an eye toward developing molecularly targeted anti-cancer therapeutics.

The DNA damage response is a network of multiple interconnected pathways responsible for repairing damaged DNA and maintaining genomic integrity. The DDR pathways are integrated with cell cycle checkpoint proteins (e.g., Rb (retinoblastoma protein) and p53 (tumor protein p53)) such that when DNA damage is sensed, progression through the cell cycle is arrested until the damage may be repaired or, if irreparable, the cell may undergo regulated cell death to prevent the passage of potentially deleterious DNA mutations to daughter cells. There are three master regulatory proteins of the DDR: ATR, ATM and DNA-PK, which have been extensively reviewed [68]. These DDR proteins have some specificity for various DNA lesions with ATM and DNA-PK acting at double-strand DNA (dsDNA) breaks, while ATR is recruited to single-strand DNA (ssDNA) at stalled replication forks. These "transducer kinases" then act differentially at various points in the cell cycle [69].

Neoplastic cells frequently harbor mutations in cell cycle checkpoints, most commonly p53. Mutations in DDR proteins including functional deletions in ATM and DNA-PK proteins are also observed [70]. However, ATR, which acts in the S (DNA synthesis) and G2 (gap 2) phases of the cell cycle to ensure that DNA synthesis is complete prior to entering mitosis, is virtually never completely eliminated. Indeed, complete loss of ATR function has not been observed in humans to our knowledge, although its expression is greatly reduced in some cases of Seckel syndrome [71]. In contrast, ATM loss of function causes ataxia telangiectasia, which occurs at rates of up to ~1:40,000 individuals and is associated with a 20–30% lifetime cancer risk [72]. ATM heterozygosity is prevalent at rates of 1–2% in the general population and is a significant risk for the development of several malignancies, breast cancer in particular [72–74]. ATM mutations are present in approximately 5% of all cancers [75]. Human germline DNA-PK loss of function mutation is very rare but is a cause of severe combined immunodeficiency [76]. Mouse studies support ATR as a critical protein, with its knockout resulting in embryonic lethality [77], while ATM [78] and DNA-PK [79] knockout mouse models are viable. While ATM and DNA-PK expression may be lost in human cancer [70,75], ATR expression is generally maintained, although mutations and reduced expression levels are sometimes observed [80]. Dysregulation of DNA-PK leading to increased activity is also associated with aggressive cancers with poor outcomes [81,82]. Loss of cell cycle checkpoints supports the unrestrained growth characteristic of neoplastic cells. DDR protein deficiencies may benefit cancer cells by allowing them to bypass these cell cycle checkpoints and harbor a greater mutational burden. ATR's role in ensuring completion of DNA synthesis, especially in the context of other cell cycle checkpoint or DDR pathway deficiencies, appears to be required in replicating cells, thus making it a particularly appealing therapeutic target.

Given the importance of cell cycle checkpoints and DDR biology in tumorigenesis, targeting DDR pathways and their effector proteins to halt cell cycle progression has been of great interest over the past two decades [83]. Inhibitors of ATR, ATM and DNA-PK have been studied in many different cancer types. They were initially explored for their abilities to sensitize cells to DNA-damaging agents, including radiation and cytotoxic chemotherapies, or to synergize with existing cell cycle checkpoint or DDR deficiencies (e.g., use of ATR inhibitors in ATM-deficient malignancies) to exert a direct cytotoxic effect [84,85]. The concept of synthetic lethality has perhaps been best demonstrated clinically with the use of PARPi in BRCA (breast cancer)-deficient cancers whereby PARP-mediated DNA damage repair becomes critical for maintaining genomic integrity with the loss of homologous recombination [86]. After more than a decade of delay between establishing that DDR proteins were desirable cancer therapy targets, potent and selective

mediated DNA damage repair becomes critical for maintaining genomic integrity with the loss of homologous recombination [86]. After more than a decade of delay between establishing that DDR proteins were desirable cancer therapy targets, potent and selective compounds eventually became available to target ATR, ATM and DNA-PK. Recent clinical studies have shown that several drug candidates appear to be tolerated in combination with radiation or a variety of chemotherapeutic agents, as discussed below.

Excitingly, in recent years, preclinical models exploring these novel, selective DDR inhibitors (DDRi) show that they have a surprising and potentially important effect: the ability to augment innate and/or adaptive anti-tumor immune responses. Here, we focus on the underlying mechanisms by which DDR pathway inhibition may augment anti-tumor immunity and potentially assist in overcoming resistance to ICI therapy (Figure 1). Combining an ATR inhibitor (ATRi) with an ICI, thereby targeting an essential regulator of cell cycle checkpoints in addition to immune checkpoint pathway blockade, may synergistically activate anti-tumor immunity while minimizing the toxicity of combined therapies.

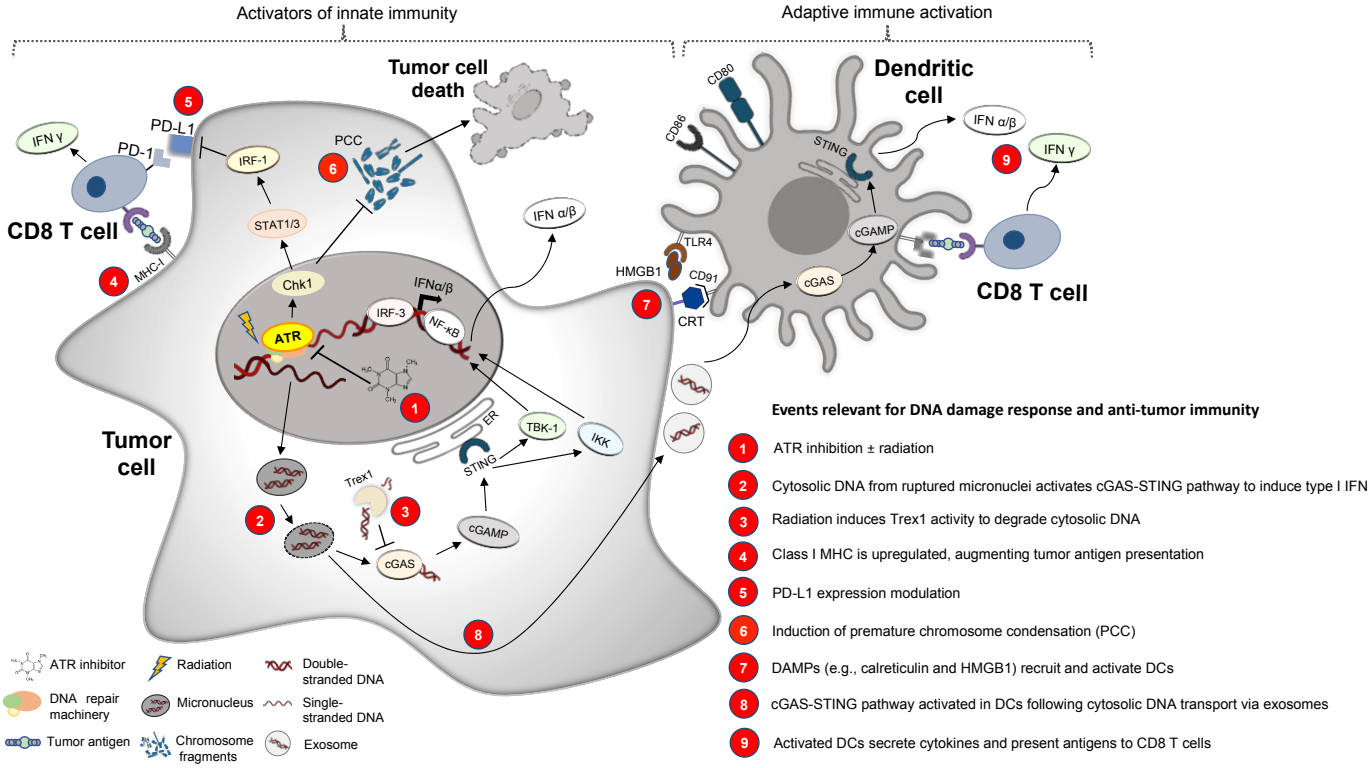

Figure 1. Events that relate targeted DDR (ATR) inhibition to anti-tumor immunity. Nine steps delineated in this figure summarize how ATR inhibition may augment innate immunity and reinvigorate adaptive immune responses via cGAS-STING pathway activation, DAMP signaling, PD-L1 expression modulation, class I MHC upregulation and enhanced T cell priming via activation of dendritic cells (see text for explanation). Abbreviations: CD80/86/91: cluster of differentiation 8/80/86/91, cGAMP: cyclic guanosine monophosphate–adenosine monophosphate, cGAS: cyclic GMP-AMP synthase, Chk1: checkpoint kinase 1, CRT: calreticulin, DAMPs: damage-associated molecular patterns, HMGB1: high mobility group box protein 1, IFN: interferon, IKK: IκB kinase, IRF-1 or 3: interferon regulatory factor 1 or 3, MHC: major histocompatibility complex, NFκB: nuclear factor κB, PD-(L)1: programmed death-ligand 1, STAT: signal transducer and activator of transcription, STING: stimulator of interferon genes, TBK-1: TANK-binding kinase 1, TLR4: Toll-like receptor 4, Trex1: three prime repair exonuclease 1.

There is substantial preclinical evidence relating targeted DDR pathway inhibition to anti-tumor immunity, as schematized in Figure 1 and described below:

(1) With the recent availability of highly selective DDR pathway-targeting agents, inhibition of ATR, ATM and DNA-PK has been heavily explored preclinically, and to a lesser extent in clinical trials, to sensitize tumors to radiation and other DNA-damaging agents [67,87–96].

(2) Interestingly, recent studies demonstrate how DDR pathway signaling regulates the innate immune response by limiting micronuclei (MN) formation and cytosolic dsDNA

accumulation [97–101]. In the presence of DDRi, however, cytosolic dsDNA leads to upregulated cGAS (cyclic GMP-AMP synthase)-STING (stimulator of interferon genes) signaling to induce type I interferon (IFN). Indeed, inhibition of ATR [102–104], ATM [105–108] or DNA-PK [109] activity results in enhanced innate immune responses in vitro and in mice.

(3) Following radiation-induced release of dsDNA into the cytosol, a DNA exonuclease, Trex1 (three prime repair exonuclease 1), suppresses anti-tumor immunity by degrading DNA and thus depriving cGAS-STING of its stimulatory signal [110,111]. Reduced expression of Trex1 in human cancer cell lines is associated with increased sensitivity to an ATRi [112].

(4) Radiation alone may upregulate MHC-I (major histocompatibility complex class I) expression and antigen presentation [113–116]. ATR, ATM and DNA-PK inhibition may also increase MHC-I expression in tumor cells to effect antigen presentation and T cell infiltration [102,107,117].

(5) Radiation upregulates PD-L1 on tumor cells which may affect their immunogenicity [45]. DDR pathway inhibition may also affect PD-L1 expression on tumor cells, although there is significant heterogeneity of the effect in different model systems. For example, ATR inhibition alleviated dsDNA break-induced PD-L1 upregulation in various cancer cell lines [118,119]. Similarly, in cultured HCC cells, ATRi treatment in combination with radiation decreased PD-L1 expression on tumor cells [120]. Conversely, targeted inhibition of Chk1 (checkpoint kinase 1, a critical effector kinase for ATR) induced PD-L1 expression in both human and murine small cell lung cancer cell lines [100]. Ionizing radiation-induced PD-L1 expression in U2OS cells was noted to be suppressed by an ATMi [119]. In human lung cancer cell lines, DNA-PK inhibition downregulated PD-L1 while increasing MHC-I expression [117] which could lead to improved activation of anti-tumor T cells. In summary, preclinical data suggest that DDR pathways often impinge on immune checkpoint biology, and this area warrants further study.

(6) ATR inhibition may selectively sensitize rapidly proliferating tumor cells via premature chromatin condensation (PCC) which can promote MN formation, subsequent innate immune signaling and potentially immunogenic cell death (ICD) [121–125] (see Figure 2 for details).

(7) Radiation induces ICD through release of damage-associated molecular patterns (DAMPs) that activate dendritic cells (DCs) and thus augment the adaptive immune response [126]. Combining ATR inhibition with DNA-damaging agents may markedly increase the expression of DAMPs (surface-exposed calreticulin, high mobility group box protein 1 (HMGB1) and adenosine 5′-triphosphate (ATP) release) [127,128]. As depicted in Figure 1, DAMPs displayed by the tumor cell, HMGB1 and calreticulin, interact with their receptors on DCs, toll-like receptor 4 (TLR4) and CD91 (cluster of differentiation 91), respectively [129–133].

(8) and (9) Cytosolic DNA released from tumor cell-derived MN is transported within exosomes to DCs [134]. This induces type I IFN production via cGAS-STING activation in DCs [135–137]. ATR inhibition may enhance cGAS-STING signaling and DC activation in murine tumors to potentiate anti-tumoral cytotoxic T cells [102,138]. In addition to inducing ICD, combining an ATRi with RT may also induce senescence in a manner that could depend upon cGAS [139,140].

Several recent and exciting preclinical studies in immune-competent mouse models have explored the potential of DDR pathway inhibition to augment anti-tumor immunity. AZD6738 (ATRi) synergized with low-dose radiation to induce T cell-mediated tumor rejection in a mouse model of Kras-driven colorectal cancer [141]. Similarly, AZD6738 synergized with low-dose radiation to activate an IFN response, promote antigen presentation and increase T and natural killer (NK) cell infiltration, thereby improving tumor control in a murine model of HPV-driven cancer [102]. In a mouse model of HCC, the addition of an ATRi to radiation plus an anti-PD-L1 antibody increased anti-tumor CD8 T cell activity, enhanced immune memory and prolonged survival relative to radiation + ICI alone [120]. The observed efficacy of ATRi + ICI + radiation was mediated via cGAS-STING signal-

ing [120]. Similarly, inhibition of Chk1 in a murine small cell lung cancer model potentiated ICI and was dependent on the cGAS-STING pathway [100]. Therefore, inhibition of ATR signaling augments innate immunity to damaged DNA in a variety of preclinical models, and an ATRi may augment ICI activity.

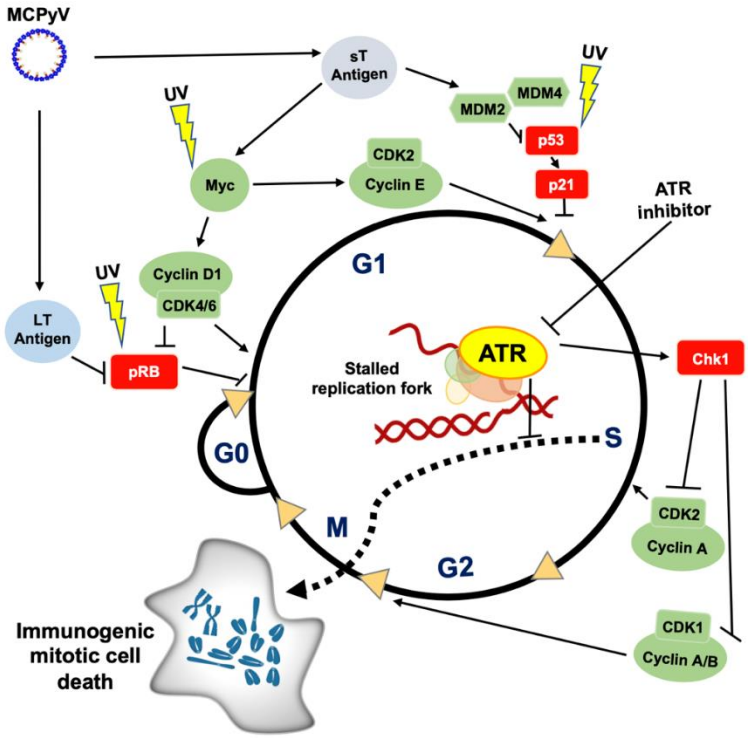

Figure 2. A model of how cell cycle dysregulation in Merkel cell carcinoma may predispose to ATR inhibition. Cellular components that restrain progression of the cell cycle are depicted in red; cell cycle progression accelerators are shown in green. In virus-positive (VP) MCC, Rb is directly inactivated by binding the MCPyV LT oncoprotein. p53 (via activation of MDM2/4) and Myc signaling are dysregulated in VP-MCC by the sT oncoprotein. Similarly, in virus-negative (VN) MCC, UV mutations disrupt Rb and p53 and promote Myc signaling. These changes disable the G1 cell cycle checkpoint in both VP- and VN-MCCs, making it potentially more reliant on ATR to ensure completion of DNA replication in S and G2 phases of the cell cycle. Stalled replication forks normally recruit ATR and lead to Chk1 activation. If ATR is inhibited, this disrupts the Chk1-dependent activation of the intra-S and G2/M checkpoints. This in-turn causes stalled replication forks to not be detected, may lead to double-strand breaks and, as depicted by the dashed arrow, promotes premature entry into M phase. This process may manifest as premature chromatin condensation (PCC) and lead to an immunogenic type of mitotic cell death. Abbreviations: CDK: cyclin dependent kinase, Chk1: checkpoint kinase 1, G0 phase: resting phase, G1 or G2 phase: Gap 1 or 2 phase, LT: Large T antigen, McPyV: Merkel cell polyomavirus, Mdm2 or 4: mouse double minute 2 or 4 homolog, M phase: mitosis phase, Myc: myelocytomatosis protein, PCC: premature chromatin condensation, p53: tumor protein p53, Rb: retinoblastoma protein, S phase: DNA synthesis phase, sT: small T antigen, UV: ultraviolet radiation.

Loss of ATM or DNA-PK signaling may also increase the immunogenicity of tumors. Cells derived from patients with ATM deficiency and ATM-deficient mice both have increased type I IFN responses via the cGAS-STING pathway [105]. ATM inhibition (via small molecule or short-hairpin RNA) enhanced anti-tumor immunity in combination with ICI and radiation in murine models of ovarian and pancreatic cancers [107,108]. Inhibition (or genetic deficiency) of DNA-PK may similarly enhance innate immunity via cGAS-STING signaling [109]. DNA-PK mutations have been associated with a high TMB and high ICI response rates in several human cancers, and a DNA-PKi enhanced the

efficacy of PD-1 pathway blockade in a murine colon cancer model [142]. In summary, there is substantial preclinical evidence that DDR pathway inhibition can augment innate and adaptive anti-tumor immunity. DDRi warrant further clinical study in the setting of ICI-refractory disease.

3. Clinical Experience with DNA Damage Response Pathway Inhibitors

Clinical testing of potent and selective inhibitors of DDR pathways has been underway for several years. The focus of this review is ATR, ATM and DNA-PK inhibitors, although PARPi have reached clinical practice, and early-phase trials of other DDRi have been conducted. Notably, Chk1 inhibitors were the first DDRi to undergo clinical trials and had unfavorable toxicity profiles [83,143]. Per review of clinicaltrials.gov in May 2021, greater than 80 trials in phases I or II are investigating ATRi, ATMi or DNA-PKi in a variety of settings, as reviewed elsewhere [82,144]. To briefly summarize the clinical landscape, there are five ATR inhibitors in clinical trials including AstraZeneca's oral drug ceralasertib (AZD6738), with 33 trials listed, in addition to EMD Serono's intravenous (IV) berzosertib (VX-970/M6620; 23 trials) and oral VX-803 (3 trials), Bayer's oral BAY1895344 (8 trials) and Atrin Pharmaceuticals' ATRN-119 (1 trial). Clinical publications describe early safety and efficacy data for ceralasertib [145], BAY1895344 [146] and berzosertib [147,148] in a variety of settings including as monotherapy or in combination with various DNA-damaging agents. ATRN-119 is a next-generation ATRi with enhanced potency and specificity that is entering early-phase trials [149]. Four ATM inhibitors, including the brain-penetrant, oral AZD1390 [150], are being studied in six trials. Five DNA-PK inhibitors are in early-phase trials. EMD Serono's oral peposertib (M3814 [151]) is the most widely tested with 14 trials in a variety of settings and combinations with chemotherapies or radiotherapy. As summarized in Table 1, three ATR inhibitors (notably ceralasertib in combination with durvalumab in nine studies) and the DNA-PKi M3814 (with avelumab and radiation) are now being clinically tested in combination with ICIs. No clinical trials combining DDRi and ICI have yet to be completed and published to our understanding. Though early meeting abstracts suggest the combinations are well tolerated.

Cancers **2021**, *13*, x 9 of 24

Table 1. Clinical trials pairing DNA damage response inhibitors (DDRi) with immune checkpoint inhibitors (ICIs). The inhibitory concentration (IC_{50}) indicates the potency of the inhibitor. ATM is not listed because no ICI combinations with ATMi were listed on clinicaltrials.gov at the time of review.

Table 1. Clinical trials pairing DNA damage response inhibitors (DDRi) with immune checkpoint inhibitors (ICIs). The inhibitory concentration (IC_{50}) indicates the potency of the inhibitor. ATM is not listed because no ICI combinations with ATMi were listed on clinicaltrials.gov at the time of review.

DDRi Agent	Chemical Structure, IC_{50}	Total No. of Trials	Total No. of Trials with ICI	Phase	ICI Agents in Combination with DDRi
ATR inhibitors					
AZD6738/ Ceralasertib Oral, AstraZeneca	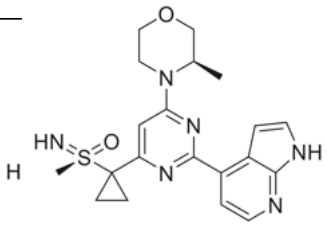 Cell-based IC_{50} = 74 nM	33	9	I/II, II	Durvalumab, Cisplatin/Carboplatin, Cisplatin/Carboplatin + Etoposide + Durvalumab
VX-970/M6620/ Berzosertib Intravenous, EMD Serono	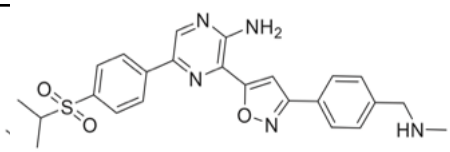 Cell-based IC_{50} = 19 nM	23	3	I, I/II	Avelumab, Avelumab + Carboplatin, Carboplatin + Gemcitabine hydrochloride, Carboplatin + Gemcitabine hydrochloride + Pembrolizumab
BAY1895344/ Elimusertib Oral, Bayer	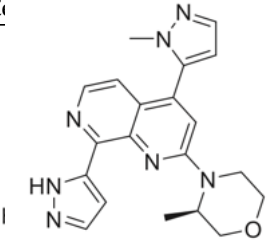	8	2	I	Pembrolizumab, Stereotactic body radiation therapy + Pembrolizumab

Table 1. *Cont.*

DDRi Agent		Total No. of Trials	Trials with ICI	Phase	ICI Agents in Combination with DDRi
VX-970/M6620/ Berzosertib Intravenous, EMD Serono	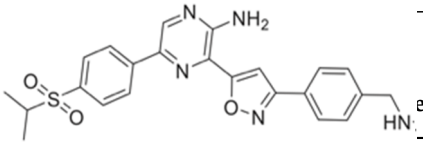	23	3	I, I/II	Avelumab, Avelumab + Carboplatin, Carboplatin + Gemcitabine hydrochloride ± Pembrolizumab
	Cell-based IC_{50} ≡ 74 nM				
BAY1895344/ Elimusertib Oral, Bayer	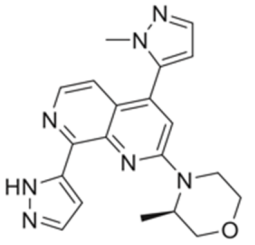	8	2	I	Pembrolizumab, Stereotactic body radiation therapy + Pembrolizumab
	Cell-based IC_{50} ≡ 36 nM				
M3814/MSC2490484A/ Nedisertib/ Peposertib Oral, EMD Serono	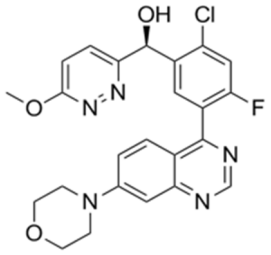	14	3	I, I/II	Avelumab ± radiotherapy, Avelumab + Radium-223 Dichloride, Avelumab + Hypofractionated radiotherapy
	Cell-based IC_{50} ≤ 0.5 μM				

4. Rationale for "Double-Checkpoint Inhibition" in Merkel Cell Carcinoma

The preclinical evidence for potential synergy between DDRi and ICIs is mounting. Investigation of DDR pathway inhibition in ICI-refractory disease is warranted, and multiple DDRi with favorable safety profiles are in early-phase clinical studies. For the reasons below, MCC may be an excellent test case to evaluate the ability of an ATRi to reinvigorate anti-tumor immunity in PD-1 pathway blockade-resistant disease.

MCC is an aggressive neuroendocrine cancer with two distinct etiologies. In the United States, ~80% of MCCs are caused by Merkel cell polyomavirus (MCPyV), whereby the viral T antigens dysregulate essential G1 (gap1) cell cycle checkpoints to effectively transform the cell and drive unconstrained growth [152]. The remaining ~20% of MCC cases result from UV-induced mutations affecting many of the same key G1 cell cycle checkpoint pathways as the MCPyV oncoproteins.

In virus-positive (VP) MCC, patient outcomes are correlated with the presence of CD8 T cells specific for viral protein antigens [153]. Both VP-MCC and virus-negative (VN) MCC are inherently immunogenic and are among the most responsive solid tumors to PD-1 pathway blockade, with approximately 50% of patients achieving durable disease control [25,154–157]. VN-MCC is characterized by an exceptionally high TMB, a well-known predictor of response to anti-PD-(L)1 therapy, as discussed above [16]. There is, however, a significant unmet medical need for MCC patients whose tumors have primary or acquired resistance to PD-1 pathway blockade. Given its characteristic immunogenicity, G1 cell cycle checkpoint deficiencies and associated sensitivity to DNA-damaging agents, we propose that MCC is a highly appealing tumor to test whether ATR inhibition can overcome resistance to PD-1 pathway blockade.

Both VP- and VN-MCC are driven by many of the major "PARCB" factors (p53, Akt1, RB1, c-Myc and Bcl2) of small cell neuroendocrine carcinogenesis [152,158,159]. As depicted in Figure 2, VP- and VN-MCCs are deficient in Rb and p53 signaling, while Myc (myelocytomatosis) signaling is upregulated. The viral Large T (LT) antigen interacts directly with Rb, a negative regulator of cell cycle progression through G1, to inhibit its activity [160]. p53 signaling is deficient in VP-MCC, although the gene is typically wild-type and the T antigens do not appear to directly inhibit its function [160,161]. Rather, small T

(sT) antigen increases the activity of MDM2 (mouse double minute 2 homolog), a ubiquitin ligase regulating p53 activity, via activation of a transcriptional complex including L-Myc [162]. sT-mediated upregulation of L-Myc activity also promotes cell cycle progression through G1 [163]. Signaling via Rb [164,165], p53 [164,166] and Myc [167] is similarly dysfunctional in VN-MCC; however, this is via direct UV-induced mutations in these critical regulatory genes [152,168–170]. The net effect of deregulating the G1 cell cycle checkpoints is a highly proliferative malignancy, as evidenced by median Ki-67 positivity of >50% [171,172] relative to <5% Ki-67-positive tumor cells in malignant melanoma [173].

Loss of these early G1 cell cycle checkpoints renders cells more reliant upon the later S and G2/M cell cycle checkpoints, coordinated by ATR and its downstream effector kinase Chk1 [174,175], to ensure that DNA is replicated prior to entering mitosis (Figure 2). ssDNA at stalled replication forks in the S phase is sensed by ATR which is recruited to regions of ssDNA that have been coated with RPA (replication protein A) [176,177]. ATR subsequently activates Chk1 which signals downstream to halt cell cycle progression via inhibition of CDK2 (cyclin dependent kinase 2)/cyclin A in the S phase or in G2/M via inhibition of CDK1 paired with either cyclin B or cyclin A. As discussed above, complete loss of ATR function is not tolerated in replicating cells in contrast to ATM and DNA-PK which may be lost in human cancers. While ATR function is critical, low-dose pharmacologic inhibition of ATR may be tolerated by untransformed cells while selectively suppressing the growth of H-ras mutant and c-Myc-overexpressing fibroblasts, suggesting an increased reliance upon ATR in oncogene-expressing cells [178] (Figure 2). In the setting of an ATRi, cancer cells proceed prematurely to mitosis prior to completion of DNA synthesis in the S phase, which may manifest as PCC [121] and potentially an immunogenic type of mitotic cell death, as schematized in Figure 2 [125]. MCC tumors are highly replicative with the majority of cells actively dividing, as evidenced by high Ki-67. As such, MCC tumor cells are under significant replication stress and should be more dependent upon ATR to induce the DDR in S/G2 phases to prevent premature entry to mitosis and subsequent cell death. Therefore, ATR inhibition may allow cells to progress through the cell cycle with accumulated DNA damage (Figure 2) and potentiate ICD (Figure 1).

Rapidly dividing cells are particularly sensitive to DNA-damaging agents, as opposed to quiescent G0 cells which are resistant. MCC is sensitive to radiotherapy with an overall response rate of greater than 90% in metastatic lesions receiving a single 8 gray treatment [179]. Responses to radiation in immune-competent patients were durable (<10% in-field progression), whereas in-field tumor progression was observed in 30% of immunodeficient patients [179]. Radiation upregulates tumor cell antigen presentation via MHC-I, the downregulation of which is a well-established and dominant escape mechanism in immunogenic cancers including MCC [180,181]. MCC is notably chemotherapy-sensitive, although responses are short-lived [182–184]. Cytotoxic regimens are lymphodepleting and likely to antagonize the activity of an ICI. Targeting tumor cells with low-dose, conformal radiotherapy and an ATRi, which is selectively cytotoxic in rapidly dividing cells, may reduce the burden of MCC without suppressing systemic immunity which is critical for controlling MCC. Using radiotherapy, particularly hypofractionated regimens which are often considered more immunogenic [42,110], to effect DNA damage and potentiate ICI has been heavily explored over the past decade. The addition of an ATRi may help to potentiate the pro-inflammatory effects of radiation rather than its immunosuppressive properties [102].

5. Clinical Trials Including Patients with Merkel Cell Carcinoma

As summarized in Table 2, more than 80 clinical trials are potentially available for MCC patients or have been recently completed per review of clinicaltrials.gov in May 2021. As MCC is a rare cancer, the majority of these are early-phase studies open to patients with several advanced solid tumors. There are currently no approved therapies for ICI-refractory MCC, and these trials may provide important data to address this area of need. As discussed above, MCC is a highly immunogenic cancer, and, accordingly, novel

immunotherapy-based treatments are well represented (Table 2) [185]. In addition to trials of novel ICIs, several classes of immunostimulatory agents are under study including T cell co-stimulatory molecules, intralesional therapies designed to activate innate immune receptors and oncolytic viruses. Adoptive T and NK cell-based strategies are being tested. Antagonists of immunosuppressive myeloid cells and associated signaling pathways are being explored [186–188]. MCC is notably sensitive to radiation, and several trial designs incorporate radiotherapy in various forms. Agents targeting cell cycle, cell death and cell proliferation pathways are also being tested and may be relevant given the biology of MCC reviewed above. While few of these trials are powered to assess efficacy, their related translational analyses and exploratory endpoints may yield insight into the development of new therapies for ICI-resistant MCC.

Table 2. Novel therapeutic agents potentially available to MCC patients on clinical trials or with recently completed trials.

Drug Class	Sub-Class	Specific Agents	Phase
Immune checkpoint inhibitors (ICI)	Combination ICI	Ipilimumab (anti-CTLA-4) + Nivolumab (anti-PD-1)	I, II
	Novel ICI	INCAGN02385 (Lag3), INCAGN02390 (Tim3)	I
	New PD-(L)1/CTLA4 mAbs	BT-001 (Treg depleting anti-CTLA-4), Tremelimumab (anti-CTLA-4), retifanlimab (anti-PD1)	I/II, II
Radiotherapy	Radiotherapy + ICI	Ipilimumab/Nivolumab + SBRT; Pembrolizumab + SBRT	II
	Novel radiosensitizer	NBTXR3 (radioenhancer hafnium oxide nanoparticle)	I
Immune agonists	T cell co-stimulatory agonist	INCAGN01949 (OX40), INCAGN01876 (GITR), Utomilumab (4-1BB)	I, I/II
	Intralesional innate immune agonists	Poly-ICLC (TLR3), Imiquimod (TLR7), NKTR-262 (TLR7/8), Cavrotolimod (TLR9)	I, I/II
	Oncolytic viruses	T-VEC (Herpes virus), Ad-p53 (adenovirus expressing p53)	I, II
	Tumor vaccines	IFx-Hu2.0 (DNA vaccine with streptococcal antigen)	I
	Cytokines	Bempegaldesleukin (CD122-preferential IL-2 pathway agonist), NT-I7 (IL-7 agonist), N-803 (IL-15 superagonist +ICI or NK cells), SO-C101 (IL-15 superagonist)	I, I/II, II
Adoptive cell therapies	T cells	MCPyV T antigen-specific polyclonal autologous CD8+ T cells	I/II
	NK cells	Allogeneic NK cell	Case only
Novel agents targeting immunosuppressive TME	NOS inhibitor	L-N^{G}-monomethyl Arginine acetate (L-NMMA)	I
	Adenosine antagonist	Etrumadenant	I
	IDO1 inhibitor	Epacadostat	I/II
Tumor antigen targeted therapy	Somatostatin	Lanreotide (SST analogue), Tidutamab/XmAb18087 (bispecific mAb targeting CD3 and SSTR)	I/II, II
	Targeted radionuclide	Lutetium-177 DOTATATE (targeting SSTR)	I/II
Antibody–drug conjugates	Anti-DLL3	Rovalpituzumab tesirine (anti-DLL3 with DNA cross-linking drug)	I
	Anti-CD56	huN901-DM1 (anti-CD56 with microtubule inhibitor)	I

Table 2. *Cont.*

Drug Class	Sub-Class	Specific Agents	Phase
Cell cycle/cell death and proliferation pathways	MDM2 inhibitor	KRT-232	II
	Anti-Bcl2	Oblimersen	II
	mTOR inhibitors	RAD001, MLN0128	I, I/II
Anti-angiogenics	Anti-VEGF mAb	Bevazicumab (with atezolizumab)	I/II, II
	Tyrosine kinase inhibitor	Vatalanib (small molecule targeting VEGF receptors, PDGF receptor beta and c-kit)	I

Abbreviations: 4-1BB: TNF receptor family co-stimulatory receptor, also known as CD137 and TNFRS9; Ad-p53: oncolytic adenovirus transgenically expressing p53; Bcl2: B cell lymphoma 2; CD 3/8/56/122: cluster of differentiation 3/8/56/122; CTLA-4: cytotoxic T-lymphocyte-associated protein 4; DLL3: delta-like protein 3; GITR: glucocorticoid-induced TNFR-related protein; ICI: immune checkpoint inhibitors; IDO1: indoleamine 2,3-dioxygenase; IL-2/7/15: interleukin-2/7/15; L-NMMA: L-NG-monomethyl arginine acetate; Lag3: lymphocyte activating 3; mAb: monoclonal antibody; MCPyV: Merkel cell polyomavirus; MDM2: mouse double minute 2 homolog; mTOR: mammalian target of rapamycin; NK cell: natural killer cell; NOS: nitric oxide synthase; OX40: tumor necrosis factor receptor superfamily, member 4, also known as CD134 and OX40 receptor; PD-1: programmed cell death-1; PDGF: platelet-derived growth factor; PD-(L)1: programmed cell death-1 ligand 1; SBRT: stereotactic body radiation therapy; SST: somatostatin; SSTR: somatostatin receptor; T-VEC: talimogene laherparepvec; Tim3: T cell immunoglobulin and mucin domain-containing protein 3; TLR3/7/8/9: Toll-like receptor 3/7/8/9; TME: tumor microenvironment; VEGF: vascular endothelial growth factor.

6. Discussion and Conclusions

Beginning with the initial approval of ipilimumab for malignant melanoma in 2011, highly immunogenic skin cancers have been important model diseases for the development of new immune-directed therapies. ICIs have been transformational for a subset of patients with advanced skin cancers and have provided us with unique insights into the importance of UV neoantigens and viral antigens in anti-tumor immunity. However, several recent immune-focused approaches have not meaningfully improved upon the early gains from targeting the CTLA-4 and PD-(L)1 pathways. While incremental improvements from new and combined immune therapies are also anticipated, it may be important to target processes beyond the immune system to augment the efficacy of ICIs. Such orthogonal approaches to enhancing immunity may provide a synergistic therapeutic benefit while avoiding excess immune toxicity. Skin cancer, particularly MCC, may again prove a fertile testing ground for understanding whether DDRi can augment immunity and potentiate existing immunotherapies. Exciting new biology and the availability of specific small molecules inhibiting central DDR pathway regulators including ATR, ATM and DNA-PK facilitate clinical trials of DDRi with a focus on enhancing anti-tumor immunity.

In addition to improving survival, maintaining the quality of life for those with advanced disease is a central goal for our patients. Widening the therapeutic window may be achievable by combining therapies with distinct cellular targets and synergistic efficacy but without known overlapping toxicities. A DDR pathway inhibitor paired with an ICI, targeting cell cycle and immune checkpoints, respectively, is one such promising combination. DDRi may slow tumor growth by restricting cell cycle progression while also promoting immune signaling and ICD to potentiate innate and systemic anti-tumor immunity (Figure 3A). The addition of very low dose radiation (potentiated by the tumor-selective radiosensitizing properties of an ATRi) may lower the tumor burden to facilitate the immune system's ability to control microscopic disease and is expected to be well tolerated.

The rationale for a study of an ATRi in advanced MCC is driven not only by the potential to restrict tumor growth via direct effects on cell cycle progression but also by the mounting preclinical evidence for ATR inhibition to promote anti-tumor immunity in this remarkably ICI-sensitive cancer. In particular, a clinical trial is envisioned for patients with ICI-refractory MCC in which an ATRi would be added while continuing PD-1 pathway blockade (Figure 3B). Such a study would assess the efficacy of an ATRi to stabilize metastatic disease and re-establish anti-tumor immunity. Targeted, low-dose radiotherapy may be employed to palliate progressive lesions and potentially synergize with "double-checkpoint inhibition". Correlative studies should address how an ATRi

may modulate innate and adaptive anti-tumor responses and what the mechanisms of resistance to an ATRi might be.

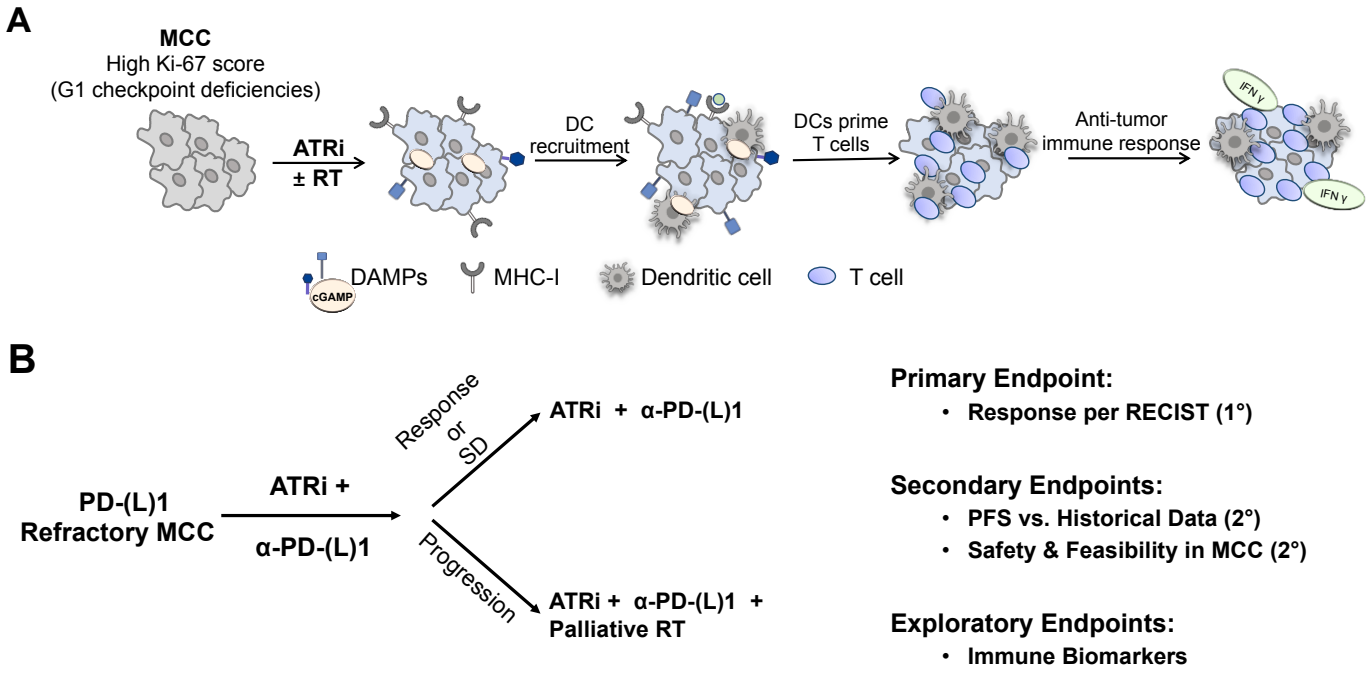

Figure 3. Potential role for an ATR inhibitor (ATRi) to overcome immune checkpoint inhibitor (ICI)-refractory Merkel cell carcinoma (MCC) and a clinical trial concept. (**A**) Prospective mechanism of action for an enhanced immune response in MCC treated with an ATRi + radiotherapy (RT). (**B**) Schematic for a potential clinical trial of an ATRi for patients with MCC refractory to ICIs wherein an ATRi would be added to a patient's ongoing PD-1 pathway blockade. Palliative RT may be utilized to control progressive lesions and potentially synergize with the ATRi. Abbreviations: cGAMP: cyclic guanosine monophosphate–adenosine monophosphate, α-PD-(L)1: anti-PD-(L)1, PFS: progression-free survival, RECIST: response evaluation criteria in solid tumors, SD: stable disease.

Figure 3. Potential role for an ATR inhibitor (ATRi) to overcome immune checkpoint inhibitor (ICI)-refractory Merkel cell carcinoma (MCC) and a clinical trial concept. (**A**) Prospective mechanism of action for an enhanced immune response in MCC treated with an ATRi + radiotherapy (RT). (**B**) Schematic for a potential clinical trial of an ATRi for patients with MCC refractory to ICIs wherein an ATRi would be added to a patient's ongoing PD-1 pathway blockade. Palliative RT may be utilized to control progressive lesions and potentially synergize with the ATRi. Abbreviations: cGAMP: cyclic guanosine monophosphate–adenosine monophosphate, α-PD-(L)1: anti-PD-(L)1, PFS: progression-free survival, RECIST: response evaluation criteria in solid tumors, SD: stable disease.

The rationale for a study of an ATRi in advanced MCC is driven not only by the potential to restrict tumor growth via direct effects on cell cycle progression but also by the mounting preclinical evidence for ATR inhibition to promote anti-tumor immunity in this remarkably ICI-sensitive cancer. In particular, a clinical trial is envisioned for patients with ICI-refractory MCC in which an ATRi would be added while continuing PD-1 pathway blockade (Figure 3B). Such a study would assess the efficacy of an ATRi to stabilize metastatic disease and re-establish anti-tumor immunity. Targeted, low-dose radiotherapy may be employed to palliate progressive lesions and potentially synergize with "double-checkpoint inhibition". Correlative studies should address how an ATRi may modulate innate and adaptive anti-tumor responses and what the mechanisms of resistance to an ATRi might be.

DDR pathway inhibitors with favorable toxicity profiles are now in phase I and II clinical trials. Preclinical data supporting a role for DDR pathway inhibition to promote innate and systemic anti-tumor immunity provide a strong rationale for clinical trials combining DDRi with immune-targeted therapies to address ICI-resistant disease. Excitingly, ceralasertib (AZD6738), an ATRi, in combination with durvalumab showed promising efficacy (overall response rate of 30% and disease control rate of 63%) in patients with melanoma resistant to anti-PD-1 therapy per an early report at ASCO in 2021 [189]. These data are encouraging when considering the potential benefit of an ATRi plus anti-PD-(L)1 therapy in MCC patients with ICI-resistant disease. Additionally, strong correlative studies to assess biomarkers of response and resistance are critical to further our understanding of the interplay between DDR pathways and the immune system in human disease.

Author Contributions: Conceptualization, P.H.G., R.B., T.H., J.P.L., E.P. and P.N.; writing—original draft preparation, P.H.G., R.B., T.H., J.P.L., E.P. and P.N.; writing—review and editing, P.H.G., R.B., T.H., J.P.L., E.P. and P.N.; funding acquisition, P.H.G., T.H. and P.N. All authors have read and agreed to the published version of the manuscript.

Funding: This work was supported in part by an ASPIRE Award from The Mark Foundation for Cancer Research, #20-002-ASP (P.N.). The authors gratefully recognize research funding from the Prostate Cancer Foundation's Kelsey Dickson Team Science Courage Research Award (PCF# 19CHAS02, P.N.), the RSNA Research and Education Foundation (RR2028, P.H.G.), the NIH/NCI (P01CA257904, P.N.; R01-CA168770, P.N.; and T32CA236621, T.H.), and the University of Washington MDC (J.P.L.).

Institutional Review Board Statement: Not applicable.

Informed Consent Statement: Not applicable.

Data Availability Statement: Not applicable.

Conflicts of Interest: P.N. reports research funding and personal fees from EMD Serono (Rockland, MA, USA) and Merck and Co. (Kenilworth, NJ, USA) not related to this work. P.H.G. reports research funding from Gilead Sciences, Inc. (Foster City, CA, USA) not related to this work.

References

1. Bagchi, S.; Yuan, R.; Engleman, E.G. Immune Checkpoint Inhibitors for the Treatment of Cancer: Clinical Impact and Mechanisms of Response and Resistance. *Annu. Rev. Pathol.* **2021**, *16*, 223–249. [CrossRef]
2. Vaddepally, R.K.; Kharel, P.; Pandey, R.; Garje, R.; Chandra, A.B. Review of Indications of FDA-Approved Immune Checkpoint Inhibitors per NCCN Guidelines with the Level of Evidence. *Cancers* **2020**, *12*, 738. [CrossRef]
3. Oaknin, A.; Tinker, A.V.; Gilbert, L.; Samouelian, V.; Mathews, C.; Brown, J.; Barretina-Ginesta, M.P.; Moreno, V.; Gravina, A.; Abdeddaim, C.; et al. Clinical Activity and Safety of the Anti-Programmed Death 1 Monoclonal Antibody Dostarlimab for Patients With Recurrent or Advanced Mismatch Repair-Deficient Endometrial Cancer: A Nonrandomized Phase 1 Clinical Trial. *JAMA Oncol.* **2020**, *6*, 1766–1772. [CrossRef] [PubMed]
4. Galienne, M.; Rodrigues, M. New drug approval: Dostarlimab-second line in advanced MSI endometrial cancer. *Bull. Cancer* **2021**, *S0007-4551*. [CrossRef]
5. Robert, C. A decade of immune-checkpoint inhibitors in cancer therapy. *Nat. Commun.* **2020**, *11*, 3801. [CrossRef]
6. La-Beck, N.M.; Jean, G.W.; Huynh, C.; Alzghari, S.K.; Lowe, D.B. Immune Checkpoint Inhibitors: New Insights and Current Place in Cancer Therapy. *Pharmacotherapy* **2015**, *35*, 963–976. [CrossRef] [PubMed]
7. Palmieri, D.J.; Carlino, M.S. Immune Checkpoint Inhibitor Toxicity. *Curr. Oncol. Rep.* **2018**, *20*, 72. [CrossRef] [PubMed]
8. Waldman, A.D.; Fritz, J.M.; Lenardo, M.J. A guide to cancer immunotherapy: From T cell basic science to clinical practice. *Nat. Rev. Immunol.* **2020**, *20*, 651–668. [CrossRef]
9. Sharpe, A.H.; Pauken, K.E. The diverse functions of the PD1 inhibitory pathway. *Nat. Rev. Immunol.* **2018**, *18*, 153–167. [CrossRef]
10. Haslam, A.; Prasad, V. Estimation of the Percentage of US Patients With Cancer Who Are Eligible for and Respond to Checkpoint Inhibitor Immunotherapy Drugs. *JAMA Netw. Open* **2019**, *2*, e192535. [CrossRef]
11. Shen, X.; Zhao, B. Efficacy of PD-1 or PD-L1 inhibitors and PD-L1 expression status in cancer: Meta-analysis. *BMJ* **2018**, *362*, k3529. [CrossRef]
12. Lee, C.K.; Man, J.; Lord, S.; Cooper, W.; Links, M.; Gebski, V.; Herbst, R.S.; Gralla, R.J.; Mok, T.; Yang, J.C. Clinical and Molecular Characteristics Associated With Survival Among Patients Treated With Checkpoint Inhibitors for Advanced Non-Small Cell Lung Carcinoma: A Systematic Review and Meta-analysis. *JAMA Oncol.* **2018**, *4*, 210–216. [CrossRef]
13. Yun, S.; Vincelette, N.D.; Green, M.R.; Wahner Hendrickson, A.E.; Abraham, I. Targeting immune checkpoints in unresectable metastatic cutaneous melanoma: A systematic review and meta-analysis of anti-CTLA-4 and anti-PD-1 agents trials. *Cancer Med.* **2016**, *5*, 1481–1491. [CrossRef]
14. Yang, F.; Markovic, S.N.; Molina, J.R.; Halfdanarson, T.R.; Pagliaro, L.C.; Chintakuntlawar, A.V.; Li, R.; Wei, J.; Wang, L.; Liu, B.; et al. Association of Sex, Age, and Eastern Cooperative Oncology Group Performance Status With Survival Benefit of Cancer Immunotherapy in Randomized Clinical Trials: A Systematic Review and Meta-analysis. *JAMA Netw. Open* **2020**, *3*, e2012534. [CrossRef]
15. Chalmers, Z.R.; Connelly, C.F.; Fabrizio, D.; Gay, L.; Ali, S.M.; Ennis, R.; Schrock, A.; Campbell, B.; Shlien, A.; Chmielecki, J.; et al. Analysis of 100,000 human cancer genomes reveals the landscape of tumor mutational burden. *Genome Med.* **2017**, *9*, 34. [CrossRef] [PubMed]
16. Yarchoan, M.; Hopkins, A.; Jaffee, E.M. Tumor Mutational Burden and Response Rate to PD-1 Inhibition. *N. Engl. J. Med.* **2017**, *377*, 2500–2501. [CrossRef] [PubMed]
17. Hodi, F.S.; O'Day, S.J.; McDermott, D.F.; Weber, R.W.; Sosman, J.A.; Haanen, J.B.; Gonzalez, R.; Robert, C.; Schadendorf, D.; Hassel, J.C.; et al. Improved survival with ipilimumab in patients with metastatic melanoma. *N. Engl. J. Med.* **2010**, *363*, 711–723. [CrossRef] [PubMed]
18. Paulson, K.G.; Lahman, M.C.; Chapuis, A.G.; Brownell, I. Immunotherapy for skin cancer. *Int. Immunol.* **2019**, *31*, 465–475. [CrossRef] [PubMed]
19. Hazarika, M.; Chuk, M.K.; Theoret, M.R.; Mushti, S.; He, K.; Weis, S.L.; Putman, A.H.; Helms, W.S.; Cao, X.; Li, H.; et al. U.S. FDA Approval Summary: Nivolumab for Treatment of Unresectable or Metastatic Melanoma Following Progression on Ipilimumab. *Clin. Cancer Res.* **2017**, *23*, 3484–3488. [CrossRef]
20. Barone, A.; Hazarika, M.; Theoret, M.R.; Mishra-Kalyani, P.; Chen, H.; He, K.; Sridhara, R.; Subramaniam, S.; Pfuma, E.; Wang, Y.; et al. FDA Approval Summary: Pembrolizumab for the Treatment of Patients with Unresectable or Metastatic Melanoma. *Clin. Cancer Res.* **2017**, *23*, 5661–5665. [CrossRef]
21. Larkin, J.; Chiarion-Sileni, V.; Gonzalez, R.; Grob, J.J.; Rutkowski, P.; Lao, C.D.; Cowey, C.L.; Schadendorf, D.; Wagstaff, J.; Dummer, R.; et al. Five-Year Survival with Combined Nivolumab and Ipilimumab in Advanced Melanoma. *N. Engl. J. Med.* **2019**, *381*, 1535–1546. [CrossRef]

22. Lebbé, C.; Meyer, N.; Mortier, L.; Marquez-Rodas, I.; Robert, C.; Rutkowski, P.; Menzies, A.M.; Eigentler, T.; Ascierto, P.A.; Smylie, M.; et al. Evaluation of Two Dosing Regimens for Nivolumab in Combination With Ipilimumab in Patients With Advanced Melanoma: Results From the Phase IIIb/IV CheckMate 511 Trial. *J. Clin. Oncol.*. **2019**, *37*, 867–875. [CrossRef]
23. Kaufman, H.L.; Russell, J.S.; Hamid, O.; Bhatia, S.; Terheyden, P.; D'Angelo, S.P.; Shih, K.C.; Lebbe, C.; Milella, M.; Brownell, I.; et al. Updated efficacy of avelumab in patients with previously treated metastatic Merkel cell carcinoma after >/=1 year of follow-up: JAVELIN Merkel 200, a phase 2 clinical trial. *J. Immunother. Cancer* **2018**, *6*, 7. [CrossRef] [PubMed]
24. D'Angelo, S.P.; Bhatia, S.; Brohl, A.S.; Hamid, O.; Mehnert, J.M.; Terheyden, P.; Shih, K.C.; Brownell, I.; Lebbe, C.; Lewis, K.D.; et al. Avelumab in patients with previously treated metastatic Merkel cell carcinoma: Long-term data and biomarker analyses from the single-arm phase 2 JAVELIN Merkel 200 trial. *J. Immunother. Cancer* **2020**, *8*. [CrossRef] [PubMed]
25. Nghiem, P.T.; Bhatia, S.; Lipson, E.J.; Kudchadkar, R.R.; Miller, N.J.; Annamalai, L.; Berry, S.; Chartash, E.K.; Daud, A.; Fling, S.P.; et al. PD-1 Blockade with Pembrolizumab in Advanced Merkel-Cell Carcinoma. *N. Engl. J. Med.* **2016**, *374*, 2542–2552. [CrossRef]
26. Nghiem, P.; Bhatia, S.; Lipson, E.J.; Sharfman, W.H.; Kudchadkar, R.R.; Brohl, A.S.; Friedlander, P.A.; Daud, A.; Kluger, H.M.; Reddy, S.A.; et al. Durable Tumor Regression and Overall Survival in Patients With Advanced Merkel Cell Carcinoma Receiving Pembrolizumab as First-Line Therapy. *J. Clin. Oncol.* **2019**, *37*, 693–702. [CrossRef]
27. Migden, M.R.; Rischin, D.; Schmults, C.D.; Guminski, A.; Hauschild, A.; Lewis, K.D.; Chung, C.H.; Hernandez-Aya, L.; Lim, A.M.; Chang, A.L.S.; et al. PD-1 Blockade with Cemiplimab in Advanced Cutaneous Squamous-Cell Carcinoma. *N. Engl. J. Med.* **2018**, *379*, 341–351. [CrossRef]
28. Cemiplimab in locally advanced basal cell carcinoma after hedgehog inhibitor therapy: An open-label, multi-centre, single-arm, phase 2 trial. *Lancet Oncol.* **2021**, *22*, 848–857. [CrossRef]
29. Liu, D.; Jenkins, R.W.; Sullivan, R.J. Mechanisms of Resistance to Immune Checkpoint Blockade. *Am. J. Clin. Dermatol.* **2019**, *20*, 41–54. [CrossRef]
30. Valero, C.; Lee, M.; Hoen, D.; Weiss, K.; Kelly, D.W.; Adusumilli, P.S.; Paik, P.K.; Plitas, G.; Ladanyi, M.; Postow, M.A.; et al. Pretreatment neutrophil-to-lymphocyte ratio and mutational burden as biomarkers of tumor response to immune checkpoint inhibitors. *Nat. Commun.* **2021**, *12*, 729. [CrossRef] [PubMed]
31. Rogado, J.; Romero-Laorden, N.; Sanchez-Torres, J.M.; Ramos-Levi, A.M.; Pacheco-Barcia, V.; Ballesteros, A.I.; Arranz, R.; Lorenzo, A.; Gullon, P.; Garrido, A.; et al. Effect of excess weight and immune-related adverse events on the efficacy of cancer immunotherapy with anti-PD-1 antibodies. *Oncoimmunology* **2020**, *9*, 1751548. [CrossRef] [PubMed]
32. An, Y.; Wu, Z.; Wang, N.; Yang, Z.; Li, Y.; Xu, B.; Sun, M. Association between body mass index and survival outcomes for cancer patients treated with immune checkpoint inhibitors: A systematic review and meta-analysis. *J. Transl. Med.* **2020**, *18*, 235. [CrossRef]
33. Strickler, J.H.; Hanks, B.A.; Khasraw, M. Tumor Mutational Burden as a Predictor of Immunotherapy Response: Is More Always Better? *Clin. Cancer Res.* **2021**, *27*, 1236–1241. [CrossRef]
34. Subbiah, V.; Solit, D.B.; Chan, T.A.; Kurzrock, R. The FDA approval of pembrolizumab for adult and pediatric patients with tumor mutational burden (TMB) >/=10: A decision centered on empowering patients and their physicians. *Ann. Oncol.* **2020**, *31*, 1115–1118. [CrossRef]
35. Gandhi, L.; Rodriguez-Abreu, D.; Gadgeel, S.; Esteban, E.; Felip, E.; De Angelis, F.; Domine, M.; Clingan, P.; Hochmair, M.J.; Powell, S.F.; et al. Pembrolizumab plus Chemotherapy in Metastatic Non-Small-Cell Lung Cancer. *N. Engl. J. Med.* **2018**, *378*, 2078–2092. [CrossRef]
36. Kato, K.; Sun, J.-M.; Shah, M.A.; Enzinger, P.C.; Adenis, A.; Doi, T.; Kojima, T.; Metges, J.-P.; Li, Z.; Kim, S.-B.; et al. LBA8_PR Pembrolizumab plus chemotherapy versus chemotherapy as first-line therapy in patients with advanced esophageal cancer: The phase 3 KEYNOTE-590 study. *Ann. Oncol.* **2020**, *31*, S1192–S1193. [CrossRef]
37. Dosset, M.; Joseph, E.L.; Rivera Vargas, T.; Apetoh, L. Modulation of Determinant Factors to Improve Therapeutic Combinations with Immune Checkpoint Inhibitors. *Cells* **2020**, *9*, 1727. [CrossRef] [PubMed]
38. Wu, J.; Waxman, D.J. Immunogenic chemotherapy: Dose and schedule dependence and combination with immunotherapy. *Cancer Lett.* **2018**, *419*, 210–221. [CrossRef]
39. Formenti, S.C.; Rudqvist, N.P.; Golden, E.; Cooper, B.; Wennerberg, E.; Lhuillier, C.; Vanpouille-Box, C.; Friedman, K.; Ferrari de Andrade, L.; Wucherpfennig, K.W.; et al. Radiotherapy induces responses of lung cancer to CTLA-4 blockade. *Nat. Med.* **2018**, *24*, 1845–1851. [CrossRef]
40. Bang, A.; Schoenfeld, J.D. Immunotherapy and radiotherapy for metastatic cancers. *Ann. Palliat. Med.* **2019**, *8*, 312–325. [CrossRef]
41. Kordbacheh, T.; Honeychurch, J.; Blackhall, F.; Faivre-Finn, C.; Illidge, T. Radiotherapy and anti-PD-1/PD-L1 combinations in lung cancer: Building better translational research platforms. *Ann. Oncol.* **2018**, *29*, 301–310. [CrossRef]
42. Demaria, S.; Guha, C.; Schoenfeld, J.; Morris, Z.; Monjazeb, A.; Sikora, A.; Crittenden, M.; Shiao, S.; Khleif, S.; Gupta, S.; et al. Radiation dose and fraction in immunotherapy: One-size regimen does not fit all settings, so how does one choose? *J. Immunother. Cancer* **2021**, *9*. [CrossRef]
43. Shaverdian, N.; Lisberg, A.E.; Bornazyan, K.; Veruttipong, D.; Goldman, J.W.; Formenti, S.C.; Garon, E.B.; Lee, P. Previous radiotherapy and the clinical activity and toxicity of pembrolizumab in the treatment of non-small-cell lung cancer: A secondary analysis of the KEYNOTE-001 phase 1 trial. *Lancet Oncol.* **2017**, *18*, 895–903. [CrossRef]
44. Wang, Y.; Deng, W.; Li, N.; Neri, S.; Sharma, A.; Jiang, W.; Lin, S.H. Combining Immunotherapy and Radiotherapy for Cancer Treatment: Current Challenges and Future Directions. *Front. Pharmacol.* **2018**, *9*, 185. [CrossRef] [PubMed]

45. Gong, J.; Le, T.Q.; Massarelli, E.; Hendifar, A.E.; Tuli, R. Radiation therapy and PD-1/PD-L1 blockade: The clinical development of an evolving anticancer combination. *J. Immunother. Cancer* **2018**, *6*, 46. [CrossRef]
46. Seiwert, T.Y.; Kiess, A.P. Time to Debunk an Urban Myth? The "Abscopal Effect" With Radiation and Anti–PD-1. *J. Clin. Oncol.* **2021**, *39*, 1–3. [CrossRef] [PubMed]
47. Yau, T.; Kang, Y.K.; Kim, T.Y.; El-Khoueiry, A.B.; Santoro, A.; Sangro, B.; Melero, I.; Kudo, M.; Hou, M.M.; Matilla, A.; et al. Efficacy and Safety of Nivolumab Plus Ipilimumab in Patients With Advanced Hepatocellular Carcinoma Previously Treated With Sorafenib: The CheckMate 040 Randomized Clinical Trial. *JAMA Oncol.* **2020**, *6*, e204564. [CrossRef]
48. Wong, J.S.L.; Kwok, G.G.W.; Tang, V.; Li, B.C.W.; Leung, R.; Chiu, J.; Ma, K.W.; She, W.H.; Tsang, J.; Lo, C.M.; et al. Ipilimumab and nivolumab/pembrolizumab in advanced hepatocellular carcinoma refractory to prior immune checkpoint inhibitors. *J. Immunother. Cancer* **2021**, *9*. [CrossRef]
49. Wang, D.Y.; Salem, J.E.; Cohen, J.V.; Chandra, S.; Menzer, C.; Ye, F.; Zhao, S.; Das, S.; Beckermann, K.E.; Ha, L.; et al. Fatal Toxic Effects Associated With Immune Checkpoint Inhibitors: A Systematic Review and Meta-analysis. *JAMA Oncol.* **2018**, *4*, 1721–1728. [CrossRef]
50. Geraud, A.; Gougis, P.; Vozy, A.; Anquetil, C.; Allenbach, Y.; Romano, E.; Funck-Brentano, E.; Moslehi, J.J.; Johnson, D.B.; Salem, J.E. Clinical Pharmacology and Interplay of Immune Checkpoint Agents: A Yin-Yang Balance. *Annu. Rev. Pharmacol. Toxicol.* **2021**, *61*, 85–112. [CrossRef]
51. Andtbacka, R.H.; Kaufman, H.L.; Collichio, F.; Amatruda, T.; Senzer, N.; Chesney, J.; Delman, K.A.; Spitler, L.E.; Puzanov, I.; Agarwala, S.S.; et al. Talimogene Laherparepvec Improves Durable Response Rate in Patients With Advanced Melanoma. *J. Clin. Oncol.* **2015**, *33*, 2780–2788. [CrossRef]
52. Ribas, A.; Dummer, R.; Puzanov, I.; VanderWalde, A.; Andtbacka, R.H.I.; Michielin, O.; Olszanski, A.J.; Malvehy, J.; Cebon, J.; Fernandez, E.; et al. Oncolytic Virotherapy Promotes Intratumoral T Cell Infiltration and Improves Anti-PD-1 Immunotherapy. *Cell* **2018**, *174*, 1031–1032. [CrossRef]
53. Chesney, J.; Puzanov, I.; Collichio, F.; Singh, P.; Milhem, M.M.; Glaspy, J.; Hamid, O.; Ross, M.; Friedlander, P.; Garbe, C.; et al. Randomized, Open-Label Phase II Study Evaluating the Efficacy and Safety of Talimogene Laherparepvec in Combination With Ipilimumab Versus Ipilimumab Alone in Patients With Advanced, Unresectable Melanoma. *J. Clin. Oncol.* **2018**, *36*, 1658–1667. [CrossRef] [PubMed]
54. Darvin, P.; Toor, S.M.; Sasidharan Nair, V.; Elkord, E. Immune checkpoint inhibitors: Recent progress and potential biomarkers. *Exp. Mol. Med.* **2018**, *50*, 1–11. [CrossRef] [PubMed]
55. Gibney, G.T.; Weiner, L.M.; Atkins, M.B. Predictive biomarkers for checkpoint inhibitor-based immunotherapy. *Lancet Oncol.* **2016**, *17*, e542–e551. [CrossRef]
56. Finn, R.S.; Qin, S.; Ikeda, M.; Galle, P.R.; Ducreux, M.; Kim, T.Y.; Kudo, M.; Breder, V.; Merle, P.; Kaseb, A.O.; et al. Atezolizumab plus Bevacizumab in Unresectable Hepatocellular Carcinoma. *N. Engl. J. Med.* **2020**, *382*, 1894–1905. [CrossRef] [PubMed]
57. Quhal, F.; Mori, K.; Bruchbacher, A.; Resch, I.; Mostafaei, H.; Pradere, B.; Schuettfort, V.M.; Laukhtina, E.; Egawa, S.; Fajkovic, H.; et al. First-line Immunotherapy-based Combinations for Metastatic Renal Cell Carcinoma: A Systematic Review and Network Meta-analysis. *Eur. Urol. Oncol.* **2021**. [CrossRef]
58. Qin, S.; Xu, L.; Yi, M.; Yu, S.; Wu, K.; Luo, S. Novel immune checkpoint targets: Moving beyond PD-1 and CTLA-4. *Mol. Cancer* **2019**, *18*, 155. [CrossRef]
59. Marin-Acevedo, J.A.; Kimbrough, E.O.; Lou, Y. Next generation of immune checkpoint inhibitors and beyond. *J. Hematol. Oncol.* **2021**, *14*, 45. [CrossRef]
60. Tolcher, A.W.; Sznol, M.; Hu-Lieskovan, S.; Papadopoulos, K.P.; Patnaik, A.; Rasco, D.W.; Di Gravio, D.; Huang, B.; Gambhire, D.; Chen, Y.; et al. Phase Ib Study of Utomilumab (PF-05082566), a 4-1BB/CD137 Agonist, in Combination with Pembrolizumab (MK-3475) in Patients with Advanced Solid Tumors. *Clin. Cancer Res.* **2017**, *23*, 5349–5357. [CrossRef] [PubMed]
61. Lee, E.K.; Konstantinopoulos, P.A. Combined PARP and Immune Checkpoint Inhibition in Ovarian Cancer. *Trends. Cancer* **2019**, *5*, 524–528. [CrossRef] [PubMed]
62. Post, C.C.B.; Westermann, A.M.; Bosse, T.; Creutzberg, C.L.; Kroep, J.R. PARP and PD-1/PD-L1 checkpoint inhibition in recurrent or metastatic endometrial cancer. *Crit. Rev. Oncol. Hematol.* **2020**, *152*, 102973. [CrossRef] [PubMed]
63. Goncalves, A.; Mezni, E.; Bertucci, F. Combining poly(ADP-ribose) polymerase inhibitors and immune checkpoint inhibitors in breast cancer: Rationale and preliminary clinical results. *Curr. Opin. Oncol.* **2020**, *32*, 585–593. [CrossRef]
64. Paluch-Shimon, S.; Cardoso, F. PARP inhibitors coming of age. *Nat. Rev. Clin. Oncol.* **2021**, *18*, 69–70. [CrossRef] [PubMed]
65. Rose, M.; Burgess, J.T.; O'Byrne, K.; Richard, D.J.; Bolderson, E. PARP Inhibitors: Clinical Relevance, Mechanisms of Action and Tumor Resistance. *Front. Cell Dev. Biol.* **2020**, *8*, 564601. [CrossRef] [PubMed]
66. Pilie, P.G.; Tang, C.; Mills, G.B.; Yap, T.A. State-of-the-art strategies for targeting the DNA damage response in cancer. *Nat. Rev. Clin. Oncol.* **2019**, *16*, 81–104. [CrossRef] [PubMed]
67. Huang, R.X.; Zhou, P.K. DNA damage response signaling pathways and targets for radiotherapy sensitization in cancer. *Signal Transduct Target Ther.* **2020**, *5*, 60. [CrossRef]
68. Blackford, A.N.; Jackson, S.P. ATM, ATR, and DNA-PK: The Trinity at the Heart of the DNA Damage Response. *Mol. Cell* **2017**, *66*, 801–817. [CrossRef]
69. Lanz, M.C.; Dibitetto, D.; Smolka, M.B. DNA damage kinase signaling: Checkpoint and repair at 30 years. *EMBO J.* **2019**, *38*, e101801. [CrossRef]

70. Kandoth, C.; McLellan, M.D.; Vandin, F.; Ye, K.; Niu, B.; Lu, C.; Xie, M.; Zhang, Q.; McMichael, J.F.; Wyczalkowski, M.A.; et al. Mutational landscape and significance across 12 major cancer types. *Nature* **2013**, *502*, 333–339. [CrossRef]
71. Klingseisen, A.; Jackson, A.P. Mechanisms and pathways of growth failure in primordial dwarfism. *Genes Dev.* **2011**, *25*, 2011–2024. [CrossRef] [PubMed]
72. Choi, M.; Kipps, T.; Kurzrock, R. ATM Mutations in Cancer: Therapeutic Implications. *Mol. Cancer Ther.* **2016**, *15*, 1781–1791. [CrossRef]
73. Jerzak, K.J.; Mancuso, T.; Eisen, A. Ataxia-telangiectasia gene (ATM) mutation heterozygosity in breast cancer: A narrative review. *Curr. Oncol.* **2018**, *25*, e176–e180. [CrossRef] [PubMed]
74. van Os, N.J.H.; Roeleveld, N.; Weemaes, C.M.; Jongmans, M.C.; Janssens, G.O.; Taylor, A.M.; Hoogerbrugge, N.; Willemsen, M.A. Health risks for ataxia-telangiectasia mutated heterozygotes: A systematic review, meta-analysis and evidence-based guideline. *Clin. Genet.* **2016**, *90*, 105–117. [CrossRef]
75. Jette, N.R.; Kumar, M.; Radhamani, S.; Arthur, G.; Goutam, S.; Yip, S.; Kolinsky, M.; Williams, G.J.; Bose, P.; Lees-Miller, S.P. ATM-Deficient Cancers Provide New Opportunities for Precision Oncology. *Cancers* **2020**, *12*, 687. [CrossRef]
76. van der Burg, M.; van Dongen, J.J.; van Gent, D.C. DNA-PKcs deficiency in human: Long predicted, finally found. *Curr. Opin. Allergy Clin. Immunol.* **2009**, *9*, 503–509. [CrossRef]
77. Brown, E.J.; Baltimore, D. ATR disruption leads to chromosomal fragmentation and early embryonic lethality. *Genes Dev.* **2000**, *14*, 397–402. [CrossRef] [PubMed]
78. Barlow, C.; Hirotsune, S.; Paylor, R.; Liyanage, M.E.M.; Collins, F.; Shiloh, Y.; Crawley, J.N.; Ried, T.; Tagle, D.e.a. Atm-Deficient Mice: A Paradigm of Ataxia Telangiectasia. *Cell* **1996**, *86*, 159–171. [CrossRef]
79. Espejel, S.; Martin, M.; Klatt, P.; Martin-Caballero, J.; Flores, J.M.; Blasco, M.A. Shorter telomeres, accelerated ageing and increased lymphoma in DNA-PKcs-deficient mice. *EMBO Rep.* **2004**, *5*, 503–509. [CrossRef] [PubMed]
80. Lewis, K.A.; Mullany, S.; Thomas, B.; Chien, J.; Loewen, R.; Shridhar, V.; Cliby, W.A. Heterozygous ATR mutations in mismatch repair-deficient cancer cells have functional significance. *Cancer Res.* **2005**, *65*, 7091–7095. [CrossRef] [PubMed]
81. Dylgjeri, E.; McNair, C.; Goodwin, J.F.; Raymon, H.K.; McCue, P.A.; Shafi, A.A.; Leiby, B.E.; de Leeuw, R.; Kothari, V.; McCann, J.J.; et al. Pleiotropic Impact of DNA-PK in Cancer and Implications for Therapeutic Strategies. *Clin. Cancer Res.* **2019**, *25*, 5623–5637. [CrossRef]
82. Mohiuddin, I.S.; Kang, M.H. DNA-PK as an Emerging Therapeutic Target in Cancer. *Front. Oncol.* **2019**, *9*, 635. [CrossRef]
83. Brandsma, I.; Fleuren, E.D.G.; Williamson, C.T.; Lord, C.J. Directing the use of DDR kinase inhibitors in cancer treatment. *Expert. Opin. Investig. Drugs* **2017**, *26*, 1341–1355. [CrossRef] [PubMed]
84. Minchom, A.; Aversa, C.; Lopez, J. Dancing with the DNA damage response: Next-generation anti-cancer therapeutic strategies. *Ther. Adv. Med. Oncol.* **2018**, *10*. [CrossRef] [PubMed]
85. Topatana, W.; Juengpanich, S.; Li, S.; Cao, J.; Hu, J.; Lee, J.; Suliyanto, K.; Ma, D.; Zhang, B.; Chen, M.; et al. Advances in synthetic lethality for cancer therapy: Cellular mechanism and clinical translation. *J. Hematol. Oncol.* **2020**, *13*, 118. [CrossRef] [PubMed]
86. Ashworth, A.; Lord, C.J. Synthetic lethal therapies for cancer: What's next after PARP inhibitors? *Nat. Rev. Clin. Oncol.* **2018**, *15*, 564–576. [CrossRef]
87. Tu, X.; Kahila, M.M.; Zhou, Q.; Yu, J.; Kalari, K.R.; Wang, L.; Harmsen, W.S.; Yuan, J.; Boughey, J.C.; Goetz, M.P.; et al. ATR Inhibition Is a Promising Radiosensitizing Strategy for Triple-Negative Breast Cancer. *Mol. Cancer Ther.* **2018**, *17*, 2462–2472. [CrossRef]
88. Fokas, E.; Prevo, R.; Pollard, J.R.; Reaper, P.M.; Charlton, P.A.; Cornelissen, B.; Vallis, K.A.; Hammond, E.M.; Olcina, M.M.; Gillies McKenna, W.; et al. Targeting ATR in vivo using the novel inhibitor VE-822 results in selective sensitization of pancreatic tumors to radiation. *Cell Death Dis.* **2012**, *3*, e441. [CrossRef]
89. Dillon, M.T.; Boylan, Z.; Smith, D.; Guevara, J.; Mohammed, K.; Peckitt, C.; Saunders, M.; Banerji, U.; Clack, G.; Smith, S.A.; et al. PATRIOT: A phase I study to assess the tolerability, safety and biological effects of a specific ataxia telangiectasia and Rad3-related (ATR) inhibitor (AZD6738) as a single agent and in combination with palliative radiation therapy in patients with solid tumours. *Clin. Transl. Radiat. Oncol.* **2018**, *12*, 16–20. [CrossRef]
90. Reaper, P.M.; Griffiths, M.R.; Long, J.M.; Charrier, J.D.; Maccormick, S.; Charlton, P.A.; Golec, J.M.; Pollard, J.R. Selective killing of ATM- or p53-deficient cancer cells through inhibition of ATR. *Nat. Chem. Biol.* **2011**, *7*, 428–430. [CrossRef]
91. Pires, I.M.; Olcina, M.M.; Anbalagan, S.; Pollard, J.R.; Reaper, P.M.; Charlton, P.A.; McKenna, W.G.; Hammond, E.M. Targeting radiation-resistant hypoxic tumour cells through ATR inhibition. *Br. J. Cancer* **2012**, *107*, 291–299. [CrossRef]
92. Biddlestone-Thorpe, L.; Sajjad, M.; Rosenberg, E.; Beckta, J.M.; Valerie, N.C.; Tokarz, M.; Adams, B.R.; Wagner, A.F.; Khalil, A.; Gilfor, D.; et al. ATM kinase inhibition preferentially sensitizes p53-mutant glioma to ionizing radiation. *Clin. Cancer Res.* **2013**, *19*, 3189–3200. [CrossRef] [PubMed]
93. Dunne, V.; Ghita, M.; Small, D.M.; Coffey, C.B.M.; Weldon, S.; Taggart, C.C.; Osman, S.O.; McGarry, C.K.; Prise, K.M.; Hanna, G.G.; et al. Inhibition of ataxia telangiectasia related-3 (ATR) improves therapeutic index in preclinical models of non-small cell lung cancer (NSCLC) radiotherapy. *Radiother. Oncol.* **2017**, *124*, 475–481. [CrossRef]
94. Durant, S.T.; Zheng, L.; Wang, Y.; Chen, K.; Zhang, L.; Zhang, T.; Yang, Z.; Riches, L.; Trinidad, A.G.; Fok, J.H.L.; et al. The brain-penetrant clinical ATM inhibitor AZD1390 radiosensitizes and improves survival of preclinical brain tumor models. *Sci. Adv.* **2018**, *4*. [CrossRef] [PubMed]

95. Ciszewski, W.M.; Tavecchio, M.; Dastych, J.; Curtin, N.J. DNA-PK inhibition by NU7441 sensitizes breast cancer cells to ionizing radiation and doxorubicin. *Breast Cancer Res. Treat.* **2014**, *143*, 47–55. [CrossRef]
96. Timme, C.R.; Rath, B.H.; O'Neill, J.W.; Camphausen, K.; Tofilon, P.J. The DNA-PK Inhibitor VX-984 Enhances the Radiosensitivity of Glioblastoma Cells Grown In Vitro and as Orthotopic Xenografts. *Mol. Cancer Ther.* **2018**, *17*, 1207–1216. [CrossRef] [PubMed]
97. Pilger, D.; Seymour, L.W.; Jackson, S.P. Interfaces between cellular responses to DNA damage and cancer immunotherapy. *Genes Dev.* **2021**, *35*, 602–618. [CrossRef] [PubMed]
98. Parkes, E.E.; Walker, S.M.; Taggart, L.E.; McCabe, N.; Knight, L.A.; Wilkinson, R.; McCloskey, K.D.; Buckley, N.E.; Savage, K.I.; Salto-Tellez, M.; et al. Activation of STING-Dependent Innate Immune Signaling By S-Phase-Specific DNA Damage in Breast Cancer. *J. Natl. Cancer Inst.* **2017**, *109*. [CrossRef]
99. Chao, H.H.; Karagounis, I.V.; Thomas, C.; Francois, N.B.; Facciabene, A.; Koumenis, C.; Maity, A. Combination of CHEK1/2 inhibition and ionizing radiation results in abscopal tumor response through increased micronuclei formation. *Oncogene* **2020**, *39*, 4344–4357. [CrossRef] [PubMed]
100. Sen, T.; Rodriguez, B.L.; Chen, L.; Corte, C.M.D.; Morikawa, N.; Fujimoto, J.; Cristea, S.; Nguyen, T.; Diao, L.; Li, L.; et al. Targeting DNA Damage Response Promotes Antitumor Immunity through STING-Mediated T-cell Activation in Small Cell Lung Cancer. *Cancer Discov.* **2019**, *9*, 646–661. [CrossRef]
101. Harding, S.M.; Benci, J.L.; Irianto, J.; Discher, D.E.; Minn, A.J.; Greenberg, R.A. Mitotic progression following DNA damage enables pattern recognition within micronuclei. *Nature* **2017**, *548*, 466–470. [CrossRef]
102. Dillon, M.T.; Bergerhoff, K.F.; Pedersen, M.; Whittock, H.; Crespo-Rodriguez, E.; Patin, E.C.; Pearson, A.; Smith, H.G.; Paget, J.T.E.; Patel, R.R.; et al. ATR Inhibition Potentiates the Radiation-induced Inflammatory Tumor Microenvironment. *Clin. Cancer Res.* **2019**, *25*, 3392–3403. [CrossRef]
103. Feng, X.; Tubbs, A.; Zhang, C.; Tang, M.; Sridharan, S.; Wang, C.; Jiang, D.; Su, D.; Zhang, H.; Chen, Z.; et al. ATR inhibition potentiates ionizing radiation-induced interferon response via cytosolic nucleic acid-sensing pathways. *EMBO J.* **2020**, *39*, e104036. [CrossRef] [PubMed]
104. Dillon, M.T.; Barker, H.E.; Pedersen, M.; Hafsi, H.; Bhide, S.A.; Newbold, K.L.; Nutting, C.M.; McLaughlin, M.; Harrington, K.J. Radiosensitization by the ATR Inhibitor AZD6738 through Generation of Acentric Micronuclei. *Mol. Cancer Ther.* **2017**, *16*, 25–34. [CrossRef]
105. Hartlova, A.; Erttmann, S.F.; Raffi, F.A.; Schmalz, A.M.; Resch, U.; Anugula, S.; Lienenklaus, S.; Nilsson, L.M.; Kroger, A.; Nilsson, J.A.; et al. DNA damage primes the type I interferon system via the cytosolic DNA sensor STING to promote anti-microbial innate immunity. *Immunity* **2015**, *42*, 332–343. [CrossRef] [PubMed]
106. Song, X.; Ma, F.; Herrup, K. Accumulation of Cytoplasmic DNA Due to ATM Deficiency Activates the Microglial Viral Response System with Neurotoxic Consequences. *J. Neurosci.* **2019**, *39*, 6378–6394. [CrossRef] [PubMed]
107. Zhang, Q.; Green, M.D.; Lang, X.; Lazarus, J.; Parsels, J.D.; Wei, S.; Parsels, L.A.; Shi, J.; Ramnath, N.; Wahl, D.R.; et al. Inhibition of ATM Increases Interferon Signaling and Sensitizes Pancreatic Cancer to Immune Checkpoint Blockade Therapy. *Cancer Res.* **2019**, *79*, 3940–3951. [CrossRef] [PubMed]
108. Wang, L.; Yang, L.; Wang, C.; Zhao, W.; Ju, Z.; Zhang, W.; Shen, J.; Peng, Y.; An, C.; Luu, Y.T.; et al. Inhibition of the ATM/Chk2 axis promotes cGAS/STING signaling in ARID1A-deficient tumors. *J. Clin. Investig.* **2020**, *130*, 5951–5966. [CrossRef] [PubMed]
109. Sun, X.; Liu, T.; Zhao, J.; Xia, H.; Xie, J.; Guo, Y.; Zhong, L.; Li, M.; Yang, Q.; Peng, C.; et al. DNA-PK deficiency potentiates cGAS-mediated antiviral innate immunity. *Nat. Commun.* **2020**, *11*, 6182. [CrossRef]
110. Vanpouille-Box, C.; Alard, A.; Aryankalayil, M.J.; Sarfraz, Y.; Diamond, J.M.; Schneider, R.J.; Inghirami, G.; Coleman, C.N.; Formenti, S.C.; Demaria, S. DNA exonuclease Trex1 regulates radiotherapy-induced tumour immunogenicity. *Nat. Commun.* **2017**, *8*, 15618. [CrossRef]
111. Yang, Y.G.; Lindahl, T.; Barnes, D.E. Trex1 exonuclease degrades ssDNA to prevent chronic checkpoint activation and autoimmune disease. *Cell* **2007**, *131*, 873–886. [CrossRef] [PubMed]
112. Krushkal, J.; Silvers, T.; Reinhold, W.C.; Sonkin, D.; Vural, S.; Connelly, J.; Varma, S.; Meltzer, P.S.; Kunkel, M.; Rapisarda, A.; et al. Epigenome-wide DNA methylation analysis of small cell lung cancer cell lines suggests potential chemotherapy targets. *Clin. Epigenetics* **2020**, *12*, 93. [CrossRef] [PubMed]
113. Reits, E.A.; Hodge, J.W.; Herberts, C.A.; Groothuis, T.A.; Chakraborty, M.; Wansley, E.K.; Camphausen, K.; Luiten, R.M.; de Ru, A.H.; Neijssen, J.; et al. Radiation modulates the peptide repertoire, enhances MHC class I expression, and induces successful antitumor immunotherapy. *J. Exp. Med.* **2006**, *203*, 1259–1271. [CrossRef]
114. Zebertavage, L.K.; Alice, A.; Crittenden, M.R.; Gough, M.J. Transcriptional Upregulation of NLRC5 by Radiation Drives STING- and Interferon-Independent MHC-I Expression on Cancer Cells and T Cell Cytotoxicity. *Sci. Rep.* **2020**, *10*, 7376. [CrossRef]
115. Sharma, A.; Bode, B.; Wenger, R.H.; Lehmann, K.; Sartori, A.A.; Moch, H.; Knuth, A.; Boehmer, L.; Broek, M. gamma-Radiation promotes immunological recognition of cancer cells through increased expression of cancer-testis antigens in vitro and in vivo. *PLoS ONE* **2011**, *6*, e28217. [CrossRef]
116. Wan, S.; Pestka, S.; Jubin, R.G.; Lyu, Y.L.; Tsai, Y.C.; Liu, L.F. Chemotherapeutics and radiation stimulate MHC class I expression through elevated interferon-beta signaling in breast cancer cells. *PLoS ONE* **2012**, *7*, e32542. [CrossRef]
117. Tsai, A.K.; Khan, A.Y.; Worgo, C.E.; Wang, L.L.; Liang, Y.; Davila, E. A Multikinase and DNA-PK Inhibitor Combination Immunomodulates Melanomas, Suppresses Tumor Progression, and Enhances Immunotherapies. *Cancer Immunol. Res.* **2017**, *5*, 790–803. [CrossRef]

118. Sun, L.L.; Yang, R.Y.; Li, C.W.; Chen, M.K.; Shao, B.; Hsu, J.M.; Chan, L.C.; Yang, Y.; Hsu, J.L.; Lai, Y.J.; et al. Inhibition of ATR downregulates PD-L1 and sensitizes tumor cells to T cell-mediated killing. *Am. J. Cancer Res.* **2018**, *8*, 1307–1316.
119. Sato, H.; Niimi, A.; Yasuhara, T.; Permata, T.B.M.; Hagiwara, Y.; Isono, M.; Nuryadi, E.; Sekine, R.; Oike, T.; Kakoti, S.; et al. DNA double-strand break repair pathway regulates PD-L1 expression in cancer cells. *Nat. Commun.* **2017**, *8*, 1751. [CrossRef] [PubMed]
120. Sheng, H.; Huang, Y.; Xiao, Y.; Zhu, Z.; Shen, M.; Zhou, P.; Guo, Z.; Wang, J.; Wang, H.; Dai, W.; et al. ATR inhibitor AZD6738 enhances the antitumor activity of radiotherapy and immune checkpoint inhibitors by potentiating the tumor immune microenvironment in hepatocellular carcinoma. *J. Immunother. Cancer* **2020**, *8*. [CrossRef]
121. Nghiem, P.; Park, P.K.; Kim, Y.; Vaziri, C.; Schreiber, S.L. ATR inhibition selectively sensitizes G1 checkpoint-deficient cells to lethal premature chromatin condensation. *Proc. Natl. Acad. Sci. USA* **2001**, *98*, 9092–9097. [CrossRef]
122. Rybaczek, D.; Kowalewicz-Kulbat, M. Premature chromosome condensation induced by caffeine, 2-aminopurine, staurosporine and sodium metavanadate in S-phase arrested HeLa cells is associated with a decrease in Chk1 phosphorylation, formation of phospho-H2AX and minor cytoskeletal rearrangements. *Histochem. Cell Biol.* **2011**, *135*, 263–280. [CrossRef]
123. Zuazua-Villar, P.; Rodriguez, R.; Gagou, M.E.; Eyers, P.A.; Meuth, M. DNA replication stress in CHK1-depleted tumour cells triggers premature (S-phase) mitosis through inappropriate activation of Aurora kinase B. *Cell Death Dis.* **2014**, *5*, e1253. [CrossRef] [PubMed]
124. Chen, J.; Harding, S.M.; Natesan, R.; Tian, L.; Benci, J.L.; Li, W.; Minn, A.J.; Asangani, I.A.; Greenberg, R.A. Cell Cycle Checkpoints Cooperate to Suppress DNA- and RNA-Associated Molecular Pattern Recognition and Anti-Tumor Immune Responses. *Cell Rep.* **2020**, *32*, 108080. [CrossRef]
125. Kiraly, G.; Simonyi, A.S.; Turani, M.; Juhasz, I.; Nagy, G.; Banfalvi, G. Micronucleus formation during chromatin condensation and under apoptotic conditions. *Apoptosis* **2017**, *22*, 207–219. [CrossRef]
126. Galluzzi, L.; Vitale, I.; Warren, S.; Adjemian, S.; Agostinis, P.; Martinez, A.B.; Chan, T.A.; Coukos, G.; Demaria, S.; Deutsch, E.; et al. Consensus guidelines for the definition, detection and interpretation of immunogenic cell death. *J. Immunother. Cancer* **2020**, *8*. [CrossRef]
127. Combes, E.; Andrade, A.F.; Tosi, D.; Michaud, H.A.; Coquel, F.; Garambois, V.; Desigaud, D.; Jarlier, M.; Coquelle, A.; Pasero, P.; et al. Inhibition of Ataxia-Telangiectasia Mutated and RAD3-Related (ATR) Overcomes Oxaliplatin Resistance and Promotes Antitumor Immunity in Colorectal Cancer. *Cancer Res.* **2019**, *79*, 2933–2946. [CrossRef] [PubMed]
128. Wang, H.H.; Wu, Z.Q.; Qian, D.; Zaorsky, N.G.; Qiu, M.H.; Cheng, J.J.; Jiang, C.; Wang, J.; Zeng, X.L.; Liu, C.L.; et al. Ablative Hypofractionated Radiation Therapy Enhances Non-Small Cell Lung Cancer Cell Killing via Preferential Stimulation of Necroptosis In Vitro and In Vivo. *Int. J. Radiat. Oncol. Biol. Phys.* **2018**, *101*, 49–62. [CrossRef] [PubMed]
129. Galluzzi, L.; Buque, A.; Kepp, O.; Zitvogel, L.; Kroemer, G. Immunogenic cell death in cancer and infectious disease. *Nat. Rev. Immunol.* **2017**, *17*, 97–111. [CrossRef]
130. Kroemer, G.; Galluzzi, L.; Kepp, O.; Zitvogel, L. Immunogenic cell death in cancer therapy. *Annu. Rev. Immunol.* **2013**, *31*, 51–72. [CrossRef]
131. Krysko, D.V.; Garg, A.D.; Kaczmarek, A.; Krysko, O.; Agostinis, P.; Vandenabeele, P. Immunogenic cell death and DAMPs in cancer therapy. *Nat. Rev. Cancer* **2012**, *12*, 860–875. [CrossRef] [PubMed]
132. Moriya, T.; Kitagawa, K.; Hayakawa, Y.; Hemmi, H.; Kaisho, T.; Ueha, S.; Ikebuchi, R.; Yasuda, I.; Nakanishi, Y.; Honda, T.; et al. Immunogenic tumor cell death promotes dendritic cell migration and inhibits tumor growth via enhanced T cell immunity. *iScience* **2021**, *24*. [CrossRef] [PubMed]
133. Garg, A.D.; Krysko, D.V.; Verfaillie, T.; Kaczmarek, A.; Ferreira, G.B.; Marysael, T.; Rubio, N.; Firczuk, M.; Mathieu, C.; Roebroek, A.J.; et al. A novel pathway combining calreticulin exposure and ATP secretion in immunogenic cancer cell death. *EMBO J.* **2012**, *31*, 1062–1079. [CrossRef] [PubMed]
134. Diamond, J.M.; Vanpouille-Box, C.; Spada, S.; Rudqvist, N.P.; Chapman, J.R.; Ueberheide, B.M.; Pilones, K.A.; Sarfraz, Y.; Formenti, S.C.; Demaria, S. Exosomes Shuttle TREX1-Sensitive IFN-Stimulatory dsDNA from Irradiated Cancer Cells to DCs. *Cancer Immunol. Res.* **2018**, *6*, 910–920. [CrossRef] [PubMed]
135. Deng, L.; Liang, H.; Xu, M.; Yang, X.; Burnette, B.; Arina, A.; Li, X.D.; Mauceri, H.; Beckett, M.; Darga, T.; et al. STING-Dependent Cytosolic DNA Sensing Promotes Radiation-Induced Type I Interferon-Dependent Antitumor Immunity in Immunogenic Tumors. *Immunity* **2014**, *41*, 843–852. [CrossRef]
136. Yokoi, A.; Villar-Prados, A.; Oliphint, P.A.; Zhang, J.; Song, X.; De Hoff, P.; Morey, R.; Liu, J.; Roszik, J.; Clise-Dwyer, K.; et al. Mechanisms of nuclear content loading to exosomes. *Sci. Adv.* **2019**, *5*. [CrossRef]
137. Huang, L.; Li, L.; Lemos, H.; Chandler, P.R.; Pacholczyk, G.; Baban, B.; Barber, G.N.; Hayakawa, Y.; McGaha, T.L.; Ravishankar, B.; et al. Cutting edge: DNA sensing via the STING adaptor in myeloid dendritic cells induces potent tolerogenic responses. *J. Immunol.* **2013**, *191*, 3509–3513. [CrossRef]
138. Golden, E.B.; Apetoh, L. Radiotherapy and immunogenic cell death. *Semin. Radiat. Oncol.* **2015**, *25*, 11–17. [CrossRef]
139. Dobler, C.; Jost, T.; Hecht, M.; Fietkau, R.; Distel, L. Senescence Induction by Combined Ionizing Radiation and DNA Damage Response Inhibitors in Head and Neck Squamous Cell Carcinoma Cells. *Cells* **2020**, *9*, 2012. [CrossRef]
140. Yang, H.; Wang, H.; Ren, J.; Chen, Q.; Chen, Z.J. cGAS is essential for cellular senescence. *Proc. Natl. Acad. Sci. USA* **2017**, *114*, E4612–E4620. [CrossRef]

141. Vendetti, F.P.; Karukonda, P.; Clump, D.A.; Teo, T.; Lalonde, R.; Nugent, K.; Ballew, M.; Kiesel, B.F.; Beumer, J.H.; Sarkar, S.N.; et al. ATR kinase inhibitor AZD6738 potentiates CD8+ T cell-dependent antitumor activity following radiation. *J. Clin. Investig.* **2018**, *128*, 3926–3940. [CrossRef] [PubMed]
142. Tan, K.T.; Yeh, C.N.; Chang, Y.C.; Cheng, J.H.; Fang, W.L.; Yeh, Y.C.; Wang, Y.C.; Hsu, D.S.; Wu, C.E.; Lai, J.I.; et al. PRKDC: New biomarker and drug target for checkpoint blockade immunotherapy. *J. Immunother. Cancer* **2020**, *8*. [CrossRef] [PubMed]
143. Qiu, Z.; Oleinick, N.L.; Zhang, J. ATR/CHK1 inhibitors and cancer therapy. *Radiother. Oncol.* **2018**, *126*, 450–464. [CrossRef] [PubMed]
144. Kantidze, O.L.; Velichko, A.K.; Luzhin, A.V.; Petrova, N.V.; Razin, S.V. Synthetically Lethal Interactions of ATM, ATR, and DNA-PKcs. *Trends. Cancer* **2018**, *4*, 755–768. [CrossRef] [PubMed]
145. Kim, S.T.; Smith, S.A.; Mortimer, P.; Loembe, A.B.; Cho, H.; Kim, K.M.; Smith, C.; Willis, S.; Irurzun-Arana, I.; Berges, A.; et al. Phase I study of ceralasertib (AZD6738), a novel DNA damage repair agent, in combination with weekly paclitaxel in refractory cancer. *Clin. Cancer Res.* **2021**. [CrossRef]
146. Yap, T.A.; Tan, D.S.P.; Terbuch, A.; Caldwell, R.; Guo, C.; Goh, B.C.; Heong, V.; Haris, N.R.M.; Bashir, S.; Drew, Y.; et al. First-in-Human Trial of the Oral Ataxia Telangiectasia and RAD3-Related (ATR) Inhibitor BAY 1895344 in Patients with Advanced Solid Tumors. *Cancer Discov.* **2020**. [CrossRef]
147. Yap, T.A.; O'Carrigan, B.P.M.S.; Penney, M.S.; Lim, J.S.; Brown, J.S.; Luken, M.J.M.; Tunariu, N.; Perez-Lopez, R.; Rodrigues, D.N.R.; Riisnaes, R.; et al. Phase I Trial of First-in-Class ATR Inhibitor M6620 (VX-970) as Monotherapy or in Combination with Carboplatin in Patients With Advanced Solid Tumors. *J. Clin. Oncol.* **2020**, *38*, 3195–3204. [CrossRef] [PubMed]
148. Thomas, A.; Redon, C.E.; Sciuto, L.; Padiernos, E.; Ji, J.; Lee, M.J.; Yuno, A.; Lee, S.; Zhang, Y.; Tran, L.; et al. Phase I Study of ATR Inhibitor M6620 in Combination With Topotecan in Patients With Advanced Solid Tumors. *J. Clin. Oncol.* **2018**, *36*, 1594–1602. [CrossRef] [PubMed]
149. Jackson, C.B.; Noorbakhsh, S.I.; Sundaram, R.K.; Kalathil, A.N.; Ganesa, S.; Jia, L.; Breslin, H.; Burgenske, D.M.; Gilad, O.; Sarkaria, J.N.; et al. Temozolomide Sensitizes MGMT-Deficient Tumor Cells to ATR Inhibitors. *Cancer Res.* **2019**, *79*, 4331–4338. [CrossRef]
150. Jucaite, A.; Stenkrona, P.; Cselenyi, Z.; De Vita, S.; Buil-Bruna, N.; Varnas, K.; Savage, A.; Varrone, A.; Johnstrom, P.; Schou, M.; et al. Brain exposure of the ATM inhibitor AZD1390 in humans-a positron emission tomography study. *Neuro. Oncol.* **2021**, *23*, 687–696. [CrossRef]
151. van Bussel, M.T.J.; Awada, A.; de Jonge, M.J.A.; Mau-Sorensen, M.; Nielsen, D.; Schoffski, P.; Verheul, H.M.W.; Sarholz, B.; Berghoff, K.; El Bawab, S.; et al. A first-in-man phase 1 study of the DNA-dependent protein kinase inhibitor peposertib (formerly M3814) in patients with advanced solid tumours. *Br. J. Cancer* **2021**, *124*, 728–735. [CrossRef] [PubMed]
152. DeCaprio, J.A. Molecular Pathogenesis of Merkel Cell Carcinoma. *Annu. Rev. Pathol.* **2021**, *16*, 69–91. [CrossRef]
153. Paulson, K.G.; Iyer, J.G.; Simonson, W.T.; Blom, A.; Thibodeau, R.M.; Schmidt, M.; Pietromonaco, S.; Sokil, M.; Warton, E.M.; Asgari, M.M.; et al. CD8+ lymphocyte intratumoral infiltration as a stage-independent predictor of Merkel cell carcinoma survival: A population-based study. *Am. J. Clin. Pathol.* **2014**, *142*, 452–458. [CrossRef] [PubMed]
154. D'Angelo, S.P.; Russell, J.; Lebbe, C.; Chmielowski, B.; Gambichler, T.; Grob, J.J.; Kiecker, F.; Rabinowits, G.; Terheyden, P.; Zwiener, I.; et al. Efficacy and Safety of First-line Avelumab Treatment in Patients With Stage IV Metastatic Merkel Cell Carcinoma: A Preplanned Interim Analysis of a Clinical Trial. *JAMA Oncol.* **2018**, *4*, e180077. [CrossRef]
155. Nghiem, P.; Bhatia, S.; Lipson, E.J.; Sharfman, W.H.; Kudchadkar, R.R.; Brohl, A.S.; Friedlander, P.A.; Daud, A.; Kluger, H.M.; Reddy, S.A.; et al. Three-year survival, correlates and salvage therapies in patients receiving first-line pembrolizumab for advanced Merkel cell carcinoma. *J. Immunother. Cancer* **2021**, *9*. [CrossRef] [PubMed]
156. Topalian, S.L.; Bhatia, S.; Amin, A.; Kudchadkar, R.R.; Sharfman, W.H.; Lebbé, C.; Delord, J.P.; Dunn, L.A.; Shinohara, M.M.; Kulikauskas, R.; et al. Neoadjuvant Nivolumab for Patients With Resectable Merkel Cell Carcinoma in the CheckMate 358 Trial. *J. Clin. Oncol.* **2020**, *38*, 2476–2487. [CrossRef]
157. Lahman, M.C.; Paulson, K.G.; Nghiem, P.T.; Chapuis, A.G. Quality Is King: Fundamental Insights into Tumor Antigenicity from Virus-Associated Merkel Cell Carcinoma. *J. Invest. Dermatol.* **2021**. [CrossRef]
158. Park, J.W.; Lee, J.K.; Sheu, K.M.; Wang, L.; Balanis, N.G.; Nguyen, K.; Smith, B.A.; Cheng, C.; Tsai, B.L.; Cheng, D.; et al. Reprogramming normal human epithelial tissues to a common, lethal neuroendocrine cancer lineage. *Science* **2018**, *362*, 91–95. [CrossRef] [PubMed]
159. Hafner, C.; Houben, R.; Baeurle, A.; Ritter, C.; Schrama, D.; Landthaler, M.; Becker, J.C. Activation of the PI3K/AKT pathway in Merkel cell carcinoma. *PLoS ONE* **2012**, *7*, e31255. [CrossRef]
160. Borchert, S.; Czech-Sioli, M.; Neumann, F.; Schmidt, C.; Wimmer, P.; Dobner, T.; Grundhoff, A.; Fischer, N. High-affinity Rb binding, p53 inhibition, subcellular localization, and transformation by wild-type or tumor-derived shortened Merkel cell polyomavirus large T antigens. *J. Virol.* **2014**, *88*, 3144–3160. [CrossRef]
161. Houben, R.; Dreher, C.; Angermeyer, S.; Borst, A.; Utikal, J.; Haferkamp, S.; Peitsch, W.K.; Schrama, D.; Hesbacher, S. Mechanisms of p53 restriction in Merkel cell carcinoma cells are independent of the Merkel cell polyoma virus T antigens. *J. Investig. Dermatol.* **2013**, *133*, 2453–2460. [CrossRef]
162. Park, D.E.; Cheng, J.; Berrios, C.; Montero, J.; Cortes-Cros, M.; Ferretti, S.; Arora, R.; Tillgren, M.L.; Gokhale, P.C.; DeCaprio, J.A. Dual inhibition of MDM2 and MDM4 in virus-positive Merkel cell carcinoma enhances the p53 response. *Proc. Natl. Acad. Sci. USA* **2019**, *116*, 1027–1032. [CrossRef] [PubMed]

163. Cheng, J.; Park, D.E.; Berrios, C.; White, E.A.; Arora, R.; Yoon, R.; Branigan, T.; Xiao, T.; Westerling, T.; Federation, A.; et al. Merkel cell polyomavirus recruits MYCL to the EP400 complex to promote oncogenesis. *PLoS Pathog.* **2017**, *13*, e1006668. [CrossRef] [PubMed]
164. Wong, S.Q.; Waldeck, K.; Vergara, I.A.; Schroder, J.; Madore, J.; Wilmott, J.S.; Colebatch, A.J.; De Paoli-Iseppi, R.; Li, J.; Lupat, R.; et al. UV-Associated Mutations Underlie the Etiology of MCV-Negative Merkel Cell Carcinomas. *Cancer Res.* **2015**, *75*, 5228–5234. [CrossRef]
165. Cimino, P.J.; Robirds, D.H.; Tripp, S.R.; Pfeifer, J.D.; Abel, H.J.; Duncavage, E.J. Retinoblastoma gene mutations detected by whole exome sequencing of Merkel cell carcinoma. *Mod. Pathol.* **2014**, *27*, 1073–1087. [CrossRef]
166. Harms, P.W.; Harms, K.L.; Moore, P.S.; DeCaprio, J.A.; Nghiem, P.; Wong, M.K.K.; Brownell, I.; International Workshop on Merkel Cell Carcinoma Research Working Group. The biology and treatment of Merkel cell carcinoma: Current understanding and research priorities. *Nat. Rev. Clin. Oncol.* **2018**, *15*, 763–776. [CrossRef]
167. Paulson, K.G.; Lemos, B.D.; Feng, B.; Jaimes, N.; Penas, P.F.; Bi, X.; Maher, E.; Cohen, L.; Leonard, J.H.; Granter, S.R.; et al. Array-CGH reveals recurrent genomic changes in Merkel cell carcinoma including amplification of L-Myc. *J. Investig. Dermatol.* **2009**, *129*, 1547–1555. [CrossRef]
168. Harms, P.W.; Vats, P.; Verhaegen, M.E.; Robinson, D.R.; Wu, Y.M.; Dhanasekaran, S.M.; Palanisamy, N.; Siddiqui, J.; Cao, X.; Su, F.; et al. The Distinctive Mutational Spectra of Polyomavirus-Negative Merkel Cell Carcinoma. *Cancer Res.* **2015**, *75*, 3720–3727. [CrossRef] [PubMed]
169. Knepper, T.C.; Montesion, M.; Russell, J.S.; Sokol, E.S.; Frampton, G.M.; Miller, V.A.; Albacker, L.A.; McLeod, H.L.; Eroglu, Z.; Khushalani, N.I.; et al. The Genomic Landscape of Merkel Cell Carcinoma and Clinicogenomic Biomarkers of Response to Immune Checkpoint Inhibitor Therapy. *Clin. Cancer Res.* **2019**, *25*, 5961–5971. [CrossRef]
170. Horny, K.; Gerhardt, P.; Hebel-Cherouny, A.; Wulbeck, C.; Utikal, J.; Becker, J.C. Mutational Landscape of Virus- and UV-Associated Merkel Cell Carcinoma Cell Lines Is Comparable to Tumor Tissue. *Cancers* **2021**, *13*, 649. [CrossRef]
171. La Rosa, S.; Bonzini, M.; Sciarra, A.; Asioli, S.; Maragliano, R.; Arrigo, M.; Foschini, M.P.; Righi, A.; Maletta, F.; Motolese, A.; et al. Exploring the Prognostic Role of Ki67 Proliferative Index in Merkel Cell Carcinoma of the Skin: Clinico-Pathologic Analysis of 84 Cases and Review of the Literature. *Endocr. Pathol.* **2020**, *31*, 392–400. [CrossRef] [PubMed]
172. Iwasaki, T.; Matsushita, M.; Nonaka, D.; Kato, M.; Nagata, K.; Murakami, I.; Hayashi, K. Phosphohistone-H3 (PHH3) is prognostic relevant in Merkel cell carcinomas but Merkel cell polyomavirus is a more powerful prognostic factor than AJCC clinical stage, PHH3, Ki-67 or mitotic indices. *Pathol. Int.* **2015**, *65*, 404–409. [CrossRef]
173. Nielsen, P.S.; Riber-Hansen, R.; Jensen, T.O.; Schmidt, H.; Steiniche, T. Proliferation indices of phosphohistone H3 and Ki67: Strong prognostic markers in a consecutive cohort with stage I/II melanoma. *Mod. Pathol.* **2013**, *26*, 404–413. [CrossRef]
174. Saldivar, J.C.; Cortez, D.; Cimprich, K.A. The essential kinase ATR: Ensuring faithful duplication of a challenging genome. *Nat. Rev. Mol. Cell Biol.* **2017**, *18*, 622–636. [CrossRef]
175. Fokas, E.; Prevo, R.; Hammond, E.M.; Brunner, T.B.; McKenna, W.G.; Muschel, R.J. Targeting ATR in DNA damage response and cancer therapeutics. *Cancer Treat. Rev.* **2014**, *40*, 109–117. [CrossRef] [PubMed]
176. Zou, L.; Elledge, S.J. Sensing DNA Damage Through ATRIP Recognition of RPA-ssDNA Complexes. *Science* **2003**, *300*, 1542–1548. [CrossRef] [PubMed]
177. Karnitz, L.M.; Zou, L. Molecular Pathways: Targeting ATR in Cancer Therapy. *Clin. Cancer Res.* **2015**, *21*, 4780–4785. [CrossRef] [PubMed]
178. Schoppy, D.W.; Ragland, R.L.; Gilad, O.; Shastri, N.; Peters, A.A.; Murga, M.; Fernandez-Capetillo, O.; Diehl, J.A.; Brown, E.J. Oncogenic stress sensitizes murine cancers to hypomorphic suppression of ATR. *J. Clin. Investig.* **2012**, *122*, 241–252. [CrossRef] [PubMed]
179. Iyer, J.G.; Parvathaneni, U.; Gooley, T.; Miller, N.J.; Markowitz, E.; Blom, A.; Lewis, C.W.; Doumani, R.F.; Parvathaneni, K.; Anderson, A.; et al. Single-fraction radiation therapy in patients with metastatic Merkel cell carcinoma. *Cancer Med.* **2015**, *4*, 1161–1170. [CrossRef] [PubMed]
180. Paulson, K.G.; Tegeder, A.; Willmes, C.; Iyer, J.G.; Afanasiev, O.K.; Schrama, D.; Koba, S.; Thibodeau, R.; Nagase, K.; Simonson, W.T.; et al. Downregulation of MHC-I expression is prevalent but reversible in Merkel cell carcinoma. *Cancer Immunol. Res.* **2014**, *2*, 1071–1079. [CrossRef]
181. Ritter, C.; Fan, K.; Paulson, K.G.; Nghiem, P.; Schrama, D.; Becker, J.C. Reversal of epigenetic silencing of MHC class I chain-related protein A and B improves immune recognition of Merkel cell carcinoma. *Sci. Rep.* **2016**, *6*, 21678. [CrossRef]
182. Iyer, J.G.; Blom, A.; Doumani, R.; Lewis, C.; Tarabadkar, E.S.; Anderson, A.; Ma, C.; Bestick, A.; Parvathaneni, U.; Bhatia, S.; et al. Response rates and durability of chemotherapy among 62 patients with metastatic Merkel cell carcinoma. *Cancer Med.* **2016**, *5*, 2294–2301. [CrossRef] [PubMed]
183. Chan, I.S.; Bhatia, S.; Kaufman, H.L.; Lipson, E.J. Immunotherapy for Merkel cell carcinoma: A turning point in patient care. *J. Immunother. Cancer* **2018**, *6*, 23. [CrossRef]
184. Voog, E.B.P.; Martin, J.P.; Blay, J.Y. Chemotherapy for Patients with Locally Advanced or Metastatic Merkel Cell Carcinoma. *Cancer* **1999**, *85*, 2589–2595. [CrossRef]
185. Colunga, A.; Pulliam, T.; Nghiem, P. Merkel Cell Carcinoma in the Age of Immunotherapy: Facts and Hopes. *Clin Cancer Res.* **2018**, *24*, 2035–2043. [CrossRef] [PubMed]

186. Tormoen, G.W.; Crittenden, M.R.; Gough, M.J. Role of the immunosuppressive microenvironment in immunotherapy. *Adv. Radiat. Oncol.* **2018**, *3*, 520–526. [CrossRef]
187. Binnewies, M.; Roberts, E.W.; Kersten, K.; Chan, V.; Fearon, D.F.; Merad, M.; Coussens, L.M.; Gabrilovich, D.I.; Ostrand-Rosenberg, S.; Hedrick, C.C.; et al. Understanding the tumor immune microenvironment (TIME) for effective therapy. *Nat. Med.* **2018**, *24*, 541–550. [CrossRef] [PubMed]
188. Vijayan, D.; Young, A.; Teng, M.W.L.; Smyth, M.J. Targeting immunosuppressive adenosine in cancer. *Nat. Rev. Cancer* **2017**, *17*, 709–724. [CrossRef]
189. Kwon, M.; Kim, S.T.; Smith, S.; Smith, C.; Mortimer, P.G.; LoembE, B.; Kozarewa, I.; Dean, E.; Lee, J. Phase II study of ceralasertib (AZD6738), in combination with durvalumab in patients with metastatic melanoma who have failed prior anti-PD-1 therapy. *J. Clin. Oncol.* **2021**, *39*, 9514. [CrossRef]

Titles

Extended treatment duration using reduced-frequency dosing of anti-PD-1 therapy in patients with advanced melanoma and Merkel cell carcinoma

Target Journal: JITC
Word Count: 3717 / 5,000
Structured Abstract: 350/ 350 words
Tables/Figures: 7/ 7
References: 39/ 50

Authors:

Lisa May Ling Tachiki[1,3], Daniel S Hippe[3,4], Karly Williams Silva[1,3], Evan Thomas Hall[1,3], William McCamy[1], Dane Fritzsche[3], Andrea Perdue[1,3], Julia Majovski[1,3], Alexandra Spallone[1,3], Thomas Pulliam[2,3], Daniel A Goldstein[5], Joshua Veatch[1,3], Joel Ho[1,3], Paul T Nghiem[2,3], John A Thompson[1,3], Shailender Bhatia[1,3]

[1]Department of Medicine, Division of Medical Oncology, University of Washington, Seattle, WA
[2]Department of Medicine, Division of Medical Oncology, University of Washington, Seattle, WA
[3]Clinical Research Division, Fred Hutchinson Cancer Center, Seattle, WA
[4]Department of Radiology, University of Washington, Seattle, WA
[5]Davidoff Cancer Center, Rabin Medical Center, Petah Tikva, Israel

Corresponding author: Lisa Tachiki

Email: ltachiki@uw.edu

Author information:
Daniel S Hippe
dhippe@uw.edu

Karly Williams Silva
karlyann@uw.edu

Evan Thomas Hall
evanh@uw.edu

William McCamy
wmccamy@seattlecca.org

Dane Fritzsche
dfritzsche@seattlecca.org

Andrea Perdue
anoordew@seattlecca.org

Julia Majovski
jmajovski@seattlecca.org

Alexandra Spallone
aspallon@seattlecca.org

Thomas Pulliam
thpullia@uw.edu

Daniel A Goldstein
danielg3@tauex.tau.ac.il

Joshua Veatch
jveatch@uw.edu

Paul T Nghiem
pnghiem@uw.edu

John A Thompson
jat@uw.edu

Shailender Bhatia
sbhatia@uw.edu

Keywords

Immune checkpoint inhibitors; reduced frequency; extended interval; immunotherapy dosing; nivolumab; pembrolizumab; melanoma; Merkel cell carcinoma

ABSTRACT

Word count: 350/350

Background: Optimal duration of treatment (DoT) with immune checkpoint inhibitors (ICI) in patients with metastatic melanoma and Merkel cell carcinoma (MCC) remains unclear. ICI discontinuation in melanoma and MCC patients, especially without CR, may be associated with higher rates of progression, compared to ICI continuation. Thus, extending DoT could improve outcomes. However, continuing ICI at standard frequency doses (SFD) is not logistically or financially viable. Reduced frequency ICI administration may provide an alternative option to sustain DoT.

Methods: This retrospective study analyzes patients with metastatic melanoma and MCC treated with reduced-frequency dosing (RFD) of anti-PD-1 antibodies every 2-3 months. RFD was implemented in patients who experienced initial clinical benefit with ICI administered at SFD then electively transitioned to RFD. Efficacy and safety endpoints included progression free survival (PFS) and immune-related adverse events (irAE), respectively. We also compared the costs between 2 years of treatment at SFD versus extended DoT at RFD.

Results: From 2014 – 2021, 23 patients with metastatic melanoma (N = 18) or MCC (N = 5) received anti-PD-1 therapy with RFD. Median DoT at SFD was 1.1 years (range 0.2 – 2.2) with best objective responses of CR (N =6), PR (N = 11), and SD (N = 6). Median DoT at RFD was 1.2 years (range 0.2 – 3.5). The median follow-up was 3.7 years after ICI initiation. The 3-year PFS in melanoma patients was 100% with CR, 89% with PR, and 50% with SD. The 3-year PFS in MCC was 100% in patients with CR and PR. The cumulative incidence of any-grade irAEs was 57% and grade 3 irAEs was 28% during the RFD period. Among the subset of 15 patients with DoT >2 years (median 3.4 yr, range 2.0 – 5.0), total savings amounted to $1.1 million in drug costs and 384 hours of clinic and travel time despite the extended DoT, as compared to the cost of 2-year DoT at SFD.

Conclusions: Efficacy and safety data suggest sustained biologic activity of ICI with RFD administration. RFD may provide an alternative approach to extending DoT in patients receiving ICI without additional logistical and financial burden, while preserving outcomes.

This part should be a total of 3-5 sentences:

- **What is already known on this topic** –

  There is no clear consensus regarding the optimal duration of immune checkpoint inhibitors. Treatment discontinuation may affect clinical outcomes in advanced melanoma patients without CR and in Merkel cell carcinoma patients, but ongoing treatment delivery must be optimized.

- **What this study adds**

  Patients who transitioned to reduced-frequency dosing of anti-PD-1 therapy every 2-3 months after initial clinical responses did not appear to have inferior

outcomes compared to historical cohorts. Clinical efficacy and safety data suggest sustained immune activity with reduced-frequency dosing administration.

- **How this study might affect research, practice or policy**

  Reduced-frequency dosing may extend the duration of treatment, while decreasing logistical and financial burdens on patients and the healthcare system. The reduced-frequency dosing approach should be studied further in prospective, randomized trials to evaluate the optimal dosing regimen for immune checkpoint inhibitors.

INTRODUCTION

Immune checkpoint inhibitors (ICI) have led to remarkable improvement in the patient outcomes in several different cancer types, including metastatic melanoma and Merkel cell carcinoma (MCC) (1-4). Although a sizable proportion of patients with these aggressive skin cancers experience initial responses and durable clinical benefit with ICIs, the optimal duration of treatment to sustain long-term disease control remains unclear (5, 6). Durable complete responses (CR) after treatment discontinuation have been observed in a select cohort of metastatic melanoma patients treated in KEYNOTE-001 (7). However, ICI discontinuation in melanoma patients without a CR and in Merkel cell carcinoma (MCC) patients may be associated with a higher rate of progression over time, as compared to historical outcomes with ICI continuation (8-11). For these patients, continuing immunotherapy may be beneficial to sustain treatment outcomes. Yet, indefinite continuation at standard frequency doses (SFD) is not logistically or financially sustainable (12, 13).

Rather than discontinue therapy, optimizing dose frequency may be an alternative way to decrease use of this expensive class of drugs while maintaining anti-tumor responses (6). In phase I studies, one infusion of nivolumab sustained PD-1 receptor occupancy up to 85 days (14). Furthermore, nivolumab saturated PD-1 receptors at doses of 0.3mg/kg, doses significantly lower than those approved by the FDA (15). These pharmacodynamic findings suggest that clinical responses to ICI therapy could be achieved with less frequent and lower doses of anti-PD-1 drug (16).

Current clinical options for patients who respond to ICI include continuing standard doses of ICI therapy until disease progression or completely discontinuing therapy after 2 years. In our clinic, we employ reduced frequency dosing (RFD) of anti-PD-1 antibodies as an alternative method to maintain patients on treatment, in lieu of permanent discontinuation, while mitigating the financial and logistical burdens of ICI therapy. We discuss this approach of de-escalating treatment with RFD (pembrolizumab or

nivolumab once every 2-3 months) with our patients after they experience objective responses to ICI therapy.

Reported clinical outcomes from extended-interval ICI dosing are limited (17). The purpose of this study was to retrospectively evaluate the efficacy and safety of RFD of anti-PD-1 antibodies at our institution in patients with advanced melanoma and Merkel cell carcinoma. To our knowledge, this is the first study to report efficacy outcomes of RFD in patients with melanoma and MCC and to provide a cost-savings analysis from implementing RFD.

METHODS

We conducted a single-center, retrospective analysis of patients with advanced melanoma or MCC treated with anti-PD-1 or anti-PD-L1 therapy at the Fred Hutchinson Cancer Center between January 2014 to June 2021. This study was approved by the local Institutional Review Board and was conducted in accordance with the Declaration of Helsinki provisions.

Eligible patients were at least 18 years of age and had a confirmed diagnosis of either melanoma (excluding uveal melanoma) or MCC with distant metastatic or unresectable locoregional disease. All patients had received systemic anti-PD-1/PD-L1 therapy administered initially at standard frequency dosing (SFD) but had subsequently transitioned to reduced frequency dosing (RFD) after individualized discussions with the treating clinicians. Transition from SFD to RFD was a shared clinical decision made by the patients after a thorough, documented discussion with their treating clinician. The decision was influenced by the timing and depth of disease response, logistical demands of SFD, toxicity considerations and importantly, patient preference and comfort around the potential risks of a non-standard dosing schedule. Hence, the time to transition was variable across this cohort of patients.

SFD was defined as any of the prior and current FDA-approved administration regimens for pembrolizumab (2mg/kg or 200 mg every 3 weeks; 400 mg every 6 weeks), nivolumab (3mg/kg or 240 mg every 2 weeks; 480 mg every 4 weeks) or avelumab (10 mg/kg or 800 mg every 2 weeks), either as monotherapy or in combination with other immunotherapy agents such as ipilimumab (18, 19). RFD was defined as pembrolizumab or nivolumab administered at a frequency less than SFD, generally once every 8-12 weeks.

We also collected patient demographics, location of metastases at initiation of anti-PD-(L)1 therapy, prior lines of treatment, dates of immunotherapy treatment, immune-related adverse events (irAE), time to progression, and date of last follow-up. Efficacy assessment included best overall response (BOR) on SFD, progression free survival (PFS), and overall survival (OS). BOR was defined as the best response category, per RECIST 1.1, recorded from the start of anti-PD-1 therapy at SFD prior to the transition to RFD. All patients were experiencing clinical benefit with SFD prior to the transition. Eligible patients were also required to have obtained ≥ 1 radiographic scan after transitioning to RFD to evaluate for disease response.

PFS was calculated as the time interval from the date of the first infusion at RFD to the earliest subsequent date of progression or death. Patients who were alive without progression were censored at last follow up. Similarly, time to irAE was calculated starting from the date of the first infusion at RFD and censored at last follow up. Progression and death were considered competing risks for irAEs. Rates of irAE were summarized for all irAEs (any grade) and for grade 3/4 irAEs. PFS was estimated using Kaplan-Meier methods, and rates of irAE were estimated using the cumulative incidence function estimator to account for competing risks. Confidence intervals (CIs) for PFS and irAE rates were

calculated using conventional standard error formulas except when the estimated rates were 0% or 100%. In those cases, CIs were calculated using the Clopper-Pearson exact method. All statistical calculations were conducted with the statistical computing language R (version 4.0.3; R Foundation for Statistical Computing, Vienna, Austria).

ECONOMIC ANALYSES

We identified a subset of patients in our retrospective cohort who received a total duration of therapy beyond two years, and we calculated the cumulative costs incurred by this subset of patients who received an extended duration of therapy. The costs of extended duration of therapy at RFD were compared to the theoretical costs of completing two years of anti-PD-1 therapy at SFD followed by treatment discontinuation. We used the average sales price (ASP) from the Center for Medicare and Medicaid Services for Part B drugs from the first quarter of 2021: $28.90 USD per mg for nivolumab and $51.35 USD per mg for pembrolizumab. We also collected estimated patient travel expenses by recording distances traveled between a patient's home address and the cancer clinic. We multiplied the miles traveled by the U.S. Internal Revenue Service travel reimbursement rate for 2021: $0.56/mile. To calculate total patient time spent in outpatient clinic visits, we used published estimates for average patient time associated with travel (32 minutes) (20), phlebotomy (51 minutes) (21), physician interaction time (29 minutes) (22), provider wait times (35 minutes) (20), infusion wait times (58 minutes) (22), and anti-PD-1 administration (30 minutes) (18, 19).

RESULTS

PATIENT CHARACTERISTICS

We identified 23 patients with either metastatic melanoma (N = 18) or MCC (N = 5) who had received anti-PD-1 therapy at RFD. The characteristics of our retrospective cohort are displayed in **Table 1**. The

median age of the patients was 61 years (range 40 – 92), and 18 patients were male (78%). Nine patients had previously received systemic therapy for advanced disease (39%). At the time of starting anti-PD-1 therapy, 7 patients had CNS metastases (30%), and 7 patients had visceral metastases without CNS disease (30%). Nine patients received nivolumab therapy (39%), and 14 patients received pembrolizumab (61%). None of the patients received avelumab.

TREATMENT OUTCOMES

Figure 1 demonstrates the clinical trajectory of each of the 23 patients, including the duration of treatment at SFD, the best overall response (BOR) achieved at SFD, duration of treatment at RFD, incidence of grade ≥ 2 irAEs, and disease progression or death, when applicable. The median duration of therapy at SFD was 13.3 months (range 2.3 - 26.3). The BOR at SFD was CR (N = 6; 26%), PR (N = 11; 48%) or SD (N = 6; 26%). The median duration of therapy at RFD was 15.7 months (range 2.1 – 42.7). At the time of data cutoff on July 8, 2021, the median follow-up duration in our cohort was 49.2 months (range 8.1 - 75.6). The 36-month PFS rate was 73% (95% CI 53 to 100) in advanced melanoma (**Figure 2A**) and 100% (95% CI 48 to 100) in advanced MCC (**Figure 2B**). By BOR in melanoma, the 36-month PFS rate was 100% (95% CI 29 to 100) for CR, 89% (95% CI 71 to 100) for PR, and 50% (95% CI 38 to 100) for SD (**Figure 2C**). In MCC, the 3-year PFS rate was 100% (95% CI 29 to 100) in patients with CR and 100% (95% CI 16 to 100) in PR (**Figure 2D**). The median PFS after transition to RFD was not reached (95% CI not estimable) in melanoma patients and was 58.2 months in MCC patients (95% CI not estimable).

SAFETY

During the SFD period, irAEs of any grade occurred in 48% of patients (N = 11), with grade 3 or higher events occurring in 9% of patients (N = 2). Two patients with irAE required systemic glucocorticoids to manage their toxicities, including grade 2 pneumonitis and grade 3 hepatitis. One patient required systemic glucocorticoids and infliximab to manage grade 3 colitis. The remaining 8 patients were

managed by withholding ICI therapy or adding hormone replacement. All patients had resolution of their irAEs prior to restarting immunotherapy. Upon reinitiating ICI therapy, only one of the 11 patients had recurrence of their prior irAE (neuropathy) during the RFD period.

There were 10 irAEs of any grade observed over the cumulative RFD period at a rate of 57% (95% CI 35 to 93). Eight of 10 events occurred within the first two years after starting RFD (1-year rate: 26%, 2-year rate: 37%). The last observed irAE occurred at 39 months after starting RFD (**Figure 3A**). The cumulative rate of grade 3 irAEs was 28% (95% CI 11 to 72) during the RFD period. Four patients experienced a grade 3 irAE events, including colitis (N=2), hepatitis (N=1), and dermatitis (N=1). IrAEs during RFD occurred at a similar rate to the SFD period. Furthermore, rates of irAE on RFD were similar between patients who had previously experienced an irAE during SFD and those without any prior irAE on SFD (**Figure 3B**).

PROGRESSION AFTER RFD

Four patients in our cohort had disease progression, summarized in **Table 2**. One out of the four patients remained on RFD when his disease progressed. The patient had a history of melanoma with brain parenchymal and leptomeningeal metastases, pulmonary metastases, and cutaneous metastases who experienced initial disease control with local radiation to CNS metastases and responded to systemic nivolumab at SFD for 16 months, followed by RFD for 7 months. He then progressed at a site of prior metastasis with new leptomeningeal disease while on RFD. Despite transitioning to BRAF/MEK inhibitor therapy for BRAFV600E-mutated melanoma, the patient died after four months due to disease progression. Conversely, the three additional patients were not receiving any systemic therapy at the time of progression. Two patients had irAEs (hepatitis and colitis) that had led to treatment discontinuation. One of these patients with metastatic melanoma underwent localized treatment with

stereotactic radiosurgery directed to progression at a solitary brain metastasis. He continues to remain free from progression. The second patient with metastatic MCC was restarted on anti-PD-1 therapy due to systemic disease progression but died without response to immunotherapy.

One patient with metastatic melanoma who electively discontinued anti-PD-1 therapy illustrated disease biology that may require ongoing PD-1 blockade for long-term disease control. This patient had achieved SD as BOR while on pembrolizumab for a total duration of 46.5 months, then elected to discontinue therapy due to ongoing stable response (Figure 4A). 14 months after elective discontinuation, his surveillance imaging demonstrated PD at sites of prior metastases (Figure 4B). He was re-initiated on systemic anti-PD-1 therapy and developed an ongoing partial response after 16 months on standard doses of nivolumab (Figure 4C). After 19 months on SFD, he was transitioned to RFD with nivolumab and continues to experience disease control.

COST SAVINGS ANALYSES

We then compared the cumulative costs of extended duration of therapy (beyond 2 years) at RFD to the costs of therapy at SFD for 2 years total. Fifteen of our 23 patients had received a duration of anti-PD-1 therapy beyond 2 years (median 3.4 years, range 2.0 - 5.0) at the data cutoff date. In this cohort, the RFD approach was associated with total cost savings of $1,124,464.63 in drug costs, $3,317.44 in travel costs to patients, and 384 hours of clinic time (**Figure 5A**). In a hypothetical treatment strategy that uses SFD for 6 months followed by subsequent treatment at RFD (every 12 weeks), the total drug costs for two years of SFD therapy could extend the duration of PD-1 blockade to 7 years with pembrolizumab and 9.5 years with nivolumab (**Figure 5B**).

DISCUSSION

We report real-world outcomes in a cohort of patients who have transitioned to reduced frequency dosing (RFD) after achieving disease control with standard frequency doses (SFD) of ICI. With limitations discussed below, implementation of RFD to extend the duration of treatment was feasible and maintained response outcomes. Efficacy and safety data suggest sustained biologic activity of ICI with RFD administration. Furthermore, drug costs and clinic time were significantly reduced with RFD. Therefore, RFD may provide an alternative approach to extend the duration of therapy with reduced financial and logistical burden.

Our reported PFS rates for RFD do not appear inferior to historical melanoma outcomes with ICI at SFD, recognizing discrepancies with cross-trial comparisons. In our melanoma cohort, the PFS at 3 years after transitioning to RFD was 100% for CR, 89% for PR, and 50% for SD. For melanoma patients who did not progress during the first 12 months of treatment, the 5-year PFS of CheckMate-067 was 88% for CR, 63% for PR and 50% for SD in the nivolumab monotherapy arm (10). For the ipilimumab/nivolumab combination arm, the 5-year PFS was 81% for CR, 79% for PR and 11% for SD (10). Similarly, outcomes from our MCC cohort appear to be maintained compared to historical cohorts. In this study's MCC cohort, the PFS rate at 3 years after RFD was 100% in patients with CR and PR. While noting differences between these studies, the KEYNOTE-017/CITN-09 trial reported 73% of MCC patients with initial objective responses experienced ongoing response at 3 years after treatment initiation (23).

Ongoing research efforts are investigating ways to de-escalate use of immune checkpoint inhibitors given their significant treatment-related toxicities, considerable economic cost, and the logistical burden for patients (6). Complete cessation of immunotherapy is one method currently under investigation (24-27). Based on early data from subgroup analyses and retrospective studies, treatment discontinuation must be considered cautiously (28). Retrospective analyses of elective ICI discontinuation in melanoma patients suggest correlation between shorter duration of treatment and higher rates of disease progression (29, 30). Furthermore, real-world PFS outcomes in patients who discontinue ICI report lower PFS rates compared to historical outcomes with ICI continuation. In a multicenter study across 14 melanoma centers in the Netherlands, 324 patients discontinued immunotherapy in the absence of disease progression. The 24-month PFS after anti-PD-1 discontinuation was 64% for CR, 53% for PR, and 31% for SD (9). Similarly, in a retrospective analysis at Memorial Sloan Kettering evaluating 396 patients

with melanoma, the 3-year probability of being alive without needing additional treatment was 72% for patients with CR (8). This rate dropped significantly to 26.9% for a response less than CR, and 3.8% for stable disease (SD) (8). Advanced Merkel cell carcinoma (MCC) patients responding to therapy may be at even higher risk of progressive disease after ICI discontinuation compared to melanoma patients (9). In a retrospective cohort of 20 advanced MCC with discontinued therapy, 2/6 patients with CR (33%), 7/11 patients with PR (64%), and 3/3 patients with SD (100%) developed disease progression after a median follow-up period of 13.2 months (11).

As an alternate to treatment discontinuation, optimizing dose frequency may provide a sustainable option to maintain treatment duration. Extending intervals between ICI doses has been studied previously. The FDA approved pembrolizumab 400 mg every 6 weeks after a preliminary analysis of KEYNOTE-555 demonstrated objective responses and toxicity rates comparable to prior historical outcomes (18, 31). A retrospective analysis conducted by the Veterans Health Administration also support the efficacy of extended-interval dosing. Among 835 veterans who received pembrolizumab, no differences in time-to-treatment discontinuation were observed between standard- and extended-interval dosing in either the all-diseases cohort (HR, 1.00; 95% CI, 1.00-1.00) or the NSCLC cohort (HR, 1.00; 95% CI, 1.00-1.00) (17). Pembrolizumab 200mg at extended intervals has also been evaluated. In a retrospective, multicenter study, patients with advanced non-small cell lung cancer (NSCLC) treated with pembrolizumab at extended intervals had outcomes comparable to patients who received standard dosing (32). Reasons for extended interval dosing included irAE, non-irAE medical issues, or patient–physician preference. Of note, 11 of the 27 patients in the retrospective cohort electively transitioned to extended-interval dosing after discussion with their physicians. Efficacy outcomes from these studies, in combination with our findings, underscore the necessity to study prospective trials using immune checkpoint inhibitors at less frequent doses.

Clinical responses at RFD challenge the utility of applying historical maximum-tolerated dose-finding strategies to new immunotherapeutic agents (33). In the phase 1b study of nivolumab, doses ranging from 0.1 mg/kg to 10 mg/kg generated similar response rates for advanced melanoma and renal cell carcinoma patients (15). One plausible explanation is that one dose of nivolumab, at concentrations ranging from 0.3mg/kg to 10 mg/kg, is able to saturate PD-1 receptors for approximately 3 months (14,

34). The non-linear relationship among the pharmacokinetic properties, pharmacodynamic properties, and response rates of ICIs suggest that lower and less frequent doses likely produce the same outcomes. Further investigation into pharmacodynamic biomarkers, such as PD-1 receptor occupancy, may be useful to identify the minimal ICI dose and frequency needed to maintain immune activation and therapeutic effect (35, 36).

Limitations of this study include retrospective analysis, small cohort size, and the selection of patients who were already responding to ICI therapy at transition to RFD. Patients who experienced severe grade 4 irAEs during SFD may be underrepresented in our cohort, as these patients likely did not proceed to RFD. Given the selective cohort evaluated in this study, PFS outcomes in this study warrant judicious application to other practice settings. RFD was not used during the induction phase of ICI therapy prior to patients' objective responses. Therefore, our results cannot be applied to upfront use of RFD prior to initial clinical response.

To our knowledge, this is the first study to report retrospective efficacy and safety outcomes for RFD of ICIs every 2 to 3 months in patients with advanced melanoma and Merkel cell carcinoma. Sustained PFS outcomes in patients with initial clinical responses to checkpoint inhibitors and rates of irAEs in our cohort suggest ongoing immune activation with RFD. Our findings provide data to support further study of dose optimization studies. Correlative studies of patient samples from prospective RFD regimens are pivotal to evaluate the pharmacokinetic and pharmacodynamic properties of RFD regimens. With increasing ICI indications across multiple tumor types, an optimized RFD schedule has significant implications for providing sustainable healthcare delivery by reducing healthcare expenditure and decreasing demands on patient time and finances. Furthermore, there is an urgent need to improve ICI access for low- and middle-income countries to this expensive class of potentially life-saving drugs. Prospective, randomized clinical trials studying regimens like RFD are underway internationally (37-39). The RFD approach may help to lower barriers to ICI access, thereby impacting cancer outcomes at a global scale.

REFERENCES

1. Robert C, Schachter J, Long GV, Arance A, Grob JJ, Mortier L, et al. Pembrolizumab versus Ipilimumab in Advanced Melanoma. N Engl J Med. 2015;372(26):2521-32. Epub 20150419. doi: 10.1056/NEJMoa1503093. PubMed PMID: 25891173.
2. Larkin J, Chiarion-Sileni V, Gonzalez R, Grob JJ, Cowey CL, Lao CD, et al. Combined Nivolumab and Ipilimumab or Monotherapy in Untreated Melanoma. New England Journal of Medicine. 2015;373(1):23-34. doi: 10.1056/NEJMoa1504030.
3. Kaufman HL, Russell J, Hamid O, Bhatia S, Terheyden P, D'Angelo SP, et al. Avelumab in patients with chemotherapy-refractory metastatic Merkel cell carcinoma: a multicentre, single-group, open-label, phase 2 trial. The Lancet Oncology. 2016;17(10):1374-85. doi: https://doi.org/10.1016/S1470-2045(16)30364-3.
4. Nghiem PT, Bhatia S, Lipson EJ, Kudchadkar RR, Miller NJ, Annamalai L, et al. PD-1 Blockade with Pembrolizumab in Advanced Merkel-Cell Carcinoma. New England Journal of Medicine. 2016;374(26):2542-52. doi: 10.1056/NEJMoa1603702.
5. Robert C, Marabelle A, Herrscher H, Caramella C, Rouby P, Fizazi K, et al. Immunotherapy discontinuation - how, and when? Data from melanoma as a paradigm. Nat Rev Clin Oncol. 2020;17(11):707-15. Epub 20200707. doi: 10.1038/s41571-020-0399-6. PubMed PMID: 32636502.
6. Hirsch I, Goldstein DA, Tannock IF, Butler MO, Gilbert DC. Optimizing the dose and schedule of immune checkpoint inhibitors in cancer to allow global access. Nature Medicine. 2022. doi: 10.1038/s41591-022-02029-1.
7. Robert C, Ribas A, Hamid O, Daud A, Wolchok JD, Joshua AM, et al. Durable Complete Response After Discontinuation of Pembrolizumab in Patients With Metastatic Melanoma. J Clin Oncol. 2018;36(17):1668-74. Epub 20171228. doi: 10.1200/jco.2017.75.6270. PubMed PMID: 29283791.
8. Betof Warner A, Palmer JS, Shoushtari AN, Goldman DA, Panageas KS, Hayes SA, et al. Long-Term Outcomes and Responses to Retreatment in Patients With Melanoma Treated With PD-1 Blockade. Journal of Clinical Oncology. 2020;38(15):1655-63. doi: 10.1200/JCO.19.01464.
9. van Zeijl MCT, van den Eertwegh AJM, Wouters M, de Wreede LC, Aarts MJB, van den Berkmortel F, et al. Discontinuation of anti-PD-1 monotherapy in advanced melanoma-Outcomes of daily clinical practice. Int J Cancer. 2022;150(2):317-26. Epub 20211002. doi: 10.1002/ijc.33800. PubMed PMID: 34520567; PubMed Central PMCID: PMC9293478.
10. Wolchok JD, Chiarion-Sileni V, Gonzalez R, Grob JJ, Rutkowski P, Lao CD, et al. Long-Term Outcomes With Nivolumab Plus Ipilimumab or Nivolumab Alone Versus Ipilimumab in Patients With Advanced Melanoma. J Clin Oncol. 2022;40(2):127-37. Epub 20211124. doi: 10.1200/jco.21.02229. PubMed PMID: 34818112; PubMed Central PMCID: PMC8718224.
11. Stege HM, Haist M, Schultheis S, Fleischer MI, Mohr P, Ugurel S, et al. Response durability after cessation of immune checkpoint inhibitors in patients with metastatic Merkel cell carcinoma: a retrospective multicenter DeCOG study. Cancer Immunol Immunother. 2021;70(11):3313-22. Epub 20210418. doi: 10.1007/s00262-021-02925-4. PubMed PMID: 33870464; PubMed Central PMCID: PMC8505278.
12. Mariotto AB, Robin Yabroff K, Shao Y, Feuer EJ, Brown ML. Projections of the Cost of Cancer Care in the United States: 2010–2020. JNCI: Journal of the National Cancer Institute. 2011;103(2):117-28. doi: 10.1093/jnci/djq495.

13. Yabroff KR, Mariotto A, Tangka F, Zhao J, Islami F, Sung H, et al. Annual Report to the Nation on the Status of Cancer, Part 2: Patient Economic Burden Associated With Cancer Care. JNCI: Journal of the National Cancer Institute. 2021;113(12):1670-82. doi: 10.1093/jnci/djab192.
14. Brahmer JR, Drake CG, Wollner I, Powderly JD, Picus J, Sharfman WH, et al. Phase I Study of Single-Agent Anti–Programmed Death-1 (MDX-1106) in Refractory Solid Tumors: Safety, Clinical Activity, Pharmacodynamics, and Immunologic Correlates. Journal of Clinical Oncology. 2010;28(19):3167-75. doi: 10.1200/JCO.2009.26.7609.
15. Agrawal S, Feng Y, Roy A, Kollia G, Lestini B. Nivolumab dose selection: challenges, opportunities, and lessons learned for cancer immunotherapy. Journal for ImmunoTherapy of Cancer. 2016;4(1):72. doi: 10.1186/s40425-016-0177-2.
16. Malmberg R, Zietse M, Dumoulin DW, Hendrikx JJMA, Aerts JGJV, van der Veldt AAM, et al. Alternative dosing strategies for immune checkpoint inhibitors to improve cost-effectiveness: a special focus on nivolumab and pembrolizumab. The Lancet Oncology. 2022;23(12):e552-e61. doi: https://doi.org/10.1016/S1470-2045(22)00554-X.
17. Strohbehn GW, Holleman R, Burns J, Klamerus ML, Kelley MJ, Kerr EA, et al. Adoption of Extended-Interval Dosing of Single-Agent Pembrolizumab and Comparative Effectiveness vs Standard Dosing in Time-to-Treatment Discontinuation. JAMA Oncology. 2022;8(11):1663-7. doi: 10.1001/jamaoncol.2022.4109.
18. Merck & Co. Keytruda (pembrolizumab) [package insert]. U.S. Food and Drug Administration website. https://www.accessdata.fda.gov/drugsatfda_docs/label/2016/125514s012lbl.pdf. Revised October 2016. Accessed August 13, 2022.
19. Bristol Myers Squibb. Opdivo (nivolumab) [package insert]. U.S. Food and Drug Administration website. https://www.accessdata.fda.gov/drugsatfda_docs/label/2021/125554s090lbl.pdf. Revised January 2021. Accessed August 13, 2022.
20. Rocque GB, Williams CP, Miller HD, Azuero A, Wheeler SB, Pisu M, et al. Impact of Travel Time on Health Care Costs and Resource Use by Phase of Care for Older Patients With Cancer. J Clin Oncol. 2019;37(22):1935-45. Epub 20190611. doi: 10.1200/jco.19.00175. PubMed PMID: 31184952; PubMed Central PMCID: PMC6804875.
21. Gjolaj LN, Gari GA, Olier-Pino AI, Garcia JD, Fernandez GL. Decreasing Laboratory Turnaround Time and Patient Wait Time by Implementing Process Improvement Methodologies in an Outpatient Oncology Infusion Unit. Journal of Oncology Practice. 2014;10(6):380-2. doi: 10.1200/JOP.2014.001499.
22. Hamel LM, Chapman R, Eggly S, Penner LA, Tkatch R, Vichich J, et al. Measuring the Use of Examination Room Time in Oncology Clinics: A Novel Approach to Assessing Clinic Efficiency and Patient Flow. Journal of Oncology Practice. 2014;10(6):e385-e9. doi: 10.1200/JOP.2013.001359.
23. Nghiem P, Bhatia S, Lipson EJ, Sharfman WH, Kudchadkar RR, Brohl AS, et al. Three-year survival, correlates and salvage therapies in patients receiving first-line pembrolizumab for advanced Merkel cell carcinoma. J Immunother Cancer. 2021;9(4). doi: 10.1136/jitc-2021-002478. PubMed PMID: 33879601; PubMed Central PMCID: PMC8061836.
24. Coen O, Corrie P, Marshall H, Plummer R, Ottensmeier C, Hook J, et al. The DANTE trial protocol: a randomised phase III trial to evaluate the Duration of ANti-PD-1 monoclonal antibody Treatment in patients with metastatic mElanoma. BMC Cancer. 2021;21(1):761. Epub 20210701. doi: 10.1186/s12885-021-08509-w. PubMed PMID: 34210290; PubMed Central PMCID: PMC8246129.
25. Mulder E, de Joode K, Litière S, Ten Tije AJ, Suijkerbuijk KPM, Boers-Sonderen MJ, et al. Early discontinuation of PD-1 blockade upon achieving a complete or partial response in patients with advanced melanoma: the multicentre prospective Safe Stop trial. BMC Cancer. 2021;21(1):323. Epub 20210325. doi: 10.1186/s12885-021-08018-w. PubMed PMID: 33765967; PubMed Central PMCID: PMC7993897.

26. Gibney GT, Lee SJ, Atkins MB, Wong TZ, Guerriero J, Marron TU, et al. A phase II study of biomarker-driven early discontinuation of anti–PD-1 therapy in patients with advanced melanoma (PET-Stop): ECOG-ACRIN EA6192. Journal of Clinical Oncology. 2022;40(16_suppl):TPS9591-TPS. doi: 10.1200/JCO.2022.40.16_suppl.TPS9591.
27. Baetz TD, Song X, Ernst DS, McWhirter E, Petrella TM, Savage KJ, et al. A randomized phase III study of duration of anti-PD-1 therapy in metastatic melanoma (STOP-GAP): Canadian Clinical Trials Group study (CCTG) ME.13. Journal of Clinical Oncology. 2018;36(15_suppl):TPS9600-TPS. doi: 10.1200/JCO.2018.36.15_suppl.TPS9600.
28. Marron TU, Ryan AE, Reddy SM, Kaczanowska S, Younis RH, Thakkar D, et al. Considerations for treatment duration in responders to immune checkpoint inhibitors. J Immunother Cancer. 2021;9(3). doi: 10.1136/jitc-2020-001901. PubMed PMID: 33653801; PubMed Central PMCID: PMC7929825.
29. Jansen YJL, Rozeman EA, Mason R, Goldinger SM, Geukes Foppen MH, Hoejberg L, et al. Discontinuation of anti-PD-1 antibody therapy in the absence of disease progression or treatment limiting toxicity: clinical outcomes in advanced melanoma. Annals of Oncology. 2019;30(7):1154-61. doi: 10.1093/annonc/mdz110.
30. Asher N, Israeli-Weller N, Shapira-Frommer R, Ben-Betzalel G, Schachter J, Meirson T, et al. Immunotherapy Discontinuation in Metastatic Melanoma: Lessons from Real-Life Clinical Experience. Cancers (Basel). 2021;13(12). Epub 20210620. doi: 10.3390/cancers13123074. PubMed PMID: 34203061; PubMed Central PMCID: PMC8234591.
31. Lala M, Akala O, Chartash E, Kalabis M, Su S-C, De Alwis D, et al. Abstract CT042: pembrolizumab 400 mg Q6W dosing: first clinical outcomes data from Keynote-555 cohort B in metastatic melanoma patients. Cancer Research. 2020;80(16_Supplement):CT042-CT.
32. Sehgal K, Bulumulle A, Brody H, Gill RR, Macherla S, Qilleri A, et al. Association of Extended Dosing Intervals or Delays in Pembrolizumab-based Regimens With Survival Outcomes in Advanced Non-small-cell Lung Cancer. Clin Lung Cancer. 2021;22(3):e379-e89. Epub 20200605. doi: 10.1016/j.cllc.2020.05.028. PubMed PMID: 32653295; PubMed Central PMCID: PMC7273162.
33. Renner A, Burotto M, Rojas C. Immune Checkpoint Inhibitor Dosing: Can We Go Lower Without Compromising Clinical Efficacy? J Glob Oncol. 2019;5:1-5. doi: 10.1200/jgo.19.00142. PubMed PMID: 31348737; PubMed Central PMCID: PMC6690659.
34. Topalian SL, Hodi FS, Brahmer JR, Gettinger SN, Smith DC, McDermott DF, et al. Safety, Activity, and Immune Correlates of Anti–PD-1 Antibody in Cancer. New England Journal of Medicine. 2012;366(26):2443-54. doi: 10.1056/NEJMoa1200690.
35. Centanni M, Moes DJAR, Trocóniz IF, Ciccolini J, van Hasselt JGC. Clinical Pharmacokinetics and Pharmacodynamics of Immune Checkpoint Inhibitors. Clinical Pharmacokinetics. 2019;58(7):835-57. doi: 10.1007/s40262-019-00748-2.
36. Osa A, Uenami T, Koyama S, Fujimoto K, Okuzaki D, Takimoto T, et al. Clinical implications of monitoring nivolumab immunokinetics in non-small cell lung cancer patients. JCI Insight. 2018;3(19). Epub 20181004. doi: 10.1172/jci.insight.59125. PubMed PMID: 30282824; PubMed Central PMCID: PMC6237460.
37. Gravis G, Olive D, Marino P, Penault-Llorca FM, Delord J-P, Lamrani-Ghaouti A, et al. A non-inferiority randomized phase III trial of standard immunotherapy versus reduced dose intensity in responding patients with metastatic cancer: MOIO study. Journal of Clinical Oncology. 2022;40(16_suppl):TPS2674-TPS. doi: 10.1200/JCO.2022.40.16_suppl.TPS2674.
38. Merrick S, Nankivell M, Quartagno M, Clarke CS, Joharatnam-Hogan N, Waddell T, et al. REFINE (REduced Frequency ImmuNE checkpoint inhibition in cancers): A multi-arm phase II basket trial testing reduced intensity immunotherapy across different cancers. Contemp Clin Trials. 2022;124:107030. Epub 20221126. doi: 10.1016/j.cct.2022.107030. PubMed PMID: 36519749.

39. Dy GPEWVEWiTPWN-sCLCCgiNUS, 2022. Accessed November 12, 2022. https://clinicaltrials.gov/ct2/show/NCT04032418.

Characteristic	N = 23
Age in years; median (range)	60.5 (40 - 92)
Male sex – no. (%)	18 (78%)
ECOG performance score – no. (%)	
0	18 (78%)
1	3 (13%)
2	2 (9%)
Disease type – no. (%)	
Cutaneous Melanoma	18 (78%)
Merkel cell carcinoma	5 (22%)
Elevated baseline LDH level – no (%)	6 (26%)
Sites of metastases at therapy initiation – no. (%)*	
CNS metastases	7 (30%)
Visceral metastases	7 (30%)
Lung metastases	3 (13%)
Skin/Lymph node only metastases	6 (26%)
Anti-PD-1 agent – no. (%)	
Nivolumab	9 (39%)
Pembrolizumab	14 (61%)
Immunotherapy regimen – no. (%)	
Monotherapy	16 (70%)
With Ipilimumab (during Induction)	7 (30%)
Line of therapy for anti-PD-1 mAb – no. (%)	
1	14 (61%)
2 or higher	9 (39%)
Best response at transition to RFD – no. (%)	
Complete response	6 (26%)
Partial response	11(48%)
Stable disease	6 (26%)

Table 1. Patient demographics and clinical characteristics. *Patients were classified by their most advanced site of metastatic disease. Patients with CNS metastases included patients with or without skin, soft tissue, lung or visceral sites of disease. Patients with visceral metastases included patients without CNS disease but may include patients with or without skin, soft tissue, and lung disease. Patients with lung metastases included patients with or without skin and soft tissue disease. Abbreviations: ECOG – Eastern Cooperative Oncology Group performance status; CNS – central nervous system; mAb – monoclonal antibody; RFD – reduced frequency dosing

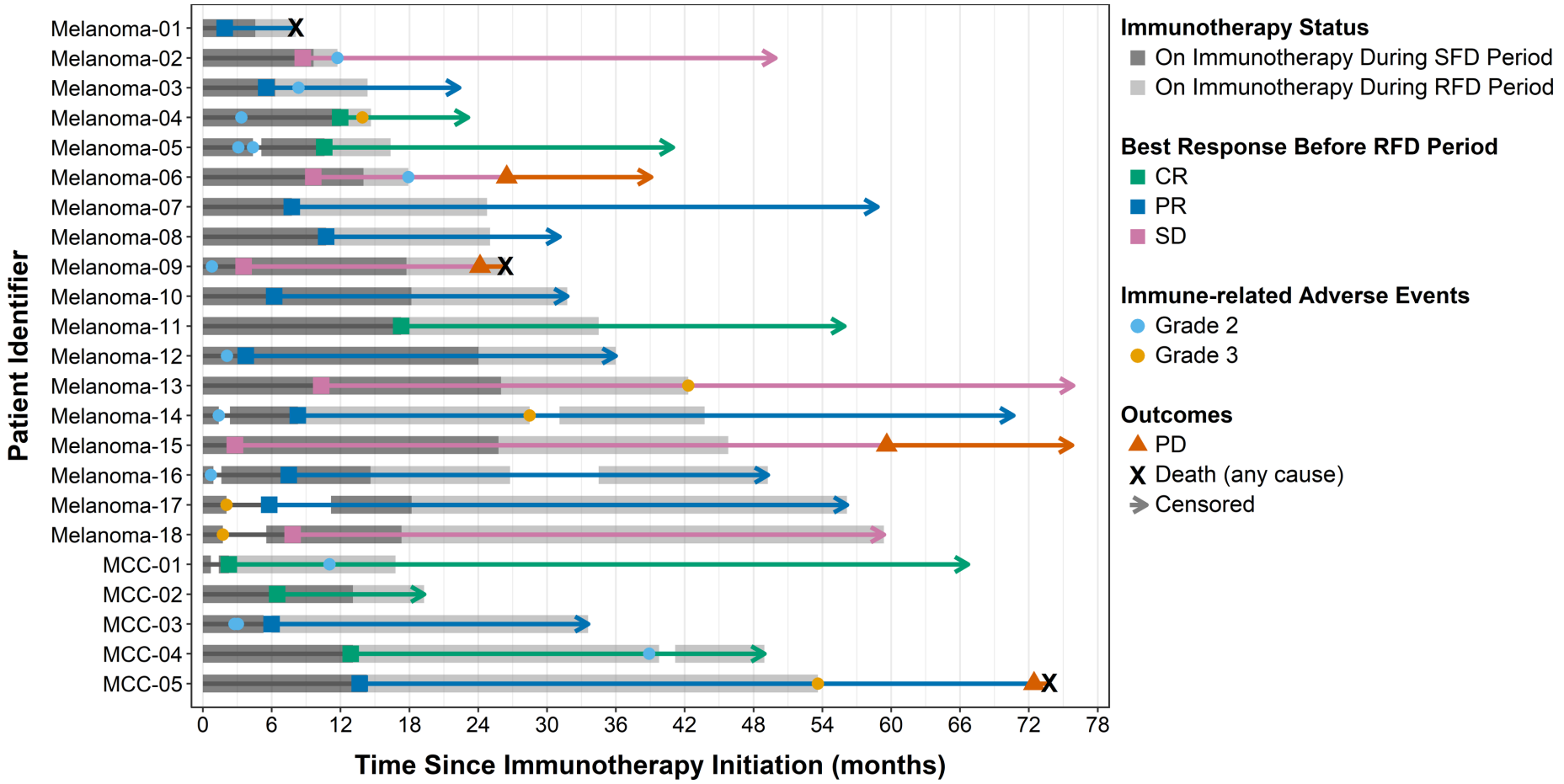

Figure 1. Clinical course of each patient receiving standard-frequency anti-PD-1 therapy followed by reduced-frequency dosing. This swimmer's plot portrays duration of treatment, best overall response, clinically significant immune-related adverse events, and disease progression or death in 23 patients who received standard frequency dosing of anti-PD-1 (SFD) then transitioned to reduced-frequency dosing (RFD). Each patient received SFD (dark gray) until objective response or disease control was achieved, followed by transition to RFD (light gray) guided by timing of disease response. The median duration of therapy at SFD was 13.3 months (range 2.3 - 26.3), and the median duration of RFD was 15.7 months (range 2.1 – 42.7).

Abbreviations: SFD – standard frequency dosing; RFD – reduced frequency dosing; CR – complete response; PR – partial response; SD- stable disease; PD- progressive disease

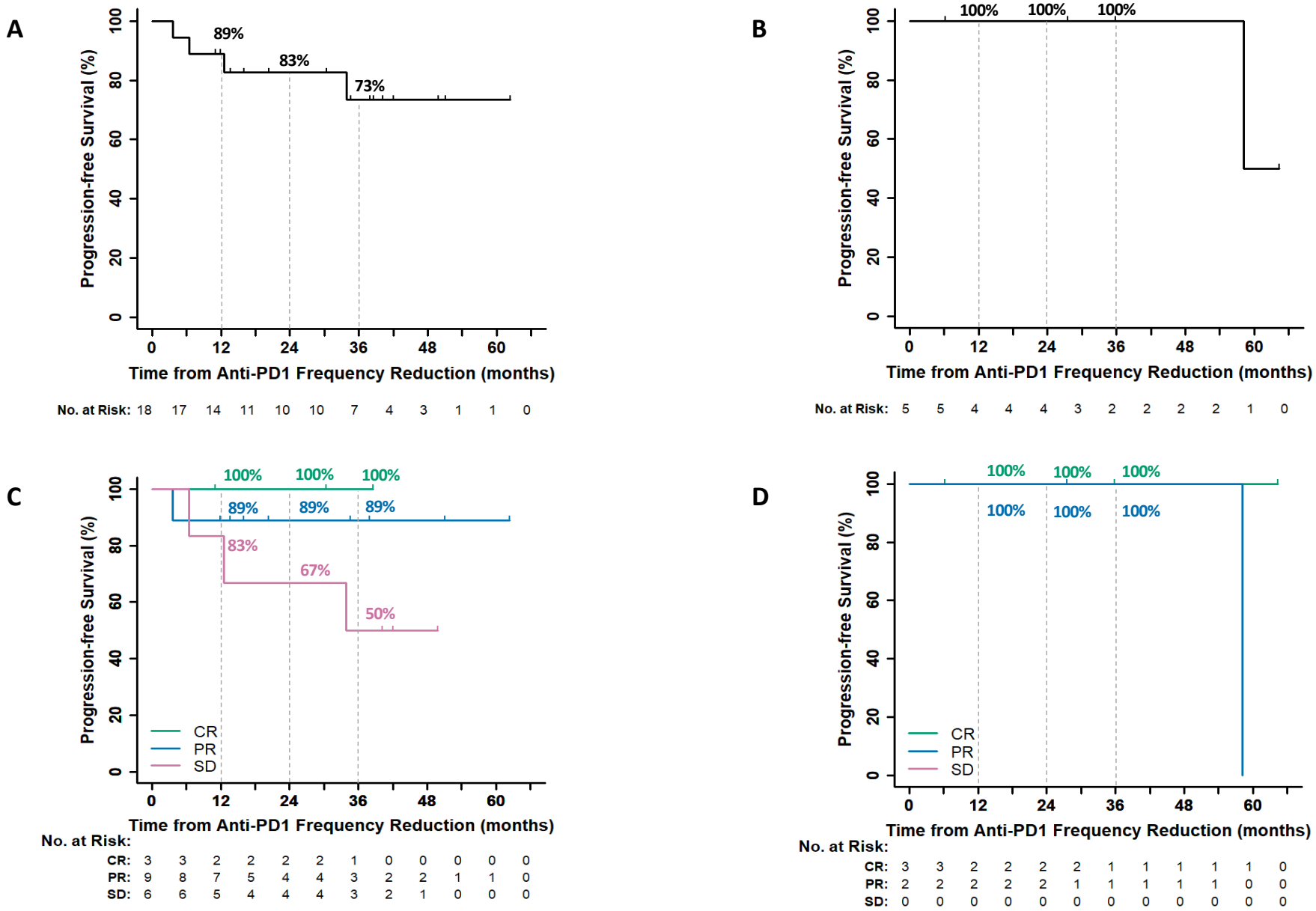

Figure 2. **Kaplan-Meier curve showing progression-free survival (PFS) for patients by disease type and by best overall response**. PFS was measured from initiation of reduced-frequency dosing to disease progression or death, whichever occurred first. Patients without an event were censored (tick mark) at the last disease assessment date. (A) From time of initiating reduced frequency dosing, the estimated 36-month PFS for melanoma patients was 73% (95% CI 53 to 100). Median PFS for melanoma patients was not reached. (B) The estimated 36-month PFS was 100% (95% CI 48 to 100). Median PFS for MCC patients was 58.2 months. (C) By best overall response (BOR) in melanoma, the estimated 36-month PFS rate for CR, PR, and SD were 100% (95% CI 29 to 100), 89% (95% CI 71 to 100) and 50% (95% CI 22 to 100), respectively. (D) By BOR in MCC, the estimated 36-month PFS rate was 100% (95% CI 29 to 100) in patients with CR and 100% (95% CI 16 to 100) in PR.

Abbreviations: PFS – progression-free survival; MCC – Merkel cell carcinoma; CR – complete response; PR – partial response; SD- stable disease; PD- progressive disease; BOR – best overall response

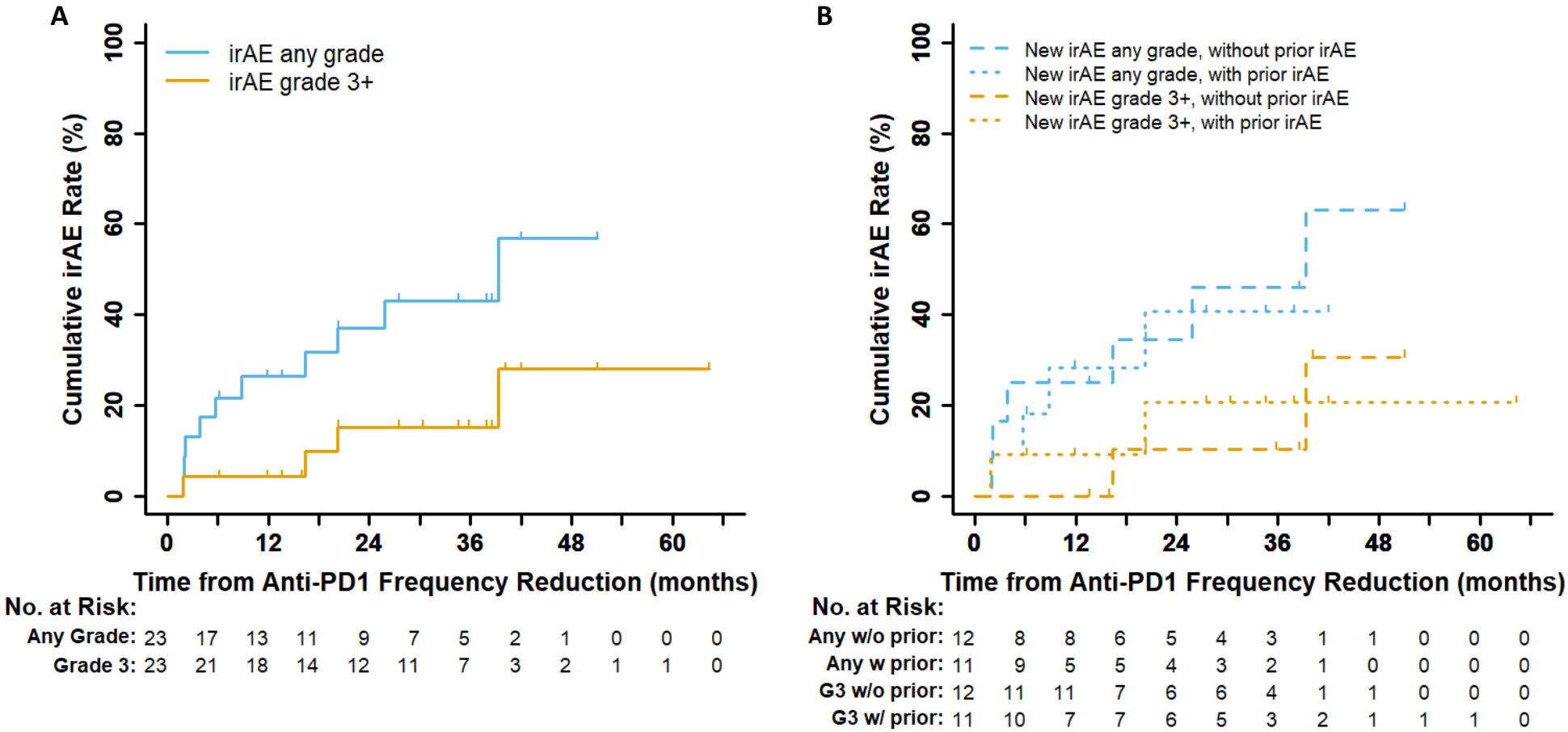

Figure 3. Cumulative rate of delayed immune-related adverse events (irAEs) in all patients on reduced frequency dosing. (A) The cumulative incidence of irAE after initiation of reduced frequency dosing was 57% (N = 10 patients) for all grades and 28% (N = 4 patients) for grade 3 irAEs. Grade 3 events included colitis (2), hepatitis, and dermatitis. (B) Rates of irAEs on reduced-frequency dosing developed at similar rates between patients with a prior irAE during standard-frequency (N = 11) and patients who had never experienced an irAE previously (N = 12). Of the 11 patients who experienced irAE on standard-frequency doses of immunotherapy, only one patient experienced a recurrence of a prior irAE. Thus, the majority of delayed irAEs that patients incurred on RFD were new toxicity events.

Abbreviations: irAE – immune-related adverse event; RFD – reduced frequency dosing

Table 2. Outcomes of patients who developed disease progression during or after reduced-frequency dosing

	Disease type	Time on anti-PD-1 therapy	BOR 1st course	Status of anti-PD-1 therapy at progression	Site(s) of progression	New site of metastatic disease?	Therapy for PD	BOR 2nd course	Time on therapy	Disease status at follow up
1	Cutaneous melanoma	16 months	SD	OFF therapy for 11 months due to ICI-induced hepatitis	Brain	Yes	SRS	SD	--	NED
2	Cutaneous melanoma	46.5 months	SD	OFF therapy for 14 months electively	Lymph nodes	No	nivolumab (standard frequency)	SD	15.5 months	Ongoing partial response
3	Cutaneous melanoma	23.2 months	SD	Receiving nivolumab 240 mg every 2 months	Leptomeninges	No	BRAF/MEK inhibitor therapy	PD	1.9 months	Died
4	Merkel cell carcinoma	50.4 months	PR	OFF therapy for 22 months due to colitis	Lymph nodes, retroperitoneum	No	RT to perinephric mass, pembrolizumab (standard frequency)	PD	2 months	Died

Table 2. Outcomes of patients who developed disease progression during or after reduced-frequency dosing.
Three melanoma patients with stable disease, and one patient with Merkel cell carcinoma with a partial response developed progressive disease. Among the four patients with disease progression, three of the patients had previously discontinued systemic therapy at the time of progression. The time interval between cessation of immunotherapy and progression of disease ranged from 11 – 22 months. Two patients restarted immunotherapy, and one of the two patients experienced a partial response to anti-PD-1 therapy after reinitiating therapy.
Abbreviations: BOR – best overall response; PD – progressive disease; SD – stable disease; SRS – stereotactic radiosurgery; NED – no evidence of disease; RT – radiation therapy

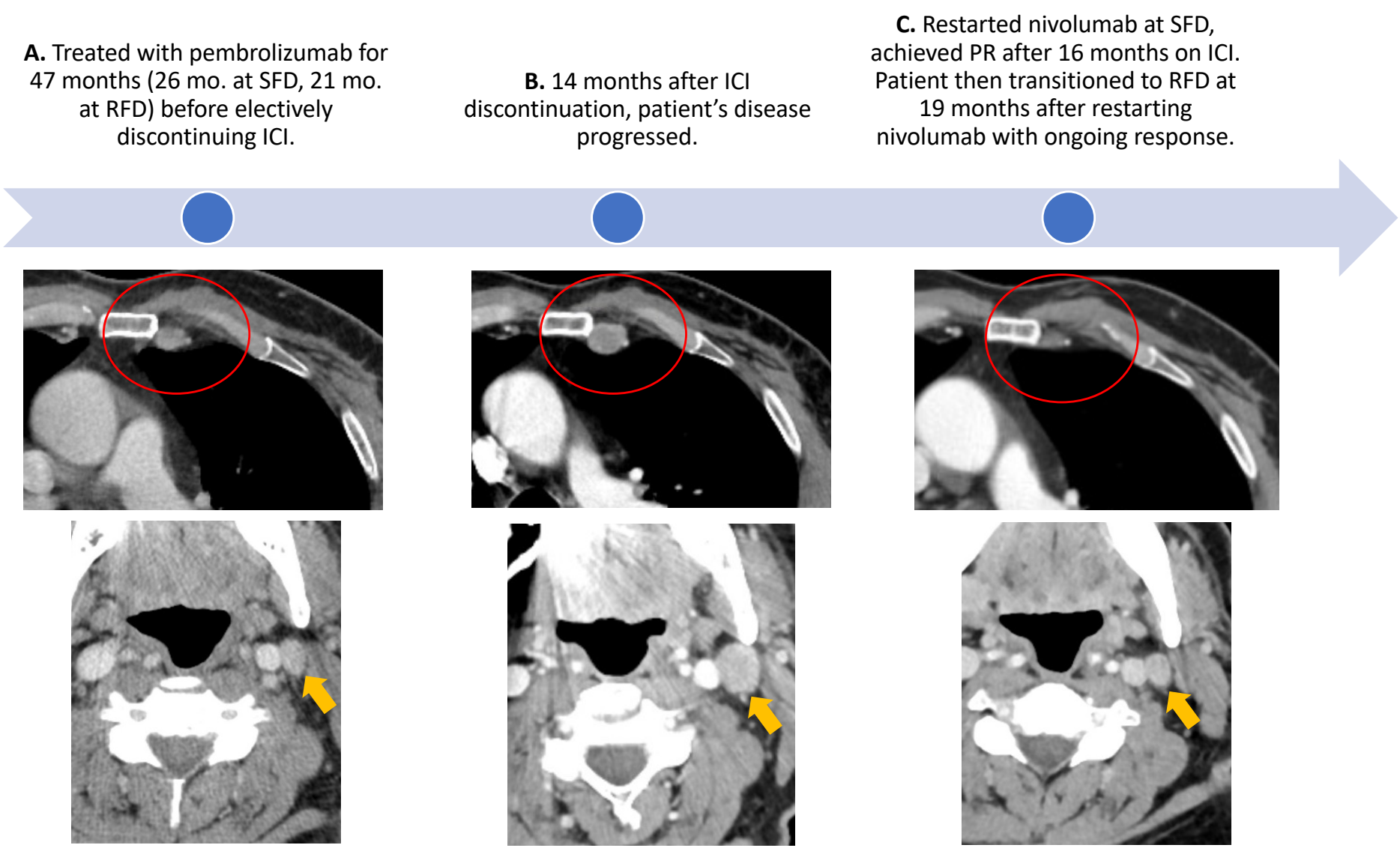

Figure 4. Case study suggesting dependence on continuous PD-1 blockade for disease control (patient Melanoma-15 from Fig 1). 71-year-old male with metastatic melanoma was treated with pembrolizumab for 47 months (26 months at SFD and 21 months at RFD) before he electively discontinued ICI (**panel A**). 14 months after elective discontinuation, his disease progressed (**panel B**), suggesting potential role of prolonged PD-1 blockade in controlling his disease. Reintroduction of nivolumab at SFD has recaptured his disease response (**panel C**), which is ongoing at 24 months after restarting nivolumab. This case suggests the importance of continuous PD-1 blockade in maintaining immune equilibrium in patients with residual disease.

A

	Total savings in 15 patients	Median savings per patient
Drug costs	$1,124,464.63	$71,888.60
Travel costs to patient	$3,317.44	$127.76
Clinic time saved	384 hrs	28 hrs

B

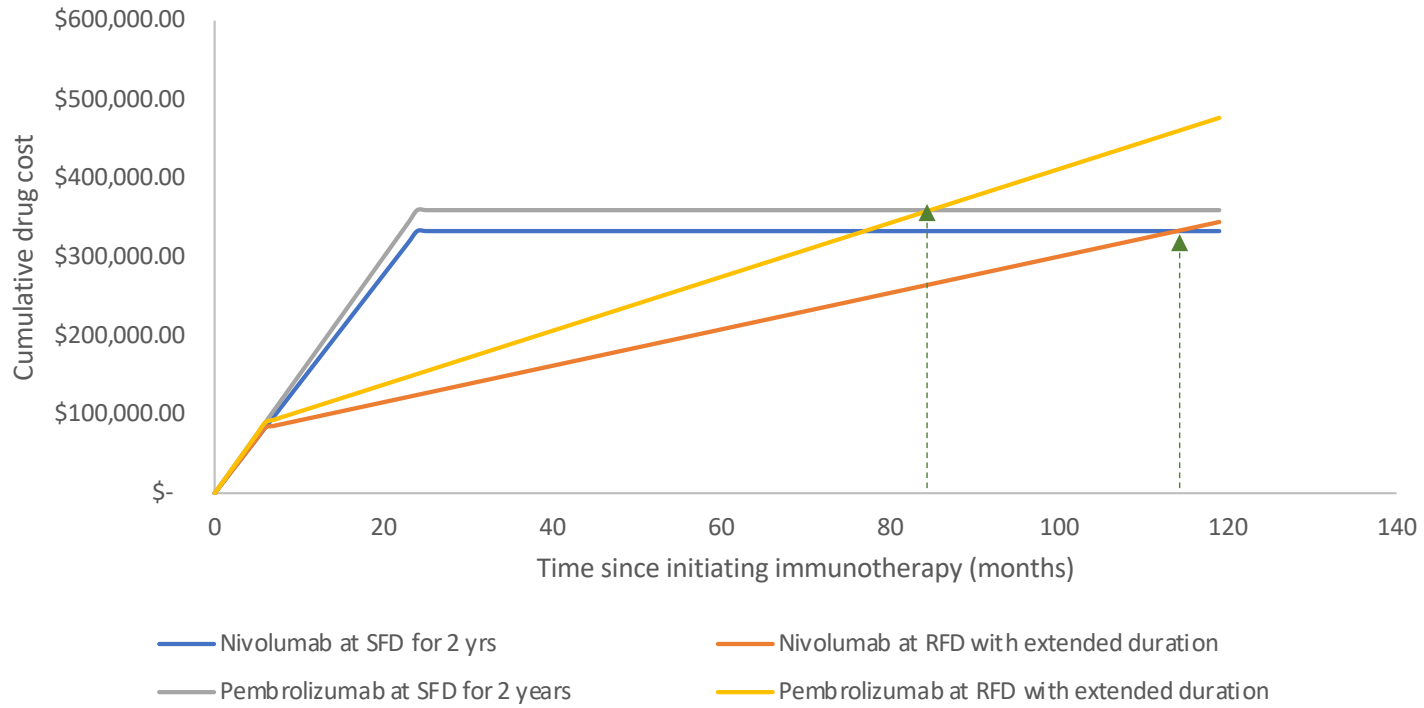

Figure 5. Savings with reduced-frequency dosing. (A) Among the subset of 15 patients with a total duration of therapy > 2 years (median 3.4 yr, range 2.0 – 5.0), we calculated savings from drug costs and patient-centered costs with the reduced-frequency approach (despite extended duration beyond 2 years) compared to the costs of 2 years of therapy at standard-frequency dosing. (B) In a hypothetical model utilizing reduced-frequency dosing after an initial 6 months of standard-frequency dosing, the total duration of treatment was extended to 84 months for pembrolizumab with reduced-frequency approach or 114 months with nivolumab with the reduced-frequency approach without incurring any additional costs.
Abbreviations: SFD – standard frequency dosing; RFD- reduced frequency dosing

Narrow excision margins are appropriate for Merkel cell carcinoma when combined with adjuvant radiation: Analysis of 188 cases of localized disease and proposed management algorithm

Erica S. Tarabadkar, MD,[a,b] Teresa Fu, MD,[a,c] Kristina Lachance, MS,[a] Daniel S. Hippe, MS,[d] Thomas Pulliam, BS,[a] Hannah Thomas, BS,[a] Janet Y. Li, MD,[e] Christopher W. Lewis, MD,[a] Coley Doolittle-Amieva, PA,[a] David R. Byrd, MD,[f] Jeremy T. Kampp, MD,[a] Upendra Parvathaneni, MD,[g] and Paul Nghiem, MD, PhD[a]

Seattle, Washington; Atlanta, Georgia; Palo Alto, California; and Houston, Texas

Background: Merkel cell carcinoma (MCC) management typically includes surgery with or without adjuvant radiation therapy (aRT). Major challenges include determining surgical margin size and whether aRT is indicated.

Objective: To assess the association of aRT, surgical margin size, and MCC local recurrence.

Methods: Analysis of 188 MCC cases presenting without clinical nodal involvement.

Results: aRT-treated patients tended to have higher-risk tumors (larger diameter, positive microscopic margins, immunosuppression) yet had fewer local recurrences (LRs) than patients treated with surgery only (1% vs 15%; $P = .001$). For patients who underwent surgery alone, 7 of 35 (20%) treated with narrow margins (defined as ≤1.0 cm) developed LR, whereas 0 of 13 patients treated with surgical margins greater than 1.0 cm developed LR ($P = .049$). For aRT-treated patients, local control was excellent regardless of surgical margin size; only 1% experienced recurrence in each group (1 of 70 with narrow margins ≤1 cm and 1 of 70 with margins >1 cm; $P = .56$).

Limitations: This was a retrospective study.

Conclusions: Among patients treated with aRT, local control was superb even if significant risk factors were present and margins were narrow. We propose an algorithm for managing primary MCC that integrates risk factors and optimizes local control while minimizing morbidity. (J Am Acad Dermatol 2021;84:340-7.)

Key words: adjuvant radiation; controversy, margin size; excision; local disease; local recurrence; Merkel cell carcinoma; nonmelanoma skin cancer; surgical margins; radiation; radiation therapy.

From the Department of Medicine, Division of Dermatology, University of Washington, Seattle[a]; Department of Dermatology, Emory University School of Medicine, Atlanta[b]; Palo Alto Medical Foundation, Palo Alto[c]; Department of Radiology, University of Washington, Seattle[d]; and Southeast Dermatology, Houston[e]; Department of Surgery, Division of Surgical Oncology, University of Washington, Seattle[f]; Department of Radiation Oncology, University of Washington, Seattle.[g]

Drs Tarabadkar and Fu contributed equally to this article.

Funding sources: Supported by National Institutes of Health (grants P01-CA-225517, K24-CA139052, R01-CA176841, P30-CA015704, T32-CA080416), the David & Rosalind Bloom Endowment for MCC Research, and the MCC Patient Gift Fund.

Disclosure: Dr Nghiem has served as a paid consultant for EMD-Serono, Merck, Pfizer, and 4SC. Drs Tarabadkar and Fu, Author Lachance, Author Hippe, Authors Pulliam and Thomas, Drs Li and Lewis, Author Doolittle-Amieva, and Drs Byrd, Kampp, and Parvanthaneni have no conflicts of interest to declare.

IRB approval status: Reviewed and approved by IRB at the Fred Hutchinson Cancer Research center (approval no.6585).

Accepted for publication July 20, 2020.

Reprint requests: Paul Nghiem, MD, PhD, UW Medical Center at Lake Union, 850 Republican St, Seattle, WA 98109. E-mail: pnghiem@uw.edu.

Published online July 22, 2020.

0190-9622/$36.00

https://doi.org/10.1016/j.jaad.2020.07.079

Merkel cell carcinoma (MCC) is a rare, aggressive cutaneous neuroendocrine malignancy. In 2015, there were approximately 2500 cases/year; this is expected to increase to 3300 by 2025.[1] Approximately 65% of patients with MCC present with localized disease based on national cancer registry data.[2] Published local recurrence (LR) rates are highly variable because historical cohorts are retrospective, heterogenous, and often combine LRs with in transit and regional recurrences. Nevertheless, LRs arise in approximately 4% to 30% of patients.[3-7]

Current guidelines for the treatment of primary cutaneous MCC include wide local excision, sentinel lymph node biopsy (SLNB) for pathologic staging, and consideration of adjuvant radiation therapy (aRT). The National Comprehensive Cancer Network (NCCN) currently recommends wide local excision, "1- 2-cm margins to investing fascia of muscle or pericranium should be performed when clinically feasible and with consideration of possible morbidity" (p MS-17).[8] However, there is no consensus on the appropriate surgical margin size.

Prior studies on the relationship between surgical margin size and LR have yielded seemingly conflicting results. An early study found a trend toward fewer recurrences in patients treated with surgical margins greater than 3.0 cm.[9] However, more recent studies found no difference in LR rates when comparing margins of 1.0 cm or less versus greater than 1.0 cm[3,5] or margins of greater than 2.0 cm versus 2.0 cm or less.[4,5] A relevant limitation of some prior studies is that they do not separately consider surgical margins in the absence and presence of aRT. This is important because numerous studies indicate that aRT markedly decreases the rate of LR.[10-13]

An exception is a study of 179 Canadian patients with MCC by Harrington et al[14] in which patients were separated based on aRT status. They found that patients treated with aRT had a low LR rate regardless of margin size.[14] A separate study of low-risk patients with MCC (primary tumor of <2 cm) who did not receive aRT also found a low (<1%) recurrence rate regardless of margin size.[15]

We sought to determine the relationship between surgical margin size, aRT, and local disease control in a large, single-center cohort of patients who presented with a primary cutaneous MCC tumor.

CAPSULE SUMMARY

- Surgical margin size in Merkel cell carcinoma is controversial; however, we found that if adjuvant radiotherapy is given, patients with narrow or even microscopically positive margins have excellent local disease control.
- If adjuvant radiotherapy therapy is planned, narrower surgical margins are adequate, reduce morbidity, and minimize delay in initiating radiotherapy.

METHODS

We performed a retrospective analysis using a Seattle-based repository of more than 1400 patients with MCC that has been enrolling individuals since 2003. We included patients with MCC with local and SLNB-detected microscopic nodal disease and excluded patients who had advanced disease including muscle/bone invasion, clinically/radiologically evident nodal disease, and metastatic disease. Patients were excluded if surgical margin, radiation therapy, and follow-up data were unavailable. Patients enrolled more than 180 days from diagnosis were excluded to eliminate ascertainment bias associated with late referral to a tertiary center that could diminish how accurately the cohort represents the natural history of the disease.

Clinical characteristics collected included age, sex, stage, site of primary tumor (head/neck vs trunk/extremities), size of primary tumor (≤1 cm, 1-2 cm, or >2 cm), and presence of immunosuppression (HIV, organ transplant, hematologic malignancy, or chronic use of T-cell immunosuppressive medication[16]). Treatment characteristics were obtained through chart review. Patients were separated based on whether they received aRT to the primary tumor bed after undergoing surgery. These groups were further separated by surgical margin size of the primary tumor as noted in operative reports (≤1 cm vs >1 cm) (Fig 1). Patients who underwent Mohs micrographic surgery were excluded.

Recurrences were categorized into 4 groups: local, in transit, regional, and metastatic. *Local* was a recurrence arising within or adjacent to the primary excision scar and within 2 cm of the primary tumor site; *in transit* was a cutaneous/subcutaneous lesion not involving regional lymph nodes and arising more than 2 cm from the primary scar; *regional* was a lesion arising in the draining lymph node basin; and *metastatic* lesions occurred beyond the draining lymph node basin.

Statistical analyses were performed using Stata software, version 14.0 (StataCorp, College Station, TX). Fisher's exact or Wilcoxon rank sum tests were used to compare clinical and tumor characteristics. LR outcomes were measured by the permutation test, with nonlocal MCC recurrences and death as competing risks.

Abbreviations used:

aRT:	adjuvant radiation therapy
LR:	local recurrence
MCC:	Merkel cell carcinoma
NCCN:	National Comprehensive Cancer Network
SLNB:	sentinel lymph node biopsy

A P value of less than .05 was considered to be statistically significant. Competing risk regression curves were used to represent local recurrence-free survival. Patients were grouped based on their aRT status and margin size. Local recurrence-free survival was defined as the length of time from the surgery date to the date of MCC LR, last follow-up, or death. All studies were performed in accordance with Declaration of Helsinki principles and were approved by the Fred Hutchinson Cancer Research Center Institutional Review Board (no. 6585).

RESULTS

Patient and tumor characteristics

A total of 188 patients were identified from the repository, of whom 140 were treated with surgery and aRT and 48 were treated with surgery alone (Fig 1). The majority of patients were male, 65 years or older, and immunocompetent. Of the patients who underwent successful SLNB, 24% had pathologic evidence of tumor invasion into the lymph nodes (Table I). The median follow-up for the entire cohort was 4 years (range, 42 days to 12 years).

The majority of patients had surgical margins of either 1 cm (81 patients) or 2 cm (59 patients), with the remaining 48 patients having other margin sizes. For several known risk factors, patients who received aRT had higher-risk tumors compared to patients who received surgery alone. Specifically, tumor size was larger for aRT-treated patients (29% of tumors ≥2 cm vs 8% for patients treated with surgery alone; $P < .001$). In addition, aRT-treated patients had higher-stage (IIIA) tumors (30% compared to 6.2% in the surgery-only group; $P = .001$). However, they were less likely to have the primary tumor on the head/neck (26% vs 63% in the surgery-only cohort; $P < .001$). Patients who received aRT with surgical margins of 1 cm or less were more likely to have a primary tumor on the head and neck ($P < .003$) and smaller primary tumor size ($P < .020$). For patients who received surgery only to the primary tumor, the only significant difference in patient characteristics between margin groups was that patients with tumors on the head and neck were more likely to receive smaller surgical margins ($P = .049$) (Table I).

Local recurrences

Among the 188 patients, there were 9 LRs (Table II). aRT-treated patients had fewer LRs than patients with surgery only (1 vs 15%, $P = .001$). After adjustment for margin size and aRT status, more LRs occurred on the head/neck versus trunk/extremities ($P = .013$) (Table II). Seven of the 9 patients with LR had salvage therapy with surgery and/or radiation, and in 1 case also immunotherapy.

In the 140 patients treated with surgery and aRT, 2 LRs occurred; for the smaller margin group, there was 1 LR on the head/neck, and for the larger surgical margin group, there was 1 LR on the lower limb. There was no statistically significant difference in local recurrence-free survival between the surgical margin groups ($P = .56$) (Fig 2).

In the 48 patients treated with surgery only, 7 LRs occurred, all of which were on the head/neck. There were 7 recurrences in the smaller margin group and none in the larger margin group. There was a significant difference in local recurrence-free survival between the surgical margin size groups ($P = .049$) (Fig 2).

MCC-specific survival

In addition to the 9 LRs, there were 8 in transit, 15 nodal, and 22 distant recurrences. Thirty-seven patients died during follow-up; 21 of these deaths were caused by MCC. Although LR was the focus of this study, we also looked at MCC-specific survival. We saw no difference in MCC-specific survival between the aRT-treated and the surgery-only groups ($P = .22$). Furthermore, within each of these groups, wide versus narrow margin size was not associated with MCC-specific survival, and results were similar when adjusted for immunosuppression, tumor size, and head/neck primary tumor.

DISCUSSION

Previous studies have shown that wider surgical margins are associated with improved local control of MCC. However, the vast majority of these studies did not report whether or not patients also received aRT, a treatment known to be highly effective in MCC local control. This is relevant because aRT is frequently included in MCC management. Specifically, 54% of MCC patients in the National Cancer Database received aRT.[17] In our Seattle-based repository, among patients who had no evidence of distant metastatic disease, 92% of 826 patients received aRT to the primary site (database accessed February 2019). Whether or not aRT is included in initial management could significantly affect the appropriate surgical margin size in MCC. Indeed, the findings presented here support the

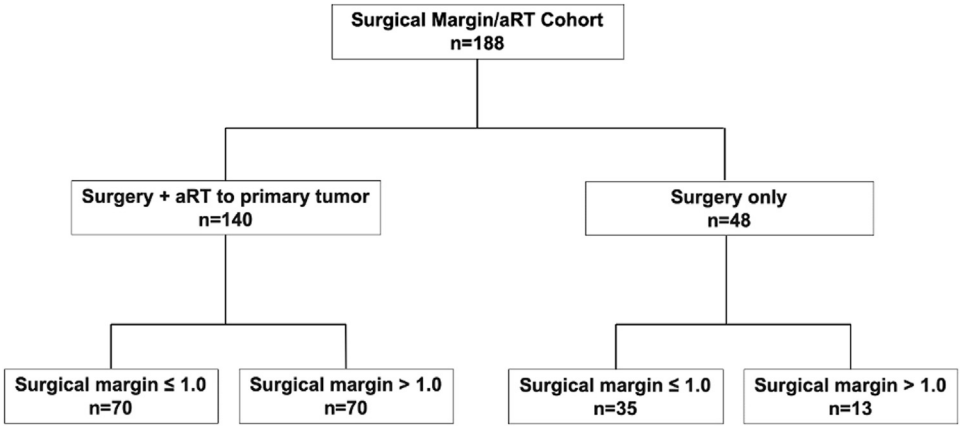

Fig 1. Flowchart of patients with MCC included in this surgical margin/aRT cohort. All 188 patients met the following 5 entry criteria: local-only MCC by clinical examination at diagnosis (stages: pathologic, I; clinical, I; pathologic, IIA; clinical, IIA; pathologic, IIIA), underwent primary lesion excision, aRT status available, surgical margin status available, and enrolled within 180 days from diagnosis. *aRT*, Adjuvant radiation therapy; *MCC*, Merkel cell carcinoma.

Table I. Comparison of clinical and tumor characteristics between all patients and specified subgroups

		Surgery + aRT			Surgery only		
Variables	**All patients**	**Margins ≤ 1 cm**	**Margins > 1 cm**	***P* value***	**Margins ≤ 1 cm**	**Margins > 1 cm**	***P* value***
n	188	70	70		35	13	
Female sex, n (%)	72 (38.3)	26 (37.1)	22 (31.4)	.59	16 (45.7)	8 (61.5)	.52
Age ≥ 65 y, n (%)	121 (64.4)	44 (62.9)	46 (65.7)	.86	24 (68.6)	7 (53.8)	.50
Immunosuppressed, n (%)	18 (9.6)	10 (14.3)	5 (7.1)	.27	3 (8.6)	0 (0.0)	.55
Nodal stage (path stage IIIA), n (%)†	45 (23.9)	17 (24.3)	25 (35.7)	.20	2 (5.7)	1 (7.7)	>.99
Head and neck primary tumor, n (%)‡	66 (35.1)	26 (37.1)	10 (14.3)	.003	25 (71.4)	5 (38.5)	.049
Size of primary tumor, cm, n (%)§				.020			.92
≤1	82 (44.1)	30 (42.9)	18 (26.5)		25 (71.4)	9 (69.2)	>.99
1-2	60 (32.3)	25 (35.7)	25 (36.8)		7 (20.0)	3 (23.1)	
≥2	44 (23.7)	15 (21.4)	25 (36.8)		3 (8.6)	1 (7.7)	
SLNB performed, n (%)	164 (87.2)	63 (90.0)	65 (92.9)	.76	25 (71.4)	11 (84.6)	.47
Unknown	36 (19.1)	13 (18.6)	17 (24.3)		3 (8.6)	3 (23.1)	

aRT, Adjuvant radiation therapy; *SLNB*, sentinel lymph node biopsy.
*Fisher's exact test or the Wilcoxon rank sum test (size of primary tumor).
†Compared to local stage of diagnosis.
‡Compared to primaries on extremities and trunk.
§Two patients did not have a tumor size available.

concept that wider surgical margins are not indicated for patients who will receive aRT.

A recent summary of the current literature on this topic suggested that the appropriate surgical margin size for primary MCC is 1- to 3 cm.[18] However, wide margins often cause significant morbidity[5,19] and can delay the start of aRT if a graft or flap is required for closure.[5] The 2020 NCCN guidelines recommend "wide excision with 1- to 2-cm margins to investing fascia of muscle or pericranium when clinically feasible" (p MS-17) but also note that if aRT is planned, then primary closure should be prioritized over wider margins.[8]

Consistent with the existing literature, in the present cohort, among patients treated with only surgery, margin size did affect the risk of LR: 20% of patients who were treated with a smaller (≤1 cm) surgical margin developed LR compared to 0% of patients with a larger (>1 cm) surgical margin. These findings are concordant with a study of 179 patients with MCC in British Columbia[14] in which surgical margin size mattered only among patients who did not receive aRT. Specifically, in the Canadian study, among patients who had narrow margin excision (<1 cm), only 5% (1/19) had LR if they received aRT, whereas 25% (3/12) who did not receive aRT

Table II. Characteristics of 9 patients who experienced local recurrence of MCC

Patient ID*	aRT	Age and sex	Stage†	Site of primary tumor	Size of primary tumor, cm	Surgical margin, cm	LVI	Narrowest radial margin via pathology, cm
1	No	73 M	C-I	Head and neck	0.7	0.5	Unknown	No residual tumor
2		59 F	P-I	Head and neck	0.5	1.0	Unknown	0.2
3		76 M	P-I	Head and neck	0.5	1.0	Absent	No residual tumor
4		58 M	P-I	Head and neck	0.5	1.0	Absent	No residual tumor
5		84 M	P-I	Head and neck	0.4	1.0	Absent	No residual tumor
6		80 M	P-I	Head and neck	0.8	1.0	Present	0.4
7		70 F	P-I	Head and neck	0.6	1.0	Absent	0.4
8	Yes	71 F	P-IIA	Lower limb	2.4	2.0	Unknown	Unknown
9		67 M	P-I	Head and neck	0.8	1.0	Absent	Unknown

aRT, Adjuvant radiation therapy; *C*, clinical; *ID*, identification; *LVI*, lymphovascular invasion; *MCC*, Merkel cell carcinoma; *P*, pathologic.
*Stage is according to American Joint Committee on Cancer staging system, 8th edition.
†No patients were immunosuppressed.

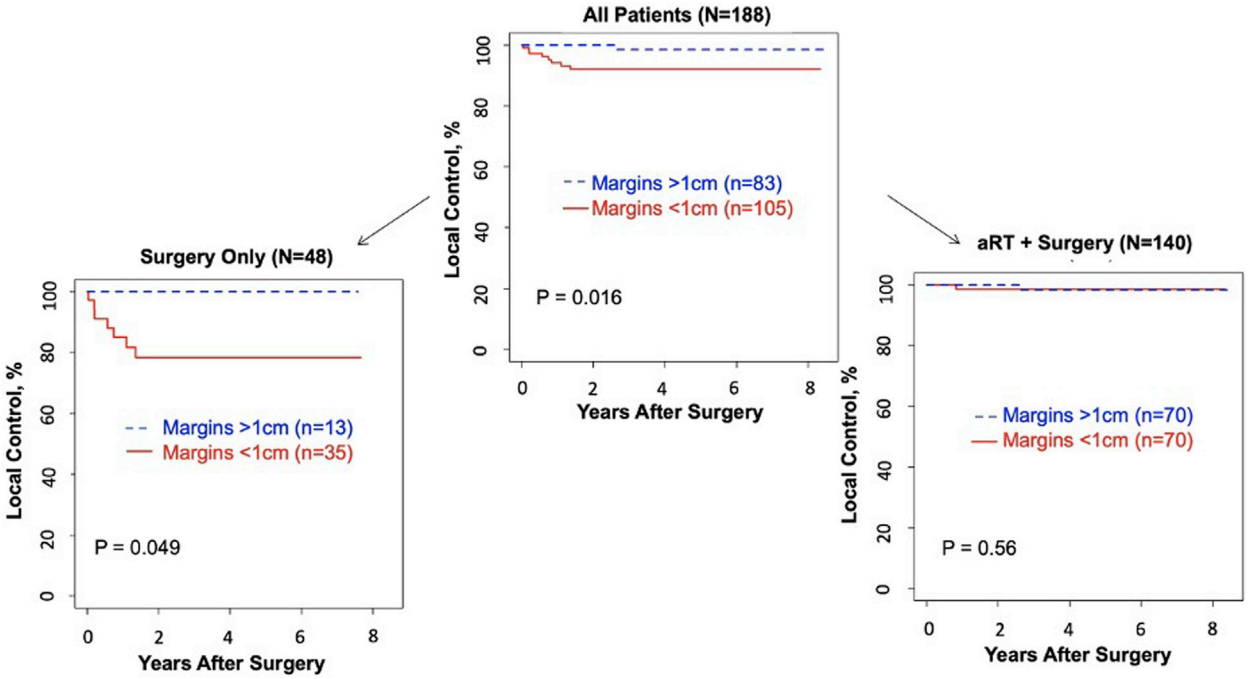

Fig 2. Control of Merkel cell carcinoma at the primary site as a function of surgical margin size and whether or not adjuvant radiation was given. Cumulative incidence curves are shown, with death and any nonlocal Merkel cell carcinoma recurrence being competing risks.

had LR.[14] Also similar to the present study, among patients who had surgical margins of 1.0 cm or greater, there was no improved local control with the addition of aRT.[14] In contrast, most of the existing literature does not separately consider whether or not patients received aRT. Interpretation of appropriate margin size from studies that do not describe aRT status is not feasible because of the high efficacy of aRT in controlling local disease. For example, in one of the larger studies, Allen et al[3] found no difference in LR rate when comparing margins of less than 1 cm versus 1 cm or greater, but the margin analysis was not stratified based on whether or not patients received aRT,[7] making it difficult to interpret the relationship between margin size and local control.

In the present study, head and neck primary tumors were associated with a higher risk of LR compared to those on the trunk and extremities, with 89% (8/9) of LRs occurring on the head or neck. The head/neck is a unique site where tissue-sparing surgery is important to optimize cosmetic and functional outcome but also where radiation adverse effects could be morbid, especially in elderly

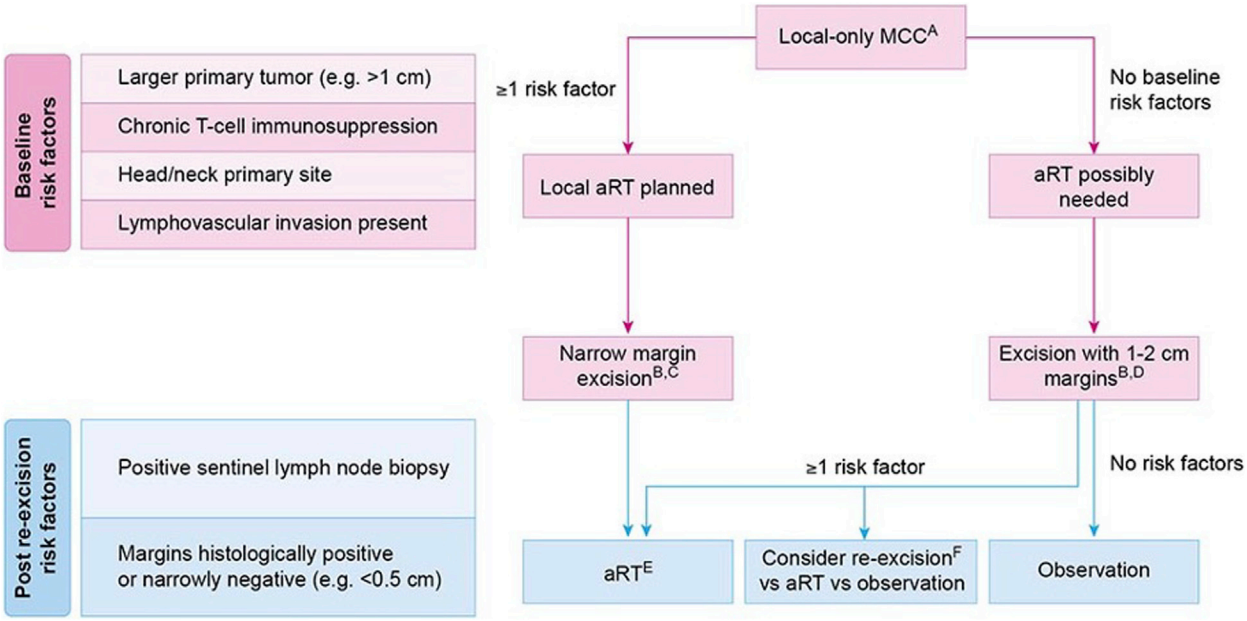

Fig 3. Suggested local MCC treatment management. This flowchart integrates treatment options with risk factors that are associated with local recurrence. Certain risk factors are available at the time of diagnosis (baseline), whereas others are available only after surgical excision (post re-excision). [A]Criteria for local-only MCC were as follows: clinically node negative, no in transit disease, and imaging negative for distant disease. [B]Sentinel lymph node biopsy was typically performed at this time. [C]Narrow excision margins minimize morbidity, and if aRT is performed microscopically positive margins are acceptable. [D]The goal should be primary tissue closure (ie, without a flap or graft) allowing aRT initiation within 3 to 4 weeks.[5,19,20] [E]If the sentinel lymph node biopsy result is positive, nodal aRT would typically be given in addition to primary site aRT. [F]The decision on re-excision is based on clinical setting (narrow path margins, eg, <0.5 cm) and patient preference: re-excision versus aRT versus observation. *aRT*, Adjuvant radiation therapy; *MCC*, Merkel cell carcinoma.

patients. In a retrospective study of 46 low-risk (primary tumor ≤ 2 cm, immunocompetent, negative SLNB results, negative pathologic margin results) head and neck tumors from the Seattle repository, the addition of aRT to the primary site significantly reduced LRs compared to surgery only.[13] Furthermore, in a separate study of 106 patients with head/neck MCC, when aRT was included, local control was more than 96%.[21] In a Tampa-based, single-institution study of 113 patients with head/neck MCC, aRT was associated with improved local control (3-year local control of 89% vs 68% with surgery only; $P = .005$).[22] In summary, multiple studies suggest that head and neck MCC tumors are at higher risk of recurrence after surgical monotherapy (perhaps because of limitations of margin size for this site) and that aRT should be considered for these tumors.

Given the important cosmetic and functional considerations for head and neck MCC management, Mohs micrographic surgery is often considered. Currently, NCCN guidelines do not routinely recommend Mohs surgery for MCC, in part because SLNB is often indicated,[8,23,24] requiring separate hospital-based surgical procedures in addition to Mohs surgery. The findings from the present study suggest that in the absence of aRT, the unique ability of Mohs surgery to attain narrow, pathologically negative surgical margins may not be as beneficial for MCC as for other skin cancers, because MCC often recurs beyond pathologically negative margins (multiple patients had LR after pathologically negative excision) (Table II).

Based on the results presented here and in the existing literature, we have created a treatment algorithm (Fig 3) to aid clinicians in determining the appropriate management for primary MCC tumors. Using clinical factors such as primary tumor size, primary site, and immunosuppression status, this algorithm first separates patients into a higher-risk group for which aRT is indicated. Such patients can then avoid the morbidity of wide surgical margins and potential delays in initiating aRT. For lower-risk patients who may not need aRT, clinicians

may consider a wider margin with primary closure at the time of SLNB. Depending on the pathology results of excision and SNLB, aRT may not be indicated.

Although aRT decreased LR among patients with narrower surgical margins (<1 cm), there was no difference in disease-specific survival. The findings presented here and from the literature[14] show that for low-risk MCCs, surgical margins of greater than 1 cm are sufficient and that aRT is not required for excellent local disease control. In contrast, if narrow surgical margins are required to reduce morbidity and obtain primary closure, there is agreement that aRT can provide excellent local control. In terms of whether survival can be affected by aRT, the present study did not observe this association. However, 3 cancer registry studies that were far larger than our study showed that aRT was associated with significantly better overall survival.[12,17,25] It is possible that with a larger sample size, we might have detected survival differences based on whether or not aRT was given. Although links to survival are controversial, current evidence suggests that optimal local control (sometimes involving aRT) can minimize LRs. This is beneficial because LR leads to patient anxiety, increased medical costs, and salvage therapies that can increase morbidity.

Limitations of this study are its retrospective design and unavailable clinical data for some cases (50/188 patients lacked pathologic margin size, and 2/188 lacked primary tumor size). Because the sample size for the surgery-only group was 48, further subgrouping of surgical margin size was not statistically feasible. Also, because our site is a tertiary referral center for MCC, patients in this cohort often received their treatment closer to their homes. This cohort represents a heterogeneous group with regard to surgery and radiation therapy techniques.

This study lends support to earlier literature that suggests if localized cutaneous MCC is also treated with aRT, then narrow surgical margins are sufficient. Although this study indicates that aRT plays an important role in the management of higher-risk MCC tumors, it is possible that emerging approaches in aRT (eg, a single fraction of 8-Gy radiation[26]) may provide good local control with markedly diminished morbidity and enhanced patient convenience. As summarized in the flowchart (Fig 3), we believe that surgical margins for patients with MCC should be determined with careful consideration of risk factors and the potential role of aRT in optimizing a patient's outcome.

REFERENCES

1. Paulson KG, Park SY, Vandeven NA, et al. Merkel cell carcinoma: current US incidence and projected increases based on changing demographics. *J Am Acad Dermatol*. 2018;78:457-463.
2. Harms KL, Healy MA, Nghiem P, et al. Analysis of prognostic factors from 9387 Merkel cell carcinoma cases forms the basis for the new 8th edition AJCC staging system. *Ann Surg Oncol*. 2016;23:3564-3571.
3. Allen PJ, Bowne WB, Jaques DP, Brennan MF, Busam K, Coit DG. Merkel cell carcinoma: prognosis and treatment of patients from a single institution. *J Clin Oncol*. 2005;23:2300-2309.
4. Gillenwater AM, Hessel AC, Morrison WH, et al. Merkel cell carcinoma of the head and neck: effect of surgical excision and radiation on recurrence and survival. *Arch Otolaryngol Head Neck Surg*. 2001;127:149-154.
5. Perez MC, de Pinho FR, Holstein A, et al. Resection margins in Merkel cell carcinoma: is a 1-cm margin wide enough? *Ann Surg Oncol*. 2018;25:3334-3340.
6. Medina-Franco H, Urist MM, Fiveash J, Heslin MJ, Bland KI, Beenken SW. Multimodality treatment of Merkel cell carcinoma: case series and literature review of 1024 cases. *Ann Surg Oncol*. 2001;8:204-208.
7. Fields RC, Busam KJ, Chou JF, et al. Five hundred patients with Merkel cell carcinoma evaluated at a single institution. *Ann Surg*. 2011;254:465-473.
8. Merkel Cell Carcinoma (Version 1.2020). National Comprehensive Cancer Network. Accessed January 1, 2020. https://www.nccn.org/professionals/physician_gls/pdf/mcc.pdf
9. Yiengpruksawan A, Coit DG, Thaler HT, Urmacher C, Knapper WK. Merkel cell carcinoma. Prognosis and management. *Arch Surg*. 1991;126:1514-1519.
10. Lewis KG, Weinstock MA, Weaver AL, Otley CC. Adjuvant local irradiation for Merkel cell carcinoma. *Arch Dermatol*. 2006;142:693-700.
11. Jouary T, Leyral C, Dreno B, et al. Adjuvant prophylactic regional radiotherapy versus observation in stage I Merkel cell carcinoma: a multicentric prospective randomized study. *Ann Oncol*. 2012;23:1074-1080.
12. Mojica P, Smith D, Ellenhorn JD. Adjuvant radiation therapy is associated with improved survival in Merkel cell carcinoma of the skin. *J Clin Oncol*. 2007;25:1043-1047.
13. Takagishi SR, Marx TE, Lewis C, et al. Postoperative radiation therapy is associated with a reduced risk of local recurrence among low risk Merkel cell carcinomas of the head and neck. *Adv Radiat Oncol*. 2016;1:244-251.
14. Harrington C, Kwan W. Radiotherapy and conservative surgery in the locoregional management of Merkel cell carcinoma: the British Columbia Cancer Agency experience. *Ann Surg Oncol*. 2016;23:573-578.
15. Frohm ML, Griffith KA, Harms KL, et al. Recurrence and survival in patients with Merkel cell carcinoma undergoing surgery without adjuvant radiation therapy to the primary site. *JAMA Dermatol*. 2016;152:1001-1007.
16. Cook M, Baker K, Redman M, et al. Differential outcomes among immunosuppressed patients with Merkel cell carcinoma: impact of immunosuppression type on cancer-specific and overall survival. *Am J Clin Oncol*. 2019;42:82-88.
17. Bhatia S, Storer BE, Iyer JG, et al. Adjuvant radiation therapy and chemotherapy in Merkel cell carcinoma: survival analyses of 6908 cases from the National Cancer Data Base. *J Natl Cancer Inst*. 2016;108(9):djw042.

18. Tello TL, Coggshall K, Yom SS, Yu SS. Merkel cell carcinoma: an update and review: current and future therapy. *J Am Acad Dermatol*. 2018;78:445-454.
19. Garbutcheon-Singh KB, Veness MJ. The role of radiotherapy in the management of non-melanoma skin cancer. *Australas J Dermatol*. 2019;60:265-272.
20. Limawararut V, Leibovitch I, Sullivan T, Selva D. Periocular squamous cell carcinoma. *Clin Exp Ophthalmol*. 2007;35:174-185.
21. Bishop AJ, Garden AS, Gunn GB, et al. Merkel cell carcinoma of the head and neck: favorable outcomes with radiotherapy. *Head Neck*. 2016;38(Suppl 1):E452-E458.
22. Strom T, Naghavi AO, Messina JL, et al. Improved local and regional control with radiotherapy for Merkel cell carcinoma of the head and neck. *Head Neck*. 2017;39:48-55.
23. Fields RC, Busam KJ, Chou JF, et al. Recurrence and survival in patients undergoing sentinel lymph node biopsy for merkel cell carcinoma: analysis of 153 patients from a single institution. *Ann Surg Oncol*. 2011;18:2529-2537.
24. Lemos BD, Storer BE, Iyer JG, et al. Pathologic nodal evaluation improves prognostic accuracy in Merkel cell carcinoma: analysis of 5823 cases as the basis of the first consensus staging system. *J Am Acad Dermatol*. 2010;63:751-761.
25. Yan L, Sun L, Guan Z, Wei S, Wang Y, Li P. Analysis of cutaneous Merkel cell carcinoma outcomes after different surgical interventions. *J Am Acad Dermatol*. 2020;82:1422-1434.
26. Cook MM, Schaub SK, Goff PH, et al. Postoperative, Single-Fraction Radiation Therapy in Merkel cell Carcinoma of the head and Neck. *Adv Radiat Oncol*. 2020;5(6):1248-1254.

Chapter 13. Conclusions

Summary of research findings

As outlined in the introduction, the studies in this dissertation focus on immunotherapy response and resistance and why only half of patients with Merkel cell carcinoma (MCC) respond to PD-1 pathway blockade. **Chapters 1 and 2** provides an introduction to MCC and reviews the use of immunotherapy in this cancer.

Original research is presented in **Chapter 3** which attempts to identify PD-1 pathway resistance mechanisms following initial treatment. We use samples from 3 cohorts of patients including a clinical trial of neoadjuvant anti-PD-1 therapy to study cancer-specific CD8 T cells over the course of immunotherapy. Frequency of cancer-specific T cells in tumor and blood, before and after therapy were quantified and cancer-specific T cells in blood were further phenotyped. We found that the frequency of MCPyV-specific CD8 T cells in the blood was most correlated with response. Further comparison of MCPyV-specific T cells in tumor versus blood show that the blood resident cells exhibit characteristics of earlier stage exhaustion compared to the tumor resident cells. These results suggest that the blood acts as a reservoir of cancer-specific T cells at an early stage of exhaustion that can expand following PD-1 pathway blockade (Figure 1).

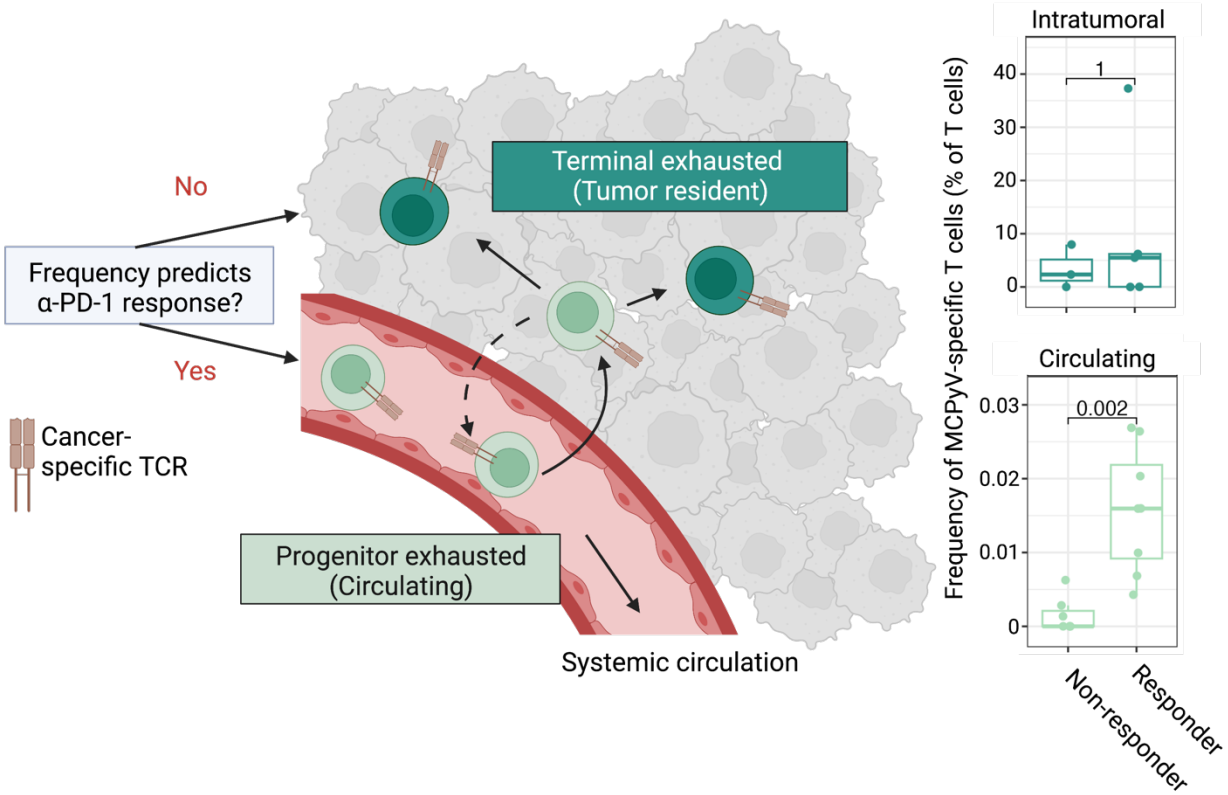

Figure 1. Overview of major findings from Chapter 3. Frequency of MCPyV-specific CD8 T cells in the blood, but not in tumors, is correlated to initial response to PD-1 blockade in MCC patients. These circulating cancer-specific cells are less exhausted than their intratumoral counterparts and could represent a population of early exhausted cells that have been shown to expand and mediate tumor regression following PD-1 pathway blockade. Data from neoadjuvant anti-PD-1 trial presented in Chapter 3. p values calculated using Wilcox test.

While the frequency of MCPyV-specific CD8 T cells in tumors predicts initial immunotherapy response, we found that patients with secondary/acquired resistance to anti-PD-(L)1 therapy often had these cells in their blood at the time of resistance. In two patients studied we found that MCC cells lacked MHC-I in this setting suggesting that may be an immune escape

mechanism when functional cancer-specific T cells are present. One of these patients was subsequently given an intralesional STING agonist as treatment for their recurrent disease (**Chapter 4**). This led to durable tumor regression in injected and non-injected lesions. Analysis of tumor cells before and after treatment show that MHC-I is upregulated on tumor cells following STING agonism suggesting this could be a beneficial therapy in patients whose MCC tumors down regulate MHC-I (Figure 2).

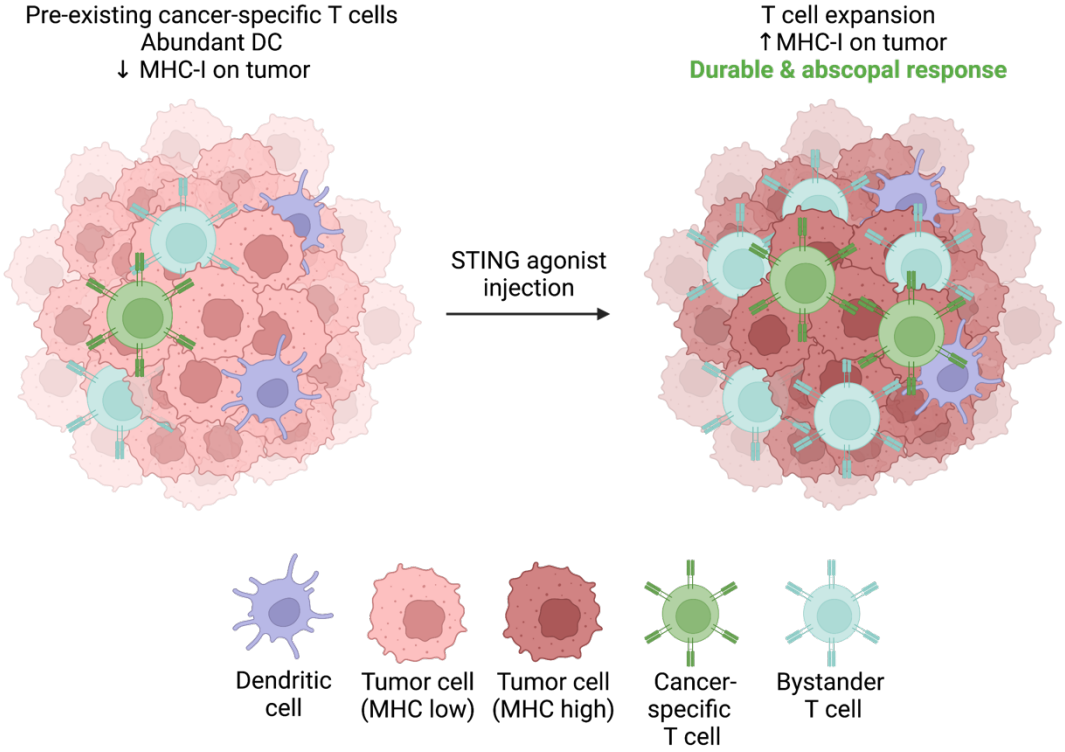

Figure 2 Mechanism of response to intralesional STING agonism. A patient with PD-L1 refractory disease had pre-existing cancer-specific T cells in their tumor but absent MHC-I expression on tumor cells. Intralesional injection of STING agonist led to durable and resolution of injected and non-injected lesions. Analyses of tumor tissues shows expansion of cancer-specific and bystander T cells and upregulation of MHC-I on tumor cells.

Chapters 5-7 further detail cancer-specific T cell responses as well as a new technique to study T cells inside tumors. In **Chapter 5**, we detail a case of a patient with a profound response to anti-PD-L1 therapy. This patient had virus-negative MCC, so we studied the neoantigen-specific T cells in this patient. Surprisingly, we only found neoantigen-specific CD4 T cells despite optimizing assays for CD8 T cells. These CD4 T cells exhibited characteristics of a T_H1 phenotype suggesting they may be supporting an anti-tumor immune response. In **Chapter 6**, we study the role of IL2 in promoting T cell exhaustion. Whereas IL2 is normally thought to support T cells and be important for T cell survival and proliferation, we show that IL2 signaling can lead to late-stage exhaustion via signaling through the high affinity IL2 receptor (CD25). Finally in **Chapter 7**, we describe a new analytic technique to study the tumor microenvironment at higher resolution. Novel techniques that link RNAseq with spatial location have been developed. However, these techniques currently measure “spots” that are 55 μm in diameter meaning that each spot is covered by up to 10 cells. We created a new technique called “BayesSpace” That can deconvolute these spots to single cell or near single cell resolution. Together, these studies provide further insights into the roles of T cells in human cancer.

<u>Future directions</u>

The data presented here contribute to the fields of MCC and cancer research in three major areas: 1) They provide a rationale and preliminary data for upcoming clinical trials, 2) They form the basis for development of a bioinformatic tool (TCR predictor) that predict immunotherapy responses by identifying MCPyV-specific T cells in the blood via deep sequencing 3) They support other studies of cancer-specific CD4, CD8 and B cells.

Future directions: Trials

Three major trials in MCC are detailed in **Chapters 8, 9 and 10**. The first trial will use combination checkpoint blockade to treat anti-PD-(L)1 refractory MCC patients. Antibodies against PD-1, TIM3 and LAG3 will be used in attempt to restore function to cancer-specific T cells at late stages of exhaustion. Data in **Chapters 3 and 8** show that immunotherapy refractory patients often have cancer-specific T cells in their tumors, but these cells are too exhausted to be rescued by PD-1 therapy alone. However, they do express high levels of immune checkpoints LAG3 and TIM3 suggesting that combination therapy could potentiate anti-cancer responses in these cells.

As a major finding in **Chapter 3** is that cancer-specific T cells in the blood are important for mediating immunotherapy responses, the remaining two trials each will attempt to replenish or support these circulating cells. One trial is supporting cancer-specific CD8 T cells by through therapeutic vaccination. One such trial began enrolling patients in 2022 (NCT05422781, described in **Chapter 9**). This phase 1 trial uses a DNA plasmid encoding the MCPyV large T antigen that will be (needlelessly) injected into MCC patients without active disease. MCPyV-specific B and T cell responses will then be measured to see if this treatment restores the number or function of cancer-specific T cells. Because the antigen is encoded on a plasmid, this vaccine is self adjuvanting as the DNA will activate several innate immune pathways including STING. The plasmid also encodes LAMP1 to improve antigen presentation to CD4 T cells. An additional MCPyV therapeutic vaccine candidate based on self-amplifying RNA is also in development.

An additional trial that aims to boost adaptive immunity is also entering clinical trials soon (2023). This trial will inhibit ataxia telangiectasia and Rad3-related (ATR) an important kinase in the DNA damage response that can induce cell cycle arrest following DNA damage. Mouse models have shown that these therapies can improve anti-cancer immunity and are in fact dependent on CD8 T cells[22,23]. Preliminary data from our lab suggests that ATR inhibition could induce immunogenic cell death and lead to more anti-cancer immune cells by acting as an *in situ* vaccine.

Future directions: TCR predictor

Another direct implication from Chapter 3 is that measuring the frequency of MCPyV-specific could predict immunotherapy response. This prediction could be incredibly valuable to clinicians and patients as it would allow us to prioritize patients who would not respond to PD-(L)1 blockade to other therapies or clinical trials. However, the complex nature of MHC multimers make performing this assay in a clinical setting infeasible. To circumvent this, a collaborative team led by Saumya Jani is working on building a sequencing-based method that could identify MCPyV-specific T cell receptors from bulk TCR sequencing. This approach is readily scalable and would build on similar tests currently available for CMV and COVID.

Future directions: Studies of cancer-specific immune cells

The studies of antigen-specific T cells described in **Chapters 3-7** have also established techniques and raised questions that are being addressed in ongoing projects. Because virally driven MCC shares two small antigens across patients, it is an ideal model to study cancer-specific adaptive immune responses and several of the techniques I helped to create pipelines for in our lab are being used by other lab members to study these cells. Specifically, the use of DNA barcoded multimers cellular indexing of transcriptomes and epitopes studies of antigen specific CD4, CD8 and B cells are all currently in progress. Of particular note are the studies of Heeju Ryu in the Newell Lab. Dr. Ryu's has also studied MCPyV-specific CD8 T cells in immunotherapy patients. She has also seen a correlation between frequency of MCPyV-specific CD8 T cells and response to PD-1 blocakde using a different cohort of patients and different technique (CyTOF).

In conclusion, we conducted detailed studies on cancer-specific T cells in MCC patients treated with immunotherapy. Our studies identified a new marker of immunotherapy response: the presence of cancer-specific CD8 T cells in the blood. These cells are highly predictive of immunotherapy response in the first-line treatment. However, we also observed that tumors of patients who initially responded to immunotherapy may downregulate MHC-I in the secondary resistance setting. We observed that intralesional STING agonism can reverse this MHC-I downregulation and produce durable responses in patients who are resistant to PD-(L)1. These findings provide important information for upcoming clinical trials, and we hope they can be translated into a clinical assay through high-throughput sequencing of T cells.

14. References

1. Becker, J.C*., et al.* Merkel cell carcinoma. *Nat Rev Dis Primers* **3**, 17077 (2017).
2. Becker, J.C*., et al.* Epidemiology, biology and therapy of Merkel cell carcinoma: conclusions from the EU project IMMOMEC. *Cancer Immunol Immunother* **67**, 341-351 (2018).
3. Bhatia, S*., et al.* Adjuvant Radiation Therapy and Chemotherapy in Merkel Cell Carcinoma: Survival Analyses of 6908 Cases From the National Cancer Data Base. *J Natl Cancer Inst* **108**(2016).
4. Paulson, K.G*., et al.* Merkel cell carcinoma: Current US incidence and projected increases based on changing demographics. *J Am Acad Dermatol* **78**, 457-463 e452 (2018).
5. Feng, H., Shuda, M., Chang, Y. & Moore, P.S. Clonal integration of a polyomavirus in human Merkel cell carcinoma. *Science* **319**, 1096-1100 (2008).
6. Nghiem, P.T*., et al.* PD-1 Blockade with Pembrolizumab in Advanced Merkel-Cell Carcinoma. *N Engl J Med* **374**, 2542-2552 (2016).
7. Kaufman, H.L*., et al.* Avelumab in patients with chemotherapy-refractory metastatic Merkel cell carcinoma: a multicentre, single-group, open-label, phase 2 trial. *Lancet Oncol* **17**, 1374-1385 (2016).
8. Pauken, K.E. & Wherry, E.J. Overcoming T cell exhaustion in infection and cancer. *Trends Immunol* **36**, 265-276 (2015).
9. Bengsch, B. & Wherry, E.J. The importance of cooperation: partnerless NFAT induces T cell exhaustion. *Immunity* **42**, 203-205 (2015).
10. Sen, D.R*., et al.* The epigenetic landscape of T cell exhaustion. *Science* **354**, 1165-1169 (2016).
11. McLane, L.M., Abdel-Hakeem, M.S. & Wherry, E.J. CD8 T Cell Exhaustion During Chronic Viral Infection and Cancer. *Annu Rev Immunol* **37**, 457-495 (2019).
12. Spranger, S., Bao, R. & Gajewski, T.F. Melanoma-intrinsic beta-catenin signalling prevents anti-tumour immunity. *Nature* **523**, 231-235 (2015).
13. Neubert, N.J*., et al.* T cell-induced CSF1 promotes melanoma resistance to PD1 blockade. *Sci Transl Med* **10**(2018).
14. Sade-Feldman, M*., et al.* Defining T Cell States Associated with Response to Checkpoint Immunotherapy in Melanoma. *Cell* **175**, 998-1013 e1020 (2018).
15. Yarchoan, M., Hopkins, A. & Jaffee, E.M. Tumor Mutational Burden and Response Rate to PD-1 Inhibition. *N Engl J Med* **377**, 2500-2501 (2017).
16. Zaretsky, J.M*., et al.* Mutations Associated with Acquired Resistance to PD-1 Blockade in Melanoma. *N Engl J Med* **375**, 819-829 (2016).
17. Wendzicki, J.A., Moore, P.S. & Chang, Y. Large T and small T antigens of Merkel cell polyomavirus. *Curr Opin Virol* **11**, 38-43 (2015).
18. Church, C.D. & Nghiem, P. How does the Merkel polyomavirus lead to a lethal cancer? Many answers, many questions, and a new mouse model. *J Invest Dermatol* **135**, 1221-1224 (2015).
19. He, R*., et al.* Follicular CXCR5- expressing CD8(+) T cells curtail chronic viral infection. *Nature* **537**, 412-428 (2016).

20. Im, S.J.*, et al.* Defining CD8+ T cells that provide the proliferative burst after PD-1 therapy. *Nature* **537**, 417-421 (2016).
21. Utzschneider, D.T.*, et al.* T Cell Factor 1-Expressing Memory-like CD8(+) T Cells Sustain the Immune Response to Chronic Viral Infections. *Immunity* **45**, 415-427 (2016).
22. Dillon, M.T.*, et al.* ATR Inhibition Potentiates the Radiation-induced Inflammatory Tumor Microenvironment. *Clin Cancer Res* **25**, 3392-3403 (2019).
23. Vendetti, F.P.*, et al.* ATR kinase inhibitor AZD6738 potentiates CD8+ T cell-dependent antitumor activity following radiation. *J Clin Invest* **128**, 3926-3940 (2018).

15. Appendix

Table of manuscripts resulting from work in Nghiem Lab

Title	Status	First author	Senior author	Journal (or target)
Cancer-specific CD8 T cell frequency at baseline in blood correlates with response to PD-1 blockade in Merkel cell carcinoma	Manuscript in preparation	Pulliam	Paul Nghiem	Nature medicine
STING agonism leads to durable clinical response in a PD-L1 refractory patient: Tumor antigen-specific, single cell level biomarker analyses	Manuscript in preparation	Pulliam	Shailender Bhatia	JITC
Transcriptional and functional analyses of neoantigen-specific CD4 T cells during a profound response to anti-PD-L1 in metastatic Merkel cell carcinoma	Accepted	Church/ Pulliam	Paul Nghiem	JITC
Merkel Cell Carcinoma in the Age of Immunotherapy: Facts and Hopes	Accepted	Colunga	Paul Nghiem	CCR
Polyomavirus-driven Merkel cell carcinoma: Prospects for therapeutic vaccine development	Accepted	Tabachnick-Cherny	Paul Nghiem	Mol. Carcinog.
Intersection of Two Checkpoints: Could Inhibiting the DNA Damage Response Checkpoint Rescue Immune Checkpoint-Refractory Cancer?	Accepted	Goff/ Bhakuni	Paul Nghiem	Cancers (Basel)
Narrow excision margins are appropriate for Merkel cell carcinoma when combined with adjuvant radiation: Analysis of 188 cases of localized disease and proposed management algorithm	Accepted	Tarabadkar/ Fu	Paul Nghiem	JAAD
Spatial transcriptomics at subspot resolution with BayesSpace	Accepted	Zhao	Raphael Gottardo	Nature methods
Programming of checkpoint blockade responsive progenitor exhausted T cells by rheostatic IL-2 signals through distinct dendritic cell subsets	In revisions/under review	Toumi	Vandana Kalia	Science
CD8+ T cell clonotypes from prior SARS-CoV-2 infection predominate during the cellular immune response to mRNA vaccination	In revisions/ under review	Ford	David Koelle	Nature immunology

Differential effects of high versus low LET radiation on type-I interferon (IFNβ) and TREX1 responses	In revisions/ under review	Miles	Keith Stantz	Clinical and Translational Radiaiton Oncology
High dimensional profiling of Merkel cell polyomavirus-specific T cells in response to PD-1 therapy in Merkel cell carcinoma	Manuscript in preparation	Ryu	Evan Newell	
MCPyV-specific B cells	Manuscript in preparation	Rodriguez	Taylor/ Nghiem	
Myeloid cells in MCC	Manuscript in preparation	Tabachnik-Cherney	Paul Nghiem	
Extended treatment duration using reduced-frequency dosing of anti-PD-1 therapy in patients with advanced melanoma and Merkel cell carcinoma	In revisions/ under review	Tachiki	Bhatia	
PD-1 extended dosing	Generating data	Tachiki	Shailender Bhatia	
Profiling MCPyV-specific CD4 T cells in Merkel cell carcinoma	Generating data		Josh Veatch	
Transcriptional profiling of circulating MCPyV-specific CD8 T cells in immunotherapy treated patients	Generating data	Jani	Paul Nghiem	
Transcriptional profiling of tumor-resident MCPyV-specific CD8 T cells in immunotherapy treated patients	Generating data		Kellie Smith	